Berichte
zur Polar-
und Meeresforschung

626
2011

Reports
on Polar and Marine Research

Towards data assimilation in ice-dynamic models: the (geo)physical basis

Olaf Eisen

HELMHOLTZ GEMEINSCHAFT

ALFRED-WEGENER-INSTITUT FÜR
POLAR- UND MEERESFORSCHUNG
in der Helmholtz-Gemeinschaft
D-27570 BREMERHAVEN
Bundesrepublik Deutschland

ISSN 1866-3192

Hinweis

Die Berichte zur Polar- und Meeresforschung werden vom Alfred-Wegener-Institut für Polar-und Meeresforschung in Bremerhaven* in unregelmäßiger Abfolge herausgegeben.

Sie enthalten Beschreibungen und Ergebnisse der vom Institut (AWI) oder mit seiner Unterstützung durchgeführten Forschungsarbeiten in den Polargebieten und in den Meeren.

Es werden veröffentlicht:

- Expeditionsberichte (inkl. Stationslisten und Routenkarten)
- Expeditionsergebnisse (inkl. Dissertationen)
- wissenschaftliche Ergebnisse der Antarktis-Stationen und anderer Forschungs-Stationen des AWI
- Berichte wissenschaftlicher Tagungen

Die Beiträge geben nicht notwendigerweise die Auffassung des Instituts wieder.

Notice

The Reports on Polar and Marine Research are issued by the Alfred Wegener Institute for Polar and Marine Research in Bremerhaven*, Federal Republic of Germany. They appear in irregular intervals.

They contain descriptions and results of investigations in polar regions and in the seas either conducted by the Institute (AWI) or with its support.

The following items are published:

- expedition reports (incl. station lists and route maps)
- expedition results (incl. Ph.D. theses)
- scientific results of the Antarctic stations and of other AWI research stations
- reports on scientific meetings

The papers contained in the Reports do not necessarily reflect the opinion of the Institute.

The „Berichte zur Polar- und Meeresforschung” continue the former „Berichte zur Polarforschung”

* Anschrift / Address
Alfred-Wegener-Institut
für Polar- und Meeresforschung
D-27570 Bremerhaven
Germany
www.awi.de

Editor in charge:
Dr. Horst Bornemann

Assistant editor:
Birgit Chiaventone

Die "Berichte zur Polar- und Meeresforschung" (ISSN 1866-3192) werden ab 2008 ausschließlich als Open-Access-Publikation herausgegeben (URL: http://epic.awi.de).

Since 2008 the "Reports on Polar and Marine Research" (ISSN 1866-3192) are only available as web based open-access-publications (URL: http://epic.awi.de)

Towards data assimilation in ice-dynamic models: the (geo)physical basis

---

Olaf Eisen

ISSN 1866-3192

PD Dr. Olaf Eisen
Alfred-Wegener-Institut für Polar- und Meeresforschung
Am Handelshafen 12
D-27570 Bremerhaven
Germany
✉ olaf.eisen@awi.de

Die vorliegende Arbeit ist die inhaltlich unveränderte Fassung einer Habilitationsschrift, die im April 2010 zur Erlangung der Venia Legendi der Fakultät für Physik und Astronomie an der Ruprecht–Karls–Universität Heidelberg vorgelegt wurde.

Contents

1 Introduction

This Habilitation considers the application of active electromagnetic reflection techniques – radar for short – to answer questions as they are raised in cryospheric sciences. The basic objective is: How can we derive physical properties from the interior on a natural ice mass by performing measurements at its surface?

The large ice masses play a key role in the planet's global hdrological cycle. They store vast amounts of water in solid form and thus influence the global sea level. Because of this property, the large ice sheets came into the focus of research and public attention during the last decades because of the changes in mass the ice sheets might experience under a chaning climate. The flow of large ice masses is controlled by processes occurring at their surface, at their base and by the spatial variation of rheological properties within the ice. The internal structure of the ice masses represents an integrated memory of the interaction of these processes and properties, knowledge of which has key implications for unraveling their history and predicting their future behaviour.
Over the last seven years my research engaged in the detection of macro-scale internal layer architecture with active electromagnetic methods. These active methods are also known as radio-echo sounding (RES), ground-penetrating radar (GPR), snow radar or alike, depending on the type of system, frequency and observational range. In general, laterally imaging the layer architecture of radar reflections yields complementary information to the direct evidence of physical properties otherwise solely provided by ice cores, which are however limited to single points.
Three main objectives were treated:

(i) understanding of physical properties on the micro-scale which cause coherent layered reflections or incoherent backscatter;

(ii) exploiting the layer architecture and related information acquired during data acquisition to deduce and understand ice kinematics and dynamic behaviour (flow);

(iii) using the lateral variation in layer depth of shallow reflections to deduce the spatio-temporal variation of specific surface mass balance, an important proxy for ground-truthing satellite-derived values of accumulation, especially in Antarctica and Greenland, and understand relevant physical processes.

Most recently, measurements from ice masses were extended to measurements of snow stratigraphy in a seasonal snow cover and changes thereof over the course of one winter season. One ultimate goal of my reasearch is to move forward the field of applied geophysics in croyspheric sciences to enable the transition from simply characterising the static components of systems towards the characterisation of transient processes to provide forecasts for near-future behaviour. A main purpose would be to advance the application of four-dimensional data assimilation techniques (4D-Var) in geophysical applications. In this context, the research presented in this Habilitation provides the physical basis for understanding what causes the reflections of electromagnetic waves in the radio frequency range in ice and how the observed features can be scientifically exploited.

2 Research synopsis: the bottom line

Before data assimilation for improving ice-dynamic models of ice sheets, shelves or glaciers can be tackled, the inherent properties of the subsystems contributing to the overall system behaviour have to be understood. The main subsystems considered in this Habilitation are:

- physical properties and characteristics of ice and snow from geophysical data
- ice dynamics and kinematics
- processes in the atmospheric boundary layer and effects on spatio-temporal distribution of accumulation

In this section I want to present a short summary of the main results. In the third section, the relevant publications are thematically grouped into these categories, followed by a compilation of the actual publications.

2.1 Physical properties and characteristics of ice and snow from geophysical data

Application of radar for imaging the snow, firn and ice column usually utilizes a transmitter and receiver moved at a certain distance from each other across the surface along the survey profile. The device is either towed by hand, a snowmobile or tractor, or carried on-board an airplane or helicopter. At defined intervals, either at equal temporal or spatial increments, the transmitter emits an electromagnetic pulse into the snow column. Distances between consecutive measurements vary, depending on the system performance, between about 0.1 and 10 m. The pulse penetrates into the snow column and is partly reflected where the complex dielectric permittivity changes. The reflected signals travel back to the receiving antenna at the surface. The complete signal is recorded as a function of traveltime of the transmitted radar pulse.
Three factors are known to change the dielectric constant in firn and ice: gradients in the real part, the permittivity, are mostly related to density; they dominate reflections in the upper 100s of meters. Variations in the imaginary part are proportional to conductivity, related to acidity, and depend on frequency. They are the governing reflection cause in deeper ice. A third mechanism involves dielectric anisotropy of the crystal fabric of ice, but it becomes significant only at the deeper levels ($>$500–1000 m) of the ice sheet, where changes in anisotropic crystal fabrics could develop. Other radar techniques are based on frequency-modulated continuous wave (FMCW) transmissions or stepped-frequency radars. Although the technical details on data acquisition and processing are different, the results are the same – an image of subsurface reflections along a profile.
One tool employed in several of the publications listed in subsection 3.1 is a finite-difference numerical code of the Maxwell equations. Based on the complex dielectric permittivity measured along an ice core by means of dielectric profiling, the code calculates the estimated response signal received at the surface for a given electromagnetic pulse emitted at the surface into the ice. By means of comparison of synthetic radargrams with measured radargrams and sensitivity studies, it became possible to attribute the physical change observed in the ice-core data to an observed continuous internal reflection horizon. This method proved very efficient for improving the depth estimate of internal reflections caused by changes in conductivity, mostly related to aerosol deposition from volcanic eruptions (e.g. Eisen et al., J.Glac., 2006). The method was later complemented by including data on the crystal orientation fabric (COF) measured along the same ice core. However, as COF data was spatially too sparse in terms of depth resolution, it has not yet been incorporated in the forward model. Nevertheless, it was possible by Eisen et al. (TC, 2007) for the first time ever to identify a continuous internal reflection horizon which is caused by a transition in COF (from elongated girdle to single maximum texture). This is especially important for establishing realistic models of rheological properties for ice-dynamic flow, as for an anisotropic ice crystal the effective viscosity differs by up to two orders of magnitude compared to an isotropic distribution of ice. An extension of this study by Drews et al. (TC, 2009) led to the possibility to relate observed macro-scale basal zonations in radargrams obtained in ice sheets (the so-called echo-free zone, on the order of several hundreds meter thick) to layer disturbances on the micro-scale (on the order of milli- to centimeters). Apart from another set of constraints for ice-dynamic

models, this is important for the selection of sites for deep ice-core drilling, as the echo-free zone hints to potential disturbances in the layer sequence – and thus age – of the ice, which could result in unusable information in an ice core.
Another field of study lead to the characterization of the thermal structure of a large Alpine glacier (Eisen et al., Ann.Glac., 2009). As the liquid water content of ice depends exponentially on its temperature below the pressure melting point, it was possible by radar methods to characterize those parts of the glacier, which were significantly below the freezing point. This study sets a starting point for future observations of the evolution of the glacier's thermal structure under changing climate conditions, but moreover implies different rheological and hydraulic behaviour for the different regimes, important to separate in envisaged modelling studies.
A third subject treated in the context of physical properties of ice and snow is the temporal characterisation of seasonal snow-pack evolution (Heilig et al., CRST 2009, Heilig et al., Hyd.Proc., 2009). With the development of an upward-looking GPR application it became possible to monitor the evolution of a seasonal snow cover from underneath. This enabled us to establish relations between the observed reflection signatures, physical properties and the underlying processes and temporal evolution. The findings are the basis to assimilate the GPR data in snowpack models for improved evaluation of snow metamorphosis, melt processes and ultimately snow-pack stability for forecasting avalanche danger.

2.2 Ice dynamics and kinematics

Ideally, an ice-dynamic model would be able to reproduce and evolve the true stress and strain distributions and correct rheological respective fabric properties from given initial and boundary conditions. However, current ice-dynamic models are still far from achieving this in three dimensions, simply for the reason of limited computing power. In order to pursue a one-dimensional approach, studies like Wesche et al. (J.Glac., 2007) provide local topography, velocities and strain fields at the surface, which can then either be incorporated into dynamic models or be used for validation purposes.
However, as especially geophysical radar surveys yield regional-scale data sets of internal layer architecture in ice sheets, and thus relative three-dimensional age distributions, direct exploitation of these data sets could allow for improved three-dimensional deduction of velocity, strain or stress fields. As an initial step, Eisen (J.Glac., 2008) investigated a kinematic approach to determine two-dimensional velocity distributions from a given age field by means of an inverse method using singular value decomposition. The age field is taken from internal radar layer architecture and is treated as a tracer field. As the system of equations is generally underdetermined, it is necessary to provide further boundary conditions at the surface, as e.g. established by Wesche et al. (J.Glac., 2007), or spatial distributions of surface accumulation, which can likewise be deduced from radar data, as discussed next. Based on these results, further developments should aim in the long run at directly assimilating layer architecture (i.e. isochrones) into ice-dynamic models to improve model quality and reliablility.

2.3 Processes in the atmospheric boundary layer and effects on spatio-temporal distribution of accumulation

The spatial distribution of accumulation has been investigated by means of ground-penetrating radar in specific areas of the dry-snow zone of Antarctica, the dry-snow zone and percolation zone of Greenland and a temperate glacier in the Swiss Alps. The underlying physical principle of utilizing GPR for accumulation studies is the layered persistence of changes in physical properties over time, from which radar waves are reflected. Several processes cause simultaneous changes of physical properties of an ice mass. For instance, density is mainly altered by seasonal temperature or radiation changes or storm events with heavy precipitation, coherently on the scale of ten to more then hundred kilometers. Another important factor, especially in the dry snow zones of the large ice sheets, is the deposition of volcanic aerosols at the surface, which lead to peaks in electric conductivity. Once a layer is formed at the surface, further accumulation on top leads to layer submergence. As such a layer forms at the surface at basically the same time, it can be considered an isochrone, i.e. a layer of equal age. By performing GPR surveys one can image the depth of these layers along the profile. The depth of a layer or the distance between layers is an indicator for the amount of ice that has been accumulated within the respective

time period (i.e. age difference) between the layers. Mapping layer architecture along single profiles or over larger areas in the form of grids or alike provides a 2D or 3D view of layer architecture. From this, averaged mass balance can be deduced. This measurement principle has been applied in numerous papers and is laid out in detail in the comprehensive review paper by Eisen et al. (Rev. Geophys., 2008), together with a presentation and overall discussion of other methods to determine specific surface mass balances on ice sheets.

The fundamental result of my research in this respect is that accumulation (i.e. the positive contribution to mass balance) is much more variable than previously assumed. In Dronning Maud Land (DML), Antarctica, a point measurement of accumulation has been found to be representative only within a distance of several kilometers. However, covariance seems to appear over a much larger area, up to several hundred kilometers. This finding is of great importance for the interpretation of accumulation from ice-core records, which usually have separations of several hundred to even thousand kilometers, and for determining the overall state of mass balance of ice sheets within the assessment of global climate change and sea-level rise. As for DML, winter accumulation was likewise found to vary significantly on a glacier in the Swiss Alps. Before this result, researchers assumed that the overall precipitation determined from weather stations over a certain period and region is a good proxy for integral accumulation on a glacier, given a calibration has been established before. However, it turned out that accumulation on a glacier can likewise vary significantly enough to cause errornous results when modelling glacier mass balance. The main reason for the observed variability of accumulation is the same in Alpine regions as well as on the Antarctic plateau: redistribution of snow by small variations in wind speed. Whereas it is obvious that the overall topography of mountains influences accumulation, it has been less clear to which extent small-scale variations in surface slope (on the order of degrees) influence the wind redistribution. Thus, it has been surprising that a topographic high in surface elevation of only one meter over a hundred meter distance is large enough to cause a signficant redistribution on the order of ten percent.

On the ice sheets, in general, these small-scale variation overlay the large-scale trend in accumulation caused by tropospheric conditions. A first-order estimate of accumulation at a point can be obtained from the distance to the coast and mean temperature. An extreme case for small-scale variations in accumulation has been investigated in Anschütz et al. (GRL, 2006). Our interpretation is that oscillations in the atmospheric surface boundary layer are initiated by a break in surface slope, where the polar plateau in DML enters an outlet glacier through a mountain range. On an undisturbed surface, these oscillation cause a variation in wind speed and thus a variation in accumulation. Once this system has been stable for a long enough time, unulations in surface elevation develop from the variation in accumulation. This, in turn, again influences wind speed and thus accumulation. The result is the development of dunes with a dominant wavelength of 5 km and undulations of $\sim$10 m. Overall, this process causes quasi-harmonic oscillations of surface undulations, surface slope and accumulation, with a clear anticorrelation of accumulation and slope at zero lag.

The significance of these findings lies in their application to other methods for determining mass balance, like numerical atmospheric modelling or satellite remote sensing, e.g. by mapping passive microwave radiation or altimetric surveys. As regional-scale atmospheric models operate on grids $>$10 km increment and satellite sensors typically have footprints in size on the order of 10–100 km^2, both methods can presently not resolve smaller-scale features or variations, but only provide grid-cell or footprint-averaged information. If processes occuring on the sub-footprint-scale are unknown or wrong processes taken into account, data analysis can lead to errorenous results, which might turn out, in the worst case, to be unusable.

3 Relevant publications in thematic order

Several publications inclcuded in this cumulative Habilitation resulted from studies in the framework of dissertation and diploma theses, for which I acted as the main advisor on the scientific and/or technical level:
Dissertations: H. Anschütz (Uni. Bremen), H. Machguth (Uni. Zürich), C. Wesche (Uni. Bremen), G. Rotschky (Uni. Bremen), A. Heilig (Uni. Heidelberg), R. Drews (Uni. Bremen);
Diploma thesis: T. Dunse (Uni. Bremen).
In these publications the doctoral or diploma candidate acted as the first author, according to the DFG "Regeln der guten wissenschaftlichen Praxis". In the following I first provide a list of publications in thematic order, according to the categories laid out above. This is complemented by the actual publications, which are usually available in the form of electronic reprints reproduced here.

3.1 Physical properties and characteristics of ice and snow from geophysical data

Drews, R., **Eisen, O.**, Hamann, I., Kipfstuhl, S., Lambrecht, A., Steinhage, D., Wilhelms, F., Miller, H. Layer disturbances and the radio-echo free zone in ice sheets, The Cryosphere, 3, 195–203, http://www.the-cryosphere.net/3/195/2009/, 2009.

Eisen, O., Hamann, I., Kipfstuhl, S., Steinhage, D., Wilhelms, F. Direct evidence for continuous radar reflector originating from changes in crystal-orientation fabric, The Cryosphere, 1, 1–10, http://www.the-cryosphere.net/1/1/2007/tc-1-1-2007.html, 2007.

Eisen, O., Bauder, A., Riesen, P., Funk, M. Deducing the thermal structure in the tongue of Gornergletscher, Switzerland, from radar surveys and borehole measurements, Annals of Glaciology, 50, 51, 63–70, 2009.

Eisen, O., Wilhelms, F., Steinhage, D., Schwander, J. Improved method to determine RES-reflector depths from ice-core profiles of permittivity and conductivity, Journal of Glaciology, 52, 177, 299–310, 2006.

Heilig, A., Schneebeli, M., **Eisen, O.** Upward-looking Ground-Penetrating Radar for monitoring snow-pack stratigraphy, Cold Regions Science and Technology, 59, 2–3, 152–162, doi:10.1016/j.coldregions.2009.07.008, 2009.

Heilig, A., **Eisen, O.**, Schneebeli, M. Temporal Observations of a Seasonal Snowpack using Upward-Looking GPR, Hydrological Processes, doi:10.1002/hyp.7749, 2010.

3.2 Ice dynamics and kinematics

Eisen, O. Inference of velocity pattern from isochronous layers in firn, using an inverse method, Journal of Glaciology, 54, 187, 613–630, 2008.

Wesche, C., **Eisen, O.**, Oerter, H., Schulte, D., Steinhage, D. Surface topography and ice flow in the vicinity of the EDML deep-drilling site, Antarctica, Journal of Glaciology, 53, 182, 442–448, 2007.

3.3 Spatio-temporal distribution of accumulation

Eisen, O., Frezzotti, M., Genthon, C., Isaksson, E., Magand, O., van den Broeke, M., Dixon, D. A., Ekaykin, A., Holmlund, P., Kameda, T., Karlöf, L., Kaspari, S., Lipenkov, V., Oerter, H., Takahashi, S., Vaughan, D. Snow accumulation in East Antarctica, Reviews of Geophysics, 46, RG2001, doi:10.1029/2006RG000218, 2008.

Anschütz, H., Steinhage, D., **Eisen, O.**, Oerter, H., Horwarth, M. Small-scale spatio-temporal characteristics of accumulation rates in western Dronning Maud Land, Antarctica, Journal of Glaciology, 54, 185, 315–323, 2008.

Dunse, T., **Eisen, O.**, Helm, V., Rack, W., Steinhage, D., Parry, V. Characteristics and small-scale variability of GPR signals and their relation to snow accumulation in Greenland's percolation zone, Journal of Glaciology, 54, 185, 333–342, 2008.

Anschütz, H., **Eisen, O.**, Steinhage, D., Oerter, H., Scheinert, M. Investigating small-scale variations of the recent accumulation rate in Coastal Dronning Maud Land, East Antarctica, Annals of Glaciology 46, 14–21, 2007.

Machguth, H., **Eisen, O.**, Paul, F., Hoelzle, M. Strong spatial variability of accumulation observed with helicopter-borne GPR on two adjacent Alpine glaciers, Geophysical Research Letters, 33, L13503, doi:10.1029/2006GL026576, 2006.

Anschütz, H., **Eisen, O.**, Rack, W., Scheinert, M. Periodic Surface Features in Coastal East Antarctica, Geophysical Research Letters, 33, L22501, doi:10.1029/2006GL027871, 2006.

Eisen, O., Rack, W., Nixdorf, U., Wilhelms, F. Characteristics of accumulation in the vicinity of the EPICA deep-drilling site in Dronning Maud Land, Antarctica, Annals of Glaciology, 41, 41–46, 2005.

Steinhage, D., **Eisen, O.**, Clausen, H. B. Regional and temporal variation of accumulation around North-GRIP derived from ground based ice-penetrating radar, Annals of Glaciology, 42, 326–330, 2005.

Rotschky, G., **Eisen, O.**, Wilhelms, F., Nixdorf, U., Oerter, H. Spatial characteristics of accumulation patterns derived from combined data sets in Dronning Maud Land, Antarctica, Annals of Glaciology, 39, 265–270, 2004.

Copyright Permissions

Physical properties and characteristics of ice and snow from geophysical data

The Cryosphere, 3, 195–203, 2009
www.the-cryosphere.net/3/195/2009/

The Cryosphere

Layer disturbances and the radio-echo free zone in ice sheets

R. Drews[1], O. Eisen[1,2], I. Weikusat[1], S. Kipfstuhl[1], A. Lambrecht[1,*], D. Steinhage[1], F. Wilhelms[1], and H. Miller[1]

[1]Alfred-Wegener-Institut für Polar- und Meeresforschung, Bremerhaven, Germany
[2]Institut für Umweltphysik, Heidelberg, Germany
[*]now at: DMT GmbH & Co. KG, Am Technologiepark 1, 45307 Essen, Germany

Received: 20 March 2009 – Published in The Cryosphere Discuss.: 28 April 2009
Revised: 22 July 2009 – Accepted: 28 July 2009 – Published: 25 August 2009

Abstract. Radio-echo sounding of the Antarctic and Greenlandic ice sheets often reveals a layer in the lowest hundreds of meters above bedrock more or less free of radio echoes, known as the echo-free zone (EFZ). The cause of this feature is unclear, so far lacking direct evidence for its origin. We compare echoes around the EPICA drill site in Dronning Maud Land, Antarctica, with the dielectric properties, crystal orientation fabrics and optical stratigraphy of the EPICA-DML ice core. We find that echoes disappear in the depth range where the dielectric contrast is blurred, and where the coherency of the layers in the ice core is lost due to disturbances caused by the ice flow. At the drill site, the EFZ onset at ∼2100 m marks a boundary, below which the ice core may have experienced flow induced disturbances on various scales. The onset may indicate changing rheology which needs to be accounted for in the modeling of ice sheet dynamics.

1 Introduction

For over 40 years radio-echo sounding (RES) has been successfully applied to determine ice thickness and internal structure of large ice bodies. Internal echoes (horizons) are caused by layers contrasting significantly in the dielectric properties of the surrounding ice. The three causes for such changes are: density variations in shallow ice, acid layers and changing crystal orientation fabric (COF) in deeper ice (Fujita et al., 1999). Changes in density and conductivity have isochronous character (Vaughan et al., 2004; Eisen et al., 2004). Changing COF might have isochronous character, but is also influenced by the ice flow (Eisen et al., 2007).

A commonly observed but hitherto unexplained phenomenon is the basal echo free zone (EFZ), a hundreds of meters thick band above the ice bed interface more or less free of radio echoes. The absence of layering was first discussed by Robin et al. (1977) and eventually named as EFZ by Drewry and Meldrum (1978). It is often characterized by an abrupt transition, and an upper onset that varies with depth. It is usually not attributed to the loss of RES sensitivity. Typically it follows the bedrock topography and increases in thickness away from ice domes (Matsuoka et al., 2003). Because direct evidence has been unavailable, it is unclear what triggers the absence of internal reflections within the EFZ, although the EFZ is observed in extensive parts of the Antarctic ice sheet (e.g. Drewry and Meldrum, 1978; Robin and Millar, 1982; Fujita et al., 1999; Siegert and Kwok, 2000; Matsuoka et al., 2003; Wang et al., 2008). Russell-Head and Budd (1979) connected the EFZ observed by Robin et al. (1977) to a layer with low shear stress in the lower third of the ice sheet by Law Dome. Robin and Millar (1982) suggested that the EFZ, observed North of Lake Vostok, is due to a buckling of layers which become increasingly deformed as the bedrock relief starts to influence stress and strain rates towards the bottom. Maccagnan and Duval (1982) proposed that the EFZ onset near the Dome C area represents an isotherm in ice. Fujita et al. (1999) argued for examples at Dome F that variable shear over an irregular surface causes folding, mixing, and faulting of layers and thus inhibits the return of coherent reflections. Siegert and Kwok (2000) discussed the EFZ observed in subglacial valleys West of Lake Vostok. They described the ice as being potentially stagnant and suggest that recrystallization and recirculation of ice may also play a role.

Correspondence to: R. Drews
(reinhard.drews@awi.de)

Published by Copernicus Publications on behalf of the European Geosciences Union.

If the EFZ is not due to the system sensitivity, Bogorodsky et al. (1985) consider it as a proxy for the reliability of ice-core records in paleoclimate resarch which relies on parallel layering for the age-depth conversion. As the EFZ likely indicates a change in flow behavior, the mechanisms are also important for the modeling of ice sheet dynamics and stability (Dowdeswell and Evans, 2004).

In order to check the existing hypotheses we compare airborne RES data around the EPICA drill site at Kohnen station in Dronning Maud Land (DML), Antarctica, with the crystal fabric, optical stratigraphy and dielectrical properties of the 2774 m long EPICA-DML (EDML) ice core. The geographical setting (Fig. 1) indicates the locations of the RES profiles used in this study (Fig. 2) . The ice core is situated on an ice divide in a flank-flow regime. Ice flows towards the Kirwanveggen mountain range, which potentially acts as a barrier for ice flow.

Along with data from dielectric profiling (DEP) and the distribution of COF, we use line-scan images to visualize the integrity of layering. Line-scan images (see Fig. 3) display the stratigraphy of high-scattering zones for light, called cloudy bands (CBs). They correlate with the impurity content of ice (Svensson et al., 2005) and we take them as a proxy for the layering of RES horizons.

So far the comparison of CB layering with RES has not been achieved, because no continuous CB stratigraphy is available for other ice cores from Antarctica. Moreover, only few CBs are seen in the deep ice cores from Byrd, Vostok, and Dome Concordia. The EDML core is the only core from Antarctica with continuous visual stratigraphy and cloudy bands enable a direct comparison with RES data. We find that radio echoes disappear below ∼2100 m at the drill site and that this transition coincides with progressive disturbances in CB-stratigraphy. We discuss possible reasons for the absence of echoes in that zone and implications for the suitability of ice for paleoclimate research and ice-sheet modeling.

2 Methods and findings

2.1 Dielectric profiling and fabric analyzer

For DEP the ice core is placed between cylindrical electrodes to measure the complex dielectric permittivity from which bulk density and conductivity can be inferred (Wilhelms et al., 1998). The 1-cm electrodes were driven with a 250 kHz signal and shifted along-core with a 0.5 cm increment. DEP records are corrected for variations in temperature, core diameter, and breaks. The data are scaled (Eisen et al., 2006) to the center frequency of the RES system (150 MHz). In the conductivity profile in Fig. 5a the number and height of peaks decreases towards greater depths. The last dominant peaks rising three times above the background

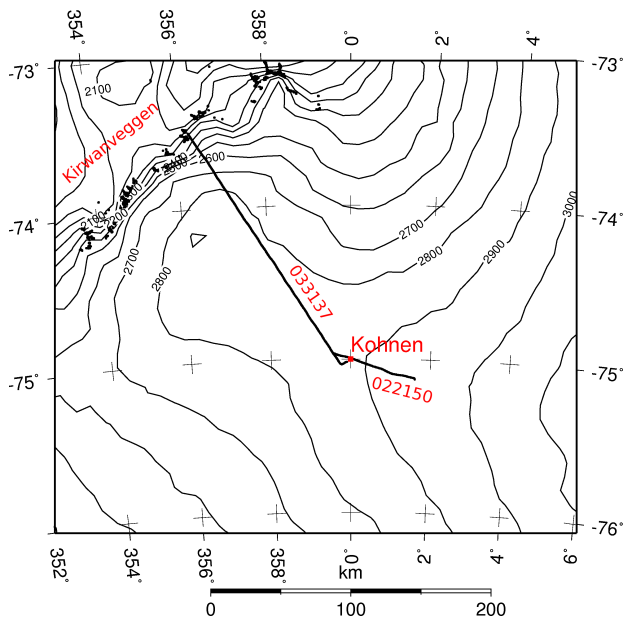

Fig. 1. Location of radar profiles 022150 and 033137 (long black lines) in the vicinity of Kohnen (red dot). Profile 033137 intersects the Kirwanveggen mountain range, which acts as barrier for ice flow. Outcrops of the mountain range are indicated with black dots.

noise occur at 2180 m. Below 2400 m the typical conductivity peaks are missing.

The fabric data in Fig. 5b are collected from thin sections between crossed polarizers (Wilson et al., 2003). The data are usually displayed in Schmidt diagrams or in terms of three Eigenvalues characterizing an ellipsoid which best approximates the c-axes distribution. Between 2025–2045 m the distribution in COF changes from a vertical girdle type to a single maximum distribution continuing to the bottom. At ∼2375 m the fabric resembles a vertical girdle distribution, but COF data in this depth interval are sparse.

2.2 Line-scans and ice-core characteristics

The line-scan camera images 1-m segments of the ice core at a resolution of 0.1 mm with light (Svensson et al., 2005). While being moved along the core, the camera records light which is scattered by grain boundaries, air-bubbles and microparticles. Transparent zones appear black, and zones with inclusions appear milky (see Fig. 3).

We see progressive disturbances in CB-stratigraphy with depth which correspond to other ice-core characteristics: above 1700 m the CBs appear straight, smooth, and parallel. They dip slightly due to the inclination of the borehole. Between ∼1700–2050 m the CBs develop mm-scale undulations. From approximately 2050 m downwards the dip of CBs increases to 10–15°. Most CBs are still parallel, but mm-scaled z-folds start to develop.

Crystals with diameters larger than 10 cm are present in the last interglacial (MIS5, ∼2300–2375 m, age-depth values are based on Ruth et al., 2007) and below ∼2600 m. A plot of mean crystal size is published by Weikusat et al. (2009) in Fig. 2a. At the transition from MIS5 to glacial MIS6 (below about 2400 m), we see a mixture of dipping and undulating CBs on various scales. In the fine-grained ice of MIS6, the CBs appear parallel, horizontal or inclined up to 30° alternated with isoclinal z-folds on the cm- to dm-scale. Below a depth of about 2400 m, CBs increasingly occur with opposite sign of dip within a single core segment of 1 m length.

We quantified the dip angle of CBs along depth via an automated image analysis. After contrast enhancement and edge detection, the line-scan image of a 1-m segment was binarized. Remaining straight lines with a maximal dip angle of ±45° from the horizontal (namely CBs) were detected by using a Hough transformation (Hough and Arbor, 1960). In this approach every line connecting two or more pixels is represented as a point in a parameter space (offset and slope), and the strongest lines are identified with a voting procedure (see for example: Burger and Burge, 2008). Between 1500 m–2100 m, CBs are clearly visbile and approximately 8–15 CBs are detected per image. From 2100 m–2370 m, stronger contrast enhancement is necessary and the stratigraphy appears more blurred. In average only 3–7 CBs are detected. Between 2370 m down to 2500 m, the stratigraphy is more pronounced again. In Fig. 3 the so detected CBs are marked with green lines. It is evident that the procedure does not capture the CBs in their full complexity, but is biased towards thick and non-undulated CBs with a strong contrast. It neglects weaker and undulated CBs. Thus the results should only be regarded as a general trend (for example the mean value of dip angles may vary, depending on the thresholds chosen for the contrast enhancement).

Figure 5d displays the absolute mean dip in a 1-m segment along depth. The mean dip angle varies gradually from 1400–2000 m depth and then exhibits larger variations. Segments with strong mean dip are intersected with segments of smaller mean dip. Below 2100 m the most of the CBs appear perturbed, but also undisturbed CBs can be found.

2.3 RES internal structure

The airborne RES system operates at a frequency of 150 MHz in a toggle mode alternately transmitting a pulse with length of 60 and 600 ns. The theoretical vertical resolution is 5 and 50 m in ice respectively. Specifics about the radar system are summarized in Table 1, and also discussed by Nixdorf et al. (1999).

Figure 2 displays two profiles in the vicinity of the drill site at Kohnen station. Conversion of two-way traveltime (TWT) to depth is based on synthetic traces (Eisen et al., 2006). Profile 022150 was recorded in 2002 and runs parallel to the ice divide. Profile 033137 was recorded in 2003 and connects Kohnen with the German overwintering station Neumayer.

Table 1. Radar system specification; for wavelength λ a permittivity of 3.15 was assumed, Δz corresponds to half the pulse length, two antennas with equal transmitting and receiving gain G are used, P_t is damped for the short pulse data to maintain a rectangular shape of the ougoing pulse.

Parameter	Variable	60 ns pulse	600 ns pulse
transm. peak power [dBm]	τ	47	62
vert. resolution in ice [m]	Δz	5	50
wave length in ice [m]	λ	2	2
center frequency [MHz]	–	150	150
antenna type (trans.& receiv.)	–	short backfire	short backfire
antenna gain [dB]	G	14.2	14.2

Detailed internal layering is evident at both pulse lengths in the upper two thirds of the ice column and prominent layers can be traced from one profile to the other. At EDML, the majority of internal reflectors below ∼900 m originate from individual conductivity peaks, with some being an interference signal of closely spaced peaks (Eisen et al., 2006). The last two detected signals in the 60 ns RES data at EDML correspond to a reflector from changes in COF at 2040 m (Eisen et al., 2007) and a conductivity peak at 2080 m. The EFZ is observed in both profiles. Figure 4a and b display an example from profile 033137 (trace 6297), where the last continuous reflector is found at 1654 m depth, 690 m above the ice-bed interface. The backscattered intensity in the long pulse data drops by 8 dB. At EDML, the EFZ is less pronounced but still evident (see Fig. 4c and d). Below about 2100 m no continuous internal layering can be found, short and long pulse data fade at similar depth. The last reflector in the long pulse data is about 2 dB above the noise level. Small signals sometimes appear within the EFZ but these are usually not continuous laterally. An example is visible in Fig. 5e between 2300 and 2400 m depth. The usually invisible signal becomes only apparent in the differentiated data of the long pulse. The backscattered power is just a few tenths of dB above the noise level. It coincides with the previously mentioned change in COF at 2375 m, and a section of undisturbed CBs below about 2385 m depth. Similar reflectors within the EFZ are also observed at other locations (Robin and Millar, 1982).

2.4 Definition of EFZ-onset and system performance

The EFZ has been characterized so far by the absence of continuous internal layering above the bedrock, which starts with a sudden drop in backscattered power. The abruptness often negates insufficient radar performance as a primary reason for the EFZ. There is no consensus how strong the drop in backscattered power should be, and since the power drop must be a function of depth, it seems inadequate to tie it to a fixed number.

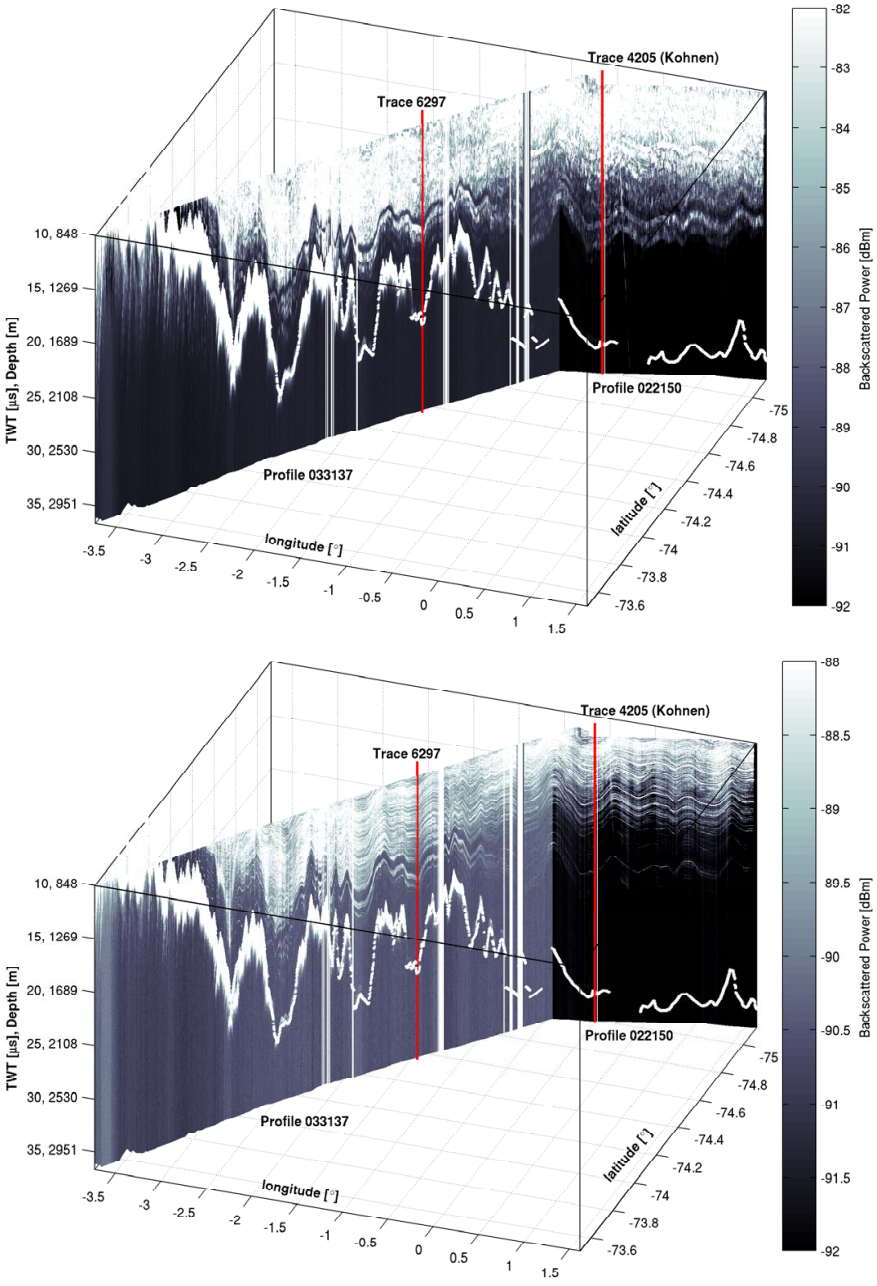

Fig. 2. Radar profiles in the vicinity of Kohnen station recorded with the 60 ns (bottom) and 600 ns (top) pulse. Bedrock was picked from differentiated data. The TWT is corrected to the first break of the surface reflection. Units of backscattered power are referenced to 1 mW (dBm). For better visibility of deeper layers the upper layers have been excluded. Profile 022150 has a length of 40 km and runs parallel to the ice divide. Ice flow is approximately 1 m/a. Profile 033137 has a length of 200 km and intersects the Kirwanveggen mountain range. Although the upper boundary of the EFZ cannot be mapped everywhere, it is clearly visible that it is variable in height and follows the bedrock topography. Traces shown in Fig. 4 are labeled at the top.

We propose two ways how to keep RES sensitivity and other physical mechanisms for the EFZ apart: firstly a comparison of calculated power reflection coefficients (PRCs) from ice-core data with the estimated detection limit of the system, and secondly an in-situ comparison of long and short pulse data.

The PRCs ($|R|^2$) approximate the scattering cross section in case of an ideal interface. We calculate them from DEP and COF data with the two-layer approximation from Paren (1981). Following Nixdorf et al. (1999), an estimate for the signal to noise ratio S/N can be parameterized with

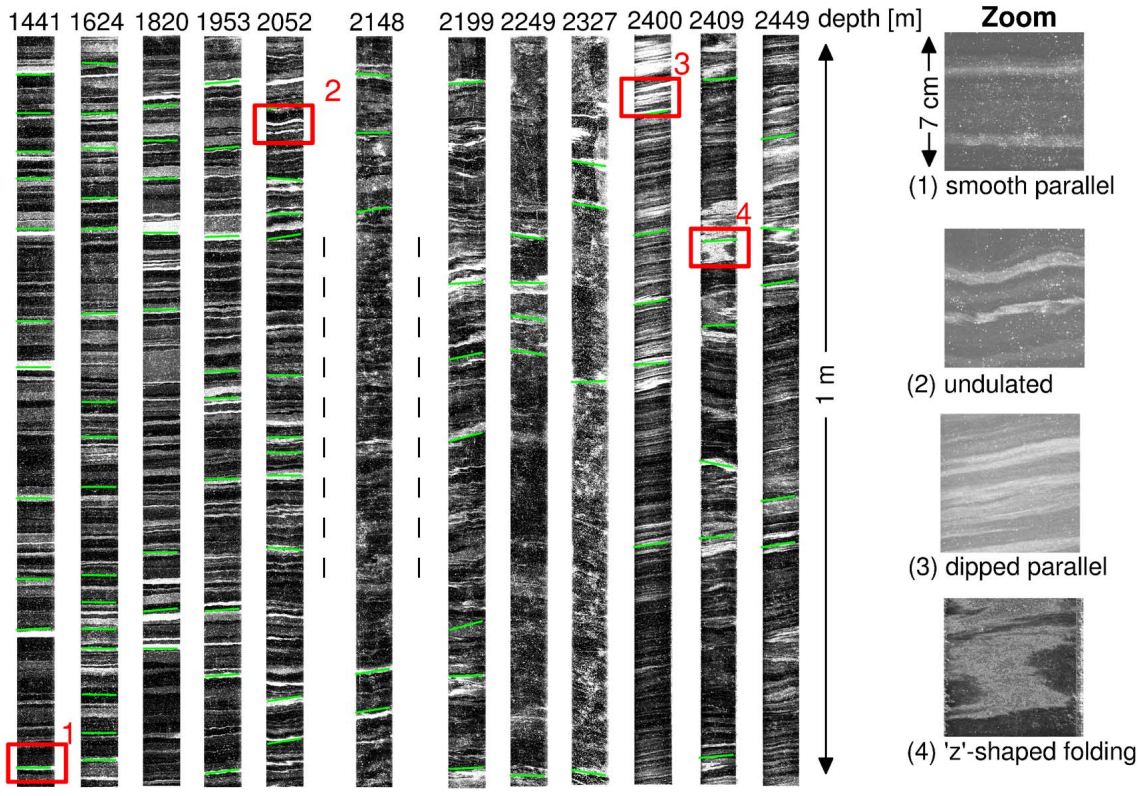

Fig. 3. Line-scan images of the EDML ice core (left) after contrast enhancement. Close-ups of the originial images are visible on the right. Cloudy bands that have been detected with the image analysis are marked in green. The EFZ onset at approximately 2100 m depth is indicated with dashed lines. Cloudy band stratigraphy appears undisturbed (zoom 1) above EFZ with small-scale undulations (zoom 2) slowly developing. Within the EFZ, layers appear partly dipped parallel (zoom 3) and partly rough as dips point into opposite directions. Dips can be intersected with z-shaped folds (zoom 4).

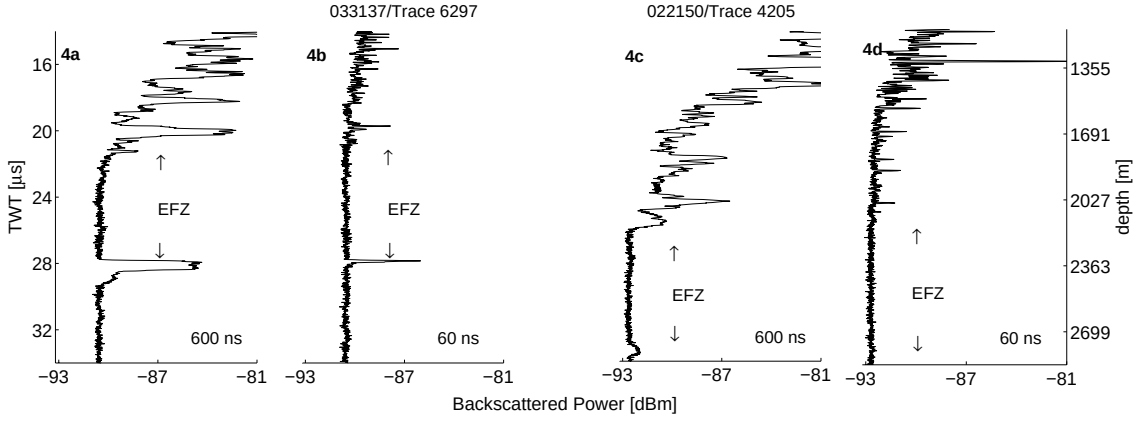

Fig. 4. The EFZ is identified by the simultaneous disappearance of continuous layers in the 60 and 600 ns data, whereby backscattered power in the 600 ns data drops by several dB. In **(a)** and **(b)** trace 6297 (profile 033137) of 600 and 60 ns data is a typical example for the EFZ. The last continuous signal is visbile at 20.1 μs in the 600 ns and at 19.7 μs (∼1654 m depth) in the 60 ns pulse. Bedrock is clearly visible in both traces at 27.9 μs (∼2344 m depth). **(c)** and **(d)** display trace 4205 (profile 022150) for both pulses at the EPICA drill site. Bedrock is visible in both traces at about 2790 m depth. Last continuous signals above the bedrock are detected at 25.4 and 25 μs TWT (∼2100 m depth). Because of the larger depth, the signal drop in the 600 ns data is smaller than in (a).

$$\frac{S}{N} = \frac{P_t \tau G^2 q g_{st} \lambda^2 |R|^2}{(4\pi)^2 [2(H+h)]^2 LkT} \quad (1)$$

where q is the refraction gain, g_{st}=200 is the stacking gain, H=500 m is the flight level above surface, k is the Boltzmann constant, T=400 K is the noise temperature and L is the attenuation at depth h. All other parameters are summarized in Table 1. The loss factor $L=L_K^2 (L_T)^2 L_A$ includes the transmission loss through the surface (L_T=1.11), the cable loss (L_K=1.99), and the two-way dielectric loss L_A. In analogy to other approaches (MacGregor et al., 2007), we neglect power loss through multiple internal reflections and calculate the total two-way dielectric loss L_A as the product of incremental attenuation rates for each measured value of the conductivity. Conductivity has been corrected for temperature with an Arrhenius relation (e.g. MacGregor et al. (2007), Eq. 2). Rearranging Eq. (1) for $|R|^2$ with an empirical signal to noise ratio of 1.02 and plotting it along depth results in the two lines displayed in Fig. 5c. These lines mark the estimated detection limit for PRCs for the two different pulses. Compared to the calculated (ideal) PRCs from ice-core data, we would expect to detect at least three more layers within the EFZ. However, the estimation of the detection limit does not take into account interference effects and the temperature dependence of the attenuation rates is not fully known. Thus this approach is only a rough estimation.

The radar is usually flown in toggle mode, so that the short pulse can be used to detect internal layering at high vertical resolution and the long pulse for the sounding of bedrock topography. Equation (1) somewhat quantifies this behaviour with the dependency on pulse length (τ) and emitted peak power (P_t). Pulse length and peak power do not always translate linearly into the signal to noise ratio, as for example R is also dependent on the pulse length (the short pulse layering results from interferences within a smaller vertical interval leading to some differences). However, there is often a direct correspondence between peaks in long and short pulse data – with a better signal to noise ratio in the long pulse data. Therefore we use the deepest layering in the short pulse data as an upper boundary for the detection limit of the long pulse. If layering in long and short pulse data vanish at similar depth, we suspect that at least the absence of layering in long pulse data in a certain interval below that depth is not caused by the system sensitivity. The vertical extent of that interval depends on the drop in backscattered power of the long pulse data. A definition of the EFZ onset in that way is inherently radar dependent, but it bypasses the uncertainties in estimating the detection limit based on the radar equation.

The single traces in Fig. 4a, b demonstrate clearly a correspondence between long and short pulse, together with an 8 dB drop in backscattered power in the long pulse data. Since it is unlikely that the long pulse is attenuated by 8 dB within 100 m below the last reflector, we assume that other mechanisms than mere running out of signal strength must be responsible for the absence of echoes. Single traces at the drill site (Fig. 4c, d) correspond well in long and short pulse data, but the drop in backscattered power in the long pulse data is smaller (≈2 dB). From this example alone, the separation between system performance and other physical mechanisms is not so clear-cut, because the long pulse could be attenuated shortly beneath the disappearance of the short pulse by a slight increase in temperature. However, since the drop in backscattered power must be a function of depth, and because we can trace the EFZ from the previous example (Fig. 4a, b) to the drill site (see also Fig. 2), we conclude that the EFZ is also evident at the drill site. The correspondence of long and short pulse data, and the lateral variation of the EFZ onset around the drill site are indicated in Fig. 5e.

3 Potential physical mechanisms of the EFZ

Using the dual-pulse technique described in Sect. 2.4 we identify the EFZ in many places of Fig. 2. An example is shown in Fig. 5e. It is evident that the EFZ's upper onset is variable in height and largely follows the bedrock topography. The onset in Fig. 2 ranges from 1600–2100 m depth, with a 600–700 m thick gap to the bedrock. Here we discuss potential mechanisms – other than the RES sensitivity – for the absence of internal layering around the EPICA-DML drill site. In particular we consider (1) a lack of dielectric contrast, (2) the role of temperature with respect to signal attenuation and the mechanical properties of ice, and (3) the lack of suitable reflecting surfaces due to layer roughness.

The DEP record changes its characteristic below about 2200 m. Conductivity peaks are broader, less distinct and not as frequent. Thus a one dimensional forward model of electromagnetic wave propagation (Eisen et al., 2006) does not predict reflections within the EFZ. The lack of strong conductivity signals can be related to the dipping of layers in the CB stratigraphy. Non-horizontal conductivity signals cause broader and less pronounced peaks, since the DEP device integrates over the entire core diameter D along the horizontal. The magnitude of this effect can be estimated by assuming the conductivity signal $\sigma(z,x)$ to be Gaussian along the vertical z and dipped with slope m along the horizontal x. This means $\sigma(z,x)=A\exp\left(-\frac{(z-mx)^2}{d^2}\right)$, with A determining the peak amplitude and d the peak width. The integration over the core diameter D yields $\sigma(z)=\int_0^D \sigma(z,x)dx = A\frac{\sqrt{\pi d}}{2m}\left[\mathrm{ERF}\left(\frac{m}{d}x-\frac{z}{\sqrt{d}}\right)\right]_0^D$, where ERF stands for the error function. The magnitude of peak broadening is mainly determined by the initial peak width and the dip angle. With an exemplary peak width of d=2.5 cm and a dip angle of 15°, the initial peak height decreases by ∼15%. However, whether ice dynamics or simple diffusion is the main reasons for the absence of strong conductivity peaks has yet to be determined. As a physical mechanism for the EFZ, a simple lack of dielectric contrast cannot be excluded.

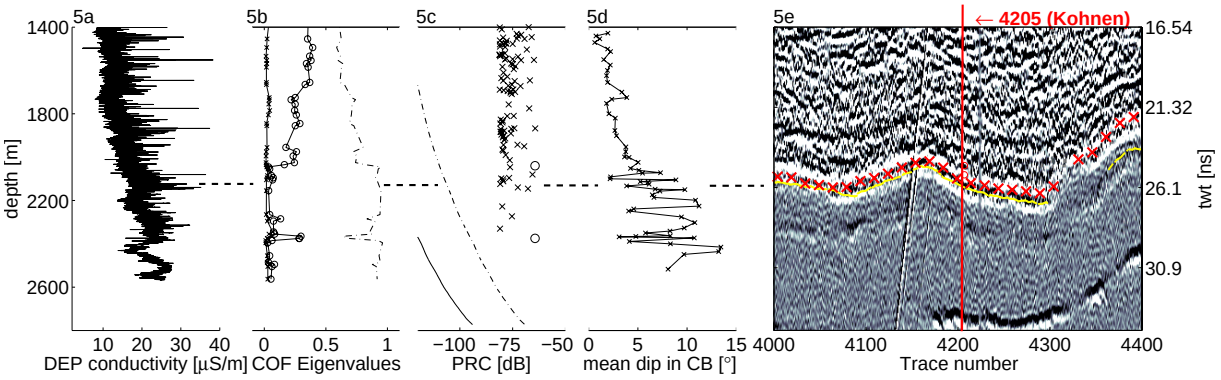

Fig. 5. DEP conductivity profile **(a)** and COF Eigenvalues **(b)** from measurements on the EPICA-DML ice core at Kohnen. Power reflection coefficients in **(c)** are calculated from peaks in DEP-data (x) and change in COF (o) based on the two-layer interface approximation after Paren (1981). The lines indicate the estimated limit of detectable power reflections coefficients for the 60 and 600 ns pulse dashed and solid, respectively (adapted from Nixdorf et al., 1999). The stratigraphic disturbances observed in the line-scan images are illustrated in **(d)** as the mean absolute dip of CBs averaged over a 1-m interval along depth. **(e)** displays differentiated radar data (600 ns) of profile 022150 centered around Kohnen. The last continuous reflector in the 600 ns data is indicated with the yellow line. The same reflector can be picked in the 60 ns data (overlaid on the 600 ns data with red crosses) between traces 4000 and 4300.

The connection of EFZ onset with an isotherm in ice was previously suggested by Maccagnan and Duval (1982). The temperature distribution in the lower third of an ice sheet is dominated by the geothermal heat flux, but it is also affected by the overburden ice column. If the EFZ onset represents an isotherm, two effects need to be considered: The effect of temperature with respect to attenuation, and the effect of temperature with respect to the mechanical properties of ice. Attenuation usually does not suggest a threshold behaviour. Whereas temperature might play a role in the example of Fig. 4c–d, it seems unlikely to be the case for Fig. 4a–b where the dielectric loss would need to be 8 dB/100 m. A change in the mechanical properties of ice around the EFZ onset is supported by the disturbances observed in the line-scan data. However, so far there is no evidence that ice develops a threshold behaviour at a certain temperature. We therefore exclude temperature for a driving mechanism for the EFZ onset at EDML.

The correspondence of progressive CB disturbances and the EFZ onset (see Fig. 5d, e) suggests a physical connection. If the CB stratigraphy is taken as a proxy for the large scale layering of RES reflectors, it seems that above the EFZ the layering is quasi-parallel, whereas below the EFZ onset the layering is disturbed. A roughening of layer surfaces within the first few Fresnel zones increases the diffuse scattering and reduces the coherent component. A dipping of layers reflects the signal away from the receiver. Studies about scattering on rough interfaces are often based on the Kirchhoff approximation (see for example Ogilvy, 1991), where random and isotropic Gaussian surfaces with a specified rms-roughness and correlation length are used. In our case, we estimate that a rms-roughness of ∼0.2 m results in ∼10 dB loss in the specular component (Peters et al., 2005). In case layers are dipped, it is possible that the main lobe of the signal is lost, and only sidelobe reflections are received. Both effects cannot be evaluated quantitvely because it is impossible to extrapolate the disturbances seen in the ice core (diameter 10 cm) to the entire Fresnel zone (≈60 m at 2100 m depth). If we assume that CB-layers do not intersect (as they are isochrones) we can linearely extrapolate dipped cloudy bands in a single core segment and estimate the layer roughness and correlation length from anticipated intersection points. However, this strongly depends on which CBs are used for extrapolation and also does not boarder the parameters with an upper or lower boundary.

We favour large-scale disturbances in the layering of RES reflectors caused by ice flow as the primary reason for the EFZ at EDML. Deformations on a larger scale are suggested by changing COF at the EFZ onset (see Fig. 5c), and by a change in borehole geometry at 2385 m depth, when drilling was interrupted for two years during 2004 and 2006 (Faria et al., 2006). The measured borehole closure of 2 mm/a indicates an increase in differential flow by an order of magnitude compared to the upper ice column. The climate record is dated to 2417 m depth. However, Ruth et al. (2007) report increasing difficulties in matching volcanic events with the Dome Concordia record below 1900 m depth. It is hypothesized that starting at 2050 m depth, complex flow history and increasing shear stress makes the climate record less reliable until dating is impossible below 2400 m (S. Faria, personal communication, 2009).

In the vicinity around Dome F an EFZ is also observed. Directly at the dome position the radar signal decreases gradually, but away from the dome in the flank-flow regions the EFZ is evident (S. Fujita, personal communication, 2003, 2008), indicating an ice-dynamical link. The EDML ice

core is situated in such a flank-flow regime likewise as the GISP2 (Greenland Ice Sheet Project) ice core in Greenland. For GISP2, Jacobel and Hodge (1995) describe the coincident loss of internal layering in analog radar data, at equal depth with dipped stratigraphy in the ice core. Therefore we suggest that for EDML layer roughness (or dip) is the main reason for the loss of internal layering. Not enough data are currently at hand to generalize our results for other places in Greenland and Antarctica.

4 Conclusions

It is not finally established whether the primary reason for the EFZ at EDML is related to the dielectric contrast, the temperature, or a larger scale layer roughness. We favour the latter: rough or dipped layers reduce the level of backscatterd power. Possibly other radar systems find the EFZ onset at EDML at a different depth, but a change in backscattered power would still be expected. It is likely that the EFZ is enhanced in flank-flow regimes. The small-scale CB features we describe may belong to disturbances on a larger scale, with overturning and thus age reversal of layers as modeled by Jacobson and Waddington (2005). If this holds true, the onset of the EFZ indicates the beginning of differential flow, with mixing and folding of layers towards greater depth. The interrelation of reflections from changing COF and the EFZ onset, which has also been observed by Matsuoka et al. (2003) and Fujita et al. (1999), has yet to be determined. It is likely that the changing rheology needs to be accounted for in ice-sheet modeling. The EFZ marks the depth within the ice, below which paleoclimate ice-core records may have been influenced by ice flow and need to be interpreted with care.

As the EFZ is detected from above the ice sheet, it is an excellent indicator of disturbances in internal stratigraphy. This is important for future surveys of ice-core sites, particularly for the upcoming search for the oldest ice within the framework of the International Partnerships in Ice Core Sciences (IPICS).

Acknowledgements. This work is a contribution to the European Project for Ice Coring in Antarctica (EPICA), a joint European Science Foundation/European Commission scientific programme, funded by the EU and by national contributions from Belgium, Denmark, France, Germany, Italy, The Netherlands, Norway, Sweden, Switzerland and the United Kingdom. The main logistic support was provided by IPEV and PNRA (at Dome C) and AWI (at Dronning Maud Land). This is EPICA Publication Number 232.

Preparation of this work was supported by the Emmy Noether-programme of the Deutsche Forschungsgemeinschaft grant EI 672/5 to O. Eisen and a scholarship of the "Evangelisches Studienwerk e.V. Villigst" to R. Drews.

Edited by: J. L. Bamber

References

Bogorodsky, V., Bentley, C., and Gudmandsen, P.: Radioglaciology, D. Reidel Publishing Co., 1985.

Burger, W. and Burge, M. J.: Digital Image Processing – An Algorithmic Introduction using Java, Springer, 2008.

Dowdeswell, J. A. and Evans, S.: Investigations of the form and flow of ice sheets and glaciers using radio-echo sounding, Reports on Progress in Physics, 67, 1821–1861, 2004.

Drewry, D. J. and Meldrum, D. T.: Antarctic Airborne Radio Echo Sounding, 1977–78, Polar Record, 19, 267–273, 1978.

Eisen, O., Nixdorf, U., Wilhelms, F., and Miller, H.: Age estimates of isochronous reflection horizons by combining ice core, survey, and synthetic radar data, J. Geophys. Res. – solid earth, 109, B04106, doi:10.1029/2003JB002858, 2004.

Eisen, O., Wilhelms, F., Steinhage, D., and Schwander, J.: Improved method to determine radio-echo sounding reflector depths from ice-core profiles of permittivity and conductivity, J. Glaciol., 52(12), 299–310, doi:10.3189/172756506781828674, 2006.

Eisen, O., Hamann, I., Kipfstuhl, S., Steinhage, D., and Wilhelms, F.: Direct evidence for continuous radar reflector originating from changes in crystal-orientation fabric, The Cryosphere, 1, 1–10, http://www.the-cryosphere.net/1/1/2007/, 2007.

Faria, S. H., Hamann, I., Kipfstuhl, S., and Miller, H.: Is Antarctica like a birthday cake?, www.mis.mpg.de/preprints/2006/preprint2006_33.pdf, mPI für Mathematik in den Naturwissenschaften. Leipzig, Communication Preprint No. 33/06, 2006.

Fujita, S., Maeno, H., Uratsuka, S., Furukawa, T., Mae, S., Fujii, Y., and Watanabe, O.: Nature of radio echo layering in the Antarctic ice sheet detected by a two frequency experiment, J. Geophys. Res., 104, 13013–13024, 1999.

Hough, P. V. C. and Arbor, A.: Method and Means for Recognizing Complex Patterns, US Patent 3069654, 1960.

Jacobel, R. W. and Hodge, S. M.: Radar internal layers from the Greenland summit, Geophys. Res. Lett., 22, 587–590, 1995.

Jacobson, H. P. and Waddington, E. D.: Recumbent folding of divide arches in response to unsteady ice-divide migration, J. Glaciol., 51, 201–209, 2005.

Maccagnan, M. and Duval, P.: Electrical behaviour of Antarctic ice and radio echo layers in ice sheets, Ann. Glaciol., 3, 195–198, 1982.

MacGregor, J. A., Winebrenner, D. P., Conway, H., Matsuoka, K., Mayewski, P. A., and Clow, G. D.: Modeling englacial radar attenuation at Siple Dome, West Antarctica, using ice chemistry and temperature data, J. Geophys. Res., 112, F03008, doi:10.1029/2006JF000717, 2007.

Matsuoka, K., Furukawa, T., Fujita, S., Maeno, H., Uratsuka, S., Naruse, R., and Watanabe, O.: Crystal orientation fabrics within the Antarctic ice sheet revealed by a multipolarization plane and dual-frequency radar survey, Geophys. Res. Solid Earth, 108(B10), 2499, doi:10.1029/2003JB002425, 2003.

Nixdorf, U., Steinhage, D., Meyer, U., Hempel, L., Jenett, M., Wachs, P., and Miller, H.: The newly developed airborne radio-echo sounding system of the AWI as a glaciological tool, Ann. Glaciol., 29, 231–238, doi:10.3189/172756499781821346, 1999.

Ogilvy, J. A.: Theory of Wave Scattering from Random Rough Surfaces, Taylor & Francis, 1991.

Paren, J.: Correspondence, J. Glaciol., 27, 203–204, 1981.

Peters, M. E., Blankenship, D. D., and Morse, D. L.: Analysis techniques for coherent airborne radar sounding: Application to West Antarctic ice streams, J. Geophys. Res., 110, B06303, doi: 10.1029/2004JB003222, 2005.

Robin, G. Q. and Millar, D. M.: Flow of ice sheets in the vicinity of subglacial peaks, Ann. Glaciol., 3, 290–294, 1982.

Robin, G. Q., Drewry, D., and Meldrum, D.: International studies of ice sheet and bedrock, Philos. T. Roy. Soc. London, 279, 185–196, 1977.

Russell-Head, D. and Budd, W.: Ice-sheet flow properties derived from bore-hole shear measurements combined with ice-core studies, J. Glaciol., 27, 117–130, 1979.

Ruth, U., Barnola, J.-M., Beer, J., Bigler, M., Blunier, T., Castellano, E., Fischer, H., Fundel, F., Huybrechts, P., Kaufmann, P., Kipfstuhl, S., Lambrecht, A., Morganti, A., Oerter, H., Parrenin, F., Rybak, O., Severi, M., Udisti, R., Wilhelms, F., and Wolff, E.: "EDML1": a chronology for the EPICA deep ice core from Dronning Maud Land, Antarctica, over the last 150000 years, Clim. Past, 3, 475–484, 2007, http://www.clim-past.net/3/475/2007/.

Siegert, M. and Kwok, R.: Ice-sheet radar layering and the development of preferred crystal orientation fabrics between Lake Vostok and Ridge B, central East Antarctica, Earth Planet. Sci. Lett., 179, 227–235, 2000.

Svensson, A., Nielsen, S. W., Kipfstuhl, S., Johnsen, S. J., Steffensen, J. P., Bigler, M., Ruth, U., and Rüthlisberger, R.: Visual stratigraphy of the North Greenland Ice Core Project (NorthGRIP) ice core during the last glacial period, J. Geophys. Res., 110, D02108, doi:10.1029/2004JD005134, 2005.

Vaughan, D. G., Anderson, P. S., King, J. C., Mann, G. W., Mobbs, S. D., and Ladkin, R. S.: Imaging of firn isochrones across an Antarctic ice rise and implications for patterns of snow accumulation rate, J. Glaciol., 50(6), 413–418, doi:10.3189/172756504781829882, 2004.

Wang., B, Tian, G., Cui, X., and Zhang, X.: The internal COF features in Dome A of Antarctica revealed by multi-polarization-plane RES, Appl. Geophys., 5, 230–237, doi:10.1007/s11770-008-0029-z, 2008.

Weikusat, I., Kipfstuhl, S., Faria, S., Azuma, N., and Miyamot, A.: Subgrain boundaries and related microstructural features in EDML (Antarctica) deep ice core, J. Glaciol., 55, 461–472, 2009.

Wilhelms, F., Kipfstuhl, S., Miller, H., Heinloth, K., and Firestone, J.: Precise dielectric profiling of ice cores: A new device with improved guarding and its theory, J. Glaciol., 44, 171–174, 1998.

Wilson, C. J. L., Russell-Head, D., and Sim, H. M.: The application of an automated fabric analyzer system to the textural evolution of folded ice layers in shear zones, Ann. Glaciol., 37(11), 7–17, doi:10.3189/172756403781815401, 2003.

The Cryosphere, 1, 1–10, 2007
www.the-cryosphere.net/1/1/2007/

The Cryosphere

Direct evidence for continuous radar reflector originating from changes in crystal-orientation fabric

O. Eisen, I. Hamann, S. Kipfstuhl, D. Steinhage, and F. Wilhelms

Alfred-Wegener-Institut für Polar- und Meeresforschung, Bremerhaven, Germany

Received: 23 May 2007 – Published in The Cryosphere Discuss.: 15 June 2007
Revised: 5 September 2007 – Accepted: 1 October 2007 – Published: 19 October 2007

Abstract. The origin of a strong continuous radar reflector observed with airborne radio-echo sounding (RES) at the EPICA deep-drilling site in Dronning Maud Land, Antarctica, is identified as a transition in crystal fabric orientation from a vertical girdle to an increased single-pole orientation seen along the ice core. The reflector is observed with a 60 ns and 600 ns long pulse at a frequency of 150 MHz, spans one pulse length, is continuous over 5 km, and occurs at a depth of about 2025–2045 m at the drill site. Changes in conductivity as reflector origin are excluded by investigating the ice-core profile, synthetic RES data, and a RES profile with different electromagnetic polarisation azimuths. The reflector's magnitude shows maximum values for polarisation parallel to the nearby ice divide and disappears for polarisation perpendicular to it, identifying the orientation of the girdle to lie in the vertical plane parallel to the ice divide. Observations allow us to extrapolate the crystal orientation feature along the reflector in space, with implications for ice-sheet dynamics and modeling.

1 Introduction

Natural ice found in ice sheets and glaciers shows anisotropic behaviour in various physical parameters (Petrenko and Whitworth, 1999). A body of ice with anisotropic orientation of crystals responds differently to applied stresses compared with isotropic ice, for which ice crystals have a random orientation. For anisotropic ice, ice flow could be enhanced by about an order of magnitude if stresses act parallel to the crystals' basal planes, but flow could be reduced by an order of magnitude if stresses act perpendicular to the basal planes (Paterson, 1994). Consequently, the general flow of ice and the response of ice sheets to changing environmental conditions depends on the degree of anisotropy within. The current demand for advanced modeling of ice sheets requires the incorporation of anisotropic properties of ice and the spatial distribution of these properties for unraveling ice sheet history and predicting the future development (ISMASS Committee, 2004). Various ways have been developed to treat anisotropic rheology, as, for instance, summarised by Marshall (2005). The correlation between fabric changes and climate transitions (e.g. Durand et al., 2007), moreover, emphasizes that valuable information is carried by vertical and lateral fabric distributions. However, information about the distribution of crystals within the ice, the crystal orientation fabric (COF), is mainly available from ice coring, and restricted, therefore, to point locations. No standard procedure exists to date to determine the spatial variation of COF within ice sheets on a routine basis. This is, however, a key to an improved understanding and modeling of ice-sheet behaviour. Here, we present direct evidence that radio-echo sounding (RES) provides a formidable tool to map strong fabric changes occurring over a few 10s of meters in the vertical, and, moreover, carries the potential to map the lateral distribution of COF continuously.

Since the beginning of operational applications of RES in glaciological research three processes were suggested to cause continuous internal reflections from within the ice column (Bogorodsky et al., 1985; Dowdeswell and Evans, 2004): changes in density (Robin et al., 1969), conductivity (Paren and Robin, 1975), and changes in COF (Harrison, 1973). Whereas the isochronous property of reflection horizons originating from changes in density and conductivity is nowadays routinely exploited for a multitude of purposes, the detection and interpretation of reflections stemming from changes in the COF is still in the early stages. Partial reflection of a propagating radar pulse occurs where either the real (ε') or imaginary part (ε'') of the complex dielectric constant (ε) changes. The possibility to detect fabric changes with RES arises from the anisotropy of permittivity

Correspondence to: O. Eisen
(olaf.eisen@awi.de)

Published by Copernicus Publications on behalf of the European Geosciences Union.

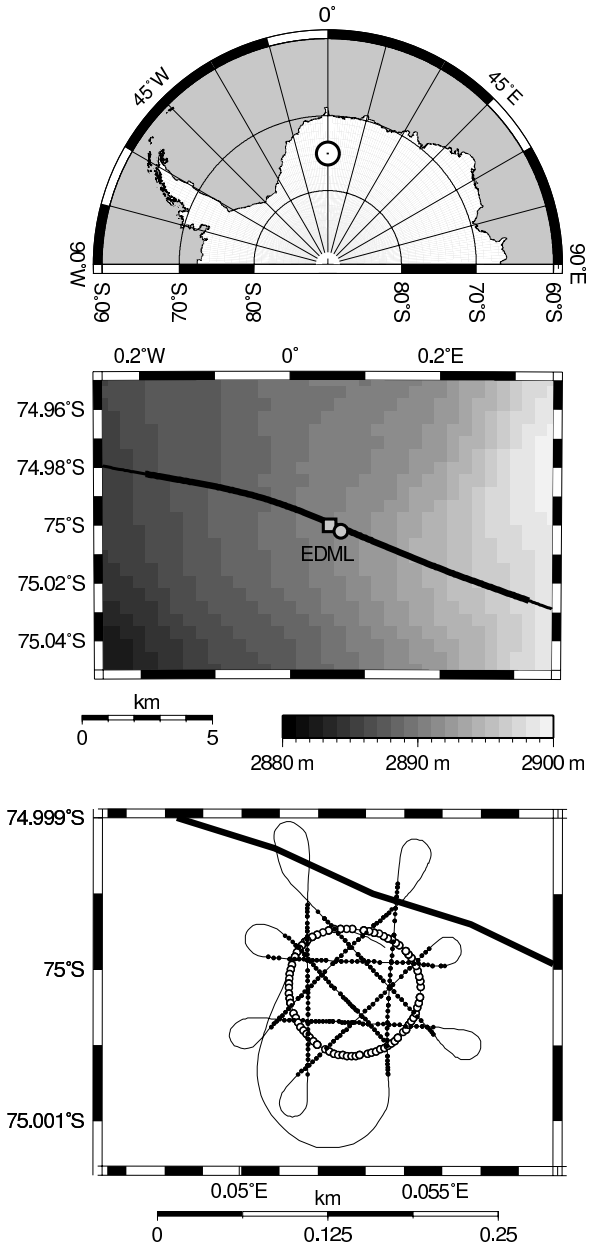

Fig. 1. Top: location of study area in Antarctica. Middle: location of EDML drill site (circle), RES flight line of profiles 022150/023150 (black line), and ground-based profile 033042 (square); bold black line: RES section shown in Fig. 2; grayscale: Radarsat Antarctic Mapping Project digital elevation model (Liu et al., 2001) on $400\times400\,m^2$ raster (meter above sea level for WGS84 ellipsoid). Bottom: close-up of profile 033042 recorded with airplane on ground (thin line) and flight line of profiles 022150/023150 (thick line). Traces of the circle segment of profile 033042 are indicated by open circles, traces belonging to linear segments are shown as black dots.

in a pure ice crystal. The latest compilation of dielectric properties of ice (Fujita et al., 2000) provides an anisotropy in ε' of $\Delta\varepsilon'=\varepsilon'_{||}-\varepsilon'_{\perp}\approx0.035$, measured parallel and perpendicular to the crystal c-axis at 1 MHz and 252 K. This value corresponds to little more than roughly 1% of the permittivity of ice, which is in the range of 3.1–3.2. $\Delta\varepsilon'$ is accurate to $\sim$0.007, or 20% (Fujita et al., 2000, Fig. 3), and varies slightly with temperature and frequency, however insignificantly to be a concern in this study.

To discriminate reflections originating from changes in COF and conductivity, multi-frequency experiments can be utilized (Fujita et al., 1999). However, as ice is also a birefringent medium at radio frequencies (Hargreaves, 1978), multi-polarisation measurements are required to resolve ambiguities arising from anisotropic reflection and wave propagation (Doake et al., 2002; Fujita et al., 2003). With such experiments, Matsuoka et al. (2003) located high-scattering zones several hundred meters thick at depths around 1000–1500 m in East Antarctica. Based on the dependence of the reflection strength on the polarisation plane, the wide zones were interpreted as alternations in COF of adjacent ice layers (Matsuoka et al., 2004), induced by past and present ice flow. Fujita et al. (2006) determined the vertical evolution of the radar phase by combining ice-core profiles of COF with a matrix-model of radar-wave propagation at the sites where polarimetric radar studies were carried out. By comparison of COF data and model results with multi-polarisation/bi-frequency RES point data, they were able to separate the general contribution of anisotropic reflection from COF and birefringence to the observed signals. However, previous studies did not provide COF profiles from ice cores for direct comparison with continuous internal reflections in RES data and reflectivity.

In this work we extend previous findings by comparing RES data with ice-core profiles of COF, permittivity, and conductivity. Moreover, we use synthetic RES data to analyse the origin of RES signals. This leads to the novel observation that a sharp, continuous internal reflection horizon, trackable over several kilometers, is caused by an abrupt transition in crystal orientation fabric occuring over just a few tens of meters. Our deduction from these comparisons is supported by the analysis of the azimuth-dependence of reflection magnitude of the reflector of interest.

2 Data and methods

Data used in the present study were acquired within the European Project for Ice Coring in Antarctica (EPICA) at the deep drill site in Dronning Maud Land, Antarctica (EDML). The drill site is located at 0.0684° E, 75.0025° S at 2891.7 m above sea level near a transient ice divide, characterised by along-flow compression and lateral extension, causing an overall vertical compression of the ice column (Wesche et al., 2007).

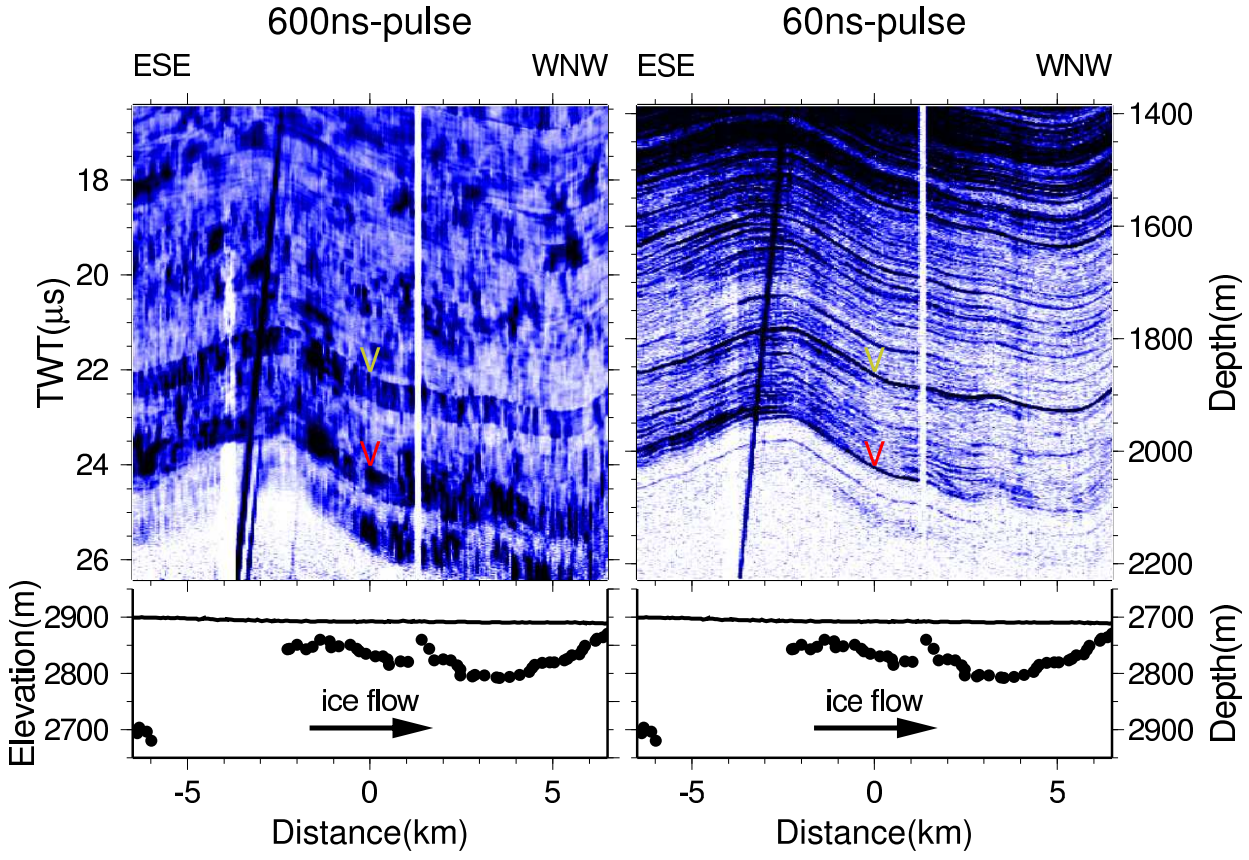

Fig. 2. Top: unfiltered 10-fold stack (65-m trace spacing) RES profile recorded with the 600-ns pulse (022150, left) and 60-ns pulse (023150, right); ordinates are the same for both panels: two-way travel time (TWT) on left ordinate is recording time corrected to the first break of surface reflection, right ordinate refers to depth below the surface for a mean wave speed of 168.7 m µs^{-1} from the surface to a 2100-m depth; color code indicates signal magnitude (increasing white-blue-black); first breaks of internal reflectors of interest are marked by yellow and red "V" at 0 km (drill site) at travel times of 22 and 24 µs, respectively; dark diagonal line between −3.8 and −2.3 km is a hyperbola leg, caused by reflections from Kohnen station (located at 0 km); white vertical line at 1.3 km is caused by system dropout. Bottom: surface elevation above mean sea level (solid line, left axis) from airplane radar altimeter and depth of detected bedrock reflection below surface (black dots, right axes). The profile runs approximately parallel to a transient ice divide (ESE–WNW), arrow indicates ice flow from left to right.

2.1 Radio-echo sounding (RES)

We use data from the RES system on board the Dornier 228-101 aircraft Polar2, operated by the Alfred Wegener Institute (AWI). The system, with an overall sensitivity of 190 dB, generates 150-MHz bursts of 60 ns and 600 ns in duration, which are transmitted alternatedly. The receiver module rectifies and logarithmically compresses the signals, stacks 200 consecutive signals after analog-to-digital conversion, and stores the stack as a single trace on tape at sample intervals of 13.33 ns over a time window of 50 µs. Data are normally acquired in-flight at an altitude of 450 m above ground at typical speeds of 65 m s^{-1} (130 knots), resulting in a trace spacing of the 200-fold stack of 6.5 m between equal pulses (Nixdorf et al., 1999). The airplane heading is equal to the polarisation of the electric field. Apart from static correction for the first break of the surface reflection, no additional filtering or gain control is applied to the RES data used here. Conversion from recorded travel time to depth domain is performed with the calibration for pure-ice permittivity derived by Eisen et al. (2006), with a mean wave speed of 168.7 m µs^{-1} over the distance from the surface to 2100-m depth.

We use two types of RES data sets here (Fig. 1): (i) airborne data from the season 2002/03, with profiles 022150 (600 ns pulse) and 023150 (60 ns pulse) running along the ice divide (ESE–WNW direction), passing the EDML drill site about 100 m to the NNE (Fig. 2); (ii) data from profile 033042 (60 ns pulse) recorded in season 2003/04 with the airplane slowly moving on the ground about 500 m downstream from the drill site, first in a circle and then crossing the circle in linear segments in eight different orientations (N, NE, E, SE, S, SW, W, NW). The airborne data enable

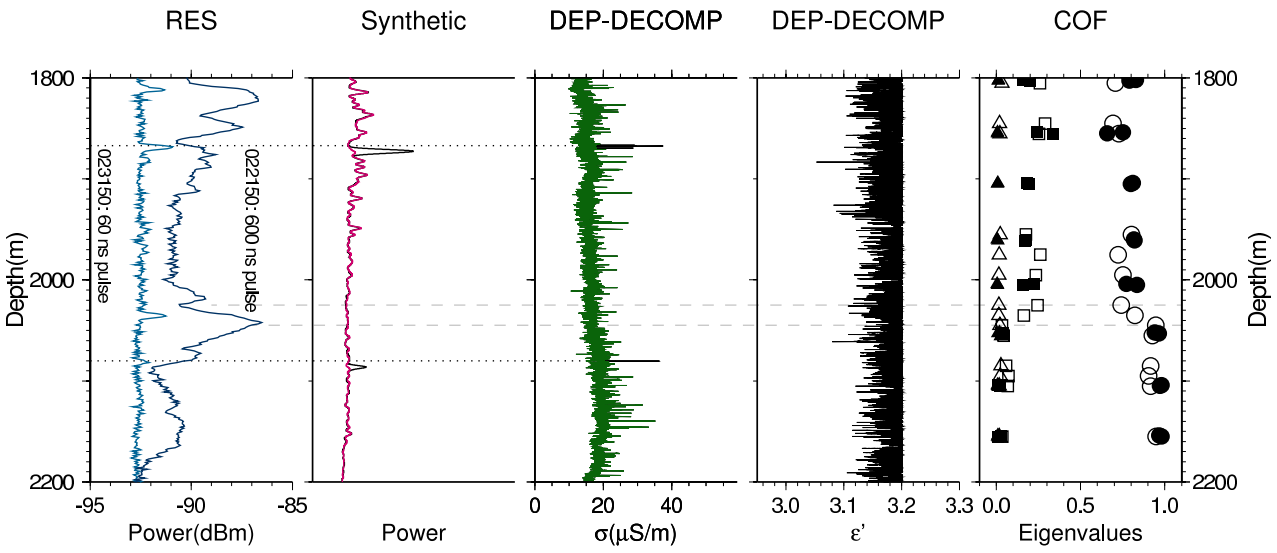

Fig. 3. Comparison of radar data and ice-core profiles at the EPICA-DML drill site. From left to right: RES signal power measured with two pulse widths for trace 4205 of profiles 022150 (600 ns pulse) and 023150 (60 ns pulse) with respect to 1 mW (dBm), representing a stack of 2000 recordings in total (200 pre-storage and 10 post-storage stacks) over a distance of 65 m; DEP-based synthetic RES trace for 60-ns pulse; DECOMP-corrected DEP conductivity (σ); DECOMP-corrected DEP-permittivity (ε', with the permittivity of pure ice as upper bound); eigenvalues (λ_1: triangle, λ_2: square, λ_3: circle) of crystal orientation tensor along horizontal (filled symbols) and vertical core samples (open symbols). The black synthetic trace is based on original conductivity data (black σ-curve); on top the red synthetic trace is plotted, based on the DEP data with conductivity peaks removed (green σ-curve); peaks originating from conductivity thus appear black, emphasized by dotted horizontal lines; dashed horizontal lines connect the depth of the strong RES reflector with transition depth of changes in COF.

us to investigate the lateral extension of continuous internal reflections. For their subsequent analysis, we additionally stack 10 traces of each pulse width (resulting in a 65-m trace spacing in Fig. 2). The traces closest to the drill site are used later for comparison with ice-core data. They are referred to as the long and short pulse RES traces, respectively (Fig. 3). The ground-based data of profile 033042 provide insights into the dependence of reflected energy on polarisation azimuth. Along each of the eight linear segments of constant heading, we stack 70 consecutive traces to increase the signal-to-noise ratio. The data from the circle segment are used unstacked.

2.2 Ice-core permittivity and conductivity profiles

Dielectric profiling (DEP) at 250 kHz and γ-attenuation profiling, simultaneously carried out in the field after core retrieval, provide dielectric properties and density along the EDML ice core (see Eisen et al., 2006, for details). The calibrated DEP record is corrected for variations in core diameter and temperature. Unreliable data in the vicinity of the core breaks are removed. Effects of density and conductivity mixed complex-valued permittivity in the two-phase system ice–air are taken into account by applying an extended volumetric mixing model (DECOMP). Thus, contributions from density and conductivity in the complex permittivity are separated (Wilhelms, 2005).

2.3 Finite-difference forward modeling

The synthetic trace, adapted from Eisen et al. (2006), simulates the 60-ns pulse (Fig. 3). It is calculated by a one-dimensional finite-difference time-domain model of Maxwell's curl equations. Ice-core profiles of permittivity and conductivity serve as model input, separated using an inverse application of DECOMP at 250 kHz, conductivity linearily scaled to 150 MHz, and merged again with forward application of DECOMP. Conductivity is provided in 0.02-m resolution. Due to the strong influence of the DEP-measurement noise in permittivity on synthetic reflections, permittivity is smoothed over 20 m for forward modeling (Eisen et al., 2006). The synthetic trace thus only contains reflections which originate from changes in conductivity. Processing comprises a synchronization of the synthetic source signal to the RES first-break signal from the surface by a time shift of +0.1 μs, application of a Hilbert magnitude transformation to obtain a signal envelope (i.e. mimic rectification), and a smoothing with a 0.1-μs Gaussian running-mean filter. Details are presented in Eisen et al. (2006)

2.4 Determination of crystal-orientation fabric

Fabric data of the EDML deep ice core were measured down to a 2560-m depth in a coldroom at a temperature of −20°C in 2005 at AWI (Bremerhaven, Germany). Ice-core sections

were drilled between 2001 and 2004 and have been stored at −30°C after the transportation at −25°C to AWI. Thin sections were prepared according to standard procedures using a microtome from horizontally ($0.5\times50\times50\,\mathrm{mm}^{-3}$) and vertically ($0.5\times50\times100\,\mathrm{mm}^{-3}$) cut samples. Orientations of c-axes were derived using an automatic fabric analyzer system (Wilson et al., 2003), which enables complete measurement of these samples in 15 to 30 min. Unfortunately, it is not yet possible to record the horizontal azimuth of the drilled core sections, so azimuth is not available for the thin sections. In addition to the Schmidt diagrams (mapping each measured crystal c-axis direction from a point on the hemisphere to a circular plane using an equal-area projection, Fig. 4), we present the data in terms of the eigenvalues λ_i of the orientation tensor (Wallbrecher, 1979). The eigenvalues (Fig. 3) represent the components along the orthogonal coordinate system $\hat{e}_i$ of an ellipsoid, which best approaches the momentum of inertia of the c-axes distribution. Measurements of samples cut horizontally and vertically from the core are jointly displayed. From the distribution of all measurements along the whole core it is evident that the eigenvalues are accurate to about a value of ±0.1. This is partly explained by the physical variations in the distribution of crystals in each sample, but also partly by local effects attributed to the immatureness of the system. Nevertheless, the eigenvalues are considered reliable within this accuracy.

3 Results and discussion

Drilling at EDML finished in January 2006, reaching bedrock at a logged ice thickness of 2774.15 m. This corresponds well with the ice thickness determined by RES (Fig. 2). The RES profiles at both pulse widths show the common internal layering of ice sheets, which increasingly follows the bedrock topography at larger depth, especially evident for profile sections spanning several 10–100 km (not shown). A sudden decrease in reflected energy and the absence of any laterally continuous signals suggest that the echo-free zone is present in the lowest 500–800 m above bedrock, starting at about 2100 m at the drill site.

The 600 ns pulse spans some 50 m in ice and integrates over a much wider depth range than the short pulse, which covers only about 5 m. As would be expected, fewer layers are therefore visible in the profile recorded with the 600 ns pulse than in the one recorded with the 60 ns pulse (Fig. 2). Looking at single traces, it is evident that several distinct peaks in the short-pulse trace have nevertheless counterparts in the long-pulse trace. This is clearly the case for strong reflections at depths of 1810 and 2035 m, and less so at 1865 and 2080 m (Fig. 3). Dominant reflections of each pulse cover about one pulse length. The first break of the concurrent reflections appear at about the same depth, but the maximum power in the long pulse occurs about 10 m deeper than in the short pulse.

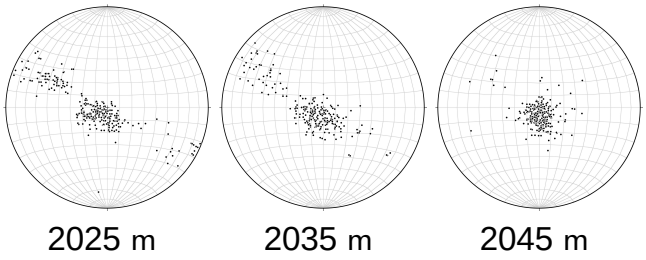

Fig. 4. Schmidt diagrams of vertical sections at three depths, showing the orientation of c-axes and the transition from vertical girdle-type to increased vertical single-maximum fabric. The orientations have been rotated into the horizontal xy-plane.

The comparison between the short pulse trace and the synthetic trace carried out by Eisen et al. (2006) demonstrates that a number of internal layers can be reproduced by forward modeling based on a conductivity profile. Removing dominant peaks by interpolation in the underlying conductivity profile causes a disappearance of the related reflections in the synthetic trace, as indicated for two cases at 1865- and 2080-m depth in Fig. 3 by the dotted line and the black peaks of the synthetic radargram. This demonstrates that these reflections originate from narrow peaks in conductivity, all less than about 0.5 m wide (Eisen et al., 2006). Interestingly, the strong signal in the short pulse at 2035 m is not reproduced in the synthetic data. The origin of this reflection and its characteritic properties will be investigated in detail in the remaining part of the paper.

3.1 RES vs. ice-core data

In comparison to the reflection at 1865 m of the short pulse, which is caused by a peak with a maximum conductivity of $38\,\mu\mathrm{S\,m}^{-1}$ on a background conductivity of $15\,\mu\mathrm{S\,m}^{-1}$, one would expect a conductivity peak of comparable size also at 2035 m. However, the conductivity profile merely displays a peak of $24\,\mu\mathrm{S\,m}^{-1}$ on a background of $17\,\mu\mathrm{S\,m}^{-1}$ at this depth. Peaks of this size appear regularly in the conductivity profile, without causing strong reflections, neither in the short pulse RES data nor in the synthetic trace. Missing data, rejected in the DEP quality check, could mask a prominent conductivity peak. Using 0.5 m as the upper limit for the width of strong conductivity peaks responsible for reflections, as identified by Eisen et al. (2006), the closest sections of data gaps >0.5 m are located at 2026.26–2027.32, 2028.29–2028.81, 2038.90–2039.93, and 2040.03–2040.65 m. Each of these gaps is further away from the reflector's depth of origin than its depth accuracy of less than 1 m (Eisen et al., 2006). We therefore exclude the possibility that a single peak in conductivity causes the reflection in the short pulse trace at 2035 m.

Another possibility for the origin of the reflection at 2035-m depth would be that interference of partial reflections at

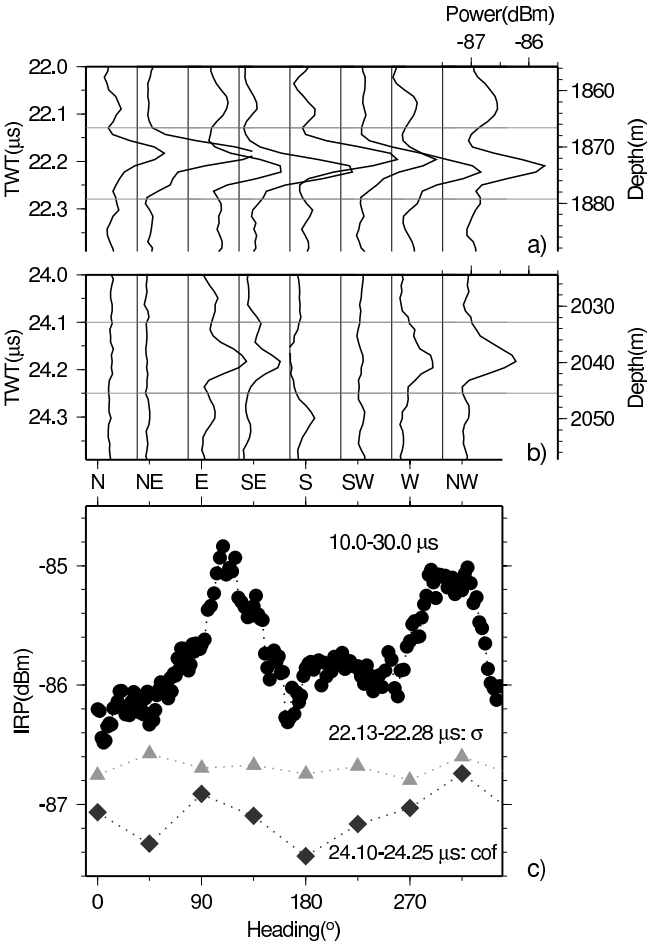

Fig. 5. Comparison of azimuth dependence for two reflectors originating from changes in **(a)** conductivity and **(b)** COF for eight airplane headings, which are equal to electric polarisation. Each trace in (a) and (b) is a stack of 70 traces along one of eight linear segements of profile 033042 (Fig. 1), recorded with the 60-ns pulse; power scale given for heading NW in a) applies for all traces; vertical baselines in (a) and (b) correspond to -87.5 dBm; horizontal lines bound time windows used for calculation of internal reflection power (IRP) displayed in (c). **(c)** IRP as a function of azimuth and time window, calculated as the power average per sample over the respective time window. Triangles and diamonds: IRP over 150-ns time window (12 samples) of traces shown in (a) and (b), respectively; black circles: IRP over 10–30 µs time window for unstacked traces of circle segment of profile. The ice divide runs along the ESE–WNW direction.

several conductivity peaks within one pulse length occurs. However, referring to the reflection's counterpart in the long-pulse data, it would be surprising that a series of small conductivity peaks of just 5–10 $\mu S\,m^{-1}$ above a background of 15–20 $\mu S\,m^{-1}$ would allow for coherent interference in both pulse lengths to produce the dominant reflections being one pulse width long. We therefore also exclude the possibility that the reflections at 2035 m in both RES traces are caused by changes in conductivity, and thus the imaginary part ε'' of the dielectric constant.

The only other possibility for reflector origin is the real part ε'. At these depths, changes in density are not present, as air bubbles already turned into air hydrates. As these have a very low volume density (Matsuoka et al., 2004), they hardly influence the bulk permittivity. One would consequently expect a profile of basically constant permittivity. The noise seen in the permittivity profile of about 0.05 on the sub-meter scale (Fig. 3) is attributed to measurement noise of the DEP bench. We therefore cannot use the permittivity profile to determine the reflection origin.

The remaining possibility to cause a change in ε' are changes in COF. The Schmidt diagrams at 2025–2045-m depth in Fig. 4 show a transition from a vertical girdle-type to a single-maximum fabric with c-axes clearly concentrated around the vertical. The eigenvalues of the distribution of c-axes (Fig. 3) show this transition very clearly in the two largest components, λ_2 and λ_3, which change by $\sim$20% over 20 m. A change from a vertical girdle-type fabric to a vertically concentrated fabric as reflector origin should result in an anisotropic response in the RES signals as a function of polarisation. This will be investigated next.

3.2 Analysis of RES polarisation azimuth

The RES data of profile 033042 were recorded with different airplane headings, and thus polarisation azimuths (Fig. 1). This data set provides an independent means to determine the origin of the internal reflections and enables us to fix the azimuth ambiguities of the COF measurements along the core.

For different time windows we calculate the internal reflection power (IRP, compare Gades et al., 2000), defined as the power average per sample (in dBm) within the time window. The azimuth dependence of the reflected energy from individual reflectors (i.e. for short time windows) is difficult to analyse for the circle segment, as the signal-to-noise ratio is very low and stacking is not feasible because of the different azimuths. However, IRP over the time window 10–30 µs indicates that for the heading E to SE and W to NW the IRP is significantly higher than for other headings (Fig. 5). The maxima lie in the vertical plane along the ice divide (ESE–WNW).

Our explanation is as follows: c-axes orientations of all types (single maximum, girdle, ...) show small statistical variations around a mean distribution with depth. Thus, the dielectric properties also vary slightly with depth, causing some incoherent backscatter of a propagating radar signal. These variations have the largest effect on the radar backscatter if they occur in the vertical plane parallel to radar polarisation. At the present location, dominated by a girdle-type fabric between 450 and 2025-m depth, polarisation perpendicular to the ice divide results in an overall lower level of backscatter, whereas for polarisation parallel to the ice divide the level of backscatter is highest. We interpret this as

an indication that the girdle fabric lies in the vertical plane parallel to the ice divide, and that variations in the girdle fabric cause the higher backscatter in that plane. For later analysis, we define this as the yz-plane of an orthogonal coordinate system, with the horizontal coordinates x and y as the across-flow (NNE) and the along-flow (WNW) directions, respectively, and the vertical coordinate z.

We next look at the variation of reflected energy as a function of azimuths of the stacked linear segments. For the reflector originating at 1865-m depth at the drill site, both the display of the raw traces (Fig. 5a), as well as the IRP calculated over a 150-ns window containing the reflection (Fig. 5c) do not show any clear systematic variation in backscatter with azimuth. This isotropic pattern is expected for reflections stemming from changes in conductivity, as from the peak present at 1865 m in the ice-core data. At the depth of the change in COF at about 2035 m at the drill site, a reflection is visible for headings E and SE, and in the opposite directions W and NW. Along the other headings no reflection is visible (Fig. 5b). The IRP, again calculated for a 150-ns time window at these depths, likewise shows maxima for the headings which also show a reflection (Fig. 5c). We interpret this to be caused by the change in COF from the anisotropic distribution of c-axes of the girdle-type fabric, which has an isotropic distribution in the horizontal plane, to the vertically concentrated fabric. If the electric polarisation is parallel to the plane in which c-axes change, i.e. parallel to the ice divide in the yz-plane, permittivity changes as well, and a reflection occurs. If, in contrast, the electric polarisation is perpendicular to the plane containing the c-axes, then any changes in COF in the yz-plane will not influence the radar wave. We therefore take the azimuth-dependence of reflectivity as an independent confirmation that the reflector at 2035 m indeed originates from the changes in COF observed in the ice core.

3.3 Reflectivity from ice-core COF

The distribution of c-axes allows us to calculate the permittivity components. Following Fujita et al. (2006), the effective permittivity in the direction of the ellipsoid's principle components $\hat{e}_i$ can be determined from the eigenvalue λ_i by $\varepsilon'_i = \varepsilon'_\perp + \Delta\varepsilon'\lambda_i$. In the present case, the principle component $\hat{e}_3$ is very close to the vertical below 1700-m depth (Fig. 4), and $\hat{e}_{1,2}$ lie in the horizontal xy-plane. Although borehole logging indicated that the core axis has a possible deviation of 1–2° from the vertical, we consider this negligible for the following analysis, as the accuracy of the fabric analyzer is on the same order of magnitude. This is moreover justified by the width of the distribution of c-axes of some tens of degrees, even for the vertically highly concentrated fabric. The results above with azimuth dependence of backscatter from the circle profile indicate that $\hat{e}_1$ corresponds to the x-direction, and $\hat{e}_2$ to the y-direction. The principle components $\hat{e}_i$ are therefore approximately aligned with the orthogonal coordinates x, y, z.

The change in COF between depths z_1=2025 and z_2=2045 m results in a change in the permittivity components $\delta\varepsilon'_i = \varepsilon'_i|_{z_1} - \varepsilon'_i|_{z_2} = \Delta\varepsilon'(\lambda_i|_{z_1} - \lambda_i|_{z_2})$. Using the eigenvalues determined in the vertical sections yields $\delta(\varepsilon'_x, \varepsilon'_y, \varepsilon'_z) = \Delta\varepsilon'\,(0.6, 21.1, -20.5)\,10^{-2} = (0.2, 7.4, -7.2)10^{-3}$. This change occurs over 20 m, well within the width covered by the long pulse. The radar wave propagates in the vertical direction, so only $\delta\varepsilon'_{x,y}$ can cause a reflection. Using the approximation from Paren (1981) to determine the power reflection coefficient for a two-layer interface with differing permittivities, $|R| = \left(\delta\varepsilon'/(4\varepsilon)\right)^2$, the change in $\delta\varepsilon'_x$ corresponds to a reflection coefficient R_x=−96.1 dB, and the change $\delta\varepsilon'_y$ yields R_y=−64.6 dB. The measurement error of 20% in $\Delta\varepsilon'$=0.035 results in an uncertainty of less than 1 dB of R_x and R_y. Whereas R_x is very small, likely too small to result in a sufficiently large reflection, R_y seems to be large enough to detect a related reflection at the surface. These reflection coefficients explain the above observation that the reflection at 2035 m only appears for polarisation in y-direction (parallel to the ice divide, Fig. 5b), but not in the x-direction (perpendicular to the ice divide).

The nearby reflections at 2080 m, appearing for both pulse lengths, provide a qualitative plausibility check for the hypothesis that the change in COF in the yz-plane is indeed strong enough to cause reflections. As shown by the synthetic trace, the reflections' origin is the conductivity peak at 2080 m with a height of 37 µS m^{-1}. The reflection coefficient corresponding to this conductivity peak (Paren, 1981) results as −75.7 dB at 150 MHz, only a few dB smaller than the reflection coefficients R_y resulting from the change in COF. The smaller reflection coefficient is consistent with the fact that the reflections' maximum peak power at 2080 m for both pulses are smaller than those at 2035 m. We can therefore indeed attribute the origin of the observed reflections at 2035 m to the change in COF, which is strong enough and occurs over a short enough distance to cause the strong reflections in the short and long pulse data.

3.4 Distribution of reflector from COF

Laterally, the reflector from COF (red "V" in Fig. 2) is quasi-parallel to other internal layers, e.g. the reflectors from conductivity at a depth of 1865 m (yellow "V") and 2080 m at the drill site, but displays stronger variations in reflection magnitude. Although the 600-ns pulse radargram contains more noise (in terms of clutter or speckle) than the 60-ns data, the reflector from conductivity at 1865 m is clearly dominant. Both reflectors from conductivity can clearly be tracked over the whole section of the 60-ns pulse in Fig. 2. The reflector from COF seems to be continuous over the whole section in the 600-ns data as well, although of very low quality. In contrast, it can only be tracked between −3 km and 2.5 km in the 60-ns data. It is very strong on the downstream

(right) side of the anticline between −3 and 1.5 km. Further upstream (to the left) from the anticline, it fades away, with several strong reflectors appearing within 20 m above it. Downstream from the drill site, it starts to fade away at 1.5 km, and is interrupted and lost in the syncline starting around 3 km. The different characteristics of the 60 ns and 600 ns emphasize that care has to be exercised when interpreting long-pulse radar data, as reflector characteristics and mechanisms could change within the pulse length without resulting in obvious changes in the reflection magnitude or depth. The variation of reflection magnitude of the reflector from COF suggests that fabric changes are less continuous than conductivity characteristics, as they are susceptible to variations of internal stresses, e.g. between upstream and downstream sides of subglacial bedrock variations.

3.5 Reflectors from COF – frequent or uncommon?

Whereas certain flow regimes are necessary for sharp transitions in COF to occur, changes in conductivity are not constrained by comparable ice-dynamic conditions. We therefore expect that continuous internal reflectors from COF do occur less often than reflectors from conductivity. It is commonly expected that changes in conductivity cause isotropic reflectors. Reflections from COF, instead, can be anisotropic or isotropic. Anisotropic reflections only occur if the underlying change in COF patterns is also anisotropic in the horizontal plane. This is usually the case in flow regimes with significant lateral strain (e.g. Fujita et al., 2003), as is the case at the EDML drilling site. In contrast, analyses at Dome Fuji down to a depth of 2500 m (about 83% ice thickness) by Fujita et al. (2006) indicate that isotropic reflections with birefringent effects prevail. They explain this by the horizontally-symmetric pattern in COF in the same depth range, caused by symmetric divide flow at the dome. Any potential reflections from changes in COF therefore also show an isotropic pattern at Dome Fuji.

Observations of either type of reflector, conductivity- or COF-based, are likely biased, as data acquisition required for ice-core analyses are more intensive for detection of COF-type reflectors. The same holds true for the type of RES measurements required to indirectly identify the reflector origin from RES measurements alone. Reflections from conductivity are independent of polarisation plane. Reflectors from COF can only be identified by azimuth-dependent polarisation measurements at a single location in the case of anisotropic reflections, or a combination with multi-frequency measurements in the case of isotropic reflections. As azimuths-dependent RES measurements require more time than simple straight RES profiles (especially if only airborne systems are available), they are carried out less often.

To date, the reflector discussed here is the only one at EDML that can be clearly attributed to changes in COF. In contrast, 13 strong internal reflectors were identified to originate from changes in conductivity at the same location (Eisen et al., 2006). However, with more COF data emerging, it might be possible that some reflectors appear to be of a mixed type, with their origin being partly from changes in COF, partly from conductivity. For instance, the reflector only present in the 600-ns pulse data at 1850-m depth could be caused by the series of conductivity peaks (Fig. 3), but it could also stem from slight changes in COF, or both. Further refinement of the COF data in at least 10-m resolution is necessary to answer this question conclusively.

Some of the few ice cores from deep-drilling sites currently available display transitions from COF patterns which are anisotropic in the horizontal plane (e.g. girdle-type), to highly concentrated single-maximum fabrics in the lower part of the ice column, as at NorthGRIP (Wang et al., 2002) or Vostok (Obbard and Baker, 2007). However, only for some of the deep-drilling ice cores are profiles of COF available in high enough resolution to search for potential reflectors from COF directly. Another promising site to identify reflections from COF is the Siple Dome. The COF data, measured in 20-m intervals, show a sharp transition from an elongated to a highly concentrated fabric between 685 and 700-m depth, with the largest eigenvalue of the COF distribution changing from 0.75 to 0.95 (DiPrinzio et al., 2005, Fig. 3). RES data from the Siple Dome (e.g. Gades et al., 2000, Fig. 3) indicate a strong continuous internal reflector at about the same depth (based on the travel time depth conversion of Gades et al., 2000). In analogy to the findings developed here, this reflector thus bears the potential to stem from an abrupt change in COF.

Ice-core deep drillings are mostly carried out at such divide or dome locations as Dome Fuji or Siple Dome. Paleoclimatic interpretation of ice-core records usually incorporates ice-flow modeling. Recent modeling studies of ice flow at Siple Dome emphasize the significance of changes in COF for ice flow. Pettit et al. (2007) implemented fabric properties from borehole measurements in an anisotropic nonlinear flow law as part of an ice-sheet flow model. They found that the band of highly vertically concentrated COF in the lower 20–30% of the ice column causes concentrated bed-parallel shearing 300 m above the bed. Moreover, compared to an isotropic fabric, the anisotropy considerably increases the size of the isochrone arch underneath the Siple Dome divide, and thus strongly influences the age–depth distribution. Pettit et al. (2007) assumed that the COF-profile is only a function of normalized depth with respect to ice thickness. The method presented here to identify continuous reflectors from changes in COF provides a way to improve this assumption. If a reflector is identified to originate from changes in COF, its true depth tracked in RES profiles could be used as a proxy for the spatial distribution of the change in COF, instead of extrapolating its normalized depth as observed in boreholes or ice cores.

4 Conclusions

The combination of ice-core profiles of COF and the conductivity with RES data of different pulse lengths in our approach identifies the origin of a defined continuous internal reflector as a sharp transition in COF, from a girdle-type to a single-maximum fabric over just a few tens of meters. This finding goes beyond the previous analyses, which related RES signals to flow-induced COF, but did not provide a direct comparison of continuous internal layers in RES data with nearby in-situ data of COF. We showed that, even at short pulse lengths, the width of the COF-related reflector is comparable to reflectors stemming from conductivity peaks, limited by the RES pulse length. The spatial variation of the reflector from COF in depth is parallel to other internal reflectors, but less continuous. However, we emphasize that we have no evidence whether the reflector from COF is an isochrone or not. These observations imply that care has to be taken when correlating ice-core data with internal reflectors, if only single-frequency single-polarisation RES data are available, as these cannot pin down the reflector origin unambiguously.

The identification of a single change in COF as the origin of a strong individual internal reflector opens new possibilities for understanding and modeling ice dynamics. The fabric properties can be extrapolated along the reflector, as long as it is continuously trackable in the RES profile. Determination of the internal distribution of stresses can thus go beyond the point information provided by ice cores. Ice-dynamic models can utilize the reflector as an ancillary condition. As the rheology of a girdle-type fabric differs from those of a single-maximum fabric, the reflector indicates a boundary of different ice-flow properties above and below the reflector within the ice sheet. A remaining challenge lies in exclusively using remote-sensing data, like RES or seismics, to discriminate physical properties from the ice sheet's surface, without requiring in-situ information from ice cores. By providing characteristic observations of the forward relation of changes in COF and reflectivity, this study provides another step towards solving the inverse problem, which should eventually be used to determine the continuous profiles of vertical and lateral physical properties within the ice sheet.

Acknowledgements. This work is a contribution to the European Project for Ice Coring in Antarctica (EPICA), a joint European Science Foundation/European Commission scientific programme, funded by the EU and by national contributions from Belgium, Denmark, France, Germany, Italy, the Netherlands, Norway, Sweden, Switzerland and the United Kingdom. The main logistic support was provided by IPEV and PNRA (at Dome C) and AWI (at Dronning Maud Land). This is EPICA publication no. 186. Preparation of this work was supported by an "Emmy Noether"-scholarship of the Deutsche Forschungsgemeinschaft grant EI 672/1 to O. Eisen.

Edited by: J. L. Bamber

References

Bogorodsky, V. V., Bentley, C. R., and Gudmandsen, P. E.: Radioglaciology, D. Reidel Publishing Company, Dordrecht, Holland, 1985.

DiPrinzio, C. L., Wilen, L. A., Alley, R. B., Fitzpatrick, J. J., Spencer, M. K., and Gow, A. J.: Fabric and texture at Siple Dome, Antarctica, J. Glaciol., 51, 281–290, 2005.

Doake, C. S. M., Corr, H. J. F., and Jenkins, A.: Polarization of radio waves transmitted through Antarctic ice shelves, AG, 34, 165–170, 2002.

Dowdeswell, J. A. and Evans, S.: Investigations of the form and flow of ice sheets and glaciers using radio-echo sounding, Rep. Prog. Phys., 67, 1821–1861, 2004.

Durand, G., Gillet-Chaulet, F., Svensson, A., Gagliardini, O., Kipfstuhl, S., Meyssonnier, J., Parrenin, F., Duval, P., and Dahl-Jensen, D.: Change of the ice rheology with climatic transitions – implications for ice flow modelling and dating of the EPICA Dome C core, Clim. Past, 3, 155–167, 2007, http://www.clim-past.net/3/155/2007/.

Eisen, O., Wilhelms, F., Steinhage, D., and Schwander, J.: Improved method to determine RES-reflector depths from ice-core profiles of permittivity and conductivity, J. Glaciol., 52, 299–310, 2006.

Fujita, S., Maeno, H., Uratsuka, S., Furukawa, T., Mae, S., Fujii, Y., and Watanabe, O.: Nature of radio echo layering in the Antarctic ice sheet detected by a two-frequency experiment, J. Geophys. Res., 104, 13 013–13 024, 1999.

Fujita, S., Matsuoka, T., Ishida, T., Matsuoka, K., and Mae, S.: A summary of the complex dielectric permittivity of ice in the megahertz range and its application for radar sounding of polar ice sheets, in: The Physics of Ice Core Records, edited by: Hondoh, T., pp. 185–212, Hokkaido University Press, 1 edn., 2000.

Fujita, S., Matsuoka, K., Maeno, H., and Furukawa, T.: Scattering of VHF radio waves from within an ice sheet containing the vertical-girdle-type ice fabric and anisotropic reflection boundaries, Ann. Glaciol., 37, 305–316, 2003.

Fujita, S., Maeno, H., and Matsuoka, K.: Radio-wave depolarization and scattering within ice sheets: a matrix-based model to link radar and ice-core measurements and its application, J. Glaciol., 52, 407–424, 2006.

Gades, A., Raymond, C., Conway, H., and Jacobel, R.: Bed properties of Siple Dome and adjacent ice streams, West Antarctica, inferred from radio-echo sounding measurements, J. Glaciol., 46, 88–94, 2000.

Hargreaves, N. D.: The radio-frequency birefringence of polar ice, J. Glaciol., 21, 301–313, 1978.

Harrison, C. H.: Radio echo sounding of horizontal layers in ice, J. Glaciol., 12, 383–397, 1973.

ISMASS Committee: Recommendations for the collection and synthetis of Antarctic Ice Sheet mass balance data, Global Planet. Change, 42, 1–15, 2004.

Liu, H., Jezek, K., Li, B., and Zhao, Z.: Radarsat Antarctic Mapping Project digital elevation model version 2, Digital media, National Snow and Ice Data Center, Boulder, CO, USA, 2001.

Marshall, S. J.: Recent advances in understanding ice sheet dynamics, E. Plan Sci. Lett., 240, 191–204, doi:10.1016/j.epsl.2005.08.016, 2005.

Matsuoka, K., Furukawa, T., Fujita, S., Maeno, H., Uratsuka, S., Naruse, R., and Watanabe, O.: Crystal orientation fabrics within

the Antarctic ice sheet revealed by a multipolarization plane and dual-frequency radar survey, J. Geophys. Res., 108(B10), 2499, doi:10.1029/2003JB002425, 2003.

Matsuoka, K., Uratsuka, S., Fujita, S., and Nishio, F.: Ice-flow induced scattering zone within the Antarctic ice sheet revealed by high-frequency airborne radar, J. Glaciol., 50, 382–388, 2004.

Nixdorf, U., Steinhage, D., Meyer, U., Hempel, L., Jenett, M., Wachs, P., and Miller, H.: The newly developed airborne RES-system of the AWI as a glaciological tool, Ann. Glaciol., 29, 231–238, 1999.

Obbard, R. and Baker, I.: The microstructure of meteoric ice from Vostok, Antarctica, J. Glaciol., 53, 41–62, 2007.

Paren, J. G.: PRC at a dielectric interface, J. Glaciol., 27, 203–204, 1981.

Paren, J. G. and Robin, G. de Q.: Internal reflections in polar ice sheets, J. Glaciol., 14, 251–259, 1975.

Paterson, W. S. B.: The physics of glaciers, 3rd edition, Oxford, New York, Tokyo, Pergamon, ix, 480 pp., ISBN 0-08037944 3, 1994.

Petrenko, V. F. and Whitworth, R. W.: Physics of Ice, Oxford University Press, 1999.

Pettit, E. C., Thorsteinsson, T., Jacobson, H. P., and Waddington, E. D.: The role of crystal fabric in flow near an ice divide, J. Glaciol., 53, 277–288, 2007.

Robin, G. de Q., Evans, S., and Bailey, J. T.: Interpretation of radio echo sounding in polar ice sheets, in: Philosophical Transactions of the Royal Society of London, vol. 146 of A, pp. 437–505, Royal Society of London, 1969.

Wallbrecher, E.: Methoden zum quantitativen Vergleich von Regelungsgraden und Formen strukturgeologischer Datenmengen mit Hilfe von Vektorstatistik und Eigenwertanalyse, N. JB. Geol. Paläontol. Abh., 159, 113–149, 1979.

Wang, Y., Thorsteinsson, T., Kipfstuhl, J., Miller, H., Dahl-Jensen, D., and Shoji, H.: A vertical girdle fabric in the NorthGRIP deep ice core, North Greenland, Ann. Glaciol., 35, 515–520, 2002.

Wesche, C., Eisen, O., Oerter, H., Schulte, D., and Steinhage, D.: Surface topography and ice flow in the vicinity of EDML deep-drilling site, J. Glaciol., 53(182), 442–448, 2007.

Wilhelms, F.: Explaining the dielectric properties of firn as a density and conductivity mixed permittivity (DECOMP), Geophys. Res. Lett., 32, L16 501, doi:10.1029/2005GL022808, 2005.

Wilson, J., Russell-Head, D. S., and Sim, H. M.: The application of an automated fabric analyzer systm to the textural evolution of folded ice layers in shear zones, Ann. Glaciol., 37, 7–17, 2003.

Deducing the thermal structure in the tongue of Gornergletscher, Switzerland, from radar surveys and borehole measurements

O. EISEN,[1,2] A. BAUDER,[1] M. LÜTHI,[1] P. RIESEN,[1] M. FUNK[1]

[1] *Versuchsanstalt für Wasserbau, Hydrologie und Glaziologie (VAW), ETH Zürich, CH-8092 Zürich, Switzerland*
[2] *Alfred-Wegener-Institut für Polar- und Meeresforschung, Postfach 120161, D-27515 Bremerhaven, Germany*
E-mail: olaf.eisen@awi.de

ABSTRACT. We present the thermal distribution in the confluence area of Gorner- and Grenzgletscher, Valais, Switzerland. The area was mapped by ice-penetrating radar at 1–5 and 40 MHz. The higher-frequency data reveal a thick surface layer of low backscatter in the center of the Grenzgletscher branch. Based on datasets of borehole-temperature measurements and flow velocity, we interpret this as a thick layer of cold ice, advected from the accumulation region of Grenzgletscher. Along seven profiles the base of the low-backscatter zone can be found at a maximum depths between approximately 100 and 200 m. Laterally, the layer extends some 400 m, ~1/3 of the width of the Grenzgletscher branch. The lower boundary of the low-backscatter zone is systematically higher than the cold–temperate transition surface found in the boreholes. This discrepancy is attributed to the direct sensitivity of radar backscatter to liquid-water inclusions, rather than to the temperature distributions as observed in boreholes. We present the current state of the cold layer and discuss its influence on other glacier characteristics.

INTRODUCTION

Polythermal glaciers are most commonly observed in polar or subpolar regions. However, some glaciers at mid-latitudes (e.g. in the European Alps) can also be considered polythermal (Paterson, 1994; Haeberli and Hoelzle, 1995; Suter and others, 2001). The presence of ice at temperatures below the pressure-melting point (pmp) influences a number of properties of the glacier, such as the temperature gradients and heat fluxes, distribution of shear stresses and characteristics of the hydrological system. This makes modelling the behaviour of polythermal glaciers more complicated than that of temperate glaciers. It has been recognized for some time that geophysical properties of ice, such as seismic wave speed (Kohnen, 1974) and dielectric permittivity (Bogorodsky and others, 1985), are influenced by ice temperature. Among geophysical methods, ground-penetrating radar, in particular, has the potential to identify cold ice because of its relatively low backscatter compared to temperate ice, as the volume fraction of liquid water is greatly reduced at ice temperatures below the pmp (Nye, 1991; Mader, 1992; Pettersson and others, 2004). As a consequence, several studies established the possibility of detecting thermal regimes within glaciers by means of radar surveys (see Pettersson and others, 2003, and references therein for a summary).

A prominent example of a glacier in the Alps which contains cold firn in the accumulation area is Gornergletscher, located in Valais, Switzerland. With a length of ~14 km and an area of ~60 km^2, it is one of the largest European glaciers. It spans an altitude range from 2200 to >4550 m a.s.l. It has been the subject of a number of scientific studies since the 1970s (e.g. Bezinge and others, 1973; Elliston, 1973; Haeberli, 1976; Aschwanden and Leibundgut, 1982; Alean and others, 1984; Haeberli and others, 1988; Haeberli and Funk, 1991; Iken and others, 1996; Lüthi and Funk, 2000, 2001; Suter and others, 2001; Huss and others, 2007; Sugiyama and others, 2007). Its accumulation region at Colle Gnifetti has been the site of several ice-core drillings, mainly to exploit palaeoclimate proxies conserved in the ice (e.g. Oeschger and others, 1978; Gäggeler and others, 1983; Döscher and others, 1995; Wagenbach and others, 1996; Smiraglia and others, 2000).

One reason for the scientific interest in Gornergletscher is a glacier-dammed lake that forms every spring above the confluence of the southern branch, Grenzgletscher, with the northern branch, the actual Gornergletscher (Fig. 1). The lake, known as Gornersee, reaches a maximum volume of ~1–4 $\times 10^6$ m^3 and usually drains during summer over a period of several days, with peak water outflow of 20–60 m^3 s^{-1} (Bezinge and others, 1973; Huss and others, 2007). This jökulhlaup, or glacier outburst flood, poses a threat to the villages located down-valley. The village of Zermatt has experienced serious damage in the past from these jökulhlaups. To investigate the ice-dynamical, thermal and hydrological properties of the glacier, an extensive field program has been carried out over the past few years. Predictions of the future response and behaviour of the glacier, as well as the drainage mechanism, are the ultimate goal of this field program. This requires a thorough understanding of the processes occurring during the jökulhlaup and related glacier dynamics. A number of different techniques (e.g. measurements of surface velocity, mass balance, borehole deformation and temperature, water pressure, tracer experiments, ground-penetrating radar, passive and active seismics) have been employed in several campaigns to obtain physical parameters and their variation over the course of the drainage.

In this study, we use radar data to determine the current thermal structure of the glacier, focusing on several cross-sections of the glacier tongue, along with data on ice thickness, bedrock topography and temperature profiles from boreholes. Implications of the deduced temperature distribution for the jökulhlaup and glacier dynamics, as well as possible future applications for detecting signals of climate change and improving palaeoclimatological methods, are discussed.

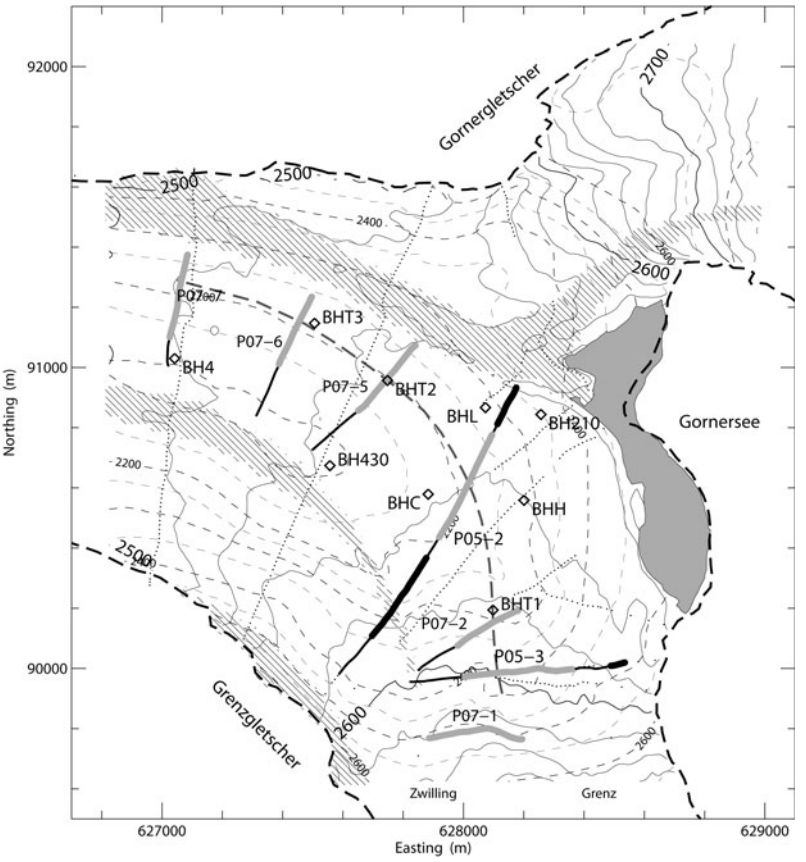

Fig. 1. Overview of study area at confluence of Gorner- and Grenzgletscher with the Gornersee (solid grey area): surface elevation with 20 m contour lines (thin solid), bedrock elevation with 50 m contour lines (dashed), borehole locations (labelled diamonds), low-frequency radar profiles (dotted lines) and extent of medial moraines at surface (hatched). Along the 40 MHz radar profiles (P05-2 to P07-7, semi-bold lines) the presence of the low backscatter at 60 m depth is indicated as a grey bold line, the presence of clutter as a black bold line. The semi-bold dashed grey line indicates a tentative flowline (BHT4–BHT2–BH3), the semi-bold dashed black line the glacier boundary.

METHODS

Radar systems and data acquisition

The glacier tongue was first surveyed with a low-frequency monopulse system, operating with resistivity loaded dipoles (Funk and others, 1994a). An example survey is shown in Figure 2a. Antenna frequency was varied between 1 and 5 MHz as a trade-off between strong reflections from the bedrock and a short transmitter pulse for improved resolution. Data acquisition and post-recording processing, including static correction, bandpass filtering, migration using the ellipse method and automatic gain control, are identical to the procedures described in detail by Bauder and others (2003). Antennae distance and shot interval were kept constant at 15 m. Transmitter and receiver positions were recorded at every shot using DGPS (differential global positioning system). Using such low frequencies and large wavelengths provides the advantage that more energy is transmitted into the ice, the absorption in ice is low and the signals are rather insensitive to metre-size englacial scatterers. Thus, the main return signals are from the ice/bed interface.

Additionally, seven profiles in the confluence area were surveyed in April 2005 and April 2007 with 40 MHz radar (Figs 2b and 3a–g), with a Narod and Clarke (1994) transmitter (Icefield Instruments, Canada) and antennae based on the system developed by Hempel and Thyssen (1993). Trans-mitter and receiver antennae each consisted of two dipoles slightly crossed in the horizontal plane, operated in parallel with a damped bow-tie antenna put on top for improved directivity. Antennae spacing and shot interval were 5 m. Data were recorded with a Tektronix storage oscilloscope at 2500 samples per trace with eight-fold stacking per shot. Oscilloscope recording was triggered by the first break of the airwave. Traces were recorded in a 10 μs window with 4 ns sample interval. Processing includes time-domain dewowing, bandpass filtering and gain control (compensation for spherical divergence and energy decay). Ice close to the surface near borehole BHH had density $\sim$900 kg m^{-3}, corresponding to a velocity of 1.70×10^8 m s^{-1}, using the empirical approximation of Kovacs and others (1995). For deeper ice the density, and thus wave speed, is expected to be lower because of higher pressure and small amounts of liquid water in temperate ice. Conversion of two-way travel time (twtt) to depth for all data is performed with a wave speed of 1.68×10^8 m s^{-1} for solid ice. Compared to the wave speed at the surface, this corresponds to a 1% difference. The wave speed used is also justified, a posteriori, by comparison with ice thicknesses derived from boreholes. The comparison of ice thicknesses derived with the two different radar systems allows us to evaluate uncertainties for ice-thickness estimates (Table 1).

Temperature logging

Between 2004 and 2007, several boreholes were drilled to bedrock with hot water (Fig. 1). After drilling, thermistor strings were deployed in the boreholes (Table 1). The strings were equipped with calibrated thermistors (Fenwal 135-107

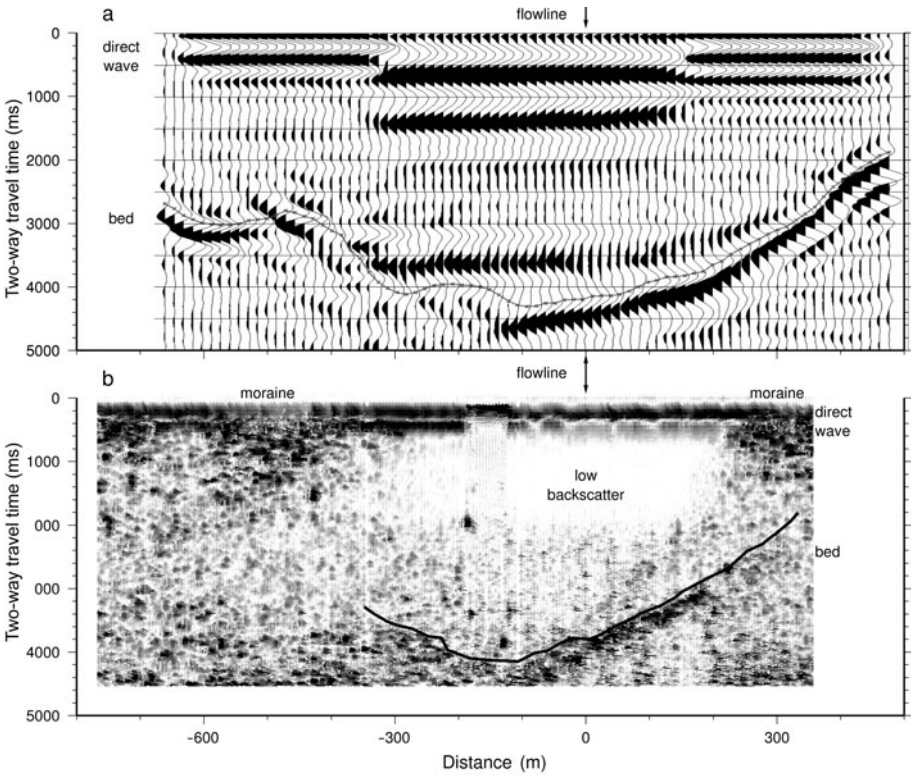

Fig. 2. Radar data along profile P05-2 recorded with (a) 1–5 MHz and (b) 40 MHz, both plotted in filled-wiggle mode. Greyscale of filled wiggles in (b) indicates signal magnitude (white: low; black: high). Thin lines in (a) indicate traced bedrock. Main backscatter features and interpretation are indicated on the plots. Vertical arrows mark the flowline (zero on *x* axis), as indicated in Figure 1. Ice flow is into the plane.

FAG-J01) and installed in the boreholes in varying increments, depicted in Figure 4. Temperatures were recorded several times after deployment, with an accuracy of 0.05 K per measurement. Logging intervals ranged between months and years, depending on the borehole, to allow for the decay of thermal perturbations caused by the drilling procedure.

RESULTS

The low-frequency data show clear reflections from the ice/bed interface along all profiles (see example in Fig. 2). They show no indication of any signals originating from the interior part of the glacier, because of the low frequency and long pulse length. In contrast, the 40 MHz data show three distinct features, as illustrated for profile P05-2 (Fig. 2). Firstly, the bedrock reflection is visible along the first two-thirds of the profile (from right to left), with a maximum ice thickness occurring around −100 m (i.e. 100 m to the left of the tentative flowline shown in Fig. 1); secondly, two areas of high backscatter (horizontal sections 200 to 350 m and −600 to −350 m) from the surface downwards are visible, decreasing to a medium backscatter level below a twtt of ∼1500 ns;

Table 1. Comparison of radar and borehole characteristics

Radar profile	Borehole	Coordinates		Distance	Drilling year	BH	Ice thickness		Thermistor range	CTS depth	RTS
		East	North				1–5 MHz	40 MHz			40 MHz
				m		m	m (%)	m (%)	m	m	m
P05-2	BHC	627883	90579	+48	2006	351	352 (<1)	335 (5)	102–350	236–286	181 ± 30
P05-2	BH210	628257	90844	−60	2004	210	210 (0)	162 (−30)	25–185	temperate	na
P05-2	BHL	628073	90867	+24	2006	248	265 (6)	226 (8)	81–248	81–141	na
P07-5	BHT2	627748	90957	−5	2007	320	na	302 (−6)	20–320	207–245	141 ± 30
P07-5	BH430	627557	90674	−43	2004	430	na	na	20–180	temperate	na
P07-6	BHT3	627506	91147	−19	2007	300	na	265 (13)	14–294	163–207	152 ± 30
P07-7	BH4	627042	91030	−12	2006	381	na	na	40–360	40–80	na

Notes: Distance refers to the distance of the borehole along a flowline from the nearest profile (>0 and <0 are down- and upstream of the profile, respectively). All depth values rounded to full metres. All boreholes drilled to bedrock. Ice thicknesses: percentage differences of radar minus borehole thicknesses in respect to radar ice thicknesses are given in parentheses. CTS depth: the ranges of cold–temperate transition surface depths result from thermistor spacings; thermistor increments vary with depth and borehole. RTS: radar transition surface, the depth of the transition from low to medium backscatter. Uncertainty range for radar depths only includes the picking uncertainty in radar data. na: not applicable (borehole outside radar profile range or no detectable bedrock/CTS signal).

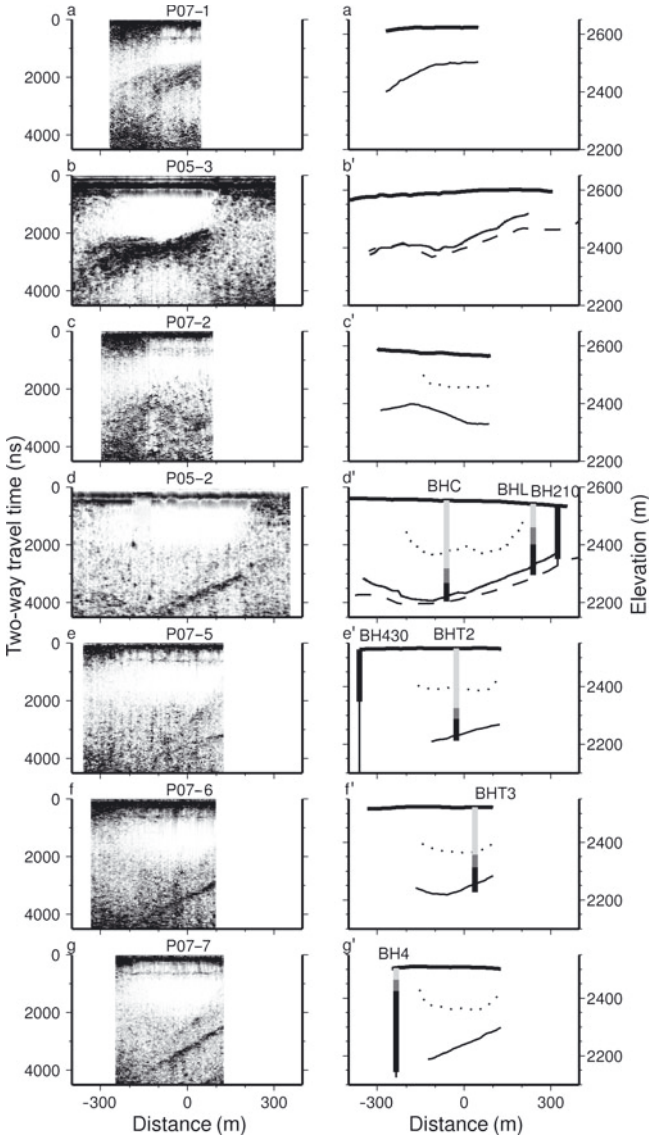

Fig. 3. (a–g) Radargrams recorded at 40 MHz, displayed in the twtt domain. (a′–g′) Ice geometry and schematic interpretation of profiles (a–g) in the depth domain, converted to elevation (m a.s.l.): surface topography (thick curves), bedrock topography (deduced from 40 MHz data: thin curves; 1–5 MHz data (only (b′) and (d′)): dashed curves), and depth of cold–temperate transition surface (CTS) 40 MHz data, dotted curves). Vertical lines (d′–g′) show projected location of boreholes onto the nearest radar profile along tentative flowlines; thin black line indicates borehole extent without thermistors; bold lines indicate thermistor chains; and line fillings indicate temperatures: below pmp (light grey); thermistor gap containing CTS (grey, see Table 1); and temperate ice (black). Ice flow is into the plane.

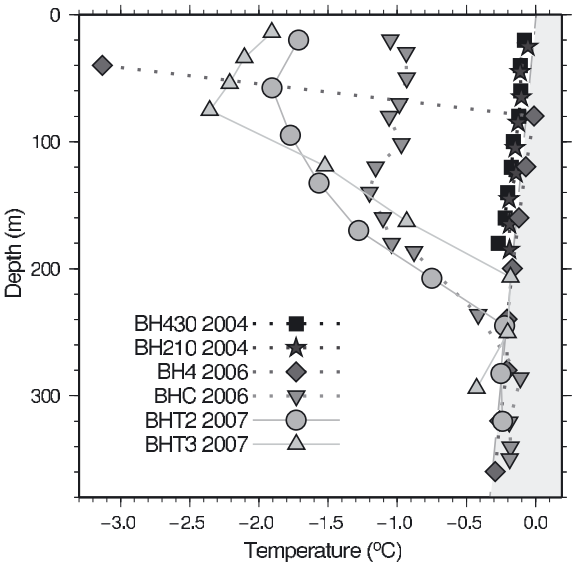

Fig. 4. Distribution of steady-state temperatures in selected boreholes. Shaded area indicates temperatures above the pmp curve for ice in equilibrium with liquid water (Paterson, 1994, p. 212). Details of boreholes are given in Table 1.

thirdly, a zone of low backscatter (horizontal section −200 to 200 m) at twtt values between 800 and 2200 ns is visible.

Bedrock topography

The resolution of the 40 MHz data is naturally better than that of the low-frequency data (i.e. the reciprocal bandwidth of either system). For the 40 MHz system, $\lambda = 4$ m in ice. Its source wavelet is ∼200 ns in duration (bandwidth 5 MHz), which corresponds to almost 34 m in ice. For a single boundary between semi-infinite half-spaces, the theoretical resolution limit is $\lambda/4$. Considering the length of the wavelet, the resolution limit of a layer detected with the 40 MHz system is ∼15–20 m.

Despite the different resolutions, the ice thicknesses derived from high- and low-frequency radar data are usually in good agreement along the profiles where both datasets were recorded (Fig. 3b′ and d′). The maximum difference of both radar-based ice thicknesses is 50 m (23% of the borehole ice thickness in the case of BH210; Fig. 3d′). The agreement of the 1–5 MHz ice thicknesses with the borehole thicknesses at three locations is very good (differences of 1, 0 and 17) given the wavelength of the system. Comparison of low-frequency-based ice thicknesses with logging data of other boreholes drilled to bedrock (not further considered here) yields an agreement better than 10% of the ice thickness, on average (Riesen and others, 2006). For the 40 MHz radar, differences with borehole-based ice thicknesses range from 16 to 48 m (Table 1). The largest percentage error, 30% of 40 MHz radar ice thickness (or 23% of borehole thickness), occurs for a relatively small radar ice thickness of 162 m (210 m borehole BH210, ∼60 m upstream of the profile). The other percentage differences (in respect to radar thickness) are 5, 8, 6 and 13% (with profile–borehole distances <50 m).

Apart from the technical resolution limits of either radar system, several other factors contribute to the overall uncertainty of estimated ice thickness. Our radar profiles are usually a few to tens of metres away from the boreholes. Although there is no systematic relation apparent in our dataset (Table 1), a larger distance obviously leads to worse agreement. The general bedrock roughness influences the time of first break for different wavelengths. Significant parts of Gornergletscher have become ice-free over the past few years. The now-exposed bedrock shows a roughness of the order of tens of metres. Naturally, the first (earliest) radar return from the bedrock will occur at bedrock highs. With the correct wave speed, one therefore expects that a radar thickness is, in general, smaller than a borehole ice thickness, as a borehole a few centimetres in diameter can easily be lowered in lows of bedrock roughness within the footprint of

the radar signal. Moreover, the bedrock is a non-planar three-dimensional (3-D) surface, but our radar data only image in two dimensions, where off-profile reflections can mask the along-profile location of the bed. Moran and others (2000) showed that ice-thickness errors for radar estimates with a steep bedrock topography on a glacier are ~15% for two-dimensional (2-D) data processing and migration, and can amount to >30% for raw data.

Another factor contributing to the observed ice-thickness differences could be the presence of sediments within the basal layer of the glacier, especially in the regions close to the medial moraines and the lake with a vivid hydrological system. Because of the large wavelength, the 1–5 MHz system would be much less sensitive to such sediments than the 40 MHz system.

We consider the roughness of the bed the primary factor responsible for the differences in ice thickness between the two radar systems, with a possible, but uncertain, contribution from the sediment content of the basal layer. From the differences in Table 1 we estimate an accuracy of 15% in ice thickness along the profiles for the 40 MHz data. Overall, these results provide a realistic uncertainty and indicate that the choice of a standard wave speed for migration and travel-time–depth conversion is acceptable. The interpolated bedrock topography is derived from a combination of both radar datasets. It shows a prominent overdeepening downstream of the confluence area (centred around coordinates 627400 E, 90750 N in Fig. 1). The interpolated topography probably has a higher uncertainty than 15% (Bauder and others, 2003).

High-backscatter zone

The high backscatter close to the surface occurs in the vicinity of two medial moraines, one between Gorner- and Grenzgletscher, the other between the Grenz- and Zwillingsgletscher branches. Both moraines rise several tens of metres above the surrounding glacier surface, are partly >100 m wide (Fig. 1) and consist of debris varying in size from centimetres to boulders several metres in diameter. Naturally, debris of medial moraines extends vertically into the ice, although the moraine width at depth is rather of the order of metres, as evident from the highest parts of the medial moraines at the surface (Fig. 1). Since the wavelength of the 40 MHz system approaches this order of magnitude, it is much more sensitive to inhomogeneities located on the surface and within the ice than the low-frequency radar. We therefore interpret the radar scatterers, for instance observed along profile P05-2 around −600 to −350 m and +250 to +350 m from the centre line (Figs 2b and 1), as clutter mainly originating from moraine material located both along- and off-track of the profile, as well as at the surface and at depth. It is obvious that the scatter is large enough to inhibit recording the bedrock reflection in the vicinity of the moraines (Fig. 2b).

Low-backscatter zone

Along all profiles, the 40 MHz data show a zone of low backscatter in the central region (Fig. 3a–g), outlined with dotted lines in the schematic cross-sections of Figure 3a′–g′ and vertically projected to the surface in Figure 1 (bold grey lines). The upper part of the data, from the surface down to ~60 m depth, is masked by the radar air- and ground waves. In profiles P07-1 and P05-3 the low-backscatter zone seems to extend all the way to the bedrock. In all other profiles, the maximum depth corresponds to ~50% of the ice thickness. Laterally, the low-backscatter zone is visible over a distance of 200–400 m, partly bounded by the zone of high backscatter (e.g. at +200 m in profile P05-2, Fig. 2b). The lower boundary of the low-backscatter zone is rather diffuse in most cases, varying by up to 30 m over the same along-profile distance. We take this value as the precision with which we can determine the depth of the lower boundary.

Borehole temperatures

Most temperatures in the boreholes approached an equilibrium value within a few weeks of deployment. At some locations (e.g. BH210 and BH430), the temperatures reached equilibrium only after 1–2 years. This rather long time is due to the fact that at these locations the borehole closure rate is very low because of high water pressure and ice temperatures very close to the melting point. Thermistors not reaching equilibrium values are considered faulty, or cables exposed to strain are excluded from further analysis (e.g. BHT1). Temperatures in boreholes BH430 and BH210 show a steady and almost linear decrease from −0.1°C to −0.3°C, close to the pmp (Fig. 4). Boreholes BH4, BHC, BHT2 and BHT3 indicate temperatures >1 K below the pmp for shallow to intermediate depths. The pmp is reached at different depths, depending on borehole location (Table 1). The cold–temperate transition surface (CTS) is believed to be located in the depth range between the two thermistors for which the upper one is below the pmp and the lower one is at the pmp.

INTERPRETATION AND DISCUSSION

Borehole vs radar CTS depth

Temperatures below the pmp greatly reduce the liquid-water content, and thus reduce the backscatter observed with radar systems. We therefore suggest that the region of low backscatter observed in our radar corresponds to ice temperatures below the pmp and that its lower boundary is related to the CTS. We now investigate whether this hypothesis is consistent with borehole observations and physical mechanisms.

To compare radar backscatter and temperature measurements, we project the location of the boreholes along the flowline to the nearest radar profile. Using data in Table 1, we can compare our inferred CTS depth from radar with that from thermistor readings. At those locations where the projected boreholes cross the outlined zone of low backscatter (dotted lines in Fig. 3), the CTS observed in boreholes is generally deeper than the lower boundary of the low-backscatter zone, in the following referred to as the radar transition surface (RTS). The values differ by 11, 55 and 66 m. The smallest difference, at BHT3, is within the measurement uncertainty and supports our hypothesis. In the other two cases, the distance between borehole and profile is +48 m (BHC) and −5 m (BHT2). For BHC, the difference amounts to 23% of the borehole depth. For a perfect interface between cold and temperate ice (no liquid water above CTS), these uncertainties are still in the range (although at the upper limit) of possible uncertainties (Moran and others, 2000), especially given the distance between borehole and radar profile. BHT2 is located almost on the profile, and the difference amounts to 32% of borehole depth. This discrepancy cannot be explained by geometric effects alone and is discussed below in further detail. BH210 and BH430 are outside the zone of low backscatter and are both temperate. BH4 is at the southern margin of profile P07-7 (Fig. 3g′), where the RTS is already masked by the high backscatter from the moraine.

All nominal temperature values determined in BH4, BHC, BHT2 and BHT3 are below the pmp curve. These data are in accordance with data from 1975 by Haeberli (1976), who measured temperatures several Kelvin below the pmp in the same area on Grenzgletscher at depths of 44, 160 and 180 m. The temperature measurements therefore indicate a massive surface layer of cold ice, with a thickness corresponding to >50% of the ice thickness in the central part of the glacier. In the vicinity of medial moraines, all boreholes indicate either temperate ice throughout (BH210, BH430), or only a shallow cold surface layer (BH4, BHL). We therefore assume that the ice at the medial moraines is temperate. This could also be assumed a priori, as, by definition, ice at medial moraines has been in contact with the bedrock upstream of the actual confluence (at elevations at or below 3000 m) where the basal ice is temperate.

The presence of cold ice in the boreholes combined with the distribution of low backscatter leads us to the conclusion that the zone of low backscatter is completely within a region of cold ice. The apparent systematic offset between the borehole CTS and RTS depth makes it, however, difficult to conclude that the RTS is related to the borehole CTS. As the radar data do not allow direct observation of temperatures, several reasons could explain this discrepancy.

It should be noted that the radar backscatter is sensitive to liquid-water content, whereas the borehole thermistors determine temperature. The liquid-water content can be inversely proportionally related to the temperature depression below the melting point, but also depends on the geometry of inclusions and the impurity content (Nye, 1991; Mader, 1992). The 40 MHz radar signal has a wavelength of ~4 m in ice. In order for liquid-water inclusions to act as individual scatterers at this wavelength, they need a diameter of about one-tenth of the wavelength, i.e. 0.4 m. This is less likely than the combined effect of a number of smaller scatterers in high number density.

Apart from liquid-water inclusions, the scatterers could, in general, also consist of boulders or sediments. However, as hot-water drilling of boreholes was unproblematic down to bedrock, the presence of a considerable amount of sediment in the ice is unlikely. As mentioned above, the onset of the scattering above the borehole-based CTS depth indicates that the lower boundary is still in cold ice. We are unable to think of an efficient mechanism to incorporate significant amounts of boulders or similar into the cold layer of Grenzgletscher from below. Area-wide deposition of boulders on the glacier surface from above (e.g. from an ancient rockfall) would rather result in a strong reflection horizon, comparable to that of the bed, and, moreover, inhibit successful drilling.

Another possibility for the observed difference is the separation of borehole location and radar profiles. The temperature measurements take place at different times in a Lagrangian frame of reference. This implies that the distance between a borehole and the position of a radar profile changes over time. However, this is only considered to be important on timescales of more than a year. For instance, BHT2 was drilled directly on the profile several months after the radar measurements, but also shows the offset in CTS depth. The nature of radar measurements and the conversion of observed signal backscatter in the travel-time domain to a depth domain along the radar profile introduce further errors. Above, we estimated an uncertainty of 30 m for the location of the RTS in the radargram. The wave speed used to convert radar travel time to depth introduces an error of ~10–15%, comparable to the uncertainty for ice thickness presented above. The CTS is a 3-D surface and shows variations with depth, details of which we do not know. It might therefore be possible that some backscatter originates from off-nadir directions. As the scatter appears as clutter and not as defined hyperbolae, it is unfortunately not possible to reduce the noise by migration processing. Whether this backscatter is caused by a rough surface of the CTS or simply single large objects above the CTS (e.g. an individual collection of water pockets along and off the profile) cannot be determined from our data.

Seasonal variations of water pressure, which is close to overburden pressure in spring (personal communication from M. Werder, 2008), could also contribute to the observed differences in borehole-CTS and RTS depths. A number of hairline cracks are present on the tongue, partly remaining from icefalls upstream, partly forming every year when the lake is filling. Although cold ice is impermeable on the intergranular scale (Paterson, 1994), the high water pressure could cause penetration of liquid water into the cracks to shallower depths and enable the formation of local water pockets, even in those parts where the bulk of the ice is cold. Despite decreasing water pressure after the melt season, some liquid water could still remain above the CTS and refreeze only slowly over time, depending on the thermal state of the surrounding ice, thus leading to the formation of liquid-water pockets acting as scatterers within the cold ice. A final contribution to backscatter above the CTS is the gradual increase of liquid-water content, again for temperatures below the pmp. However, Pettersson and others (2003) showed that these inclusions cause very little backscatter.

Summarizing these considerations, we conclude that the first part of our hypothesis is correct: the low-backscatter zone detected with the 40 MHz radar does indeed correspond to a zone of low liquid-water content, indicating cold ice. For the second part of our hypothesis, however, we conclude that at the utilized frequency the lower boundary of the low-backscatter zone should only be considered a critical transition in liquid-water content in respect to the characteristics of the radar system, indicating some upper limit of the CTS, rather than a direct proxy for the CTS.

Relevance of a cold surface layer

The surface layer of cold ice influences various properties of the glacier. Its significance for hydrology is most easily recognizable by the abundance of superficial lakes and channels on the glacier tongue. The properties of the ice dam blocking the lake, as well as the closure rate of the drainage channel, located either sub- or intraglacially, depend on ice viscosity, which, in turn, depends on ice temperature. The presence of cold ice could thus potentially influence the drainage mechanism of the lake and the characteristics of the jökulhlaup. Although the distribution of glacier velocity, dominated by basal motion, is probably not influenced by cold ice most of the time, the exceptional behaviour occurring during the lake outburst flood, as observed by Sugiyama and others (2007), could be influenced by the different properties and the spatial distribution of cold ice.

Determining the distribution of cold ice on the surface of the glacier tongue could open several opportunities for palaeoclimate research. Firstly, if the bubbles enclosed by cold ice have lain undisturbed since formation, they will contain past atmospheric information (Haeberli, 1976). Secondly, large volumes of old ice could be used for

improving and developing analytical methods for palaeoclimate research (e.g. carbon dating). Gornergletscher thus provides easy access to an atmospheric archive of past European climate at its surface, with fewer logistical problems than encountered in ice-core drilling operations.

Previous studies provided a sequence of the thermal spatial regime of Grenzgletscher based on borehole measurements alone. Based on our interpretation of the radar and temperature data and the general behaviour and properties of the Grenzgletscher branch, we can extend the distribution of the thermal regime along the centre flowline in the following sequence:

1. Cold ice originates in the accumulation region at high elevations where the glacier is cold throughout and frozen to bed (Haeberli and Funk, 1991; Lüthi and Funk, 2001; Suter and others, 2001; Eisen and others, 2003).
2. In the lower accumulation region and the upper ablation region (including the equilibrium line), temperate firn and ice are present as a surface layer on top of a cold layer of ice.
3. At some point, strain heating and geothermal heat flux cause the onset of melting at the base. The exact position of this onset is unknown. It could be at a higher elevation than the appearance of zone 2 at the surface.
4. In the intermediate ablation area, including our area of investigation, the temperate surface layer from zone 2 has completely melted. Thus cold ice originating from zone 1 emerges at the surface. Temperate ice persists underneath as a basal layer. In the confluence area of Gorner- and Grenzgletscher the cold layer occupies about the central half of the width of the Grenzgletscher branch at the surface. The thickness of the temperate basal layer amounts to ~50% of the ice thickness at maximum.
5. In the lowest ablation region, temperate surface ice from zone 2 and the cold-ice layer from zone 1 have completely melted. The temperate basal ice layer is present throughout the glacier. Apart from zone 1, the lateral parts of Grenzgletscher (including the medial moraines) are temperate.

Under a changing climate forcing, as currently experienced (Huss and others, 2007), the position of the CTS will change. The different contributions to a changing CTS (advection and temperature forcing) can be analysed by modelling approaches. Earlier studies (Blatter and Haeberli, 1984) employed a 2-D model to determine the temperature distribution in Grenzgletscher along a flowline, using local temperature measurements as boundary conditions. Although a 2-D flow model can provide information about the present thermal regime of an ice body (e.g. Funk and others, 1994b), it is likely that such an approach will not suffice to pin down all components of the energy balance for a CTS's 3-D geometry, as presented here. Although a time-dependent 2-D model will improve results, full 3-D modelling in a non-steady state seems necessary, if all components of the thermal regime need to be quantified.

CONCLUSION AND OUTLOOK

We have related the backscatter properties of 40 MHz radar on the Grenzgletscher branch of Gornergletscher to the thermal distribution in the glacier. The transition from a massive surface layer of low backscatter to a basal layer of medium backscatter in the central part of the glacier probably corresponds to a change in liquid-water content. It indicates an upper limit of the CTS depth, as evident from thermistor records in several boreholes. We cannot provide a conclusive reason for the difference in the larger CTS depth observed in boreholes and the onset of medium backscatter, the RTS, at smaller depths in the radar data. A relationship to the presence of local pockets of liquid water, caused by seasonal penetration of liquid water under high pressure into cracks within cold ice, is likely, as are uncertainties in radar depths and geometric effects. As Grenzgletscher is not in steady state, this problem can only be resolved with a transient 3-D thermomechanical model, taking into account time-dependent vertical and also lateral heat fluxes.

Our measurements provide a baseline for future observations. Comparable interpretations for linking observed climate warming and changing CTS depth and distribution, as carried out by Pettersson and others (2003) at Storglaciären, Sweden, mainly require improved accuracy of the radar measurements. Extrapolating the negative mass-balance trend observed over the last 70 years (Bauder and others, 2007; Huss and others, 2007), it can be expected that the volume of cold ice will decrease. Firstly, increasing mean air temperatures in the firn region leads to a higher firn temperature and thus reduced flux of cold ice downglacier; secondly, increased ablation reduces the flux of cold ice downwards of the confluence area; and, thirdly, the ongoing thinning of the glacier tongue will further reduce the volume of near-surface cold ice.

ACKNOWLEDGEMENTS

The Gorner Project is funded under grants 200021-103882 and 200020-111892 of the Schweizerischen Nationalfonds. O. Eisen is funded by the 'Emmy Noether' programme of the Deutsche Forschungsgemeinschaft. The Swiss military provided logistical support with helicopter transports and the International Foundation High Altitude Research Stations Jungfraujoch and Gornergrat (HFSJG) provided support for personnel transport. We acknowledge comments of two anonymous referees and W. Haeberli for improving an earlier version of this work. Special thanks to casa Mark, Sotto Il Vigno.

REFERENCES

Alean, J., W. Haeberli and B. Schädler. 1984. Snow accumulation, firn temperature and solar radiation in the area of the Colle Gnifetti core drilling site (Monte Rosa, Swiss Alps): distribution patterns and interrelationships. *Z. Gletscherkd. Glazialgeol.*, **19**(2), 131–147.

Aschwanden, H. and C. Leibundgut. 1982. Die Markierung der Wasser des Gornerseeausbruchs mit drei Fluoreszenztracern. *Beitr. Geol. Schweiz*, **28**, 535–549.

Bauder, A., M. Funk and G.H. Gudmundsson. 2003. The ice-thickness distribution of Unteraargletscher, Switzerland. *Ann. Glaciol.*, **37**, 331–336.

Bauder, A., M. Funk and M. Huss. 2007. Ice-volume changes of selected glaciers in the Swiss Alps since the end of the 19th century. *Ann. Glaciol.*, **46**, 145–149.

Bezinge, A., J.P. Perreten and F. Schafer. 1973. Phénomènes du lac glaciaire du Gorner. *IASH Publ.* 95 (Symposium at Cambridge 1969 – *Hydrology of Glaciers*), 65–78.

Blatter, H. and W. Haeberli. 1984. Modelling temperature distribution in Alpine glaciers. *Ann. Glaciol.*, **5**, 18–22.

Bogorodsky, V.V., C.R. Bentley and P.E. Gudmandsen. 1985. *Radioglaciology*. Dordrecht, etc., D. Reidel Publishing Co.

Döscher, A., H.W. Gäggeler, U. Schotterer and M. Schwikowski. 1995. A 130 years deposition record of sulfate, nitrate and chloride from a high-Alpine glacier. *Water, Air, Soil Pollut.*, **85**(2), 603–609.

Eisen, O., U. Nixdorf, L. Keck and D. Wagenbach. 2003. Alpine ice cores and ground penetrating radar: combined investigations for glaciological and climatic interpretations of a cold Alpine ice body. *Tellus*, **55**(5), 1007–1017.

Elliston, G.R. 1973. Water movement through the Gornergletscher. *IASH Publ.* 95 (Symposium at Cambridge 1969 – *Hydrology of Glaciers*), 79–84.

Funk, M., G.H. Gudmundsson and F. Hermann. 1994a. Geometry of the glacier bed of the Unteraarglacier, Bernese Alps, Switzerland. *Z. Gletscherkd. Glazialgeol.*, **30**, 187–194.

Funk, M., K. Echelmeyer and A. Iken. 1994b. Mechanisms of fast flow in Jakobshavns Isbrælig, West Greenland: Part II. Modeling of englacial temperatures. *J. Glaciol.*, **40**(136), 569–585.

Gäggeler, H., H.R. von Gunten, E. Rössler, H. Oeschger and U. Schotterer. 1983. ^{210}Pb-dating of cold Alpine firn/ice cores from Colle Gnifetti, Switzerland. *J. Glaciol.*, **29**(101), 165–177.

Haeberli, W. 1976. Eistemperaturen in den Alpen. *Z. Gletscherkd. Glazialgeol.*, **11**(2), 203–220.

Haeberli, W. and M. Funk. 1991. Borehole temperatures at the Colle Gnifetti core-drilling site (Monte Rosa, Swiss Alps). *J. Glaciol.*, **37**(125), 37–46.

Haeberli, W. and M. Hoelzle. 1995. Application of inventory data for estimating characteristics of and regional climate-change effects on mountain glaciers: a pilot study with the European Alps. *Ann. Glaciol.*, **21**, 206–212.

Haeberli, W., W. Schmid and D. Wagenbach. 1988. On the geometry, flow and age of firn and ice at the Colle Gnifetti core drilling site (Monte Rosa, Swiss Alps). *Z. Gletscherkd. Glazialgeol.*, **24**(1), 1–19.

Hempel, L. and F. Thyssen. 1993. Deep radio echo soundings in the vicinity of GRIP and GISP2 drill sites, Greenland. *Polarforschung*, **62**(1), 11–16.

Huss, M., A. Bauder, M. Werder, M. Funk and R. Hock. 2007. Glacier-dammed lake outburst events of Gornersee, Switzerland. *J. Glaciol.*, **53**(181), 189–200.

Iken, A., K. Fabri and M. Funk. 1996. Water storage and subglacial drainage conditions inferred from borehole measurements on Gornergletscher, Valais, Switzerland. *J. Glaciol.*, **42**(141), 233–248.

Kohnen, H. 1974. The temperature dependence of seismic waves in ice. *J. Glaciol.*, **13**(67), 144–147.

Kovacs, A., A.J. Gow and R.M. Morey. 1995. The in-situ dielectric constant of polar firn revisited. *Cold Reg. Sci. Technol.*, **23**(3), 245–256.

Lüthi, M. and M. Funk. 2000. Dating of ice cores from a high Alpine glacier with a flow model for cold firn. *Ann. Glaciol.*, **31**, 69–79.

Lüthi, M.P. and M. Funk. 2001. Modelling heat flow in a cold, high-altitude glacier: interpretation of measurements from Colle Gnifetti, Swiss Alps. *J. Glaciol.*, **47**(157), 314–324.

Mader, H.M. 1992. The thermal behaviour of the water-vein system in polycrystalline ice. *J. Glaciol.*, **38**(130), 359–374.

Moran, M.L., R.J. Greenfield, S.A. Arcone and A.J. Delaney. 2000. Delineation of a complexly dipping temperate glacier bed using short-pulse radar arrays. *J. Glaciol.*, **46**(153), 274–286.

Narod, B.B. and G.K.C. Clarke. 1994. Miniature high-power impulse transmitter for radio-echo sounding. *J. Glaciol.*, **40**(134), 190–194.

Nye, J.F. 1991. Thermal behaviour of glacier and laboratory ice. *J. Glaciol.*, **37**(127), 401–413.

Oeschger, H., U. Schotterer, B. Stauffer, W. Haeberli and H. Röthlisberger. 1978. First results from Alpine core drilling projects. *Z. Gletscherkd. Glazialgeol.*, **13**(1–2), 193–208.

Paterson, W.S.B. 1994. *The physics of glaciers. Third edition*. Oxford, etc., Elsevier.

Pettersson, R., P. Jansson and P. Holmlund. 2003. Cold surface layer thinning on Storglaciären, Sweden, observed by repeated ground penetrating radar surveys. *J. Geophys. Res.*, **108**(F1), 6004. (10.1029/2003JF000024.)

Pettersson, R., P. Jansson and H. Blatter. 2004. Spatial variability in water content at the cold–temperate transition surface of the polythermal Storglaciären, Sweden. *J. Geophys. Res.*, **109**(F2), F02009. (10.1029/2003JF000110.)

Riesen, P., A. Bauder and O. Eisen. 2006. Dual-frequency radar investigations on an alpine valley glacier. *Geophys. Res. Abstr.* 8, 02289. (1607-7962/gra/EGU06-A-02289.)

Smiraglia, C., V. Maggi, A. Novo, G. Rossi and P. Johnston. 2000. Preliminary results of two ice core drillings on Monte Rosa (Colle Gnifetti and Colle del Lys), Italian Alps. *Geogr. Fís. Din. Quat.*, **23**(2), 165–172.

Sugiyama, S., A. Bauder, P. Weiss and M. Funk. 2007. Reversal of ice motion during the outburst of a glacier-dammed lake on Gornergletscher, Switzerland. *J. Glaciol.*, **53**(181), 172–180.

Suter, S., M. Laternser, W. Haeberli, R. Frauenfelder and M. Hoelzle. 2001. Cold firn and ice of high-altitude glaciers in the Alps: measurements and distribution modelling. *J. Glaciol.*, **47**(156), 85–96.

Wagenbach, D., S. Preunkert, J. Schaefer, W. Jung and L. Tomadin. 1996. Northward transport of Saharan dust recorded in a deep Alpine ice core. *In* Guerzoni, S. and R. Chester, *eds. The impact of African dust across the Mediterranean*. Dordrecht, etc., Kluwer Academic Publishers, 291–300.

Instruments and Methods

Improved method to determine radio-echo sounding reflector depths from ice-core profiles of permittivity and conductivity

Olaf EISEN,[1,2] Frank WILHELMS,[1] Daniel STEINHAGE,[1] Jakob SCHWANDER[3]

[1]*Alfred-Wegener-Institut für Polar- und Meeresforschung, Postfach 120161, D-27515 Bremerhaven, Germany*
E-mail: oeisen@awi-bremerhaven.de
[2]*Versuchsanstalt für Wasserbau, Hydrologie und Glaziologie, Eidgennössische Technische Hochschule, ETH-Zentrum, CH-8092 Zürich, Switzerland*
[3]*Physikalisches Institut, Universität Bern, Sidlerstrasse 5, CH-3012 Bern, Switzerland*

ABSTRACT. We present a technique that modifies and extends down-hole target methods to provide absolute measures of uncertainty in radar-reflector depth of origin. We use ice-core profiles to model wave propagation and reflection, and then cross-correlate the model results with radio-echo sounding (RES) data to identify the depth of reflector events. Stacked traces recorded with RES near the EPICA drill site in Dronning Maud Land, Antarctica, provide reference radargrams, and dielectric properties along the deep ice core form the input data to a forward model of wave propagation that produces synthetic radargrams. Cross-correlations between synthetic and RES radargrams identify differences in propagation wave speed. They are attributed to uncertainties in pure-ice permittivity and are used for calibration. Removing conductivity peaks results in the disappearance of related synthetic reflections and enables the unambiguous relation of electric signatures to RES features. We find that (i) density measurements with γ-attenuation or dielectric profiling are too noisy below the firn–ice transition to allow clear identification of reflections, (ii) single conductivity peaks less than 0.5 m wide cause the majority of prominent reflections beyond a travel time of about 10 μs (~900 m depth) and (iii) some closely spaced conductivity peaks within a range of 1–2 m cannot be resolved within the RES or synthetic data. Our results provide a depth accuracy to allow synchronization of age–depth profiles of ice cores by RES, modeling of isochronous internal structures, and determination of wave speed and of pure-ice properties. The technique successfully operates with dielectric profiling and electrical conductivity measurements, suggesting that it can be applied at other ice cores and drill sites.

1. INTRODUCTION

The interpretation of glacial radio-echo sounding (RES) profiles exploits the distribution of reflected energy with travel time, distinct reflection patterns and the absorption and scattering of the radio waves. Profile features are interpreted to locate the ice–bedrock interface, internal layers and other physical transitions like temperature or crystal structure (see, e.g., Siegert, 1999; Lythe and others, 2001; Dowdeswell and Evans, 2004; Matsuoka and others, 2004a). Over recent decades, the coverage of the Greenland and Antarctic ice sheets with RES has considerably increased and it is being further extended within programs like EPICA (European Project for Ice Coring in Antarctica), ITASE (International Trans-Antarctic Scientific Expedition) and the IPY (International Polar Year) scheduled for 2007/08. The depths of internal reflections are often linked to age–depth profiles established along firn and ice cores or within snow pits to investigate recent patterns of accumulation (Richardson and others, 1997; Nereson and others, 2000; Richardson-Näslund, 2001; Frezzotti and others, 2002; Pälli and others, 2002; Eisen and others, 2004; Spikes and others, 2004; Vaughan and others, 2004; Karlöf and others, 2005; Steinhage and others, 2005) or to short- and long-term glaciological processes (Morse and others, 1998; Fahnestock and others, 2001; Leonard and others, 2004; Siegert and others, 2004). Most importantly for paleoclimate research, several ice-core deep-drilling sites have been (or will be in the near future) stratigraphically linked by RES (e.g. the Antarctic sites Vostok and Dome Concordia (Siegert and others, 1998), EPICA Dronning Maud Land (EDML) and Dome Fuji (Steinhage, unpublished information), and the major Greenland sites GRIP, GISP and NorthGRIP (Dahl-Jensen and others, 1997)). The isochronous properties of most continuous internal reflection horizons detected with RES have the potential to physically link the ice-core profiles, thus providing additional constraints for climatic interpretations. In the context of present research dealing with the evolution of ice sheets and the prediction of their future behavior, spatial age–depth distributions calculated from ice-sheet models (e.g. Clarke and others, 2005) require field data for calibration and validation, which can only be provided by RES profiles.

Although the principal physics and mechanisms underlying RES have been known for a long time (Evans, 1965; Robin and others, 1969; Millar, 1981), improved radar devices and techniques to determine the in situ physical properties have led to progress in understanding the detailed processes that cause reflections. High-resolution data have made it possible to augment the interpretation of ice cores (Jacobel and Hodge, 1995; Dahl-Jensen and others, 1997) and to cross-correlate ice-core profiles and radargrams (Hempel and others, 2000). Improved ice-core profiling has made it feasible to calculate synthetic radargrams by

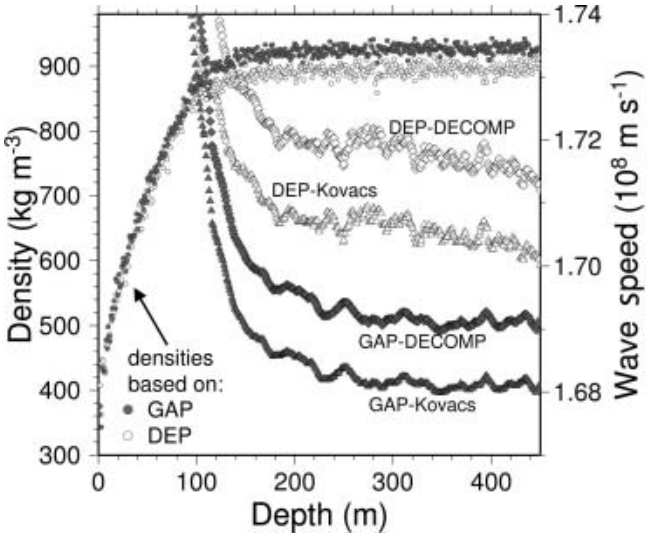

Fig. 1. Distribution of density (circles) and wave speed with depth based on γ-attenuation profiling (GAP; filled symbols) and inverted dielectric profiling (DEP; empty symbols) data in top 450 m of ice core. Densities and wave speeds are filtered over 1 and 10 m bins, respectively, with values displayed in 1 m increments. Conversions of density to wave speed are based on the Kovacs and others (1995) approximation (triangles) and DECOMP (Equation (2)) (diamonds).

forward modeling, focusing on the upper parts of the ice column (Moore, 1988; Miners and others, 1997; Kanagaratnam and others, 2001; Eisen and others, 2003; Kohler and others, 2003), but also employing data over the full length of a deep ice core (Miners and others, 2002).

As all RES systems basically yield the data in the domain of travel time, the conversion of travel time to depth is the essential processing step for all quantitative applications. Naturally, the determination of RES reflector depths involves uncertainties. Uncertainties in age estimates along RES profiles are relatively small in the firn column. However, they increase in the deeper parts, where annual layer thickness decreases. The deeper regions are of special interest, because they harbor the oldest ice and contain the largest expressions of ice dynamics. The improvement of depth estimates of RES reflectors is the topic of this paper.

In general, time–depth conversions are based on measured or assumed distributions of wave speed with depth. The most simple way, widely applied, is to use a constant electromagnetic wave speed for solid ice (e.g. Morse, 1997; Siegert and others, 1998; Fahnestock and others, 2001; Matsuoka and others, 2004a; Vaughan and others, 2004). In some cases a correction for the higher wave speed in the firn column is added, varying with geographic location (Dowdeswell and Evans, 2004). Most direct measurements of wave speeds are derived from ice-core profiles of density or permittivity (Robin and others, 1969; Clough and Bentley, 1970; Kovacs and others, 1995; Richardson and others, 1997; Eisen and others, 2002) or tomography between boreholes or pits (Fortin and Fortier, 2001; Kravchenko and others, 2004). Indirect measurements depend on knowledge of reflector depth and travel time, as is needed for down-hole radar methods (Jezek and Roeloffs, 1983; Clarke and Bentley, 1994), or on a defined survey geometry for wide-angle reflection measurements (Annan and Davis, 1976) and common-midpoint surveys (Fisher and others, 1992; Hempel and others, 2000; Murray and others, 2000; Eisen and others, 2002).

Wave speeds in snow, firn and ice mainly depend on density (Bogorodsky and others, 1985). A recent compilation of the few available wave-speed measurements in ice for the Antarctic continent (Popov and others, 2003), however, demonstrates that a spatial variation on the order of 3% seems to exist. Furthermore, there are various models available that relate density and permittivity, which are used for the conversion of density measured along an ice core to wave speed. The determination of wave speed from ice-core measurements depends sensitively on the choice made and the device used for density measurements because results differ on the order of 1% (Fig. 1). Any uncertainties in wave speed from density or permittivity translate to a relative uncertainty in depth, which implies an increasing absolute error with travel time and depth. For deep reflections depth errors can therefore be large enough to significantly influence the geophysical interpretation. Among the methods mentioned above, the down-hole radar technique is the only means that directly establishes a time–depth relationship without using information of wave-speed distribution. Therefore, it has to be considered the most accurate method. All other approaches indirectly relate time to depth by integrating a wave-speed distribution, and are thus subject to cumulating errors with depth.

The objective of this paper is to develop a new accurate method to determine the depth of RES reflections. We feed ice-core data to a numerical model of electromagnetic wave propagation to generate synthetic radargrams, and then cross-correlate the radargrams with RES profiles to determine depths. In this way we avoid the propagation of errors in wave speed that may be introduced by first determining the wave-speed distribution and then integrating it to relate travel time and depths. We test our method with data from EPICA in Dronning Maud Land (75° S, 0° E), where 2565 m of a deep ice core (EDML) had been retrieved by 2004, with about 210 m left to bedrock. Physical properties are available from dielectric profiling (DEP) (Moore and Paren, 1987) to provide permittivity and conductivity for RES interpretation. From sensitivity studies we identify the origin of depths of unambiguous, distinct reflection characteristics present in the RES and synthetic radargrams. These are then linked to the observed travel time of the reflection. Thus, in principle, our approach is comparable to down-hole target techniques.

We find that single conductivity peaks are mostly responsible for individual reflections, especially in the intermediate and deeper parts of the ice sheet. This is contrary to earlier findings, that only closely spaced boundaries of dielectric interfaces lead to internal reflections at greater depth in ice sheets (Millar, 1982; Siegert and others, 1998) and similar implications for ice streams (Jacobel and others, 1993). By-products are in situ permittivity of pure ice and mean wave speed.

We first introduce the ice-core measurements, followed by a description of the RES data and the modeling approach, including a detailed layout of several processing steps for the input data. The main part of the paper treats the identification of reflector depths by sensitivity studies and discusses the results. Utilization of permittivity and conductivity profiles measured with different devices leads us to the conclusion that the method can also be applied at other sites.

2. ICE-CORE MEASUREMENTS

In the field γ-attenuation profiling (GAP) and DEP were used to simultaneously measure density and dielectric properties along the EDML ice core. The system and bench fixture, performance and measurement uncertainties are described by Wilhelms (2000). Electrical conductivity measurements (ECM) (Hammer, 1980) were performed along the EDML ice core during ice-core processing and cutting in the cold room after the core was transported to the Alfred Wegener Institute in Bremerhaven, Germany.

2.1. GAP (γ-attenuation profiling)

The absorption and scattering of γ-rays originating from a radioactive source (^{137}Cs) and passing in the transverse direction through the ice core to the detector (Wilhelms, 1996, 2000) are used for γ-attenuation profiling. The radiation is monochromatic and thus the mass absorption coefficient is known with 0.1% relative error. The statistical intensity measurement errors of the free-air reference and at each sampling position are determined from direct analysis of the recorded data collection of at least 20 measurements. The calibrated detector signal is corrected for variations in core diameter. Furthermore, the possible influence at maximum misalignment of the core within the bench is estimated and a propagation of error is performed for each single measurement. The precision of the density measurement is typically in the range 0.006–0.01 g cm^{-3} for a 100 mm diameter core. Unreliable data in the vicinity of core breaks are removed from the dataset. Along the EDML ice-core density was measured to 450 m depth in 5 mm increments (Fig. 1).

2.2. DEP (dielectric profiling)

We express the complex parts of the relative dielectric permittivity as

$$\varepsilon^* = \varepsilon' - \mathrm{i}\varepsilon'', \tag{1}$$

where the real part, ε', is the ordinary relative permittivity of the medium. The imaginary part, the dielectric loss factor, is related to conductivity, σ, and radian frequency, ω, by $\varepsilon'' = \sigma(\varepsilon_0\omega)^{-1}$, where ε_0 is the permittivity of free space. Both parts of ε^* can be determined with DEP (Moore and Paren, 1987). An improved DEP scanner (Wilhelms, 2000), operating at 250 kHz, was used over the full depth of the EDML ice core (2565.55 m). The upper 12.6 m of the dataset are missing because of the operational set-up of the deep drilling. They are replaced by adjusted profiles of the shallow ice core B32, located 1.5 km to the west. The calibrated DEP record is corrected for variations in core diameter and temperature. Unreliable data in the vicinity of core breaks, as for GAP, are removed. The correct interpretation of DEP requires that the effects of mixing of air and ice are taken into account. This is done by applying the formula for density and conductivity mixed permittivity (Wilhelms, 2005) explained below.

2.3. ECM (electrical conductivity measurements)

ECM is essentially a measure of d.c. conductance. It has traditionally been carried out by dragging a pair of electrodes with a high voltage between them along a core, and measuring the current between the electrodes (Hammer, 1980; Neftel and others, 1985). A new ECM system, developed at the University of Bern, was used in the field at Dome Concordia (Wolff and others, 1999) and later in the laboratory for measuring the EDML ice core. In brief, a flat surface is prepared in the ice-core processing line along its full length using a horizontal band-saw and a microtome knife. The electrode assembly consists of seven electrodes at an inter-electrode spacing of 8 mm across the core. The electrodes are made of a carbon-doped silicon rubber. They are lowered onto the flat surface of the core and 350 V is applied across each adjacent pair of electrodes in turn. The current between the electrodes is sampled at regular intervals after a settling time, and averaged. The electrodes are lifted and moved 1 mm along the core and the sequence is repeated. This procedure yields six sets of data at 1 mm resolution. The data presented here are averaged over 10 mm and corrected to –15°C. Documented major core breaks and ends are removed from the ECM record. To date, corrected ECM data are available along the EDML ice core from 113.01 to 2563.98 m depth.

2.4. DECOMP (density and conductivity mixed permittivity)

Kovacs and others (1995) match a comprehensive dataset with a simple empirical formula relating the ordinary relative permittivity ε' to density ρ: $\varepsilon' = (1 + 0.845\rho)^2$. They obtain a standard error of ± 0.031 for ε', about 1% of the permittivity of pure ice (i.e. ice without bubbles and impurities). Looyenga (1965) derives a theoretical mixing model for air distributed in a dielectric medium based on spherical approximations of bubbles. Extension of his relation to complex space (Wilhelms, 2005) leads to

$$\varepsilon^{*1/3} = \frac{\rho}{\rho_{\mathrm{ice}}}\left[\left(\varepsilon'_{\mathrm{ice}} - \mathrm{i}\frac{\sigma_{\mathrm{ice}}}{\omega\varepsilon_0}\right)^{1/3} - 1\right] + 1, \tag{2}$$

where the subscript 'ice' refers to values of the pure-ice (i.e. bubble-free) volume fraction, taking into account impurities that contribute to conductivity, like acids. Variables without a subscript refer to bulk values of the ice–air mixture. Wilhelms (2005) demonstrates that neglect of complex mixing for the density–permittivity relation could result in significant errors in ε^*. Combination of γ-attenuation density and DEP data for the upper 450 m of the EDML core, analogously to Wilhelms (2005), yields $\varepsilon'_{\mathrm{ice}} = 3.094$ and $\rho_{\mathrm{ice}} = 926\,\mathrm{kg\,m^{-3}}$. Based on these values for the pure-ice fraction, which are the most consistent available for our site, we numerically invert Equation (2) to derive density and conductivity from the DEP measurements at 250 kHz (Fig. 1). Directly applying Equation (2) to the inverted DEP density and conductivity yields ε^* at 150 MHz, assuming that ε' does not change with frequency. This is done for the combinations of density (GAP and DEP) and DEP conductivity shown in Table 1. Each combination serves as input to a run of the wave-propagation model described below and results in a synthetic trace, designated S_i ($i = 1, \ldots, 5$) (Table 1). For ice, a Debye relaxation occurs below 10 kHz (Bittelli and others, 2004). Its tail causes a tiny frequency dependence of complex permittivity ε^* in the MHz range (Fujita and others, 2000, figs 2 and 3). Our calibration of the pure-ice permittivity described later implicitly takes care of this small effect for ε'. Moreover, Equation (2) suffices to scale the conductivity with frequency, as the Debye relaxation frequency has been found to be constant near and at conductivity peaks (Wilhelms, unpublished data).

Table 1. Description of radargram origin

	Density	Conductivity	ε'_{ice}	$l\langle\varepsilon'\rangle$ m	σ peaks
Synthetic radargram					
S_1	DEP	DEP	3.09	0.2	–
S_2	GAP	DEP	3.09	0.2	–
S_3	DEP	DEP	3.09	20	–
S'_3	DEP	DEP	3.20	20	–
$\tilde{S}'_3$	DEP	DEP	3.20	20	li
S_4	GAP	DEP	3.09	20	–
S_5	DEP	ECM	3.09	20	–
S'_5	DEP	ECM	3.20	20	–
$\tilde{S}'_5$	DEP	ECM	3.20	20	li
Reference radargram					
R_1	trace 4204 of airborne RES profile 023150				
R_2	stack of ground-based RES profile 033042				

Notes: Plain symbols, S_i, imply $\varepsilon' = 3.09$; primed symbols, S'_i, imply $\varepsilon' = 3.20$; symbols with a tilde, $\tilde{S}'_i$, and li indicate that selected conductivity peaks in ε'' are removed and the gaps are linearly interpolated for the sensitivity studies; $l\langle\varepsilon'\rangle$indicates the filter length for ε'. Details are given in the text.

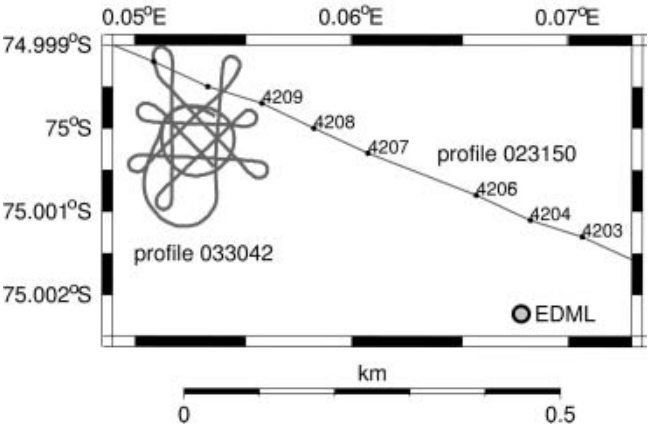

Fig. 2. Location of airborne profile 023150 and of ground-recorded profile 033042. The numbers refer to 10-fold stacked traces along profile 023150. The circle indicates the position of the EPICA drilling site. Reference radargram R_1 corresponds to trace number 4204, which is closest to the drilling site. R_2 is calculated from stacking all ~14 000 traces of profile 033042.

ECM measurements along the EDML core were not carried out simultaneously with GAP and DEP, therefore restricting the use of Equation (2). An exact transfer of measured d.c.-ECM conductivity values to the frequency of radio waves requires knowledge of chemical composition and frequency-dependent properties of the constituents (Moore and others, 1992, 1994). Moreover, ECM is not a direct measure of electrical d.c. conductivity, as currents depend on the contact area of the electrodes which is difficult to keep constant, and are predominantly influenced by the conductivity in the vicinity of the contact area. ECM currents are also affected by electrode polarization (Maidique and others, 1971). For our 'proof-of-concept' study, which is based on conductivity changes rather than on the absolute values, we choose a simpler approach. We scale the ECM record so that the mean ECM conductivity equals the mean DEP conductivity, the latter corrected for dielectric mixing and transferred to the MHz range, so that their means agree over the whole depth range. For all model runs S_5 (Table 1) the DEP-conductivity data are then replaced by the scaled ECM-conductivity record.

3. LINKING RES DATA TO ICE-CORE PROFILES

Based on combinations of the above ice-core records we calculate synthetic radargrams. After calibrating in situ properties of the pure-ice fraction within their uncertainty range by comparing the synthetic radargrams to measured RES reference data, we perform sensitivity studies to identify the origin of individual reflections.

3.1. Reference radargrams from airborne RES

We use RES data obtained with the Alfred Wegener Institute airborne system operated on the *Polar2*, a Dornier 228-101 aircraft, from Antarctic seasons 2002 and 2003. The system generates a 150 MHz burst of 60 ns duration with a peak power of 1.6 kW and 20 MHz bandwidth (Nixdorf and others, 1999). The receiver system includes a logarithmic amplifier and rectifies the received signal, i.e. the phase information is not recovered. An analog-to-digital converter samples at an interval of 13.33 ns and records over a window of 50 μs. Two hundred consecutive traces are stacked and the averaged traces are stored on tape. The overall system performance figure is 190 dB. During airborne surveys the ground speed is 65 m s^{-1} (130 knots), resulting in a trace spacing of 6.5 m (Nixdorf and others, 1999).

Two RES profiles are considered, the locations of which are displayed in Figure 2. Profile 023150 was recorded during flight at an altitude of 450 m. It runs parallel to the ice divide in an east-southeast–west-northwest direction and passes the drilling location at a distance of ~100 m to the north-northeast. Horizontal stacking was applied to ensembles of ten consecutive traces stored on tape. The stacked trace 4204 is used as reference radargram R_1. To provide a higher spatial coverage and at the same time avoid uncertainties in the orientations of the airplane during flight, profile 033042 was recorded with the airplane sliding on the ground. An area of 200 × 300 m^2 about 500 m west-northwest of the drilling site was covered with some 14 000 traces recorded with multiple orientations of the airplane. Stacking of all traces results in the reference radargram R_2. No additional filtering or gain control is applied to the RES data. The reference radargrams $R_{1,2}$ (Fig. 3) are shifted in time such that their first break (the reflection from the surface) occurs at 0. We omit the time interval 0–2 μs as the strength of the surface reflection saturated the RES system receiver.

It is obvious from Figure 3 that the signal-to-noise ratio (SNR) in R_2 is remarkably lower than in R_1 because of the much higher stacking coverage. Despite the higher SNR, maximum amplitudes of reflections are slightly lower than for R_1 for two reasons. First, the profile 033042 covers an area that is larger than the first Fresnel zone of the transmitted wave. Second, the stacked traces were recorded with different antenna orientations, and thus did not take account of the anisotropic and birefringent properties of the ice (Hargreaves, 1978; Fujita and others, 2000). Both these contribute to destructive interference and thus lower

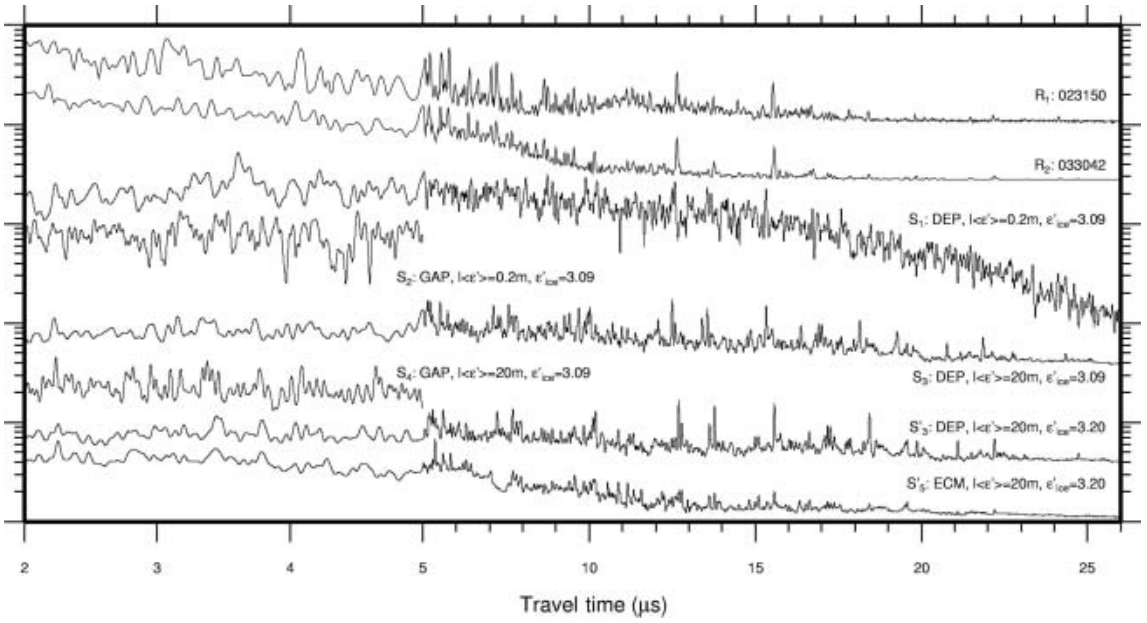

Fig. 3. Comparison of RES- and FD-radargram envelopes on a logarithmic scale (arbitrary units). From top to bottom: trace 4204 of profile 023150 (R_1); 14 000-trace stack of profile 033042 (R_2); nomenclature of synthetic radargrams (Table 1): plain symbols, S_i: $\varepsilon' = 3.09$; primed symbols, S'_i: $\varepsilon' = 3.20$; $l\langle\varepsilon'\rangle$ indicates the filter length for ε'; specifically: S_1 and S_2 are based on DEP and GAP profiles, respectively, and using $\varepsilon'_{\mathrm{ice}} = 3.094$ and a 0.2 m running mean filter applied to ε' (indicated by $l\langle\varepsilon'\rangle$); S_3 and S_4, which are the same as S_1 and S_2, respectively, but with a 20 m running mean filter applied to ε'; S'_3,which is the same as S_3, but using $\varepsilon'_{\mathrm{ice}} = 3.20$; and S'_5 based on DEP-density and ECM-conductivity profiles with $\varepsilon'_{\mathrm{ice}} = 3.20$ and $l\langle\varepsilon'\rangle = 20$ m. The magnitude of the synthetic radargrams is linearly scaled with travel time to compensate for the logarithmic pre-amplification of the RES system. Note the different scale of the 2–5 μs (the length of the GAP record) and 5–20 μs range.

amplitudes. At times >18 μs the reflections are very close to the system noise level, and result in a lower boundary in amplitude with no further decrease with travel time. In this interval, several reflections can be more clearly identified in R_2 than in R_1. Within each radargram a reflection maximum can be located with an uncertainty of one sample interval (±13 ns). The position of numerous major reflections, rising more than three times above the surrounding magnitude and present in each reference radargram, are in very good agreement with each other. The remaining differences in travel times of temporally corresponding reflections in R_1 and R_2 are most likely caused by the 0.5 km separation of the locations. For the differences in travel time we obtain $0 \geq \Delta t_{R_2-R_1} \geq -50$ ns for travel times less than 10 μs, that is reflections of R_1 occur slightly later than those of R_2. For travel times beyond 20 μs, $0 \leq \Delta t_{R_2-R_1} \leq 80$ ns, reflections of R_1 occur earlier than those of R_2.

3.2. Calculation of synthetic radargrams

We use a one-dimensional version of the parallelized finite-difference (FD) time-domain model successfully applied to the simulation of shallow ground-penetrating radar radargrams by Eisen and others (2003), which are based on the staggered-grid formulation of Maxwell's curl equations (Yee, 1966). The model operates with a spatial increment of 0.02 m and a time-step of 0.02 ns, ensuring numerical stability and dispersion criteria (Eisen and others, 2003). The data domain extends from 0 to 2565 m (the ice-core length). The model domain is chosen large enough that reflections from the model boundaries do not interfere with physical reflections caused by ice-core properties. Profiles of ε^* at 150 MHz serve as model input, which are calculated from different combinations of DEP-, GAP- and ECM-based permittivity and conductivity data introduced above (Table 1).

The rectification and logarithmic amplification of the RES receiver signal prevents the phase retrieval of the signal transmitted into the ice. Theoretically, the 60 ns burst should contain nine sinusoidal waves of 150 MHz. Hardware-related finite rise and decay times of the burst-trigger switches, common for RES transmitters (Matsuoka and others, 2004b), and the limited bandwidth of the transmitter antenna (Nixdorf and others, 1999) lead to signal broadening and changes in the frequency spectrum. This is evident from the envelope shape of the received reflection from the air–ice interface. It has a total width of roughly 140 ns at half maximum, i.e. more than twice the theoretical pulse length (which partly results from reverberations of the surface).

Radargrams produced by wave-propagation modeling as well as real measurements are sensitive to the transmitted signal (e.g. Miners, 1998). Especially long wavelets easily lead to interference and reduced resolution; in the worst case even destructive interference. Unfortunately, the exact characteristics of the radiated wavelet of the airborne system are unknown. We have two aims: first, our main concern is to identify the depth of origin of a reflector at high resolution; and, second, we aim to determine the type of physical signal that causes the reflection. For the first aim a short synthetic source pulse should be used, as a long one could cause a degradation in the quality of the synthetic radargrams, which do not occur in the real measurements. However, our second aim requires a longer pulse, as a short one (e.g. a Ricker wavelet) could not reproduce the physical smoothing effect, i.e. interference, of a longer pulse. As a trade-off we use a synthetic wavelet consisting of only 2.5 150 MHz cycles of unit amplitude for modeling. In addition,

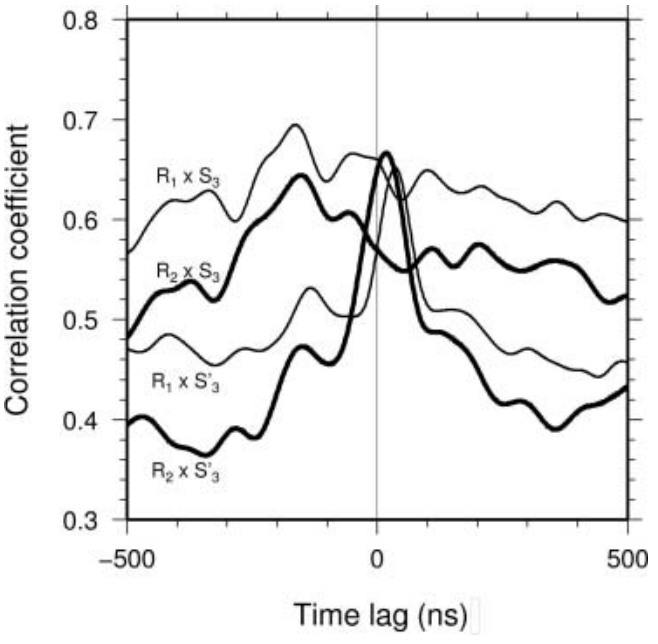

Fig. 4. Cross-correlation functions of S_3 ($\varepsilon'_{ice} = 3.094$) and S'_3 ($\varepsilon'_{ice} = 3.20$) with R_1 (thin line) and R_2 (thick line) for the time interval 10–26 μs with a maximum lag of ±500 ns.

half-wavelength oscillations of lower amplitude are added that precede and follow the synthetic wavelet, as is typical for burst and pulse radar systems (Miners and others, 2002).

The following processing steps could be regarded as a filtering procedure that aims to conciliate our apparently incompatible aims. To synchronize the occurrence of maximum power of the RES direct coupling signal and the synthetic transmitter signal, the FD radargrams are shifted by +0.1 μs. Further processing includes application of a Hilbert magnitude transformation to the synthetic radargrams to obtain envelopes. Additional smoothing with a 100 ns Gaussian running mean filter adjusts the visual effect of the shorter FD-source signal to that of the broader RES reflection characteristics.

To reduce the effect of differences in resolution and statistical uncertainty of the various ice-core measuring devices on the synthetic results discussed below, we first apply a 2 cm running mean to all input data. This filter length is below the typical peak width of conductivity signals (e.g. from volcanic eruptions). Statistical noise is thus reduced, but the signal is preserved. The characteristics of ε' show fluctuations at scales of centimeters to decimeters. As will be shown next, these are related to the measurements so that additional filtering is necessary to recover the reflections present in the RES reference radargrams.

3.3. RES vs FD: the role of ε'

Over the whole travel-time range of 2–26 μs the comparison of the synthetic radargram S_1 calculated from DEP data, with an additional 0.2 m running mean filter applied to ε' (Table 1), shows few features in common with the RES reference radargrams $R_{1,2}$ (Fig. 3). However, the synthetic radargram S_3, based on ε' data filtered with a 20 m window and ε'' data with a 0.02 m running mean, contains several events which are found in both reference radargrams. The higher variability in S_1 reflectivity relative to that of radargram S_3 implies that the density signal underlying S_1 is too noisy to reproduce reflections present in RES radargrams. Moreover, the stronger decrease of reflected magnitude in S_1 with travel time beyond 10 μs in comparison to S_3 indicates that the unrealistic noise present in ε' produces higher reflection loss, meaning that less energy is transmitted to deeper ice.

A second set of numerical modeling runs based on the GAP-density and DEP-conductivity records in the depth range 0–450 m (a time range of 5 μs) produces the same result (S_2 and S_4 in Fig. 3). Despite the different origin of the GAP-density data, low-pass filtering on the order of tens of meters of ε' (S_4) is necessary to achieve an agreement in the reflection pattern, with the synthetic radargram S_3, as well as the reference radargrams R_1 and R_2. Therefore density signals derived from either DEP or GAP contain too much noise to reproduce radargrams with a sufficiently high SNR for regions below the firn–ice transition, in a depth range where conductivity signals become important. In the remaining part of the paper we consequently restrict our RES–FD comparison to synthetic data for which ε' has been filtered over 20 m. Note that the smoothing has a negligible influence on the travel-time–depth relation (which depends on integrated ε'); it merely improves the quality of reproduced reflections.

3.4. RES vs FD: characteristic peaks and time shift

A number of reflection patterns visible in the RES reference radargrams R_1 and R_2 are reproduced in the synthetic radargram S_3 (Fig. 3). However, the synthetic reflections in S_3, which is based on $\varepsilon'_{ice} = 3.094$, occur earlier than the corresponding RES signals. To reduce this systematic time shift we model another set of synthetic radargrams S'_i, $i = 3, 5$ (Fig. 3), based on ε^* calculated with $\varepsilon'_{ice} = 3.20$ in the forward mixing application at 150 MHz of the DECOMP formula (2). Possible reasons for this observation will be discussed below.

A cross-correlation analysis of the synthetic radargrams with the reference radargrams (denoted by $S \times R$) for the time interval 10–26 μs demonstrates the improved agreement (Fig. 4). (As density variations contribute to reflections down to 10 μs, extending the cross-correlation to shorter travel times includes the uncertainty related to density measurements and leads to less clear results, but is nevertheless feasible.) Prior to cross-correlation all synthetic and RES radargrams are unified to a common sample interval of 1 ns by linear interpolation. The cross-correlation is applied to the logarithmic magnitudes, which are, in the case of the synthetic radargrams, linearly scaled with time to compensate for the RES system's pre-amplification, and for the progressive decrease of magnitudes caused by geometric spreading and losses. The cross-correlation function of $S_3 \times R_1$ and $S_3 \times R_2$ has a broad maximum (Fig. 4). S_3 leads R_1 and R_2 by 164 and 153 ns, with correlation maxima of 0.69 and 0.65, respectively. The cross-correlation of $S'_3 \times R_1$ and $S'_3 \times R_2$ results in slightly changed maximum correlation coefficients of 0.64 and 0.66, respectively. However, the time shift now changes to a lag of S'_3 with respect to R_1 and R_2 of 36 and 12 ns, respectively, that is only 1–3 RES sample points. Moreover, the cross-correlation function related to S'_3 shows a more pronounced peak of maximum correlation than is the case for S_3. Based on these results, the in situ travel time underlying the RES radargrams appears to be about 1.6% lower than that arising from the ice-core data in

the synthetic radargrams. To identify the originating depth of reflections, our main goal, we use ice-core data processed with $\varepsilon'_{ice} = 3.20$ for our further modeling. The related synthetic traces are marked with primed symbols (S'_i, where only $i = 3$ and 5 will be used; see Table 1).

Several sections of S'_3 show exceptionally good agreement with R_1 and R_2 (Fig. 5) Most prominent are the series of signals at 5–6 μs and 19.5–20.5 μs, the double peaks at 12.6 and 13.7 μs, and the single events at 7.2, 7.7, 10.2, 15.5, 18.4, 22.1 and 24.7 μs. Not only do the times of the reflections correspond to each other, in several cases their structures are also similar. For example, the narrow double peak at 12.6 μs, almost at the limit of temporal resolution in the RES radargrams, is reproduced in the synthetic radargram. Distressingly, the synthetic reflection at 21.1 μs occurring in S'_3 has no counterpart in R_1 or R_2. Possible reasons are discussed at the end of section 4.3.

To investigate the reproducibility of the above comparison based on DEP conductivity, we calculate another synthetic radargram, based on ECM conductivity (S'_5; Table 1). The reflection sequences (Figs 3 and 5) are in general very similar to S'_3, especially at 5–6, 7.7, 10–12, 12.6, 13.8, 15.5, 18.4, 19.5 and 22.1 μs. However, the reflections resulting from ECM conductivity are less significantly greater than the background variability, compared to the reflections from DEP conductivity (e.g. at 12.6 and 15.5 μs). The low amplitudes of S'_5 around 7.3 μs are caused by missing ECM data. The reflections produced by DEP conductivity at 19.8–20.5 and 24.7 μs are not reproduced by the ECM conductivity.

4. RESULTS AND DISCUSSION

4.1. Depth and type of reflector origin

Having identified a number of reflections in the reference radargrams that are reproduced in the synthetic radargrams, we now proceed to determine the physical origin of the synthetic peaks, and thus their originating depth. A correlation between conductivity and reflections has been demonstrated by other studies (Hempel and others, 2000; Miners and others, 2002). We therefore test if individual conductivity peaks present in the DEP and ECM data are also responsible for the strong reflections. (Remember that the permittivity for all S_3 radargrams is smoothed so that all synthetic reflections should be caused only by conductivity signals.) A number of strong conductivity peaks in the ε^* profile are removed (Table 2). The gaps are then closed by linear interpolation (Fig. 6). All of the considered conductivity peaks rise about 2–5 times above the background conductivity of ~10 μS m^{-1}, are less than 0.5 m wide and are most likely of volcanic origin. The synthetic radargrams calculated from these data with truncated conductivity peaks (denoted with a tilde, $\tilde{S}'_3$ and $\tilde{S}'_5$) lack a number of the prominent reflections present in S'_3 and S'_5, respectively, which have counterparts in the RES radargrams (Fig. 5). For $\tilde{S}'_3$, clear correspondence occurs for the reflections at 7.2, 7.7, 12.6, 13.7, 15.5, 18.4, 22.1 and 24.7 μs. In these unambiguous cases the good agreement between synthetic and reference radargrams and the identification of reflection origins enables us to relate the travel time observed in the RES radargrams to the depth of the removed single conductivity peaks. For $\tilde{S}'_5$, the agreement and effect of the truncation is somewhat different. Unambiguous cases occur

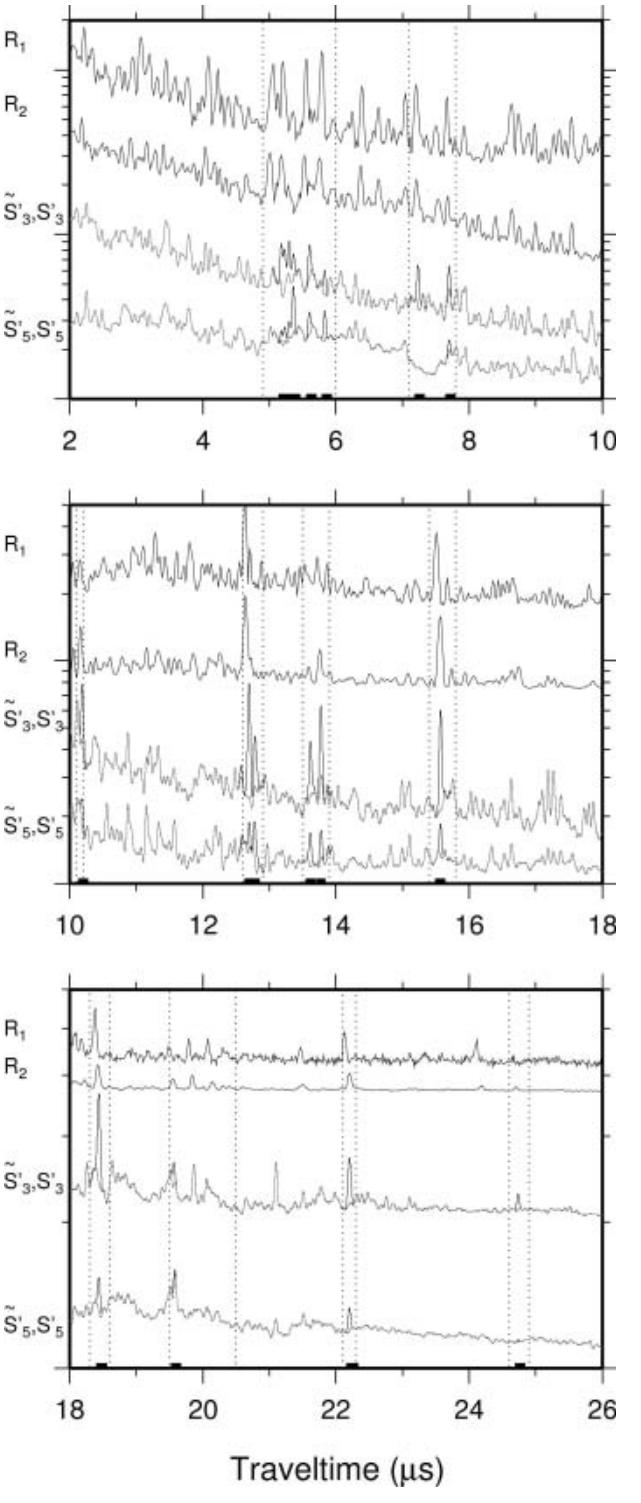

Fig. 5. Comparison of RES- and FD-radargram envelopes on a logarithmic scale in arbitrary units. For nomenclature of FD radargrams see Table 1. On top of S'_3 (black) radargram $\tilde{S}'_3$ (gray) is plotted. Reflections not present in $\tilde{S}'_3$ therefore appear black. The same is the case for S'_5 and $\tilde{S}'_5$. Dominant reflections mentioned in the text are enframed by gray dotted lines. Black boxes on the *x* axis indicate truncated conductivity peaks used in $\tilde{S}'_3$ and $\tilde{S}'_5$. No time-variant scaling is applied above 18 μs. Beyond 18 μs the square root of S'_i magnitudes multiplied by travel time is displayed to compensate for logarithmic pre-amplification and decreasing SNR of the reference radargrams.

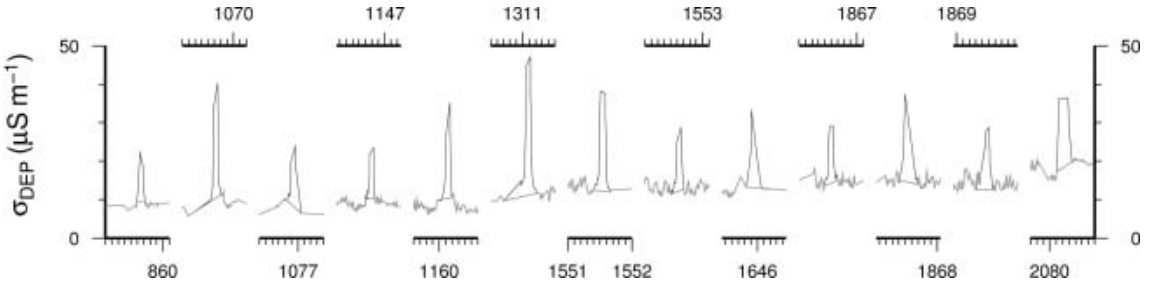

Fig. 6. DEP-conductivity peaks (black) for the depth range 800–2100 m (~10–25 μs), considered in the sensitivity study to calculate $\tilde{S}_3'$ for comparison with S_3'. The peaks are removed and the gaps subsequently linearly interpolated (gray), plotted on top of the original curve. Each *x*-axis segment covers 1 m depth with ticks every 0.1 m.

at 12.6 and 19.5 μs. The RES travel times are taken from R_1, as this radargram stems from a continuous long-distance profile which is closest to EDML, in contrast to the spatially confined radargram R_2. We determine the travel time at maximum amplitudes for ten reflections (Table 2). They are accurate with respect to other reflections to within one sample interval, in our case 13 ns.

Two observations indicate not only that single large conductivity peaks cause reflections, but that constructive interference between reflected signals also occurs. The reflections at 18.4 and 22.1 μs require that a series of two and three conductivity peaks, respectively, has to be truncated to completely remove the reflections (Table 2). Interpolation of only one peak of the series merely results in a reduced amplitude of the corresponding reflection. In other cases, the truncation of conductivity peaks does not lead to a significant change in the reflection structure. For instance, the reflection sequence in the range 5–6 μs, the three broad reflections from 19.5 to 20.5 μs and the single reflection at 10.2 μs.

4.2. Error analysis

The accuracy of the established travel-time–depth relations differs for the different types of reflections selected here. According to Ricker's criterion for resolution limits, two signals can be resolved if the separation of their maxima is larger than the full width at half maximum. The RES reflections typically have a full width at half maximum of some 50 ns travel time, which corresponds to about 4 m depth in solid ice. For the processed synthetic traces this value is around 25 ns or 2 m, the higher accuracy because of the shorter source wavelet. Where a single strong conductivity peak causes a synthetic reflection which is in accordance with the RES radargrams, the relation of reflection travel time and reflector depth is unambiguous. The centers of the conductivity peaks in the DEP profile are taken as the depths of origin of the reflections, and the peak width determines the accuracy in depth (Table 2). As all conductivity peaks are less than 0.5 m wide, the error of the depth estimate is less than ±0.5 m. This accuracy cannot be achieved for reflections stemming from constructive interference occurring at closely spaced conductivity peaks, such that the resolution criterion given above is not fulfilled. Nevertheless, it is still possible to pin down the depth of origin, though with a larger uncertainty. The two conductivity peaks related to the reflection at 18.4 μs are separated by 1.1 m and together cover a total depth range of 1.3 m, implying a depth estimate accurate to within ±0.7 m. The series of three peaks from 1866.5 to 1869.6 m are separated by at most 1.9 m and cover a range of 3.1 m, which is still smaller than the possible resolution of the RES radargrams. In other cases, for instance for the groups of reflections around 5.3 and 19.5–20.5 μs, several meters of the conductivity profile have to be truncated to completely remove the reflection signature. The uncertainty of the depth estimates in these cases ranges from 2 to 5 m, depending on the profile structure.

4.2.1. Inferences on physical properties

The mean wave speeds are calculated from the surface to the reflector depths, and show a small minimum at intermediate depth (Table 2). In addition to travel-time uncertainties, the logged ice-core depth is subject to errors which enter the wave-speed estimates. They mainly arise from hole inclination, core relaxation, temperature dependence of measuring devices and lost core fraction. Although the individual errors are small, logging-depth errors could add up to meters over an ice core of several kilometers. The wave speeds have an accuracy of better than 3×10^5 m s^{-1} in the case of a single conductivity peak as reflection origin. The uncertainty increases to up to 7×10^5 m s^{-1} if the depth of origin is less clear, either due to ambiguities in the reflection pattern or large errors in logging depth. A thorough discussion of the wave-speed–depth profile and errors requires comparison with logged temperature and crystal orientation fabric data, which is beyond the scope of this paper.

Our results rely on the correlation between reflections in RES and synthetic radargrams. Apart from manual inspection, the cross-correlation analysis shows that correction of ε'_{ice} from 3.094 to 3.20 leads to improved agreement between the reflection patterns. An exact match of RES and synthetic radargrams was possible for a slightly different value of ε'_{ice}, along with a zero time-lag of the cross-correlation function, but it does not change our results and is not necessary for the purpose of this study. The most comprehensive compilation to date of dielectric properties of ice, by Fujita and others (2000), indicates that at 150 MHz only the poorly documented data of W.B. Westphal is available as a laboratory reference. Measurements of artificial and natural single crystal and polycrystalline ice at lower frequencies allow a range of 3.14–3.23 (Fujita and others, 2000). However, indirect deductions from travel times as summarized by Bogorodsky and others (1985, table IX) and Popov and others (2003) indicate that our value of 3.09 is comparable to other estimates. This is supported by the work of Kravchenko and others (2004), who found from

tomography at the South Pole a refractive index of 1.76 ± 0.03 (equal to a permittivity of 3.09) at 150 m depth (although bubbles are still present at this depth). The systematic difference in the ε'_{ice} values from the two methods used here could arise from various technical, physical or methodological factors. For the sake of completeness we briefly discuss possible reasons for the observed variation.

4.2.2. Error in ice-core data

Calculation of the synthetic radargrams fundamentally depends on the ice-core properties. Wilhelms (2005) derived a systematic uncertainty on the order of 1% for ε'_{ice}. Reasons for this uncertainty are the accuracy of the GAP and DEP devices as well as inversion of the DECOMP formula. The application of forward mixing includes the transfer of the dielectric properties from 250 kHz to 150 MHz. Frequency dependence and the slightly anisotropic behavior of ice has been observed and studied by different authors (see Fujita and others, 2000, for a summary). Frequency dependence of dielectric anisotropy is well known, although a gap exists in the MHz range. At 252 K, ε' values perpendicular (parallel) to the c axis are 3.18 (3.21) at 1 MHz and 3.13 (3.16) at 9.7 GHz (Fujita and others, 2000). For a temperature increase of 40 K both components increase on the order of 1% for the temperature ranges observed in ice sheets (Fujita and others, 2000). The applied frequency scaling could, in principle, also contribute to the observed difference in ε'_{ice} of the methods applied here, although the relaxation frequency of ice is below 10 kHz (Bittelli and others, 2004) and should have a negligible influence in the MHz range. In any case, neglecting relaxation would have the opposite effect, namely lead to an overestimated permittivity.

4.2.3. System errors

The reference radargrams depend on the RES system properties. The statistical variation of the length of a sample interval of the RES system is reduced to below 0.5% by the system's 200-fold averaging procedure for each stored trace. However, we cannot exclude a small dependence on operation temperature and ambient pressure. Prior to and after ice-sheet campaigns, the RES system's calibration is checked with mirror flights over sea ice and open water by comparing RES and radar-altimetry altitudes. Differences are around 0.5%.

4.2.4. Geometrical errors

Logging depths are subject to small uncertainties, as mentioned above, and the internal structure is not parallel to the surface, but has small gradients of 0–0.04. The separation of R_1 and EDML by ~100 m results in small differences between the reflector depths determined from the EDML profiles and the real depths of origin of the matched reflections at the site of R_1. The same is, of course, true for R_2. To completely explain the observed difference by sloping internal layers, however, would require the depth at the location of R_1 to be more than 1% higher. This corresponds to a slope >0.2, which is not observed.

Unfortunately, we cannot provide a final physical interpretation because of the various systematic and partly unknown measurement uncertainties involved. We have to assume that several of the above factors contribute to the difference.

Table 2. Travel-time–depth relationship for selected reflections from trace R_1

Travel time	Width	Depth range	Peak width	Mean wave speed
ns	ns	m	m	$\times 10^8$ m s^{-1}
Single peak				
7201	75	611.0–611.4	0.4	1.698
7665	55	650.1–650.4	0.3	1.697
12 628	55	1069.6–1069.8	0.2	1.694
12 709	45	1076.8–1077.0	0.2	1.695
13 527	45	1146.6–1146.9	0.3	1.696
13 716	50	1160.0–1160.2	0.2	1.692
15 502	75	1310.8–1311.2	0.4	1.691
24 666	20	2080.0–2080.4	0.4	1.687
Double peak				
18 385	50	1551.4–1551.6	0.2	1.688
		1552.5–1552.7	0.2	1.689
Triple peak				
22 128	50	1866.5–1866.7	0.2	1.687
		1867.4–1867.7	0.3	1.688
		1869.3–1869.6	0.3	1.690

Notes: Travel times are taken from R_1, ranges from the truncated conductivity peaks from the DEP-conductivity profile (Fig. 6). Mean wave speed is calculated for the travel time from the surface to the reflector depth.

4.3. Comparison to other methods

Usually a certain wave-speed–depth function is integrated from the surface to a certain depth to determine the relevant travel time. As any wave-speed estimate is subject to an error, the integration results in an increasing absolute uncertainty with increasing travel time and depth and thus also for the subsequent travel-time–depth conversion. A relative error in wave speed is linearly translated into an equivalent error in depth.

The method introduced here significantly reduces this relative uncertainty by correlating synthetic and RES radargrams in the time domain based on reflection patterns to identify the reflection origin in the depth domain of the ice-core data. Given the physical properties, the model produces the reflections at the right position and enables us to accurately connect reflectors and ice-core properties. Our travel-time–depth relationship is subject to an absolute uncertainty, which mainly depends on the quality of correspondence between the RES and synthetic reflections. Simultaneously, it takes into account the small depth-dependent variations of wave speed. Given a 1% uncertainty in measured wave speeds (a realistic estimate as demonstrated in Fig. 1), the corresponding depth uncertainty for an ordinary travel-time–depth conversion will likewise be 1%, increasing from 1 m at 100 m depth to 20 m at 2000 m depth. In contrast, our travel-time–depth relationship established above is only subject to an absolute error on the order of 1 m, independent of depth. This simple example illustrates that our method is therefore especially useful for deeper reflections.

A tough constraint for reliable functionality is put on the method by the high SNR demanded of RES and synthetic radargrams. As demonstrated, RES data with high SNR can be produced by increased spatial and temporal coverage. Whereas this is no problem for ground-based surveys, it might not be always possible during airborne measurements.

In polar ice, reflection coefficients for electromagnetic waves at radio frequencies are dominated by changes in ε', and are less sensitive to impedance contrasts of ε''. Masking of most reflections originating from conductivity peaks in the synthetic radargrams by noise in the density profiles can be overcome by low-pass filtering of ε'. Unfortunately, this also eliminates the information related to small-scale variations in ε' (from permittivity or anisotropy) in the synthetic radargram. This explains why the agreement of RES and synthetic traces is better below 10 μs than above.

In general, core breaks or only a few centimeters of cracks could also easily mask reflections from conductivity peaks or lead to a rejection of a core section in the quality check. Apart from the difference in conduction mechanisms, this is probably one reason why some reflectors appear in the DEP radargrams, but not in the ECM radargrams (e.g. at 19.8–20.5 and 24.7 μs Fig. 5). In addition, it can also happen that reflections in the reference radargrams are not reproduced by the DEP or the ECM conductivity. As recently shown by Wolff and others (2005), it is difficult to reproduce the conductivity profile for replicate ice cores. In their study at Dome Concordia, two 800 m long conductivity profiles of two ice cores 10 m apart do reproduce individual peaks, but their magnitude varies, typically by a factor of 1.5. Some signals are even completely missing in one of the cores. It is therefore unlikely that synthetic radargrams will reproduce all the RES radargram peaks, even if the measurements take place at exactly the same location, and more so if the locations are separated by a few tens to hundreds of meters.

5. CONCLUSIONS

We have presented a method to determine the depth of origin of reflections observed in RES profiles that is more accurate than previous, standard methods. We find that single conductivity peaks are responsible for the majority of individual reflections, especially in the intermediate and deeper parts of the ice sheet, complementing earlier findings on reflection origin (Millar, 1982; Siegert and others, 1998; Miners and others, 2002). Together with the observed insensitivity of the numerical model results to the type of electrical conductivity data used as an input, this implies that the approach can be applied at most deep-drilling locations, as RES and conductivity profiling are standard measurements and are usually available. Moreover, coarse-resolution density profiles, and possibly even theoretical assumptions for the density distribution with depth, are sufficient as the applied physical properties for the pure-ice fraction can be calibrated within a reasonable uncertainty limit by cross-correlation analysis. Apart from reflection origin we also demonstrate the application to determine the in situ permittivity of the pure-ice fraction and the wave speed–depth function.

The most significant potential, however, lies in the connection of RES and ice-core profiles for the synchronization of deep ice cores. A number of authors proved the long-range traceability of internal reflections in Antarctica (e.g. Siegert and Hodgkins, 2000; Steinhage and others, 2001; Jacobel and Welch, 2005) to connect drilling locations. As demonstrated here, we are now able to identify the origin of selected individual reflections to within 1 m accuracy in depth, even for a lower RES resolution, given that single events cause the reflections. Performing a comparable study at either end of RES profiles that connect deep-drilling locations imposes sound geophysical constraints on the age–depth scales of the ice cores. These constraints are independent of other dating methods, which are usually based on ice-sheet modeling or ice-core records like gas and isotope profiles. Another application is the accurate dating of ice cores drilled in outcropping older ice (Siegert and others, 2003), where no continuous temporal record is available. The good coverage of Greenland with RES profiles combined with this method should be used to improve the accuracy of age–depth distributions. In Antarctica, we hope that the connection of all deep-drilling locations by high-resolution RES, for instance during the IPY 2007/08, will provide a fundamental basis for a comprehensive age–depth map to improve understanding of ice-sheet evolution and phase relations of climate change.

ACKNOWLEDGEMENTS

During the review process we had some stimulating discussions with J. Moore and another, anonymous, reviewer. We greatly acknowledge and appreciate the effort they put into their reviews and suggestions. Preparation of this work was supported by the Deutsche Forschungsgemeinschaft grant WI 1974/2 and an 'Emmy Noether' scholarship EI 672/1 to O.E. This work is a contribution to the European Project for Ice Coring in Antarctica (EPICA), a joint ESF (European Science Foundation)/EC scientific program, funded by the European Commission and by national contributions from Belgium, Denmark, France, Germany, Italy, the Netherlands, Norway, Sweden, Switzerland and the United Kingdom. This is EPICA publication No. 155.

REFERENCES

Annan, A.P. and J.L. Davis. 1976. Impulse radar sounding in permafrost. *Radio Science,* **11**(4), 383–394.

Bittelli, M., M. Flury and K. Roth. 2004. Use of dielectric spectroscopy to estimate ice content in frozen porous media. *Water Resour. Res.,* **40**(4), W04212. (10.1029/2003WR002343.)

Bogorodsky, V.V., C.R. Bentley and P.E. Gudmandsen. 1985. *Radioglaciology* Dordrecht, etc., D. Reidel Publishing Co.

Clarke, G.K.C., N.M. Lhomme and S.J. Marshall. 2005. Tracer transport in the Greenland ice sheet: three-dimensional isotopic stratigraphy. *Quat. Sci. Rev.,* **24**, 155–171.

Clarke, T.S. and C.R. Bentley. 1994. High-resolution radar on Ice Stream B2, Antarctica: measurements of electromagnetic wave speed in firn and strain history from buried crevasses. *Ann. Glaciol.,* **20**, 153–159.

Clough, J.W. and C.R. Bentley. 1970. Measurements of electromagnetic wave velocity in the East Antarctic ice sheet. *In Symposium at Hanover 1968 – Antarctic Glaciological Exploration (ISAGE).* Wallingford, Oxon., International Association of Scientific Hydrology, 115–128. (IAHS Publication 86.)

Dahl-Jensen, D. *and 9 others.* 1997. A search in north Greenland for a new ice-core drill site. *J. Glaciol.,* **43**(144), 300–306.

Dowdeswell, J.A. and S. Evans. 2004. Investigations of the form and flow of ice sheets and glaciers using radio-echo sounding. *Rep. Prog. Phys.,* **67**, 1821–1861.

Eisen, O., U. Nixdorf, F. Wilhelms and H. Miller. 2002. Electromagnetic wave speed in polar ice: validation of the common-midpoint technique with high-resolution dielectric-profiling and γ-density measurements. *Ann. Glaciol.,* **34**, 150–156.

Eisen, O., F. Wilhelms, U. Nixdorf and H. Miller. 2003. Revealing the nature of radar reflections in ice: DEP-based FDTD forward modeling. *Geophys. Res. Lett.,* **30**(5), 1218–1221.

Eisen, O., W. Rack, U. Nixdorf and F. Wilhelms. 2005. Characteristics of accumulation around the EPICA deep-drilling site in Dronning Maud Land, Antarctica. *Ann. Glaciol.,* **41**, 41–56.

Evans, S. 1965. Dielectric properties of ice and snow – a review. *J. Glaciol.,* **5**(42), 773–792.

Fahnestock, M.A., W. Abdalati, S. Luo and S. Gogineni. 2001. Internal layer tracing and age–depth–accumulation relationships for the northern Greenland ice sheet. *J. Geophys. Res.,* **106**(D24), 33,789–33,797.

Fisher, E., G.A. McMechan and A.P. Annan. 1992. Acquisition and processing of wide-aperture ground-penetrating radar data. *Geophysics,* **57**(3), 495–504.

Fortin, R. and R. Fortier. 2001. Tomographic imaging of a snowpack. *In Proceedings of the 58th Annual Eastern Snow Conference*. Hanover, NH, US Army Engineer Research and Development Center–US Army Cold Regions Research and Engineering Laboratory.

Frezzotti, M., S. Gandolfi and S. Urbini. 2002. Snow megadunes in Antarctica: sedimentary structure and genesis. *J. Geophys. Res.,* **107**(D18), 4344. (10.1029/2001JD000673.)

Fujita, S., T. Matsuoka, T. Ishida, K. Matsuoka and S. Mae. 2000. A summary of the complex dielectric permittivity of ice in the megahertz range and its applications for radar sounding of polar ice sheets. *In* Hondoh, T., *ed. Physics of ice core records.* Sapporo, Hokkaido University Press, 185–212.

Hammer, C.U. 1980. Acidity of polar ice cores in relation to absolute dating, past volcanism, and radio-echoes. *J. Glaciol.,* **25**(93), 359–372.

Hargreaves, N.D. 1978. The radio-frequency birefringence of polar ice. *J. Glaciol.,* **21**(85), 301–313.

Hempel, L., F. Thyssen, N. Gundestrup, H.B. Clausen and H. Miller. 2000. A comparison of radio-echo sounding data and electrical conductivity of the GRIP ice core. *J. Glaciol.,* **46**(154), 369–374.

Jacobel, R.W. and S.M. Hodge. 1995. Radar internal layers from the Greenland summit. *Geophys. Res. Lett.,* **22**(5), 587–590.

Jacobel, R.W. and B.C. Welch. 2005. A time marker at 17.5 kyr BP detected throughout West Antarctica. *Ann. Glaciol.,* **41**, 47–51.

Jacobel, R.W., A.M. Gades, D.L. Gottschling, S.M. Hodge and D.L. Wright. 1993. Interpretation of radar-detected internal layer folding in West Antarctic ice streams. *J. Glaciol.,* **39**(133), 528–537.

Jezek, K.C. and E.A. Roeloffs. 1983. Measurements of radar wave speeds in polar glaciers using a down-hole radar target technique. *Cold Reg. Sci. Technol.,* **8**(2), 199–208.

Kanagaratnam, P., S.P. Gogineni, N. Gundestrup and L. Larsen. 2001. High-resolution radar mapping of internal layers at the North Greenland Ice Core Project. *J. Geophys. Res.,* **106**(D24), 33,799–33,811.

Karlöf, L. 2004. Temporal and spatial variability of snow accumulation and redistribution, and its impact on the interpretation of ice cores. (PhD thesis, University of Oslo.)

Karlöf, L. *and 11 others.* 2005. Accumulation variability over a small area in east Dronning Maud Land, Antarctica, as determined from shallow firn cores and snow pits: some implications for ice-core records. *J. Glaciol.,* **51**(174), 343–352.

Kohler, J., J.C. Moore and E. Isaksson. 2003. Comparison of modelled and observed responses of a glacier snowpack to ground-penetrating radar. *Ann. Glaciol.,* **37**, 293–297.

Kovacs, A., A.J. Gow and R.M. Morey. 1995. The in situ dielectric constant of polar firn revisited. *Cold Reg. Sci. Technol.,* **23**(3), 245–256.

Kravchenko, I., D. Besson and J. Meyers. 2003. In situ measurements of the index of refraction of the south polar firn with RICE detector. *J. Glaciol.,* **50**(171), 522–532.

Leonard, K., R.E. Bell, M. Studinger and B. Tremblay. 2004. Anomalous accumulation rates in the Vostok ice-core resulting from ice flow over Lake Vostok. *Geophys. Res. Lett.,* **31**(24), L24401. (10.1029/2004GL021102.)

Looyenga, H. 1965. Dielectric constant of heterogeneous mixtures. *Physica,* **31**(3), 401–406.

Lythe, M.B., D.G. Vaughan and BEDMAP consortium. 2001. BEDMAP: a new ice thickness and subglacial topographic model of Antarctica. *J. Geophys. Res.,* **106**(B6), 11,335–11,351.

Maidique, M.A., A. von Hippel, D.B. Knoll and W.B. Westphal. 1971. Transfer of protons through 'pure' ice I_h single crystals. III. Extrinsic versus intrinsic polarization; surface versus volume conduction. *J. Chem. Phys.,* **54**, 150–160.

Matsuoka, K., S. Uratsuka, S. Fujita and F. Nishio. 2004a. Ice-flow induced scattering zone within the Antarctic ice sheet revealed by high-frequency airborne radar. *J. Glaciol.,* **50**(170), 382–388.

Matsuoka, K., R. Saito and R. Naruse. 2004b. A novel backpackable ice-penetrating radar system. *J. Glaciol.,* **50**(168), 147–150.

Millar, D.H.M. 1981. Radio-echo layering in polar ice sheets and past volcanic activity. *Nature,* **292**(5822), 441–443.

Millar, D.H.M. 1982. Acidity levels in ice sheets from radio echo-sounding. *Ann. Glaciol.,* **3**, 199–203.

Miners, W.D. 1998. Electromagnetic reflections inside ice sheets. (PhD thesis, Open University.)

Miners, W.D., A. Hildebrand, S. Gerland, N. Blindow, D. Steinhage and E.W. Wolff. 1997. Forward modeling of the internal layers in radio echo sounding using electrical and density measurements from ice cores. *J. Phys. Chem., Ser. B,* **101**(32), 6201–6204.

Miners, W.D., E.W. Wolff, J.C. Moore, R. Jacobel and L. Hempel. 2002. Modeling the radio echo reflections inside the ice sheet at Summit, Greenland. *J. Geophys. Res.,* **107**(B8), 2172. (10.1019/2001JB000535.)

Moore, J.C. 1988. Dielectric variability of a 130 m Antarctic ice core: implications for radar sounding. *Ann. Glaciol.,* **11**, 95–99.

Moore, J.C. and J.G. Paren. 1987. A new technique for dielectric logging of Antarctic ice cores. *J. Phys.* (Paris), **48** (C1), 155–160.

Moore, J.C., E.W. Wolff, H.B. Clausen and C.U. Hammer. 1992. The chemical basis for the electrical stratigraphy of ice. *J. Geophys. Res.,* **97**(B2), 1887–1896.

Moore, J.C., E.W. Wolff, H.B. Clausen, C.U. Hammer, M.R. Legrand and K. Fuhrer. 1994. Electrical response of the Summit-Greenland ice core to ammonium, sulphuric acid, and hydrochloric acid. *Geophys. Res. Lett.,* **21**(7), 565–568.

Morse, D.L. 1997. Glacier geophysics at Taylor Dome, Antarctica. (PhD thesis, University of Washington.)

Morse, D.L., E.D. Waddington and E.J. Steig. 1998. Ice age storm trajectories inferred from radar stratigraphy at Taylor Dome, Antarctica. *Geophys. Res. Lett.,* **25**(17), 3383–3386.

Murray, T. *and 6 others.* 2000. Glacier surge propagation by thermal evolution at the bed. *J. Geophys. Res.,* **105**(B6), 13,491–13,507.

Neftel, A., E. Moor, H. Oeschger and B. Stauffer. 1985. Evidence from polar ice cores for the increase in atmospheric CO_2 in the past two centuries. *Nature,* **315**, 45–47.

Nereson, N.A., C.F. Raymond, R.W. Jacobel and E.D. Waddington. 2000. The accumulation pattern across Siple Dome, West Antarctica, inferred from radar-detected internal layers. *J. Glaciol.,* **46**(152), 75–87.

Nixdorf, U. *and 6 others.* 1999. The newly developed airborne radio-echo sounding system of the AWI as a glaciological tool. *Ann. Glaciol.,* **29**, 231–238.

Pälli, A. *and 6 others.* 2002. Spatial and temporal variability of snow accumulation using ground-penetrating radar and ice cores on a Svalbard glacier. *J. Glaciol.,* **48**(162), 417–424.

Popov, S.V., A.N. Sheremet'yev, V.N. Masolov, V.V. Lukin, A.V. Mironov and V.S. Luchininov. 2003. Velocity of radio-wave propagation in ice at Vostok station, Antarctica. *J. Glaciol.,* **49**(165), 179–183.

Richardson, C., E. Aarholt, S.E. Hamran, P. Holmlund and E. Isaksson. 1997. Spatial distribution of snow in western Dronning Maud Land, East Antarctica, mapped by a ground-based snow radar. *J. Geophys. Res.,* **102**(B9), 20,343–20,353.

Richardson-Näslund, C. 2001. Spatial distribution of snow in Antarctica and other glacier studies using ground-penetrating radar. (PhD thesis, Stockholm University.)

Robin, G.de Q., S. Evans and J.T. Bailey. 1969. Interpretation of radio echo sounding in polar ice sheets. *Philos. T. Roy. Soc. London, Ser. A.* **265**(1166), 437–505.

Siegert, M.J. 1999. On the origin, nature and uses of Antarctic ice-sheet radio-echo layering. *Prog. Phys. Geog.,* **23**(2), 159–179.

Siegert, M.J. and R. Hodgkins. 2000. A stratigraphic link across 1100 km of the Antarctic ice sheet between the Vostok ice-core site and Titan Dome (near South Pole). *Geophys. Res. Lett.,* **27**(14), 2133–2136.

Siegert, M.J., R. Hodgkins and J.A. Dowdeswell. 1998. A chronology for the Dome C deep ice-core site through radio-echo layer correlation with the Vostok ice core, Antarctica. *Geophys. Res. Lett.,* **25**(7), 1019–1022.

Siegert, M.J., R.C.A. Hindmarsh and G.S. Hamilton. 2003. Evidence for a large surface ablation zone in central East Antarctica during the last Ice Age. *Quat. Res.,* **59**, 114–121.

Siegert, M.J. *and 9 others.* 2004. Ice flow direction change in Interior West Antarctica. *Science,* **305**(5692), 1948–1951.

Spikes, V.B., G.S. Hamilton, S.A. Arcone, S. Kaspari and P. Mayewski. 2004. Variability in accumulation rates from GPR profiling on the West Antarctic plateau. *Ann. Glaciol.,* **39**, 238–244.

Steinhage, D., U. Nixdorf, U. Meyer and H. Miller. 2001. Subglacial topography and internal structure of central and western Dronning Maud Land, Antarctica, determined from airborne radio echo sounding. *J. Appl. Geophys.,* **47**, 183–189.

Steinhage, D., O. Eisen and H.B. Clausen. 2005. Regional and temporal variation of accumulation around NorthGRIP derived from ground-penetrating radar. *Ann. Glaciol.,* **42**, 326–330.

Vaughan, D.G., P.S. Anderson, J.C. King, G.W. Mann, S.D. Mobbs and R.S. Ladkin. 2004. Imaging of firn isochrones across an Antarctic ice rise and implications for patterns of snow accumulation rate. *J. Glaciol.,* **50**(170), 413–418.

Wilhelms, F. 1996. Leitfähigkeits- und Dichtemessung an Eisbohrkernen. *Ber. Polarforsch.* 191.

Wilhelms, F. 2000. Messung dielektrischer Eigenschaften polarer Eiskerne. *Ber. Polarforsch.* 367.

Wilhelms, F. 2005. Explaining the dielectric properties of firn as a density-and-conductivity mixed permittivity (DECOMP). *Geophys. Res. Lett.,* **32**(16), L16501. (10.1029/2005GL022808.)

Wolff, E., I. Basile, J.R. Petit and J. Schwander. 1999. Comparison of Holocene electrical records from Dome C and Vostok, Antarctica. *Ann. Glaciol.,* **29**, 89–93.

Wolff, E.W., E. Cook, P.R.F. Barnes and R. Mulvaney. 2005. Signal variability in replicate ice cores. *J. Glaciol.,* **51**(174), 462–468.

Yee, K.S. 1966. Numerical solution of initial boundary value problems involving Maxwell's equations in isotropic media. *IEEE Trans. Antennas and Propagation,* **14**, 302–307.

MS received 21 September 2005 and accepted in revised form 10 May 2006

Upward-looking Ground-Penetrating Radar for monitoring snowpack stratigraphy

Achim Heilig[1,2], *Martin Schneebeli*[3], *Olaf Eisen*[1,4]

[1]IUP Institute of Environmental Physics, Heidelberg, Germany

[2]r-hm Risk and Hazard-Management, Hausham, Germany

[3]WSL Institute for Snow and Avalanche Research, Davos Dorf, Switzerland

[4]Alfred Wegener Institute for Polar and Marine Research, Bremerhaven, Germany.

Abstract

Operational remote monitoring of snowpack stratigraphy, melt water intrusions and their evolution with time for forecasting snowpack stability is not possible to date. Determination of the spatial variability of snowpack conditions on various scales requires a number of point measurements with various methods. These methods are either destructive or do not provide information about the internal structure. In this study we present results from upward-looking ground-penetrating radar (GPR) surveys from a horizontal cave dug in the front wall of a snow profile at the bottom of the snowpack. GPR data are compared with vertical profiles of snow hardness and density, obtained in the snow profile. Data were acquired in different areas with varying snow conditions with various GPR impulse systems, frequencies and polarizations. Radar experiments with high frequencies (above 1 GHz) in dry snow detect internal layers in the snowpack, but fail to provide clear reflections at the upper snow-air transition. In wet snow, the radar signals below 1 GHz are capable of penetrating a meter-thick snowpack and detecting the snow surface, although the signal is strongly attenuated. Consequently, commercial GPR systems with frequencies above 1 GHz likely provide insufficient penetration for operational applications. Analysis of reflection phases and magnitude allows interpretation of their physical origin in terms of electrical permittivity. Varying antenna polarization caused a strongly different signal response, likely caused by the snow-pit wall present in our set-up. Forward calculation of density-based reflection coefficients between neighboring layers of varying hardness yields ambiguous results in terms of correspondence with observed radar reflections despite of interferences of neighboring reflections. Moreover, we identify several pitfalls for future applications. The system set-up used here is capable of improving information of spatial and temporal snowpack characteristics.

Keywords: Upward-looking Ground-Pentrating Radar GPR, snowpack monitoring, snow stratigraphy;

1 Introduction

Avalanche warning centers forecast the snowpack stability and monitor the current snow distribution and precipitation amounts for areas that range from mountain regions to provinces and to entire countries in alpine mountains. The spatial and temporal variability of seasonal snowpacks is large, even when focusing on homogeneous slopes (Schweizer et al., 2008). Regarding a whole mountain region, a few observations are definitely insufficient to determine the spatial and temporal variability of e.g. internal weak layers or snow drift accumulations at ridges and in avalanche paths. Evaluation of snow height, snow distribution and observations of the temporal evolution of the snowpack are some of the major tasks facing avalanche forecasting. Temporal snowpack monitoring of the same bulk of snow is impossible if the method is destructive (e.g. conventional snow profiles). Ultrasonic snow-height sensors can be used only in flat areas (Gubler, 1981). No reliable results can

be gathered in snow-deposition areas along ridges or in avalanche paths, where snow displacements are large and inhomogeneous and dangerous to observe on-site. The use of explosives for determining and reducing the current avalanche danger in such areas is an insufficient trial and error method. For the validation and improvement of snowpack simulation models, it is of high importance to measure snowpack conditions with a high spatial resolution in real-time on various scales (Lehning and Fierz, 2008). Additionally, ground-truth measurements for evaluation of remote satellite-based snow monitoring is a task which will be in high demand in the future (Wingham et al., 2005). Snowpack monitoring on steep slopes, avalanche paths or along ridges requires a system working independently of the current avalanche danger. Furthermore, it must not be destroyable by avalanches and should provide data in all weather conditions. A feasible solution would be a system monitoring the snowpack from below. Upward-looking GPR is a suitable method to fullfill these requirements. Data gathered with this GPR-application, i.e. snow height, specific layer features and locations (including wet layers), their changes with time and changes in density in the snowpack above the antennas, provide a supplemental data set of standard observations, which can support avalanche warning centers.

The non-destructive recording of snowpack properties has been of major interest to snow scientists for more than 30 years. The use of impulse radars with high frequencies (2-7 GHz) to measure snow stratigraphy in an alpine snowpack was firstly described by Vickers and Rose (1973). Ellerbruch et al. (1977) and Boyne and Ellerbruch (1979) measured snow properties with a frequency modulated continuous wave radar (FMCW). Gubler and Hiller (1984) conducted similar measurements with a FMCW system from above and beneath the snowpack. Marshall and Koh (2008) review the research done on the use of FMCW for snow analysis. Their radar system provided convincing results for measuring the snow stratigraphy from above the surface. On the other hand, the used FMCW X- and Ku-band frequencies failed to penetrate a moist snowpack (e.g. Gubler and Hiller, 1984; Gubler and Weilenmann, 1986). Only C-band frequencies were able to penetrate a moist snowpack (Marshall et al., 2004). Moreover, a few FMCW-radar systems are used for near-continuous observations of avalanche flow dynamics and avalanche entrainment measurements (e.g. Sovilla and Bartelt, 2002). Nevertheless, there exists no commercial manufacturer of FMCW-systems in the frequency range for applications from beneath the snowpack. Previous studies used custom-made single unit productions which makes it very difficult to establish the method as a standard monitoring tool. Single unit productions differ usually in various system parameters as no standard manufacturing norm exists. This fact complicates the development of normalized processing steps to reduce clutter and noise. Furthermore, the price and the feasibility of reproduction in higher unit numbers favor the concentration on pulsed radar antennas. Other methods such as time domain reflectrometry (TDR), turned out to be not suitable for an application in slope areas (Schneebeli et al., 1998; Waldner et al., 2001). The installation of TDR requires poles reaching the transition from snow to air above the surface, which makes the system prone to avalanche destruction.

Recently, various research has been conducted on the use of impulse radar for estimating snowpack properties. These radar systems are commercially available and have a wide field of applications. In Scandinavia and in alpine regions, impulse radar systems such as Ground Penetrating Radar (GPR) are used to measure snow-water equivalent (SWE) (Lundberg et al., 1999; Lundberg and Thunehed, 2000; Marchand et al., 2001), snow depth and snow accumulation variability (Harper and Bradford, 2003; Machguth et al., 2006) as well as to detect avalanche victims (Modroo, 2004; Heilig et al., 2008). In Arctic and Antarctic regions, GPR was successfully applied in snow and glacier studies, e.g. determining internal layering in the firn column for accumulation studies (e.g. Richardson et al., 1997; Eisen et al., 2008).

For the development of an automatic snowpack monitoring system focusing on snow height and internal layering based on GPR technology, it is essential to evaluate various system components, to investigate their capabilities and pitfalls. This study analyzes the potential of GPR in snow stratigraphy mapping for both dry and wet snow conditions. Our approach considers three main objectives: (i) find a measurement arrangement for impulse radar antennas from beneath the snowpack, which is able to provide reliable measurements of the snowpack for short-time data requests

at several times during a day; (ii) analyze the reflection response of different snow stratigraphic boundaries and the penetration depth for various snow conditions; (iii) compare various antennas, set-ups and GPR systems in terms of their reliability as an automated snowpack monitoring system. We first describe the utilized systems and the theoretical background, measurement set-ups and conducted studies . Subsequently the measurements are analyzed separately for dry and wet snow conditions and polarization and frequency dependencies. The results suggest that further research on this topic is necessary and the improvement of hardware components for a remote controlled operation desirable.

2 Methods

2.1 Data acquisition

GPR-system

We used a RIS One GPR instrument (IDS, Pisa, Italy) with shielded 900 MHz and 2 GHz bipolar antennas and a RAMAC system (MALA Geoscience, Malå, Sweden) with shielded 800 MHz antennas. In all measurements the signals were time-triggered. For further processing and interpretation steps it is important to distinguish between snow stratigraphic reflections and noise or internal antenna reflections caused by the antenna design or other external influences. The antenna noise in pulsed radar from beneath the snowpack masks the reflections caused by the snow stratigraphy, which makes it impossible to detect the snow signals. In order to remove this effect, we generated an alternation of the response signal for different recordings (i.e. with time of the whole acquisition consisting of several tens of traces, which is not identical to the recording time of an individual trace). We moved the antenna for the alternation of the signal. For this feasibility study, the option to operate the radar at various locations with different antennas systems argued against a long-time installation of the system.

Additionally, we used a bipolar antennas concept (No. 4, Table 1) operating at 2 GHz. The bipolar antennas measured one pulse after another with each antenna measured separately. Thus, with one test arrangement, we created two different measurements almost simultaneously while each antenna operated individually. The antennas were orientated orthogonal to each other. To investigate polarization effects with the conventional 900 MHz and 800 MHz antennas in a similar manner as for the bipolar antennas, we also rotated each shielded transmitter/receiver pair horizontally by 90°.

Snow-data

A conventional snow profile (e.g. Colbeck et al., 1990) with high resolution density measurements was made to interpret the radar measurements and compare the resulting reflections with snowpack properties. We took at least two snow samples of 100 cm^3 of each recognized layer to determine the average layer density. The hand hardness values were determined according to the guidelines of Colbeck et al. (1990) where different objects are gently pushed into the snow with a penetration force of about 50 N. The different objects are the fist (F) describing the most loose part of the snowpack following by four fingers (4Fi), one finger (1Fi), pencil (P) and finally a knife blade (K) to penetrate the hardest layers. The determination of the liquid water content in our study is qualitative since we were not able to use instruments for moisture measurements. We used an approximation by Colbeck et al. (1990), who defined four terms of liquid water content in the snowpack and distinguished between the four classes by an approximate range of water volume fraction. Wetness class I corresponds to moist conditions, where the liquid water is not yet visible at 10 times magnification (approximate range of liquid water content in the snowpack $\nu_w < 3\%$). Class II - wet - and III - very wet - contain visible liquid water and are distinguished by the possibility to press out water by moderately squeezing the snow in the hands (class II: $3 < \nu_w < 8\%$; class III: $8 < \nu_w < 15\%$). Class III contains an appreciable amount of air between the pores in contrary to the next higher class IV, which is defined as "slush" ($\nu_w > 15\%$). We determined the liquid water content of the whole snowpack using the collected wetness classes of the field data and applying the upper and lower borders from Colbeck et al. (1990).

Data-processing

The raw data sets were all processed in a similar way. We applied a dewow filter of 5 ns length

to calculate a running mean value which is subtracted from the central point for each trace independently. A linear gain helped to enhance upper parts of the radargram (i.e. snow surface) and a bandpass-butterworth filter was employed to reduce clutter and noise with the cut-offs set at about ±50 % of the nominal frequency. A background removal was only applied if remarkable improvement of the visibility of non horizontal reflections was achieved. Subsequently, a static correction was used to change the height-frame of reference from the antennas direct wave to the snow surface. From this it followed that all reflections parallel to the snow surface were horizontally planar after the correction whereas the direct wave and other instrumentally caused reflections appear in an inverse (triangular) oscillation to the vertical movement. The resulting radargram was stacked over a fraction of all scans (about a tenth or a third of the whole data set). Next, the resulting scans (typically 10 or 3) were averaged over the number of samples of one reflection half cycle. With this processing reflections not parallel to the surface were remarkably attenuated and the parallel reflections not significantly influenced. A deconvolution function (Sandmeier, 1998) was utilized to improve the visibility of the existing reflections, if the record parameters were not optimally set. With this processing we were able to isolate recognizable snow reflections, which were generated by stratigraphy, and to separate multiple reflections and antenna ringing caused by the set-up and antenna design. To be consistent in all radargrams, we decided to define signals' first arrival as the start of the first half cycle of a reflection of recording.

2.2 Test arrangement

Measuring from below the snowpack requires either horizontal or vertical movement of the antenna to apply the mentioned data processing. Otherwise the impulse radar must be operated over a time period with considerable modifications of the observed snowpack. Applying a reasonable effort to the test arrangement from beneath the snowpack (maximal 0.5 m - 1.0 m horizontal movement), the horizontally moved antenna did not produce data which could be evaluated sufficiently. Therefore we arranged an experiment set-up with vertically moved antennas (Figure 1). We tried different test arrangements and varied the movement distance as well as the speed and manner. The variation of the vertical movement ranged between 0.1 m and 0.3 m.

After recording of the conventional snow profile the GPR antennas were buried in an excavated cave at the bottom of the snowpack, in which they were moved by a lever system (Figure 1). The cave was about 60 cm wide and 60 cm long. The distance of the antennas to the profile wall was usually about 10 to 20 cm. We measured the snowpack conditions with two different antenna arrangements: the polarization of the antennas parallel ($\parallel$-polar) or orthogonal ($\top$-polar) to the profile wall. After the antennas were installed beneath the snowpack, the duration of each measurement was only about 1 to 2 minutes.

2.3 Field data

Measurements were conducted in two Austrian Alpine regions, the Stubai Valley and the Oetz Valley, Tyrol as well as on the Colle Gnifetti, Monte Rosa, Valais, Switzerland. At all sites we measured far above the treeline, at an elevation of about 2700 m a.s.l in Austria and above 4400 m a.s.l. in Switzerland. One data set was created in high-winter conditions in January with temperatures below the melt point (No.1, Table 1), another one in spring conditions (April-May) at a mean daytime temperature significantly above the melting point (+ 7°C) (No.2, Table 1). The same snowpack was investigated the next morning again after a cold night with a temperature minimum of -7°C (No. 3, 4). The wet snowpack from the day before was refrozen after the night. The third test arrangement was conducted in August at almost high-winter conditions above 4400 m (No.5).

2.4 Theory

Dry snow conditions

Kovacs et al. (1995) and Mätzler (1996) state that in dry snow relative dielectric permittivity ε_r is

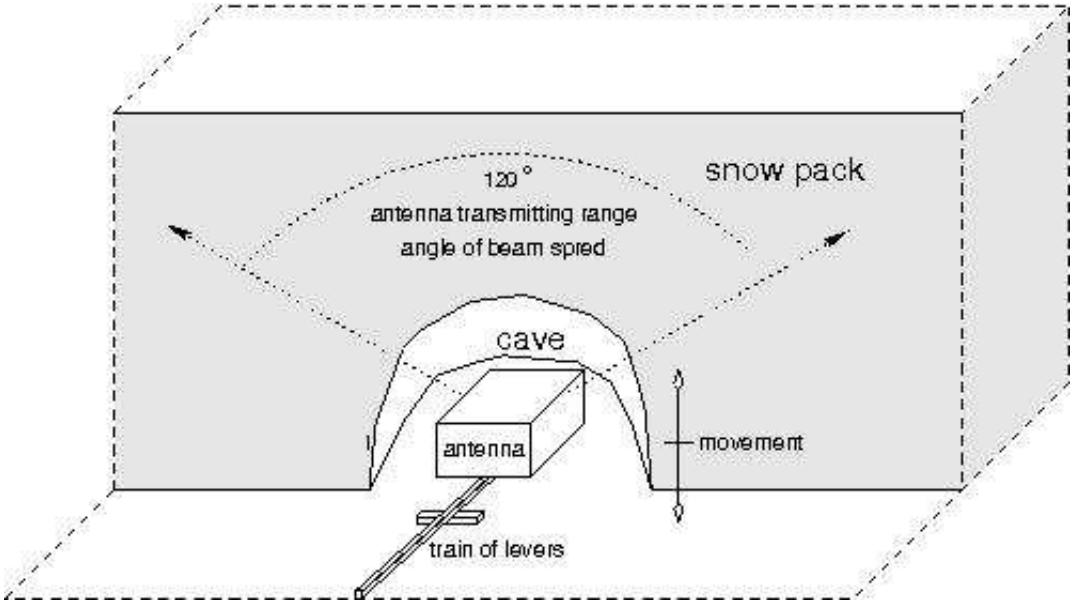

Fig. 1: Sketch of the test arrangement for measurements with vertically moved antennas with the use of a lever. The antennas and the lever are operated from a snow pit.

solely a function of density. Kovacs slightly improved the fit of the equation by Robin et al. (1969) to

$$\varepsilon^{'} = (1 + 0.845\rho)^2 \tag{1}$$

with ρ the density of snow or ice in [g/cm^3]. Mätzler (1996), however, applied several mixing formulas on known ice-volume fractions in various snowpacks and compared the results to the effective medium formula of Polder and van Santen (1946). He concluded that an influence of a liquid layer is not detectable in dry snow conditions. In his results the Looyenga formula (2) (Looyenga, 1965) with the empirical fitting parameters of $\varepsilon_a = 0.9974$ and $\varepsilon_I = 3.215$ with b $= \frac{1}{3}$ provided good results and the parameter are in between 1.1 % compared to the available values (e.g. Daniels, 2004)

$$\varepsilon^b = (1 - \nu) \cdot \varepsilon_a^b + \nu \cdot \varepsilon_I^b \tag{2}$$

ν describes the ice volume fraction, the quotient of snow density and ice density. Both equations (1) and (2) differ less than 2 % in the resulting dielectric permittivity when applying density records measured at the test sites in the Austrian Alps of the last three winters (Table 2).

Tab. 2: Comparison of the two different dielectric permittivity determinations of density based on Eq. (1) and Eq. (2) The ratio of the equations and the sample size (N) of the respective data sets are displayed.

	N	mean $\varepsilon_{Kov}/\varepsilon_{Maet}$ [%]
06	50	1.8
07	57	1.9
08	14	1.9

As the wave speed of radar in snow and therefore the stratigraphic relation of the radargram depends on the relative dielectric permittivity, we analyzed various data sets for changes in the calculated dielectric permittivity. These values were derived from manual density measurements. To calculate the electromagnetic waves speed in snow, we use the approximation for low-loss media (Daniels, 2004)

$$v = c \cdot (\varepsilon_r)^{-\frac{1}{2}} \tag{3}$$

where v is the velocity in snow and c the speed of light in vacuum.

The determination of the mean wave speed in dry snow is displayed in Table 3. The average value of

Tab. 1: Date, time, location, altitude, used antennas and snow conditions for the different radar antenna tests.

No.	date time	location	altitude [m] a.s.l.	antennas [MHz]	snow conditions
1	21.01.08 10:00	Stubai Glacier Austria	2840	900	dry
2	29.04.08 17:30	Vernagtferner Austria	2740	900	wet
3	30.04.08 7:30	Vernagtferner Austria	2740	900	refrozen
4	30.04.08 7:30	Vernagtferner Austria	2740	2000 bipolar	refrozen
5	28.08.08 11:00	Colle Gnifetti Switzerland	4450	800 both polarizations	dense dry

the velocity is $\mu = 0.237$ m·ns^{-1}, the standard deviation (stdv) of these 121 measurements is $\sigma = 0.015$ and the resulting coefficient of variation (defined as $CV = \frac{\sigma}{\mu}$) amounts to $CV = 6$ %.

Reflection coefficient

For the conditions present the magnitude of a reflection is theoretically proportional to the permittivity changes. If in dry snow the density is the sole parameter influencing the permittivity (Kovacs et al., 1995; Mätzler, 1996), we can use the magnitude to estimate the dielectric permittivity values at a two-media transition. The reflection coefficient r for a single interface between two semi-infinite half spaces is determined by

$$r_i = \frac{\sqrt{\varepsilon_i} - \sqrt{\varepsilon_{i+1}}}{\sqrt{\varepsilon_i} + \sqrt{\varepsilon_{i+1}}} \tag{4}$$

with i counting the layers vertically upwards. To cover more realistic scenarios in a natural snowpack, Marshall et al. (2007) applied an equation which takes the layer thickness and the used frequency at each layer transition into account to determine the effective reflectivity R_i .

$$R_i = |\Gamma_i|^2 \tag{5}$$

Γ_i is the reflection response of the i-th snow layer in the direction of wave propagation (from the ground upwards in our application),

$$\Gamma_i = \frac{r_i + \Gamma_{i+1} e^{-2jk_i\Delta z_i}}{1 + r_i\Gamma_{i+1} e^{-2jk_i\Delta z_i}} \tag{6}$$

with k_i the wave number, Δz_i the layer thickness and $\Gamma_{i=1}$ the reflection response of the lowest boundary, in our case the transition from air to snow in the cave. Contrary to Marshall et al. (2007), who measured from above the snow surface, $\Gamma_{i=m}$ is the uppermost transition at the snow surface as we measured from beneath the snowpack. The iteration is initialized at the snow surface with $\Gamma_m = r_m$. The layer thickness Δz_i was determined from the snow profile.

Wet snow conditions

In wet snow conditions the equations for relating density to permittivity as in dry snow are no longer applicable (e.g. Lundberg and Thunehed, 2000). Dielectric permittivity and electric conductivity are influenced by the moisture content in the snowpack. Thus, the moisture fraction has to be taken into account. Empirical relationships between the effective permittivity of wet snow ε_{eff} and the water-volume fraction ν_w were performed by various re-

Tab. 3: Converted dielectric permittivity values (ε) for density measurements conducted between 2006 and 2008 for dry snow conditions. The permittivity has been calculated with (1) and the velocity of propagation values (υ) were calculated with (3). N is the sample size, stdv: standard deviation of the respective data set.

year	ε mean	ε stdv	CV	υ mean [m·ns^{-1}]	υ stdv	CV	N
06	1.6552	0.2298	14 %	0.235	0.017	7 %	50
07	1.5889	0.1674	10.5 %	0.239	0.013	5.5 %	57
08	1.5839	0.5839	8.5 %	0.239	0.011	5 %	14
mean	1.6162	0.1946	12 %	0.237	0.015	6 %	121

search groups (e.g. Sihvola and Tiuri, 1986; Denoth, 1989; Roth et al., 1990; Denoth, 1994). Based on these previous studies Lundberg and Thunehed (2000) determined a parameter for the calculation of an average permittivity and thus the SWE in wet snow. They used the empirical relation

$$\varepsilon_w = 1 + c_3\rho_s + c_4\rho_s^2 + c_5\nu_w + c_6\nu_w^2 \qquad (7)$$

for the wet-snow permittivity based on the snow density and the volume fraction of water previously defined by Sihvola and Tiuri (1986); Sihvola and Kong (1988) and Denoth (1989, 1994). This equation was derived from the three phase mixing model of the existing media ice, air and water

$$\varepsilon_{eff}^{\frac{1}{3}} = \nu_I\varepsilon_I^{\frac{1}{3}} + \nu_a\varepsilon_a^{\frac{1}{3}} + \nu_w\varepsilon_w^{\frac{1}{3}} \qquad (8)$$

applied to the model of Looyenga (1965) and discussed in detail by Wilhelms (2005) for firn with two media. The indices refer to ice (I), air (a) and water (w).

The variables c_j in (7) are constants derived by Roth et al. (1990), where $\nu_w + \nu_s + \nu_a = 1$ and $\rho_s = \nu_w\rho_w + \nu_a\rho_a + \nu_I\rho_I$ is the measured density of snow. Roth et al. (1990) found a good agreement between calculated and measured ε using the phase mixing model with the derived constants of $c_3 = 1.7 \cdot 10^{-3}$, $c_4 = 7.244 \cdot 10^{-7}$, $c_5 = 15.06$, $c_6 = 56.7$, the permittivity of water $\varepsilon_w = 88$ and the permittivity of ice $\varepsilon_I = 3.18$ (Daniels, 2004) (note that Roth et al., 1990 state that ε_w is temperature and frequency dependent and therefore different to the known $\varepsilon_w = 81$ for 20°C e.g. Daniels, 2004). Sihvola and Kong (1988) developed an empirical model to compare measured data with theoretically calculated relative dielectric permittivity values for wet snow,

$$\varepsilon_{eff} = 1+1.7\rho_d+0.7\rho_d^2+(0.1\nu_w\rho_w+0.8(\nu_w\rho_w)^2)\varepsilon_w \qquad (9)$$

with the density of dry snow $\rho_d = \rho_s - \nu_w\rho_w$. Furthermore we applied equation 3 for an additional determination of ε_{eff}.

In these approaches different forms for the water inclusions (spherical, ellipsoidal, etc.) are not considered. However, this is not important in snow, because the shape of water inclusions is always similar unless heavy melting takes place and drainage pathways might develop. This influence is, however, beyond the scope of this paper.

3 Results

3.1 Dry snow conditions

Utilizing a lever system, the height of the uplift of the antennas has an influence on the radargram.The antenna describes a circular movement on the lever (Figure 1). The longer the uplift the more of a circular movement the antenna will describe. We applied various movement heights with the lever system. The longer the uplift the more the divergence angle between the perpendicular of the profile and the antenna increases. With an uplift of $d = 0.1$ m the antenna will be turned by $\alpha_{0.1}$= 5.7°, with an uplift of $d = 0.3$ m, α will increase to $\alpha_{0.3} = 17.5°$. A 5° turn of the antenna is negligible in our opinion. To keep the results reliable we only considered data sets with a maximum uplift of about 0.1 m. An error occurs by the conversion of two-way travel time values to depth values. We used the calculated mean wave speed in dry snow (Table 3), but measured across two medias, air and snow. Therefore the conversion of

the transition air - snow above the snow cave is not correct. We disregarded this error due to the fact that our focus lies on the correct reproduction of the snow depth. Nevertheless, estimating layer positions with the determined mean average wave speed in snow results in a slight impreciseness in the displayed snow-height and layer-position accuracy converting two-way travel time to height values (Table 3). We compared the calculated wave speed of each layer of the two referred measurements using equation 1 to the mean average velocity of propagation in dry snow of Table 3. The mean values were calculated according to the respective layer thickness, neglecting the snow layers where the snow cave was excavated. Even the radar measurements in August 2008 on a high alpine site is within the variation range of the determined average wave speed for dry snow conditions (Table 3).

Tab. 4: Calculated mean values of the density determinations of the referred measurements No.1 and No.5 (Table 1) in comparison to the mean wave speed of Table 3.

Date	21.01.08	28.08.08
mean ρ [kg/m^3]	291.63	396.08
mean ε	1.554	1.781
CV ε	0.08	0.14
mean v_s	0.241	0.225
CV v_s	0.04	0.06
Δv_{mean} [%]	1.7	5.3

The radargrams from the operation of different systems from beneath the snowpack in dry snow conditions are compared with the hand hardness and density profile. Figure 2 shows a radar record with the IDS system (No.1, Table 1) and Figure 3 a record with the RAMAC system (No.5, Table 1). To investigate the relation between prominent internal layers visible in the radargram with the transitions in the physical properties data set, as determined from the snow profiles, both radargrams are turned upside down to have the snow surface at the top of the figure. The effective reflectivity values of $R_i \gtrsim -70$ dB of snow-pit density records are listed in tables 5, 6 as well as the corresponding layer thicknesses and density gradients.

In both figures the reflections related to the transitions from air to snow at the cave ceiling and from snow to air at the snow surface are distinctly developed (Figure 2, 3; black bars). The direct wave and the reflection caused by the transition air - snow beneath the snowpack overlap. Therefore the phase sequence cannot be clearly related. However, various internal reflections can be related to the recorded snow parameter. The measured dominant change in density of $+80$ kg/m^3 in radar wave propagation direction (Table 5) at 107 cm snow height result in a remarkable reflection in the radargram (referred to as ref#2, Figure 2). Furthermore the strong density decrease above 133 cm can be related to the respective reflection (ref#1). Other density steps resulting in lower reflectivity values in Table 5 are not distinguishable in the radargram. Likely constructive interference at 146 cm and destructive interference at 62 cm prevented the evolution of these reflections in the radargram. Additionally, both layers causing the reflection are thicker or equal to the theoretical layer resolution in snow (Table 5) (Daniels, 2004). The utilized processing standard for these data enabled a visualization without artifacts via the static correction and the stack of the scans.

The measurements conducted on the Colle Gnifetti (No.5, Table 1) indicates that the snowpack stratigraphy causes various reflections. With the applied static correction at the snow surface, we were able to attenuate multiple reflections and antenna noise but could completely remove them. The range in the radargram (Figure 7) between 132 cm snow height and the surface is dominated by multiple reflections, as analyzed by comparison of different polarization measurements further discussed below in section 3.3.The radar records of this high alpine site (Figure 3) are more influenced by artifacts caused by the system design (several half cycles of the direct wave, test arrangement, etc.) than the records performed in January 2008 (Figure 2). Several strong changes in density and hand hardness are observeable at about 130 cm (ref#1), below 118 cm (ref#2), below 80 cm and between 48 - 62 cm (ref#3) snow height (Figure 3). These snow stratigraphy changes correspond to reflections in the processed radargram (displayed in greyscale) as well as in the averaged wiggles (reflection values displayed as a sinusoidal oscillation). The ice layer at a depth of 132 cm in the snow profile is difficult to assign to ref#1 in the radargram. It is likely that the ice layer corresponds to the remarkable reflec-

tion. The transition from snow to ice can cause a reflection although the layer thickness is too thin for the vertical resolution of the radar (Marshall et al., 2007). The next remarkable internal reflection (ref#2), at first sight, has only a corresponding snowpack structure in the hand hardness to explain the reflection occurrence. The analyzed snowpack was influenced by several melting periods resulting in various ice lenses, which were more or less horizontally consistant. Ref#3, however, can be related to the density step of $\Delta_\rho \simeq +50$ kg/m^3 at 50 - 62 cm snow height, also recorded as a remarkable hardness increase in the profile. The calculated effective reflectivity (Eq. 6) is about -70 dB (Table 6). The density and hardness rise from 70 - 80 cm has a slight equivalence in reflection response. The effective reflectivity hardly differs from that of at 50 cm snow height (Table 6). The radar responses situated below 30 cm snow height are characterized by the dominant overlap of the direct wave. Similar to the measurement No.1 (Table 1), the dominant reflections at the transitions from air to snow and snow to air are interfering with the reflections likely caused by the near-surface and the near-cave ceiling layers.

Tab. 5: Location, density gradient in radar direction, reflectivity and layer thickness of specific snow layers with a reflectivity larger than -70 dB of the analyzed measurement No.1 from the Stubai Glacier, Austria.

height	$\Delta\rho$[kg/m^3]	R$_i$[dB]	layer thickness [cm]
150	-332.34	-18.5	
146	201.69	-46.2	4
133	-123.20	-54.4	13
128.5	-55.64	-68.9	5
119	-58.12	-68.5	3
107	80.48	-62.8	12
68	57.61	-68.5	14
62	-81.47	-62.6	6
55	362.64	-33.6	7

3.2 Wet snow conditions

In a moist snowpack the previously applied conversions of travel time to depth or density to dielectric permittivity values are no longer possible.

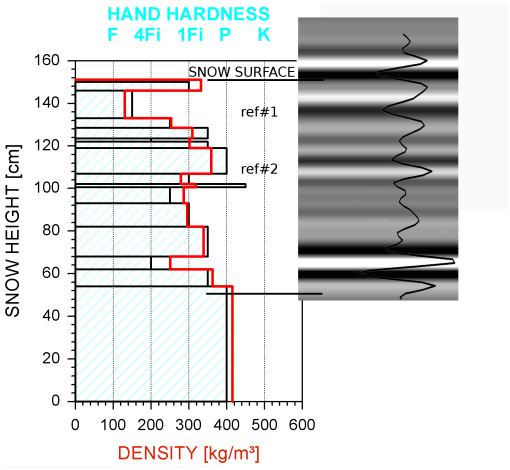

Fig. 2: Data set No. 1 measured on the Stubai glacier, Austria (Table 1). Comparison of radar records obtained with the 900 MHz system in dry snow conditions to snow hardness (blue) and density (red line). The black bars relate the snow surface and the cave ceiling to the corresponding reflections. Visualized is the statically corrected and stacked radargram and an averaged wiggle view over 30 traces of the presented range.

The roughly determined average volume fraction of water for the entire analyzed snowpack (Figure 4) was about $\nu_w = 4.2$ % utilizing the upper boundaries of the ranges defined by Colbeck et al. (1990) and $\nu_w = 2.9$ % if the lower boundaries are utilized. This results in an uncertainty of about 30 % for the average water volume fraction. Calculating the effective permittivity of the snow results in different values for all introduced equations (Eq. 3, 7, 9). The effective permittivity calculated with the measured two-way travel time in the analyzed wet snowpack using Eq. 3 results in $\varepsilon_{eff3} = 2.76$ (the subscripts indicates the respective equation). The empirical approach by Lundberg and Thunehed (2000) result in $\overline{\varepsilon}_{eff7} = 2.36\pm0.12$ ($\pm5\%$) for the given wetness range and the equation by Sihvola and Kong (1988) result in $\overline{\varepsilon}_{eff9} = 2.08\pm0.08$ ($\pm4\%$). The differences for these assumed values is 14 % between the empirical approaches and almost 30 % between Eq. 3 and Eq. 9. If regarding the wettest layer in the profile and adopting the upper range given by Colbeck et al. (1990) the difference

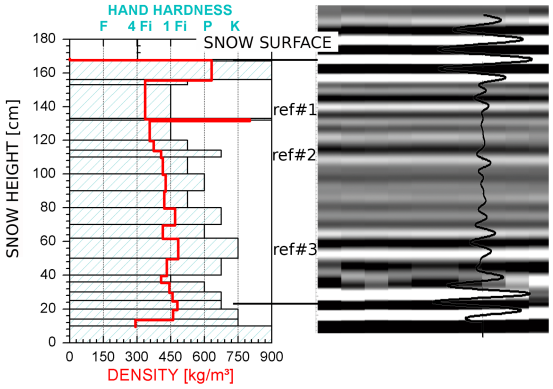

Fig. 3: Data set No. 5 ⊤-polar measured on the Colle Gnifetti, Switzerland (Table1). Comparison of radar records obtained with the 800 MHz system in dry snow conditions to snow hardness (blue) and density (red line). The black bars relate the snow surface and the cave ceiling to the corresponding reflections. Visualized is the statically corrected and stacked radargram with an averaged wiggle view over 30 traces of the presented range.

between the two empirical equations increases to 17 %. The values determined with Eq. 9 correspond adequately within the three-phase mixing model Eq. 8 ($\bar{\varepsilon}_{eff8} = 2.18 \pm 0.08$ ($\pm 3.5\%$). Independently of the used equation, the average effective permittivity of the whole snowpack and the permittivity of certain wet layers differ by more than a factor of 2 at most. This variation is higher than the dielectric permittivity variation of dry snow (e.g. Heilig et al., 2008). Additionally, this variation has no linear gradient with depth, but can be present from one layer to the next. In Figure 4 the wetness variations are displayed in addition to hardness and density. The occurrence of different wetness classes one after another in the snowpack in Figure 4 result in travel-time conversion to depth with respect on each layer separately in contrary to dry snow conditions, where permittivity differences among snow layers can be neglected for the wave speed determination.

In the completely isothermal snowpack (temperature constant at 0° C in the snowpack) in Figure 4, the snow surface reflection is strongly attenuated.

Tab. 6: Location, density gradient in radar direction, reflectivity and layer thickness of specific snow layers with a reflectivity larger than -70 dB of the analyzed measurement No.5 from the Colle Gnifetti, Switzerland.

height	$\Delta\rho$[kg/m^3]	R$_i$[dB]	layer thickness [cm]
167	-631.31	-13.6	
156	295.25	-41.5	7
133	-465.22	-34.2	20
132	445.16	-35.0	1
70	55.24	-70.3	10
62	-69.55	-66.3	8
50	51.79	-71.5	12
24	457.73	32.0	6

The used 900 MHz antenna is still able to penetrate the snowpack as proven by targets (Aluminum shovel put onto the snow surface for short time, see reflection hyperbola in Fig. 4) in the radargram, but the detection of the surface reflection is hardly possible without such target reflections (Figure 4). However, it is clearly visible that wet layers are represented in the radar record. In addition to density steps, wetness differences cause reflections in this radargram and actually seem the major cause. The two remarkable internal reflections seem to correspond to the strong increases in wetness at about 110 cm and 150 cm in the snow profile (Figure 4).

3.3 Polarization and frequency dependency

The application of pulsed radar systems, where the bandwidth is predetermined according to the used antennas, allows two possibilities of variation, which influence the radar record. Firstly, it is possible to vary the frequency and, secondly, one can vary the polarization of the antennas. The frequency determines the penetration depth and the bandwidth the vertical resolution (Marshall et al., 2007). A lower frequency enables a deeper penetration into the media and a higher frequency has higher sensitivity to layer transitions. A larger bandwidth or frequency range results in improved vertical resolution. Figure 5 illustrates these rela-

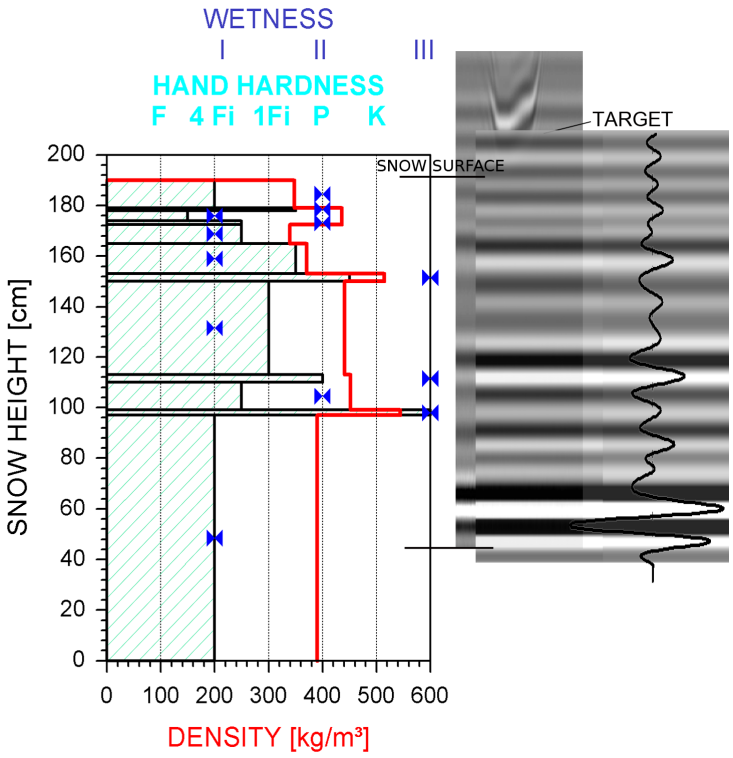

Fig. 4: Data set No. 2 measured on the Vernagtferner, Austria (Table 1). Comparison of radar records obtained with the 900 MHz system in wet snow to snow hardness (light blue), density (red line) and wetness (blue stars). The black bars relate the snow surface and the cave ceiling to the corresponding reflections. Visualized is the statically corrected and stacked radargram with an averaged wiggle view over 30 traces of the presented range. Furthermore the reflection from the snow surface-target (Aluminum shovel) is displayed in the background.

tions by the use of two different antenna systems for analyzing the same snowpack (Table 1, No. 3 and 4). The previously mentioned 900 MHz antenna (Figure 5 A) is compared with a 2 GHz bipolar antenna (Figure 5 B and C). The measurements were conducted before the daily warming occurred.

The three radargrams of the same snowpack are plotted together in Figure 5 to compare corresponding reflections. The most obvious differences occur at the snow surface. While for the 900 MHz antennas (Figure 5 A, at about 15 ns) the transition from snow to air at the snow surface is distinctly visible, the appearance of this transition for the 2 GHz antennas is very much attenuated and hardly recognizable (Figure 5 B, C). Reflections from the surface target in the 2 GHz antennas are only visible by applying an extra gain at the snow surface range. Below the surface transitions, the next horizontal persistant reflections which occur in all three radar records are located at about 12 - 13 ns. The 900 MHz antenna shows a strong reflection structure, while in both 2-GHz records the signal is strongly attenuated. Further persistant reflections consistently occurring in all three radargrams are situated at about 10 ns and the reflection from the cave ceiling. However, radargram B and C recorded with two different polarizations are not identical. Differences in reflection strength of the signal and the location of the reflection with height occur. Both records were processed in the same way. The only horizontally persistant reflections which are observable in both radargrams are at 12 ns, at about 10 ns and above 8 ns. The occurrence of other reflections are not corresponding to each other. This is for instance the case between 13 - 14 ns and below 6 ns. This indicates that these

signals depend on the polarization of the antenna and should rather be considered some kind of noise, which is not a proxy for the snowpack stratigraphy.

Furthermore, especially for the parallel-polarized arrangement, various artifacts are observable throughout the profile (Figure 5C). We also observed these occurrences of artifacts in the data set No.5 conducted with 800 MHz antennas (Figure 7). The strong symmetrical phase and amplitude structures in the wiggle view and the radargrams indicate that these reflections are very likely multiples or ringing. Interestingly, these artifacts occur mainly at the areas before and after the uplift with air between the antennas and the cave ceiling. In contrast, regarding the orthogonal-polarized arrangement (Figure 7), these artifacts are concentrated on the range of the antennas' uplift and thus deleted or strongly attenuated by the applied processing procedure.

3.4 Physical origin of reflections

Studies of GPR in Antarctic regions (Arcone et al., 2004, 2005) showed that the radar phase structure enables interpretation of the stratigraphic characteristics in dry snow. Arcone et al. (2005) and Hubbard and Glasser (2005) describe the relation between permittivity and phase polarity sequences. We analyzed the phase structure of two data sets in dry snow conditions (No. 1, Stubai Glacier, Austria; No.5, Colle Gnifetti, Switzerland, Table 1) and one data set obtained in wet snow conditions (No. 3, Vernagtferner, Austria, Table 1) with respect to the above mentioned results. The observed source wavelet's phase structure for the IDS antennas is a sequence of 3 half cycles with a negative-positive-negative amplitude sequence (- + -) while the used RAMAC antennas have at least 4 half cycles also starting with a negative half cycle (- + - +). We display the radar data such that a positive half cycle corresponds to a white colored amplitude and a negative half cycle to a black colored amplitude (Figure 2; 3, wiggle) in the greyscale plot. From the physical principles laid out in Section 2.4 (Eq. 4) we would therefore expect that a change from low to high permittivity (air-snow interface at the cave ceiling) causes a phase reversal ($r < 0$), whereas a change from high to low permittivity (snow-air interface at the snow surface) causes a reflection without a phase reversal ($r > 0$) . As mentioned above, in dry snow conditions, density is the sole parameter (Kovacs et al., 1995; Mätzler, 1996) influencing the permittivity. Therefore phase polarity changes can be related to the sign of a density change (Arcone et al., 2004; Arcone et al., 2005). The phase structure of the reflection from the cave ceiling in Figure 2 consists of 4 half cycles starting with a positive amplitude (+ - + -) and at the snow surface of 2.5 half cycles (- + (-)) without phase reversal. The phase sequences of this two reflections are consistent with the underlying changes in permittivity. In Figure 2, the first positive oscillation at the cave ceiling is interfering with the direct wave and therefore slightly attenuated, but visible in the wiggle display. The internal reflection at 107 cm height (ref#2) in this figure has a reversed phase characteristic (+ - +) and the reflection at 133 cm (ref#1) has no reversal of 2 half cycles starting with a negative amplitude. Both reflections correspond to the recorded density gradient resulting in a phase reversal at 107 cm and no reversal at 133 cm. The reflectivity values of these two changes in density of Table 5 are both above $R = -70$ dB (Fig. 6). For the data set no. 5 (Figure 3) obtained on Colle Gnifetti, Switzerland, the cave ceiling is difficult to define due to interferences and overlapping of the direct air and ground wave, therefore no phase analysis is reliable. At the snow surface the reflection starts with a strong positive half cycle due to the strong density change to the uppermost layer ($R = -41.5$ dB, Table 6). It is not possible to distinguish the transition from snow to air from the snow surface to this layer reflection because of the length of the wavelet which is at least 3 half cycles long. The three previously discussed internal reflections (Figure 3, ref#1 - ref#3) have a similar phase sequence starting with a positive amplitude (+ -). Comparing to the measured densities for ref#1 and ref#3 these phase reversals are reproduced in the corresponding density increase (Figure 3). As the density increase related to ref#2 is missing in the snow pit data (Fig. 3), we assume that a strong, thin increase in density existed but has not been measured. An increase in hand hardness at this depth was observed at 110 cm height (Figure 3). The phase sequence is in accordance with the previously mentioned theoretical principles as well. The reflectivity values (Table 6; Figure 7) are at

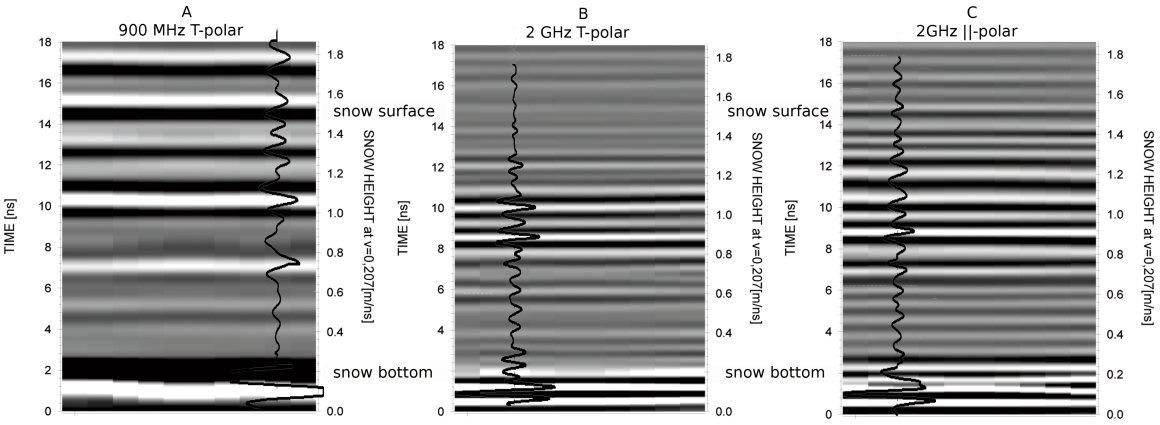

Fig. 5: Data set No. 3 and No. 4 measured on the Vernagtferner, Austria (Table 1). Comparison of radar records of the same refrozen snowpack obtained with 900 MHz (A) and 2GHz (B,C) bipolar antennas. The two-way travel time is related to depth values. Visualized are the statically corrected and stacked radargrams with an averaged wiggle view over 30 traces of the presented range.

about $R_i \simeq -70$ dB and above. The density step at 70 cm height can be related to a slightly recognizable reflection in the radargram (Fig. 3, wiggle view). The calculated reflectivity is $R = 70.3$ dB.

Also for the reflections in wet snow conditions the observed phase structure corresponds to permittivity changes. In this case the dielectric permittivity depends in addition on moisture content. The internal layer with a higher moisture content at 110 cm and 155 cm in Figure 4 are represented by a + - phase structure, indicating an increase in dielectric permittivity. The snow-surface transition displays the opposite structure (- +), although it is hardly recognizable.

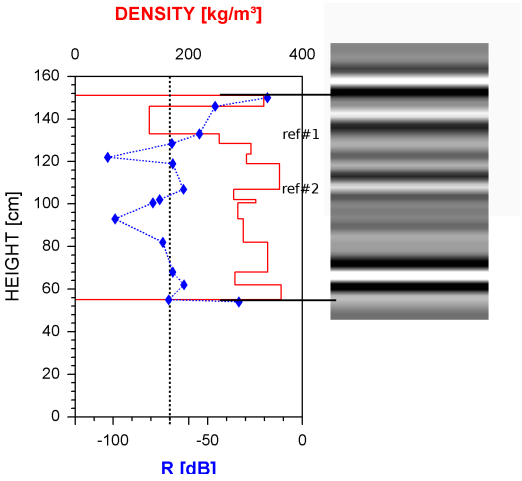

Fig. 6: Data set No. 1 measured on the Stubai glacier, Austria (Table 1). Reflectivity (blue diamonds) determined with Eq. 5 and density (red line) compared to observed reflections in the radargram recorded with 900 MHz antennas. The diamonds display the effective reflectivity where the density changes from one layer to another.

4 Discussion

In the following we address the three objectives: (i) find a measurement arrangement for the application of radar beneath the snowpack which is able to provide reliable results for short-time data requests at specific times during a day; (ii) analyze the reflection response of different snow stratigraphies and the penetration depth for various snow conditions; (iii) compare various antenna and GPR systems in terms of their reliability as an automated snowpack monitoring system.

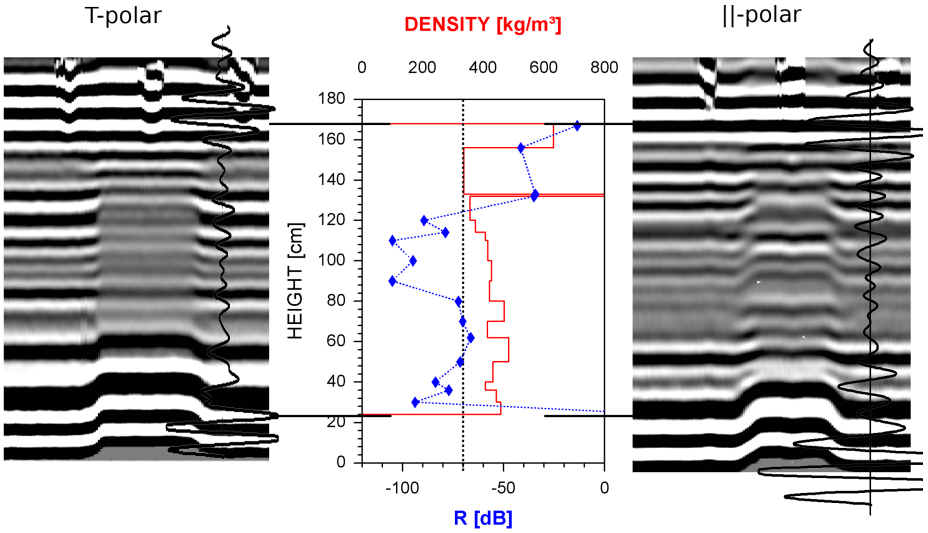

Fig. 7: Data set No. 5 measured on the Colle Gnifetti, Switzerland (Table 1). Effective reflectivity (blue diamonds) determined with Eq. 5 and density (red line) compared to recorded radargrams. Visualized are a $\top-$and a $\|$-polarization in respect to the profile wall recorded with 800 MHz antennas. The diamonds display the effective reflectivity where the density changes from one layer to another. The radar records are additionally processed via a static correction but not stacked for a better visualization of the multiple reflections.

For a short-term data request it is essential that one is able to distinguish between antenna effects and snow stratigraphy causing reflections. As the snowpack is usually not changing while a measurement is conducted and the frequency of the source signal is constant for impulse systems, moved antennas will improve the interpretability and the reliability of the received data. A horizontal movement requires a movement which is not applicable beneath the snowpack. Therefore the vertical uplift is the most effective solution. Reflections caused by the snow stratigraphy or by media transitions will be reproduced in the radar record with a significant movement structure. This structure is the basis for further processing steps. We were able to identify artifacts and multiples (Figure 2-7) by our processing procedure. The applied static correction allowed us to separate reflections non-parallel to the snow surface, the stacking over selected scan ranges helped to identify artifacts and the horizontal average attenuates the non-horizontally planar reflections. Reflections caused by the stratigraphy in the snowpack can be separated via the applied test arrangement and processing. The presented movement technique via a lever system is naturally not applicable for an installation of the system on the top ground surface. A remote controlled lifting platform is essential for a long-term installation. Nevertheless, for this feasibility study the lever system worked well and provided reliable results with an uplift of about 0.1 m.

Dry snow

The results of the field measurements in dry snow conditions are very motivating. Strong density changes with an adequate layer thickness produce distinct reflections. In high winter conditions without a melt period affecting the snowpack, which means that no ice lenses are in the snow cover, the reflections were caused by density changes with a layer thickness larger than the resolution limit of the applied antennas (Daniels, 2004; Marshall et al., 2007). If thinner layers could possibly be detected cannot be answered with this data set. Thin layers with a distinct density step and therefore a calculated reflectivity $R_i > -70$ dB were situated too close to the snow-air media transitions in the radargram. The transition from air to snow

and snow to air caused constructive and destructive interferences which prevented identification of possible layer reflections of these thin layers (Tab. 5; Fig. 2). While melt processes have affected the snowpack, resulting thin ice layers were detectable because of the strong density transitions and the resulting strong increase in dielectric permittivity (Figure 3, ref#1). Occasionally their vertical location in the snow pit does not exactly corresponds with the location of the reflection. This could happen if the snowpack was not undisturbed and the recorded layer in the profile not perfectly parallel to the snow surface. However, application of an average wave speed also slightly influences the traveltime-depth conversion and contributes to small depth differences. In the profile in Figure 3 more than one ice lens was observed. However, horizontally non-persistant ice layers were not recorded in the observed profile. It is very much likely that the reflection ref#2 was caused by other ice intrusions of which the density was not recorded because of their lateral discontinuity. Nevertheless, a corresponding strong increase in hand hardness could be recorded in the profile. The location of internal layers and the determined snow height calculated with an average wave speed is within the variation range of 6 % (Table 3;4), even for the measurements in August on a high alpine site. Considering a snow height with a two-way travel time of 20 ns, a variation range of 6 % to the mean average wave speed will result in 2.31 m snow height with an uncertainty of ± 0.15 m. This is an adequate accuracy regarding the spatial variability of probed snow heights (Föhn, 1989).

Wet snow

Due to the lack of an adequate instrument for the measurement of the water volume fraction in snow, the presented results cannot be taken as a fully quantitative analysis of the influence of specific amounts of liquid water on radar reflections. The uncertainty in the determination of the water volume fraction of the whole snowpack is about 30 %. By regarding the calculated permittivity values this uncertainty decreases to about $\pm 5\%$. Two different empirical approaches for the calculation of the effective permittivity were used. The values of the approach by Lundberg and Thunehed (2000) differ by more than 15 % from the results by Sihvola and Kong (1988). This is why permittivity values were not converted to reflectivity. Lundberg and Thunehed used the measured density of wet snow and Sihvola and Kong developed an empirical relation for the density of dry snow. Which empirical conversion of water volume fraction to effective permittivity fits best, has to be analyzed in a future measurement series with objective determinations of the moisture fraction in the snowpack. However, various qualitative relations can be derived from this data set. The signal of the utilized GPR 900 MHz antenna was strongly attenuated by the moisture in the snowpack, but it was still able to penetrate the snow all the way to the surface and back. The assumed average moisture values for the whole snowpack were probably at the lower end of the actual values, especially for the upper parts of the profile. Though, distinct layers reached water contents up to 12 % and more, which is very wet (Colbeck et al. (1990)). We conclude that the analyzed snow conditions defined the upper-end member of possible moisture contents where the application of impulse radar systems with higher frequencies seems still be possible and reliable. Two internal layers were recorded with radar, which corresponded to layers of high moisture content. A temporal observation of wet layers in snowpacks is a strong argument for the intended sensor system and can be a decisive application possibility for the prediction of wet slab avalanches. However, more field work is required for the application in wet snow conditions, e.g. to determine an average wave speed value for the snow height estimation or an algorithm for the snow surface identification.

Comparison of density-base reflectivity distribution with observed reflections

The introduction of the phase structure and the reflection coefficient or effective reflectivity relates specific reflections in dry snow to specific snow parameter. The analyzed phase structures for dry and wet snow conditions correlated well with the observed density or calculated dielectric permittivity changes. This result helped to identify and follow specific snow layers with time. The results of the calculated reflectivity showed that potentially a reflection is caused by an effective reflectivity threshold larger than $R = -70$ dB. It is not possible yet to quantitatively analyze reflections. In the cur-

rent study a quantitative analysis is hampered by the fact that we utilized two different radar systems and that for this scope our sample size is too small. However, further development and application of the radar equation seems possible. Note that in a homogeneous medium (without ice layers) the detectable thickness of snow layers is inversely proportional to the used frequency range or bandwidth. For a reliable conclusion about the reflectivity more field data are needed to relate thresholds to snowpack parameters.

Comparison of different antenna and GPR system

In this feasibility study we employed different radar systems and various antennas. The aim of the variation was to identify the best radar set-up for future long-term field measurements and to define the possible problems in snowpack monitoring by GPR. The most obvious problems occurred with the application of the 2 GHz antennas. Even a dry snowpack with a high average density caused so much attenuation that the snow surface reflection and targets at the snow surface were hardly detectable. Furthermore, the penetration length was only about 1.4 m. On the contrary, the 900 MHz antennas provided distinct surface reflections and were able to detect the targets even in a wet snowpack. This lets us conclude that the 2 GHz impulse radar is not feasible for a whole season application especially if water infiltrates the snowpack. Additionally, the two different polarizations with 2 GHz created reflections which could not be assigned to snowpack features and therefore are likely noise or multiples. Especially in the upper parts of the snowpack, reflections caused by the stratigraphy were hardly detectable in the radargrams and a different reflectivity between both polarizations was apparent. Supplemental radar records for the two analyzed different polarizations were measured with the 800 MHz antennas as well. The 800 MHz antennas confirm the polarization results observed with the 2 GHz antennas. Antennas polarized parallel to the snow-pit wall produce remarkably more multiples in the radargram than orthogonal polarized antennas. The generation of the multiples and side reflections is propably due to the fact that the emittance of the radar covered not a laterally homogeneous snowpack. The discussed test arrangement obviously contributes to the problem, as one side of the snowpack was excavated and could cause reflections from the vertical wall. As the records were measured closely to the profile wall it is very much likely that the multiple reflections and artifacts are caused by radar waves traveling at the profile wall up and down and reaching media transitions at slightly different travel times than the direct waves. The antenna touched the snowpack at the cave while it was uplifted. This is probably the reason for the occurrence of these artifacts in the orthogonal-polar arrangement. A polarization parallel to the profile wall means that the main part of the emitted radar lobe is orthogonal to the profile wall, resulting in a large portion of the radar wave being radiated to the media transition at the snow-pit wall. While the antenna is uplifted the range transmitted in the open space is reduced and thus less multiples are generated.

A future permanent installation of the system beneath a snowpack for the entire season will prevent these polarization problems. We estimate the influence of polarization relatively marginal for our usage. It is assumed that the stratigraphy is very homogeneous and quasi-parallel for the small section the radar footprint is covering, even in steep slopes.

5 Conclusion

The imaging of snow stratigraphy with an upward-looking GPR system deployed beneath the snow pack is feasible. Even a wet snowpack was penetrable by the utilized radar system. The use of 800-900 MHz antennas for commercial pulsed radar systems provides the best trade-off between vertical resolution and penetration depth. 2 GHz antennas were not able to penetrate a snowpack with a higher average density. For very wet snowpacks or for larger snow heights the performance of higher frequencies than 1 GHz are insufficient. The application of theoretical and empirical relations to allocate reflections to changes in snow density and moisture content was possible, especially for the phase structure. The allocation of the reflections magnitude provided qualitative results. If these results will be confirmed in further field works, it will be possible to follow a temporal development of the snowpack especially in snow height and specific

density changes (crusts). Continuous radar profiles and some evaluation measurement in combination with weather data can provide detailed information about the further evolution of the snowpack and by this validate snowpack models. For a reliable quantification of the reflectivity, more field data is required, especially highly resolved density records and for wet snow conditions continuous measurements of the moisture content. Application of dielectric profiling on the centimeter scale within the area of the GPR footprint could provide very detailed information about the coherences of snow density variations and permittivity, enabling a better comparison of snow-based reflection coefficients and observed GPR reflections.

Acknowledgement

This research is partly funded by grant DFG EI672/5-1 to O.Eisen, PIEPS GmbH, WSL Swiss Federal Institute for Snow and Avalanche Research SLF and r-hm Risk and Hazardmanagement. For assistance in the field we thank the Comission of Glaciology of the Bavarian Academy of Sciences, S. Leimgruber, P. Bohleber, R. Drews and C. Hofstede. We would also like to thank H.-M. Schuler and K.J. Sandmeier for discussions that helped to improve the paper and the anonymous referees for valuable suggestions.

References

Arcone, S. A., Spikes, V. B., Hamilton, G. S., 2005. Phase structure of radar stratigraphy horizons within antarctic firn. Annals of Glaciology 41, 10–16.

Arcone, S. A., Spikes, V. B., Hamilton, G. S., Mayewski, P., 2004. Stratigraphic continuity in 400mhz short-pulse radar profiles of firn in west antarctica. Annals of Glaciology 39, 195–200.

Boyne, H., Ellerbruch, D., 1979. Microwave measurements of snow stratigraphy and water equivalence. In: Proc. 47th Annual Western Snow Conference.

Colbeck, S., Akitaya, E., Armstrong, R., Gubler, H., Lafeuille, J., Lied, K., McClung, D., Morris, E., 1990. The international classification for seasonal snow on the ground. Tech. rep., International Commission of Snow and Ice of International Association of Scientific Hydrology / prep. by Working group on Snow Classification.

Daniels, D., 2004. Ground Penetrating Radar, 2nd Edition. The Institution of Electrical Engineers, London, UK.

Denoth, A., 1989. Snow dielectric measurements. Advanced Space Research 9, 233–243.

Denoth, A., 1994. An electronic device for long-term snow wetness recording. Annals of Glaciology (Proceedings of the Symposium on Applied Ice and Snow Research 1993) 19, 104–106.

Eisen, O., Frezzotti, M., Genthon, C., Isaksson, E., Magand, O., van den Broeke, M., Dixon, D., Ekaykin, A., Holmlund, P., Kameda, T., Karlöf, L., Kaspari, S., Lipenkov, V., Oerter, H., Takahashi, S., Vaughan, D., 2008. Ground-based measurements of spatial and temporal variability of snow accumulation in east antarctica. Reviews of Geophysics 46 (RG2001).

Ellerbruch, D., Little, W., Boyne, H., Bachman, D., 1977. Microwave characteristics of snow. In: Proc. 45th Annual Western Snow Conference.

Föhn, P., 1989. Snow cover stability tests and the areal variability of snow strength. In: Proceedings ISSW International Snow Science Workshop 1988, Whistler, B.C. Canada. pp. 262–273.

Gubler, H., 1981. An inexpensive remote snow-depth gauge based on ultrasonic wave reflection from the snow surface. Journal of Glaciology 27 (95), 157–163.

Gubler, H., Hiller, M., 1984. The use of microwave FMCW radar in snow and avalanche research. Cold Regions Science and Technology 9, 109–119.

Gubler, H., Weilenmann, P., 1986. Seasonal snow cover monitoring using fmcw radar. In: ISSW International Snow Science Workshop 1986. pp. 87–97.

Harper, J., Bradford, J., 2003. Snow stratigraphy over a uniform depositional surface: spatial variability and measurement tools. Cold Regions Science and Technology 37, 289–298.

Heilig, A., Schneebeli, M., Fellin, W., 2008. Feasibility study of a system for airborne detection of avalanche victims with ground penetrating radar and a possible automatic location algorithm. Cold Regions Science and Technology 51 (2-3), 178–190.

Hubbard, B., Glasser, N., 2005. Field Techniques in Glaciology and Glacial Geomorphology. Wiley and son, Chichester. Great Britain.

Kovacs, A., Gow, A., Morey, R., 1995. The in-situ dielectric constant of polar firn revisited. Cold Regions Science and Technology 23, 245–256.

Lehning, M., Fierz, C., 2008. Assessment of snow transport in avalanche terrain. Cold Regions Science and Technology 51, 2-3 (2-3), 240–252.

Looyenga, H., 1965. Dielectric constant of heterogeneous mixtures. Physica 21, 401–406.

Lundberg, A., Thunehed, H., 2000. Snow wetness influence on impulse radar snow surveys theoretical and laboratory study. Nordic Hydrology 31 (2), 89–106.

Lundberg, A., Thunehed, H., Bergström, J., 1999. Impulse radar snow surveys - influence of snow density. Nordic Hydrology 31 (1), 1–14.

Machguth, H., Eisen, O., Paul, F., Hoelzle, M., 2006. Strong spatial variability of snow accumulation observed with helicopter-borne GPR on two adjacent Alpine glaciers. Geophysical Research Letters 33 (13).

Marchand, W.-D., Bruland, O., Killingtveit, A., 2001. Improved measurements and analysis of spatial snow cover by combining a ground based radar system with a differential global positioning system receiver. Nordic Hydrology 32 (3), 181–194.

Marshall, H., Koh, G., 2008. FMCW radars for snow research. Cold Regions Science and Technology 52, 118–131.

Marshall, H., Koh, G., Forster, R., 2004. Ground-based frequency-modulated continuous wave radar measurements in wet and dry snowpacks, Colorado, USA: an analysis and summary of the 2002/03 NASA CLPX data. Hydrological Processes 18, 3609–3622.

Marshall, H., Schneebeli, M., Koh, G., 2007. Snow stratigraphy measurements with high-frequency FMCW radar: Comparison with snow micropenetrometer. Cold Regions Science and Technology 47 (1-2), 108–117.

Modroo, J. J., 2004. Ground penetrating radar location of buried avalanche victims. Master's thesis, Colorado School of Mines, [Online]. Available: http://www.modroo.com/files/JjM2004MSc.PDF. URL `[Online].Available:http://www.modroo.com/files/JjM2004MSc.PDF`

Mätzler, C., 1996. Microwave permittivity of dry snow. IEEE Transactions on Geoscience and Remote Sensing 34 (2), 573–581.

Polder, D., van Santen, J., 1946. The effective permeability of mixtures of solids. Physica 12 (5), 257–271.

Richardson, C., Aarholt, E., Hamram, S.-E., Holmlund, P., Isaksson, E., 1997. Spatial distribution of snow in western dronning maud land, east antarctica, mapped by a ground-based snow radar. Journal of Geophysical Research 102 (B9), 20, 343–353.

Robin, G. d., Evans, S., Bailey, C., 1969. Interpretation of radio echo sounding in polar ice sheets. Phil. Trans. R. Soc., Ser. A 265 (116), 437–505.

Roth, K., Schulin, R., Flüler, H., Attinger, W., 1990. Calibration of time domain reflectrometry for water content measurement using a composite dielectric approach. Water Resources Research 26, 226–273.

Sandmeier, K., 1998. ReflexW Version 4.1 manual. URL `http://www.sandmeier-geo.de/Download/reflexwmanual.pdf`

Schneebeli, M., Coléou, C., Touvier, F., Lesaffre, B., 1998. Measurement of density and wetness in snow using time-domain reflectometry. Annals of Glaciology 26, 69–72.

Schweizer, J., Kronholm, K., Jamieson, B., Birkeland, K., 2008. Review of spatial variability of snowpack properties and its importance for avalanche formation. Cold Regions Science and Technology 51 (2-3), 253–272.

Sihvola, A., Kong, J., 1988. Effective permittivity of dielectric mixtures. IEEE Transactions on Geoscience and Remote Sensing 26 (4), 420–429.

Sihvola, A., Tiuri, M., 1986. Snow fork for field determination of the density and wetness profiles of a snow pack. IEEE Transactions of Geoscience and Remote Rensing 24, 717–721.

Sovilla, B., Bartelt, P., 2002. Observations and modelling of snow avalanche entrainment. Natural Hazards and Earth System Sciences 2, 169–179.

Vickers, R., Rose, G., 1973. High resolution measurements of snowpack stratigraphy using a short pulse radar. In: Proceedings of the Eighth International Symposium on Remote Sensing of the Environment. pp. 261–277.

Waldner, P., Huebner, C., Schneebeli, M., Brandelik, A., Rau, F., 2001. Continuous measurements of liquid water contents and density in snow using tdr. In: Dowding, C. (Ed.), Proceedings 2. International Symposium and Workshop on Time Domain Reflectometry for Innovative Geotechnical Applications. pp. 446–556.

Wilhelms, F., 2005. Explaining the dielectric properties of firn as a density-and-conductivity mixed permittivity (decomp). Geophysical Research Letters 32.

Wingham, D., Francis, C., Baker, S., Bouzinac, C., Brockley, D., Cullen, R., de Chateau-Thierry, P., Laxon, S., Mallow, U., Mavrocordatos, C., Phalippou, L., Ratier, G., Rey, L., Rostan, F., Viau, P., Wallis, D., 2005. Cryosat: A mission to determine the fluctuations in earth's land and marine ice fields. Natural Hazards and Oceanographic Processes from Satellite Data 37 (4), 841–871.

HYDROLOGICAL PROCESSES
Hydrol. Process. (2010)
Published online in Wiley InterScience
(www.interscience.wiley.com) DOI: 10.1002/hyp.7749

Temporal observations of a seasonal snowpack using upward-looking GPR

Achim Heilig,[1,2]* Olaf Eisen[1,3] and Martin Schneebeli[4]

[1] *Institute of Environmental Physics (IUP), Heidelberg, Germany*
[2] *r-hm Risk and Hazard-Management, Hausham, Germany*
[3] *Alfred Wegener Institute for Polar and Marine Research, Bremerhaven, Germany*
[4] *WSL, Institute for Snow and Avalanche Research, Davos Dorf, Switzerland*

Abstract:

An increase of the spatial and temporal resolution of snowpack measurements in Alpine or Arctic regions will improve the predictability of flood and avalanche hazards and increase the spatial validity of snowpack simulation models. In the winter season 2009, we installed a ground-penetrating radar (GPR) system beneath the snowpack to measure snowpack conditions above the antennas. In comparison with modulated frequency systems, GPR systems consist of a much simpler technology, are commercially available and therefore are cheaper. The radar observed the temporal alternation of the snow height over more than 2·5 months. The presented data showed that with moved antennas, it is possible to record the snow height with an uncertainty of less than 8% in comparison with the probed snow depth. Three persistent melt crusts, which formed at the snow surface and were buried by further new snow events, were used as reflecting tracers to follow the snow cover evolution and to determine the strain rates of underlaying layers between adjacent measurements. The height in two-way travel time of each layer changed over time, which is a cumulative effect of settlement and variation of wave speed in response to densification and liquid water content. The infiltration of liquid water with depth during melt processes was clearly observed during one event. All recorded reflections appeared in concordance with the physical principles (e.g. in phase structure), and one can assume that distinct density steps above a certain threshold result in reflections in the radargram. The accuracy of the used impulse radar system in determining the snow water equivalent is in good agreement with previous studies, which used continuous wave radar systems. The results of this pilot study encourage further investigations with radar measurements using the described test arrangement on a daily basis for continuous destruction-free monitoring of the snow cover. Copyright © 2010 John Wiley & Sons, Ltd.

KEY WORDS upward-looking GPR; temporal observation seasonal snowpack

Received 23 September 2009; Accepted 12 April 2010

INTRODUCTION

The determination and forecast of snowpack properties is an important feature contributing to the daily avalanche warning bulletin as well as to the prediction of hydrological hazards and run-off. In hydrological forecasting, the snow water equivalent (SWE) and therefore the possible melt rates for the prediction of streamflow and reservoir inflow are of high interest (Turcotte *et al*., 2007). In Arctic regions, spring snow melt amounts up to 80% of the annual river flow (König and Sturm, 1998). In the European Alps, slightly lower rates are observable. Snow melt in spring contributes about 60% of the annual run-off in a mountainous area in the Austrian Alps (Escher-Vetter *et al*., 2009; Comm. Glaciology, 2009). Spring run-off rates are concentrated to relatively short time periods. Therefore, to forecast run-off, it is important for the management of hydroelectric power plants or for regional hazard authorities to determine the amounts of SWE in a catchment area as accurate as possible. Furthermore, seasonal snow covers and glaciers contribute almost exclusively to the water supply of more than one-sixths of the world's population (Barnett *et al*., 2005). An early determination of the SWE in catchment areas is essential for the water management of these regions. Spatially highly resolved information of snow coverage in a catchment area can be gathered with airborne or spaceborne imaging, but there exists a lack of ground truth data points (e.g. Bindschadler *et al*., 2005). Ground truth point data on snow height and average density in dry snow conditions to estimate the SWE can be provided by upward-looking radar measurements together with snow height sensors. For hydrological questions, weekly, spatially highly resolved information about the snowpack in the catchment area is sufficient. For dry-snow conditions, only the corresponding SWE is of interest for the run-off prediction. On the contrary, in spring while liquid water is situated in the snowpack the location and the thickness of the water intrusions become more important.

However, for avalanche forecasting, information of snowpack conditions and changes thereof on a daily basis is necessary. For the prediction of avalanches, the spatial snow distribution in combination with snowpack stability is a key parameter (Kronholm and Schweizer, 2003; McClung and Schaerer, 2006). The determination of the

* Correspondence to: Achim Heilig, r-hm Risk and Hazard-Management, Hausham, Germany. E-mail: heilig@r-hm.de

snowpack stability, however, relies on data on the internal layering, preferable in combination with stability tests (Schweizer and Wiesinger, 2001). The data volume of snowpack changes and internal layering, especially in slope and ridge regions, is limited by accessibility, if the data acquisition is performed manually. Furthermore, a temporal observation of snowpack evolution is impossible if the method is destructive as is for instance the case for manual snow pits. To date, no other method than radar exists to observe internal snowpack stratigraphy. Alternatively, to determine snowpack evolution several snow cover models exist, for example, SNOWPACK (Lehning *et al*., 1999) or the French model combination SAFRAN–CROCUS–MEPRA (Brun *et al*., 1989, 1992). The accuracy and spatial resolution of these models depend on the input data (Bales *et al*., 2006). To date, the simulated snow height is dependent on the spatial distribution of automatic snow height stations, which means that any small-scale variation affecting the snow measurement is problematic (Bavay *et al*., 2009). Verification of the simulated development of internal layering with time in combination with environmental parameters (e.g. temperature, load of new snow) over a whole winter requires non-invasive measurement methods. As reliable automatic snow height data with sonic sensors are usually only gained in almost flat areas (Gubler, 1981), a lack of data exists especially in slope areas. The regional representativeness of point measurements at weather stations concerning the daily amount of new snow, which is an important factor for daily avalanche hazard prediction and artificial avalanche release (McClung and Schaerer, 2006), shows an increasing uncertainty with increasing daily new snow amounts (Schneebeli and Laternser, 2004). Schneebeli and Laternser noticed that large daily new snow events with about 50 cm accumulated snowfall and more are often unobserved by automatic snow height stations. It is recommended by Egli (2008) that the measuring site must be placed as close as possible to the critical hazard zone. Additionally, redistribution by wind is mostly neglected in snowpack simulations, which leads to uncertainties in the total amount of snow and the addition of potential slab structures over former surface features at ridges or in slopes. This information is especially important for the forecasting of self-released avalanches (Schweizer and Wiesinger, 2001). An increase in the number of automatic snow-monitoring sensors will improve the spatial resolution of snowpack models. For further developments in predicting the spatially distributed avalanche danger automatically, the lack of data representing snowpack features, especially for mountainous areas, is an additional weakness for approaches like nearest neighbour methods (Pozdnoukhov *et al*., 2008). Either in hydrological application for the prediction of melt rates or for avalanche warning services, further non-invasive automatic sensor systems, working on both plane and slope areas, are an important support for the regional risk and hazard management, as well as for resource managements (Bales *et al*., 2006).

In regions where avalanches occur, an automatic monitoring system must be secured against destruction by avalanches. A possible snowpack sensor system could be realized by the application of upward-looking pulsed radar systems (Heilig *et al*., 2009). Our implemented radar system operates from beneath the snowpack measuring in an upward direction. Gubler and Hiller (1984) performed early snow cover observations with frequency modulated continuous wave (FMCW) radars in a similar way but with much higher frequencies. The previous work on the application of FMCW radar for the record of the snow cover is summarized by Marshall and Koh (2008). However, in this study, the feasibility of impulse radar systems with a centre frequency of approximately 800–900 MHz is analysed. Special regard is set on the ability to adequately record the snowpack stratigraphy and the ability to penetrate both dry and wet snow covers with the same frequency. As radar systems determine the snowpack non-destructively, a temporal observation of the evolution of the snow height, internal layers and settlement speed is possible. Heilig *et al*. (2009) described the system requirements for an all-season penetration of the snowpack with sufficient layer resolution. On the basis of Heilig *et al*. (2009), we designed a test arrangement for the installation of an upward-looking ground-penetrating radar (GPR) system at a single test site.

METHODS

Data acquisition

To measure the temporal evolution of a snowpack throughout a winter season (Table I), GPR antennas were installed at a fixed position and running from the middle of January 2009 until the beginning of April 2009 at a test site in the Bavarian Alps on an almost flat area (5–9° slope angle). The test site is located at 1420 m above sea level (a.s.l.) at the Lake Grünsee (47·6525°N/11·8681 °E), Germany. Although the site is below treeline, it is situated in open space, but it is located nearby a slight terrain ridge. This ridge is potentially the reason for different snow heights and variabilities in layer locations between the position of the antennas and within the test site. We used a RAMAC system (MALA Geoscience, Malå, Sweden) with shielded 800 MHz antennas. The

Table I. Radar measurements in winter 2009 to record the temporal evolution of snowpack properties

Date	Notation	Snowpack conditions
13.02.09	a	Dry
19.02.09	b	Dry
20.02.09	c	Dry
06.03.09	d	Dry
12.03.09	e	Dry
14.03.09	f	Dry
18.03.09	g	Dry
25.03.09	h	Dry
06.04.09	i	Wet

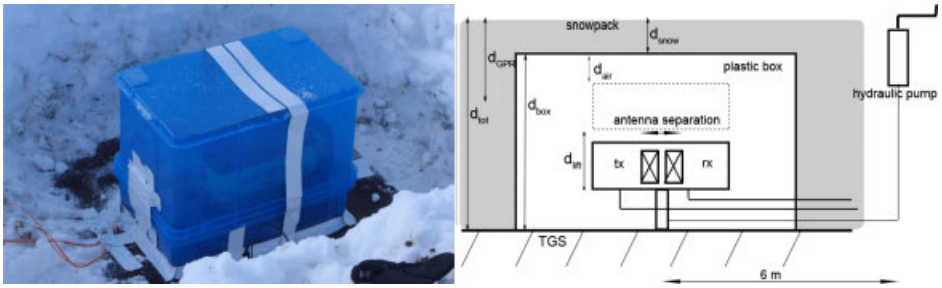

Figure 1. The test arrangement of the field work. On the left a picture of the installation, and on the right the sketch is displayed. See text for details

antennas (transmitter and receiver) were mounted on a hydraulic hoist system, which was fixed at the top ground surface (TGS) on a wooden plate. To enable the vertical movement and to secure the antennas from direct water contact, a plastic cover box was installed surrounding the antennas (Figure 1). Fibre optic cables and a 12 V battery connected via a cable facilitated the remote energy supply and data transfer to the control unit of the system. The hydraulic hoist system was connected via a tube to a hydraulic pump at a distance of 6 m from the antennas. During a radar record, the antennas were lifted and lowered several times with various speeds. We installed the whole system when the snow height above ground corresponded almost exactly to the height of the plastic box. Therefore, it was possible to measure with the GPR system naturally layered snow with properties comparable with the surrounding snowpack. Figure 1 illustrates the test arrangement. For the comparison of the recorded reflections, we conducted manual snow pit measurements inside the marked and undisturbed test site. The largest distance from the location of the antennas to a snow pit was approximately 8 m. We discuss a selection of nine radar measurements later on. The different distances d in Figure 1 are d_{tot}: the total height of the snowpack, $d_{\mathrm{box}} \sim 45$ cm, $d_{\mathrm{GPR}} = \Delta d_{\mathrm{air}} + d_{\mathrm{snow}}$ the actually measured distance to the surface, $d_{\mathrm{air}} < 10$ cm in lifted position of the antennas, which was usually cut off from the data. The lift of the antennas was $d_{\mathrm{lift}} = 14$ cm.

Snow data acquisition

According to the guidelines of the International Classification of Seasonal Snow on the Ground (ICSSG) (e.g. Colbeck *et al.*, 1990), conventional manual snow profiles with high-resolution density measurements were conducted to interpret the radar data and to compare the resulting reflections with snowpack properties. We took at least two snow samples of 100 cm^3 of each recognized layer in the snow pit to determine the average layer density. For conditions with recognized melt processes in the snowpack (snowpack temperature of 0 °C), we made additional manual qualitative wetness determinations according to the ICSSG guidelines, described in detail by Colbeck *et al.* (1990).

GPR data processing

For a good comparison of all radar records obtained throughout the winter 2009 at different times and under

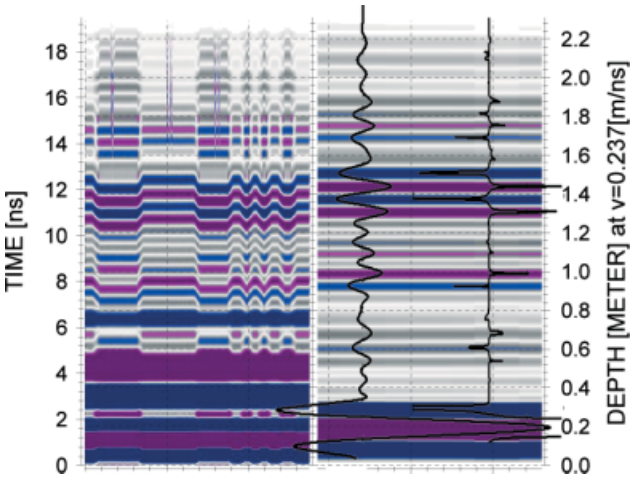

Figure 2. Effect of the applied processing steps and the visualization procedure. The left part displays the status of the radargram prior the static correction. The right part shows the final conditions after the whole processing. The compaction of the signal via the visualization procedure is displayed by the two wiggles, the left one shows the mean trace of the right radargram and the right wiggle the compressed pulses according to the procedure described in Section GPR data visualization and magnitude retrieval

different environmental conditions, we normalized the amplitude of all raw data sets using a constant factor. We applied the normalization function of the REFLEXW program, in which one scaling factor is calculated from the quotient of the overall mean energy value of all profiles and the total energy value of the individual profile (Sandmeier, 1998). The energy values are determined within the given time range of each radar measurement. After the normalization, we processed the data as described in detail by Heilig *et al.* (2009). We applied a dewow filter for the removal of low-frequency components from each trace in the profile, a linear gain function, bandpass filters and start time corrections depending on the particular data set. In all cases, we used a background removal for reflection ranges above the location of the direct wave (usually at a two-way travel time of approximately 2–7 ns). These areas were very much dominated by multiples of the direct wave and therefore not interpretable (example shown in Figure 2, left part between 2·4–6·8 ns). The background removal filtered out the horizontally constant reflections in the travel time-trace-number domain. Subsequently, processing steps were applied as described by Heilig *et al.* (2009). As the snow surface was uniquely detectable in the radargrams by

the use of a target (aluminium shovel at the surface, Figure 2), we applied a static correction on this signal pattern. A stack of the traces followed the static correction and finally, we applied an average filter over the length of one half-cycle of the surface reflection. The effect of the processing is clearly visible in Figure 2. Reflections with a vertical movement in the left part of the figure are still displayed after processing, whereas most of the signals, which occur originally horizontal in the raw data and originate from the system, are filtered out.

GPR data visualization and magnitude retrieval

Pulse compression. Ideally, a source wavelet would comprise only two half-cycles and thus would be one wavelength long. Our source wavelet comprises more than two half-cycles. The resolution is therefore not limited by the wavelength, but by the length of our wavelet, making the overlap of wavelets reflected from different layer boundaries more likely. To improve the visualization of the GPR data, we examine various methods of pulse compression.

We first employed the deconvolution technique, a standard technique routinely applied to seismic and GPR data (e.g. Xia *et al*., 2004). Unfortunately, the application to our data sets did not provide significant improvements in signal compression. As deconvolution algorithms are usually written for the processing of data with higher signal-to-noise ratios (see Figure 2, left wiggle), we find that a deconvolution algorithm is not sufficient for the data sets presented here.

Instead of a deconvolution, we weigh the reflected signals with the source wavelet referred to as the P-visualization (see Equation (2) below). This processing is applied to each of the nine analysed data sets independently to obtain a normalized visualization of each measurement. After applying the processing steps described above, the final ten traces of each measurement are averaged resulting in the mean trace $\vec{b} = (b_1, b_2, \ldots, b_N)$, a vector with N elements, that is, the data samples. (In the following, a subscript will refer to the respective element of a vector.) The number of elements N correspond to the number of samples of the recorded signal. As the reflected return signal in GPR systems is a convolved multiple of the emitted signal, independent of the phase structure and amplitude (Annan, 2002), we extract the first complete positive half-cycle of the mean trace $\vec{b}$ and define it as the mother wavelet $\vec{m} = (m_1, m_2, \ldots, m_I)$, a vector with $I < N$ elements (Perrin *et al*., 2000). This mother wavelet, assumed to be generated as part of the direct wave in air, is resampled to resemble a wavelet in snow, each sample at time t' in air is shifted to $t = t'c/\overline{v}$ in snow, where $\overline{v} = 0{\cdot}237$ m/ns is the mean wave speed in snow and c is the speed of light. We next define a series of $Q = N - I$ vectors $\vec{k}^q = (k_1^q, k_2^q, \ldots, k_I^q)$, $q = 1, \ldots, Q$, the I elements of which are the components of $\vec{m}$ element-wise weighted with a sub-vector $\vec{b}^q = (b_q, b_{q+1}, \ldots, b_{q+I-1})$ of the mean trace vector $\vec{b}$ with I elements. The i-th element of $\vec{k}^q$ is calculated from

$$k_i^q = \frac{m_i}{b_i^q}. \tag{1}$$

This division is performed Q times to cover all elements of $\vec{b}$. We next determine the standard deviation σ_q of each vector $\vec{k}^q$, yielding a vector $\vec{\sigma}$ with Q elements σ_q. On the basis of the mean trace vector $\vec{b}$, we define another subvector $\vec{b}^*$, defined as the part of $\vec{b}$ for the scan range above the direct wave. To exclude the influence of the direct wave for pulse compression, which dominates the signal, when comparing different measurements (Figure 3), we will use the maximum $\overline{b}^* = \max|\vec{b}^*|$ for vector normalization. Finally, the element-wise operation

$$P_q = \frac{b_q}{\overline{b}^* \sigma_q}, \tag{2}$$

where b_q is the q-th element of $\vec{b}$ and again $q = 1, \ldots, Q$, yields the elements of a normalized trace vector $\vec{P}$ of length Q with compressed signal appearance. (The last I elements of $\vec{b}$ are not considered in this operation.) The traces $\vec{P}$ for each measurement are compared in Figure 3. Note that the processed traces are individually normalized with respect to the total energy content of the trace, so reflection amplitudes cannot be qualitatively compared among traces yet. This will be performed next.

Amplitude normalization for comparison of measurements. The temporal evolution of the snowpack can be characterized by a time series of observed reflection magnitude of specific snow layers. For this comparison, we started off with the individually normalized radar signals as described in Section GPR data processing, but no further processing was applied to avoid processing-related changes in reflection amplitudes. Subsequently, we used the maximum and minimum value of the amplitude of two half-cycles of the mother wavelet $\vec{m}$ to determine the scaling factor $\hat{m} = \max(\vec{m}) - \min(\vec{m})$.

For the comparison of the amplitudes of different measurements, we performed the static correction to the surface reflection for each normalized raw trace and calculated the mean of the static corrected traces of each measurement, $\vec{b}^{\text{raw}} = (b_1^{\text{raw}}, b_2^{\text{raw}}, \ldots, b_N^{\text{raw}})$. Furthermore, we included a simple correction for geometrical spreading, finally yielding $b^{\ddagger}$. The mean trace for each measurement is normalized according to

$$b_i^{\ddagger} = \frac{b_i^{\text{raw}} z_i}{\hat{m}}, \tag{3}$$

where z_i is the respective range of the retrieved sample in the space domain from the antenna. The such normalized reflection amplitudes are displayed in Figure 4a.

Meteorological data set

An automatic weather station (AWS) was not available in the direct neighbourhood of the radar antennas. The next AWS was in an air-line distance of about 2 km

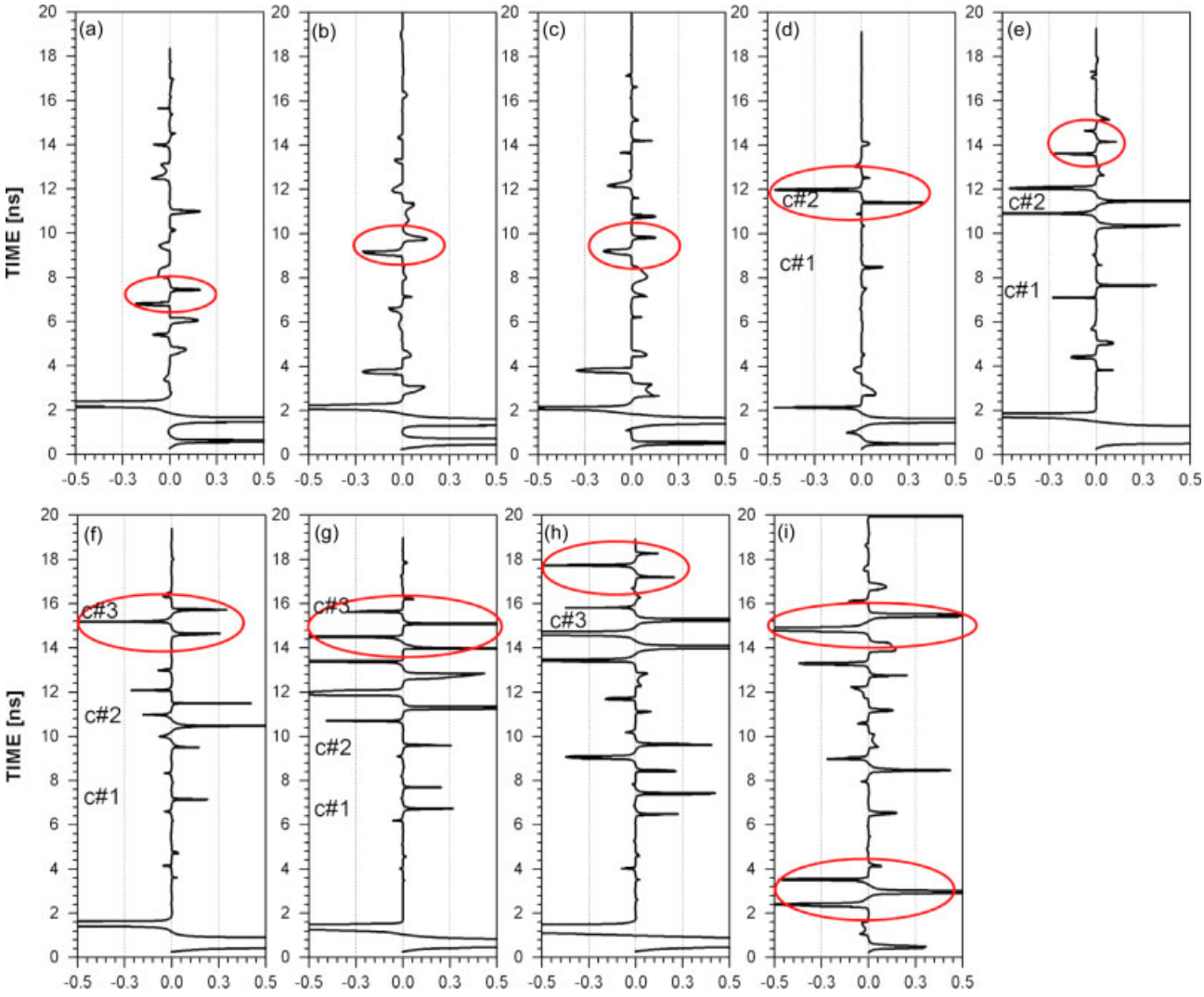

Figure 3. P-visualization of all discussed radar measurements, eight for dry-snow (a–h) and one for wet-snow conditions. The notations are in accordance with Table I; a: 13.02.09, b: 19.02.09, c: 20.02.09, d: 06.03.09, e: 12.03.09, f: 14.03.09, g: 18.03.09, h: 25.03.09, i: 06.04.09. Ordinates: two-way travel time; abscissas: compressed amplitudes according to Equation (2). Ellipses indicate the snow surface and for measurement *i* the transition from air to snow below the snowpack as well

north-east and at 320 m lower altitude. For the time periods in between the manual ground truth measurements at Grünsee, we use the data of the AWS to compensate for the lack of data. The recorded temperature at the AWS corresponds very well to the measurements at the test site (light blue line with markers, Figure 4b). The probed snow depth is always above the measured snow height (Figure 4b) of the ultrasonic snow height sensor beside some large new snow events at the end of February, when we did not visit the station. Likely the snow height at Grünsee was higher than at the AWS. The main reason for the on average lower snow height at the weather station is that it is located in a forest. Nevertheless, the precipitation and settlement tendency of the seasonal snowpack is well represented by the AWS. The weather conditions at the test site during the winter season 2009 were characterized by a high pressure period in January with almost no precipitation and cold temperatures with just sporadic peaks above melting point in a 2 h average temperature record (Figure 4b). February and March were characterized by several large snow fall events, which resulted in an over-average snow height from mid of February until April. In combination with some embedded melt processes, the snowpack stratigraphy was structured by various crusts and density differences. Figure 4b shows a comparison between probed snow depth and manually measured temperatures at the test site and the snow height and temperature of the AWS recorded at 10 min intervals.

RESULTS AND DISCUSSION

Snow height evolution

Using the P-visualization (Figure 3, ellipses), the development of the snow height determined from GPR is clearly displayed. Backscatter above the snow surface with an approximately similar amplitude to the surface reflection occurred only during strong precipitation events (Figures 3a, c and 7, 13.02.09, 20.02.09). The radargrams of both measurements influenced by the

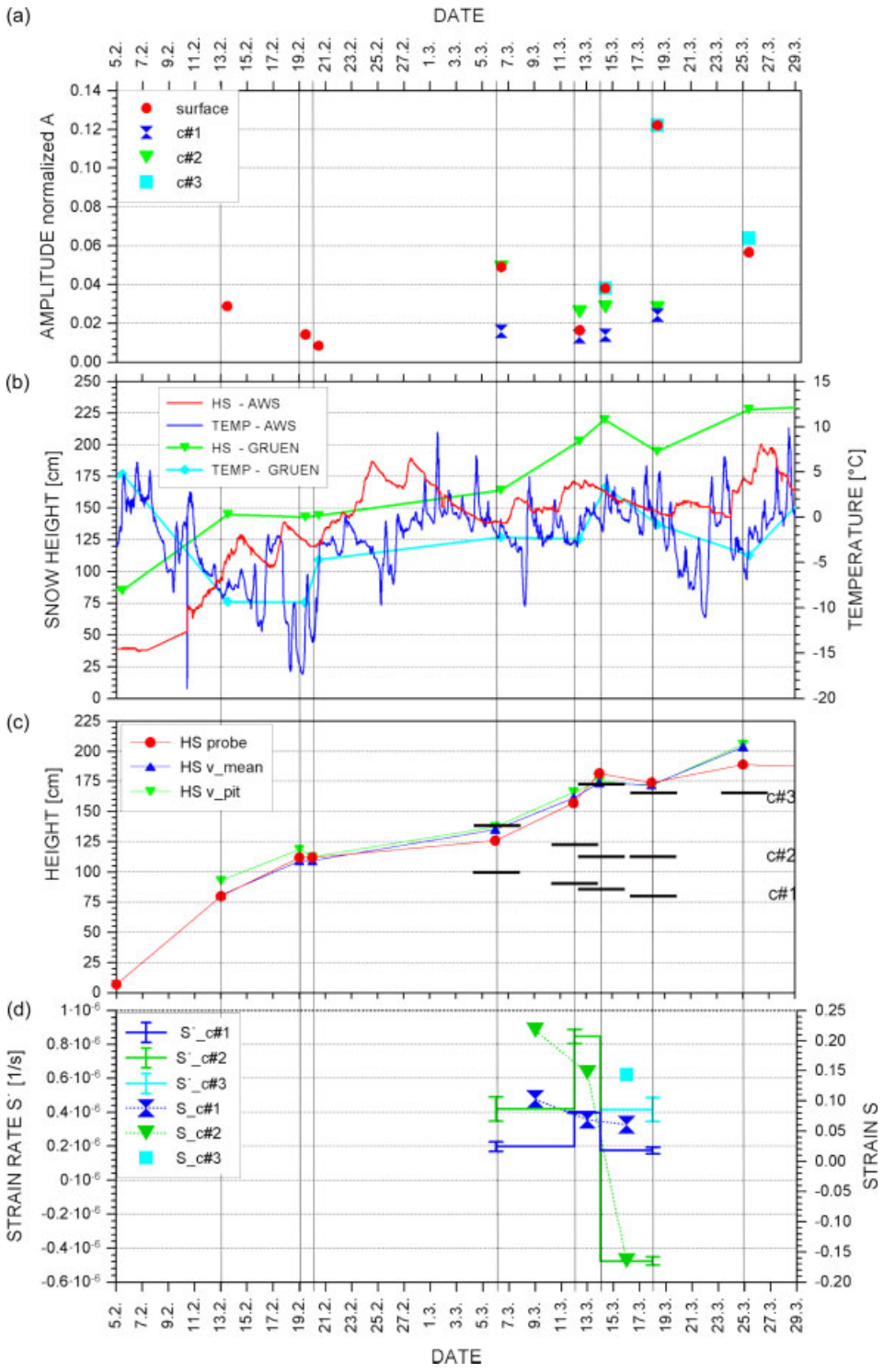

Figure 4. (a) Values of the recorded reflection amplitude of the addressed snow layers and the snow surface. (b) Meteorological parameters manually recorded at the test site (GRUEN) in comparison with the measured snow height (HS) and temperature (TEMP) at the AWS. (c) Comparison of the three differently determined snow heights above the radar box: the probed HS (HS probe), HS calculated with $\overline{v}$ (HS v_mean) and HS calculated utilizing the density of the corresponding snow pits (HS v_pit). The black horizontal line segments indicate the position of the internal layers calculated with $\overline{v}$. (d) The strain rates $\dot{S}$ (Equation (5)) of the respective layers (left ordinate) and the strain S (Equation (4)), each determined for the respective measurement interval. Error bars for $\dot{S}$ were calculated with regard to the different average wave speeds for each radar measurement (see Section *Settling—Compaction of the Snowpack*)

precipitation show horizontally non-persistent incoherent reflections above the snow surface. As the measurements were conducted in the time domain, the effect is comparable with weather radar applications, that is, moving snow flakes generate backscatter during illumination by the radar beam. In comparison, other automatic snow height sensors also receive a more noisy signal during snow precipitation events (e.g. ultrasonic sensors, Bavay *et al.*, 2009). In our data set, the surface reflection is in all cases clearly detectable. No further data calibration

Table II. Comparison of different snow height determinations

Date	Probed snow depth (cm)	Radar snow height ($\overline{v}$) (cm)	Radar snow height (v_{pit}) (cm)	v_{pit} (m/ns)
13.02.09	80	80·8 (1·0)	92·8 (16·0)	0·272
19.02.09	112	109·0 (−2·7)	118·7 (6·0)	0·258
20.02.09	112	109·3 (−2·4)	112·5 (0·4)	0·244
06.03.09	126	135·2 (7·3)	137·5 (9·1)	0·241
12.03.09	157	161·3 (2·7)	166·0 (5·7)	0·244
14.03.09	181·5	173·7 (−4·3)	175·2 (−3·5)	0·239
18.03.09	174	172·1 (−1·1)	171·3 (−1·6)	0·236
25.03.09	189	203·8 (7·8)	205·8 (8·9)	0·239

The probed snow depth is compared with radar-determined snow height d_{snow} either by using the mean wave speed in dry snow $\overline{v} = 0{\cdot}237$ m/ns or the mean wave speed determined at each snow pit individually for each measurement day, v_{pit}. The relative deviances (%) to the respective probed snow depths are written in parentheses.

is necessary. The radar-determined snow height using an average wave speed in dry snow, $\overline{v} = 0{\cdot}237$ m/ns (Heilig *et al*., 2009) varies for all measurements in dry snow conditions in winter 2009 by less than 8% in comparison with the probed snow depth above the radar box (Table II). In a 2·0 m high snowpack, the miscalculated snow height is therefore ±16 cm. This error is, on the one hand, due to inhomogeneous vertical snowpack conditions, which result in variations in the wave speed between adjacent layers and, on the other hand, due to uncertainties in snow probing. It is very likely that the box (Figure 1) was compressed by the snow masses and therefore had no plane surface as discovered after digging out the antennas in April. A difference in snow height of up to 10 cm above the box could occur due to the compression in the middle of the box. While calculating a separate mean wave speed value for each radar measurement, the difference to the probed snow depth increased up to 16% for the measurement of the 13.02.09 and less than 10% for all other measurements. A contributing factor to these specific variations is that the spatial variability of the snowpack conditions above the antennas and within the test site was larger than expected. This results in distinct variability in the characteristics of specific snow layers such as layer thicknesses or layer locations. Even two measurements on adjacent days without melt processes but with low precipitation rates (Figure 4b) and just about 3 m next to each other resulted in different calculated average wave speed values (Table II, 19.02.09, 20.02.09). The accuracy of the snow height determination using $\overline{v}$ for the conversion of the two-way travel time of the radar data could have been distinctly higher, if the uncertainty in snow probing was lower. Our estimate is based on a maximum uncertainty of 10 cm in snow probing. Disregarding this error, the accuracy of the radar-measured snow height utilizing $\overline{v}$ is slightly above the accuracy range of ultrasonic snow sensors (±3 cm, Egli and Jonas, 2009). In comparison with the measurements of Gubler and Hiller (1984), who determined the snow water equivalent with an inaccuracy of less than 5% in comparison with manually conducted measurements for dry snow densities between 200–400 kg/m^3, the data presented here is at approximately 7% slightly above this range, if the mismeasurement of the probed snow depth is not corrected. Recent work of Marshall *et al*. (2005) presents FMCW radar measurements with an uncertainty in SWE and snow depth of about 10%. For other climatic regions, such as maritime areas with distinctly higher average densities or on the opposite more continental areas with distinctly lower mean density values, respective $\overline{v}$ have to be determined. Of course the utilization of height-dependent wave speeds $v(h)$ are desirable but seldomly easily obtained. Using a mean wave speed for a certain climatic region and time of the year is a justified approximation. If similar variabilities in density records of dry snow conditions to the values presented by Heilig *et al*. (2009) with a coefficient of variability of CV = 6% are observable, we assume that the accuracy range of snow height determination utilizing upward-looking GPR is adequately accurate for other climatic regions as well. The SWE in dry snow conditions can be determined in combination with an external snow height measurement directly. If the snow height is known, a mean density for the radar measured snowpack above the antennas can be calculated and therefore the SWE be determined.

Internal layers detected by GPR

Internal layers in the snowpack were observed in all radargrams of this measurement period. Because of the spatial snowpack variability within the test site, the direct one-to-one relation of reflections to snowpack properties is not exact. We related the snow surface reflections to the respective observed snow surface in the density plots and related the signals, which were caused by interferences between the direct wave and the transition air–snow beneath the snowpack, to the location of the strong persistent crust nearby the ground at about 40–50 cm (Figure 5).

In February, with average snowpacks of relatively low density, internal reflections are mainly caused by slight density changes. On 13.02.09 (Figure 5a), the density decrease at 118 cm height indicates the transition to the last new snow event. This event occurred during the previous 48 h before the measurement and can be related to the reflection at 5–6 ns in two-way travel time τ (TWT) shortly below the surface in Figure 3a. Likely, the density decrease of the measurement b at about 92 cm height (Figure 5b) resulted in another reflection at $\tau = 7$ ns in the radargram (Figure 3b). For measurement c, the next day, probably the same density decrease is responsible for the similar reflection. The thin layer of higher density at 110 cm (Figure 3c) is possibly the reason for the broad reflection at 8 ns (Figure 3c). Because of the snowfall with graupel during the radar measurements, this record also contains reflections above the snow surface (Figure 7, 20.02.09). In contrast, the internal reflections in March are very much dominated by strong crusts, which formed at the snow surface through starting melt processes and buried by new snow

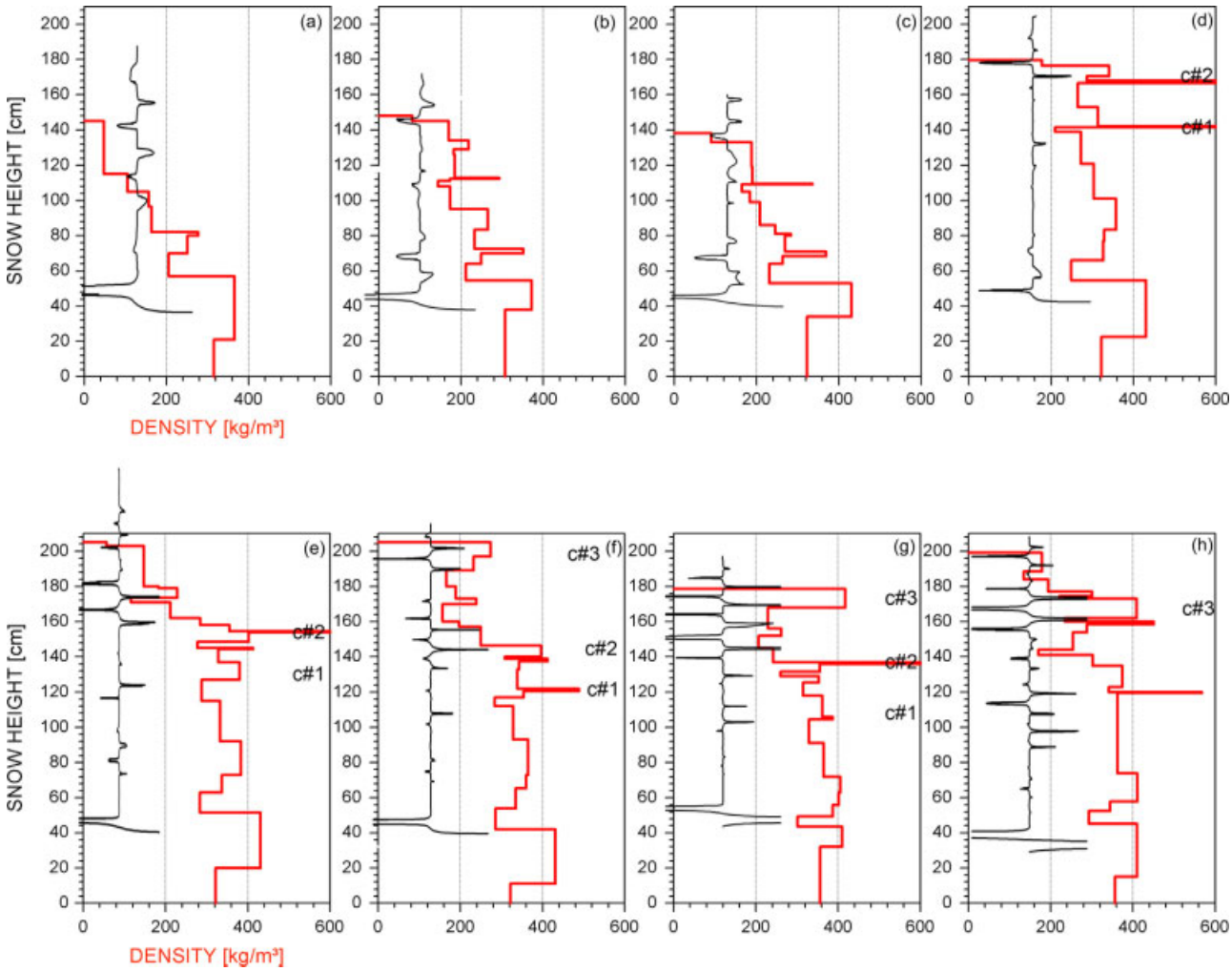

Figure 5. Densities from snow pits measured nearby the radar measurements in relation to the compressed radar traces (black) processed as described in Section GPR-data visualization and magnitude retrieval. The notations are in accordance with Table I; a: 13.02.09, b: 19.02.09, c: 20.02.09, d: 06.03.09, e: 12.03.09, f: 14.03.09, g: 18.03.09, h: 25.03.09

events. Multiple internal layers in the snowpack are traceable over several weeks. After the accumulation of an adequate amount of snow above the antennas, which was clearly discriminable from the direct-wave signal (13.02.09), the first meteorologically remarkable influence on the snowpack, besides large new snow events, happened at the end of February. Figure 4b gives an overview of the temperature and snow height conditions at the AWS location for the measurement period. On 24.02.09, the snowpack at the weather station decreased by 20 cm in height in less than 2 days. The snow surface was additionally wetted by some rain initializing the next snow fall period with again more than 20 cm of new snow in less than 24 h. This snowpack was compacted again and decreased in height by more than 50 cm towards the 06.03.09. Temperatures far above 0 °C (up to 9·5 °C, Figure 4b) and a temperature decrease on the measuring day resulted in a strong melt crust at the snow surface, as obvious from the density increase in Figure 5d. The snowpack layers, which preliminarily compacted on 26.02.09 resulted in another melt crust, which was buried by the following snowfall event. These two melt crusts are visible in the P-visualization of the 06.03.09 (Figure 3d) as well as in the manually recorded density profile (Figure 5d). At $\tau = 8{\cdot}2$ ns (Figure 3d), the buried crust (c#1) is indicated by the positive peak and at about 11–12 ns a very strong amplitude with a positive–negative phase sequence (Figure 7, 06.03.09) is visible, which represents the snow surface crust (c#2) that developed on that day. The absolute position of these events is also indicated in Figure 4c. Another strong precipitation event with more than 30 cm of new snow followed this measurement campaign. Both crusts are still visible in the measurements on 12.03.09. Towards the 14.03.09, the snow height above the GPR antennas increased another 20 cm (Table II; Figure 3f), which was not measured by the AWS. Most likely a strong wind event, which was recorded by a nearby station on the evening of the 12.03.09 caused some snow accumulation at the test site. A strong increase in air temperature on 14.03.09 resulted in high radar reflection rates at the snow surface as visible in Figure 3f. This snow surface formed the third crust (c#3) during the day, recognizable in all later radargrams until the 25.03.09. Due to the higher temperatures in the middle of March (Figure 4b) and therefore likely melt processes,

c#3 covers a large range of reflections in TWT at the snow surface as visible in Figure 3g. Likely, this large reflection range is caused by at least two strong reflections, one at the lower border of the crust and the other one at the upper border at the transition to air (Figure 5g). At the following measurement (25.03.09), c#3 was buried by 40 cm of new snow the previous day. Because of the strong temperature differences ($\Delta T =$ 17 K) in the period between the last measurement and this campaign (Figure 4b), the internal crusts c#1 and c#2 were strongly influenced by melting–freezing processes and therefore the surrounding snowpack assimilated in density and hardness to hardly distinguishable layers. The measurement at the beginning of April was even more influenced by melt processes. We recorded an isothermal snowpack, with wetness intrusions down to 96 cm in the profile. The strong reflection amplitude at about $\tau = 8{\cdot}6$ ns (corresponding to this depth) confirms this observation (Figure 3i). Additional wetness and density differences were recorded as reflections.

Snow wetness

In general, dry snow conditions were prevailing during the field measurements. However, significant wetness influence on the radar measurements is visible on 14.03.09 (Figure 6). The first radar record was obtained in the morning with already positive air temperatures but no measurable melting at the snow surface. The second measurement was conducted in the afternoon with observable melt processes, and infiltration limited to the top 20 cm. We measured an isothermal snowpack at 0 °C down to approximately 20 cm below the surface in a renewed snow pit at 14 : 00 h. The near-surface reflection in Figure 6 is in accordance with these observations. The snow surface has a completely different reflection signature in the afternoon, whereas the lower parts are equal

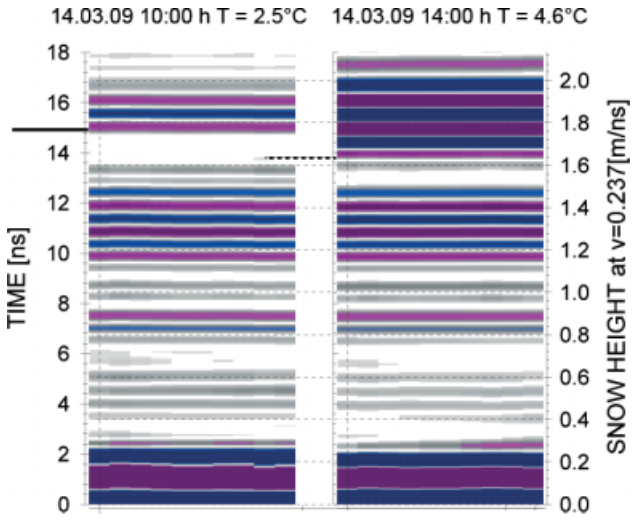

Figure 6. Influence of infiltrating wetness in the snowpack on two radar measurements recorded the same day at different time periods, which are indicated above together with the prevailling air temperature. The horizontal lines indicate the reflection of the snow-surface crust (left) and the depth of the wetness infiltration (right; dashed line)

concerning the reflection and phase structures. Additionally, one can determine very accurately the depth of the melt intrusion on that day, which is an important gain of knowledge for the prediction of wet snow avalanches. Our results indicate that radar measurement from beneath the snowpack is a sufficient technique to record melt intrusions with depth and observe these intrusions temporally. The digging of a snow pit, however, does not provide a comparable information. Recording infiltrating water in snow pits is difficult, because the pit acts as a drainage and distorts the flow path. Because of its destructive nature, it is also not possible to make comparisons from day to day, or only statistically, because there is a large spatial variability (Machado, 2000). Furthermore, the pit wall is exposed to ambient air temperature and solar irradiance and thereby altering the depth of the melt influence. Radar measurements from above the surface, however, are strongly influenced by the melt layer, making a clear detection of the melt front very difficult, because a transition dry–wet is easier detectable than wet–dry. This information can only be provided by upward-looking radar systems.

Settling—compaction of the snowpack

Especially the continuous destruction-free observation of the same snow column over time enables insights into the characteristics of settlement and involved processes. To investigate the related features, we define as $z_n(t_i)$ the position of reflector c_n ($n = 0, 1, 2, 3$) at time t_i (with $n = 0$ being the constant snow–ground interface). The thickness of layer n between two reflectors n and the one below, $n - 1$,

$$d_n(t_i) = z_n(t_i) - z_{n-1}(t_i) = \frac{1}{2}[\tau_n(t_i)\overline{v}_n(t_i) - \tau_{n-1}(t_i)\overline{v}_{n-1}(t_i)]$$

changes in the period t_i to t_{i+1} by

$$\Delta d_n|_{t_{i+1}}^{t_i} = d_n(t_i) - d_n(t_{i+1}),$$

where $\tau_n(t_i)$ is the two-way travel time of the n-th reflector at time t_i and $\overline{v}_n(t_i)$ the mean wave speed over the whole column from the antenna to the reflector at time t_i. To simplify, we use a temporally and vertically constant $\overline{v} = 0{\cdot}237$ m/ns. We normalize the absolute thickness change Δd_n by the mean layer thickness

$$\overline{d}_n|_{t_{i+1}}^{t_i} = \frac{1}{2}[d_n(t_i) + d_n(t_{i+1})]$$

in the respective time period to derive the relative change in thickness of layer n, which yields the dimensionless strain

$$S_n|_{t_{i+1}}^{t_i} = \frac{\Delta d_n|_{t_{i+1}}^{t_i}}{\overline{d}_n|_{t_{i+1}}^{t_i}} \tag{4}$$

observed in the time interval t_i to t_{i+1}. From this, the strain rate follows as

$$\dot{S}_n|_{t_{i+1}}^{t_i} = \frac{S_n|_{t_{i+1}}^{t_i}}{t_{i+1} - t_i} \tag{5}$$

Table III. Location of the three temporal traceable internal reflectors and their spacings in the time domain of $[\triangle\tau|_{n_i}^{n_{i+1}}(t_i)]$, the number of days between the measurements, as well as the average (mean) and the upper quartile (Q3) of the temperature within the time period between the measurements

Date time t_i	c_1 $\tau_1(t_i)$ (ns)	c_2 $\tau_2(t_i)$ (ns)	Spacing $\Delta\tau|_{c_1}^{c_2}(t_i)$ (ns)	c_3 $\tau_3(t_i)$ (ns)	Spacing $\Delta\tau|_{c_2}^{c_3}(t_i)$ (ns)	Days	Mean/Q3 temperature (°C)
06.03.10 : 20	8·5	11·87	3·37				
12.03.10 : 30	7·67	10·38	2·71			6	−2·05/−1
14.03.10 : 00	7·16	9·5	2·34	14·66	5·16	2	−0·10/+0·4
18.03.10 : 00	6·74	9·5	2·76	13·97	4·47	4	+0·97/+2
25.03.10 : 30				13·97		7	−2·86/−0·1

with dimension 1/time, for which we will use the units 1/s. Note that as we have only a limited number of observations at times t_i, we can only use the difference quotient but cannot approximate the differential quotients of the actual strain rate.

Table III displays the change in position above ground of specific layer reflectors in TWT, and Figure 4 shows the strain, strain rates (Figure 4d) and the radar measured location (TWT-depth conversion by $\overline{v}$) of the layers in comparison with the snow surface (Figure 4c). The radar-measured change in snow height of these layers is due to two reasons, which can have an opposing effect on travel time. First, an altered TWT is caused by the physical change of the reflector location due to settlement of the snowpack. Second, due to densification or melt water intrusions, the wave speed is reduced and therefore the TWT of the observed reflection increases. For example, a compaction of the underlaying 1·0 m thick snowpack of $\Delta\rho = +100$ kg/m^3 decreases the wave speed by approximately 6–7% for reasonable density values (100–500 kg/m^3) in snow, resulting in an increased TWT. The apparent strain rates of specific layers can become negative if the TWT of the radar waves changes variably for various reflectors in the snow cover. This is the case for the reflectors c_2 and c_1 at the time range between 14.03.09 and 18.03.09 (Table 3; Figure 4). While the snow layer between the antennas and c#1 is decreasing by approximately 4% in TWT, c#2 is recorded as being constant in time. As the reflector c_1 is situated below c_2, and the TWT of c_1 decreases, we would therefore expect a density increase of approximately 50 kg/m^3 in the layer between c_1 and c_2 to reduce the wave speed to result in a constant TWT of c_2 in the measurements with a time period of 4 days. This density increase between c#1 and c#2 was not observed in the snow pits (Figure 5f, g). Nevertheless, in this case, we expect a settling of c#2 and the underlying layers closer to c#1, which likely caused reflection interferences. Therefore, the first half-cycle of the c#2-reflection is probably not visible and we compared the third half-cycle of the 18.03.09 with the first half-cycle of the 14.03.09. The phase reversal of this reflection, visible in Figure 7, confirms our assumption.

We calculated error bars for the determination of the strain rates using a mean wave speed for all radar measurements (Figure 4). We utilized the recorded densities below the respective reflector and compared the strain rates calculated with the average densities in relation to the layer thicknesses of the snow pits with the strain rates determined with $\overline{v}$. The relative differences between both strain rates range from 1 to 17%, whereas the wave speed differences are always $< 7\%$ and thereby in good agreement with the previously observed wave speed variations in dry snow conditions (Heilig *et al.*, 2009).

Obviously, the highest strain rates were present in the period from 12.03.09 to 14.03.09 (Figure 4d). This is due to the strong new snow load the days before the 12.03.09 and the increasing temperatures in this time period (Figure 4b). At this time of the winter season, the lower parts of the snowpack still participated remarkably in the settlement, which resulted in an increase in density below c#1 (Figure 5f, g). Additionally, for snow conditions without melt water percolation, the strain rates are usually higher for layers closer to the snow surface, due to on average lower densities and a stronger influence of meteorological parameters at the upper parts of the snow cover (e.g. Figure 6). With specific layers as tracers, it seems possible to determine and quantify the strain rates of the snowpack in relation to prevailing snow and weather parameter, given that wave speed is either constant or adequately measured. If compaction or moisture intrusions are not uniformly vertically distributed, wave speed values have to be considered for each layer individually.

INTERPRETATION: PHYSICAL ORIGIN OF REFLECTIONS

The gathered physical information of the presented radar records are the occurrence and the location of a reflection in the snowpack, the reflection's magnitude and its phase structure. The physical origin defines the radar signal response yielding these information. In dry snow conditions, density variation is the sole parameter influencing the dielectric permittivity (Kovacs *et al.*, 1995; Mätzler, 1996). Therefore, reflections are caused by the magnitude of density variation at a two-media transition. In Figure 5, the recorded reflections are compared with the measured density characteristics. Conditionally on the spatial variability of the snowpack, which was larger than expected for a plane measurement field, strong density steps can be related to peaks in the compressed reflection pulse. As the antennas together with the cover box were arranged

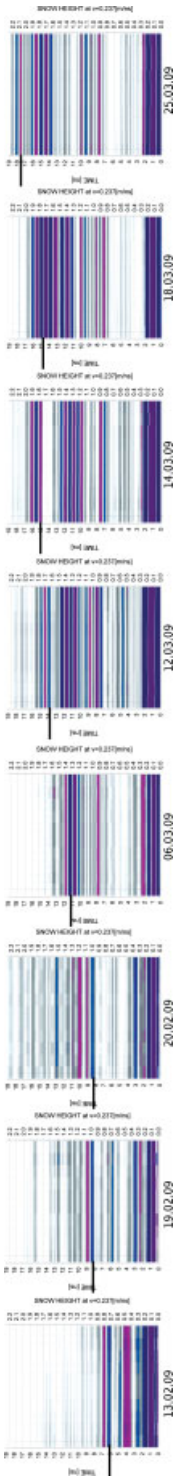

Figure 7. All recorded radargrams of the measurement series in dry snowpack conditions at the Grünsee location. The horizontal lines indicate the snow surface. The snow height values are calculated utilizing $\overline{v} = 0{\cdot}237$ m/ns

in a snowpack at approximately 50 cm snow height, all snow parameters beneath these 50 cm are not recorded. Additionally, the strong influence of the direct waves prevented singularly evaluable reflections of the first 20 cm above the plastic box. Considering only density steps above 80–90 cm in the snow pits, the density characteristics correlate well with the recorded reflections.

Regarding the phase sequences, we can first state that all reflections correspond to dielectric permittivity changes. In dry snow conditions, an increase or decrease in density influence the appearance in phase sequences. The direct wave or mother wavelet, as the first signal observable in all raw radargrams, has a negative–positive phase sequence $(-+)$ for the radar system used. A phase reversal occurs in dry snow conditions, when the density increases is negative in radar-wave direction (from the ground to the snow surface). Therefore, the strong positive density gradients in the measurements according to items a and b (Figure 5) at approximately 118 cm (a) and approximately 92 cm snow height (b) are obtained with a negative–positive phase sequence. All snow surface reflections before the measurement of panel d have a $(-+)$-sequence, too, and appear to be in agreement with the prevailing conditions of a density and permittivity decrease from snow to air (Figure 3). Strong negative density gradients, on the contrary, result in a phase reversal with a $(+-)$-sequence. This is observable for all crusts within the snowpack and at the surface, apart from crust c#1 for some measurements (Figure 3, panels d, f, g). The circumstances in which some c#1-reflections do not result in a phase reversal are not contradictory to the physical principles. Likely, the reflections of the density decreases slightly below the crust interfere with the crust reflection, which causes the observed phase structure. Especially, the measurement shown in item e (Figure 5) shows a remarkable decrease in density below the crust and thus an almost comparable negative phase amplitude in relation to the positive oscillation. The smaller and with a lower gradient developed density decreases in the measurements according to panels f and g (Figure 5) appear in a distinctly less developed negative phase and by this support this interpretation.

Especially, the phase reversal of the near surface signal for the two measurements in mid-March (panels e, f) is a clear example for the influence of temporal changes of the dielectric permittivity on the phase sequence. In panel e, the low-density new snow below the surface has a phase sequence in correspondence to the mother wavelet, whereas in panel f the sequence appears inversely (Figure 3). A crust evolution at the surface altered the reflection response and a moisture intrusion later in the afternoon increased this phase appearance (Figure 6).

Regarding the normalized amplitude, a quantitative comparison is not possible. In this study, the values should only be regarded as qualitative indicators, as a real normalization is not possible so far. The antennas were buried in the snowpack for over two months, with the consequence that influences of different temperatures

and humidity occurrences within the plastic box cannot be completely neglected. However, the maximum amplitude values of specific reflections confirm qualitatively the previous observations. Apart from the first measurement (13.02.09), where the surface amplitude is still influenced by the direct wave and therefore shows a far too high amplitude, all surface reflection magnitudes of loose snow at the surface have distinctly lower amplitudes than surface–crust reflections (Figure 4a). Especially the new-snow layer of the 12.03.09, above the surface of the previous radar record, confirms this. The magnitude of internal reflections appears always in the same graduation (c#1 < c#2 < c#3).

CONCLUSION

We could show that it is possible to observe the temporal evolution of the snowpack using upward-looking GPR technique from beneath the snow cover. The results are encouraging in several aspects, technically and scientifically. Regarding the difficulties concerning the antenna coverage of an uneven surface, the accuracy of the snow height determination of the radar measurements is in good agreement with the probed snow depth. We achieved an accuracy slightly below the one of ultrasonic snow height sensors. In contrast to the sonic sensors, the used radar is feasible of recording internal layers and following their temporal evolution. In the determination of SWE values, this study is in good agreement with previous works using FMCW radar systems. The utilized system is a suitable technique to measure automatically the infiltration of liquid water with depth due to melt processes at the surface. These measurements could be a supplemental contribution to the predictability of wet snow-avalanche events. By the use of internal layers as tracers, we determined different strain rates for layers, which are situated closer to the surface than for deeper layers. The phase sequences enabled the relation of snow layers to reflections. For the case of a highly resolved temporal observation of the snowpack with the utilized pulsed radar systems, it might be possible to improve the predictability of avalanches (e.g. wet snow avalanches or avalanches triggered by large accumulation rates) and to gather spatial information of internal layering in areas, which are difficult and dangerous to access. In combination with regularly recorded snow pits, a more detailed conclusion on the evolution of internal layers with time is possible, and thereby a better validation of snowpack simulation models is achievable.

ACKNOWLEDGEMENTS

This research is partly funded by grant DFG EI672/5-1 to O. Eisen, PIEPS GmbH, WSL Swiss Federal Institute for Snow and Avalanche Research and r-hm Risk and Hazard Management. The radar equipment was provided by the Alfred Wegener Institute for Polar and Marine Research. For assistance in the field we thank W. Alkofer, S. Deeg and T. Herrmann and the Alpenbahnen Spitzingsee for their support. We thank H.-M. Schuler for discussions that helped to optimize the test arrangement and the anonymous referees for valuable suggestions.

REFERENCES

Annan A. 2002. GPR-History, Trends and Future Developments. *Subsurface Sensing Technologies and Applications* **3**: 4 253–266.

Bales R, Molotch N, Painter TH, Dettinger M, Rice R, Dozier J. 2006. Mountain hydrology of the Western United States. *Water Resources Research* **42**: W08432.

Barnett T, Adam J, Lettenmaier D. 2005. Potential impacts of a warming climate on water availability in snow-dominated regions. *Nature* **438**: 303–309.

Bavay M, Lehning M, Jonas T, Löwe H. 2009. Simulations of future snow cover and discharge in Alpine headwater catchments. *Hydrological Processes* **23**: 95–108.

Bindschadler R, Choi H, Shuman C, Markus T. 2005. Detecting and measuring new snow accumulation on ice sheets by satellite remote sensing. *Remote Sensing of Environment* **98**: 388–402.

Brun E, David P, Sudul M, Brugnot G. 1992. A numerical model to simulate snowcover stratigraphy for operational avalanche forecasting. *Journal of Glaciology* **38**: 13–22.

Brun E, Martin E, Simon V, Gendre C, Coleou C. 1989. An energy and mass model of snowcover suitable for operational avalanche forecasting. *Journal of Glaciology* **35**: 333–342.

Colbeck S, Akitaya E, Armstrong R, Gubler H, Lafeuille J, Lied K, McClung D, Morris E. 1990. The International Classification for Seasonal Snow on the Ground. Technical report. International Commission of Snow and Ice of International Association of Scientific Hydrology. Prepared by Working group on Snow Classification.

Comm. Glaciology. 2009. Mass balance Vernagtferner. http://www.lrz-muenchen.de/~a2901ad/webserver/webdata/massbal/index.html [accessed: 31 July 2009].

Egli L, 2008. Spatial variability of new snow amounts derived from a dense network of Alpine automatic stations. *Annals of Glaciology* **49**: 51–55.

Egli L, Jonas T. 2009. Hysteretic dynamics of seasonal snow depth distribution in the Swiss Alps. *Geophysical Research Letters* **36**: L02501: DOI:10.1029/2008GL035545.

Escher-Vetter H, Kuhn M, Weber M. 2009. Four decades of winter mass balance of Vernagtferner and Hintereisferner, Austria: Methodology and results. *Annals of Glaciology* **50**: 87–95.

Gubler H. 1981. An inexpensive remote snow-depth gauge based on ultrasonic wave reflection from the snow surface. *Journal of Glaciology* **27**: 95 157–163.

Gubler H, Hiller M. 1984. The use of microwave FMCW radar in snow and avalanche research. *Cold Regions Science and Technology* **9**: 109–119.

Heilig A, Schneebeli M, Eisen O. 2009. Upward-looking ground-penetrating radar for monitoring snowpack stratigraphy. *Cold Regions Science and Technology* **59**: 2–3 152–162.

König M, Sturm M. 1998. Mapping snow distribution in the Alaskan Arctic using aerial photography and topographic relationships. *Water Resources Research* **34**: 12 3471–3483.

Kovacs A, Gow A, Morey R. 1995. The in-situ dielectric constant of polar firn revisited. *Cold Regions Science and Technology* **23**: 245–256.

Kronholm K, Schweizer J. 2003. Snow stability variation on small slopes. *Cold Regions Science and Technology* **37**: 453–465.

Lehning M, Bartelt P, Brown R, Russi T, Stöckli U, Zimmerli M. 1999. Snowpack model calculations for avalanche warning based upon a new network of weather and snow stations. *Cold Regions Science and Technology* **30**: 145–157.

Machado A. 2000. Spatial and temporal variability of meltwater pathways in a continental subalpine snowpack. Master's thesis, University of Colorado, Boulder.

Marshall H, Koh G. 2008. FMCW radars for snow research. *Cold Regions Science and Technology* **52**: 118–131.

Marshall H, Koh G, Forster R. 2005. Estimating alpine snowpack properties using FMCW radar. *Annals of Glaciology* **40**: 157–162.

McClung D, Schaerer P. 2006. *The Avalanche Handbook*, 3rd edn, The Mountaineers: Seattle.

Mätzler C. 1996. Microwave permittivity of dry snow. *IEEE Transactions on Geoscience and Remote Sensing* **34**: 2 573–581.

Perrin S, Bibaut A, Duflos E, Vanheeghe P. 2000. Use of Wavelets for Ground-Penetrating Radar Signal Analysis and Multisensor Fusion in the Frame of Landmines Detection. *IEEE International Conference on Systems, Man and Cybernetics*, vol. 4, Nashville, TN 2940–2945.

Pozdnoukhov A, Purves R, Kanevski M. 2008. Applying machine learning methods to avalanche forecasting. *Annals of Glaciology* **49**: 107–119.

Sandmeier K. 1998. *ReflexW Version* 4·1 *Manual*. Sandmeier KJ: Karlsruhe, Germany; http://www.sandmeier-geo.de/Download/reflexw manual.pdf [accessed: 2009].

Schneebeli M, Laternser M. 2004. A Probalistic Model to Evaluate the Optimal Density of Stations Measuring Snowfall. *Journal of Applied Meteorology* **43**: 711–719.

Schweizer J, Wiesinger T. 2001. Snow profile interpretation for stability evaluation. *Cold Regions Science and Technology* **33**: 179–188.

Turcotte R, Fortin L-G, Fortin V, Fortin J-P, Villeneuve J-P. 2007. Operational analysis of the spatial distribution and the temporal evolution of the snowpack water equivalent in southern Québec, Canada. *Nordic Hydrology* **38**: 3 211–234.

Xia J, Franseen E, Miller R, Weis T. 2004. Application of deterministic deconvolution of ground-penetrating radar data in a study of carbonate strata. *Journal of Applied Geophysics* **56**: 3 213–229.

Ice dynamics and kinematics

Inference of velocity pattern from isochronous layers in firn, using an inverse method

Olaf EISEN[1,2]

[1] *Versuchsanstalt für Wasserbau, Hydrologie und Glaziologie (VAW), ETH Zürich, CH-8092 Zürich, Switzerland*
[2] *Alfred-Wegener-Institut für Polar- und Meeresforschung, PO Box 120161, D-27515 Bremerhaven, Germany*
E-mail: olaf.eisen@awi.de

ABSTRACT. The suitability of a kinematic approach for finding the velocity field from dated internal-layer architecture in firn is investigated. Internal layers are isochrones and the depositional age of a layer particle is treated as a tracer. The forward problem uses two-dimensional steady-state advection of age and conservation of mass to predict layer architecture. Different combinations of constraints on horizontal and vertical velocity properties are added. The inverse problem can be formulated as the solution of underdetermined and overdetermined systems of equations. The systems are solved using singular-value decomposition, allowing analysis of the singular-value spectrum, model resolution and data resolution. Solutions of the inverse problem are evaluated by comparing the velocity-field solutions with synthetic input velocity data. Unlike conventional accumulation estimates, the new approach takes lateral advection into account, enabling improved separation of spatial and temporal variations in accumulation. Two glaciological applications are presented: the determination of the migration velocity of a spatially non-stationary accumulation pattern and reconstruction of past accumulation and its stationarity over time.

1. INTRODUCTION

Internal layering is widely observed by radar sounding in cold firn and ice, on high-alpine and polar glaciers as well as ice sheets. Layer architecture results from the interplay of spatio-temporal variation of surface accumulation, bottom melting and advection caused by ice dynamics. Most layers are isochrones, i.e. surfaces of equal age. Whereas age information retrieved from ice cores is representative only for the immediate vicinity of the drilling location, the layer architecture provides a spatial picture. It represents an integrated view of the temporal evolution of an ice mass.

Several studies have exploited this property to enhance the view of past conditions and to understand present conditions. The simplest application is the one-dimensional (1-D) direct inversion of layer depth and density distribution for accumulation, covering shallow depth and a few millennia at most (see *Annals of Glaciology* 39 and 41 for a summary of studies).

However, effects of horizontal advection are not considered; these effects can introduce errors into the inferred accumulation. Recently, Arcone and others (2005) used an accumulation-rate model to investigate how accumulation-rate anomalies and ice velocity affect stratigraphic variations of internal layers.

Other approaches use forward modelling of the whole ice column and least-squares techniques to solve for the accumulation rate by minimizing differences between calculated and measured internal-layer architecture (Siegert and others, 2003; Jacobel and Welch, 2005). Parrenin and Hindmarsh (2007) provide analytical solutions for layer stratigraphy, depending on mass balance, flow field and ice thickness. Of special interest is the reconstruction of trajectories of particle flow to improve firn and ice-core dating and separate spatial from temporal variations. Based on observed thickness anomalies between isochrones, Leonard and others (2004) identified a high-accumulation region upstream of the Vostok (Antarctica) ice core and quantified its effect on the paleoclimatic reconstruction. Morse (1997) iteratively solved a non-linear least-squares minimization problem to invert the surface velocity field at Taylor Dome, Antarctica, for ice rheology and flow parameters. Waddington and others (2007) used a forward model for calculating surface height, particle paths and internal layer shapes to infer an accumulation pattern that reproduces the observed layer architecture. They apply the method to the area around Taylor Dome.

A formal inverse approach is formulated in this study, using observed and dated layer architecture in firn, i.e. the age–depth distribution, to kinematically determine horizontal and vertical velocities. The direct solution for the flow field from internal layers in the firn column with depth-dependent density poses a problem that has not been investigated previously. Because of the variation of density with depth, the modelling of firn rheology is much more difficult than that of solid ice. Studies concerned with deeper layers (below a few hundred metres depth) therefore usually consider density to be constant over the whole ice column. The kinematic approach has the advantage that no assumptions about firn rheology are needed and a true density distribution can be used.

2. INFERRING VELOCITIES FROM TRACER FIELDS

The debate in the oceanographic community around the question of whether or not a tracer field can be inverted for velocity, as formulated by Wunsch (1985), showed that it is in principle possible. It can be said that useful information about the underlying flow field can be extracted from a tracer distribution, even for underdetermined problems (i.e. there are fewer known equations than unknowns; see Appendix).

A number of physical and chemical parameters can be used as tracers in ice masses. Of particular interest is the age of deposition at the ice-sheet surface of a certain material particle, hereafter simply referred to as age. In comparison

Table 1. Simulation parameters

Scenario*	$\bar{u}^{\mathrm{ref}}$	$\partial_x u^{\mathrm{ref}}$	$\breve{u}^{\mathrm{ref}}$
	$\mathrm{m\,a^{-1}}$	$\mathrm{a^{-1}}$	
NF	0	0	0
SF	1	0	0
MF	10	0	0
MDF	10	4×10^{-5}	$\neq 0$
Dimension	**Min.**	**Max.**	**Increment**
Prognostic forward model:			
x	0	5 km	100 m
z	0	100 m	1 m
SVD solution:			
x	0	5 km	500 m
z	0	50 m	5 m

*NF: no flow; SF: slow flow; MF: moderate flow; MDF: moderate divergent flow with a 20% increase in u over the x domain. $\bar{u}$ is the mean horizontal velocity averaged over the entire domain.

to physical or chemical tracers, such as isotopic composition or aerosols, age can definitely be considered a conservative tracer in the sense that it is subject to neither diffusion nor reaction. In the context of ice-core deep drilling for paleoclimate research, glaciological applications focused mainly on forward modelling of this tracer underestimated environmental and dynamical conditions (e.g. Nereson and Waddington, 2002; Clarke and others, 2005). Typical application examples are reconnaissance for suitable drilling sites or ice-core dating by flow modelling.

Before solving the inverse problem for the kinematic model with real field data, it is important to understand the strengths and identify the pitfalls of the kinematic model. This can best be achieved by creating synthetic data to test algorithms, as all parameter fields are known beforehand. As a result, the solution of the inverse problem can be checked. A simple prognostic forward model is used here to create synthetic stationary age distributions under prescribed conditions for a range of flow scenarios of varying complexity for the upper 100 m of the ice sheet, i.e. the firn column. Subsequently, a diagnostic inverse approach is applied to the synthetic age distribution to solve for the velocity field.

The inversion is based on singular-value decomposition (SVD). SVD has several advantages over other schemes (e.g. least-squares normal equations) especially in terms of analyzing the inversion results (Wunsch, 1996). Various combinations of boundary conditions and constraints are used to set up systems of equations to be solved, covering the full range from under- to overdetermined systems. Comparison of reference velocities calculated by the prognostic model with inferred velocities from the inverse problem provides a means of evaluating the performance and reliability of the SVD for different constraints.

Flow scenarios, the inversion formalism and constraints are introduced in sections 2–4. The main body of the paper (section 5) exploits SVD properties to interpret the results. Finally, the kinematic model is applied to two glaciological problems (section 6). The first problem deals with application of the inverse approach to determine the migration velocity of an accumulation pattern from the age–depth distribution and an accumulation proxy at the surface. The second problem aims to reconstruct the past distribution of accumulation and determine its stationarity over time.

2.1. Kinematic equations

The approach presented here is based on a kinematic consideration of the firn volume; the equations for conservation of energy and momentum are therefore not taken into account. In general, the distribution of any tracer in a medium can be described by an advection–diffusion equation. Details of the tracer transport and formulation in ice sheets are discussed extensively by Clarke and others (2005). In our case, the corresponding tracer is depositional age $A = A(\mathbf{r}, t)$, a non-diffusive property, which obeys

$$\partial_t A + \mathbf{v} \cdot \nabla A = 1, \tag{1}$$

where $\mathbf{v} = (u, w) = \mathbf{v}(\mathbf{r}, t)$ is velocity, ∂_t denotes partial derivative with respect to the subscript variable (here time t) and all calculations are carried out in two-dimensional (2-D) space $\mathbf{r} = (x, z)$ (z positive and increasing downward). See the Appendix for conventions and a list of notation.

Equation (1) is sometimes referred to as the age equation (e.g. Hindmarsh and others, 2006). The righthand side represents a source term, which is responsible for the actual aging of the firn with time.

The second governing equation is the conservation of mass,

$$\partial_t \rho + \nabla \cdot (\rho \mathbf{v}) = 0, \tag{2}$$

where $\rho = \rho(\mathbf{r}, t)$ is density. These two equations form the fundamental system of linear equations used in the forward problem.

2.2. Assumptions and boundary conditions

A number of assumptions are made for the sake of simplicity; however, they do not reduce the general applicability of the inverse-problem formulation. The considered firn volume extends from the surface $z = 0$ to an arbitrary depth $z = z_{\max}$. The density distribution is assumed to be laterally homogeneous and independent of time, i.e. $\partial_x \rho = \partial_y \rho = \partial_t \rho = 0$ (Sorge's law), but depth dependence is maintained ($\partial_z \rho \neq 0$). This assumption is well justified on a regional scale for ice-sheet plateaus (e.g. Frezzotti and others, 2004; Richardson-Näslund, 2004; Rotschky and others, 2004; Arcone and others, 2005), but has to be considered with care on cold alpine glaciers.

Note that the depth dependency of density is a prominent deviation from the incompressibility assumption often used in ice-sheet modelling. Time dependence of Equations (1) and (2) is maintained in the prognostic forward model. The system of equations to be solved, however, is formulated in a time-independent way so that $\partial_t(\cdot) = 0$ (where $(\cdot)$ denotes any term to be differentiated) as the forward model produces a steady-state age distribution as output.

No forces appear in the above equations, simplifying matters such that the upper boundary can be taken as a horizontal surface, i.e. parallel to x. Position and direction of scalar and vector quantities therefore always refer to this surface. (Consider a radargram as an illustrative example. It contains records of the reflector depth with respect to the relative surface. A topographic correction is applied only during data processing.) The kinematic boundary condition at the surface

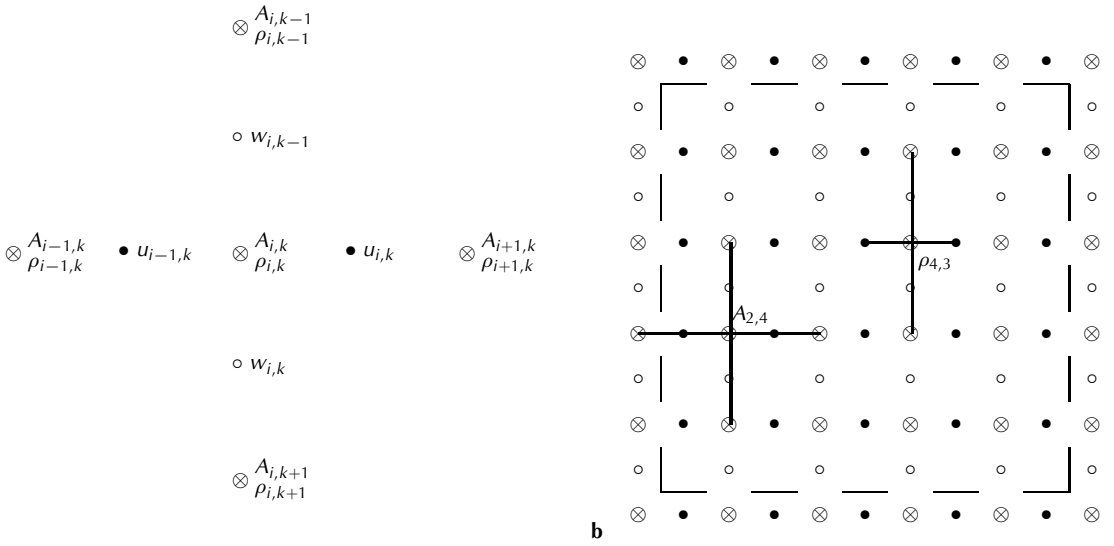

Fig. 1. (a) Unit-cell scheme of the numerical grid used for solving the linear system of Equation (3). (b) Scheme of the triplex-staggered numerical grid for $I = K = 6$. The uppermost row corresponds to the surface. Distance between nodes of similar types is Δx and Δz and between nodes of different types is $\Delta x/2$ and $\Delta z/2$ in the horizontal and vertical directions, respectively. The cross centred on the $\otimes$-node labeled $A_{2,4}$ represents the unit cell in (a) and strikes all nodes involved in the age equation for the $A_{2,4}$ node. Likewise, the cross labeled $\rho_{4,3}$ strikes all nodes involved in the conservation-of-mass equation for the $\rho_{4,3}$-node. Both equations can therefore only be solved for those A-nodes within the region bounded by the dashed line, referred to as solution domain. The $\otimes$-nodes on the corners are displayed for completeness, but not used in the inverse problem.

is $w(x, z = 0) = \dot{b}(x)/\rho_0$, where $\dot{b}(x)$ is the surface accumulation and $\rho_0 = \rho(z = 0)$ is the density at the surface. Additional constraints are introduced in section 4.2, primarily as prescribed velocity properties.

2.3. Prognostic forward model

The forward model runs under prescribed stationary allocations of density, horizontal velocity and accumulation on an ordinary grid, discretized with finite differences. It calculates the vertical velocity from the combined effect of accumulation at the surface, advection and densification, and yields the synthetic age–depth distribution. Starting from an initial laterally homogeneous, vertically increasing age distribution, the prognostic model runs in a transient mode until a steady state is reached, i.e. when the particles from the surface at $t = 0$ reach the edge of the domain. As a boundary condition, age is set to zero at the surface. At the inflow of the model domain, the horizontal age gradient is set to zero.

Details of grid parameters are listed in Table 1. The age–depth distribution constitutes the essential output, which is passed to the inverse problem. The prescribed horizontal velocities $\mathbf{u}^{\mathrm{ref}}$ and calculated vertical velocities $\mathbf{w}^{\mathrm{ref}}$ of the forward model are defined for all gridpoints. We later refer to them as the reference-velocity field (denoted by the superscript 'ref'), against which the inferred velocity field (denoted by the superscript 'est') is compared.

2.4. Linear system for inverse model

The time-independent forms of Equations (1) and (2) are

$$u\partial_x A + w\partial_z A = 1 \tag{3a}$$

$$\rho\partial_x u + \rho\partial_z w + w\partial_z \rho = 0. \tag{3b}$$

The discretization schemes for solving this linear system on a triplex-staggered grid (a grid consisting of three subgrids shifted relative to each other) are adapted from Fiadeiro and Veronis (1982) and Wunsch (1985). The input fields of age and density are prescribed on a rectangular grid, the A-grid, with a grid spacing of Δx and Δz in the x and z directions, respectively. The A-grid has $I \times K$ nodes. Corresponding indices for the gridded variables are $i = 1, \ldots, I$ for the horizontal coordinate (increasing downstream, left to right) and $k = 1, \ldots, K$ for the vertical coordinate (increasing downwards, top to bottom), as indicated in Figure 1a. The grid nodes representing u and w (u and w grid) are shifted by half the grid spacing in the horizontal and vertical direction, respectively, relative to the nodes on which the input parameters for age A and density ρ are prescribed (Fig. 1).

The application of staggered-grid differences to Equation (3) leads to a discrete system, which for a unit cell (Fig. 1a) can be expressed as

$$\begin{pmatrix} c^{\alpha}_{i-1,k} & c^{\beta}_{i,k} & c^{\gamma}_{i,k-1} & c^{\delta}_{i,k} \\ c^{\kappa}_{i-1,k} & c^{\lambda}_{i,k} & c^{\mu}_{i,k-1} & c^{\nu}_{i,k} \end{pmatrix} \begin{pmatrix} u_{i-1,k} \\ u_{i,k} \\ w_{i,k-1} \\ w_{i,k} \end{pmatrix} = \begin{pmatrix} 1 \\ 0 \end{pmatrix}. \tag{4}$$

Detailed expressions of the staggered-grid differences and coefficients $\{c^{\alpha,\ldots,\nu}_{i,k}\} = f(A, \rho)$ are given in the Appendix. As sketched in Figure 1b for the node labeled $A_{2,4}$, five A-nodes are involved in the discretized representation of the age equation for a single node. Consequently, the $u_{i,k}, w_{i,k}$ for a unit cell always depend on the values of A and ρ at the neighbouring nodes. These values are contained in the $c_{i,k}$-coefficients in Equation (4). The $u_{i,k}, w_{i,k}$ therefore cannot be fully determined on the boundaries, but only within the dashed region shown in Figure 1. This region is termed the solution domain. This formulation has the advantage that no other specific conditions are necessary at the boundaries of the domain where the inverse problem is solved with SVD.

As can also be seen in Figure 1b, in each dimension, x and z, the total number n of nodes for unknown variables u

and w differs. Within the solution domain, the number n_u^x of variables u in a row (x direction) is $n_u^x = I - 1$. Analogously, the number of variables along a column (z direction) is $n_u^z = K - 2$. For the variable w, $n_w^x = I - 2$ and $n_w^z = K - 1$. The total number of elements of each variable within the solution domain is $n_u = n_u^x n_u^z$ and $n_w = n_w^x n_w^z$. Defining the vectors and matrix

$$\begin{aligned}
\mathbf{d} &= \{d_p\} = (1, 1, \ldots, 0, 0)^T \in \mathcal{R}^M, \qquad M = 2 n_u^z n_w^x, \\
\mathbf{v} &= \{v_q\} = \left(\{u_{i,k}\}, \{w_{i,k}\}\right)^T \\
&= (\mathbf{u}^T, \mathbf{w}^T)^T \in \mathcal{R}^N, \qquad N = n_u + n_w, \\
\mathbf{M} &= \{M_{p,q}\} = \left(\{c_{i,k}^{\alpha}\}, \ldots, \{c_{i,k}^{\nu}\}\right) \in \mathcal{R}^{M \times N},
\end{aligned} \tag{5}$$

allows us to set up the matrix equation

$$\mathbf{M}\mathbf{v} = \mathbf{d}. \tag{6}$$

The variables p, q are merely indices of vector and matrix elements, to be distinguished from the coordinate indices i, k of the actual grid. The vector $\mathbf{d}$ represents the data in data space $\mathcal{R}^M$, and the vector $\mathbf{v}$ represents the model parameters in model space $\mathcal{R}^N$. M is the number of (known) equations and N is the number of unknowns, in our case the velocities within the solution domain. The relationship between model parameters and data is described by the model matrix $\mathbf{M}$, sometimes referred to as the data kernel (Menke, 1989, p. 9).

The reader might wonder how it is actually possible to define uncertainties of the data vector $\mathbf{d}$, which contains only ones and zeros. For this particular inverse problem, the measurable quantities age and density appear on the lefthand side in the matrix elements of the data kernel. The uncertainty of the data vector is therefore a measure of how the uncertainties of the data kernel cause the vector on the righthand side of Equation (6) to differ from exactly ones and zeros, even for exact velocities $\mathbf{v}$. This point is explored in more detail using a Monte Carlo-based approach in section 5.5.

3. SINGULAR-VALUE DECOMPOSITION

3.1. Principles

The SVD of a matrix $\mathbf{M}$ is a generalization of the spectral decomposition of a square to a rectangular matrix. The spectral decomposition of a rectangular matrix always exists. Here we apply SVD to calculate the pseudo-inverse (or generalized inverse) of $\mathbf{M}$, mainly following the notation of Wunsch (1996). Any rectangular matrix $\mathbf{M}$ can be decomposed into a factorization of the form

$$\mathbf{M} = \mathbf{U}\mathbf{\Lambda}\mathbf{V}^T, \tag{7}$$

where $\mathbf{U}$ and $\mathbf{V}$ are both unitary rectangular matrices, $\mathbf{U} \in \mathcal{R}^{M \times M}$, $\mathbf{V} \in \mathcal{R}^{N \times N}$ and $\mathbf{V}^T$ denotes the transpose of $\mathbf{V}$. The generally non-square matrix $\mathbf{\Lambda} \in \mathcal{R}^{M \times N}$ contains the singular values (square root of eigenvalues) of $\mathbf{M}$ in decreasing order on the main diagonal, $\Lambda_{p,q} = \delta_{pq}\lambda_p$, with the Kronecker symbol δ_{pq}. The matrix $\mathbf{V}$ contains a set of orthogonal base-vectors of $\mathbf{M}$, spanning the N-dimensional model (or solution) space, whereas the matrix $\mathbf{U}$ contains a set of orthogonal base-vectors spanning the M-dimensional data (or observation) space. The number R of non-zero singular values is the rank of $\mathbf{M}$. If some singular values are zero or $M \neq N$, one or more of the rows or columns of $\mathbf{\Lambda}$ must all be zeros. Those columns of $\mathbf{U}$ and $\mathbf{V}$ that are multiplied by zeros only can be dropped, thus reducing the matrices in Equation (7) to the expression

$$\mathbf{M} = \mathbf{U}_R \mathbf{\Lambda}_R \mathbf{V}_R^T , \tag{8}$$

where the subscript R indicates the number of columns with $\mathbf{U}_R \in \mathcal{R}^{M \times R}$ and $\mathbf{V}_R \in \mathcal{R}^{N \times R}$. $\mathbf{\Lambda}_R \in \mathcal{R}^{R \times R}$ is the square submatrix of $\mathbf{\Lambda}$ with non-vanishing singular values. It can be shown (e.g. Wunsch, 1996) that $\mathbf{V}_R \mathbf{\Lambda}_R^{-1} \mathbf{U}_R^T$ is the pseudo-inverse of $\mathbf{M}$, which we use to solve Equation (6) for the unknown model vector. We obtain the solution

$$\mathbf{v} = \mathbf{V}_R \mathbf{\Lambda}_R^{-1} \mathbf{U}_R^T \, \mathbf{d} , \tag{9}$$

where $\mathbf{\Lambda}_R^{-1}$ is the inverse of $\mathbf{\Lambda}_R$, i.e. with λ_p^{-1} on the main diagonal ($\lambda_p \neq 0$) and zeros elsewhere.

The above expressions for $\mathbf{M}$, $\mathbf{U}$ and $\mathbf{V}$ define four spaces: the model range $\mathbf{V}_R \in \mathcal{R}^{N \times R}$ (column space of $\mathbf{M}$); the model nullspace $\mathbf{V}_0 \in \mathcal{R}^{N \times (N-R)}$; the data range $\mathbf{U}_R \in \mathcal{R}^{M \times R}$ (row space of $\mathbf{M}$); and the data nullspace $\mathbf{U}_0 \in \mathcal{R}^{M \times (M-R)}$. Depending on the size of M, N and R, not all of these spaces need to exist (in the sense that they are not empty sets). Conditions for existence of these spaces, definition for over- and underdetermined systems of equations and combinations of these are listed in the Appendix.

If there is a data nullspace $\mathbf{U}_0$ ($R < M$), and if the data have components in it, then it will be impossible to fit the data exactly. This data mismatch between true data and estimated data, referred to as the residual norm, will then be different from zero. (As a norm we will use the L_2 norm or Euclidean length of a vector, denoted by the operator $\| \cdot \|$; see Appendix for definition and further information.) On the other hand, if the model has components in the model nullspace $\mathbf{V}_0$ ($R < N$) then it will be impossible to determine the model exactly: hence the term model nullspace. In that case, the model solution can be presented as a sum of the particular solution given by Equation (9), which contains only range vectors and solves Equation (6), and an arbitrary homogeneous solution $\mathbf{V}_0 \boldsymbol{\alpha}$ which solves the homogeneous system of equations $\mathbf{M}\mathbf{v} = \mathbf{0}$. The vector $\boldsymbol{\alpha}$ contains $(N-R)$ coefficients for the linear combination of the $(N-R)$ column vectors of $\mathbf{V}_0$ in the model nullspace, about which the equations provide no information.

The SVD is related to the least-squares approach. All of the structure imposed by SVD is also present in least-squares solutions. One commonality is that the SVD simultaneously minimizes the residual and solution norms (e.g. Scales and others 2001, p. 66). However, the SVD solution generalizes the least-squares solution to the case where the matrix inverses of $\mathbf{M}^T\mathbf{M}$ or $\mathbf{M}\mathbf{M}^T$, the simplest forms, do not exist, for example if the system is not full rank (Wunsch, 1996, 157f). An important advantage of the application of SVD and the interpretation of the solution is that only a single algebraic formulation is necessary for over-, under- or just-determined systems. The SVD provides its control over the solution norms, uncertainties and covariances through choice of the effective rank $\hat{R} \leq R$, which leads to the so-called truncated SVD, demonstrated in section 5.1. The truncated form makes a clear separation between range and nullspace in both solution and data spaces.

3.2. Resolution

A useful feature of the SVD is that it provides direct access to the resolution obtainable when mapping between model

and data spaces (see Menke, 1989, p. 62f; Wunsch, 1996, p. 165). The model resolution matrix, defined as

$$\mathbf{T_V} = \mathbf{V}_R\mathbf{V}_R^T, \tag{10}$$

determines the relationship between the general solution and the particular solution. If no model nullspace exists ($R = N$), the general and particular solution are equal. Then $\mathbf{T_V} = \mathbf{I}_N$, the $N \times N$-dimensional identity matrix, meaning that the model is completely resolved. If a nullspace exists, non-zero terms will appear off the main diagonal in Equation (10), so only averages of some model parameters can be resolved.

Analogously, the data resolution matrix

$$\mathbf{T_U} = \mathbf{U}_R\mathbf{U}_R^T \tag{11}$$

provides information on how well the observed data are estimated when the model solution obtained with the generalized inverse is used in the forward model to predict observable quantities.

Both resolution matrices are functions of the data kernel $\mathbf{M}$, which contains the a priori information about the physical representation of the problem, i.e. by the time-independent Equations (3). When the problem is linear, resolution matrices depend on neither the model parameters $\mathbf{v}$ nor the data $\mathbf{d}$.

3.3. Error covariance and uncertainty

Solving the inverse problem yields an estimate of model parameters, denoted $\mathbf{v}^{\text{est}}$, which are subject to uncertainties. Using the estimated $\mathbf{v}^{\text{est}}$ in the forward problem, Equation (6) yields a prediction of the data vector $\mathbf{d}^{\text{est}}$ which differs from the true data vector $\mathbf{d}$ by some residuals, denoted $\mathbf{n} = \mathbf{d} - \mathbf{d}^{\text{est}}$. The residuals can generally arise from two contributions: noise from errors in the measurement of data and inadequacy of the forward algorithm to describe the problem exactly.

The covariance $\mathbf{C_{vv}}$ of the estimated model parameters depends on the residual covariance $\mathbf{R_{nn}}$ (the second moment or covariance matrix of $\mathbf{n}$; see Appendix for details). It can be shown to be (Wunsch, 1996, p. 143)

$$\mathbf{C_{vv}} = \mathbf{V}_R\mathbf{\Lambda}_R^{-1}\mathbf{U}_R^T\mathbf{R_{nn}}\mathbf{U}_R\mathbf{\Lambda}_R^{-1}\mathbf{V}_R^T\ . \tag{12}$$

In the case of uncorrelated uniform variance σ_n^2 of the data, Equation (12) simplifies to

$$\mathbf{C_{vv}} = \sigma_n^2\mathbf{V}_R\mathbf{\Lambda}_R^{-2}\mathbf{V}_R^T\ . \tag{13}$$

The covariance of the model parameters arises from uncertainties present in the data and generates uncertainty in the coefficients of the model range vectors. Data covariance is thus mapped onto model covariance. To obtain the complete solution uncertainty $\mathbf{P_{vv}}$ of the model parameters, the influence of the missing nullspace contribution also has to be taken into account. According to Wunsch (1996),

$$\mathbf{P_{vv}} = \mathbf{C_{vv}} + \mathbf{V}_0\mathbf{R}_{\boldsymbol{\alpha\alpha}}\mathbf{V}_0^T, \tag{14}$$

where $\mathbf{R}_{\boldsymbol{\alpha\alpha}}$ is the second-moment matrix (or covariance matrix; see Appendix) of the coefficients $\boldsymbol{\alpha}$ of the model nullspace $\mathbf{V}_0$, forming the homogeneous solution $\mathbf{V}_0\boldsymbol{\alpha}$. The matrix $\mathbf{R}_{\boldsymbol{\alpha\alpha}}$ may be entirely unknown, or an estimate from a priori information might be available. The uncertainty of the residuals $\mathbf{P_{nn}}$ follows from the variance of the estimated residuals about their mean (Wunsch, 1996, p. 117), which can be written as

$$\mathbf{P_{nn}} = \mathbf{U}_0\mathbf{U}_0^T\mathbf{R_{nn}}(\mathbf{U}_0\mathbf{U}_0^T)^T. \tag{15}$$

The covariance Equation (12) of the estimated model parameters is very sensitive to small non-zero singular values. Solution variance can be reduced by choosing an effective rank $\hat{R} < R$ to exclude small λ_p. Inspecting the singular-value spectrum of the data kernel enables one to choose an appropriate cut-off size for contributing singular values (Menke, 1989, p. 122). This artificial reduction of model- and data-space dimensions leads to rank deficiency and therefore lower resolution as well as increased dimensions of the nullspaces, but decreases model covariance. The choice of the effective rank $\hat{R}$ therefore provides a means to trade-off variance and resolution, or solution norm and residual norm, respectively.

3.4. Scaling and weighting

Weighting is in general used to give more importance to certain observations than to others, mainly to correct for uncertainty. An undesired weighting effect occurs if a system consists of different physical equations, involving different physical quantities.

In our case, the conservation-of-mass and the age equation involve the quantities age and density. In the linear system Equation (6), the rows of $\mathbf{M}$ represent these equations. Their different physical origin leads to different norms of the row vectors (i.e. Euclidean length) of the matrix $\mathbf{M}$.

To correct for this effect, we first perform row scaling of the matrix $\mathbf{M}$ by multiplying each row with the reciprocal of its row norm (see Appendix for details). This is carried out below by operations with the matrix $\mathbf{W}$, which contains the row norms of $\mathbf{M}$ on its diagonal. Likewise, the column vectors of $\mathbf{M}$ have different norms. We therefore require column scaling after the row scaling is performed. This is done by operations with the matrix $\mathbf{S}$. Performing row scaling first and column scaling second transforms our linear system Equation (6) from the original space to the so-called scaled space, denoted by a tilde. The transformation has the form

$$\mathbf{W}^{-T/2}\mathbf{M}\mathbf{S}^{T/2}\mathbf{S}^{-T/2}\mathbf{v} = \mathbf{W}^{-T/2}\mathbf{d} \tag{16}$$

which we abbreviate as

$$\widetilde{\mathbf{M}}\tilde{\mathbf{v}} = \tilde{\mathbf{d}}. \tag{17}$$

The notation for $\mathbf{W}$ stems from its Cholesky decomposition $\mathbf{W} = \mathbf{W}^{T/2}\mathbf{W}^{1/2}$ (Wunsch, 1996, p. 159). Similarly, $\mathbf{S}$ has the Cholesky decomposition $\mathbf{S} = \mathbf{S}^{T/2}\mathbf{S}^{1/2}$ and contains the column norms of the already row-scaled matrix $\mathbf{W}^{-T/2}\mathbf{M}$ on its diagonal.

The SVD is applied in the scaled space. Back transformation of the solution $\tilde{\mathbf{v}}$ in the scaled space to the desired solution $\mathbf{v}$ in the original space is carried out by $\mathbf{v} = \mathbf{S}^{T/2}\tilde{\mathbf{v}}$. It can be shown that for a full-rank underdetermined (overdetermined) system, row (column) scaling is irrelevant as the respective scaling matrix is no longer present in the solution (Wunsch, 1996, p. 161, 164). Despite this fact, we always apply both scalings to cover all general cases. In addition to scaling, the use of $\mathbf{W}$ and $\mathbf{S}$ allows a degree of control of the relative norms of solution and residual.

3.5. Separation of mean and variation

Depending on the problem we are dealing with, information about the variations of the velocity around an average is more interesting than the average velocity, as the velocity variations tell us more about the processes occurring at the ice-sheet surface and their interaction with ice dynamics.

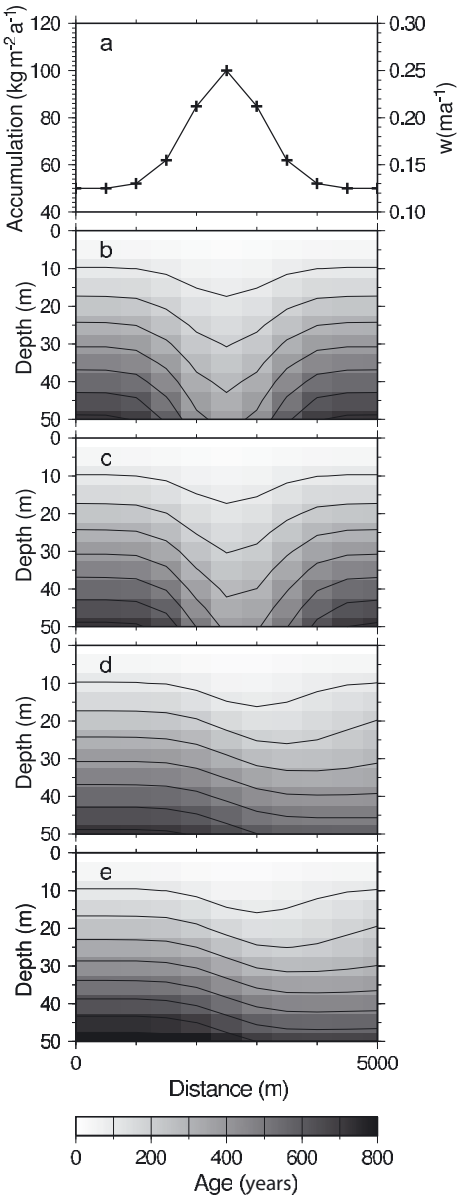

Fig. 2. (a) Accumulation forcing and (b–e) resulting age–depth distributions using different horizontal velocities. Scenarios include: (b) no flow, NF; (c) slow flow, SF; (d) moderate flow, MF; and (e) moderate divergent flow, MDF, for the upper 50 m of the firn column (Table 1). Greyscale represents age values at grid nodes, with the spatial resolution of the greyscale corresponding to the resolution used for discretizing the inverse problem. Contours are lines of equal age. Horizontal flow is from left to right. Crosses in (a) indicate position of nodes on *A*-grid and scale on the right is vertical velocity at the surface.

Unfortunately, the minimum-norm property of the SVD will result in a solution that is smallest, in the sense of being closest to zero. This means that we might derive the wrong velocity field structure. It is therefore feasible to consider only the variations of the flow field on a homogeneous background. Hence, we separate the mean flow from its spatial variations by

$$\mathbf{v} = \overline{\mathbf{v}} + \check{\mathbf{v}}, \tag{18}$$

where $\overline{\mathbf{v}} = (\overline{\mathbf{u}}^T, \overline{\mathbf{w}}^T)^T$ is the mean flow field and $\check{\mathbf{v}} = (\check{\mathbf{u}}^T, \check{\mathbf{w}}^T)^T$ is the spatial variation. Separate mean values $\bar{u} = \langle \mathbf{u} \rangle$ and $\bar{w} = \langle \mathbf{w} \rangle$, each averaged over the entire domain, are used for horizontal and vertical velocities, respectively. $\overline{\mathbf{u}} = \bar{u}\,\mathbf{i}_{n_u}$ and $\overline{\mathbf{w}} = \bar{w}\mathbf{i}_{n_w}$, where $\mathbf{i}_n$ is a vector of length n with all ones. Our linear system Equation (3) can then be reformulated as

$$\mathbf{M}\check{\mathbf{v}} = \check{\mathbf{d}} = \mathbf{d} - \mathbf{M}\overline{\mathbf{v}}. \tag{19}$$

In the case that the mean velocities used for this separation are incorrect, the SVD solution of the inverse problem will try to correct this error (e.g. by providing a velocity variation on average very different from zero). For the rest of the paper we drop the tilde. We assume that separation of mean and variation and subsequent scaling has been applied prior to SVD. The results are then discussed in terms of the variational component of the velocity field $\check{\mathbf{v}}$, as well as the complete velocity field $\mathbf{v}$.

4. SIMULATIONS AND INVERSE PROBLEMS

4.1. Scenarios

Synthetic scenarios of flow are created with the forward model, using physical parameters chosen to mimic real conditions. The horizontal flow field $\mathbf{u}^{\mathrm{ref}}$ is prescribed. A Gaussian variation in surface accumulation $\dot{b}(x)$ is superimposed, i.e.

$$\dot{b}(x) = \dot{b}_0 \left(1 + \exp\left[-\frac{(x - x_\mu)^2}{x_\sigma^2}\right]\right), \tag{20}$$

where $\dot{b}_0 = 50\,\mathrm{kg\,m^{-2}\,a^{-1}}$ is the background accumulation, a typical value for the Antarctic plateau. The maximum accumulation occurs at $x_\mu = 0.5(x_{\min} - x_{\max})$, the centre of the x domain, with $\dot{b}(x_\mu) = 2\dot{b}_0$. $x_\sigma = x_\mu/6$ determines the width of the distribution (Fig. 2a). Following Richardson and Holmlund (1999), density is parameterized as

$$\rho(z) = \rho_{\mathrm{i}} + (\rho_0 - \rho_{\mathrm{i}})\mathrm{e}^{-c_\rho z}. \tag{21}$$

The variables $\rho_0 = 400\,\mathrm{kg\,m^{-3}}$ and $\rho_{\mathrm{i}} = 900\,\mathrm{kg\,m^{-3}}$ represent the density at the surface and the density of solid ice, respectively, and $c_\rho = 0.05\,\mathrm{m^{-1}}$. Such a density distribution is commonly observed in Antarctica.

For the numerical forward model and the inverse problem, the continuous functions defined in Equations (20) and (21) are discretized onto the respective grids. The triplex-staggered grid used in the inverse problem of the linear system Equation (3) was explained in section 2.4, with more specifications given below. The forward model is implemented on a grid spanning 5 km in the horizontal and 100 m in the vertical direction, containing 51 × 101 nodes (Table 1). This volume is sufficient to cover the firn region of cold polar or high-altitude sites. It also comprises those length scales which show prominent variations in internal-layer architecture over short distances, as imaged by radar at various places in Antarctica (Rotschky and others, 2004; Arcone and others, 2005; Anschütz and others, 2006).

The effect of four different flow regimes of firn with prescribed horizontal velocity field (Table 1) on the age–depth distribution is displayed in Figure 2. In the simplest case, no horizontal advection takes place (scenario 'no flow', NF). This could be considered the case on a broad ice dome or along an ice divide. The other cases consider constant slow flow (SF) $\bar{u} = 1\,\mathrm{m\,a^{-1}}$ and constant moderate flow (MF) $\bar{u} = 10\,\mathrm{m\,a^{-1}}$, which are also typical for polar ice sheets (Bamber and others, 2000; Xiaolan and Jezek, 2004) or high-altitude alpine glaciers (e.g. Lüthi and Funk, 2001; Schwerzmann and others, 2006). For these three scenarios the prescribed velocity variation $\check{\mathbf{u}}^{\mathrm{ref}} = \mathbf{0}$.

For the moderate velocity of $\bar{u} = 10\,\mathrm{m\,a^{-1}}$, a fourth scenario considers divergent flow (MDF) of the form $u(x) = \bar{u} + c_u(x - x_\mu)$ (c_u is such that $u(x)$ increases by 20% from $0.9\bar{u}$ to $1.1\bar{u}$ over the x domain); therefore $\breve{\mathbf{u}}^{\mathrm{ref}} \neq \mathbf{0}$. A scenario with non-constant horizontal velocities is the most likely case to be encountered in reality, so it will be the special focus of the analysis in section 5. Typical velocities for fast ice-stream flow are not taken into account in the main part of this feasibility study, but a set-up with a higher flow velocity of $50\,\mathrm{m\,a^{-1}}$ is treated in the application of the inverse approach to glaciological problems in section 6. The scenarios clearly show how the varying horizontal advection affects the resulting age–depth distribution (Fig. 2). For scenario SF, the effect of the accumulation variation tapers off before an affected ice particle leaves the model domain. For both MF scenarios, advection is larger so the accumulation effect is still present at the outflow of the model boundary.

4.2. Additional constraints

A standard approach to determine the parameters of a physical model, assumed to be a compatible description of a system, is to minimize an objective function that gauges the misfit between measurements and model results. Model physics are usually enforced as constraints on the minimization in the form of exact equations, so-called hard constraints (e.g. Wunsch, 1996). For ice-flow modelling, this was presented by MacAyeal (1993) in the case of estimating the basal friction of an ice stream and later applied to real data (MacAyeal and others, 1995; Vieli and Payne, 2003; Joughin and others, 2004; Larour and others, 2005). Truffer (2004) estimated the basal velocity of valley glaciers.

In addition to the basic physical description of a system, certain aspects of a solution such as structure, norm or boundary values are also sometimes known a priori. This information is valuable and helps to restrict the lack of uniqueness in solutions of inverse problems. It can be included in the objective function either as a hard constraint by Lagrange multipliers, or as a soft constraint by trade-off between the norm of the solution and the norm of the data mismatch. The trade-off can be implemented in several ways (e.g. by weighting, tapered least squares or damped least squares (Menke, 1989, p. 52)). Although the SVD does not explicitly employ an objective function, constraints can likewise be imposed. An example is provided by Waddington and others (2007), who also use SVD to invert a linear system of equations representing a thermomechanical ice-flow model.

Each of the different sets of constraints applied in the following exercises with a synthetic scenario can, in reality, also be determined from measured data. For the problem addressed here – the flow and deformation of firn – a first guess of the flow field at the surface is usually made. Horizontal surface velocities can be measured directly (e.g. ground-based global positioning system surveys of stakes) or indirectly (e.g. observations with satellite-based interferometric synthetic aperture radar). Here, the reference velocity field $\mathbf{v}^{\mathrm{ref}}$ represents possible measurements and thus provides a priori information about various velocity characteristics. (For real field applications, these $\mathbf{v}^{\mathrm{ref}}$ would be subject to measurement errors. For the synthetic scenario, however, they are the true values.)

It is therefore possible to prescribe the horizontal velocity at one or more positions at the surface ($z = 0$). From this point onwards, discrete index notation is used. The surface corresponds to index $k = 1 = k_0$, so that

$$u_{i,k_0} = u^{\mathrm{ref}}_{i,k_0} \tag{22}$$

can be prescribed on one or more horizontal nodes i at the surface. In addition to the velocity, other properties such as the derivative of horizontal velocity (e.g. uniform, divergent or convergent flow) can also be prescribed. With $\Delta_x u^{\mathrm{ref}}_{i,k}$ denoting the horizontal difference of the horizontal reference velocity at the node (i, k) between neighbouring nodes, we can constrain

$$u_{i-1,k_0} - u_{i,k_0} = \Delta_x u^{\mathrm{ref}}_{i,k_0}. \tag{23}$$

Distribution of horizontal velocities with depth is deducible from measurements of borehole deformation, enabling us to use $k \neq k_0$ in Equation (22) for values at depth at the borehole location $i = i_\mathrm{b}$. We can also infer properties of surface-parallel shearing, i.e.

$$u_{i_\mathrm{b},k} = u^{\mathrm{ref}}_{i_\mathrm{b},k}, \tag{24}$$

$$u_{i_\mathrm{b},k-1} - u_{i_\mathrm{b},k} = \Delta_z u^{\mathrm{ref}}_{i_\mathrm{b},k}, \tag{25}$$

where $\Delta_z u^{\mathrm{ref}}_{i_\mathrm{b},k}$ is the vertical difference of horizontal reference velocity at (i_b, k). The case $\Delta_z u^{\mathrm{ref}}_{i_\mathrm{b},k} = 0$, i.e. constant horizontal velocity along the vertical, is commonly referred to as plug flow. This case is used in sections 5 and 6 below.

Not only can horizontal deformations be deduced from borehole deformation, it is also possible to directly determine the vertical velocities by different methods. One way is to observe the movement of markings in a borehole wall (Hawley and others, 2004; Schwerzmann and others, 2006). This provides similar information for the vertical velocities, i.e.

$$w_{i_\mathrm{b},k} = w^{\mathrm{ref}}_{i_\mathrm{b},k}, \tag{26}$$

$$w_{i_\mathrm{b},k-1} - w_{i_\mathrm{b},k} = \Delta_z w^{\mathrm{ref}}_{i_\mathrm{b},k}. \tag{27}$$

To infer information about the properties of the problem posed here, such as stability of the solution and general solution structure, different combinations of the equations constraining the linear system Equation (3) are used to increase the degree of determinacy. The constraints are enforced by expanding the number of rows of the model matrix $\mathbf{M}$ and the data vector $\mathbf{d}$ in Equation (6). Each combination of constraints is referred to as an inverse problem, which is then applied to a simulation scenario (Table 2). The simplest case (denoted *Plain*) does not employ further constraints and simply considers equations for age advection and conservation of mass. Other constraints are set up by prescribing conditions for u or w: the horizontal or vertical velocity at the surface as boundary condition (denoted *Bu* or *Bw*, respectively), plug flow (*Pf*) and horizontal divergence (*Du*). Moreover, combinations of these constraints are also used in the inverse problems (e.g. *BwPf*, *BuPf*, *BwDu*, *BuDu* and *BwPf*).

The inverse problem *Plain* shows that the principal property of the kinematic approach is underdeterminacy, i.e. there are fewer known equations M than unknowns N ($M = 162 < N = 180$). All other inverse problems with constraining equations are less underdetermined, with the majority being overdetermined systems (Table 2). Only the rather complex MDF scenario (moderate flow with divergence) is solved with several constraints and is used in section 5 below to discuss the solution properties in detail.

The SVD inversion is implemented with the linear algebra package (LAPACK) routines integrated in Matlab™. As most

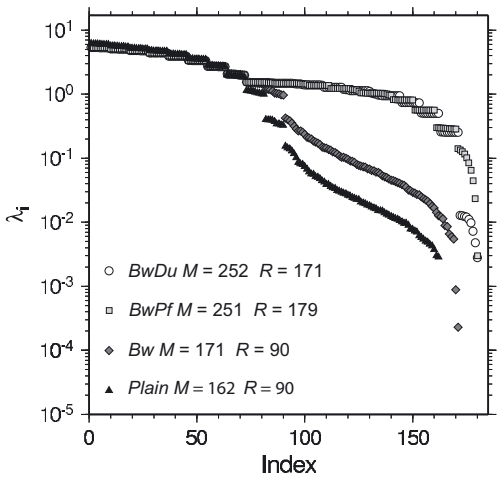

Fig. 3. Singular-value spectrum for four inverse problems with different constraints applied to the MDF scenario (see Table 1). $N = 180$, the number of unknown variables, for all inverse problems.

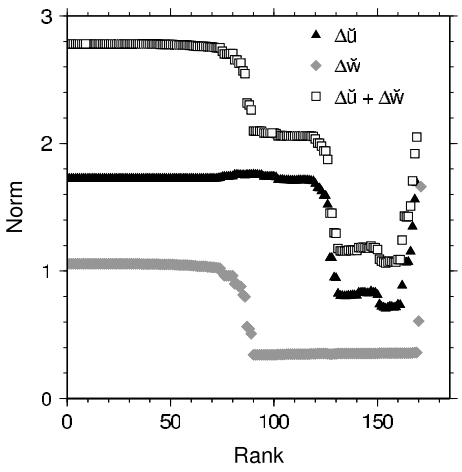

Fig. 4. Distribution of velocity-difference norms $\|\Delta\breve{\mathbf{u}}\|$, $\|\Delta\breve{\mathbf{w}}\|$, and $\|\Delta\breve{\mathbf{u}}\|+\|\Delta\breve{\mathbf{w}}\|$ as a function of reduced rank $\hat{R}$ for inverse problem *Bw* for the MDF scenario. The norms are scaled with the square root of their mean.

of the densification of snow takes place in the upper part of the firn column, the inverse problems only address the upper 50 m. The grid used for the inverse problems spans 11×11 nodes, with increments of 500 m and 5 m in the horizontal and vertical, respectively. It has a five-fold lower resolution, but its nodes coincide with a subset of the grid used in the forward problem. As a result, the fields of age and density input to the inverse problems do not have to be interpolated. A linear interpolation of the *u* and *w* reference velocity fields ($\mathbf{u}^{\text{ref}}$ and $\mathbf{w}^{\text{ref}}$) is carried out to project these values onto the triplex-staggered grid (Fig. 1). Evidently, the lower resolution and the interpolation will have some influence on the results. However, this effect could be considered equivalent to small measurement errors for real data. The influence of data errors on the results is considered at the end of section 5.

5. RESULTS AND ANALYSIS

This section compares the solutions of the different inverse problems for the MDF scenario. The advantages of SVD-based concepts for comprehensive analyses are first illustrated by investigating the singular-value spectrum (Fig. 3) together with some norm properties (Fig. 4) and resolution matrices (Fig. 5) for the MDF scenario. The velocity fields of the solutions are presented (Fig. 6) for three inverse problems. Subsequently, the distribution of several norms (Fig. 7) is discussed, which enables us to evaluate the solutions and compare the results for the inverse problems.

Table 2. Prescribed constraints and system properties

Problem*	u, w	$\partial_x u$	$\partial_z u$	M	R	$\hat{R}$
Plain	–	–	–	162	162	90
Bw	$w_{i,0}$	–	–	171	171	90
Bu	$u_{i,0}$	–	–	172	172	100
Pf	–	–	$0\,\forall(i,k)$	242	180	170
Du	–	$\Delta_x u\,\forall(i,k)$	–	243	180	171
BwPf	$w_{i,0}$	–	$0\,\forall(i,k)$	251	180	180
BuPf	$u_{i,0}$	–	$0\,\forall(i,k)$	252	180	180
BwDu	$w_{i,0}$	$\Delta_x u\,\forall(i,k)$	–	252	180	171
BuDu	$u_{i,0}$	$\Delta_x u\,\forall(i,k)$	–	253	180	172

*Age advection and conservation of mass are considered for all cases. Inverse-problem coding: *Plain*: no additional constraints; *Bw*: boundary conditions of *w* at surface prescribed; *Bu*: boundary conditions of *u* at surface prescribed; *Du*: horizontal divergence of *u* prescribed at all depths; and *Pf*: plug flow (no shear) prescribed. Constraints are enforced by additional equations to model matrix **M**.

The first norm type is the L_2-norm (see Appendix) of the residual and solution vectors, $\|\breve{\mathbf{n}}\|$ and $\|\breve{\mathbf{v}}\|$, respectively. (We consider the solution of the velocity variation $\breve{\mathbf{v}}$, our main interest, instead of the complete velocity field $\mathbf{v}$.) The residual norm is a measure of the mismatch between the data and the model predictions of the data by the estimated model parameters $\breve{\mathbf{v}}$. The solution norm is a measure of the length of the solution vector $\breve{\mathbf{v}}$. The SVD simultaneously minimizes these norms to produce the particular solution, with the rank $\hat{R}$ determining the trade-off between residual and solution norm.

The second type of norm determines the misfit between the reference velocities $\breve{\mathbf{v}}^{\text{ref}}$ (which is the right 'answer' from the prognostic forward model linearly interpolated to the *u* and *w* grid) and the velocity-field solution $\breve{\mathbf{v}}^{\text{est}}$. This misfit norm is calculated separately for horizontal and vertical velocities

$$\|\Delta\breve{\mathbf{u}}\| = \|\breve{\mathbf{u}}^{\text{ref}} - \breve{\mathbf{u}}^{\text{est}}\|$$

and

$$\|\Delta\breve{\mathbf{w}}\| = \|\breve{\mathbf{w}}^{\text{ref}} - \breve{\mathbf{w}}^{\text{est}}\|.$$

Hereafter, these misfit norms are referred to as velocity-difference norms. They provide a measure of how well the inversion for a specific inverse problem performed with respect to the known reference dataset.

5.1. Singular-value spectrum

We focus on four inverse problems with different constraints to determine the solution for the velocity field of the MDF scenario: the underdetermined and simplest case *Plain*; the almost-determined inverse problem *Bw* (boundary conditions of *w* at surface prescribed); and the overdetermined inverse problems *BwPf* and *BwDu* (as *Bw*, additionally with plug flow *Pf* or horizontal divergence *Du* prescribed as constraints, respectively (Table 2)).

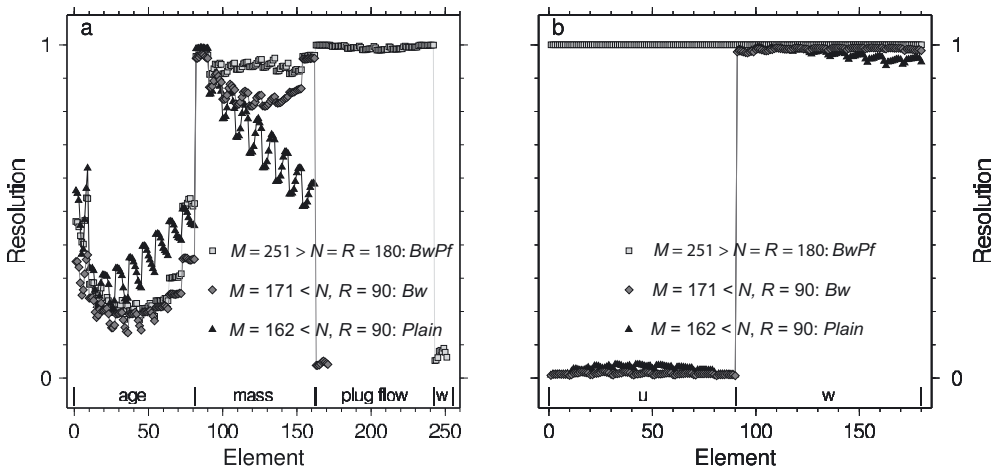

Fig. 5. Diagonal elements of (a) data resolution matrix $\mathbf{T_U}$ and (b) model resolution matrices $\mathbf{T_V}$ for the inverse problems *BwPf*, *Bu* and *Plain*, applied to the MDF scenario with $N = 180$. In (a), components of $\check{\mathbf{d}}$ (element of data for *BwPf*) correspond to the age equation, conservation-of-mass equation, plug-flow constraint and constraint of vertical velocity at the surface, as indicated on the abscissa. In (b), components of $\check{\mathbf{v}}$ (element of model parameter corresponding to u and w, respectively) are also indicated.

The first third of the ordered singular values (up to index 72 in Fig. 3) is basically identical for all inverse problems. Beyond this index, up to index 170, the spectra of the overdetermined inverse problems fall off slowly in several steps up to index 170, whereas the underdetermined inverse problems show only one or two further steps before falling steadily.

All spectra show a final discrete drop at singular values of ~0.25–0.5. Such an abrupt and final discrete drop in a singular-value spectrum is a typical phenomenon for various problems (Menke, 1989). Beyond the final discrete drop, all spectra fall continuously on the log scale. The spectra for underdetermined inverse problems decrease with increasing index faster than the overdetermined inverse problems. Whereas the rate of decrease of the spectrum for *Plain* does not change significantly, the other inverse problems show an increasing rate of decrease for the smallest singular values on the log scale.

In general, the spectra show greater differences for approximately the smallest 20–30% of the singular values. This has important implications for the residual norms and solution norms. Using the untruncated spectra for estimating the model parameters usually results in very small residual norms, equivalent to high parameter resolution, but larger solution norms. The corresponding velocity fields show very detailed velocity structures which, however, need not be correct.

To demonstrate the influence of the choice of the reduced rank $\hat{R}$, Figure 4 displays the resulting difference norms for the inverse problem *Bw* of the whole range of possible values for $\hat{R}$. The difference norm of vertical velocities $\|\Delta\check{\mathbf{w}}\|$, weighted with the square root of its mean, is constant at about 1 for $\hat{R} \leq 80$, then falls off rapidly to steady values around 0.26 before it rapidly increases for $\hat{R} > 169$. This distribution indicates that the vertical reference velocity structure is best approached for $90 \leq \hat{R} \leq 169$, although not exactly matched. This can be confirmed by checking the complete velocity structure for other $\hat{R}$ in figures comparable to Figure 6 (omitted for brevity).

The distribution of $\|\Delta\check{\mathbf{u}}\|$ for *Bw*, likewise weighted with the square root of its mean, is constant around 1.7–1.8 for $\hat{R} < 120$. Two plateaux are present for $130 \leq \hat{R} \leq 160$. In this region, the mismatch of horizontal reference and solution velocities is at its minimum. For $\hat{R} > 160$, $\|\Delta\check{\mathbf{u}}\|$ increases with rank $\hat{R}$.

Adding both velocity-difference norms, each weighted with the square root of its mean velocity, a broad minimum with two plateaux for $\|\Delta\check{\mathbf{v}}\|$ is apparent again for $130 \leq \hat{R} \leq 160$. This range corresponds to the tail of the singular-value spectrum (Fig. 3), where the singular values fall continuously. Similar analysis for the variation of difference norms with reduced rank for the other inverse problems yields equivalent findings: the velocity-difference norms always show a minimum for a range of singular values before showing the tendency to decrease more rapidly with larger indices. Within this minimum region, the choice of $\hat{R}$ leads only to small differences of the final velocity solution. The inverse problems which constrain the horizontal velocity at the surface, i.e. *Bu*, *BuPf* and *BuDu*, basically display the same features.

One choice for $\hat{R}$ is the index of the last step-like drop-off as the lower bound of the singular-value spectrum, used for estimating the solution of our inverse problem in Equation (9). The continuously and rapidly falling part of the singular spectra is thus truncated, a common practice when using SVD for solving inverse problems (e.g. Wunsch, 1996).

This leads to poorer resolution, but smaller solution norms and velocity-difference norms, and yields sufficiently realistic results for most inverse problems (Fig. 6). Although the resulting smallest singular value of the truncated spectra is about the same order of magnitude for all inverse problems, the corresponding reduced rank $\hat{R}$ differs significantly (Table 2). This results from the fact that, depending on the number and type of constraints, the equations show a varying degree of linear independence. The smaller the singular values, the more linearly dependent are the equations. For *BwPf*, however, this choice of $\hat{R} = 171$ at the final discrete drop produces a field of almost constant horizontal velocities, implying that important information is still present in the tail of small singular values for larger $\hat{R}$. For *BwPf* it is actually possible to maintain the full rank and obtain realistic solutions.

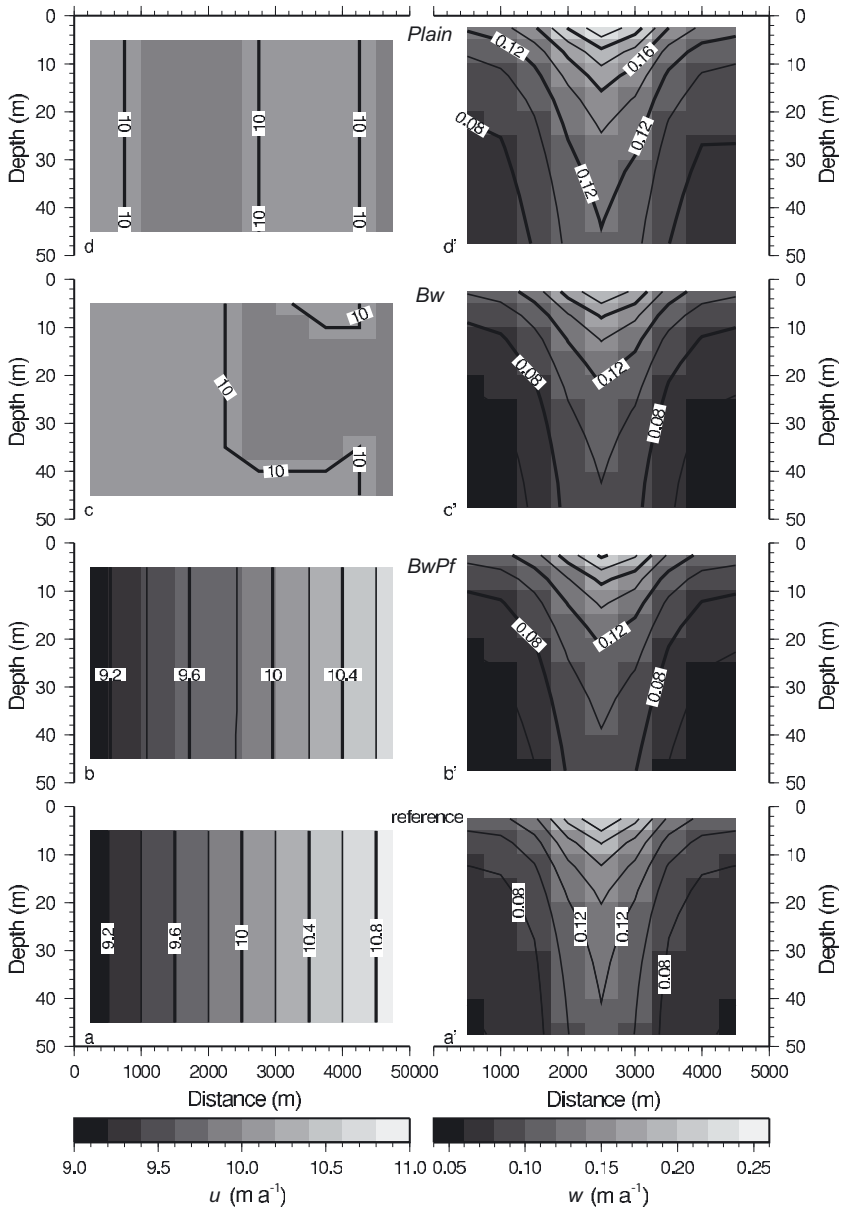

Fig. 6. Solutions for the horizontal (left, a–d) and vertical (right, a′–d′) velocity fields for the MDF scenario of inverse problems *Plain* (d, d′), *Bw* (c, c′), *BwPf* (b, b′), and the reference fields (a, a′). The different horizontal and vertical spatial domains of **u** and **v** result from the different grids used (Fig. 1).

To accommodate this observation, a more subjective choice for $\hat{R}$ would be to choose a singular value of 0.2 as the cut-off value for all inverse problems. Which choice to make is in general difficult, especially if no further details are available from a priori information. The final discrete step-like drop-off was chosen for all inverse problems, apart from *BuPf* and *BwPf* for which full rank is maintained. This is justified as *BuPf* does not display a falling tail of singular values (not shown) and the drop for *BwPf* occurs only for a very large index and is less severe than for the comparable spectrum of *BwDu* (Fig. 3).

5.2. Model and data resolution

The resolution matrices $\mathbf{T_U}$ and $\mathbf{T_V}$ provide other means of judging the solution of an inverse problem. If non-diagonal elements are non-zero the related main-diagonal element must be less than unity, indicating that this parameter is not fully resolved, i.e. only averages of nearby parameters can be determined.

The solution of three inverse problems with different constraints for the MDF scenario is now discussed. At full rank, the data are fully resolved for all underdetermined inverse problems, and the model parameters are fully resolved for all overdetermined inverse problems. The latter is the case for *BwPf*, for which the full rank $R = 180$ is maintained (Fig. 5). For the truncated underdetermined solutions (*Plain* and *Bu*) discussed for the MDF scenario above, the model resolution matrix $\mathbf{T_V}$ indicates that the horizontal velocities are only poorly resolved (Fig. 5b). The vertical velocities are equally well resolved for both inverse problems. It will become evident that this is in accordance with a comparison of the actual velocity fields shown in Figure 6. Without checking the reference velocity field it is therefore possible to assume that, in the underdetermined cases, the vertical velocity solutions are more reliable than the horizontal velocity solutions.

For all overdetermined or truncated underdetermined cases, the data cannot be fitted exactly. This gives rise to larger residuals. The order of the diagonal elements of the data-resolution matrix $\mathbf{T_U}$ in Figure 5a follows from that of the structure of $\mathbf{M}$ of the linear system Equation (6), rearranged as a vector. This vector represents groups of equations or constraints (as indicated on the abscissa of Fig. 5a). Within each group of equations, the elements are sequentially ordered by horizontal rows of grid nodes. The diagonal elements now indicate that the data predicted by the age equations are poorly resolved for all inverse problems.

The equations for conservation of mass are better resolved, though not fully. In particular, they show a decreasing resolution trend with depth (larger element index) without further constraints (*Plain*). For *BwPf*, the plug-flow constraint is well resolved. This result is evident in the horizontal velocity structure discussed in section 5.3. For both *Bw* and *BwPf*, the equations prescribing the vertical velocities at the surface are very badly resolved. The oscillations in data resolution are not arbitrary. The variations visible in Figure 5a seem to systematically depend on the position of the underlying node. The variations are smaller in the horizontal than in the vertical direction. Overall, the model-parameter and data-resolution matrices allow us to judge and improve the quality of the solution by inspecting the residual and solution norms and the singular-value spectrum without requiring a reference velocity field.

5.3. Solution vs reference velocity fields

The principal results obtained in section 5.2 are clearly seen in the velocity distribution (Fig. 6). The reference velocity fields $\mathbf{u}^{\mathrm{ref}}$ and $\mathbf{w}^{\mathrm{ref}}$, which are the correct solutions being sought, are shown in Figure 6a and a′. The underdetermined solution *Plain* without constraints does not reproduce the horizontal velocity, but gives an idea of what the vertical velocity field might look like. In the almost-determined case *Bw*, the vertical structure is reproduced correctly but the vertical velocities in the solution are smaller than the reference velocities. The horizontal velocities again do not show the expected divergence. The vertical velocities in the overdetermined case *BwPf* are very similar to the almost-determined case *Bw*, but differ slightly more from the reference values.

Because plug flow was used as a constraint for this inverse problem, the horizontal velocities $\mathbf{u}^{\mathrm{est}}$ are now in very good agreement with the reference field $\mathbf{u}^{\mathrm{ref}}$, although with smaller values overall. The better agreement of the horizontal velocities of the solution and reference is consistent with the fact that the horizontal velocities are well resolved for this inverse problem (see diagonal elements of model resolution matrix in Fig. 5b).

5.4. Norm properties of solutions

We next discuss the different norm properties of the inverse problem with different constraints as listed in Table 2. The difference norm for horizontal velocities $\|\Delta\check{\mathbf{u}}\|$ is very sensitive to the choice of the mean velocity $\bar{u}$. To provide a similar foundation for all inverse problems, the mean velocity $\bar{u}$ is always provided as the mean of the reference velocity field for each scenario, such that only the variations in the velocity solutions are compared (Table 1). The influence of zero-mean velocities is discussed below.

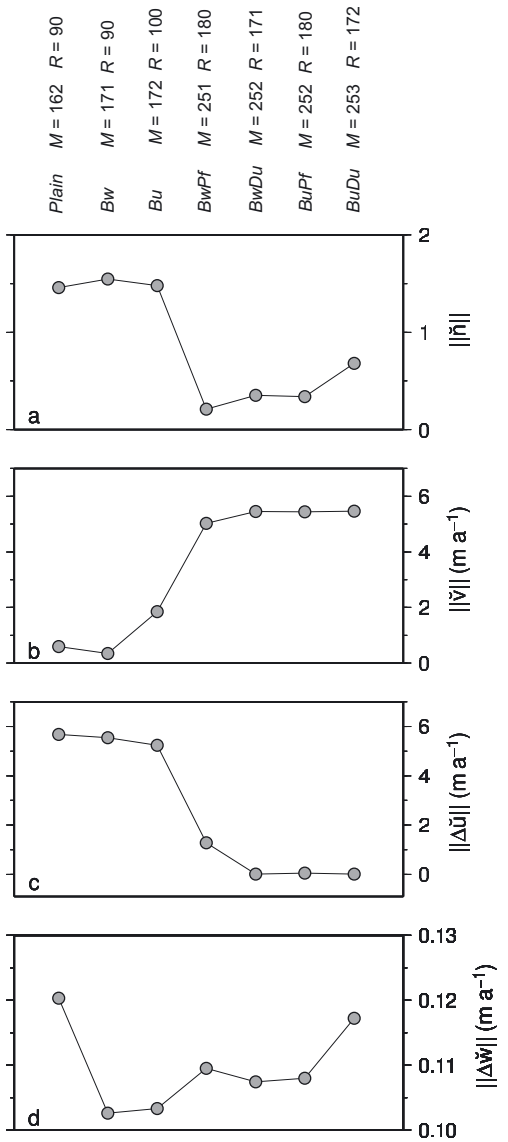

Fig. 7. (a) Residual norm $\|\check{\mathbf{n}}\|$, (b) velocity norm $\|\check{\mathbf{v}}\|$, (c) horizontal velocity-difference norm $\|\Delta\check{\mathbf{u}}\|$ and (d) vertical velocity-difference norm $\|\Delta\check{\mathbf{w}}\|$ of the MDF scenario (Table 1). The inverse problems are indicated on the top abscissa, ordered with increasing number of equations M. $N = 180$, the number of unknowns, for all inverse problems.

For full-rank SVD, ordering the different inverse problems with increasing M (the number of equations) as in Figure 7 would generally illustrate the dependence of the residual norm on determinacy. Naturally, for full-rank underdetermined systems ($M < N$) the data can be fit exactly, resulting in $\|\check{\mathbf{n}}\| = 0$. For reduced rank, however, the residual norm $\|\check{\mathbf{n}}\|$ increases, but yields a smaller solution norm $\|\check{\mathbf{v}}\|$. For the MDF scenario, the residual norm $\|\check{\mathbf{n}}\|$ is more than a factor of two times larger for the underdetermined problems (*Plain, Bw, Bu*) than for the overdetermined problems (*BwPf, BwDu, BuPf, BwDu*) (Fig. 7a). In each of these two groups, the residual norm is quite constant. The velocity norm $\|\check{\mathbf{v}}\|$ spans an order of magnitude (Fig. 7b), with the opposite ratio for under- and overdetermined inverse problems than for the residual norm, as expected.

More interesting from an application point of view is the residual between reference and solution velocities (Fig. 7c

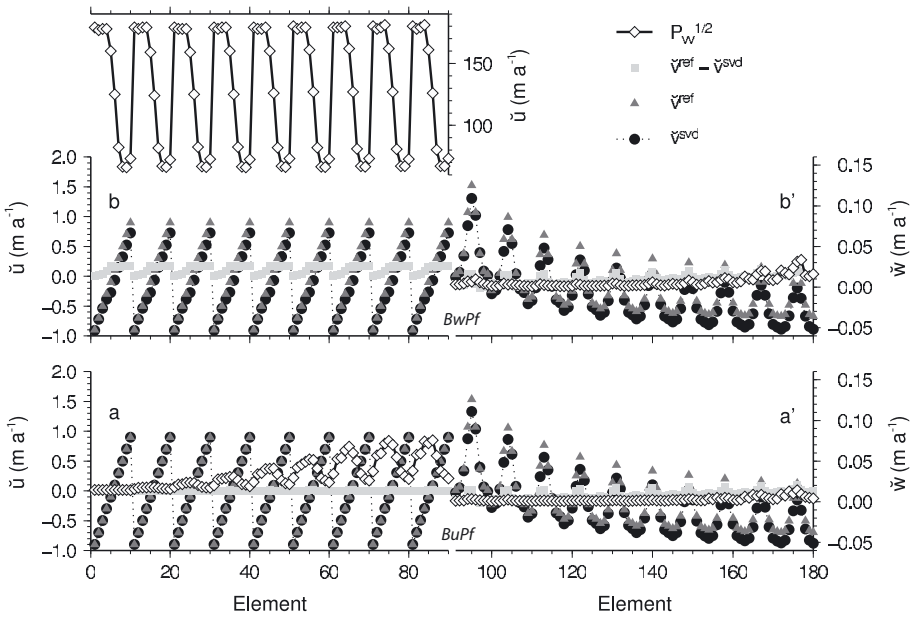

Fig. 8. Elements of the solution vector $\check{\mathbf{v}}^{est}$ and the reference $\check{\mathbf{v}}^{ref}$ for velocity variation, the solution and reference residual vector $\Delta\check{\mathbf{v}} = \check{\mathbf{v}}^{ref} - \check{\mathbf{v}}^{est}$ (and solution uncertainty) and the diagonal of $\mathbf{P}_{\mathbf{vv}}^{1/2}$ for the inverse problems (a, a′) *BuPf* and (b, b′) *BwPf* at full rank $\hat{R} = N = 180$ for the MDF scenario (Table 1). The display is split into (a, b) horizontal velocities $\check{\mathbf{u}}$ and (a′, b′) vertical velocities $\check{\mathbf{w}}$. In (b) the *y* axis on the right corresponds to the elements of $\mathbf{P}_{\mathbf{vv}}$, as they are two orders of magnitude larger than the velocity variation $\check{\mathbf{u}}$. The components of each vector correspond to sequentially ordered horizontal rows of grid nodes. For instance, the uppermost horizontal velocities of the solution domain correspond to elements 1–11 and the nodes in the row below to elements 12–22.

and d). The difference norms of horizontal velocities drop from $\|\Delta\check{\mathbf{u}}\| \approx 0.5$–$0.6\,\mathrm{m\,a^{-1}}$ for underdetermined problems to values close to zero for overdetermined problems. The difference norms of vertical velocities vary around $\|\Delta\check{\mathbf{w}}\| \sim 0.10$–$0.11\,\mathrm{m\,a^{-1}}$ for the over- and underdetermined problems, except for the cases *Plain* and *BuDu* which are only slightly larger with $\|\Delta\check{\mathbf{w}}\| \approx 0.12\,\mathrm{m\,a^{-1}}$.

In some experiments, a priori information on horizontal velocity fields may be unavailable. In those cases, $\bar{u} = 0$ would have to be used. Employing this case for the MDF scenario, the velocity-difference norm remains quasi-constant, but the residual norm significantly increases for those inverse problems that do not incorporate boundary values for $\mathbf{u}$ at the surface. Without a non-zero estimate for mean velocities, the solution produces the smallest velocity norm as a consequence of the minimum-norm property of the SVD. Reducing the rank does not provide a remedy in this case.

5.5. Error and covariance estimates

The final point to investigate, fundamental to all inverse problems, is the solution uncertainty. The quantities density ρ and age A are part of the data kernel $\mathbf{M}$. Density measurements along ice cores are very accurate, usually with an uncertainty of <2%. However, our assumption of a laterally homogeneous density distribution might be wrong, even if mean distributions are considered. The uncertainty of the age–depth distribution determined from radar surveys depends on factors including: conversion of radar travel time to depth based on integrated density; estimating age from ice cores; transferring the ice-core age to the internal horizons; tracking of individual horizons; and interpolation of the age distribution onto the SVD grid.

From analysis of Antarctic field data, Eisen and others (2004) found a maximum error of approximately 2% for the age–depth distribution in firn. In alpine regions, or regions with a laterally inhomogeneous density distribution, this error might be larger.

An error estimate of the model parameters $\check{\mathbf{v}}$ requires knowledge of the data covariance $\mathbf{C}_{\mathbf{vv}}$, according to Equations (12) and (14). For the linear system considered here, uncorrelated uniform variance for the data cannot be assumed, as different physical equations are taken into account. Instead of prescribing an arbitrary data covariance we perform a Monte Carlo-based estimate of covariances, using perturbed reference velocities, age and density distributions as input to a forward calculation using Equation (6).

A total of 10^3 experiments, each of which uses a normally distributed random error of 10% for A, 2% for ρ and 1% for $\mathbf{v}^{ref}$, results in a distribution of estimated data vectors. From this, the corresponding distribution of residuals $\mathbf{n}$ follows. Subsequent analysis finally yields an estimate of the residual covariance $\mathbf{R}_{\mathbf{nn}}$. As could be expected from the numerical set-up, the different equations are not uncorrelated. Although the main diagonal dominates $\mathbf{R}_{\mathbf{nn}}$, secondary diagonals also exhibit significant components. The contribution of the covariance of the nullspace vectors through $\mathbf{R}_{\boldsymbol{\alpha\alpha}}$ to the model uncertainty is neglected, as a priori information about its structure is not available.

We compare the model uncertainty for the solution obtained with inverse problems *BuPf* and *BwPf*. Following Equations (18) and (19), both inverse problems with constraints for the MDF scenario solve the velocity variation $\check{\mathbf{v}}$ on a background velocity of $\bar{u} = 10\,\mathrm{m\,a^{-1}}$ and $\bar{w} = 0.1\,\mathrm{m\,a^{-1}}$. The model uncertainties $\mathbf{P}_{\mathbf{vv}}$ for $\check{\mathbf{u}}$ and $\check{\mathbf{w}}$ of the solution of *BuPf* at full rank increase with element, i.e. depth (Fig. 8a and b). (Note that according to Equation (5), the

elements of the vector $\check{\mathbf{v}}$ are sequentially ordered by horizontal rows of grid nodes.) For the horizontal velocity variation $\check{\mathbf{u}}$, maximum uncertainties occur at larger depth and are approximately equal to the maximum velocity variation (Fig. 8a). For the vertical velocity variation $\check{\mathbf{w}}$, uncertainties for near-surface nodes are an order of magnitude smaller than the velocity variation, and at larger depths are approximately equal to the maximum variation (Fig. 8b). The uncertainty estimates for $\check{\mathbf{u}}$ are always at least one order of magnitude larger than the actual residual between the solution of *BuPf* and the reference velocity. For $\check{\mathbf{w}}$, residuals and uncertainties are of comparable magnitude.

For the inverse problem *BwPf*, also solved at full rank $\hat{R} = 180$, the uncertainty of the horizontal velocities is about two orders of magnitude larger than the maximum velocity variation (Fig. 8c). The uncertainty for the vertical velocity variation is comparable to those of *BuPf* (Fig. 8d).

Although *BuPf* and *BwPf* produce very similar solutions for the velocity field, the uncertainties of their horizontal velocities of the solution are very different. This can be attributed to the different constraints for the horizontal velocity. For *BuPf* the horizontal surface velocities are prescribed as a constraint. By constraining plug flow, the horizontal velocities at larger depth are also a constraint. For *BwPf*, merely plug flow is a constraint. The actual value of the horizontal velocities is therefore more influenced by the age–depth field for *BwPf* than for *BuPf*, and thus subject to larger uncertainties.

The uncertainty of the residuals $\mathbf{n}$, and therefore of the model covariance $\mathbf{C}$, depends significantly on the rank chosen. Generally, for $\hat{R}$ close to the full rank R, the uncertainties of the solution are larger than for smaller $\hat{R}$. For example, for $\hat{R} = 178$ the uncertainties for the horizontal velocities of *BwPf* are comparable with those of *BuPf* for full rank with $\hat{R} = 180$. Reducing the rank used for the solution leads to smaller uncertainties, but decreases the resolution of the model parameters. Again, this is the manifestation of the trade-off between resolution and model covariance. Moreover, for $\hat{R} < R$ the covariance of the nullspace vectors $\mathbf{R}_{\alpha\alpha}$ contributes to the model uncertainty of Equation (14), but cannot be estimated without a priori information.

6. APPLICATION TO TWO GLACIOLOGICAL PROBLEMS

In this final section, the inverse approach is applied to answer two fundamental questions which emerge from the analysis of radar data.

1. What is the migration velocity of an accumulation pattern relative to that of the underlying ice?
2. Was an accumulation pattern constant over time?

6.1. Variation of the migration velocity

Under certain conditions, an accumulation pattern is migrating at a different velocity from the underlying ice. This is the case for megadunes on the Antarctic plateau (Fahnestock and others, 2000; Frezzotti and others, 2002) and smaller dune-like features in coastal areas (Anschütz and others, 2006). Although estimates of the horizontal velocity of the ice might be available, we cannot use it to deduce the migration velocity of the accumulation pattern. The internal-layer structure provides the key to the answer, however, as it is influenced by the relative velocity between the accumulation pattern and the ice and not by the absolute velocity of the ice itself. Using the surface ice-velocity constraints under such conditions would not result in a realistic pattern of vertical velocity and accumulation. It would be more reasonable to prescribe additional flow conditions and determine the migration velocity of the accumulation pattern relative to the ice surface by solving the resulting inverse problem.

Assume that from a field survey, ground-penetrating radar (GPR) data and dated firn or shallow ice cores are available. The age–depth distribution results from merging the GPR profile with the age and density profiles of the core. For brevity, let us assume that the true distribution of the migration velocity and other physical properties corresponds to the MDF scenario as treated before. We now take the shallowest internal layer as a proxy for surface accumulation and use it as the first constraint *Bw*. Although this internal layer is subject to advection relative to the accumulation pattern, as are the deeper layers, the advected distance will in general be small enough to provide a first guess of the surface accumulation. As we only have shallow GPR data covering the firn column, we can assume plug flow in the firn and use this as the second constraint *Pf*. We therefore have the inverse problem with constraints *BwPf*, different properties of which have been determined and discussed for the MDF scenario in section 5.5. The horizontal and vertical velocity fields of the solution to the inverse problem are those shown in Figure 6.

For the glaciological problem assumed here, the horizontal velocity field now corresponds to the relative horizontal migration velocity of the accumulation field with respect to the ice. If the ice velocity is also available, the absolute migration velocity of the accumulation pattern can be calculated. This example shows how useful a kinematic inverse approach can be in providing an estimation of the horizontal advection velocity field, even if no further velocity information is available.

6.2. Estimation and stationarity of an accumulation pattern over time

The reader may wonder why it is actually necessary to use a mathematically complex inversion scheme under the simplifying assumption of plug flow in firn. If the flow is indeed plug flow, then all information on the horizontal field could be deduced from measurements at the surface. However, determination of accumulation from the age distribution produces significantly different results for conventional techniques and for inverse-problem solutions. With the conventional technique, accumulation is estimated as the quotient of cumulative mass difference and age difference between two isochronous layers. The effect of advection on layer architecture for an inhomogeneous accumulation pattern can lead to non-intuitive results, as demonstrated for a number of cases by Arcone and others (2005).

A spatially varying accumulation pattern and strong advection cause convolution of surface signals to appear in the internal-layer structure. From the conventional approach, even if a correction for advection is included, it is impossible to tell whether the accumulation pattern and value was constant in the past. Misinterpretations of internal-layer data are therefore possible.

To demonstrate the capability of the kinematic inverse approach in providing the answer for this case, the problem of a

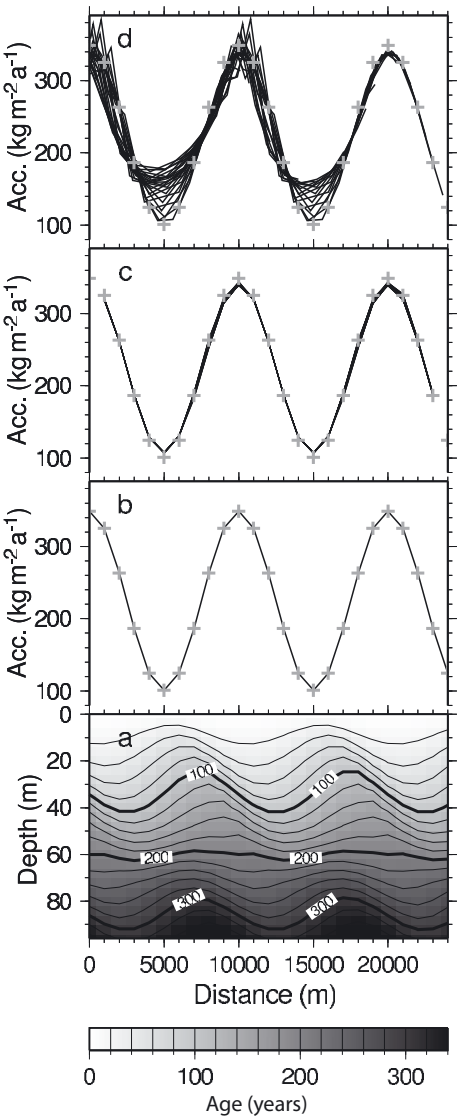

Fig. 9. SVD solution vs conventional accumulation estimates and prescribed values. (a) Age–depth distribution according to the scenario presented by Arcone and others (2005, fig. 10c) with ice flow $u = 50\,\mathrm{m\,a^{-1}}$ from left to right (note the almost horizontal isochrones for an age of around 200 years); (b) prescribed surface accumulation (black line and grey crosses) producing the age–depth distribution of (a); (c) accumulation solution for the inverse problem *BuPf* calculated from the vertical velocity solution and the prescribed density–depth distribution; and (d) conventional accumulation estimates with correction for horizontal advection according to layer age. Grey crosses in (b–d) indicate reference values for accumulation at numerical nodes at the surface.

spatially oscillating accumulation pattern and a constant advection velocity (Arcone and others, 2005, fig. 10c) is now discussed. This problem is comparable to the MF scenario (Table 1) with a higher horizontal velocity. For the analysis, the age–depth field (Fig. 9a) is produced by the forward model for a model domain of 30 km in the x direction and 100 m in the z direction. Cyclic boundary conditions are used at the inflow of the model domain, mimicking an infinite extension of the accumulation pattern at the surface. Accumulation and flow parameters are comparable to the scenario of Arcone and others (2005, fig. 10c): a constant horizontal velocity $u = 50\,\mathrm{m\,a^{-1}}$, a stationary cosine-like accumulation pattern with a wavelength of 10 km, a mean accumulation of $\dot{b}_0 = 225\,\mathrm{kg\,m^{-2}\,a^{-1}}$ and a spatial amplitude of $0.55\dot{b}_0$ (Fig. 9b). The density–depth function is the same as before. We consider only the first 25 km as the model domain of the inverse problem.

For the conventional accumulation estimate, advection can simply be taken into account by shifting the accumulation distribution determined from neighbouring internal layers upstream by the distance covered with the mean horizontal flow velocity, since the layers were deposited at the surface (Fig. 9d). The result shows that, apart from the accumulation pattern derived from the layer closest to the surface, the accumulation values calculated from deeper layers vary considerably from the actual accumulation pattern at the surface.

For accumulation minima at the surface, the accumulation derived from the deepest layers determined with the conventional approach is up to $70\,\mathrm{kg\,m^{-2}\,a^{-1}}$ higher than the actual accumulation at the surface, equivalent to ~70% of the reference value. For accumulation maxima, it varies by about $\pm 30\,\mathrm{kg\,m^{-2}\,a^{-1}}$ (8.5% of the reference value). In addition, the conventional accumulation pattern cannot be reconstructed over the complete x domain, because the layer architecture essentially necessary for a complete reconstruction has been partly advected outside the domain of the known age–depth distribution (the deepest continuous layer has an age of about 340 years, corresponding to an advection of 17 km). For a detailed analytical discussion on the related topic of causal relations between changes in accumulation, layer architecture and particle trajectories, see Parrenin and Hindmarsh (2007).

For solving the kinematic inverse problem, we assume that the horizontal surface velocities are known from measurements and that plug flow prevails. We can then use the constraints *BuPf*. To provide enough numerical nodes per wavelength of the accumulation pattern, it is necessary to increase the resolution of the grid to 25×25 nodes. This yields a total of $M = 1609$ equations and $N = 1104$ unknowns. As for the comparable case mentioned earlier, the full rank $R = 1104$ is applicable to the inverse problem *BuPf*.

The accumulation can be determined from the vertical velocities of the solution. It provides a congruent distribution for the accumulation derived from the vertical velocities at all depths. For accumulation maxima, the solution is about $5\,\mathrm{kg\,m^{-2}\,a^{-1}}$ smaller than the actual accumulation pattern, equivalent to –1.4% of the reference values. For minima, it is about $5\,\mathrm{kg\,m^{-2}\,a^{-1}}$ larger, equivalent to +5.2%. The congruent shape of the accumulation pattern derived by the inverse approach implies that the assumption of steady state is correct. This in turn tells us that the accumulation was constant over time. Again, this result cannot be achieved from the conventional accumulation estimates alone.

7. SUMMARY

The feasibility of inferring the velocity field in an advective flow regime in firn by employing age–depth data and a kinematic inverse-problem approach has been investigated. The inverse problem was solved by means of a singular-value decomposition of a linear system of equations. The comparison of inverse problems with different constraints shows that all kinematic systems provide a generally stable solution, given that the singular spectrum is adequately truncated and that

the choice of the reduced rank can be based on objective criteria. For the underlying system of equations, the given advection scenario and the prescribed spatially inhomogeneous accumulation, the inverted horizontal velocity is much more sensitive to the constraints used than is the vertical velocity solution.

The amount of information retrieved about the velocity field naturally varies with the degree of determinacy of the underlying linear system. For all inverse problems, the prescription of some surface velocities seems necessary to retrieve small velocity variations superimposed on a mean flow field. Without any quantitative information on horizontal velocity, the minimum-norm property of the SVD makes realistic solutions difficult.

A detailed investigation of the solution is possible by exploiting the mathematical advantages of the SVD. The solutions were examined in terms of resolution, error estimates and a trade-off of resolution and solution covariance.

The inverse-problem approach is also likely to be applicable to other flow scenarios. Two applications to realistic scenarios were presented. Interaction of a spatially constant accumulation pattern with a high-velocity flow field was analyzed to exclude temporal variations in accumulation by removing the advective components of accumulation estimates. Although the approach presented here assumes a steady-state pattern, larger temporal variations in accumulation derived from layer ages at different depths reveal temporally varying accumulation.

A possible extension of the presented kinematic inversion approach would be the use of more unknown parameters (e.g. we could use a certain density parameterization and also solve for those parameters). Another possibility is introducing a form of time dependence. We could also include dynamical equations and then solve an inverse problem to find parameters for a flow law of firn.

ACKNOWLEDGEMENTS

I am deeply indebted to E. Waddington. Without his critical and constructive reviews this work would not have come to this state. His linguistic and stylistic recommendations improved the text tremendously, and I hope that his mission is not as quixotic as it might seem. The efforts by scientific editor R. Greve and an anonymous reviewer are likewise acknowledged. M. Losch deserves thanks for pointing out oceanographic fundamentals and analogies at the very beginning of this study. Preparation of this work was supported by the 'Emmy Noether' programme of the Deutsche Forschungsgemeinschaft.

REFERENCES

Anschütz, H., O. Eisen, W. Rack and M. Scheinert. 2006. Periodic surface features in coastal East Antarctica. *Geophys. Res. Lett.*, **33**(22), L22501. (10.1029/2006GL027871.)

Arcone, S.A., V.B. Spikes and G.S. Hamilton. 2005. Stratigraphic variation in polar firn caused by differential accumulation and ice flow: interpretation of a 400 MHz short-pulse radar profile from West Antarctica. *J. Glaciol.*, **51**(174), 407–422.

Bamber, J.L., R.J. Hardy and I. Joughin. 2000. An analysis of balance velocities over the Greenland ice sheet and comparison with synthetic aperture radar interferometry. *J. Glaciol.*, **46**(152), 67–74.

Clarke, G.K.C., N.M. Lhomme and S.J. Marshall. 2005. Tracer transport in the Greenland ice sheet: three-dimensional isotopic stratigraphy. *Quat. Sci. Rev.*, **24**(1–2), 155–171.

Eisen, O., U. Nixdorf, F. Wilhelms and H. Miller. 2004. Age estimates of isochronous reflection horizons by combining ice core, survey, and synthetic radar data. *J. Geophys. Res.*, **109**(B4), B04106. (10.1029/2003JB002858.)

Fahnestock, M.A., T.A. Scambos, C.A. Shuman, R.J. Arthern, D.P. Winebrenner and R. Kwok. 2000. Snow megadune fields on the East Antarctic Plateau: extreme atmosphere–ice interaction. *Geophys. Res. Lett.*, **27**(22), 3719–3722.

Fiadeiro, M.E. and G. Veronis. 1982. On the determination of absolute velocities in the ocean. *J. Mar. Res.*, **40**(Suppl.), 159–182.

Frezzotti, M., S. Gandolfi and S. Urbini. 2002. Snow megadunes in Antarctica: sedimentary structure and genesis. *J. Geophys. Res.*, **107**(D18), 4344. (10.1029/2001JD000673.)

Frezzotti, M. *and 12 others*. 2004. New estimations of precipitation and surface sublimation in East Antarctica from snow accumulation measurements. *Climate Dyn.*, **23**(7–8), 803–813.

Hawley, R.L., E.D. Waddington, G.W. Lamorey and K.C. Taylor. 2004. Vertical-strain measurements in firn at Siple Dome, Antarctica. *J. Glaciol.*, **50**(170), 447–452.

Hindmarsh, R.C.A., G.J.M. Leysinger Vieli, M.J. Raymond and G.H. Gudmundsson. 2006. Draping or overriding: the effect of horizontal stress gradients on internal layer architecture in ice sheets. *J. Geophys. Res.*, **111**(F2), F02018. (10.1029/2005JF000309.)

Jacobel, R.W. and B.C. Welch. 2005. A time marker at 17.5 kyr BP detected throughout West Antarctica. *Ann. Glaciol.*, **41**, 47–51.

Joughin, I., D.R. MacAyeal and S. Tulaczyk. 2004. Basal shear stress of the Ross ice streams from control method inversion. *J. Geophys. Res.*, **109**(B9), B09405. (10.1029/2003JB002960.)

Larour, E., E. Rignot, I. Joughin and D. Aubry. 2005. Rheology of the Ronne Ice Shelf, Antarctica, inferred from satellite radar interferometry data using an inverse control method. *Geophys. Res. Lett.*, **32**(5), L05503. (10.1029/2004GL021693.)

Leonard, K., R.E. Bell, M. Studinger and B. Tremblay. 2004. Anomalous accumulation rates in the Vostok ice-core resulting from ice flow over Lake Vostok. *Geophys. Res. Lett.*, **31**(24), LZH401. (10.1029/2004GL021102.)

Lüthi, M.P. and M. Funk. 2001. Modelling heat flow in a cold, high-altitude glacier: interpretation of measurements from Colle Gnifetti, Swiss Alps. *J. Glaciol.*, **47**(157), 314–324.

MacAyeal, D.R. 1993. A tutorial on the use of control methods in ice-sheet modeling. *J. Glaciol.*, **39**(131), 91–98.

MacAyeal, D.R., R.A. Bindschadler and T.A. Scambos. 1995. Basal friction of Ice Stream E, West Antarctica. *J. Glaciol.*, **41**(138), 247–262.

Menke, W. 1989. *Geophysical data analysis: discrete inverse theory. Revised edition.* San Diego, CA, Academic Press.

Morse, D.L. 1997. Glacier geophysics at Taylor Dome, Antarctica. (PhD thesis, University of Washington.)

Nereson, N.A. and E.D. Waddington. 2002. Isochrones and isotherms beneath migrating ice divides. *J. Glaciol.*, **48**(160), 95–108.

Parrenin, F. and R. Hindmarsh. 2007. Influence of a non-uniform velocity field on isochrone geometry along a steady flowline of an ice sheet. *J. Glaciol.*, **53**(183), 612–622.

Richardson, C. and P. Holmlund. 1999. Spatial variability at shallow snow-layer depths in central Dronning Maud Land, East Antarctica. *Ann. Glaciol.*, **29**, 10–16.

Richardson-Näslund, C. 2004. Spatial characteristics of snow accumulation in Dronning Maud Land, Antarctica. *Global Planet. Change*, **42**(1–4), 31–43.

Rotschky, G., O. Eisen, F. Wilhelms, U. Nixdorf and H. Oerter. 2004. Spatial distribution of surface mass balance on Amundsenisen plateau, Antarctica, derived from ice-penetrating radar studies. *Ann. Glaciol.*, **39**, 265–270.

Scales, J.A., M.L. Smith and S. Treitel. 2001. *Introductory geophysical inverse theory.* Golden, CO, Samizdat Press.

Schwerzmann, A., M. Funk, H. Blatter, M. Lüthi, M. Schwikowski and A. Palmer. 2006. A method to reconstruct past accumulation rates in alpine firn regions: a study on Fiescherhorn, Swiss Alps. *J. Geophys. Res.*, **111**(F1), F01014. (10.1029/2005JF000283.)

Siegert, M.J., R. Hindmarsh and G. Hamilton. 2003. Evidence for a large surface ablation zone in central East Antarctica during the last Ice Age. *Quat. Res.*, **59**(1), 114–121.

Truffer, M. 2004. The basal speed of valley glaciers: an inverse approach. *J. Glaciol.*, **50**(169), 236–242.

Vieli, A. and A.J. Payne. 2003. Application of control methods for modelling the flow of Pine Island Glacier, Antarctica. *Ann. Glaciol.*, **36**, 197–204.

Waddington, E.D., T.A. Neumann, M.R. Koutnik, H.-P. Marshall and D.L. Morse. 2007. Inference of accumulation-rate patterns from deep layers in glaciers and ice sheets. *J. Glaciol.*, **53**(183), 694–712.

Wunsch, C. 1985. Can a tracer field be inverted for velocity? *J. Phys. Oceanogr.*, **15**(11), 1521–1531.

Wunsch, C. 1996. *The ocean circulation inverse problem.* Cambridge, etc, Cambridge University Press.

Xiaolan, W.U. and C. Jezek. 2004. Antarctic ice-sheet balance velocities from merged point and vector data. *J. Glaciol.*, **50**(169), 219–230.

APPENDIX

Notation

Note that vectors and matrices are represented by lower-case bold letters (e.g. $\mathbf{u}$) and upper-case bold letters (e.g. $\mathbf{M}$), respectively.

Section 2.1

$A, A_{i,k}$	Depositional age of particle
$\rho, \rho_k, \rho_{i,k}$	Density
t	Time
x, z	Horizontal, vertical spatial coordinate
$\mathbf{r} = (x, z)$	Coordinate vector
∂_i	Partial derivative with respect to $i \in \{x, z, t\}$
$u, u_{i,k}$	Horizontal velocity component
$w, w_{i,k}$	Vertical velocity component
$\mathbf{u}, \mathbf{w}$	Horizontal, vertical velocity field
$\mathbf{v}$	Velocity (= model) vector $\in \mathcal{R}^N = (\mathbf{u}^T, \mathbf{w}^T)^T$

Section 2.2

$\dot{b}$	Accumulation
ρ_0	Density at surface

Section 2.3

$\mathbf{u}^{\text{ref}}, \mathbf{w}^{\text{ref}}$	Reference horizontal, vertical velocity field, i.e. the correct solution
$\mathbf{u}^{\text{est}}, \mathbf{w}^{\text{est}}$	Estimated model parameters: the SVD solution of horizontal and vertical velocity field

Section 2.4

$\Delta x, \Delta z$	Horizontal, vertical spatial increment
$\{c_{i,k}^{\alpha,\ldots,\nu}\}$	Coefficients of linear system
I, K	Number of horizontal, vertical nodes
i, k	Horizontal, vertical index
n_u, n_u^x, n_u^z	Number of nodes for u: total, x, z direction
n_w, n_w^x, n_w^z	Number of nodes for w: total, x, z direction
M	Dimension of data space (number of observations)
N	Dimension of model space (number of unknowns)
$\mathbf{d}$	Data vector $\in \mathcal{R}^M$
d_p	Components of $\mathbf{d}$
v_q	Components of $\mathbf{v}$
$\mathbf{M}$	Model matrix $\in \mathcal{R}^{M\times N}$
$M_{p,q}$	Components of $\mathbf{M}$
p, q	Element indices

Section 3.1

R	Mathematical rank of $\mathbf{M}$
$\hat{R}$	Effective/reduced rank of $\mathbf{M}$
$\mathbf{\Lambda}$	Singular-value matrix $\in \mathcal{R}^{M\times N}$
$\Lambda_{p,q}$	Components of $\mathbf{\Lambda}$
$\mathbf{\Lambda}_R$	Submatrix of $\mathbf{\Lambda} \in \mathcal{R}^{R\times R}$
λ_p	Singular value
$\mathbf{U}$	Data/observation space $\in \mathcal{R}^{M\times M}$ $= \{\mathbf{U}_R\ \mathbf{U}_0\}$
$\mathbf{V}$	Model/solution space $\in \mathcal{R}^{N\times N}$ $= \{\mathbf{V}_R\ \mathbf{V}_0\}$
$\mathbf{U}_R$	Data range $\in \mathcal{R}^{M\times R}$
$\mathbf{V}_R$	Model range $\in \mathcal{R}^{N\times R}$
$\mathbf{U}_0$	Data nullspace $\in \mathcal{R}^{M\times M-R}$
$\mathbf{V}_0$	Model nullspace $\in \mathcal{R}^{N\times N-R}$
$\boldsymbol{\alpha}$	Coefficients of data nullspace
δ_{ij}	Kronecker symbol

Section 3.2

$\mathbf{T_V}$	Model/solution resolution matrix $= \mathbf{V}_R\mathbf{V}_R^T$
$\mathbf{T_U}$	Data/observation resolution matrix $= \mathbf{U}_R\mathbf{U}_R^T$
$\mathbf{I}_N$	Unit matrix $\in \mathcal{R}^{N\times N}$

Section 3.3

$\mathbf{n}$	Vector of residuals $\in \mathcal{R}^M$
$\mathbf{R_{nn}}$	Residual covariance
$\mathbf{R}_{\boldsymbol{\alpha\alpha}}$	Covariance of nullspace coefficients
$\mathbf{C_{vv}}$	Model covariance
$\mathbf{P_{vv}}$	Model uncertainty
$\mathbf{P_{nn}}$	Residual uncertainty

Section 3.4

$\mathbf{S}, \mathbf{W}$	Column-, row-scaling matrix
$\mathbf{M}^T$	Transpose
$\mathbf{\Lambda}^{-1}$	Inverse
$\mathbf{W}^{1/2}$	Square root (Cholesky decomposition)
$\tilde{\mathbf{M}}, \tilde{\mathbf{d}}, \tilde{\mathbf{v}}$	Linear system in scaled space

Section 3.5

$\bar{\mathbf{d}}, \bar{\mathbf{v}}$	Vectors corresponding to flow-field mean
$\breve{\mathbf{d}}, \breve{\mathbf{v}}, \ldots$	Vectors corresponding to flow-field variations
$\langle\mathbf{u}\rangle, \langle\mathbf{w}\rangle$	Mean of vectors $\mathbf{u}, \mathbf{w}$
$\mathbf{i}_N$	Diagonal of $\mathbf{I}_N$, vector with all ones

Section 4.1

$x_{\min}, x_{\max}, z_{\max}$	Boundaries of x and z dimension
$\dot{b}_0, x_\sigma, x_\mu$	Parameters of accumulation distribution
ρ_i, c_ρ	Parameters of density distribution
c_u	Parameter of horizontal velocity distribution

Section 4.2

k_0	Vertical index at surface
i_b	Horizontal index of borehole position
$\Delta_x u, \Delta_z u$	Horizontal, vertical difference of u over one spatial increment

Section 5

$\Delta\check{\mathbf{v}}, \Delta\check{\mathbf{u}}, \Delta\check{\mathbf{w}}$	Residuals of velocity variation (reference minus solution)
$\|\Delta\check{\mathbf{u}}\|, \|\Delta\check{\mathbf{w}}\|$	Norm of velocity residuals
$\|\check{\mathbf{n}}\|, \|\check{\mathbf{v}}\|$	Norm of residual, solution/model vector

Staggered-grid differences and coefficients

Applying finite differences to Equation (3) on the triplex-staggered grid yields the discrete equations

$$\frac{1}{2\Delta x}\left[(A_{i+1,k}-A_{i,k})u_{i,k}+(A_{i,k}-A_{i-1,k})u_{i-1,k}\right] + \frac{1}{2\Delta z}\left[(A_{i,k+1}-A_{i,k})w_{i,k}+(A_{i,k}-A_{i,k-1})w_{i,k-1}\right] = 1 \quad \text{(A1a)}$$

$$\rho_k\frac{1}{\Delta x}(u_{i,k}-u_{i-1,k})+\rho_k\frac{1}{\Delta z}(w_{i,k}-w_{i,k-1}) + \frac{1}{2\Delta z}\left[(\rho_{k+1}-\rho_k)w_{i,k}+(\rho_k-\rho_{k-1})w_{i,k-1}\right] = 0, \quad \text{(A1b)}$$

where the i index for density $\rho_{i,k}$ has been dropped since density is laterally homogeneous and depends only on depth index k. Rearranging and combining factors of the coefficients $\{c_{i,k}^{\alpha,\ldots,\nu}\}$ results in the expression for a unit cell (Fig. 1):

$$c_{i-1,k}^{\alpha}u_{i-1,k}+c_{i,k}^{\beta}u_{i,k}+c_{i,k-1}^{\gamma}w_{i,k-1}+c_{i,k}^{\delta}w_{i,k} = 1 \quad \text{(A2a)}$$

$$c_{k}^{\kappa}u_{i-1,k}+c_{k}^{\lambda}u_{i,k}+c_{i,k-1}^{\mu}w_{i,k-1}+c_{i,k}^{\nu}w_{i,k} = 0, \quad \text{(A2b)}$$

which can be written in the matrix notation of Equation (4).

The coefficients are given by

$$\begin{aligned} c_{i-1,k}^{\alpha} &= \frac{1}{2\Delta x}(A_{i,k}-A_{i-1,k}),\\ c_{i,k}^{\beta} &= \frac{1}{2\Delta x}(A_{i+1,k}-A_{i,k}),\\ c_{i,k-1}^{\gamma} &= \frac{1}{2\Delta z}(A_{i,k}-A_{i,k-1}),\\ c_{i,k}^{\delta} &= \frac{1}{2\Delta z}(A_{i,k+1}-A_{i,k}),\\ c_{k}^{\kappa} &= -\frac{\rho_k}{\Delta x},\\ c_{k}^{\lambda} &= \frac{\rho_k}{\Delta x},\\ c_{k-1}^{\mu} &= -\frac{1}{2\Delta z}(\rho_k+\rho_{k-1}),\\ c_{k}^{\nu} &= \frac{1}{2\Delta z}(\rho_{k+1}+\rho_k). \end{aligned} \quad \text{(A3)}$$

Cases of determinacy and conditions for existence of nullspaces

Let us denote by $\{\}$ empty sets of the model nullspace $\mathbf{V}_0$ or the data nullspace $\mathbf{U}_0$. If a data nullspace exists, $\mathbf{U}_0 \neq \{\}$ and the data vector has components in it. It will then be impossible to fit the data exactly (Scales and others, 2001). If a model nullspace exists, $\mathbf{V}_0 \neq \{\}$ and the true model vector has components in it. It will then be impossible to find the correct model. The following combinations are possible:

$M = N$	just-determined $\mathbf{V}_0 = \mathbf{U}_0 = \{\}$
$M = N > R$	deficient-rank just-determined $\mathbf{V}_0 \neq \{\}$, $\mathbf{U}_0 \neq \{\}$
$M > N = R$	full-rank overdetermined $\mathbf{V}_0 = \{\}$, $\mathbf{U}_0 \neq \{\}$
$M > N > R$	deficient-rank overdetermined $\mathbf{V}_0 \neq \{\}$, $\mathbf{U}_0 \neq \{\}$
$N > M = R$	full-rank underdetermined $\mathbf{V}_0 \neq \{\}$, $\mathbf{U}_0 = \{\}$
$N > M > R$	deficient-rank underdetermined $\mathbf{V}_0 \neq \{\}$, $\mathbf{U}_0 \neq \{\}$.

Definition of moments, norms, scaling and weighting

Second-moment or covariance matrix

Let x be a random variable with samples $(x_1, x_2, \ldots, x_n)$ drawn from the population. The kth sample moment of x is defined as

$$\frac{1}{n}\sum_{i=1}^{n}x_i^k. \quad \text{(A4)}$$

The sample mean $\langle x\rangle$ follows as the first moment of x. The kth central moments are defined as

$$\frac{1}{n}\sum_{i=1}^{n}\left(x_i-\langle x\rangle\right)^k. \quad \text{(A5)}$$

The sample variance of x is the second central moment,

$$\frac{1}{n}\sum_{i=1}^{n}\left(x_i-\langle x\rangle\right)^2. \quad \text{(A6)}$$

Assuming that the true mean of x is zero, the second moment is equal to the second central moment or variance, i.e.

$$\frac{1}{n}\sum_{i=1}^{n}x_i^2. \quad \text{(A7)}$$

Renaming x with ${}^1x$ with samples $\{{}^1x_i\}$, $(i = 1, \ldots, n)$, considering a second random variable ${}^2x$ with samples $\{{}^2x_i\}$ and further assuming that ${}^1x$ and ${}^2x$ have zero mean, we can estimate the covariance of ${}^1x$ and ${}^2x$ as

$$r_{12} = \frac{1}{n}\sum_{i=1}^{n}{}^1x_i{}^2x_i. \quad \text{(A8)}$$

Extending this further to the random variable ${}^Nx$ with samples $\{{}^Nx_i\}$, we can define the random vector $\mathbf{x} = ({}^1x, {}^2x, \ldots, {}^Nx)$ with samples $\mathbf{x}_i = ({}^1x_i, {}^2x_i, \ldots, {}^Nx_i)$. The covariance (or second moments) for pairs of variables ${}^px$ and ${}^qx$ follows as

$$r_{pq} = \frac{1}{n}\sum_{i=1}^{n}{}^px_i{}^qx_i. \quad \text{(A9)}$$

The r_{pq} are the components of the covariance or second-moment matrix $\mathbf{R_{xx}}$, as introduced in section 3.3 for vectors $\mathbf{n}$ and $\boldsymbol{\alpha}$.

L_2-norm

The norm of a vector is a measure of its length. A general definition for the norm of a vector $\mathbf{x} = (x_1, x_2, \ldots, x_n)$ is given by

$$\|\mathbf{x}\|_p = \left(|x_1|^p + |x_2|^p + \cdots + |x_n|^p\right)^{1/p}, \quad \text{(A10)}$$

where $|x_i|$ denotes the absolute value of the component x_i and $p \geq 1$ is a real number. For $p = 1$, Equation (A10) is the so-called L_1-norm. For $p = 2$, we obtain the L_2-norm which is usually referred to as the length of the vector $\mathbf{x}$ in Euclidean space, i.e. the square root of the sum of squares of its components. The L_2-norm is used throughout.

Row and column scaling

Let $M_{p,q}$ be the components of the matrix $\mathbf{M}$, with $p = 1, \ldots, M$ denoting the row number and $q = 1, \ldots, N$ denoting the column number. The L_2-norm of the ith row is calculated as

$$\|\mathbf{M}\|_p^{\text{row}} = \left(|M_{p,1}|^2 + |M_{p,2}|^2 + \cdots + |M_{p,N}|^2\right)^{1/2}. \quad \text{(A11)}$$

For row scaling, each element $M_{p,q}$ of the pth row is divided by the row norm $\|\mathbf{M}\|_p^{\text{row}}$. This leads to the row-scaling matrix $\mathbf{W}$ which has components $W_{p,q}$, defined as

$$W_{p,q} = \delta_{pq}\|\mathbf{M}\|_p^{\text{row}}, \quad \text{(A12)}$$

i.e. $\|\mathbf{M}\|_p^{\text{row}}$ on the main diagonal and zero elsewhere.

Now taking $M'_{p,q}$ as the components of the already row-scaled matrix $\mathbf{M}'$, the L_2-norm of the qth column is determined from

$$\|\mathbf{M}'\|_q^{\text{col}} = \left(|M'_{1,q}|^2 + |M'_{2,q}|^2 + \cdots + |M'_{M,q}|^2\right)^{1/2}. \quad \text{(A13)}$$

For column scaling, each element $M'_{p,q}$ of the qth column is divided by the column norm $\|\mathbf{M}'\|_q^{\text{col}}$. The components of the column-scaling matrix $\mathbf{S}$ are defined as

$$S_{p,q} = \delta_{piq}/\|\mathbf{M}'\|_q^{\text{col}}, \quad \text{(A14)}$$

so that $\mathbf{S}$ has the $1/\|\mathbf{M}'\|_q^{\text{col}}$ on the main diagonal and zeros elsewhere.

MS received 5 May 2006 and accepted in revised form 4 April 2008

Surface topography and ice flow in the vicinity of the EDML deep-drilling site, Antarctica

Christine WESCHE,[1] Olaf EISEN,[1,2] Hans OERTER,[1] Daniel SCHULTE,[1] Daniel STEINHAGE[1]

[1]*Alfred Wegener Institute for Polar and Marine Research, PO Box 120161, D-27515 Bremerhaven, Germany*
E-mail: christine.wesche@awi.de
[2]*Laboratory of Hydraulics, Hydrology and Glaciology (VAW), ETH Zürich, CH-8092 Zürich, Switzerland*

ABSTRACT. Interpretation of ice-core records requires accurate knowledge of the past and present surface topography and stress–strain fields. The European Project for Ice Coring in Antarctica (EPICA) drilling site (75.0025° S, 0.0684° E; 2891.7 m) in Dronning Maud Land, Antarctica, is located in the immediate vicinity of a transient and forking ice divide. A digital elevation model is determined from the combination of kinematic GPS measurements with the GLAS12 datasets from the ICESat. Based on a network of stakes, surveyed with static GPS, the velocity field around the drilling site is calculated. The annual mean velocity magnitude of 12 survey points amounts to 0.74 m a^{-1}. Flow directions mainly vary according to their distance from the ice divide. Surface strain rates are determined from a pentagon-shaped stake network with one center point close to the drilling site. The strain field is characterized by along-flow compression, lateral dilatation and vertical layer thinning.

INTRODUCTION

Within the framework of the European Project for Ice Coring in Antarctica (EPICA) a deep ice core (EDML) was drilled in Dronning Maud Land (DML), Antarctica, near the German summer station, Kohnen (EPICA Community Members, 2006). To obtain high-resolution climate information of the last glacial cycle, a drilling site was chosen that provides comparatively high accumulation rates, large ice thickness and nearly undisturbed layering of the ice. The EDML drilling site (75.0025° S, 0.0684° E; 2891.7 m above the World Geodetic System 1984 (WGS84) ellipsoid) is located in the Atlantic sector of Antarctica (Fig. 1) and is used to investigate the connection between Northern and Southern Hemisphere climate variability in the past. The area surrounding the EDML drilling site is situated between two transient ice divides which fork at approximately 75.1° S, 1° E, according to the elevation model of Bamber and Bindschadler (1997). The deep ice-core drilling was carried out in the austral summer seasons 2000/01 to 2005/06. The ice thickness in this region is 2782 ± 5 m, as measured by airborne radio-echo sounding, and the total recovered core length was 2774.15 m (personal communication from F. Wilhelms, 2006). The drilling finished when subglacial water entered the borehole. The recent accumulation rate in the surroundings of the EDML drilling site is 64 kg m^{-2} a^{-1} (Eisen and others, 2005), with small-scale spatial variability of ~10%.

Accurate interpretation of the EDML ice-core data (e.g. past accumulation from annual layer thicknesses) requires knowledge of the complete strain field to correct for dynamic layer thickness variation. In this paper, we determine the topography, flow and strain field in the wider surroundings of the drilling site. Similar investigations were previously made at several drilling sites in Antarctica and Greenland. For example, Vittuari and others (2004) present a velocity field at Dome C (the first EPICA deep-drilling site (EPICA Community Members, 2004)) in the Indo-Pacific sector of the Antarctic ice sheet. In Greenland, Hvidberg and others (2002) investigated the ice flow at NorthGRIP, a drilling site that is also located in the vicinity of a transient ice divide. For the EDML site, a digital elevation model (DEM) is derived from the combination of ground-based kinematic GPS (global positioning system) and ICESat (Ice, Cloud and land Elevation Satellite) laser altimetry, providing highly accurate surface topography in the region of interest. This forms, together with ice velocity data, the basis for estimating and interpreting deformation in the upper part of the ice sheet.

DATA AND METHODS

Static and kinematic GPS measurements were used for our investigation. The elevation data derived from the kinematic GPS data were complemented by NASA's ICESat satellite laser altimetry data (US National Snow and Ice Data Center (NSIDC) http://nsidc.org/data/icesat/).

Kohnen Reference Station (KRS)

Kohnen Reference Station (KRS), which is located at the German summer station Kohnen (75.0018° S, 0.0667° E), is used for processing our GPS measurements. This is a non-permanent GPS station, providing data at 1 s intervals only during the drilling campaigns 2000/01 to 2005/06 (with interruptions in the season 2004/05). The KRS GPS antenna was mounted on the northern corner of the Kohnen station. With the aid of the International Global Navigation Satellite Systems Service (IGS) network, the daily position of KRS was determined using the GPS stations Mawson, Sanae IV, Syowa, Davis, Casey and O'Higgins (Fig. 1). The KRS positions were determined with the post-processing software GAMIT, assuming motion of the site was negligible during the processing window (Scripps Institution of Oceanography, http://sopac.ucsd.edu/processing/gamit/).

Surface profiles from kinematic GPS measurements

Kinematic GPS measurements combined with ground-penetrating radar (GPR) recorded during the 2000/01 field campaign (Eisen and others, 2005) form the basis for generating a DEM with a higher accuracy and resolution

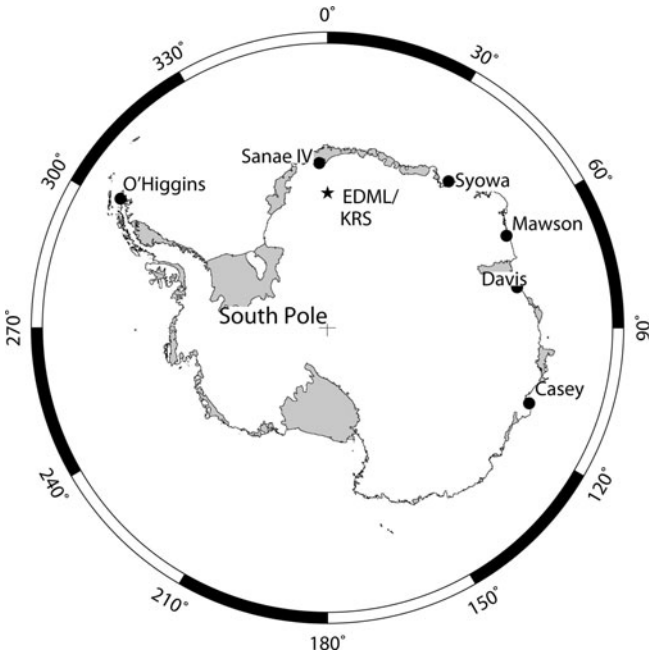

Fig. 1. Location map of the EDML drilling site in Antarctica, marked with a star. Six International Global Navigation Satellite Systems Service (IGS) reference stations are indicated with filled circles. They were used for determining the position of the local reference point Kohnen Reference Station (KRS) adjacent to the EDML drilling site.

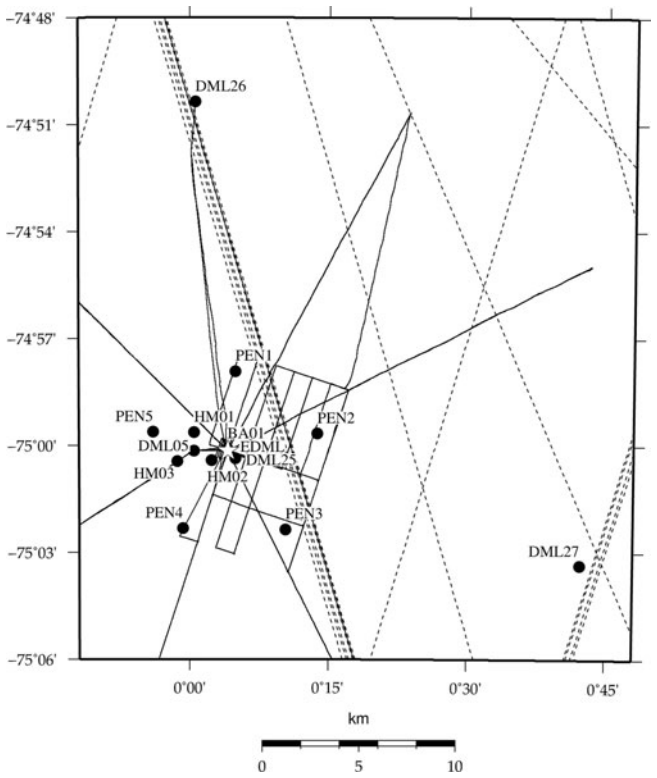

Fig. 2. Data coverage for the DEM derived in the present study. The solid lines present the kinematic GPS profiles, and the dotted lines the ICESat GLAS12 ground tracks. Sites used for static GPS measurements are marked with filled circles; the star marks the EDML drilling site.

than former DEMs in the surroundings of the EDML drilling site. A Trimble SSI 4000 GPS receiver was mounted on a snowmobile which was navigated at a velocity of about 10 km h^{-1} along predefined tracks (Fig. 2, solid lines) in the area of investigation (74.8–75.1° S, 0.2° W–0.8° E). There are two networks of kinematic GPS profiles, both centered on the EDML drilling site. The length of the edges of the first grid is 10 km with a profile spacing of 1–3 km. The second grid is a star-like pattern, which consists of seven 20–25 km legs. The kinematic GPS data were processed with Trimble Geomatics Office™ (TGO™), including precise ephemeris and ionosphere-free solution.

Flow and strain networks using static GPS measurements

In order to determine horizontal velocities and strain rates, static GPS measurements around the EDML drilling site were carried out with Ashtech Z-12 and Trimble SSI 4000 GPS receivers in the austral summer seasons between 1999/2000 and 2005/06. For the velocity network 13 points in the surroundings of the EDML drilling site were used (Fig. 2). These points are marked with aluminium stakes and were surveyed for approximately 1 hour per season to find their positions. The static GPS data were also processed with TGO™. All determined positions are available in the PANGAEA database (doi: 10.1594/PANGAEA.611331).

Surface profiles from satellite altimetry

The Geoscience Laser Altimeter System (GLAS) on board NASA's ICESat provides global altimetry data with a wavelength of 1064 nm up to 86° N and 86° S. The laser footprint has a diameter of 60 m, and the along-track distance between the footprints is 172 m. The positioning error is 35 m (Zwally and others, 2002). In this paper, GLAS12 altimetry data for the periods L1a (20 February to 20 March 2003) and L2a (25 September to 18 November 2003) are used to determine the surface elevation model of the investigated area. The ground tracks of these measurements across the investigated area are plotted in Figure 2 as dotted lines. The GLAS12 satellite laser altimetry data and the corresponding NSIDC GLAS Altimetry elevation extractor Tool (NGAT) are provided by NSIDC (http://nsidc.org/data/icesat/).

DATA ACCURACY

Knowledge of potential errors is essential for determining the quality of the kinematic and static GPS data. The general GPS errors and those of our solutions are presented in this section. The distance between the reference station and the survey point or profile is the principal factor affecting the accuracy of the position to be determined.

GPS errors

GPS observations at high latitudes are affected by the relatively weak satellite geometry, and hence formal errors are larger here than at other latitudes. Ionospheric and tropospheric effects were minimized by adopting the ionosphere-free linear combination and applying a tropospheric model. Further error reduction occurs through the double-differencing approach used in TGO™ and the relatively short baselines.

Kinematic GPS measurements

Since we used KRS, located in the center of the kinematic GPS profiles, systematic positioning errors are negligible. The accuracy of the kinematic GPS measurements is

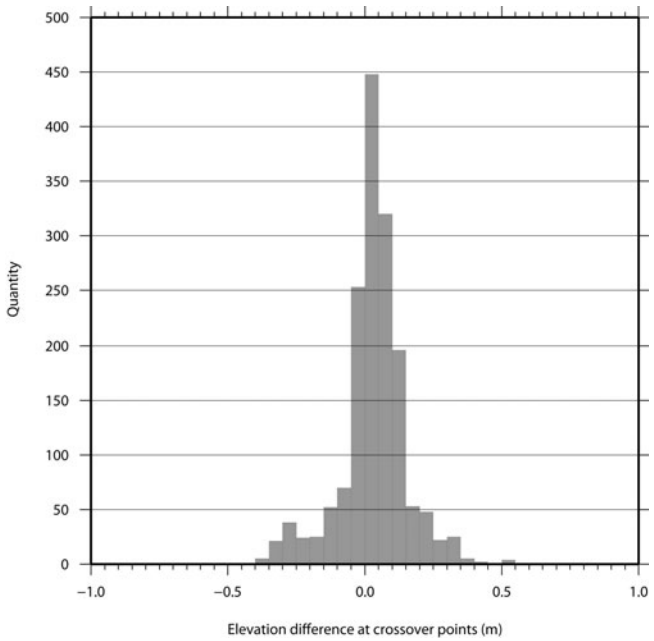

Fig. 3. Histogram of elevation differences at 1615 crossover points of the surveyed kinematic GPS profiles.

estimated by a crossover-point analysis. The histogram in Figure 3 shows the elevation differences at the 1615 crossover points. The mean elevation difference is 0.03 m with a standard deviation of 0.12 m.

Static GPS measurements

All stakes (Fig. 2) were occupied for an observation period of ~1 hour in several campaigns. The length of the baselines to KRS varied between 0.03 km (BA01) and 19.4 km (DML27). The positions of all stakes were computed using TGO™, and the formal horizontal and vertical errors (Table 1) were derived for every point in a processing report. The formal errors issued by GPS software are usually over-optimistic. Experience shows that these errors need to be scaled by a factor of 5–20, to be closer to the true uncertainty of the static GPS (personal communication from M. King, 2007). We take a factor of 20 as a conservative estimate of the precision of the GPS positions. As the accuracy depends on the baseline length, we use the points BA01 and DML27 to estimate the accuracy of the static GPS measurements.

The positions of these two points were calculated against KRS for two campaigns. They have quite different horizontal and vertical errors, which can be attributed to the longer baseline length between KRS and DML27. However, there are also significant differences between campaigns for the same point. For DML27, the horizontal and vertical errors in 2002/03 are almost an order of magnitude larger than in 2005/06. This may stem from the high sunspot activity in 2002/03 (http://solarscience.msfc.nasa.gov/SunspotCycle.shtml) in combination with the baseline length, despite using the ionosphere-free solution of TGO™. We assume that the maximum horizontal and vertical errors for our solutions are given by the values for DML27 of 0.30 m and 0.82 m, respectively, from the campaign in 2002/03.

Table 1. Error estimates for BA01 and DML27

Point	Campaign	Horizontal $1-\sigma$ error*	Vertical $1-\sigma$ error*	Baseline length
		m	m	m
BA01	2002/03	0.01	0.04	29.4
BA01	2005/06	0.01	0.02	29.7
DML27	2002/03	0.30	0.82	19 359.7
DML27	2005/06	0.04	0.10	19 358.9

*Based on formal errors issued by the GPS software, TGO™, scaled by a factor of 20.

Table 2. Calculated mean annual horizontal ice-flow velocities

Point	Magnitude	Direction	Period of averaging
	$m\,a^{-1}$	°	
BA01	0.682	272.6	Jan. 2003–Dec. 2005
DML05	0.660	270.4	Jan. 2001–Dec. 2005
DML25	0.830	274.2	Jan. 2004–Dec. 2005
DML26	1.066	335.9	Jan. 2001–Dec. 2005
DML27	0.963	287.5	Feb. 2003–Dec. 2005
HM01	0.642	273.7	Jan. 2000–Dec. 2005
HM02	0.684	270.0	Jan. 2000–Dec. 2005
HM03	0.674	266.6	Jan. 2000–Dec. 2005
PEN1	0.643	291.3	Jan. 2000–Dec. 2005
PEN2	0.767	282.9	Jan. 2000–Dec. 2005
PEN3	0.859	265.9	Jan. 2000–Dec. 2005
PEN4	0.841	257.9	Jan. 2000–Dec. 2005
PEN5	0.624	269.8	Jan. 2000–Dec. 2005

GLAS data

ICESat's positioning precision is stated as 35 m and the predicted elevation data accuracy is 0.15 m (Zwally and others, 2002). Shuman and others (2006) presented a new elevation accuracy assessment of ~0.02 m for low-slope and clear-sky conditions. Our area of investigation is a low-slope region, but clouds during the observation period cannot be excluded over the whole period. The elevation measurements of the ICESat laser altimeter refer to the TOPEX/Poseidon ellipsoid. Differences in elevation between the TOPEX/Poseidon ellipsoid and the WGS84 ellipsoid are approximately 0.71 m in the region of interest (personal communication from T. Haran, 2005). When transforming to the WGS84 ellipsoid we subtract this value from all GLAS12 elevation data.

RESULTS

Surface topography

The derived surface topography in the area of investigation refers to the WGS84 ellipsoid and is a combination of the GPS and the GLAS12 datasets (Fig. 4, contours). A crossover-point analysis was performed before combining the datasets to identify systematic offsets and to estimate the uncertainties. As crossover points for the GPS data we use the average of all GPS measurements within the diameter of the GLAS footprint of about 60 m. Considering all crossover points, the GLAS12 data (transformed to the WGS84 ellipsoid) are found to be 0.119 m lower than the GPS data, on average. This elevation difference was added to the GLAS12 data, i.e. we corrected the elevations to the GPS

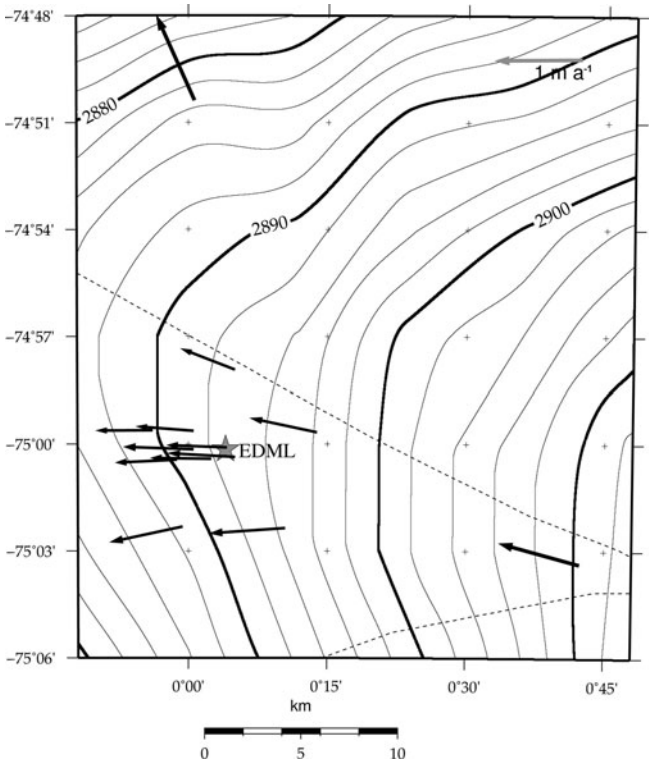

Fig. 4. Surface flow-velocity vectors in the area of interest, plotted on the contour map of the combined and gridded (5 km × 5 km) GPS/GLAS12 elevation model. The contour interval is 2 m. The dotted curves indicate the ice divide corresponding to the DEM of Bamber and Bindschadler (1997).

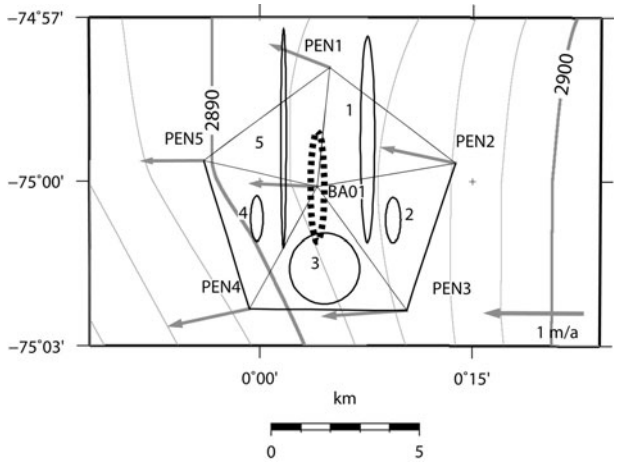

Fig. 5. Velocity vectors of the pentagon-shaped network (PEN1–PEN5) and BA01. Strain ellipses are plotted for the five strain triangles, indicated by numbers 1–5. The mean strain ellipse (dotted) is centered on BA01. See text for the calculation of the mean strain ellipse. The elevation contour interval is 2 m.

profiles. To get sufficient spatial coverage of elevation data over the whole area of investigation, we interpolated the combined dataset with a minimum-curvature algorithm (Wessel and Smith, 1991) on a 5 km × 5 km grid (Fig. 4). With this grid size, at least one data point was available for each gridcell, even several tens of kilometers away from the drilling site.

Surface velocity

The velocity magnitude at the survey points between the two ice divides varies between 0.62 m a^{-1} (PEN5) and 0.96 m a^{-1} (DML27). The flow direction varies between 257.9° (PEN4) and 291.3° (PEN1). The flow velocity of DML26, north of the divide, is outside this range, moving in a direction of 335.9° with a magnitude of 1.07 m a^{-1} (Table 2; Fig. 4).

The location of the EDML drilling site was surveyed on 10 January 2001, before the drilling operation started, yielding 75.0025° S, 0.068° E and 2891.7 m at the snow surface. As excavation of the drill trench does not allow accurate remeasurements, we use the mean velocities of the points next to it, DML25 and BA01. We thus obtain a value of 0.756 m a^{-1} in the direction of 273.4° for the ice velocity at the drilling site. The precision of the velocity measurements differs, depending on the period and data used (see Table 1). We therefore perform a propagation of errors by

$$\delta v^2 = \left(\frac{v}{s}\,\delta s_\mathrm{m}\right)^2 + \left(\frac{v}{t}\,\delta t\right)^2. \qquad (1)$$

Only the horizontal errors are used; the vertical errors are neglected for calculating the propagated error (δv) of the annual movement. Here, v is the velocity magnitude and s the horizontal offset of the survey point over the measurement interval (t). The term δs_m is the mean of the horizontal errors for the survey point of the two campaigns used for the determination of the velocities. The time error, δt, is assumed to be a constant of 1 day (1/365.25 years), because the start and end time is rounded by the day. The resulting errors for sites DML27 and BA01 are 0.059 and 0.003 m a^{-1}, respectively. As discussed above, we take the error at DML27 as the maximum error of the velocity determination, as it has the longest baseline.

Surface strain rates

Strain rates were determined from a pentagon-shaped network (PEN1–PEN5) with BA01 as the center reference pole (Fig. 5). Using the horizontal surface velocities in Table 2, with the geodetical nomenclature of y as the eastward and x as the northward components, we determine the strain-rate components from (Paterson, 1994)

$$\dot{\varepsilon}_x = \frac{\Delta v_x}{\Delta x}, \qquad \dot{\varepsilon}_y = \frac{\Delta v_y}{\Delta y}, \qquad (2)$$

and the combined strain rate as

$$\dot{\varepsilon}_{xy} = \frac{1}{2}\left(\frac{\Delta v_x}{\Delta y} + \frac{\Delta v_y}{\Delta x}\right), \qquad (3)$$

where Δv_x and Δv_y are the differences of the x and y velocity components of the considered pair of survey points, and Δx and Δy are the distances between the stakes in the x and y directions. Distances from the reference pole to each pentagon point vary between 3961.85 m (BA01–PEN5) and 5173.28 m (BA01–PEN3). Using Equation (3) the combined surface strain rate is calculated for every pair of neighboring points (west–east and south–north), yielding ten values (Table 3).

To determine the strain rates, we divide the pentagon into five strain triangles (Fig. 5) and assume the strain is constant over the area of the triangle. We calculate the average of the strain for each triangle (e.g. the mean of BA01/PEN1, BA01/PEN2 and PEN1/PEN2 for the northeastern triangle, numbered 1). The principal components are calculated using the

Table 3. Strain rates for pairs of survey points

Pair of points	$\dot{\varepsilon}_{xy}$	$\dot{\varepsilon}_x$	$\delta\dot{\varepsilon}_x$	$\dot{\varepsilon}_y$	$\delta\dot{\varepsilon}_y$	Δv_x	Δv_y
	a^{-1}	a^{-1}	a^{-1}	a^{-1}	a^{-1}	$m\,a^{-1}$	$m\,a^{-1}$
BA01/PEN1	-2.20×10^{-4}	-2.02×10^{-5}	1.47×10^{-5}	-9.61×10^{-4}	2.85×10^{-4}	–0.08	–0.20
BA01/PEN2	-5.44×10^{-5}	6.73×10^{-5}	5.83×10^{-5}	-2.74×10^{-5}	1.29×10^{-5}	0.07	–0.13
BA01/PEN3	-1.57×10^{-5}	-4.35×10^{-5}	1.49×10^{-5}	2.86×10^{-5}	1.86×10^{-5}	–0.18	0.09
BA01/PEN4	-5.81×10^{-5}	-3.32×10^{-5}	1.41×10^{-5}	-9.90×10^{-5}	2.87×10^{-5}	–0.14	–0.21
BA01/PEN5	-3.12×10^{-5}	-8.24×10^{-5}	8.63×10^{-5}	-8.49×10^{-5}	1.54×10^{-5}	–0.06	–0.03
PEN1/PEN2	-4.73×10^{-5}	-4.97×10^{-5}	1.97×10^{-5}	1.70×10^{-5}	1.36×10^{-5}	–0.15	0.08
PEN1/PEN5	-3.79×10^{-5}	-7.38×10^{-6}	1.78×10^{-5}	-5.73×10^{-5}	1.46×10^{-5}	–0.02	–0.24
PEN2/PEN3	-5.96×10^{-5}	-2.10×10^{-5}	1.18×10^{-5}	-1.57×10^{-4}	4.28×10^{-5}	–0.11	–0.22
PEN3/PEN4	-2.71×10^{-4}	1.65×10^{-4}	2.87×10^{-4}	-2.16×10^{-5}	1.13×10^{-5}	0.03	–0.11
PEN4/PEN5	-3.72×10^{-5}	-4.01×10^{-5}	1.21×10^{-5}	9.63×10^{-5}	3.32×10^{-5}	–0.20	0.17

Note: Combined ($\dot{\varepsilon}_{xy}$) and directional ($\dot{\varepsilon}_x$ and $\dot{\varepsilon}_y$) strain rates with conservative error estimates ($\delta\dot{\varepsilon}_x$ and $\delta\dot{\varepsilon}_y$); differences of the velocity components in north–south (Δv_x) and east–west (Δv_y) direction for BA01 and PEN1–PEN5. In this work, the differences of the velocity components were calculated by west minus east values, and south minus north values. Negative strain rates thus correspond to compression, and positive strain rates to extension.

rotation, θ, of the x and y axes

$$\tan 2\theta = \frac{2\dot{\varepsilon}_{xy}}{\dot{\varepsilon}_x - \dot{\varepsilon}_y}. \quad (4)$$

This provides one of two values for θ, which are 90° apart. One gives the direction of the maximum strain rate, $\dot{\varepsilon}_{max}$, the other of minimum strain rate, $\dot{\varepsilon}_{min}$. The strain-rate magnitudes along these directions follow from

$$\dot{\varepsilon}_{max,\,min} = \dot{\varepsilon}_x \cos^2\theta_{max,\,min} + \dot{\varepsilon}_y \sin^2\theta_{max,\,min} + 2\dot{\varepsilon}_{xy} \sin\theta_{max,\,min} \cos\theta_{max,\,min}. \quad (5)$$

This calculation is repeated for every strain triangle. The direction of maximum strain rate varies between 30.1° and 75.0°. Using the incompressibility condition (Paterson, 1994)

$$\dot{\varepsilon}_x + \dot{\varepsilon}_y + \dot{\varepsilon}_z = 0, \quad (6)$$

we estimate the flow-induced vertical strain rate $\dot{\varepsilon}_z$. It varies between 1.31×10^{-6} and $3.79\times10^{-4}\,a^{-1}$ (Table 4), with a standard variation of $6.49\times10^{-5}\,a^{-1}$. To estimate a strain rate representative of the EDML drilling site, we determine the average horizontal deformation and its direction at BA01. For this purpose, the arithmetic means of $\dot{\varepsilon}_{xy}$, $\dot{\varepsilon}_x$ and $\dot{\varepsilon}_y$ from the strain triangles are calculated and used in Equations (4) and (5) (Table 4). The maximum rate is $-1.85\times10^{-4}\,a^{-1}$, acting in the direction of 65.8°. The minimum rate, $2.32\times10^{-5}\,a^{-1}$, acts in the direction of 155.8°. In addition to the arithmetic mean, we determine the weighted mean for the directional and vertical strain-rate components ($\dot{\varepsilon}_{x,\,y,\,z}$), using the strain-rate error weights (Table 4). The arithmetic mean of the vertical strain rate, $\dot{\varepsilon}_z$, is $(1.62\pm1.25)\times10^{-4}\,a^{-1}$, and the weighted mean is $(1.09\pm1.25)\times10^{-4}\,a^{-1}$.

DISCUSSION

The DEM presented here is compared with the DEM generated by Bamber and Bindschadler (1997) from European Remote-sensing Satellite-1 (ERS-1) radar altimetry, which is also available on a 5 km × 5 km grid. For comparison, we subtract the Bamber and Bindschadler (1997) DEM from our combined GPS/GLAS12 DEM. The northeastern edge of the area of investigation is striking, where the elevations of the Bamber and Bindschadler (1997) DEM are about 2 m higher than those in our DEM (Fig. 6). Calculating the mean difference between the combined GPS/GLAS12 DEM and the Bamber and Bindschadler (1997) DEM for every 5 km × 5 km gridcell, we determine a mean elevation difference of –0.33 m. That is, the DEM of Bamber and

Table 4. Strain rates for the strain triangles

Strain triangle	$\dot{\varepsilon}_{xy}$	$\dot{\varepsilon}_x$	$\delta\dot{\varepsilon}_x$	$\dot{\varepsilon}_y$	$\delta\dot{\varepsilon}_y$	$\dot{\varepsilon}_z$	$\delta\dot{\varepsilon}_z$	$\dot{\varepsilon}_{max}$	θ_{max}	$\dot{\varepsilon}_{min}$	θ_{min}
	a^{-1}	a^{-1}	a^{-1}	a^{-1}	a^{-1}	a^{-1}	a^{-1}	a^{-1}	°	a^{-1}	°
1	-9.30×10^{-5}	-8.70×10^{-7}	3.66×10^{-5}	-3.24×10^{-4}	1.65×10^{-4}	3.25×10^{-4}	1.69×10^{-4}	-3.49×10^{-4}	75.03	2.40×10^{-5}	165.03
2	-4.32×10^{-5}	9.60×10^{-7}	3.54×10^{-5}	-5.18×10^{-5}	2.80×10^{-5}	5.09×10^{-5}	4.51×10^{-5}	-7.61×10^{-5}	60.71	2.52×10^{-5}	150.71
3	-1.15×10^{-4}	2.94×10^{-5}	1.66×10^{-4}	-3.07×10^{-5}	2.08×10^{-5}	1.31×10^{-6}	1.67×10^{-4}	-1.20×10^{-4}	52.32	1.18×10^{-4}	142.32
4	-4.22×10^{-5}	-5.19×10^{-5}	5.10×10^{-5}	-3.74×10^{-6}	2.68×10^{-5}	5.56×10^{-5}	5.76×10^{-5}	-7.64×10^{-5}	30.13	2.07×10^{-5}	120.13
5	-9.63×10^{-5}	-3.67×10^{-5}	5.18×10^{-5}	-3.42×10^{-4}	1.65×10^{-4}	3.79×10^{-4}	1.73×10^{-4}	-3.70×10^{-4}	73.89	-8.83×10^{-6}	163.89
Arithmetic mean	-7.80×10^{-5}	-1.18×10^{-5}	3.76×10^{-5}	-1.50×10^{-4}	4.74×10^{-5}	1.62×10^{-4}	6.05×10^{-5}	-1.85×10^{-4}	65.83	2.32×10^{-5}	155.83
Weighted mean		-1.54×10^{-5}		-5.64×10^{-5}		1.09×10^{-4}					

Note: Combined ($\dot{\varepsilon}_{xy}$), directional ($\dot{\varepsilon}_x$ and $\dot{\varepsilon}_y$), vertical strain rate ($\dot{\varepsilon}_z$), maximum and minimum strain rate ($\dot{\varepsilon}_{max}$ and $\dot{\varepsilon}_{min}$) and the direction of maximum and minimum strain rate (θ_{max} and θ_{min}). The conservative error estimates for the directional and vertical strain rates for the five triangles are denoted by $\delta\dot{\varepsilon}_{(x,y,z)}$. Weighted mean refers to the weighting by corresponding errors. See text for the calculation of the arithmetic and weighted means.

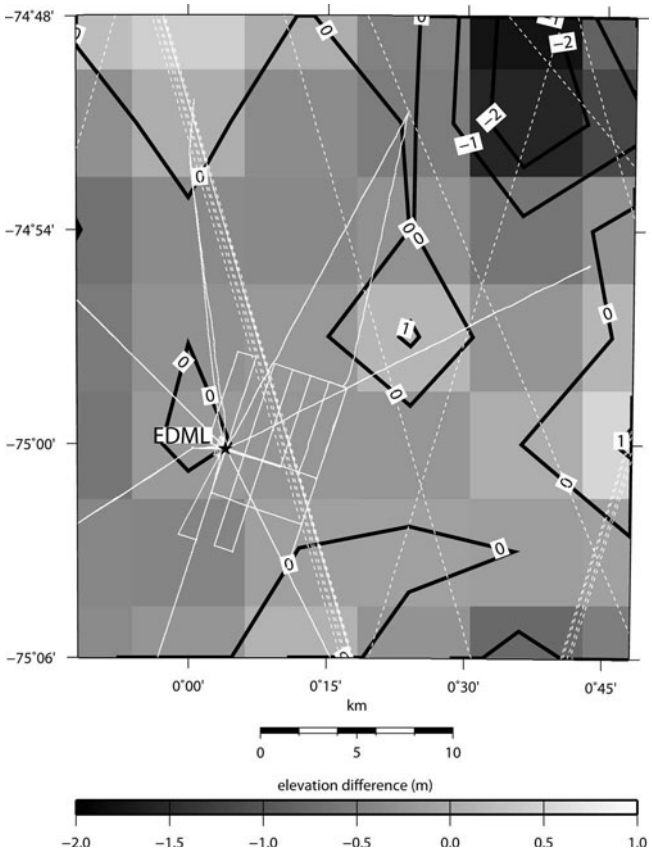

Fig. 6. Elevation differences of our GPS/GLAS12 DEM minus the Bamber and Bindschadler (1997) DEM. The contour interval is 1 m. Kinematic GPS and GLAS12 data coverage used in this paper (Fig. 2) are plotted as white dotted (GLAS12) and solid (GPS) lines.

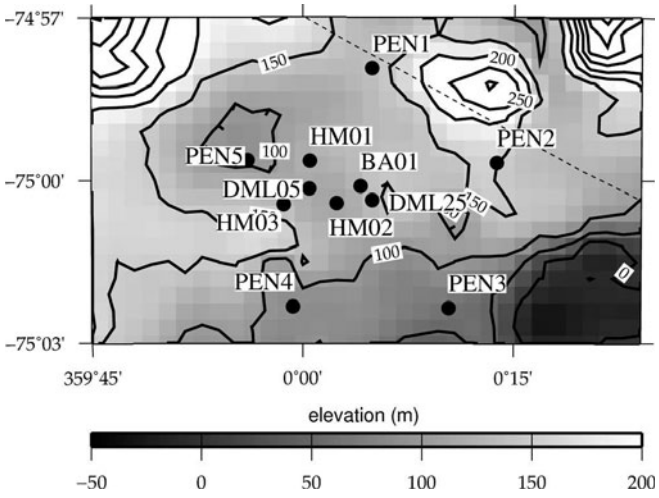

Fig. 7. Subglacial topography of the area of investigation gridded on a 500 m × 500 m raster after Steinhage and others (1999). The spacing between the contours is 50 m. The dotted line represents the ice divide corresponding to Bamber and Bindschadler (1997).

Bindschadler (1997) is about 0.3 m higher than our combined GPS/GLAS12 DEM.

The topography in the region of interest shows a smooth surface, slightly sloping down to the west. One major feature is a transient ice divide, which splits ~20 km upstream of the drilling location, thus separating three drainage basins. Of our 13 survey points, 12 are located between the two branches of the ice divide; only DML26 is located north of both ice branches (Fig. 4). As it represents a different drainage basin and flow regime, we exclude DML26 from further analysis. The ice divide and the local surface elevation are the largest factors determining the flow and strain field. This is evident from comparison of the mean slope direction at the drilling site with the mean flow direction of 273.5° from the GPS-based velocity measurements. Small differences in magnitude and direction of the horizontal ice-flow velocities of the survey points are likewise mainly caused by the relative location of the survey point in respect to the ice divide. Points very close to the ice divide are generally slower and the direction of movement is nearly parallel to the course of the divide (Fig. 4 and Table 2, e.g. PEN1). The magnitude of the flow velocity increases with increasing distance from the divide, and the northward flow component is reduced (Fig. 4; Table 2). An exception is PEN5, which has a slightly lower velocity (0.624 m a^{-1}) than PEN1 (0.643 m a^{-1}) despite the greater distance from the divide. Although this difference is smaller than the estimated conservative maximum velocity error of 0.059 m a^{-1}, we try to identify the origin of this variation.

Investigating the local bedrock topography in the vicinity of PEN5, available from airborne radio-echo soundings (Steinhage and others, 1999), PEN5 is found to be located above a depression of the subglacial topography (Fig. 7). The depression is ~5 km wide and several tens of meters deep, with respect to the surrounding average bedrock elevation. Because of the smoothing effect of ice dynamics, the surface elevation is much smoother than the bedrock topography. Surface topography varies only in the order of meters. The depression therefore simply causes locally increased ice thickness, but not a significant feature at the surface. The slightly lower velocity at PEN5, compared to the other stakes, is thus a consequence of the flux balance required by the larger ice thickness.

The surface strain rate at BA01, averaged from the strain triangles of the five pentagon points (PEN1–PEN5), is considered to be representative for the EDML ice core, as BA01 is only 93 m to the northeast of the drilling site. Most error estimates for the strain rates (Tables 3 and 4) are about equal to or smaller than the nominal value of the strain rate. For some strain rates with very small nominal values, the error is more than one order of magnitude larger (e.g. $\dot{\varepsilon}_x$ triangle 3, Table 4). We emphasize that the velocity errors are very conservative estimates, so the strain-rate errors are also conservative estimates. The average maximum principal component of the strain rate at BA01 is negative (-1.85×10^{-4} a^{-1}). It acts as a compressing force in the direction of 65.8°. The minimum principal component of the strain rate at BA01 is positive (2.32×10^{-5} a^{-1}). It therefore corresponds to a dilatational force and acts along an axis in the direction of 155.8°. This results from the low magnitude of the velocity at PEN5. Both BA01 and PEN2 (upstream of PEN5) are moving faster than PEN5, which induces the along-flow compression of the ice mass. The average vertical strain rate, as calculated above, shows that the compression in the northwest–southeast direction only partly compensates the dilatational component of the strain field in the northeast–southwest direction, perpendicular to the ice flow at EDML, and layer thinning is required in the vertical component to achieve balance.

CONCLUSION

We provide an improved dataset for the surface topography and flow velocity in the vicinity of the EDML drilling site. A DEM of high accuracy was derived from a combination of kinematic surface GPS measurements and satellite laser altimetry from ICESat's GLAS12 data. Static GPS measurements at 13 stakes between the austral summer seasons 1997/98 and 2005/06 provided the basis for deriving the flow velocity field and resulting strain rates. The flow velocity field is, in general, divergent along the course of and in between the two branches of the ice divide. On top of this general field, small velocity variations are superimposed, which are caused by local variations in ice thickness resulting from undulations in bedrock topography. The horizontal strain field, calculated from the velocities, shows lateral extension and smaller longitudinal compression. This results in layer thinning in the EDML ice core, which has to be accounted for to yield a correct interpretation of ice-core data.

ACKNOWLEDGEMENTS

The data of GPS reference stations were allocated by A. Rülke of the Institute for Planetary Geodesy of the Technical University of Dresden (http://www.tu-dresden.de/ipg/). Satellite altimetry data were provided by the US National Snow and Ice Data Center, Boulder, CO (http://nsidc.org/data/icesat/). The authors thank D. Jansen for helpful discussions. This work is a contribution to the European Project for Ice Coring in Antarctica (EPICA), a joint European Science Foundation (ESF)/European Commission (EC) scientific program, funded by the EC and by national contributions from Belgium, Denmark, France, Germany, Italy, The Netherlands, Norway, Sweden, Switzerland and the UK. The main logistic support at Dronning Maud Land was provided by AWI. This is EPICA publication No. 177. Preparation of this work was supported by Deutsche Forschungsgemeinschaft with the 'Emmy Noether' scholarship EI-672/1 to O.E. This paper was enhanced significantly by the comments of M. King, R. Jacobel and R. Bindschadler.

REFERENCES

Bamber, J.L. and R.A. Bindschadler. 1997. An improved elevation dataset for climate and ice-sheet modelling: validation with satellite imagery. *Ann. Glaciol.,* **25**, 439–444.

Eisen, O., W. Rack, U. Nixdorf and F. Wilhelms. 2005. Characteristics of accumulation around the EPICA deep-drilling site in Dronning Maud Land, Antarctica. *Ann. Glaciol.,* **41**, 41–56.

EPICA Community Members. 2004. Eight glacial cycles from an Antarctic ice core. *Nature,* **429**(6992), 623–628.

EPICA Community Members. 2006. One-to-one coupling of glacial climate variability in Greenland and Antarctica. *Nature,* **444**(7116), 195–198.

Hvidberg, C.S., K. Keller and N.S. Gundestrup. 2002. Mass balance and ice flow along the north-northwest ridge of the Greenland ice sheet at NorthGRIP. *Ann. Glaciol.,* **35**, 521–526.

Paterson, W.S.B. 1994. *The physics of glaciers. Third edition.* Oxford, etc., Elsevier.

Shuman, C.A. *and 6 others*. 2006. ICESat Antarctic elevation data: preliminary precision and accuracy assessment. *Geophys. Res. Lett.,* **33**(L7), L07501. (10.1029/2005GL025227.)

Steinhage, D., U. Nixdorf, U. Meyer and H. Miller. 1999. New maps of the ice thickness and subglacial topography in Dronning Maud Land, Antarctica, determined by means of airborne radio-echo sounding. *Ann. Glaciol.,* **29**, 267–272.

Vittuari, L. *and 6 others*. 2004. Space geodesy as a tool for measuring ice surface velocity in the Dome C region and along the ITASE traverse. *Ann. Glaciol.,* **39**, 402–408.

Wessel, P. and W.H.F. Smith. 1991. Free software helps map and display data. *Eos,* **72**(41), 441, 445–446.

Zwally, H.J. *and 15 others*. 2002. ICESat's laser measurements of polar ice, atmosphere, ocean and land. *J. Geodyn.,* **34**(3–4), 405–445.

MS received 26 October 2006 and accepted in revised form 15 April 2007

Spatio-temporal distribution of accumulation

GROUND-BASED MEASUREMENTS OF SPATIAL AND TEMPORAL VARIABILITY OF SNOW ACCUMULATION IN EAST ANTARCTICA

Olaf Eisen,[1,2] Massimo Frezzotti,[3] Christophe Genthon,[4] Elisabeth Isaksson,[5] Olivier Magand,[4] Michiel R. van den Broeke,[6] Daniel A. Dixon,[7] Alexey Ekaykin,[8] Per Holmlund,[9] Takao Kameda,[10] Lars Karlöf,[11] Susan Kaspari,[7] Vladimir Y. Lipenkov,[8] Hans Oerter,[2] Shuhei Takahashi,[10] and David G. Vaughan[12]

Received 31 October 2006; revised 2 July 2007; accepted 25 September 2007; published 11 April 2008.

[1] The East Antarctic Ice Sheet is the largest, highest, coldest, driest, and windiest ice sheet on Earth. Understanding of the surface mass balance (SMB) of Antarctica is necessary to determine the present state of the ice sheet, to make predictions of its potential contribution to sea level rise, and to determine its past history for paleoclimatic reconstructions. However, SMB values are poorly known because of logistic constraints in extreme polar environments, and they represent one of the biggest challenges of Antarctic science. Snow accumulation is the most important parameter for the SMB of ice sheets. SMB varies on a number of scales, from small-scale features (sastrugi) to ice-sheet-scale SMB patterns determined mainly by temperature, elevation, distance from the coast, and wind-driven processes. In situ measurements of SMB are performed at single points by stakes, ultrasonic sounders, snow pits, and firn and ice cores and laterally by continuous measurements using ground-penetrating radar. SMB for large regions can only be achieved practically by using remote sensing and/or numerical climate modeling. However, these techniques rely on ground truthing to improve the resolution and accuracy. The separation of spatial and temporal variations of SMB in transient regimes is necessary for accurate interpretation of ice core records. In this review we provide an overview of the various measurement techniques, related difficulties, and limitations of data interpretation; describe spatial characteristics of East Antarctic SMB and issues related to the spatial and temporal representativity of measurements; and provide recommendations on how to perform in situ measurements.

Citation: Eisen, O., et al. (2008), Ground-based measurements of spatial and temporal variability of snow accumulation in East Antarctica, *Rev. Geophys.*, *46*, RG2001, doi:10.1029/2006RG000218.

1. INTRODUCTION

[2] The development of the Earth's climate is strongly linked to the state of the polar regions. In particular, the large ice sheets influence components of the climate system, including the global water cycle by locking up or releasing large amounts of fresh water; the radiation budget through the high albedo of ice- and snow-covered surfaces; and the thermohaline circulation through the amount of fresh water released to the ocean by melting or iceberg calving. Since the termination of the last glacial period, the only remaining large ice sheets are located in Antarctica and Greenland.

[3] The polar ice sheets are not only active participants in the global climate system (including being a major control on global sea level), but they also provide the only archive which gives direct access to the paleoatmosphere. *Ice cores* collected from polar regions and analyzed for atmospheric gases, stable isotopes, major ions, trace elements, etc.,

[1]Laboratory of Hydraulics, Hydrology and Glaciology, ETH Zurich, Zurich, Switzerland.
[2]Alfred Wegener Institute for Polar and Marine Research, Bremerhaven, Germany.
[3]Laboratory for Climate Observation, Italian National Agency for New Technologies, Energy and the Environment, Rome, Italy.
[4]Laboratoire de Glaciologie et Géophysique de l'Environnement, CNRS, University Joseph-Fourier, Grenoble, France.
[5]Norwegian Polar Institute, Tromsø, Norway.
[6]Institute for Marine and Atmospheric Research, Utrecht University, Utrecht, Netherlands.
[7]Climate Change Institute, University of Maine, Orono, Maine, USA.
[8]Arctic and Antarctic Research Institute, St. Petersburg, Russia.
[9]Department of Physical Geography and Quaternary Geology, Stockholm University, Stockholm, Sweden.
[10]Kitami Institute of Technology, Kitami, Japan.
[11]SWIX Sport AS, Lillehammer, Norway.
[12]British Antarctic Survey, Cambridge, UK.

8755-1209/08/2006RG000218$15.00
Paper number 2006RG000218

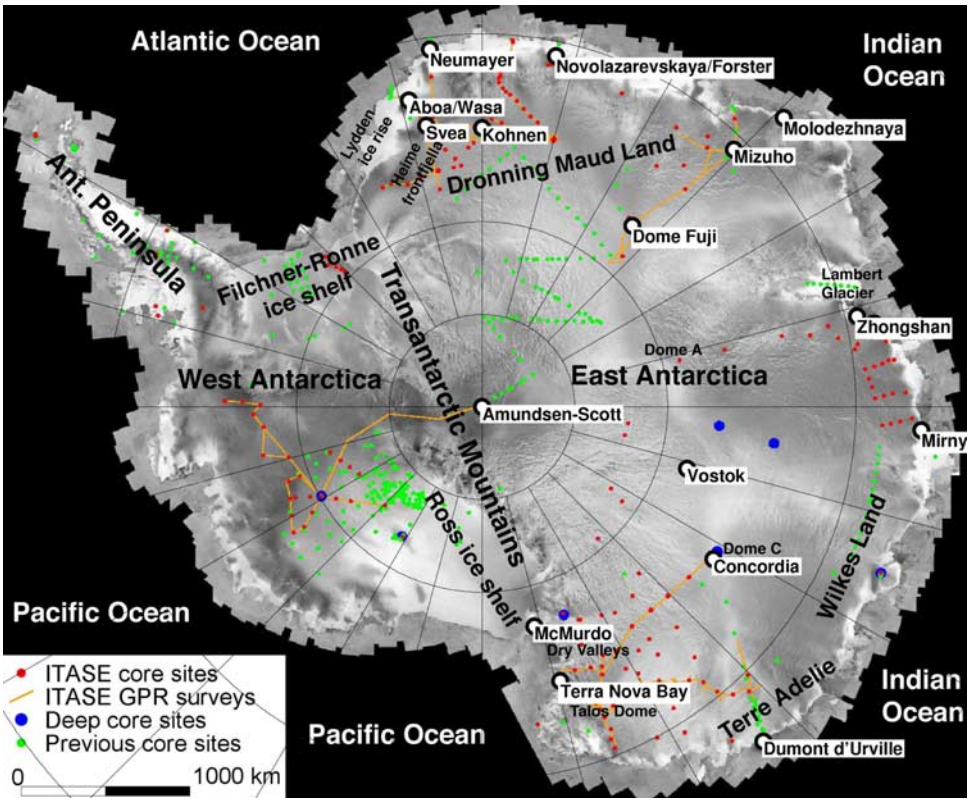

Figure 1. Map of Antarctica with some topographic names, drilling sites, radar profiles, and stations mentioned in the text (underlain by white rectangles), adapted from *Mayewski et al.* [2005] with permission of the International Glaciology Society. Radarsat mosaic in the background. ("Terra Nova Bay" station was renamed to "Mario Zucchelli station" in 2004.)

enable past climate conditions to be reconstructed [e.g., *Mayewski et al.*, 1993; *Dansgaard et al.*, 1993]. (Italicized terms are defined in the glossary, after the main text.) These records, currently spanning as far back in time as the past 800 ka [*Jouzel et al.*, 2007], are an important key to identification of the causes and forcing mechanisms of climate change.

[4] Understanding past conditions of the ice sheets and determining their present state are essential to predict their behavior under future climate conditions. The most important physical variable in assessing past and current ice sheet conditions is the *surface mass balance*. The current state-of-the-art ground-based techniques used to determine surface mass balance and its spatial and temporal characteristics in East Antarctica are the topic of this paper. Surface mass balance has been termed differently by many authors. Most completely, it is described as *mean net annual surface mass balance* and includes all terms that contribute to the solid, liquid, and gaseous transfer of water across the surface of the ice sheet. Hereafter, we will abbreviate this to "surface mass balance" (SMB) while maintaining the averaging implied by the full description. We also note that this term is the aggregate of many processes, such as precipitation from clouds and clear skies, the formation of hoarfrost at the surface and within the snowpack, sublimation, melting and runoff, wind scouring, and drift deposition.

1.1. Principal Processes

[5] Antarctica consists of West and East Antarctica, divided by the Transantarctic Mountains (Figure 1), and the Antarctic Peninsula. Whereas floating ice shelves form a considerable part of West Antarctica, the largest ones being the Filchner-Ronne and Ross ice shelves, East Antarctica is mainly formed by the inland ice sheet plateau, roughly comprising two thirds of the continent. Our main aim is to present the characteristics of SMB of the East Antarctic plateau area, which despite its apparent homogeneity shows large spatial variability. Nevertheless, we include findings based on data from West Antarctica and near-coastal sites as well for a larger context.

[6] On the *Antarctic ice sheet*, few places display a constantly negative SMB (e.g., *blue ice areas*) [e.g., *Bintanja*, 1999; *van den Broeke et al.*, 2006b]. Unlike in Greenland and the Antarctic Peninsula [*Vaughan*, 2006] where melting is an important process, wind erosion and sublimation are the key factors for negative SMB of the West and East Antarctica ice sheets. On the interior plateau of the Antarctic ice sheet, large areas have a mass balance close to zero, and negative mass balance has been reported for some areas [*Frezzotti et al.*, 2002b]. Nevertheless, annual SMB is generally positive in the long term. We will therefore use the term *accumulation* or accumulation rate synonymously to refer to a positive SMB.

[7] Solid atmospheric precipitation (snowfall or diamond dust) is deposited at the surface of the East Antarctic Ice Sheet. Atmospheric precipitation is homogeneous over tens to hundreds of kilometers. Wind erosion, wind redistribution, sublimation, and other processes during or after the precipitation event lead to a deposition at the surface which is spatially less homogeneous than the original precipitation. Variations in accumulation over tens of kilometers have been observed since the 1960s [*Black and Budd*, 1964; *Pettré et al.*, 1986]. These accumulation variations and surface processes result in surface features including sastrugi, longitudinal dunes [*Goodwin*, 1990], dunes on the 100-m scale [*Ekaykin*, 2003; *Karlöf et al.*, 2005b], and, most impressively, megadunes on a kilometer scale [*Fahnestock et al.*, 2000; *Frezzotti et al.*, 2002a]. Once the snow is permanently deposited, further accumulation is responsible for the submergence of surface layers. In the firn column, the snow densifies under the overburden weight, and the interplay with ice dynamics like advection begins to deform the surface layer.

[8] The spatial and temporal distribution of SMB is a primary concern for numerous issues: for determining the current state of the ice sheet and estimating mass balance changes over regional, basin-wide, and continental scales and the associated contribution to sea level change [e.g., *Joughin et al.*, 2005, and references therein]; for ice flow modeling of the age-depth relationship and subsequent application to ice cores; for calibration of remote sensing measurements of SMB; for understanding of the SMB–surface meteorology–climate relationship; and for improving, verifying, and validating various types of models, in particular, the climate models from which predictions (future) or reconstructions (paleoclimate) of accumulation are tentatively obtained. Unfortunately, there exists a discrepancy between assumptions and needs of these applications in terms of spatiotemporal coverage and resolution of SMB and the actual data characteristics available. For instance, dating of ice cores by flow modeling usually assumes rather smooth accumulation patterns, mainly formed by larger features, accumulation time series, and ice dynamical history. Surface accumulation, on the other hand, is not smooth in time and space. Because of interaction with surface features, such as varying surface slopes, significant surface accumulation variations occur on much smaller spatial scales than precipitation, as will be demonstrated here. Analysis of *firn cores* and meteorological observations integrated with validated model reanalysis data of European Centre for Medium Range Weather Forecasts 40-Year Reanalysis (ERA 40) pointed out high variability of snow accumulation at yearly and decadal scales over the past 50 years but without a statistically significant trend [*Monaghan et al.*, 2006].

1.2. General Difficulties

[9] While measurement of precipitation has been a routine part of worldwide observations for more than a hundred years, there is still no practical technique that can be used to measure SMB in East Antarctica in realtime as part of a meteorological measurement program. This is largely due to the technical difficulties involved in making measurements without disturbing natural patterns of snow drift and measuring changes at depth in the snowpack. Thus, knowledge of SMB seasonality, trends, and spatial variability is limited. For this reason, we rely heavily on after-the-fact measurements obtained from ice cores, snow accumulation stakes, etc. Acquiring information about surface accumulation on the ice sheets with adequate sampling intervals is thus labor intensive. Only along a few selected profiles (ITASE, EPICA, JARE, RAE) (ITASE, International Transantarctic Scientific Expedition; EPICA, European Project for Ice Coring in Antarctica; JARE, Japanese Antarctic Research Expedition; RAE, Russian Antarctic Expedition) and in certain areas has area-wide information on accumulation been obtained (Figure 1).

[10] SMB observations cannot be easily extrapolated in time and space because spatial variations in SMB amount to considerable percentages of the absolute values, and often exceed these; the magnitude of the temporal variations is small compared to spatial variability, depending on the considered timescale; and the structure of the SMB covariance is unknown. To overcome these limitations, two other important techniques are therefore used to achieve area-wide information: satellite remote sensing and numerical climate modeling.

1.3. Remote Sensing and Numerical Modeling

[11] Currently, there is no definitive way to determine SMB from remote sensing data. There are signals in some remote sensing fields that are related to SMB as has been discussed widely by *Zwally and Giovinetto* [1995], *Winebrenner et al.* [2001], *Bindschadler et al.* [2005], *Rotschky et al.* [2006], and *Arthern et al.* [2006], but these are not solely dependent on accumulation rate and are thus to some extent ''contaminated'' by other factors. For this reason, most authors have attempted to use remote sensing fields to guide interpolation of field measurements. The most recent attempt at this by *Arthern et al.* [2006], who used a formal scheme to incorporate estimates of uncertainty and models of covariance, probably provides the most defensible estimate of the remotely sensed broadscale pattern of SMB across East Antarctica (Figure 2a). The typical footprint of these compilations is 20 km horizontally.

[12] In contrast to measuring area-wide precipitation in situ, as attempted by *Bindschadler et al.* [2005], numerical models are used to simulate atmospheric processes and related accumulation features [e.g., *Gallée et al.*, 2005]. The first step for successful modeling is detailed understanding of the physical processes involved. The second step involves model validation. Because of computing resource limitations, there is currently no way to explicitly resolve processes that induce spatial variability of SMB at kilometer scales or less (e.g., sastrugi and dunes) with an atmospheric model run in climate mode, that is, over several years. Such features have to be at best statistically parameterized, or considered as noise, when comparing field data with model results [*Genthon et al.*, 2005]. Although most

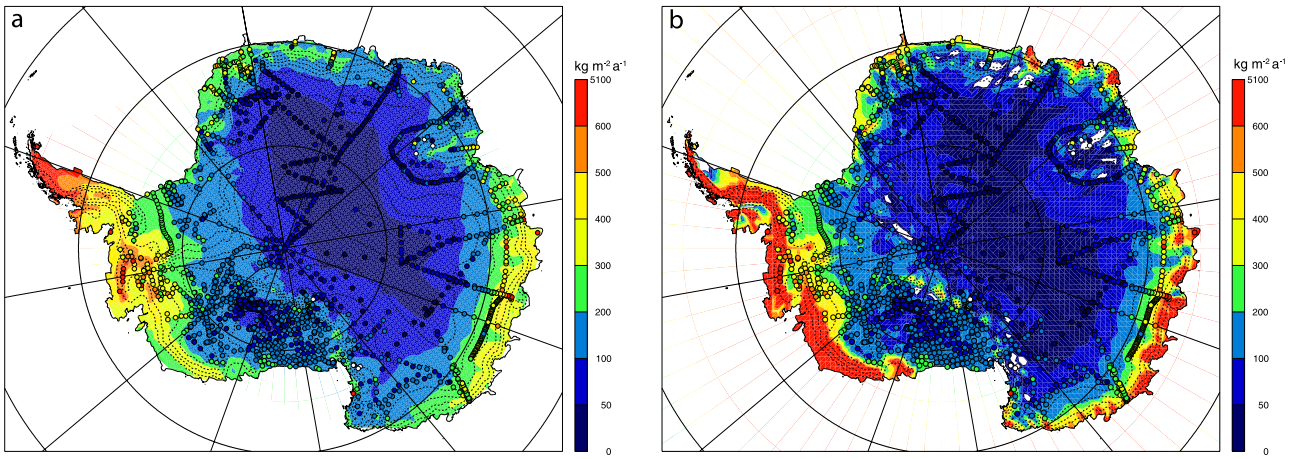

Figure 2. Examples for interpolated distributions of SMB (in kg m^{-2} a^{-1}) based on point observations (circles) in Antarctica. (a) Interpolation of SMB observations guided by passive microwave remote sensing (adapted from *Arthern et al.* [2006]); (b) numerical climate modeling of SMB (solid precipitation minus sublimation and melt) [*van den Broeke et al.*, 2006a] with ground-based SMB data collection indicated by circles [*van de Berg et al.*, 2006].

global models have spatial resolutions of 100 km and greater [*Genthon and Krinner*, 2001], grid stretching in global models [*Krinner et al.*, 2007] and regional climate modeling [*van Lipzig et al.*, 2004a; *van de Berg et al.*, 2006] allow resolutions on the order of 50–60 km that can better capture the mesoscale impacts of topography on SMB distribution such as diabatic cooling of air mass along slopes, air channeling, or barrier effects. Most of the boundary conditions needed to run global (including stretchable grid) and regional atmospheric models, such as topography, sea surface temperature and sea ice, and radiatively active gases and aerosols, are the same. On the other hand, regional models also need lateral boundary conditions such as temperature, winds, and moisture. This is generally provided by meteorological analyses for recent and present-day climate simulations, but data from global climate models are necessary to run realistic climate change experiments. In this respect, stretchable grid global models are self-consistent. As an example, Figure 2b shows mass balance from RACMO2/ANT for the period 1980–2004 [*van den Broeke et al.*, 2006a], with a horizontal resolution of 55 km, as well as a selection of observed mass balance values (updated from *Vaughan et al.* [1999b]). The model is clearly capable of reproducing the large-scale features of the Antarctic SMB (direct correlation with 1900 SMB observations yields $R = 0.82$) but cannot resolve the finer-scale features [*van de Berg et al.*, 2006] that are known to exist and that are one focus of the present paper. Double or triple nesting of models up to 3-km resolution is successfully used to improve weather forecasts in topographically complex regions, and could also be used to improve the model footprint of accumulation variability, once the governing processes (wind-driven snow redistribution) are properly parameterized [*Bromwich et al.*, 2003].

[13] One major use of SMB observations is to verify and validate climate models that are used to better understand the climate and SMB of Antarctica and to predict its future evolution. Therefore, using climate model results for driving interpolations and building maps of the Antarctic SMB from the field observations [*van de Berg et al.*, 2006] requires more care to avoid circular reasoning than for satellite data [*Vaughan et al.*, 1999b; *Arthern et al.*, 2006], as these are more independent from ground observations. However, the models do provide the means for hindcasting accumulation and may be used to identify areas where additional data or verification of existing data are most needed, such as areas where several models disagree with field reports or with interpolations [*Genthon and Krinner*, 2001; *van den Broeke et al.*, 2006a]. This approach has been used to select the sites of some of the recent Italian-French ITASE surveys, and the new data have confirmed problems with the previous estimates [*Magand et al.*, 2007].

[14] Despite significant advances in either discipline (remote sensing or numerical modeling), both techniques fail in detecting or explaining small-scale (<50 km) variability in SMB observations. The processes playing part in the ice sheet–climate–weather interaction act on a broad range of spatial and temporal scales. As mentioned in section 1.1, precipitation is homogeneous on scales of roughly 10^4 km^2, mainly on the plateau, and is subject to redistribution in the atmospheric boundary layer on scales of centimeters to kilometers. The scale of temporal variability increases from a scale related to the movement, dynamic, and lifetime of frontal systems on the order of days to seasonal variations and interannual variability. Partly related to larger-scale oscillatory atmospheric and oceanographic patterns are variations on interannual to decadal scales. Variations that occur over centuries and millennia are of relevance for climate conditions. The longest variations are on the timescale of glacial cycles with a period of 10^4–10^5 years (Table 1). The different techniques employed to observe these changes operate in a rather limited spatiotemporal window and with limited spatiotemporal resolution (Figure 3). Satellite sensors have

TABLE 1. Relevance and Scales of Surface Mass Balance Measurements

Target	Temporal Scales	Spatial Scales
Mass balance changes	1 to 10^5 years	basin to ice sheet
Climate-SMB relationship	hours to 100 years	centimeter to 100–1000 km
Climate models[a]	hours to 100 years 10^4–10^5 years in snapshots	10–100 km to ice sheet
Remote sensing[b]	hours to 30 years	submeter to ice sheet
Ice flow modeling[c]	10 to 10^5 years	100 m to ice sheet

[a]For (in)validation of models, the model output is compared with actual measurements. This permits judging the usability of models.
[b]Some remote sensing applications (altimetry, gravity, passive microwave, scatterometers, etc.) profit or even require data calibration for retrieval algorithms at specific test sites for correct interpretation and further extensions of the measurements to other areas. Validations are likewise important.
[c]Input of SMB to ice flow models is especially important for interpreting deep ice cores.

a comparably large range of footprint sizes and spatial coverage but are usually limited in temporal resolution and length of time series. Numerical models, in contrast, can cover temporal scales from hours to millennia, but their spatial coverage and resolution depend on each other in a reciprocal manner, thus yielding either low resolution at large spatial coverage or vice versa.

1.4. Outline

[15] With this background on surface accumulation in mind, the purpose of this review paper is to provide the glaciological community and those outside with a reference to measurement techniques of SMB and characteristics thereof in East Antarctica. We present the different types of measurements in section 2, including point measurements at the surface (*stakes* and *ultrasonic sounders*), point measurements at depth (*snow pits*, firn cores, and ice cores), and continuous lateral measurements (*ground-penetrating radar*). Sections 2.1–2.5 each contain a description of the mode of operation and type of analysis for the individual measurements, the basic measurement procedure for each technique and all required input quantities to derive the accumulation estimate, and an account of error estimates for each data type. We also present selected sample data to illustrate typical results obtained from these measurements and how the SMB data can form the input to other studies. Section 3 summarizes findings derived from the different measurement techniques, addresses their pros and cons, and judges the spatial and temporal representativity and limitation of SMB data. In section 4 we discuss the application of measurement data. We provide recommendations and principles for proper usage without stressing the data beyond physically justified limits to avoid misinterpretations. Additionally, we emphasize that observers in the field should be aware of end-users' needs.

2. MEASUREMENT TECHNIQUES

[16] Common for all measurements of SMB at the surface is the observation of deposited mass over a certain time period, or proxies thereof. The different methods not only cover a wide spectrum of technical modes of operation, they also yield information about mass balance for varying spatial and temporal scales and resolutions, as schematically illustrated in Figures 3, 4, and 5. SMB measurements derived from stakes, ultrasonic sounders, snow pits, and firn or ice cores provide information from a single point at the surface (Figure 4). In contrast, ground-penetrating radar (GPR) is carried out along profiles in such high resolution that it can be considered a quasi-continuous measurement. Whereas stakes and ultrasonic sounders have to be operated for a longer period to obtain a time series, snow pits, firn/ice cores, and GPR are able to provide a time series from a single deployment. One could thus classify the measurements into instantaneous and retrospective methods, with unclear boundaries. Owing to the different variables measured, the methods provide accumulation rates on very different timescales and resolution, as schematically illustrated in Figure 5. The detailed differences will be set forth in this section. Before introducing the individual methods, we first discuss the important role of snow density and how it is measured.

2.1. Prerequisite: Determination of Snow Density

[17] All techniques aimed at the determination of SMB perform some sort of difference-length measurement (height

Figure 3. Schemes to illustrate the (a) resolutions and (b) coverage of the different types of measurements in time (x axis) and space (y axis) used to derive surface mass balance. In Figure 3a, the rectangles indicate the typical resolutions of the various techniques. In addition to the characteristics of an individual measurement (e.g., a snow pit or a GPR profile), the combination of these with groups and larger entities are also displayed (e.g., stake lines or GPR grids). In this sense, "single snow pit" indicates the resolution within an individual pit, whereas "(snow pits at different sites)" refers to the distance between different snow pits. Likewise for ultrasonic sounders at different sites and GPR distance between different profiles. In Figure 3b, the rectangles indicate typical temporal and spatial coverage of measurements. For instance, stake lines may be hundreds of meters to more than 1000 km long. The time series derived from such a line could be just a year or up to several decades. In contrast, a single stake covers only an area of a few square centimeters. For implementing measurement programs, the question arises as to what can be achieved by a three- to four-person team in a single season. As logistics often impose the largest constraints in Antarctica, the resolution and coverage provided here could serve as a guideline to which combination of methods seems most effective.

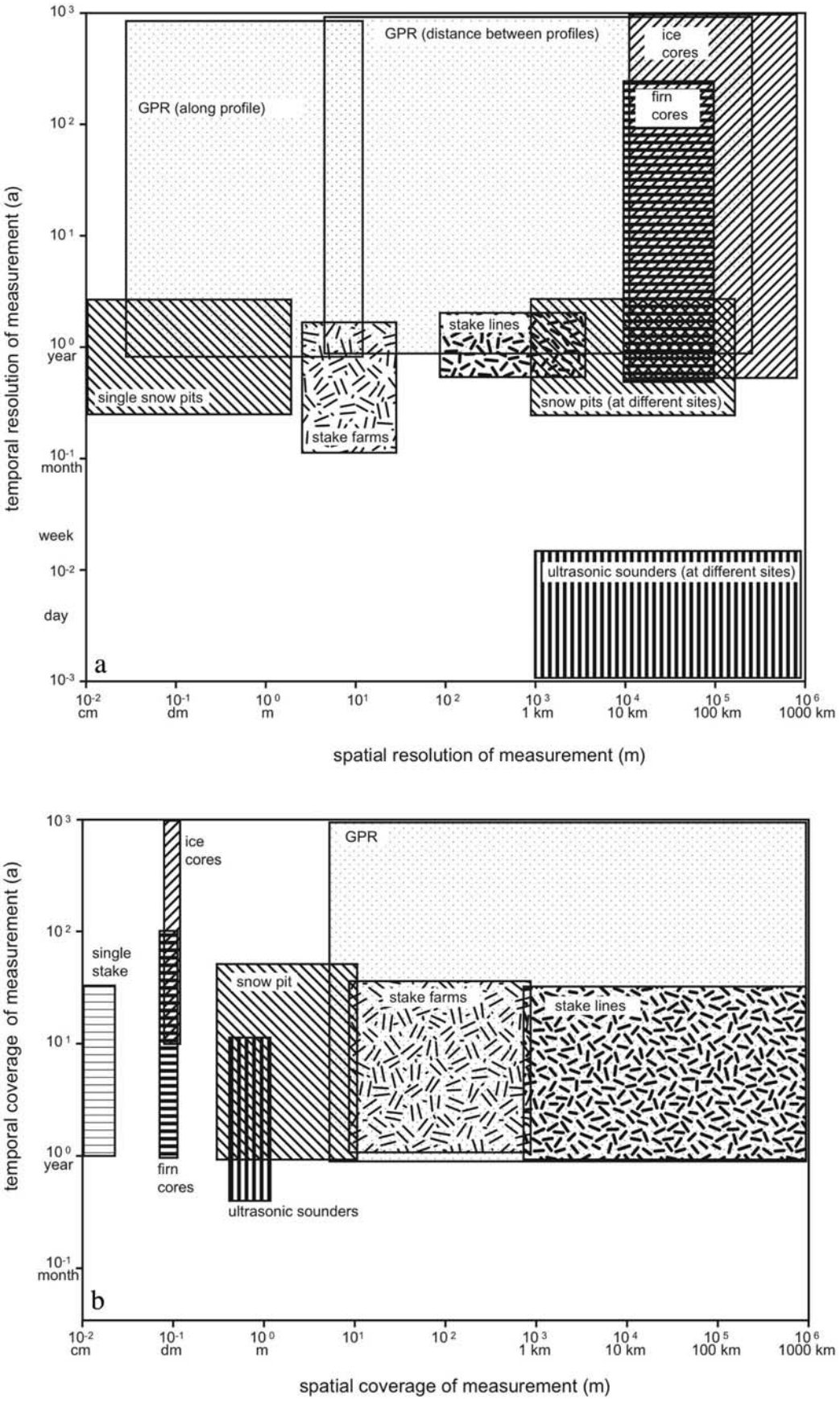
temporal resolution of measurement (a)
GPR (distance between profiles)
GPR (along profile)
ice cores
firn cores
stake lines
single snow pits
stake farms
snow pits (at different sites)
ultrasonic sounders (at different sites)
year
month
week
day
a
spatial resolution of measurement (m)
temporal coverage of measurement (a)
single stake
ice cores
GPR
snow pit
stake farms
stake lines
firn cores
ultrasonic sounders
b
spatial coverage of measurement (m)

Figure 3

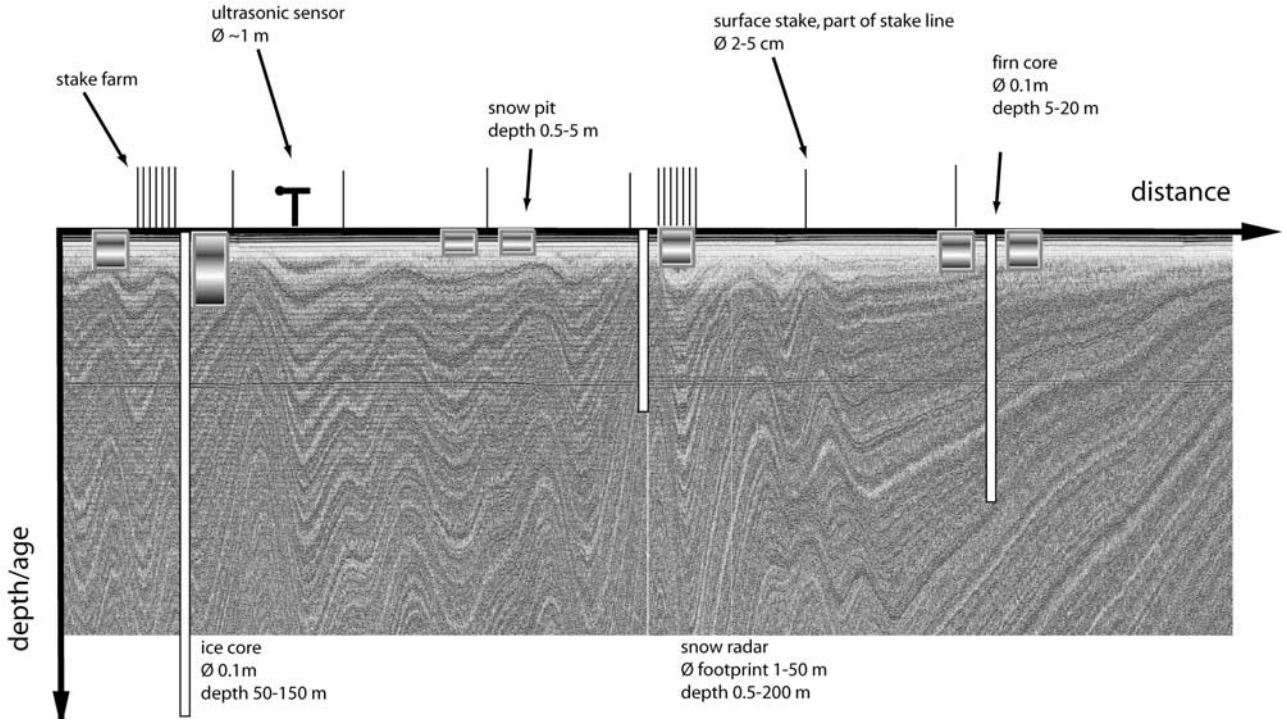

Figure 4. Scheme to illustrate spatial sampling interval and sample depths of different methods: stakes and ultrasonic sounders, at surface; snow pits, up to a few meters depth; firn cores, few tens of meters; ice cores, up to several tens to hundreds of meters, reaching below the firn-ice transition; GPR, tens to hundreds of meters. GPR data acquired along a 50-km profile [*Anschütz et al.*, 2007] are shown as background to illustrate the lateral variation. Continuous reflections present layers of equal age (isochrones). The canceled circle indicates the horizontal distance over which SMB is determined. (Note that ice core deep drilling is possible to some kilometers depths, but we are not concerned with that technique here.)

change, layer thickness, etc.) over certain time periods. To convert this length measurement to a SMB value, knowledge of the density distribution of the observed sample is fundamental. Determination of the snow density is usually more difficult and less accurate compared to the length measurements for a number of reasons. One of few exceptions for direct snow density measurements is the only recent adaptation of a neutron-scattering probe [*Morris and Cooper*, 2003; *Hawley et al.*, 2006].

[18] The classic method calculates density from snow sample volume and mass; however, accurately determining snow sample volume is a hard task under field conditions. The easiest method is to use a sampling probe with known volume. It is possible that each national Antarctic expedition uses different types of snow-sampling devices, which introduces additional uncertainties in the final values. A suitable field method for density measurements in snow pits is proposed in the ITASE guidelines by *Mayewski and Goodwin* [1997]. Because of the strong densification within the uppermost layers, density should be sampled at high vertical resolution. To avoid the risk of disturbing the underlying snow during sampling, the snow can be collected in a crossover pattern (see Figure 9c in section 2.4). Moreover, sampling snow pits from the bottom upward to the surface avoids the risk of contaminating the lower levels by snow falling down from previous sampling above. Depth control and minimizing depth error is most easily obtained by constantly leveling the sample depth with two adjacent rulers. Depending on the equipment used, the sample volume error is around several percent, and the error in the mass determination depends on the balance used. An optimistic volume error of ~1% and an accuracy of the balance of ±1 g would yield an uncertainty of about 1.4% for the density sampled in a snow pit [*Karlöf et al.*, 2005b]. The balance error increases to about ±5 g if spring scales are used.

[19] Density measurements are mainly made during the austral summer season (December or January), which may introduce additional errors because of seasonal changes in snow density that can result from numerous processes. For instance, surface density differs between snowfall events and precipitation-free periods, as wind can cause erosion, hardening, and redistribution of the snow. General factors causing seasonal density variations are changing wind speed and temperature, larger or smaller portions of low-density fresh snow, and vapor transfer between the surface, atmosphere, and deeper snow layers. It is not obvious which seasonal (or annual) density value best characterizes the ''effective'' annual density. These effects are different for snow density in the first meter in high-accumulation coastal areas (density on the order of 400 kg m^{-3}) compared to low-accumulation inland areas (around 300 kg m^{-3}). Sea-

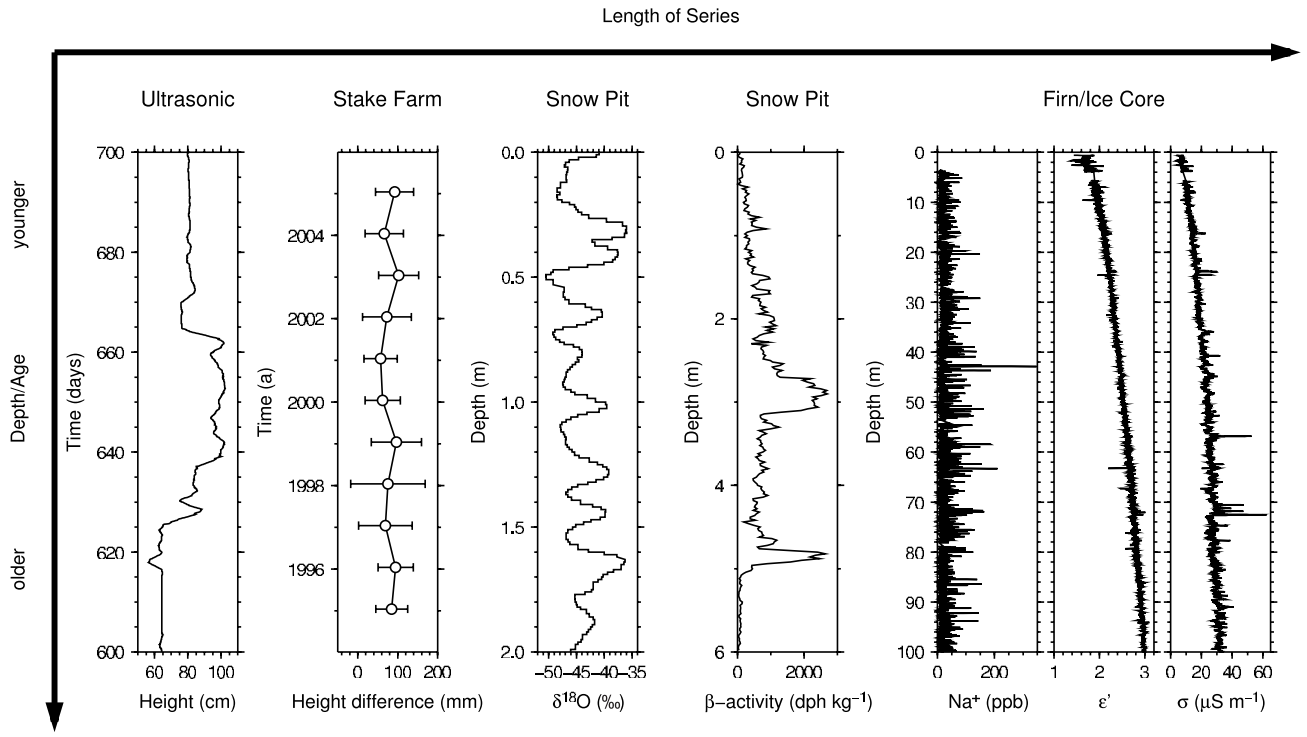

Figure 5. Data series obtained from various measurement techniques for single locations. The vertical axis indicates depth (for measurements made at depth) and time (for measurements made at the surface: ultrasonic sounders and stakes), respectively, increasing downward. The covered time/depth span differs between graphs. The temporal scale of the time/depth series lengths tentatively increases to the right. From left to right, 100 days of an ultrasonic sounder time series from the automatic weather station AWS9 (height above surface) [*van den Broeke et al.*, 2004b] at site DML05, near the EPICA deep drilling at Kohnen station in Dronning Maud Land (DML), illustrating the accumulation of snow and subsequent partly erosion; 11-year time series of measured height differences to previous year from a stake farm at Dome Fuji [*Kameda et al.*, 2008]. The circle indicates the average of 36 stakes, and the bar indicates the spatial standard deviation of the measurements; the oxygen stable isotope record is from a 2-m-deep snow pit (DML25 [*Oerter*, 2005, available at http://doi.pangaea.de/10.1594/PANGAEA.264585; *Oerter et al.*, 2004]), spanning roughly 10 years. Annual cycles are clearly visible; β activity record is from a 6-m-deep snow pit at the South Pole from 1978 [*Pourchet et al.*, 1983] spanning several decades; example of chemistry measurements (Na^+ content) [*Sommer et al.*, 2000b] and dielectric profiling record (relative permittivity ε' and conductivity σ) is from core B32 at site DML05 [*Wilhelms*, 2000] near the EPICA deep drilling in DML. The shown depth section corresponds to an 1100-year period from A.D. 883 to 1997.

sonally varying density is especially a problem for SMB measurements performed at the surface (introduced in sections 2.2 (stakes) and 2.3 (ultrasonic sounders)), in which case, density variations should be tracked in the snow layer accumulated during the given period of time (month or year). Unfortunately, almost no data are available that describe the seasonal change of the near-surface snow density and thus the actual density for the measured height difference, e.g., in the case of ultrasonic sounders. Although density values can be taken from adjacent snow pit studies, the question then arises as to which depth of the surface snow best approximates the average density. For instance, Vostok mean annual snow accumulation is only 7 cm on average (varying from negative values to more than 20 cm on individual stakes). A study of density in 17 snow pits showed that snow density does not change much with depth in the uppermost 20 cm of the snow. Consequently, the mean density from this layer is used for converting snow accumulation to SMB at Vostok. Nevertheless, at Vostok the mean density of the uppermost 20 cm changes between 310 kg m^{-3} in winter and 330 kg m^{-3} in summer, which means that the uncertainty related to this source of errors may be as much as 6%.

2.2. Point Measurements at the Surface: Stakes

[20] The easiest way to measure SMB is based on stakes planted in the snow by simply measuring the amount of accumulation over a certain time period. Despite its simplicity, this method is valuable as it allows a rough estimate of the local or regional distribution of SMB. Sources of error include the conversion of the accumulated snow to SMB, density measurements (see section 1.1), and the subsidence of the stake bottom. This simple technique is

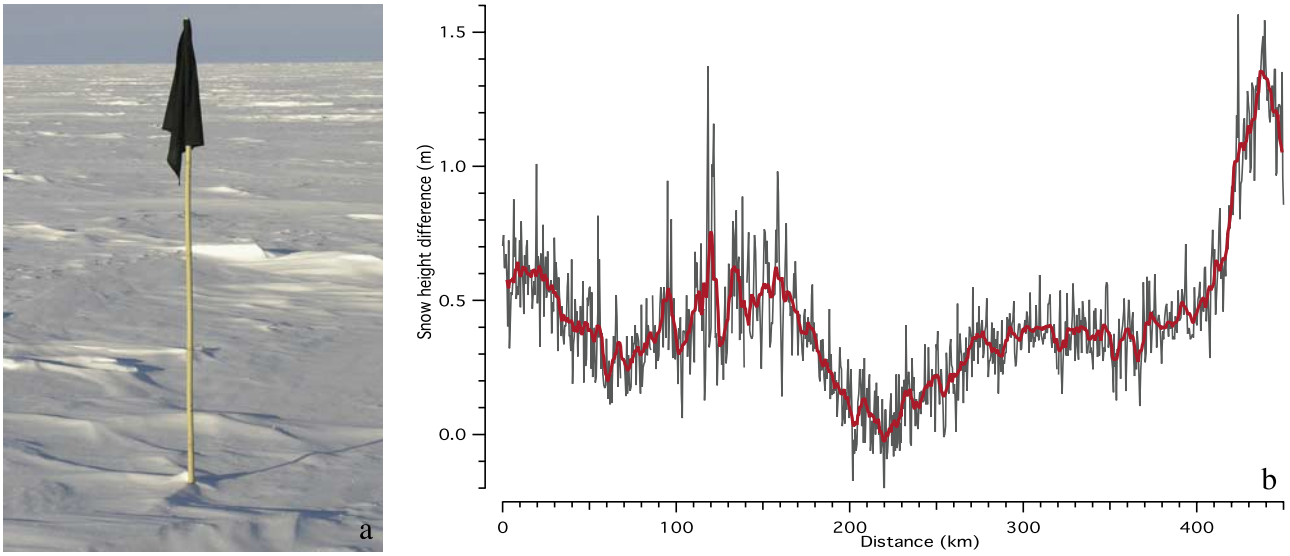

Figure 6. (a) Typical bamboo stake with a fabric flag at the top. Note the microrelief surrounding the stake base, which complicates height readings. (b) One year (2003) of sample data from the 450-km stake line from Neumayer station to Kottasberge, Heimefrontfjella, in DML; grey, single measurements every 500 m; bold, moving average over 5 km.

used by almost every nation in Antarctica. Examples are given in section 2.2.4.

[21] In addition to single stakes, *stake lines* and *stake farms* have also been used. Stake farms are more common at year-round stations, whereas stake lines may be established along traverse routes which are visited in more than one season. A stake farm gives single measurements for a well-defined small area, e.g., on the order of 10^4–10^6 m^2 (tens of meters to kilometer side length) which are averaged to produce a single accumulation value. By using several stakes the small-scale depositional noise can be reduced. Additionally, continuous monitoring of stake farms provides a record of the buildup of the snow cover during the year and information on seasonal variations [see, e.g., *Fujii*, 1981; *Mosley-Thompson et al.*, 1999; *Schlosser et al.*, 2002], an important fact further explained in section 2.2.4. Measurements in stake farms are influenced by a slight disturbance of the natural snow deposition through the stakes themselves, the disturbance of the snow surface when people have to pass through the stake farm for measuring the stakes, and the accuracy of the height measurements itself. Stake readings are usually done on the leeward side of the prevailing wind direction to minimize the effect of footprints on the snow surface.

[22] Single stakes of a stake line are usually used primarily as markers for way points. They provide one value for each stake but over a larger distance (Figure 6). These measurements are helpful in measuring the spatial distribution of accumulation with a spacing on the order of kilometers. Single measurements are still affected by small-scale depositional noise, but because the time span for reading these lines is normally 1 year or more, the noise is a small source of error compared to the measured accumulation. The use of Global Positioning System (GPS) receivers for positioning the stakes is an important tool to relocate the stakes. Stake locations can also be used to calculate surface velocities. In the case of traverse routes, the stakes are regularly replaced over the years and placed back in the original position. Determination of the accumulation rate from the stake observations consists of two types of observations: stake height measurements (allowing to determine the accumulation over a given time period) and density measurements.

2.2.1. Stake Height and Correction for Densification

[23] Stake height measurements are only possible if the stake bottom is immobile relative to the surrounding snow layer. This can be achieved by fixing the stake bottom on a horizontal slab, or by fixing it on a natural hard layer (wind slab). Usually, it is assumed that the stake bottom is firmly anchored in the snow and the stakes move down with the snow layer on which the stake bottom is fixed. Using a light weight stake, of which the bulk density is close to that of near-surface snow (e.g., commonly used bamboo stakes, 250–350 kg m^{-3}, 2–3 cm in diameter and 2.5 m in length), this condition is fulfilled in a first approximation. In the past, aluminum and bamboo stakes have been used, but they frequently have failed because of blizzard winds or melting due to solar radiation in coastal areas. Polycarbonate snow poles (50 mm diameter, 6 mm wall diameter), which have recently been used, are less fragile than bamboo and aluminum poles but are more expensive. However, the logistical costs of deployment and resurvey of stakes are much higher, and stake loss due to extreme environmental conditions is a critical issue. The maximum stake height for strong wind is around 4 m, being initially buried about 1.5 m in the snow (a ratio of about 35%). Additional factors that can cause uncertainty in reading the height appear if wind scouring or sastrugis with strong microrelief occur

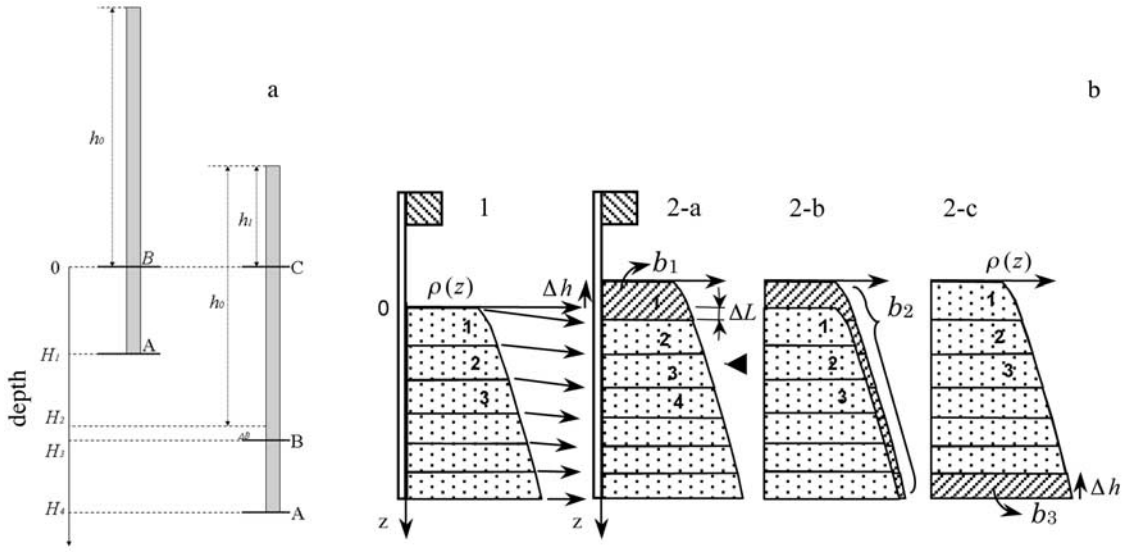

Figure 7. (a) Position of a stake in two moments in time. (b) Schematic diagram of the density-depth profile at Dome Fuji with flag stake for first (1, dotted area) and second year (2-a, 2-b, 2-c) to illustrate the effect of compaction and accumulation for determination of SMB from changes in stake height (redrawn from *Takahashi and Kameda* [2007] with permission of the International Glaciology Society). The mass accumulated in the second year is shown as the hatched areas b_1, b_2, and b_3 (with $b_1 = b_2 = b_3$) in the second year's panels; previous layers are labeled 1–3 from the surface downward. In diagram 2-a, the first year's surface is lowered by ΔL due to compaction. Δh is the change in stake height from first to second year. New snow layer is labeled 1, while the first year's layer 1 becomes layer 2, likewise for layers 2 and 3. Accumulation is thus the layer b_1 of thickness $\Delta h + \Delta L$. In diagram 2-b, density-depth profiles for first year (dotted) in respect to first year's surface and first year's layer numbering, overlaid on profile from second year in respect to second year's surface. Assuming Sorge's law and a firmly anchored stake bottom, the density-depth profiles in both years have the same shape. Accumulation is then the (hatched) area b_2 between both density profiles. 2-c: Shifting the first year's density profile upward by Δh to overlap with the second year's profile to the same surface level, the accumulation appears to be the hatched area at the stake base of thickness Δh.

around the stake (Figure 6a), and if a flexible stake is used, it can become bent.

[24] Accumulation values obtained as a difference of stake height at two moments in time must then be corrected for snow settling (densification), illustrated in Figure 7. In Figure 7 the same stake is shown at two moments in time. In the beginning, the stake bottom is fixed in the snow layer A at the depth H_1, while snow layer B is located at the surface. The stake height above the surface is h_0. Some time later, the stake has apparently sunk into the snow due to accumulation, and the new stake height is h_1. However, the actual accumulation is higher than the difference $h_0 - h_1$ due to the snow densification (note the thinning of the AB layer). The correction ΔB is the difference between the thickness of the AB layer in the beginning and in the end ($H_3 - H_2$ in Figure 7a). In order to calculate the corrected snow accumulation, we have to define the snow mass in the BC layer (i.e., layer accumulated during the given period of time), which is equal to the difference of the mass in AC layer and AB layer. The latter masses can be easily determined as soon as we know the snow density profile to the depth of H_4. This approach is only valid when two conditions are met: (1) the density profile is stable in time (known as Sorge's law) and (2) the snow mass between two fixed snow layers is constant (i.e., vapor mass transport is negligible).

[25] One can derive the equation for the correction of annual snow accumulation (the length measurement):

$$\Delta(\Delta h) = \dot{b}\left(\frac{1}{\rho_0} - \frac{1}{\rho_b}\right), \tag{1}$$

where $\dot{b}$ is the mean annual SMB, ρ_b is the snow density at the depth of stake bottom, and ρ_0 is the density of surface snow. From equation (1) it is seen that the correction value is positively related to the vertical gradient of snow density (Figure 7).

[26] Similar studies have been made by *Takahashi and Kameda* [2007]. They showed that the snow density at the stake bottom should be used for SMB calculations as

$$\dot{b} = \bar{\rho}_b \Delta h, \tag{2}$$

where Δh is the difference in stake height between two measurements, which is the same as the change of stake bottom depth; $\bar{\rho}_b$ is the average snow density between the two depths of the stake bottom, assuming a stable density profile. This correction is 1 – 27% of the annual snow accumulation at inland sites like Vostok and Dome

TABLE 2. Some Error Sources of SMB Estimates for Different Methods[a]

Source	Type of Error	Affects
Stakes		
Length measurement	height	mass
Anchoring/submergence	height	mass
Surface roughness	height	mass
Density	mass	mass
Ultrasonic Sounders		
Air temperature and profile	sound velocity	mass
Sound velocity	height	mass
Density	mass	mass
Fallen rime	height	mass
Anchoring/submergence	height	mass
Surface roughness	height	mass
Drifting snow	height	mass
Cores		
Annual cyclicity	ambiguities in age	time
Hiatus (erosion)	ambiguities in age	time
Time markers	time of deposition	time
Density from weighing	mass, core volume	mass
Density from profiling	mass, core volume	mass
Dynamic layer thinning	layer thickness	mass
GPR		
IRH resolution and tracking	traveltime	time, mass
Wave speed profile	depth	time, mass
Age-depth profile	age	time
Transfer of age to IRH	age	time
Density measurements	mass, wave speed	time, mass
Extrapolating wave speed	depth error	time, mass
Interpolating/extrapolating density	mass	mass
Dynamic layer thinning	layer thickness	mass

[a]The source is the determined property or the assumption being made. The type of error indicates which error is physically being made. Finally, the affects indicate which of the three properties of SMB (mass per area and time) are affected by the error. For stakes and ultrasonic sounders, the date of measuring is known best, so time is not affected. For cores, the annual cyclicity is variation in signals used for counting years. For GPR, tracking is the uncertainty when following a reflection horizon along the profile, and extrapolation is estimation of density and wave speed profile between different core locations.

Fuji and cannot be neglected. Information on density is not always available (particularly for older records); thus conversion of changed snow height to mass may not be possible or will have a large uncertainty.

2.2.2. Accumulation Uncertainties From Stakes

[27] The uncertainty of the stake-based accumulation determination consists of two main sources: (1) measurement errors, briefly described in section 2.2.1 for accumulation and density measurements and (2) natural noise predominantly caused by the small-scale relief-related spatial variability of snow accumulation and density (Table 2). Apparent accumulation uncertainties for field data are based on all possible sources of error; however, natural noise is the largest source of error, with all other sources at least 1 order of magnitude less. It is worth noting that the uncertainty is inversely related to the number of stakes and the period of observation. As an example, the standard deviation of accumulation, as measured at an individual stake in terms Δh, is $\sigma(\Delta h) = 5.3$ cm, i.e., nearly equal to the mean annual accumulation at Vostok. The corresponding standard deviation for the surface (at 20 cm depth) snow density is $\sigma(\rho) = 33$ kg m^{-3}, i.e., about 10% of the mean. This means that the density is a comparatively less noisy parameter than the height measurement. The standard error in accumulation (calculated from the equation $\sigma(\dot{b})/\dot{b} = \sigma(\Delta h)/h + \sigma(\rho)/\rho$) from a single stake is thus 18 kg m^{-2} a^{-1}, or about 85% of the mean annual accumulation at Vostok. This means that a single-stake observation in low-precipitation areas of central Antarctica provides practically no information about the mean accumulation rate. The standard error of annual accumulation decreases as the period of observations increases. One could expect that the error would follow the known equation $\sigma(\dot{b}) = \sigma(\dot{b}_i)/\sqrt{n}$, where $\sigma(\dot{b}_i)$ is the standard error of accumulation for a 1-year period and n is the number of 1-year observation periods. Thus, after 30 years of observations the error must be about 3 kg m^{-2} a^{-1}. Instead, previous research (not published) showed that the standard accumulation rate error for a single stake in a stake farm at Vostok after a 30-year period of observations is as low as 1.7 kg m^{-2} a^{-1}. This is related to the fact that as the observation period becomes longer, the given stake becomes representative for a wider area and thus the accumulation at the adjacent stakes becomes correlated. In this case, the uncertainty versus time function shown above becomes closer to linear: $\sigma(\dot{b}) = \sigma(\dot{b}_i)/n$. The uncertainty in the 1-year accumulation value from the whole stake farm is inversely proportional to the number of stakes k: $\sigma_k(\dot{b}) = \sigma(\dot{b})/\sqrt{k}$. For the Vostok Station stake network ($k = 79$) we can expect that the error for accumulation is 0.6 cm. In fact, this value may be slightly higher because, as we showed before, the accumulation at the adjacent stakes is not completely independent. Corresponding errors for density and accumulation values are 3 kg m^{-3} and 2.0 kg m^{-2} a^{-1}. The error of the mean annual accumulation value from the Vostok Station stake network is difficult to evaluate properly, but on the basis of the data discussed here we estimate it as $1.7/\sqrt{79} = 0.2$ kg m^{-2} a^{-1}. This value is less than the 0.8 kg m^{-2} a^{-1} determined from the time series of annual accumulation values over the last 30 years, but the latter value also includes the natural temporal variability of accumulation. In general, only long-term observations will result in reliable accumulation values. Spectral analyses of accumulation measurements from single stakes with respect to annual average accumulation of a stake farm in the Dome C drainage area show that single stakes or cores are not representative on an annual scale. Even for a site with high accumulation (250 kg m^{-2} a^{-1}), sastrugi with a height of about 20 cm cause significant noise in the individual measurements [*Frezzotti et al.*, 2007].

2.2.3. Optimal Parameters for Stake Farms and Lines

[28] When planning to set up a stake network in Antarctica, the first question to be addressed after defining the accumulation scale aimed at, is "What are the optimal parameters of the network (in terms of data quality, effort needed to make the measurements) for this particular area?" Large networks containing more stakes will produce more accurate results, but more time and effort are required to make the measurements. The network size and stake number also depend on the temporal and spatial scales of

accumulation one is interested in. A trade-off has to be made between the error of the estimated accumulation mean (decreasing with the number of stakes) and the size of the area for which the estimate is representative. The distance between stakes is determined by the size of the stake farm or line and is often restricted by logistic constraints. Unfortunately, the best sampling strategy for a specific area is often made clear only after measurements of the stake farm have already been made.

[29] As an example, optimal parameters (see Appendix A) have been determined for the Vostok area from a stake farm [*Barkov and Lipenkov*, 1978]. For comparatively small (within first hundred meters) stake farms the accuracy of the obtained accumulation values is much more dependent on the size of the farm than on the number of stakes, which is due to the influence of microrelief of the snow surface. Keeping the same amount of stakes but increasing the size of the stake network rapidly decreases the standard error of the accumulation value. At the size of 500–1000 m a saturation value is achieved. This value depends on the dominant larger-scale glacier relief forms. For example, in the megadune areas the saturation value must be of the order of the megadune length, i.e., less than 5 km. Further increasing the stake network dimensions does not significantly change the accuracy, although it does increase the represented area.

2.2.4. Examples for Long-Term Measurements and Current Approaches

[30] In Wilkes Land, the Indian-Pacific sector of Antarctica, stake measurements have been performed for half a century. An early overview of measurements and results is presented by *Young et al.* [1982]. Stake measurements of Antarctic SMB by the Russian (Soviet at that time) Antarctic Expedition (RAE) began with the opening of the first Russian base, Mirny (in 1956). Subsequently, stake networks were established at all permanent Russian stations (Vostok, Novolazarevskaya, Molodezhnaya, Bellingshausen, Leningradskaya; for a list of Antarctic stations see the Scientific Committee on Antarctic Research (SCAR) Web site http://www.scar.org), with varying network shapes, size, and number of stakes to obtain optimal setups. The most extensive data were obtained at Molodezhnaya (~11 stake networks and profiles operating from 1966 to 1981) and Novolazarevskaya. Stake lines were established along the RAE routes (Pionerskaya–Dome C, Komsomolskaya–Dome B, Mirny–Vostok). The best results were achieved from the permanent 1410-km-long Mirny–Vostok traverse, where about 800 stakes were set up in intervals of 0.5–3 km, as summarized by *Lipenkov et al.* [1998]. In addition, seven stake farms (1×1 km^2, 20–40 stakes each) were organized along the traverse in the 1970s and annually visited until the 1980s. The stake network at Vostok was set up in 1970 and is still in operation. Monthly observations allow for a robust characterization of SMB in this region and provide a prototype for the extremely low accumulation areas of central Antarctica. Results were obtained on the interannual and seasonal variability of SMB and responsible mechanisms [*Barkov and Lipenkov*, 1996; *Ekaykin*, 2003]. Among these results are the exclusion of temporal trends of mean accumulation rate (22 kg m^{-2} a^{-1}) over the observation period and the identification of different relief forms of intermediate scale, between microrelief and megadunes, called mesodunes [*Ekaykin*, 2003]. Migration of these mesodunes causes a relief-related (nonclimatic) temporal variability of SMB at a single point with periods of up to 20–30 years [*Ekaykin et al.*, 2002]. In eastern Wilkes Land, seasonal surface observations of stakes and relief forms were carried out by Australian expeditions [*Goodwin*, 1991].

[31] Since the International Geophysical Year (1957–1958), a variety of stake networks have been established at South Pole Station. These include a 42-stake pentagon and an 11-km cross consisting of six arms with a stake interval of 300 m. Details are summarized by *Mosley-Thompson et al.* [1995]. Remeasurements were carried out at irregular intervals. In November 1992, Ohio State University (OSU) set up a network of 236 stakes radiating outward from South Pole Station as six 20-km-long arms, at an interval of ~500 m. Remeasurements are performed annually in November. Results from the first 5 years of measurements indicate that earlier estimates, that one in 10 years has negative SMB [*Gow*, 1965; *Mosley-Thompson and Thompson*, 1982], are probably too high. At least in recent times at the South Pole [*Mosley-Thompson et al.*, 1999], less than 1% of all observations revealed zero or negative SMB. Moreover, the same study by *Mosley-Thompson et al.* [1999] reveals that the net accumulation of about 85 kg m^{-2} a^{-1} during the period 1965–1994 is the highest 30-year average of the last 1000 years at the South Pole.

[32] *Pettré et al.* [1986] report SMB data along a transect from the coast near Dumont d'Urville to Dome C. Most of the data are from stakes, with the stakes from the coast to 32 km inland being surveyed over as long as 21 years (1971–1983). During the old Dome C deep ice core drilling, a stake farm was measured during 1978–1980 to study spatiotemporal variability of a single core [*Palais et al.*, 1982; *Petit et al.*, 1982]. Between 1998 and 2001, at Talos Dome and along the traverse in the Dome C drainage area [*Magand et al.*, 2004; *Frezzotti et al.*, 2005, 2007], 17 stake farms were set up by the Italian Antarctic Programme, each including from 30 to 60 stakes at 100-m intervals in the shape of a cross within an area of 4 km^2, each centered on a core site. Measurements were carried out annually at four sites where automatic weather stations (AWS) have been installed. Other stake farms have been remeasured only 2–4 times. Stake farm readings show that accumulation hiatuses (no accumulation or even ablation) can occur at sites with average accumulation rates below 120 kg m^{-2} a^{-1}.

[33] In the Lambert Glacier Basin (LGB) area, stake measurements were performed by the Australian and Chinese National Antarctic Research Expeditions (ANARE, CHINARE). Results of early stake lines (1960s and 1970s) along the ANARE LGB traverse routes are summarized by *Morgan and Jacka* [1981] and *Budd and Smith* [1982]. Later measurements included stake networks (1983–1993) and multiannual combinations of networks and stakes (2 km interval) (about 1989–1994), comple-

mented by cores [*Goodwin et al.*, 1994; *Ren et al.*, 1999, 2002; *Goodwin et al.*, 2003; *Xiao et al.*, 2005]. Extension of earlier routes with 2-km stake intervals provides a continuous line over 1100 km from Zhongshan station to Dome A (1996–1999 [*Qin et al.*, 2000]).

[34] Farther to the west a number of stake lines and farms have been and are still being operated along the Dronning Maud Land coast. In eastern Dronning Maud Land, the Japanese Antarctic Research Expeditions (JAREs) deployed stakes since 1968 [*Takahashi and Watanabe*, 1997]. Stakes spaced at 2-km intervals were set from the coastal area to inland sites at Dome Fuji over a distance of more than 1000 km. Eleven stake farms were set en route from Dome Fuji to the plateau (e.g., 6 × 6 at 20 m intervals, 50 rows of stakes over 100 m; see *Kameda et al.* [2007] for details). Six stake farms from the coast to Mizuho were established in 1971. Most of these stakes and stake farms have been surveyed at least once per year. Results are given by *Takahashi and Watanabe* [1997], *Takahashi et al.* [1994], *Fujiwara and Endoh* [1971], *Endo and Fujiwara* [1973], and *Kameda et al.* [1997, 2008].

[35] At the former Georg Forster station (GDR), three stake lines, each 85–115 km in length with stake spacings of 1–5 km, were operated from 1988 to 1993 in an area of strongly differing accumulation regimes containing blue ice areas [*Korth and Dietrich*, 1996]. Other examples are the stake farm operated near the German Georg-von-Neumayer station 1981–1993 and near Neumayer station since 1992 [*Schlosser et al.*, 2002]. Measurements were extended by a 450-km stake line (500-m interval) between Neumayer station at the coast and the Heimefrontfjella (Figure 6) [see *Rotschky et al.*, 2006] (half of the traverse route to the EPICA deep drilling at Kohnen station), which has been revisited annually since 1996. A stake line between the Swedish stations Svea and Wasa was established in January 1988 [*Stroeven and Pohjola*, 1991] and partly surveyed until 1998 [*Isaksson and Karlén*, 1994]. A new 300-km profile was established in 2002/2003 for a long-term SMB monitoring [*Swedish Antarctic Research Programme*, 2003]. Shorter lines, also partly in conjunction with GPR, were investigated near the Finnish Aboa station [*Isaksson and Karlén*, 1994; *Sinisalo et al.*, 2005] and on Lydden ice rise (Brunt ice shelf) [*Vaughan et al.*, 2004]. In blue ice areas occurring in mountain regions of East Antarctica, stake networks were surveyed to gain information on *ablation* rates and to study meteorite traps [*Bintanja*, 1999; *Folco et al.*, 2002]. The data suggest that ablation rates decrease with increasing distance from the ice sheet edge, with values from 350 to 30 kg m^{-2} a^{-1}.

[36] An example of a contemporary integrated SMB approach is the Les Glaciers, un Observatoire du Climat (GLACIOCLIM) Surface Mass Balance of Antarctica (SAMBA, see http://www-lgge.obs.ujf-grenoble.fr/~christo/glacioclim/samba) observation system, a French-Italian cooperation. The French GLACIOCLIM glacier observation system consists of a ~1-km^2 stakes network (50-m interval) located on the coast of Adélie Land, with year-round surveys performed monthly. Additionally, various meteorological instruments in the area are used to study the warm/ablating region to develop an understanding of SMB genesis and to verify local modeling capabilities in such a region. An ~100-km stake line (interval 0.5–2.5 km with annual observations), recently extended to 150 km from the coast toward Dome C, is used for sampling the coast to plateau transition and sampling spatial scales consistent with climate models and with satellite data. Along the stake lines, two AWS are deployed, one of which is accompanied by a 1-km^2 stake network (250-m interval). Aiming at the sampling of both small and large scales of accumulation (model, satellite), three 1-km^2 stake networks (40-m interval) were set up in the Dome C area in 2005/2006, with the stake farms located 25 km apart. This network is surveyed at least once a year and may be surveyed more frequently now that the Concordia station is permanently inhabited. Meteorological data are available from the station. The focus of future projects is the short-term variability at various sites by measuring precipitation with spectronivometers and accumulation with ultrasonic sounders. The observation system and monitoring are expected to last at least 10 years. Examination of the data should allow us to address the climate–accumulation interaction as well as climate–model validation on subannual to multiannual scales, which will also enable analysis of interannual variations and processes.

2.3. Point Measurements at the Surface: Ultrasonic Sensors

[37] A relatively recent (~10–15 years) technique for monitoring SMB in East Antarctica is tracking surface height changes by way of ultrasonic height rangers. These sensors determine the vertical distance to the snow surface by measuring the elapsed time between emission and return of an ultrasonic pulse. An air temperature measurement is required to correct for variations of the speed of sound in air.

[38] Until quite recently, ultrasonic height rangers were mainly used to study the growth and decay of the seasonal snowpack in the Northern Hemisphere. As the design evolved (for instance, by including a multiple echo processing algorithm that stores several reflected signals to improve operational efficiency and to decrease the problem of obstacles), ultrasonic height rangers also found their way into mass balance research of high-altitude/high-latitude ice masses, such as Alpine and Arctic valley glaciers [*Oerlemans*, 2003; *Klok et al.*, 2005] and the Greenland ice sheet [*Steffen and Box*, 2001; *Van de Wal et al.*, 2005; *Smeets and van den Broeke*, 2008]. With rugged housing and improved low-temperature specification (nowadays typically down to −45°C), application of ultrasonic height rangers in Antarctic mass balance studies has become widespread. They are deployed in a wide range of climate settings, such as the McMurdo Dry Valleys [*Doran et al.*, 2002], the high accumulation coastal zone of East Antarctica [*McMorrow et al.*, 2001] and West Antarctica [*van Lipzig et al.*, 2004b], and the dry East Antarctic interior [*Reijmer and Broeke*, 2003; *van den Broeke et al.*, 2004b] as well as in the intermediate

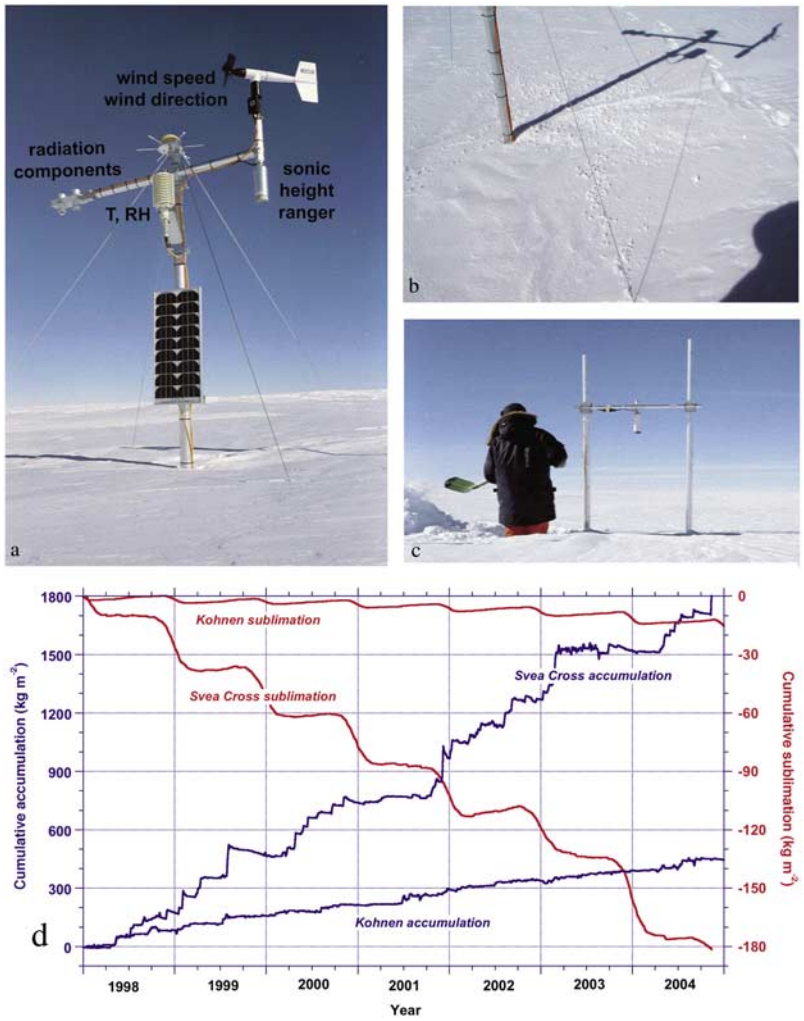

Figure 8. (a) Picture of AWS9 (near EPICA deep drilling in DML at Kohnen station), taken 4 years after installation, i.e., after about 1 m of snow has accumulated. The data logger and pressure sensor are buried in the snow. (b) Rime from the mast fallen on the ground might cause artificial accumulation. (c) Picture of stand-alone ultrasonic height meter, near AWS9. The data logger and pressure sensor are buried in the snow [*van den Broeke et al.*, 2004b]. (d) Sample data from ultrasonic sounders: scale on left side is cumulative accumulation at AWS6 (Svea Cross) and AWS9 (Kohnen station) for the period 1998–2004; scale on right side is cumulative sublimation as calculated from AWS data. Note different *y* axis scales.

katabatic wind zone [*Helsen et al.*, 2005] and on the ice shelves [*Braaten*, 1994].

[39] In East Antarctica and elsewhere, it is advantageous to mount the ultrasonic height ranger on or next to an automatic weather station (AWS, Figure 8). The AWS usually observes a range of atmospheric variables such as air pressure, air and snow temperature, air relative humidity, air velocity, and occasionally also radiation components [*van den Broeke et al.*, 2004a]. This means that surface height changes can be interpreted in a mass balance framework, including sublimation from the surface and from drifting snow particles [*Fujii and Kusunoki*, 1982; *Kaser*, 1982; *Clow et al.*, 1988; *Stearns and Weidner*, 1993; *King et al.*, 1996, 2001; *Bintanja*, 2003]. Moreover, ultrasonic height data can be accepted/rejected on the basis of prevailing meteorological conditions (see section 2.3.4). Finally, the ultrasonic height ranger can be coupled to the AWS's power and data logging system. If more information is required on the spatial variability of accumulation, several ultrasonic height rangers can be deployed in stand-alone mode, using a dedicated energy/data logger system (Figure 8c).

2.3.1. Typical Sensor Specifications

[40] As a typical example, here we list the specifications of a widely used ultrasonic height ranger, the SR50 produced by Campbell in Canada. Its limited dimensions (length 31 cm, diameter 7.5 cm, and weight 1.3 kg) make it convenient for use in AWS. With an operating temperature range down to −45°C and proven working capacity down to −70°C [*van den Broeke et al.*, 2004b] it is suitable for operation in most parts of East Antarctica. The power requirement is 9–16 Vdc (volts direct current), so that it can be powered by the data logger's 12-Vdc power supply that is standard equipment on most AWS. The low power consumption (250 mA during measurement peaks) is favorable for operation on unmanned remote platforms. The measurement range (0.5–10 m) is suitable for operation in

accumulation as well as in ablation areas. The beam acceptance (maximum deviation from the vertical) of $\sim 22^\circ$ poses no problem, as ablation-induced tilt of the mast normally does not occur in East Antarctica. The measurement accuracy is ±1 cm or 0.4% of the distance to the surface, whichever is greatest, and data can be stored at a maximum resolution of 0.1 mm. To account for the temperature-dependent speed of sound, a correction for the deviation of the mean layer air temperature from a fixed calibration temperature (273 K) must be applied.

2.3.2. Advantages of Ultrasonic Height Rangers for Mass Balance Studies

[41] The obvious advantage of ultrasonic height rangers in comparison to stakes, snow pits, and cores is that individual accumulation/ablation events are unambiguously dated. This means that the temporal variability (e.g., the seasonal cycle or the summer and winter balance) of accumulation/ablation can be quantified. This has important applications in ice core paleoclimatology: if, for instance, a significant seasonal cycle in accumulation is present that changes in time, this introduces a bias in the climate signal extracted from cores. Case studies of chemical and physical anomalies in the firn can be based on individual accumulation events identified in the ultrasonic time series. In combination with AWS data, the accumulation/ablation time series of ultrasonic height rangers can also be used to force snowpack models at their upper boundary or serve as a starting point for atmospheric trajectory calculations [*Noone et al.*, 1999; *Reijmer et al.*, 2002; *Helsen et al.*, 2004]. Moreover, the temporal distribution of accumulation/ablation events is essential for validation of meteorological and/or mass balance models [*Gallée et al.*, 2001; *van Lipzig et al.*, 2004a]. Finally, for accurate energy balance calculations from single or multilevel AWS data it is desirable to know the exact height of the wind speed, temperature, and humidity sensors above the surface, as well as the depth of snow temperature sensors [*van den Broeke et al.*, 2004b].

2.3.3. Technical Problems

[42] The ultrasonic height ranger needs to be mounted on a rack or mast so that its beam is perpendicular to the surface and is not obstructed. In accumulation areas, such as in East Antarctica, the sensor needs to be kept at least 0.5 m from the surface. This requires regular, expensive, servicing visits, the frequency of which depends on the rate of accumulation, the battery, and data storage capacity. In practice, the servicing interval will typically be once per year for coastal East Antarctica and once every 2–3 years for the interior plateau.

[43] Ultrasonic height rangers are susceptible to failure from ageing, corrosion, or freeze-thaw delaminating of the acoustic membrane. Membrane failure rate has been observed to increase with age. Therefore, regular replacement of the acoustic membrane as a preventive measure should be considered for each visit. The proximity of open sea and/or an effective transport of sea salt to the observation site significantly reduce the lifetime of the acoustic membrane. In East Antarctica, this is usually not a big problem, and lifetimes of the membranes are typically 5 years or more.

[44] A common problem that prevents correct operation of the ultrasonic height sensor is that the acoustic membrane becomes obstructed by snow/rime. Sometimes mounting a cone around the sensor can prevent this, but this carries with it the risk of spurious ice accretion on the cone and subsequent structural failure of the mast. Riming problems are considerably reduced on the ice sheet slopes, away from the flat domes in the interior and the flat ice shelves near the coast. The reason is that along these slopes, semipermanent katabatic winds heat and dry the lower atmosphere resulting in a continuous flow of subsaturated air past the sensor, keeping it free of rime.

2.3.4. Data Interpretation Problems and Uncertainties

[45] Measurements from an ultrasonic height ranger performed at a single site suffer from the same problems of poor spatial representativity as single core or stake measurements (see section 2.1). These problems can be partly solved by using the same solutions as for the other techniques, i.e., operating a farm of stakes (or drilling several shallow cores) in the surroundings of the ultrasonic height sensor or deploying several sensors.

[46] Naturally, the measuring site should be far enough upwind from obstacles to avoid spurious lee accumulation or snow erosion on a flat surface. In East Antarctica, it is usually easy to find an upwind measurement site with a large fetch because surface conditions are usually very homogeneous and (katabatic) wind direction is exceptionally constant [*van den Broeke and van Lipzig*, 2003]. Dominant sastrugi orientation from surface or aerial surveys or a modeled wind field [*van Lipzig et al.*, 2004a] can help in determining the prevailing wind direction if no local meteorological data are available.

[47] Once a suitable spot is found, raw distance data should be collected and the temperature-dependent speed of sound correction applied after data collection. In-sensor temperature measurements on older sensor types should preferably not be used because the sensor can overheat significantly under low wind speed/strong insolation conditions, fouling the surface height data. It is best to measure the air temperature independently with a ventilated dedicated sensor placed approximately halfway between the ultrasonic height ranger and the surface. A more elaborate alternative is to measure temperature at sensor height and at the surface (e.g., using a longwave radiation sensor), to calculate the temperature profile (using similarity theory and appropriate stability functions [e.g., *Andreas*, 2002; *Holtslag and Bruijn*, 1988]) and to take the mean temperature of the air layer. In East Antarctica, it is worthwhile to spend some effort to correctly perform the temperature correction because the radiation balance at the surface is often negative so that the temperature difference between the ultrasonic height ranger and the surface in the stably stratified surface layer can be considerable, up to 5–10 K in the first couple of meters during calm, clear conditions.

[48] At sites where riming occurs frequently, rime collected on the mast structure can fall off and collect at the surface, leading to artificially enhanced accumulation

(Figure 8b). This will only affect low-accumulation sites on the interior plateau.

[49] Once the wind speed exceeds a certain threshold, snowdrift occurs in the near surface air layer [*Li and Pomeroy*, 1997; *Mann et al.*, 2000]. This can lead to an erroneous height reading from a reflection from a dense drifting snow layer. Usually, AWS data can be used to detect snowdrift events so that these readings can be discarded.

[50] The technical and operational difficulties described in this section and section 2.3.3 (see also Table 2) reduce the 1-cm accuracy under laboratory conditions to an operational accuracy of typically 2–3 cm. This accuracy is sufficient for high-accumulation sites, but it is not good enough to detect the often much smaller precipitation events that are common on the interior plateau of East Antarctica. Here, small events (<1 kg m^{-2}) make up most of the total accumulation [*Reijmer et al.*, 2002].

[51] A large uncertainty is introduced when converting instantaneous height changes from the ultrasonic ranger to mass changes. In practice, continuously measured height changes are converted to mass changes through multiplication by the average density of the accumulated snowpack since the last visit, as measured in a snow pit or firn core (see section 2.1). Although this yields a correct value of the total accumulation integrated over the time interval between the pit studies, the sometimes considerable density variations in the upper firn layers result in an uncertainty of up to 20% or worse for mass changes on the event timescale.

[52] Another problem affecting ultrasonic height measurements in East Antarctica is the depth and temperature dependence of the firn densification rate. Under idealized steady state conditions, assuming continuous accumulation and a constant temperature, the vertical speed in the firn depends only on the local density (Sorge's law). Under these assumptions, knowing the anchor depth of the structure holding the ultrasonic height ranger and the density profile suffices to correct for this. Unfortunately, accumulation is not a continuous, steady state process: after a stepwise increase in surface height due to an accumulation event, the densification rate of a freshly fallen snow layer decreases with time. In addition, the densification process depends on temperature, causing accelerated summertime densification of the upper snowpack [*Dibb and Fahnestock*, 2004; *Li and Zwally*, 2002] and on the microstructure [*Freitag et al.*, 2004]. The summer heat wave slowly penetrates the firn, locally enhancing firn densification rates when it passes. This implies that only time-dependent firn densification modeling along the lines of *Li and Zwally* [2004], at least taking into account temperature, can account for the differential densification effect in a physically realistic way.

2.3.5. A Data Example From East Antarctica

[53] The following data example demonstrates both the great value and the problems of using ultrasonic height ranger data in East Antarctic mass balance research. Figure 8d shows 7 years (1998–2004) of accumulation derived from ultrasonic height ranger data from two AWS sites in western Dronning Maud Land (DML; left scale). The first AWS is located at Svea Cross (74°28.9′S, 11°31.0′W, 1160 m above sea level (asl)), at the foot of the Heimefrontfjella in the katabatic wind zone. The second is located adjacent to Kohnen station (75°00.2′S, 0°00.4′E, 2892 m asl, see Figure 8) on the Amundsenisen of the flat East Antarctic plateau. In addition to surface height changes, the AWSs measure wind speed and direction, temperature, relative humidity, shortwave and longwave radiation fluxes, air pressure, and snow temperatures. The sampling frequency typically is 6 min from which 1-h averages are calculated and stored in a Campbell CR10 data logger with separate memory module.

[54] The ultrasonic data (Figure 8d) have been corrected for temperature but not for differential firn densification. To convert height changes to mass changes, we applied a mean density of 396 kg m^{-3} at Svea Cross and 307 kg m^{-3} at Kohnen. Missing data, mainly due to riming (20% at Kohnen, <1% at Svea Cross), have been linearly interpolated. To remove some residual noise, a cubic spline fit was applied to the data. Applying linear fits to the cumulative mass balance curve yields values for the specific SMB of 243 kg m^{-2} a^{-1} at Svea Cross and 64 kg m^{-2} a^{-1} at Kohnen. These values agree with accumulation derived from shallow firn cores drilled at these sites.

[55] The data show that the measurement accuracy of the ultrasonic height ranger is insufficient to unambiguously resolve individual precipitation events at the low-accumulation site Kohnen. The record rather shows a continuous, slow accumulation interspersed with occasional larger events. No significant surface lowering is observed between accumulation events. At Kohnen, even during summer, temperatures are apparently too low to force strong sublimation and a seasonal cycle in the densification.

[56] This is very different at Svea Cross, where the accumulation occurs in large, well-defined events, some of which can also be found in the record of Kohnen. In between these accumulation events, dry periods lasting up to 8 months occur at Svea Cross. During these dry episodes, significant surface lowering occurs in the summer period (November–February). To determine which part of the surface lowering is caused by sublimation, AWS data were used to calculate the turbulent flux of latent heat [*van den Broeke et al.*, 2004b]. The scale on the right in Figure 8d indicates the resulting cumulative sublimation/deposition. As can be seen, sublimation dominates during summer, averaging typically 25 mm water equivalent (about 6.5 cm of snow) at Svea Cross and about 10 times less at Kohnen. At Svea Cross, this accounts for part but not all of the surface lowering that is observed during summer; enhanced summer densification of the firn layer enclosed by the AWS anchor depth and the surface accounts for the residual surface lowering.

2.4. Point Measurements at Depth: Snow Pits, Firn, and Ice Cores

[57] Snow pits and core drilling (Figure 9) are used to access older snow and ice below the surface. Their deployment retrieves sequences of buried snow and ice from only a single operation, as layers of different age are accessed at

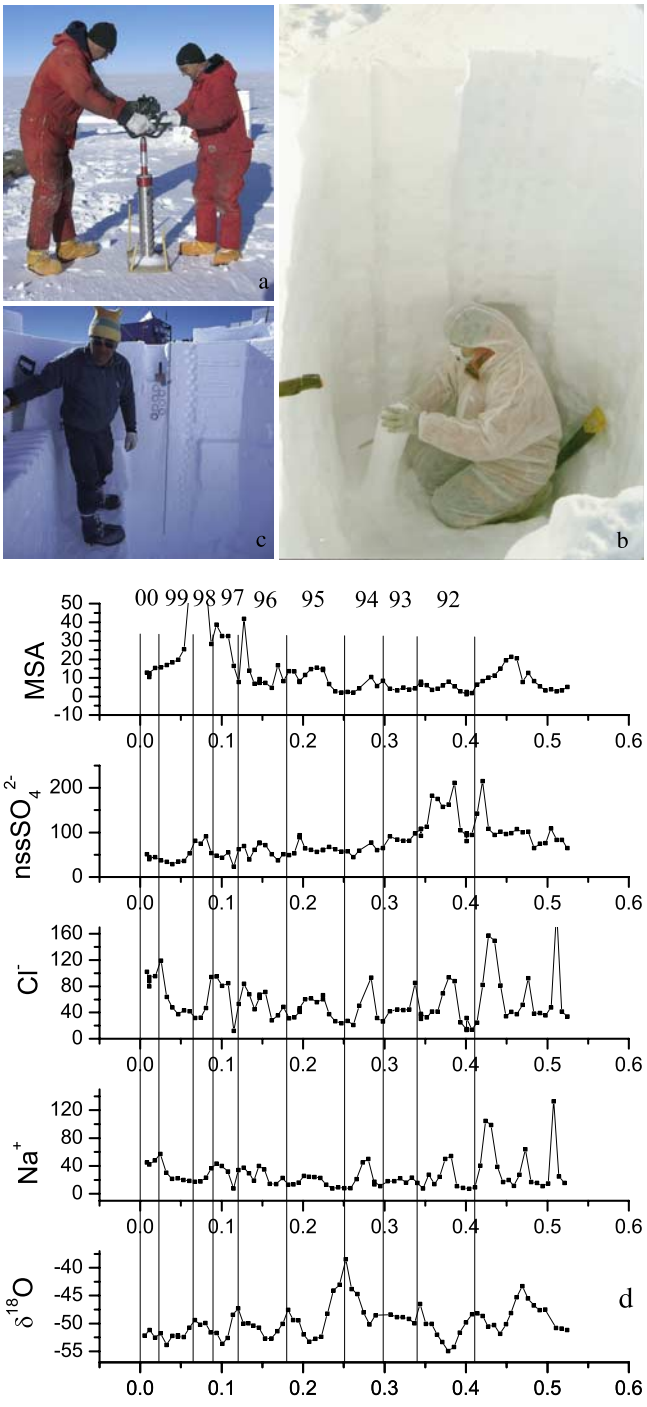

Figure 9. (a) Firn core drilling. Typical drill diameters are 3 inches (7.6 cm) and 4 inches (10.2 cm). The wooden board marks the reference level of the snow surface. (b) Taking samples in a 3-m-deep snow pit. To avoid sample contamination, the person wears a clean room suite. (c) Taking density measurements with tubes in a snow pit with a crossover pattern (visible to the left of the ruler in the center). (d) Example from pit MC in DML on how several different species have been used in dating the pits [*Karlöf et al.*, 2005b] (with permission of the International Glaciology Society). They mainly used the oxygen isotope data with support of ions to date the pits. Years (1992–2000) are indicated at the top; year transitions are marked with vertical lines.

once. Apart from accumulation, time series for a number of other parameters are established as well.

[58] The SMB corresponding to a sample in a certain depth interval (and thus age interval) is most generally derived from the ratio of mass (or water equivalent depth) of the considered sample to the time span that the sample range covers. As for stake and ultrasonic measurements, determination of density is thus one important key. In contrast to those methods, which monitor the surface and obtain time series of surface accumulation only by repeated observations of surface height at an accurately known point in time, the determination of the age as a function of depth is the other key parameter. One derives this function for instance by interpolating discrete *time markers* (e.g., *volcanic horizons*) or counting of layers of known origin, like annual signals [*Whitlow et al.*, 1992].

2.4.1. Density Measurements

[59] The techniques presented in sections 2.4.1.1–2.4.1.3, used to determine density as a function of depth along cores, complement the classic surface snow density measurement methods described in section 2.1.

2.4.1.1. Classic Technique

[60] Firn core density is most often determined by measuring core length and diameter and weighing each core section on an electronic scale directly after core retrieval in the field [*Isaksson et al.*, 1996; *Oerter et al.*, 1999; *Magand et al.*, 2004; *Frezzotti et al.*, 2005]. However, problems with this simple method are that the snow in the uppermost meter is usually poorly consolidated and loss of material is therefore unavoidable, reducing the accuracy of volume calculations. It is therefore common practice for firn core retrieval that density is measured in a pit (about 2 m depth) in direct connection to the drill site where stratigraphic studies and snow sampling can also be performed. Another problem is that the diameter of the core pieces changes depending on the snow type. For instance, less dense snow can be compacted or lost, resulting in an overestimation of density [*Karlöf et al.*, 2005b]. Cores with a wider diameter (e.g., 4 inch, 10.2 cm) reduce the uncertainty in density measurements. Core imperfections that can occur during drilling alter the volume of the core segment and can thus affect density measurements.

2.4.1.2. Radiation Attenuation Profiling

[61] Radiation attenuation profiling is based on the absorption and scattering of hard radiation to determine ice density. The ratio between transmitted and received ray intensity is a measure for absorption and scattering, which can be related to snow, firn, and ice density. Currently, three types of radiation are utilized: γ rays, X rays, and neutrons. In the case of γ attenuation profiling (GAP) [*Gerland et al.*, 1999; *Wilhelms*, 1996, 2000] the γ ray originates from a radioactive source (e.g., ^{137}Cs) and passes through the core in transverse direction to a detector. For monochromatic radiation the mass absorption coefficient is known with 0.1% relative error. The statistical intensity measurement error is determined by free-air reference. To reduce statistical errors, multiple (usually more than 10) measurements are averaged. The calibrated detector signal has to be

corrected for variations in core diameter. For high-quality cores, the diameter is accurate to $\leq$1 mm. The possible influence at maximum misalignment of the core within the measurement bench has to be accounted for, as well as cracks from core breaks at the end of an ice core. The precision of the GAP density measurements is typically around 10 kg m^{-3} for a 100-mm-diameter core. The depth resolution of GAP depends on the characteristics of the radioactive source, like ray diameter and dispersion characteristics. Typical resolution is on the order of 1 cm, with measurements carried for redundancy to the subcentimeter level.

[62] For X-ray attenuation profiling [*Hori et al.*, 1999], the accuracy is about 1%, the same as for the γ attenuation method. However, field measurements by the X-ray method are difficult since a large experimental system is required. It is therefore mostly applied in the laboratory.

[63] In contrast to these two methods, neutron probes (Walingford probe) [*Morris and Cooper*, 2003] are operated in the borehole instead of along the core. The neutron probe method thus has the advantage that only a (reasonably smooth) hole instead of a core is necessary for determining density profiles. The depth resolution, however, is physically limited to 10 cm. The uncertainty of the derived density is on the order of 10 kg m^{-3}.

2.4.1.3. Dielectric Profiling

[64] The complex dielectric constant is expressed as $\varepsilon^* = \varepsilon' - i\varepsilon''$. In the case of ice, the real part ε', the ordinary complex permittivity of the medium, mainly depends on density. The imaginary part ε'', the dielectric loss factor, is related to conductivity σ and radian frequency ω by $\varepsilon'' = \sigma(\varepsilon_0\omega)^{-1}$, where ε_0 is the permittivity of free space. Both parts of ε^* can be determined with dielectric profiling (DEP) [*Moore and Paren*, 1987]. A DEP device is essentially a calibrated and guarded scanning capacitor. The core is put between two semispheres. Its conductance and admittance are determined by applying alternating current potentials, typically at a single frequency of 10 kHz to a few hundred kilohertz, which are then converted to ε^*. For accurate devices, the real and imaginary components can each be determined to within 1% [*Wilhelms*, 2000]. A widely used formula relating the ordinary relative permittivity ε' and density ρ is based on the approximation derived by *Looyenga* [1965] from theoretical consideration of air distributed in a dielectric medium, with spherical approximations of bubbles, $\varepsilon' = ((\rho/\rho_{ice})[\sqrt{[3]}\varepsilon'_{ice} - 1] + 1)^3$. Other approximations were derived from comparison of density and permittivity measurements, e.g., by *Robin et al.* [1969], *Tiuri et al.* [1984], or *Kovacs et al.* [1995]. The latter refined an empirical approximation, $\varepsilon' = (1 + 0.845\rho)^2$, which is now widely used for permittivity-density conversions [*Kovacs et al.*, 1995]. They obtained a standard error of $\pm$0.031 for ε'. Both of the above formulae take only the real part of ε^* into account, causing a mixing of the complex components [e.g., *Barnes et al.*, 2002]. Recently, *Wilhelms* [2005] demonstrated that neglect of complex mixing for the density-permittivity relation could result in errors in ε^* and suggested extension of Looyenga's formula into complex space. In general, integration of the density-depth profile to obtain cumulative mass results in a higher accuracy, as statistical uncertainties of abnormally high or low values are averaged out.

2.4.2. Age Estimates

[65] Two main methods are used to date firn and ice cores (from seasonal to century scales): counting of seasonal variations of various parameters (physical, chemical, isotopic) that show cyclic variations during the year (Figure 9d) and identifying prominent horizons of known age, such as acid layers from dated volcanic eruptions or radioactive fallout from atmospheric thermonuclear bomb tests. A third method exploits the natural decay of radioactive materials. The method used depends on the purpose of the study and the accumulation rate at the site; however, many studies utilize all three methods.

2.4.2.1. Seasonal and Annual Layer Counting

[66] 1. The stable isotope (δ^{18}O and δD) stratigraphy [*Dansgaard et al.*, 1973] is a method commonly used to determine annual layers [e.g., *Morgan et al.*, 1991] in areas with higher accumulation (above about 80–100 kg $m^{-2}a^{-1}$). The oxygen and hydrogen isotopic composition of polar snow is mainly related to the condensation temperature [*Dansgaard*, 1964]. One advantage of the stable isotope stratigraphy is that no special precautions during the sampling procedure are necessary to prevent sample contamination [*Legrand and Mayewski*, 1997]. However, at least seven to eight samples per year are needed to correctly resolve seasonal and thus annual signals. The seasonal cycle of δ^{18}O (or δD) is usually well developed only in the upper part (5–10 m) of the snowpack because of diffusion during densification [*Johnsen*, 1977; *Legrand and Mayewski*, 1997] in the postdepositional process. As few studies have been dedicated to the analysis of postdepositional effects on Antarctic snow composition, the possibility that wind-driven ablation [*Ekaykin et al.*, 2002; *Frezzotti et al.*, 2004] as well as sublimation [*Neumann and Waddington*, 2004; *Neumann et al.*, 2005; *Satake and Kawada*, 1997] may induce systematic effects on isotope levels has to be kept in mind. These could affect seasonal and annual signals [*Masson-Delmotte et al.*, 2008] and thus SMB measurements. As suggested by Masson-Delmotte et al., systematic measurements of water vapor and snow isotopic composition should provide a means of disentangling the effect of depositional and postdepositional processes and, as a consequence, allow a better understanding of their effect on SMB estimates.

[67] 2. Chemistry of discrete firn/ice core samples has been routinely analyzed for major ion content (e.g., via ion chromatography). Over the last decade, continuous flow analysis (CFA), high-resolution fast ion chromatography (FIC), and continuous melting discrete sampling (CMDS) methods have been improved such that a quasi-continuous record of a number of different species is measured simultaneously along a single core [*Fuhrer et al.*, 1993; *Sigg et al.*, 1994; *Fuhrer et al.*, 1996; *Röthlisberger et al.*, 2000; *Sommer et al.*, 2000b, 2000a; *Udisti et al.*, 2000; *Traversi et al.*, 2002; *Rasmussen et al.*, 2005; *Osterberg et al.*, 2006].

Typical markers for seasonal layer counting are methanesulphonic acid (MSA) and nonsea-salt (nss) sulphate (nss SO_4^{2-}), the main oxidation products of dimethylsulphide (DMS), which are mainly produced by marine biogenic activity [*Saigne and Legrand*, 1987]. Study of seasonal cycles of sulfur aerosol carried out in coastal Antarctica have shown that MSA and nss SO_4^{2-} exhibit a strong seasonal cycle characterized by summer maxima [*Jourdain and Legrand*, 2001; *Curran et al.*, 1998]. Another seasonal indicator is Na^+, a tracer of sea salt. Na^+ concentrations peak during the winter as a consequence of more frequent advection of marine air masses over the Antarctic ice sheet [*Legrand and Delmas*, 1984], with the strongest seasonal signal near the coast. Among the commonly used ions, sodium, nss sulphate, and nitrate often show well-developed seasonal variations on the polar plateau [*Isaksson et al.*, 1996; *Stenni et al.*, 2000, 2002; *Traufetter et al.*, 2004; *Kaspari et al.*, 2005; *Dixon et al.*, 2004; *Karlöf et al.*, 2005b]. Also for these species it is important to sample with high enough frequency to capture their variations, i.e., at least seven to eight samples per year [*Mayewski and Goodwin*, 1997]. However, it is worth keeping in mind that nitrate diffuses and is probably reemitted from the upper layers of the ice sheet [*Wolff et al.*, 1995; *Weller et al.*, 2004]. Nitrate reemission is inversely related to accumulation rate and usually obliterates its seasonal signature at low accumulation sites. Therefore, SO_4^{2-} and Na^+ provide the most robust annual peaks within cores. In order to avoid using occasional double peaks as dividing lines for years, multiple ions with different seasonal timings can be used to define the annual horizons [e.g., *Legrand and Mayewski*, 1997].

[68] 3. Some gases also display a seasonal cycle, in addition to isotopes and ions. One example is hydrogen peroxide (H_2O_2, e.g., measured via spectrofluorimeter methods), which is principally produced in the atmosphere by photochemistry in summer. Its maximum concentration occurs in the period of maximum solar radiation, from late spring to late summer [*Neftel*, 1991]. H_2O_2 is subject to postdepositional change, caused by reemission to the atmosphere, the same as some other species. Utilization of H_2O_2 for annual layer counting is thus restricted to high-accumulation areas (>200 kg m^{-2} a^{-1}).

[69] 4. For electrical methods, the varying concentrations of ions are a major cause of variations in alternating current (AC) and direct current (DC) electric conductivity. Two techniques are used to determine quasi-continuously the variation of conductivity along a core. The electric conductivity method (ECM) [*Hammer*, 1980] is a measure of the electrical current from which acidity concentration levels may be inferred in cores. ECM is performed in a cold room with stable temperature conditions as well as in the field. In contemporary systems, two to seven electrodes with an applied high voltage of several hundred volts (AC or DC) are moved along a freshly cut ice surface, and measurements are typically taken at millimeter resolution. The original method has been modified in various ways and is used by different groups [*Isaksson et al.*, 1996; *Kaczmarska et al.*, 2004; *Wolff et al.*, 1999; *Taylor and Alley*, 2004]. A direct current flowing between the electrodes is dominated by the acid content and the temperature of the ice [*Schwander et al.*, 1983; *Moore and Mulvaney*, 1989] but is only slightly dependent on the salt concentration under normal conditions [*Schwander et al.*, 1983; *Wolff et al.*, 1997]. For alternating currents, salts have an increasing effect on conductivity [*Barnes et al.*, 2002]. The imaginary part of the dielectric constant determined from DEP, ε'', already introduced in section 2.4.1.3 in the context of density measurements, likewise reveals variations in AC conductivity [*Moore and Mulvaney*, 1989]. As an alternating current technique, which is nondestructive as it does not require direct contact between the ice and the electrodes [*Wilhelms et al.*, 1998], it also responds to both the acidity and the total salt content in the ice [*Barnes et al.*, 2002]. Measurements are performed in millimeter to centimeter increments. There is evidence that the DEP and ECM electrical methods respond to different chemical compositions. *Minikin et al.* [1994] suggested that DEP peaks represent winter maxima of sea salts, while peaks in ECM respond mostly to summer maxima of nss sulphate and partly to high values of NO_3^-, MSA, and HCl^-. *Hammer et al.* [1994] and *Mulvaney et al.* [2002] confirm that ECM is a sufficient method for detecting both volcanic peaks and seasonal changes in acidity. Apart from identifying volcanic signals in conductivity, ECM is also used to analyze annual peaks if conditions are favorable enough.

[70] 5. Dating firn and ice cores via visual stratigraphy is based on visual differences in summer and winter snow due to changes in atmospheric conditions and radiative fluxes [*Alley et al.*, 1997]. To aid the identification of annual layers, the surface of the core is prepared with a microtome knife. The core is placed on a light table to identify seasonal variations in transparency and scattering associated with annual layering. Summer layers are characterized by coarse-grained, low-density hoar layers, whereas winter layers have higher density and finer grain size. Below the firn-ice transition, summer layers have fewer and larger bubbles compared to winter layers and can also be identified by the presence of summer melt layers in coastal regions. Because of annual layer thinning, annual layers become more difficult to identify with depth. In regions with low accumulation, postdepositional processes such as drifting and melting (e.g., near coastal blue ice areas or very low accumulation areas on the plateau) can preclude the presence of visible annual layers [*Taylor et al.*, 2004]. An advantage of visible stratigraphy is that it can also be applied in the field if stratigraphic changes are strong enough to be identified without preparation of the core. At least for higher accumulation sites, and thus favorable conditions, visual stratigraphy provides an initial approximation of annual accumulation rates [*Morgan et al.*, 1991], useful for later decisions on core processing (e.g., sampling resolution). Although the visual stratigraphy is commonly applied to derive on-site information in snow pits, accumulation rates derived from pit stratigraphy alone involve personal and subjective interpretation, which can lead to unreliable results, as pointed out by *Picciotto et al.* [1971].

[71] 6. New techniques build on the greater availability of more advanced chemical analysis instrumentation, such as inductively coupled plasma–mass spectrometry (ICP-MS), allows the accurate determination of many tens of chemical elements at the parts per billion, parts per trillion, and parts per quadrillion levels. Improved instrumentation coupled with advances in sample generation, e.g., by laser ablation [*Reinhardt et al.*, 2001], ultraclean sample analysis, and continuous sampling [*Knüsel et al.*, 2003; *Osterberg et al.*, 2006], will likely yield new firn and ice core dating methods. This would be particularly advantageous for dating ice cores from low-accumulation sites (such as the East Antarctic plateau).

2.4.2.2. Reference Horizons

[72] There are several valuable reference horizons that have been used in Antarctic accumulation studies for validating the depth-age scale developed from annual layer counting or for use as a time horizon, which can then be used for calculating the accumulation rate between horizons. Below we discuss the two most commonly used reference horizons (volcanic peaks and artificial radionuclides) and suggest additional horizons that could be worthwhile to explore further.

[73] 1. For volcanic peaks, sulphate (in the form of atmospheric H_2SO_4) is generally the dominant ion in high-altitude Antarctic snow, with the dominant source from marine biogenic emissions and sporadic input from volcanic activity. For the Antarctic polar plateau, historical volcanic eruptions such as Pinatubo 1991, Mount Hudson 1991, Mount Agung 1963, Krakatau 1883, and Tambora 1815 (plus an unknown eruption 1809) have been shown to be easily distinguishable peaks that can be used as unambivalent time markers, either from chemical analysis or conductivity measurements [e.g., *Cole-Dai et al.*, 1997; *Oerter et al.*, 1999; *Nishio et al.*, 2002; *Stenni et al.*, 2002; *Traufetter et al.*, 2004; *Dixon et al.*, 2004]. Because of oxidation of SO_2, H_2SO_4 forms within about 1 month following the eruption [*Coffey*, 1996]. Once in the stratosphere, the atmospheric residence time of SO_4^{2-} is a few years, during which it can be transported to the polar regions and subsequently scavenged by snowfall. An increase of nss SO_4^{2-} concentrations in polar snow is observed in a period up to 3 years after a major volcanic eruption [*Cole-Dai and Mosley-Thompson.*, 1999]. For example, the eruption of Tambora (located in Indonesia) occurred in April 1815. The rise of SO_4^{2-} above background noise is observed in late austral winter 1816, with maximum concentrations during the austral summer of 1816/1817 [*Cole-Dai et al.*, 1997; *Palmer et al.*, 2001] due to the lag between the eruption and nss SO_4^{2-} deposition in Antarctica. In several papers from the EPICA presite and ITASE surveys, attempts have been made to develop a useful volcanic chronology spanning the last millennium to aid in the correlation between cores [*Karlöf et al.*, 2000; *Traufetter et al.*, 2004; *Hofstede et al.*, 2004]. The Tambora double peak has served as the main time horizon for the dating of many firn cores in the ITASE program [*Isaksson et al.*, 1996, 1999; *Oerter et al.*, 1999, 2000; *Stenni et al.*, 1999, 2001; *Karlöf et al.*, 2000; *Ekaykin et al.*, 2004; *Dixon et al.*, 2004; *Karlöf et al.*, 2005b; *Frezzotti et al.*, 2005; *Steig et al.*, 2005]. The most prominent eruptions during the last millennium in addition to Tambora are the A.D. 1259 eruption suggested to be El Chichon [*Palais et al.*, 1992] and the A.D. 1452 eruption suggested to be Kuwae [*Delmas et al.*, 1992]. These eruptions have been identified in many Antarctic ice cores [i.e., *Moore et al.*, 1991; *Cole-Dai et al.*, 1997, 2000; *Watanabe et al.*, 1997]. However, the volcanic signal at high-accumulation, low-elevation sites located near the Ross Sea coast in West Antarctica has been overwritten by large amounts of biogenic SO_4 that is released by marine organisms [*Dixon et al.*, 2004]. This may be a problem at other low-elevation coastal sites that are situated close to polynyas, too. Currently, on the polar plateau (SMB < 70 kg m^{-2} a^{-1}), $\sim$2.5-m-deep snow pits are deep enough to reach the 1991–1992 layer from the Mount Pinatubo and Mount Hudson eruptions. Attempts have been made to determine if dating horizons as shown in time series of DEP, ECM, and sulfate are significant with respect to natural and measurement-induced noise [*Cole-Dai et al.*, 1997; *Fischer et al.*, 1998; *Karlöf et al.*, 2005a, 2006; *Steig et al.*, 2005].

[74] 2. Time markers from artificial radionuclides are based on radioisotopes from atmospheric nuclear weapon tests (United States, United Kingdom, Soviet Union, France, China, and India) carried out between 1953 and 1980. They were deposited in Antarctica after transport in the upper atmosphere and stratosphere [*Picciotto and Wilgain*, 1963; *Wilgain et al.*, 1965; *Feely et al.*, 1966; *Picciotto et al.*, 1971; *Lambert et al.*, 1977; *Carter and Moghissi*, 1977; *Jouzel et al.*, 1979; *Kamiyama et al.*, 1989]. Since the signing of the Limited Nuclear Weapon Test Ban Treaty in 1963, the number of atmospheric nuclear weapon tests greatly decreased with tests being carried out mainly underground. Other sources of anthropogenic fallout post-1963 may be linked to the nuclear disaster in Chernobyl in 1986 [*Dibb et al.*, 1990]. Very sensitive analytical techniques and procedures have been developed and improved over the last 40 years to detect and measure both artificial and natural radionuclides present in the ice sheets [*Picciotto and Wilgain*, 1963; *Delmas and Pourchet*, 1977; *Pinglot and Pourchet*, 1979, 1994]. The high solubility of most fission products induces the formation of distinct and stable radioactive reference horizons in areas of dry snow facies or with moderate percolation of meltwater. Among the radioactive fallout, ^{90}Sr and ^{137}Cs radionuclides (referred to gross β activity), plutonium isotopes, and ^{241}Am [*Pourchet et al.*, 2003] are best suited for the formation of distinct radioactive horizons owing to their high production yield and their low volatility, which prevents vertical migration in the firn layers as long as they remain dry [*Picciotto et al.*, 1971]. Another artificial product, tritium (^{3}H), behaves differently during its injection into the global system (by thermonuclear explosions) and its deposition than the fission products previously cited [*Picciotto et al.*, 1971]. Nevertheless, very distinct radioactive peaks in continuous tritium profiles are also observed [*Jouzel et*

al., 1979; *Oerter et al.*, 1999; *Stenni et al.*, 2002; *Frezzotti et al.*, 2005]. The timing of radioactive deposition from the nuclear tests is well known in Antarctica [*Wilgain et al.*, 1965; *Feely et al.*, 1966; *Jouzel et al.*, 1979; *Oerter et al.*, 1999; *Pourchet et al.*, 1983, 1997, 2003; *Magand et al.*, 2004], with the maximum radioactivity peaks in 1954–1955 and 1965–1966 used as convenient horizons for dating snow and ice layers and measuring SMB. *Jouzel et al.* [1979] observed the largest tritium peak at the South Pole during 1966. On the basis of comparison between the tritium profile in snow layers at Dronning Maud Land and the tritium distribution at the Kaitoke (New Zealand) International Atomic Energy Agency (IAEA) station, *Oerter et al.* [1999] attributed the highest values to the 1964–1969 years. Best fit depth–time scales were used to transform the measured depth profiles to time series similar to the tritium content of precipitation at Kaitoke. In Antarctica, total β counting remains the most frequent radioactivity measurement [*Picciotto and Wilgain*, 1963; *Lambert et al.*, 1977; *Pourchet et al.*, 2003]. As a consequence, there is a great deal of data on the history of artificial radioactive fallout over Antarctica since the 1950s; thus total β activity is a well-constrained method used to identify radioactive reference horizons for estimating SMB in accumulation areas. In situ γ ray spectrometers for ice boreholes [*Pinglot and Pourchet*, 1981] enable a rapid determination of the mean annual accumulation from 1965 to present by measuring the radioactive fallout layers. This provides valuable information in the field to estimate the depth range necessary to reach dating horizons (like volcanic signals) as previously cited.

2.4.2.3. Radiochronology

[75] As in many geoscientific disciplines, the natural decay of radioactive isotopes can be used to determine the age of an investigated sample, commonly referred to as *radionchronology*. A common example for ice is ^{210}Pb, a natural β emitter. It is a long-lived daughter nuclide (half-life 22.3 years) belonging to the ^{238}U family [*Picciotto et al.*, 1971]. Its presence in the atmosphere is a result of the α radioactive decay of radon gas (^{222}Rn). The atmosphere is the major source of ^{210}Pb deposited on the Antarctic ice sheet. Many factors contribute to the low radon (and its daughter nuclide) concentrations in Antarctica [*Pourchet et al.*, 1997, 2003]. These include ice that prevents the escape of radon from the Antarctic geological basement, the surrounding ocean without radon emission, and the time required for air masses to move from continental areas (the main source of radon emission) to the south polar region. Very little ^{210}Pb was produced by the nuclear explosions during the 1960s.

[76] Studies carried out during this period show that the quantity of ^{210}Pb deposited at a given place, averaged over a year or more, appears to be constant and not to have changed significantly since the advent of H-bombs [*Bull*, 1971]. As a result, the natural ^{210}Pb continuous flux deposition over the Antarctic ice sheet could be used for dating purposes over periods of the past 100 years. Because of radioactive decay, the natural ^{210}Pb activity decreases with depth of the firn and ice layers. The age of a firn layer at z meters depth is thus given by

$$t = \frac{1}{\lambda} \ln \frac{A_0}{A_z}, \tag{3}$$

and the average rate of accumulation of snow above this depth is given by

$$\dot{b} = \frac{z\lambda}{\ln \frac{A_0}{A_z}}, \tag{4}$$

where A_0 and A_z are the ^{210}Pb activities per unit weight of snow at the surface and at a depth of z meters, respectively, and λ is the ^{210}Pb decay constant. The first attempts at dating firn or ice layers in the polar regions with the ^{210}Pb method were successfully validated by other direct measurements [*Goldberg*, 1963; *Picciotto et al.*, 1964; *Crozaz et al.*, 1964; *Nemazi et al.*, 1964; *Crozaz and Langway*, 1966]. We have to stress that accurate dating of snow by ^{210}Pb is only possible with the following assumptions: (1) The mean ^{210}Pb activity in precipitation has remained constant during the last two centuries, (2) the ^{226}Ra concentrations within the firn/ice samples are negligible, (3) no diffusion of air into the ice sheet occurs (bearing additional ^{222}Rn), and (4) ^{210}Pb remains at its initial place of deposition (no vertical transportation by water from melting snow). Even if none of these assumptions are perfectly fulfilled, we argue that a generally reliable determination of SMB over the past few decades is achievable by this method in areas exempt from melting, i.e., in accumulation zones [*Pourchet et al.*, 1997, 2003].

2.4.2.4. Optimal Strategies for Age Estimates

[77] Counting seasonal cyclicity of chemical/isotopic parameters (δ^{18}O, δD, H_2O_2, MSA, Na^+, NO_3^-, nss SO_4^{2-}, etc.) is the most precise dating method, but it is also the most time- and equipment-intensive method. A multiparameter approach using several high-resolution chemical records (as shown in Figure 9d) is therefore the most reliable way to derive annual dating. Because several atmospherically derived chemical species peak during different times of the year, it may thus be possible to ensure that no year is missing [e.g., *Udisti*, 1996; *Steig et al.*, 2005]. In general, however, seasonal cycles are difficult to observe at sites with low accumulation (below about 80–100 kg m^{-2} a^{-1}), such as the polar plateau, because the seasonally deposited chemical or physical signals often have been strongly erased or reworked by the action of wind at the surface. Applying these methods to discrete samples (as from snow pits) is ineffective in the inner part of East Antarctica, e.g., in the Dome C area, unless a high (subcentimeter) sampling resolution is used. At most low accumulation areas, high-resolution continuous electric (DEP and ECM) and chemical measurements (CFA, FIC, CMDS) and the simultaneous analysis of multiple-parameter records have to be performed in order to detect seasonal signals in the physical and chemical properties of cores and thus achieve annual dating. During the past decade, high-

resolution continuous methods have been used in many studies, such as for the EPICA presite surveying in Dronning Maud Land [*Sommer et al.*, 2000b]. Thus, it was possible to perform annual layer counting back several hundred years at several places on the East Antarctic plateau with SMB below 80 kg m^{-2} a^{-1}, e.g., at the South Pole [*Meyerson et al.*, 2002] or Dronning Maud Land [*Sommer et al.*, 2000a], and even below 50 kg m^{-2} a^{-1} from an ice core site located approximately 600 km south of Dome A (D. A. Dixon, personal communication). Such results imply that wind scouring does not suffice to erode annual signals at these sites. However, the identification of annual layers does not unequivocally imply the possibility of resolving accumulation history with representative values (±10%) of annual resolution [*Frezzotti et al.*, 2007]. When continuous sampling is not available, reference horizon dating may be the only available method at low accumulation sites. In such cases, only a mean accumulation rate between two reference horizons can be calculated. This precludes these records from studies interested in the interannual variability in accumulation, for instance, to assess changes in climate, to account for flux of chemical compounds, etc.

2.4.3. Accumulation Errors From Pit and Core Measurements

[78] Annual layer counting using seasonal cyclicity of multiparameters can be fine tuned using atmospheric thermonuclear bomb test layers and volcanic peaks as fixed time markers to achieve the best accuracy for the evaluation of snow accumulation in cores. Dating errors may arise from incorrect or nonidentification of seasonal signals (e.g., hiatus in accumulation or erosion) and from incorrect identification or errors in identification of historical volcanic or nuclear bomb layer markers. Dating errors could be ±1 year for the depth coincident with the marker, but they could be higher at points that are far from dated reference horizons [e.g., *Steig et al.*, 2005].

[79] The associated relative errors in accumulation $\dot{b}$ derived from snow pits, firn, and ice cores (Table 2) can be expressed as

$$\frac{\delta\dot{b}}{\dot{b}} \leq \sqrt{2\left(\frac{<0.5l}{\Delta z}\right)^2+\left(\frac{\delta(\Delta t)}{\Delta t}\right)^2+\left(\frac{\delta(\Delta m)}{\Delta m}\right)^2}, \qquad (5)$$

where l is sample length, Δz and Δt are the depth and age difference between the dating horizons used, and Δm is the mass difference of the two columns above the two dating horizons, sometimes expressed in meter water equivalent depth; $\delta(\ )$ is the uncertainty of the parenthesized variable, e.g., the error in the date of volcanic deposition. When the sample length is relatively large compared to the depth between dating horizons, the first term on the right-hand side is important. On the other hand, if the age–depth profile is derived from high-resolution measurements like electrical methods, the first term can be neglected. The error estimate only applies at the identified dating horizons. Any physical variation, i.e., change in accumulation, between the dating horizons is not captured by this error estimate. The typical error $\delta\dot{b}$ in $\dot{b}$ is less than 10% for both snow pits and cores.

[80] The extraction of snow accumulation values from cores requires estimating the effects of thinning due to ice dynamics (densification, compression, flow, etc.). Vertical thinning of surface layers is predictable from the sum of horizontal strain rates. As firn cores are relatively shallow (less than 50–100 m) in comparison to the total thickness of ice sheets (more than 1000 m), thinning could be assumed to be less than 5%, implying negligibility. In cold, large ice sheets like the one in East Antarctica, the strain rates are expected to be around 10^{-4} a^{-1}. On fast moving glaciers, ice streams, and ice shelves, they can sometimes get close to 10^{-2} a^{-1}, and as a result, cores that represent several hundred years can be significantly affected by thinning. As an example, consider a 100-year-old layer. If both horizontal strain rates are 10^{-4} a^{-1}, the 100-year-old layer should have thinned by only 2%, but if strain rates are 10^{-2} a^{-1}, the layer is thinned to 13% of its original thickness. For a 100-m core with around 200 kg m^{-2} a^{-1} accumulation, corresponding to 300 years of accumulation history, and at a strain rate of 10^{-3} a^{-1}, a 55% thinning of the original layer thickness should result. Whether layer thinning takes place or not has thus to be evaluated for each site individually.

2.5. Laterally Continuous Measurements: Ground-Penetrating Radar

[81] GPR maps the internal structure of the firn column along a profile from the surface. Variation in depth of continuous internal layers of equal age along the profile yields information about the accumulation pattern. Combining GPR with highly resolved ice core data is required to date the internal layers.

[82] Over the last few decades, a number of methodological studies have been carried out to investigate the suitability of high-resolution GPR for mapping accumulation rates along surface profiles. The results demonstrate that GPR profiling of firn stratigraphy, coupled with precise GPS measurements is capable of complementing traditional methods like stakes, snow pits, and cores to map accumulation rates and to improve the understanding of spatial accumulation patterns. In the literature, terms like GPR (traditionally used in engineering geophysics), ice-penetrating radar, snow radar, and sometimes radio echo sounding are used synonymously. Here, we stick to the first term and imply investigations with a phase-sensitive radar. Commercial and easily transportable GPR systems have become available and are widely used to survey the near-surface firn (<100–200 m). Over recent years this had the consequence that GPR was routinely employed during operational surveys to map the internal structure of the firn column and to determine regional surface accumulation, e.g., during most campaigns related to ITASE and EPICA [*Isaksson and Karlén*, 1994; *Richardson et al.*, 1997; *Richardson and Holmlund*, 1999; *Nereson et al.*, 2000; *Richardson-Näslund*, 2001; *Urbini et al.*, 2001; *Frezzotti et al.*, 2002b; *Frezzotti and Flora*, 2002; *Sinisalo et al.*, 2005; *Richardson-Näslund*, 2004; *Rotschky et al.*, 2004; *Karlöf*, 2004; *Spikes et al.*, 2004; *Eisen et al.*, 2005; *Frezzotti et al.*, 2005; *Arcone et al.*, 2005a, 2005b; *Jacobel et al.*, 2005; *Anschütz et al.*,

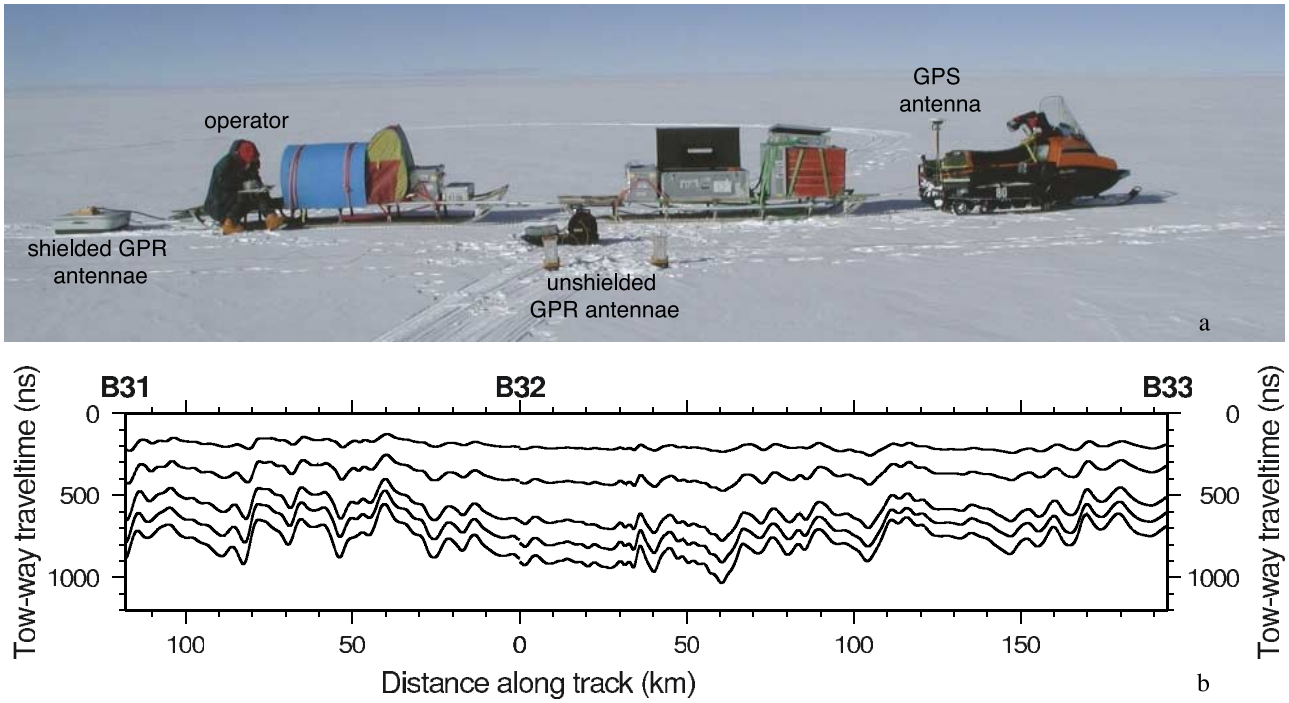

Figure 10. (a) Setup of GPR measurements: For common offset surveys, a shielded antenna (left) is pulled by a snowmobile. The GPS antenna is mounted at the rear of the vehicle (right). Common midpoint surveys utilize separate transmitter and receiver (front). (b) Sample profile of five internal horizons tracked in common offset GPR data over 300 km in Dronning Maud Land [*Eisen et al.*, 2004].

2007, 2008]. High-frequency GPR in the range of 100 MHz to 1 GHz is capable of imaging the structure of the upper tens to hundreds of meters of the ice column in high resolution. On the Antarctic inland plateau, this provides a means to derive information about the local SMB over the last tens of years to about 1000 years. It has thus become possible to map accumulation rates and their spatial variations along continuous profiles within the upper parts of the snowpack.

2.5.1. Technical Background and Functional Principle

[83] Application of GPR for imaging the snow and firn column at shallow depths usually utilizes a transmitter and receiver moved at a fixed distance from each other across the surface along the survey profile. This setup is called common offset (CO), referring to the constant distance between transmitter and receiver. The device is either towed by hand, snowmobile, or tractor, and the geographical position is usually obtained from kinematic GPS measurements (Figure 10a). At defined intervals, either at equal temporal or spatial increments, the transmitter emits an electromagnetic pulse into the snow column. Distances between consecutive measurements vary, depending on the system performance, between about 0.1 and 10 m. The pulse penetrates into the snow column and is partly reflected where the complex dielectric ε^* constant changes. The reflected signals travel back to the receiving antenna at the surface. The complete signal is recorded as a function of traveltime of the transmitted radar pulse.

[84] Three factors are known to change the dielectric constant in firn and ice: gradients in the real part, the permittivity, are mostly related to density; they dominate reflections in the upper hundreds of meters. Variations in the imaginary part are proportional to conductivity, are related to acidity, and depend on frequency. They are the governing reflection cause in deeper ice. A third mechanism, proposed by *Harrison* [1973], involves dielectric anisotropy of the crystal fabric, but it becomes significant only at the deeper levels (>500–1000 m) of the ice sheet where changes in anisotropic crystal fabrics could develop [*Fujita et al.*, 1999; *Matsuoka et al.*, 2003, 2004; *Eisen et al.*, 2007]. Other radar techniques are based on frequency-modulated continuous wave (FMCW) transmissions or stepped-frequency radars [*Kanagaratnam et al.*, 2001; *Corr et al.*, 2002]. Although the technical details on data acquisition and processing are different, the results are the same, an image of subsurface reflections along a profile (Figure 4).

[85] Studies of dielectric properties of ice and internal radar reflection horizons (IRHs, outlined in Figure 10b) show that most processes forming electromagnetic reflectors take place at the glacier surface at approximately the same time [*Gudmandsen*, 1975]. (Details on physical structure and processes related to the origin of reflections in firn are given by *Kohler et al.* [2003], *Eisen et al.* [2003a, 2003b], and *Arcone et al.* [2005a].) While some significant progress in understanding this process has been made in recent years [*Eisen et al.*, 2003b; *Arcone et al.*, 2005a], it is still not entirely clear how the GPR produces a continuous reflecting horizon in the ice, visible over hundreds to even thousands of kilometers. At present, there remains some uncertainty about how the material properties in firn combine to form the continuous reflecting horizons. It does

seem apparent that both density and chemical properties in the ice contribute, but since layers are visible even where the wavelength of the radar exceeds the annual layer thickness, it is clear that at least in the shallow regions some complex interference pattern is generally being observed. However, the isochronity of observed reflections has been proven heuristically by connecting firn and ice core drill sites [*Jacobel and Hodge*, 1995; *Spikes et al.*, 2004; *Eisen et al.*, 2004; *Frezzotti et al.*, 2005] and by comparing accumulation rates deduced from GPR with those measured along surface stake lines [*Vaughan et al.*, 2004]. The submergence rate of an isochrone surface is determined by interaction of the surface accumulation with the flow field [*Robin et al.*, 1969; *Gudmandsen*, 1975; *Clough*, 1977; *Millar*, 1981; *Bogorodsky et al.*, 1985; *Moore*, 1988]. Continuously moving the radar system along a surface profile and recording individual traces at high enough spatial repetition rates (on the order of decimeters to meters) makes it possible to continuously image the internal reflections along the profile (Figure 10b). As the continuous internal reflection horizon corresponds to an isochronous layer, the spatial variation of layer depth provides information on variations in the accumulation rate and changes due to ice sheet dynamics. The latter can mostly be neglected in the upper meters of the ice column in regions of slow flow (see previous discussion on accumulation errors from cores in section 2.4.2.3).

2.5.2. Accumulation Estimates From GPR

[86] On the Antarctic plateau, the isochronous reflections can be followed over hundreds of kilometers. The variation in depth of an individual reflector already provides a qualitative picture about the variation of surface accumulation along the profile. To determine quantitative accumulation estimates, several processing steps are necessary [*Arcone et al.*, 2005a; *Rotschky et al.*, 2004]: (1) track one or more internal reflections along the profile; (2) convert the radargram from time to depth domain along the whole profile; (3) date the isochrones at one or more points (the isochronity assures that the age can be distributed along the profile); (4) determine the cumulative mass as a function of depth from the surface to the reflector depth along the profile; and (5) calculate the average SMB by dividing the cumulative mass by the respective age of the reflector.

[87] These processing steps involve several other input properties. We now discuss details and peculiarities of each step.

2.5.2.1. Tracking Internal Reflections

[88] After digital data processing of the raw radar data (horizontal stacking, filtering, gain control), continuous reflections can be followed in the radargrams. Depending on data processing and display, it is possible to identify a single phase, for instance, the first break, and track that along the whole profile, or track the maximum amplitude when the signal envelope is used. Tracking can be performed manually, trace by trace, or semiautomatically. Semiautomatic tracking is implemented in a number of programs, mainly based on experiences in the seismic exploration industry. The tracking algorithm exploits the coherency of signal features (e.g., minimum, maximum, or zero amplitude) above noise level to automatically detect the same feature within a prescribed time window in adjacent traces and follows it as long as a similarity criterion is fulfilled. The tracking process is observed by the user and requires manual interaction in case of a low signal-to-noise ratio.

2.5.2.2. Time-to-Depth Conversion

[89] Knowledge of the variation of the electromagnetic wave speed with depth is necessary in order to be able to convert the observed reflections from time to depth domain. Some authors directly calculate water equivalent depth of a horizon to derive accumulation [*Vaughan et al.*, 1999b; *Spikes et al.*, 2004]. The wave speed is mainly a function of density; contributions from conductivity can be neglected at radio frequencies. Different methods were developed to determine the wave speed–depth function. The most direct method involves the measurement of the dielectrical properties along cores by means of DEP (see section 2.4.1) [*Moore and Paren*, 1987; *Wilhelms et al.*, 1998; *Karlöf*, 2004; *Wilhelms*, 2005], from which the interval velocities can be directly calculated. Instead of the dielectrical properties, density profiles from snow pits, firn, or ice cores are also often used to determine the electromagnetic wave speed from mixture models [*Robin et al.*, 1969; *Clough and Bentley*, 1970; *Kovacs et al.*, 1995; *Richardson et al.*, 1997; *Urbini et al.*, 2001; *Eisen et al.*, 2002; *Spikes et al.*, 2004; *Anschütz et al.*, 2006]. The downhole radar technique makes use of a drilled hole to record traveltimes as a function of depth of a reflecting target lowered in the hole [e.g., *Jezek and Roeloffs*, 1983; *Clarke and Bentley*, 1994]. Interval velocities can then be derived from the transmitter–target–receiver traveltime as a function of depth. An indirect method known from reflection seismic exploration is the common midpoint (CMP) survey technique [*Yilmaz*, 1987]. It is a special case of the radar wide-angle reflection and refraction measurement [*Annan and Davis*, 1976; *Jezek and Roeloffs*, 1983; *Morey and Kovacs*, 1985; *Bogorodsky et al.*, 1985] and has been widely applied for radar measurements in glaciology [e.g., *Blindow*, 1994; *Hempel et al.*, 2000; *Murray et al.*, 2000; *Eisen et al.*, 2002]. It makes use of a special setup of linear geometry, such that the points of reflection at a certain depth remain constant with increasing offset between transmitter and receiver. The velocity-depth function can be inferred from the increase of traveltime with offset, assuming near-horizontal reflectors.

2.5.2.3. Age Estimates of Reflection Horizons

[90] Dating IRHs is achieved by transferring age-depth distribution, as obtained from snow pit and cores as described in section 2.4.2, to the respective depth of the IRH at the location where the age-depth distribution was measured. This is usually achieved by mere comparison or correlation techniques in the depth domain. A new approach utilizes numerical forward modeling of radargrams, based on dielectric profiling of ice cores, to relate depth (and thus age) to the time domain of the radar data [*Eisen et al.*, 2004]. A problem related to the dating of snow layers by core analysis comes along with the spatial separation of GPR

profiles and coring sites. In several cases, the GPR soundings were not always made directly over the exact coring point or in the same year; in some cases, the distance between the coring site and the radar survey exceeded 10 m [*Richardson-Näslund*, 2001]. In other cases, it is not possible to follow isochrones all the way to a coring site, and thus it is not always possible to determine the age of a snow layer by direct comparison with core or pit data. Such a layer can still be dated indirectly using overlapping sections of other internal layers that could be dated directly against cores and pits. This method allows one to obtain approximate estimates of spatial variability in accumulation rate that would otherwise be unobtainable [*Richardson-Näslund*, 2001]. Even if absolute dating is not possible, a qualitative interpretation of spatial accumulation variability can still be achieved [*Vaughan et al.*, 2004].

2.5.2.4. Cumulative Mass

[91] Integration of measured density profiles yields the distribution of cumulative mass with depth. (For more details on density measurements, see section 2.1.) Generally, snow/firn density increases with increasing depth. Thus, the density-depth profile influences the wave speed–depth profile and cumulative mass value. Cumulative mass is usually calculated from the surface down to the depth of the radar reference layer. However, depending on the time interval of interest, it is also possible to calculate the mass difference between two internal reflectors to determine spatial variability of past accumulation rates, similar to firn and ice core studies.

[92] One question coming along with the spatial extent of radar profiles is the lateral homogeneity of density-depth distributions. Snow and firn densities in the dry zone are predominantly determined by overburden pressure, which is governed by local meteorological parameters: temperature, wind, and accumulation rate [*Craven and Allison*, 1998; *Kameda et al.*, 1994]. Depending on the study area, the distributions can be homogeneous over hundreds of kilometers on the polar plateau and in particular at ice divides and domes [*Frezzotti et al.*, 2004; *Richardson-Näslund*, 2004; *Rotschky et al.*, 2004; *Arcone et al.*, 2005b] or could vary considerably at places with high spatial accumulation variability due to strong wind erosion [*Richardson et al.*, 1997; *Spikes et al.*, 2004; *Frezzotti et al.*, 2005]. At Dome C and Talos Dome, dedicated density profile analyses from a number of cores and pits reveal no detectable geographical variation in density or compaction within a 50-km diameter of the dome areas [*Frezzotti et al.*, 2005, 2007; *Urbini et al.*, 2008]. In contrast, especially in coastal regions, variations on short distance scales can be significant [*Richardson-Näslund*, 2004; *Vaughan et al.*, 2004; *Frezzotti et al.*, 2005; *Anschütz et al.*, 2006]. In the latter case, density profiles need to be laterally interpolated to provide information along the GPR profiles. The largest variability in density is usually in the uppermost 3–20 m.

[93] Density data surveyed by core and pit are fitted with polynomial or logarithmic functions, usually yielding a correlation coefficient (R^2) of more than 0.9 for measured and computed densities [e.g., *Richardson et al.*, 1997; *Frezzotti et al.*, 2005]. Because of a change of density function with depth, the density profiles should cover the snow radar investigation depth. The uncertainties associated with each cumulative mass measurement vary with depth.

2.5.3. Errors of GPR-Based Accumulation Estimates

[94] A number of factors determine the final uncertainty of an accumulation estimate based on GPR (Table 2). They can be separated by errors related to determining the depth of the reflector, the age of the reflector, and the cumulative mass above the reflector. Other errors arise by spatially interpolating or extrapolating the density information along a radar profile. Depending on the region of investigation, the density–depth and thus the mass–depth and wave speed–depth distributions can be very homogeneous, e.g., in undisturbed regions on the Antarctic plateau, or very inhomogeneous, as near coastal sites and slope areas.

[95] The operation frequency of the radar system and the characteristic of the source signal determines the possible vertical resolution of a reflector. Theoretically, a quarter of the wavelength is the highest resolution that can be achieved. Another consideration is the ability to separate two neighboring reflectors. According to the Ricker criterion, they can be separated when the traveltime difference in the reflected signals is larger than half the cycle duration of the signal. However, most radars transmit a source signal which contains more than a single cycle, thus reducing the resolution. Two signals can then be separated when the traveltime difference exceeds half the pulse width. GPR is usually operated in a bistatic mode, which means separate antennae at a certain distance (dm to m, depending on frequency) for transmission and reception of the radar signal. This causes an error in estimated depth, especially for reflectors close to the surface (see *Pälli et al.* [2002] for a discussion).

[96] Accuracy of the traveltime–depth conversion depends on the source of information for the velocity profile (e.g., density measurement along a core or from common midpoint radar). Uncertainties in the age estimate of a reflector are caused by the initial uncertainty of the underlying age–depth scale (snow pit, firn, or ice core) and the transfer of the age information for, e.g., a core to the reflector. (For more details on age estimates, see section 2.4.2.) The error in accumulation depends finally on the accuracy of the depth-integrated density profile. Small-scale variations in density, like ice lenses or wind crusts, are averaged out by the integration, and neither cause large errors in cumulative depth or wave speed.

[97] *Spikes et al.* [2004] pointed out that uncertainties are based mainly on the three components: layer thinning due to ice advection, the procedure for depth calibration, and the isochronal accuracy of each horizon. Their results indicate that uncertainties at a firn depth of 10 m are about 4% of the calculated snow accumulation and decrease to 0.5% at a firn depth of 60 m. In general, conservative uncertainty estimates of SMB derived from GPR are some 5% on the polar plateau, most of which stems from the uncertainty in dating. A summary of factors contributing to errors is provided in Table 2.

2.5.4. Spatial Variability of SMB From GPR

[98] Along the Terra Nova Bay–Dome C traverse, standard deviation of variability decreases generally from the coast (47%) to the ice divide (3%) [*Frezzotti et al.*, 2004]. However, sites characterized by relatively complex surface morphology with abrupt changes in slope along wind direction show higher standard deviation (34–47%) than sites that have a low slope along wind direction (5–10%). High standard deviation in spatial variability is also observed inland in the areas of megadune fields (24% [*Frezzotti et al.*, 2002b, 2005]). The lowest values are observed at domes and ice divides (3–9%). Changes in spatial distributions have been observed over the last few centuries using GPR, with a decrease in SMB gradient along the wind direction at Talos Dome and a counterclockwise rotation of SMB distribution in the northern part of Dome C. Observations at Dome C reveal a significant increase in accumulation since the 1950s, which could correlate to altered snow accumulation patterns due to changes in snowfall trajectory. Snow accumulation mechanisms are different at the two domes: a wind-driven snow accumulation process operates at Talos Dome, whereas snowfall trajectory direction is the main factor at Dome C [*Urbini et al.*, 2008].

[99] Along the transect that crosses Talos Dome, analysis of spatial variability shows that in the coastal area, spatial variability reaches 200 kg m^{-2} a^{-1} over 1 km and wind-driven sublimation values may be as high as 260 kg m^{-2} a^{-1}. In the plateau area, spatial variability reaches 40 kg m^{-2} a^{-1} over 1 km, and wind-driven ablation is as high as 50 kg m^{-2} a^{-1} [*Frezzotti et al.*, 2007]. Redistribution processes are only present on a local scale; wind-driven sublimation values represent 20–75% of solid precipitation. Depositional features are very rare, related to the formation of transverse dunes and negligible in the SMB. The spatial variability of SMB at the kilometer scale is 1 order of magnitude higher than its temporal variability (20–30%) at the centennial timescale [*Frezzotti et al.*, 2004].

[100] The spatial variability at sites very close to the coast in Adélie Land is less than 10%. Along coastal and inland slopes the spatial standard deviation, also based on stake line data, increases from 20% to more than 50%. On the plateau the spatial variability varies up to about 20%, but in the undisturbed part of the plateau it was below 10%. Variations of the same order in the three regimes, coastal, transition, and plateau, are evident from stake line data [*Pettré et al.*, 1986], although measurements are less sound than GPR results.

[101] On the plateau in DML, the small-scale variation in accumulation is on the order of 5–15% of the mean accumulation [*Richardson-Näslund*, 2001; *Rotschky et al.*, 2004; *Eisen et al.*, 2005]. Small-scale means over distances of 10 km compare to mean values over 100 km. In the perimeter of the EPICA deep drilling site, accumulation variability is less than 15% on average, but accumulation gradients can be up to 2.5 kg m^{-2} a^{-1} over 1 km [*Eisen et al.*, 2005]. Averaged SMB values for the last 150 years decorrelated over a distance of about 10 km [*Rotschky et al.*, 2004]. In contrast, increased variability of up to 45% [*Richardson and Holmlund*, 1999] occurs on slopes and near the coast. At Camp Victoria, Amundsenisen (2400 m above sea level), and Camp Maudheimvidda (362 m asl), both in DML, *Holmlund et al.* [2000] performed $10–20 \times 20$ km^2 grid net studies to determine the spatial variability in an area with rather low ice flow velocities. They mapped the top 30–40 m and related the observed layers to the layer depth at a drilling spot at the center of the grid. At Maudheimvidda, the variation in layer depths amounted to 40 to 240% of the layer depth at the center of the grid. According to radar data, the pattern seen at the surface could be seen some tens of meters down into the snowpack. At altitudes around 2200–2500 m, at Camp Victoria, the variability was somewhat less pronounced but still on the order of 10%.

2.5.5. Point Measurements Versus GPR-Based SMB Estimates

[102] One could expect that point measurement and GPR yield principally different results because they sample different areas: the cores, stakes, and ultrasonic sensors sample centimeter-scale areas (2–10 cm), while GPR works at the meter scale. Accumulation rates derived by point measurements and GPR methods [*Richardson-Näslund*, 2001, 2004; *Rotschky et al.*, 2004; *Vaughan et al.*, 2004; *Frezzotti et al.*, 2005; *Anschütz et al.*, 2007; *Frezzotti et al.*, 2007] agree fairly well, the discrepancy ranged from a few percent to 20%, and the results do not indicate any systematic errors. *Frezzotti et al.* [2005] found major differences between point measurements and GPR (20%) along the Terra Nova Bay–Dome C traverse in regions of large spatial variability in SMB (47% over 15 km at maximum). At this site, two cores were drilled a few tens of meters apart and show a 13% difference in accumulation for the tritium/β marker horizons [*Frezzotti et al.*, 2005]. Detailed chemical studies in 16×6 m snow pits combined with GPR measurements on the polar plateau in DML found that the variability of snow layer thickness at the microscale was on average 9% [*Stenberg et al.*, 1999]. A qualitatively good comparison between stake line measurements and GPR layer architecture enabled *Vaughan et al.* [2004] to deduce that the observed IRH are isochrones. For layers several tens of meters deep, covering more than a century, a problem exists when comparing core and GPR measurements when GPR traverses pass several kilometers away from the core. Although values are still comparable, a detailed match is difficult [*Rotschky et al.*, 2004].

3. REPRESENTATIVITY AND LIMITATIONS

[103] Section 2 presented the different techniques carried out on the ground to determine accumulation, discussed difficulties associated with the measurements, and provided error estimates. Once values for the SMB are available, one asks what these values actually mean? Are they just valid for a short period of time, or just in the very vicinity of the measurement locations, or both? This brings us to the issue of the representativity, which is fundamental, as the inter-

pretation of SMB requires consideration of the climatic context, also on larger temporal and spatial scales. In this section we summarize important accumulation characteristics derived from the different measurement techniques and discuss the spatial and temporal representativity of the data.

[104] For the application of SMB data for the different purposes described in section 1, the three key questions are (1) What is the temporal representativity? (2) What is the spatial representativity? (3) Are spatial and temporal signals linked? Related issues are the stability of accumulation patterns in time. Do values at different locations with different mean SMB fluctuate synchronously, i.e., do they covary? Or do temporal changes, for instance, induced by short- and long-term local climate changes, also change the accumulation pattern, resulting in independent fluctuations? Likewise, the effect of ice flow has to be taken into account for core and GPR interpretations on longer timescales, as advection causes mixing of temporal signals with spatial information. For a reliable interpretation of SMB data, these factors have to be separated.

3.1. Temporal Representativity

[105] Time series obtained from stakes and ultrasonic measurements indicate a large interannual variability in accumulation, with variations of up to nearly 50% with respect to the 50-year average accumulation from firn cores [*Frezzotti et al.*, 2007]. *Monaghan et al.* [2006] combine model simulations and observations primarily from cores. They point out that yearly and decadal snowfall variability at local and continental scales is very large. Comparison between stake and core values makes it possible to measure the frequency distribution and thus to infer the probability of identifying missing layers and also the lowest and highest SMB values in cores. Significant differences between core and stake measurements have been observed at sites with SMB < 200 kg m^{-2} a^{-1} [*Frezzotti et al.*, 2007]. Reasons could be the misidentification of annual layers from seasonal signals and the consequent error in the definition of high and low values (values with differences >40% with respect to average value) or/and the slight variations in input timing of the chemical or isotopic composition (e.g., interannual variability in peak-input timing of sulphate could vary by weeks). The misidentification could be due to large annual peaks that could be interpreted as a double year or to two adjacent peaks that will not be stratigraphically detectable because they are sufficiently narrow and could therefore be interpreted as a single year. Signal noise is produced principally by postdepositional processes such as wind erosion, drift, and redeposition. Postdepositional noise primarily influences the high frequencies [*Fisher et al.*, 1985], and misidentification of an annual layer results in overestimation of accumulation in 1 year and to an underestimation in the preceding or following year. Both noise and error reduce the temporal representativeness of the time series.

[106] At the South Pole, the frequency distribution of stratigraphic layer thicknesses in cores and in a snow pit is not compatible with a significant number (between 1% and 5% probability) of missing layers associated with zero accumulation years inferred from measurements of stake heights. The original implication that a large percentage of years (about 10%) is missing from the ice core stratigraphy [*Van der Veen and Bolzan*, 1999; *Mosley-Thompson et al.*, 1995] has been found to be an overestimate [*Mosley-Thompson et al.*, 1999] (see also section 2.2.4). In general, stake or ultrasonic measurements are the only way to detect zero accumulation or erosion values on an annual or seasonal scale.

[107] Analysis of Gaussian distributions of accumulation versus SMB from stake farms shows that only sites with SMB > 750 kg m^{-2} a^{-1} have present values that are representative to within ±10% at an annual scale [*Frezzotti et al.*, 2007]. The SMB distribution shows that more than 80% of stakes at sites with low SMB around 80 kg m^{-2} a^{-1} and more than 40% of stakes at high SMB sites ($\sim$250 kg m^{-2} a^{-1}) present SMB differences of more than ±10% with respect to the mean. The temporal representativity increases with multiyear averages: for high SMB, values are representative at ±10% using three cumulative years; for a SMB of 80–150 kg m^{-2} a^{-1}, using 5–7 cumulative years is necessary [*Frezzotti et al.*, 2007]. *Goodwin et al.* [2003] propose that the 3-year running mean accumulation data from eastern Wilkes Land cores (235–570 kg m^{-2} a^{-1}) are representative for the precipitation minus evaporation signal rather than the local microrelief noise. The same timescale is found to be significant by wavelet analyses of electrical records by *Karlöf et al.* [2006]; that is, the correlation between different records is highest in the 1- to 3-year period. This is attributed to the fact that most material emitted by volcanic eruptions is removed from the atmosphere within 3 years of eruptions, including deposition on the ice sheets. Their study implies that the temporal and spatial representativity of SMB and the records from which it is derived are not necessarily the same. At the South Pole, *McConnell et al.* [1997] computed the average time (310 years) required to statistically ensure that each monthly SMB record within the year is adequately represented in the time average. They also pointed out that the averaging of adjacent cores would decrease the time window proportionally. *Van der Veen and Bolzan* [1999] pointed out that noise could be removed using a Gaussian weighting function with a standard deviation of about 5 years. At the coastal region of Adélie Land, reevaluation of older stake line data from *Pettré et al.* [1986] indicates interannual standard variations on the order of 45%.

[108] *Genthon* [2004] calculates the variability and the radius of decorrelation of precipitation and precipitation minus evaporation over Antarctica from climate models and meteorological analyses. Interannual variability ranges from 5 to 40% of the mean. On the century scale, however, a number of GPR studies (aiming at the spatial characteristics presented next) reveal that the accumulation patterns are stable in time.

3.2. Spatial Homogeneity and Variations

[109] Stake farms and lines have given an indication of the spatial variability in SMB on various scales, e.g., the quasi-uncorrelated annual accumulation caused by microrelief at low-accumulation sites on the plateau. Given the amount of resources required to deploy and maintain stake networks, however, the volume of data that they have produced is generally low. The emergence of GPR techniques has dramatically increased our ability to measure, and therefore understand, the spatial variability in SMB. A number of GPR surveys (see section 2.5.4) reveal that spatial variability of SMB at the kilometer scale can be up to 1 order of magnitude higher than its temporal variability (maximum 20–30%) at the multidecadal/secular and centennial timescale. Generally, the patterns of spatial variability are stable in time at least over a couple of decades to centuries. Stationary features are of comparable length scales (kilometers to tens of kilometers) [*Richardson-Näslund*, 2004; *Vaughan et al.*, 2004; *Frezzotti et al.*, 2004; *Eisen et al.*, 2005]. In rare cases, like the East Antarctic megadune fields, migrating accumulation patterns occur [*Frezzotti et al.*, 2002b]. Recently, migrating features on the 5-km scale were observed close to the coast [*Anschütz et al.*, 2006], although their variations are less pronounced and laterally extensive than megadunes.

[110] Several authors demonstrate the dependence of SMB on temperature, elevation, saturation vapor pressure, and distance from the open ocean [e.g., *Muszynski and Birchfield*, 1985; *Giovinetto et al.*, 1990; *Fortuin and Oerlemans*, 1990]. Although common, large-scale patterns are not always simple [e.g., *Smith et al.*, 2002]. The high spatial variability of SMB on the 1- to 10-km scale is mostly explained by wind-driven processes, being a function of surface slope [*King et al.*, 2004; *Frezzotti et al.*, 2004]. Likewise, the SMB of annual stake measurements is also related to morphology via the surface slope [*McConnell et al.*, 1997; *Frezzotti et al.*, 2005]. However, *Frezzotti et al.* [2004] point out that along some transects (Talos Dome, Dome C) the maximum value of snow accumulation is highly correlated with firn temperatures and represents the snow precipitation minus surface sublimation (ablation not induced by wind). The difference between the maximum and minimum SMB values at these sites represents mainly ablation processes driven by katabatic winds. These wind-driven sublimation phenomena, controlled by the slope along the prevalent wind direction, have considerable impact on the spatial distribution of SMB. They sublimate and export huge quantities of snow into the atmosphere and then into the ocean, leading to a nonnegligible term in continental SMB studies [*Frezzotti et al.*, 2004, 2007]. The direct snow redistribution process is local (e.g., sastrugi formation) and has a strong impact on the annual variability of accumulation at the annual/meter scale (i.e., noise in ice cores).

[111] Whereas SMB based on GPR and stake lines shows that decadally averaged spot measurements are only representative within a small area of a few square kilometers around the site (i.e., indicate relatively short correlation lengths), precipitation is much more homogeneous. On the basis of the analysis of climate models and meteorological data, the decorrelation length of precipitation and precipitation minus evaporation of about 500 km is comparatively large [*Genthon*, 2004]. Nevertheless, as for SMB features, large differences occur between the coast and the interior, with particularly low values on the ridges and domes. The correlation length for real SMB is much shorter than that of precipitation or precipitation minus evaporation due to depositional and postdepositional processes. However, by spatially smoothing the small-scale noise (e.g., as defined by *Genthon et al.* [2005]), one may expect a correlation with precipitation at the 100-km scale.

3.3. Associations Between Spatial and Temporal Variability

[112] The spatial scale of significance for a single firn or ice core record is a critical issue for the interpretation of the accumulation time series. Microrelief (sastrugis) introduces a high-frequency, quasi-stochastic variability into core records of annual layer thickness [*Fisher et al.*, 1985; *Van der Veen and Bolzan*, 1999]. Medium-scale undulations (wavelengths < 20 km) in surface topography up stream from a core-drilling site can cause variations in measured accumulation rates. One of the earliest results on this topic reveals that accumulation in troughs can be 30–50% more than on exposed surface crests [*Gow and Rowland*, 1965]. Meanwhile, as demonstrated in section 3.2, knowledge about the spatial variability has increased significantly. The stratigraphic record of a core is affected by the flow of ice, so the material at depth is slowly moved away from the original deposition site. If topographic features capable of changing the accumulation are located up stream of a core site, they can generate decadal to centennial long periods of accumulation consistently above or below the long-term mean because layers deeper in the record will have been deposited at these topographic troughs and crests [*Richardson and Holmlund*, 1999; *Kaspari et al.*, 2005; *Hamilton*, 2004]. The only way to really understand the significance of a core record is to know something about the spatial field of SMB surrounding the core and also to have a good idea of the rate of movement of the ice through this field. Analysis of these data would allow some separation of the spatial and temporal variability that the core represents. This is the only way to understand the true significance of accumulation rate histories in cores. Any core for which these data are not available, or that is collected on fast moving ice, or is sufficiently deep to have moved more than a fraction of the correlation length for SMB, contains an accumulation rate history that is a mixed signal and is likely not interpretable.

[113] *Richardson and Holmlund* [1999] demonstrate the importance of determining the spatial significance of cores and recommend radar surveys prior to drilling, as this is the easiest way to get this information. The timescale for which this influence is important depends on the specific SMB and flow velocities at the site. However, it is possible to resolve temporal signals if the effects of local topography and ice

flow are considered [*Spikes et al.*, 2004]. The length of periodic variations due to mesoscale relief and/or megadunes depend on ice velocity and SMB and can therefore vary in space and time. *Frezzotti et al.* [2005] point out that in megadune areas the distortion of records is characterized by a SMB periodicity of about 1500 years. In coastal areas with relatively large flow velocities and significant topographic variations, spatial SMB variations can influence temporal records on scales as short as a few decades [*Anschütz et al.*, 2006]. *Arcone et al.* [2005b] demonstrate how the same effect is present in the GPR data themselves and must be corrected for. Consequently, several techniques have been developed to deconvolve spatial from temporal effects by employing GPR data [*Hamilton*, 2004; *Arcone et al.*, 2005b; *Parrenin et al.*, 2006].

3.4. Spatial Interpolation

[114] There are probably several different length scales for coherence in the true field of SMB. There may be greater complexity in places, but in general, we might argue that the shortest length scale is governed by the sastrugi length (0.1–100 m), the next is governed by the topography over which the wind transport of snow occurs (10–10,000 m), and the longest is governed by the regional differences in the supply of precipitation governed by synoptic climate (100–4000 km). The efforts at interpolation on the continental scale have usually been focused on producing a map of the third correlation scale, accepting that there is variability on the other two length scales that are not represented (see treatment by *Vaughan et al.* [1999a]). Understood in this way, attempts to use local measurements to draw a continental-scale map make some sense, although they are fraught with pitfalls. Improved interpolation can also be achieved by subdividing data sets of local measurements in regions of comparable properties (e.g., coastal areas and plateau region) and then performing interpolation for each region separately [*Rotschky et al.*, 2007]. The complexity and quality of the efforts have undoubtedly increased in the last few decades, culminating with the explicit and formal treatment of uncertainty given by *Arthern et al.* [2006]. The map presented in their study will not be definitive in any sense but is a major step forward, since it includes a formal assessment of the uncertainty involved with the gridding process.

4. CONCLUSION AND RECOMMENDATIONS

[115] We have presented a summary of East Antarctic SMB characteristics and techniques used to acquire these. Our goal is to improve the knowledge of potential users about the difficulties associated with interpretation of measurements but also to highlight the need to perform more measurements and to use the ones currently available. We have demonstrated that SMB varies significantly in time and space on various scales. None of available measurement techniques are able to capture all scales simultaneously, neither can they be combined to provide area-wide measurements on basin scales, mainly as a result of logistical constraints. Nevertheless, regionally confined studies provide valuable information from which a number of recommendations for data acquisition and potential data users can be proposed:

[116] 1. Decadal SMB values decorrelate on the 1- to 10-km scale but covary over length scales of hundreds of kilometers. The recent discovery from GPR data that on this scale, there exists a static (topographically induced) pattern of SMB, which cannot be observed in or estimated from sparse point measurements of SMB, is of utmost importance. These observations clearly indicate the potential pitfalls of using isolated measurements as being representative of a larger region. These pitfalls can be avoided and point measurements (usually cores) given regional significance by the simple expedient of acquiring GPR data around the core location. Ideally, the GPR profiles should span several ice thicknesses up flow, down flow, and across flow and should be tuned to acquire layer information at least as deep as the core. A well-dated core combined with GPR data will allow independent calculation of spatial and temporal means and variations for the region, plus their errors. These are the parameters that need to be routinely acquired and used if we are to substantially advance our understanding of continent-wide patterns of SMB across the Antarctic ice sheet.

[117] 2. Spatial variability increases as topographic complexity increases, caused by wind deposition/erosion. It is important to consider aeolian processes in general but especially when selecting sites for firn and ice coring in areas with relatively complex topography. Slope variations of only a few meters per kilometer have a significant impact on wind-derived snow accumulation processes and also therefore on the accumulation records. To fully understand the dominant processes that affect SMB and to incorporate these into global climate reconstructions, high-resolution representativity of SMB from cores is needed. Statistically meaningful reconstructions at annual and/or seasonal scale can be produced using multiple cores for each "center of action."

[118] 3. The effective use of ultrasonic height ranger data in East Antarctic mass balance research requires that meteorological data are collected simultaneously and at the same location, so that the individual components of the SMB (sublimation, melt, snowdrift sublimation) can be quantified or at least estimated. Because of the operational accuracy of 2–3 cm, ultrasonic height ranger data are less useful to the study of individual accumulation events on the dry interior plateau of Antarctica. However, they are very valuable to to determination of intraannual variability and seasonal cycles, which at many places are not known, not even qualitatively.

[119] 4. A considerable problem, which presently remains unsolved, is the conversion of height to mass changes for both stakes and ultrasonic sounders. This needs urgent attention, especially if the use of ultrasonic height ranger and stake data increases in the future. Moreover, the spatial interpolation and extrapolation of density profiles require further input.

TABLE 3. Possible Usage of Ground Truth SMB Estimates[a]

Source	Estimated SMB Property	Ground Truth Application
Stake farm	decorrelation and covariance on (sub)annual and subkilometer scale	laser altimetry
Stake line	decorrelation and covariance on (sub)annual and kilometer scale	laser altimetry, gravimetry
Ultrasonic sounders	high temporal resolution of single events, covariance	regional climate modeling
Snow pits	high-resolution time series	regional climate modeling, microwave radiometry
Cores	high-resolution and long-term record	regional climate modeling, microwave radiometry
GPR	temporally averaged decorrelation	altimetry, gravimetry

[a]All methods provide estimates of SMB. Specific properties, however, can only be determined by specific methods.

[120] 5. An apparently trivial aspect is documentation. Experience with older data sets shows that documentation is essential but, unfortunately, often neglected and partly even missing. The documentation should contain an exact description of how the raw data sets (e.g., length measurements) were obtained, which auxiliary parameters (e.g., density) were determined, and how measured quantities were finally converted to SMB.

[121] 6. For subsurface measurements, it is a great advantage if one can determine in the field if a good dating horizon has been reached. This can be achieved by several nondestructive measurements, either in the hole, in the pit, or along the core. Cores should be drilled to a depth covering the period back to the eruption of Tambora in A.D. 1815 and the unknown eruption in A.D. 1809.

[122] 7. When retrieving a firn core, there is often some unrecoverable loss of core material. This occurs predominantly in the upper meters. A correction scheme similar to a procedure described by *Whillans and Bolzan* [1988] is recommended, with special attention to an accurate measurement of diameter. To facilitate the identification of overlap between the core and a snow pit, the pit should be deep enough to cover one dating horizon that can also be captured in the adjacent drilled core. This latter task, however, is difficult and not always possible.

[123] 8. Accumulation on the plateau is, in general, more "well behaved" in terms of spatial representativity (apart from megadune fields) than the transition region from the plateau to the coastal areas, where high katabatic winds occur frequently and the morphological variability is often high (e.g., nunataks, valley glaciers). We need more sampling in the coastal regions if we are to improve continental average assessments.

[124] Ground truthing is essential for methods like remote sensing and numerical modeling, which require (and provide) estimates of decorrelation lengths, covariance, and associated uncertainties. The serviceability depends on the type of field data and their usage (Table 3). As a suitable combination, stake farms and GPS surveys in 1 km^2 areas provide a reference for laser altimetry. Decadal measurements of stake lines provide covariance on an annual scale for gravimetry, and ultrasonic sounders provide single events for regional models. Pits, cores, and GPR provide longer-term records for regional- or continental-scale modeling as well as spatial characteristics for remote sensing.

[125] From the point of view of specific mass balance estimates, the potential that with increasing precipitation, the East Antarctic Ice Sheet could be the single largest ameliorator of sea level rise, and could balance a few tens of centimeters of sea level rise over the coming century, means that setting and understanding the baseline (current rates and trends in accumulation) are highly important. The accounting methods reviewed in this paper to determine the mean net annual SMB provide a significant contribution to this aim. Although they may never be suitable to infer the specific mass balance of the entire ice sheet, or even regions of it, by ground-based measurements alone, the records of SMB history and its spatial characteristics are definitely required to determine if the ice sheet's SMB is changing in a secular fashion and whether or not this pattern is related to anthropogenic climate change. Assessments of ice sheet surface elevation changes [*Davis et al.*, 2005; *Zwally et al.*, 2005] will continue to yield the most precise results for mass balance estimates of specific drainage basins or ice sheets as a whole. In the intermediate-term perspective, gravity measurements and related time series may potentially become more accurate than they are at present [e.g., *Chen et al.*, 2006; *Velicogna and Wahr*, 2006; *Ramillien et al.*, 2006], thus providing valuable contributions to other techniques.

[126] New airborne techniques for determining the internal layering near the surface of ice masses are currently being developed, mainly in the context of calibration and validation campaigns for satellite remote sensors. The Airborne Synthetic Aperture and Interferometric Radar Altimeter (ASIRAS) System [*Mavrocordatos et al.*, 2004] and the D2P (delay/Doppler phase monopulse) radar [*Stenseng et al.*, 2005], for instance, do not only operate as classical altimeters or synthetic aperture radar (SAR) but also utilize an interferometric SAR mode. They are basically a replicate of the SAR/Interferometric Radar Altimeter (SIRAL) instrument to be operated on board CryoSat-2. The systems provide vertical resolution comparable to high-frequency GPR. The larger footprints cause less horizontal resolution than GPR but allow a higher spatial coverage. The advantage lies in operating such a system from an airplane, covering a relatively large area with profiles over a short period of time. Recent ASIRAS results from the dry snow zone [*Hawley et al.*, 2006] and percolation zone [*Helm et al.*, 2007] of the Greenland ice sheet, accompanied by ground-based measurements [*Scott et al.*, 2006], indicate that annual layers can be continuously detected by this system, promising extended future measurements in Antarctica. The combination of satellite remote sensors with airborne surveys and

dedicated ground measurements will likely remain the primary line of action for the next decade to obtain mass balance estimates for large parts of the ice sheet.

APPENDIX A: OPTIMAL ESTIMATION OF STAKE INTERVAL

[127] By studying the accumulation correlation of nearby stakes as a function of distance, *Barkov and Lipenkov* [1978] evaluated the optimal distance between stakes (putting the stakes too close to each other will not significantly increase the accuracy due to accumulation correlation at the adjacent stakes) using a "structural function" $b_{\Delta h}(\lambda)$ as a measure of correlation:

$$b_{\Delta h}(\lambda) = 2\sigma^2_{\Delta h}(1 - r_{\Delta h}(\lambda)), \tag{A1}$$

with snow buildup Δh, its spatial variability $\sigma_{\Delta h}$, distance between stakes λ, and the correlation coefficient between snow buildup at two stakes $r_{\Delta h}$. The optimal distance is reached as soon as the correlation turns insignificant (and $b_{\Delta h}$ reaches a saturation value). They found that at Vostok Station the annual accumulation at two points is practically not correlated at the distance of 65 m. Thus, Vostok stake farm with its distance between adjacent stakes of 25 m is close to optimum and even slightly oversampled. This implies that for studies aiming at smaller scales, stake distances on the order of several tens of meters are sufficient. However, both optimal distance and the saturation values vary over Antarctica.

[128] The structural function is used to determine optimal parameters (stake farm size/profile length and amount of stakes) of the stake farm/profile [*Barkov and Lipenkov*, 1978]:

$$\sigma^2_{\bar{\Delta h}} = \sigma^2_{\Delta h} - \frac{1}{n^2}\sum_{i=1}^{n-1}(n-i)b_{\Delta h}(i\Delta l) \tag{A2}$$

where $\sigma_{\bar{\Delta h}}{}^2(l, n)$ is the total error of snow buildup depending on the length of the route (l) and amount of stakes (n); $\sigma^2_{\Delta h}$ is the spatial variability of snow buildup (standard deviation); i is the index number of a given stake; Δl is the interval between adjacent stakes; and $b_{\Delta h}(i\Delta l)$ is the value of the structural function for the distance $i\Delta l$. The optimal parameters of the stake farm correspond to the minimum value of $\sigma_{\bar{\Delta h}}{}^2(l, n)$. This method is well suited for a series, members of which are not independent, which is the case for the snow buildup spatial distribution.

GLOSSARY

Ablation: Negative surface mass balance.

Accumulation: Positive surface mass balance.

Antarctic ice sheet: Grounded part of the Antarctic polar ice cap, divided in the East and West Antarctic ice sheets.

Blue ice area: Area of negative surface mass balance, where ice formed up stream emerges to the surface. Because of the higher density of the ice this appears blue. Surrounding areas with positive mass balance appear white because of the lower density of firn and snow compared to ice.

Firn core: Core extracted from the upper tens of meters from the firn, above the pore close-off depth, where no bubbles are yet present.

Ground-penetrating radar: Geophysical tool that emits electromagnetic waves from the surface into the ground; measures the round-trip traveltime of the wave that is returned from reflecting horizons.

Ice core: Core extracted from below the pore close-off depth, where bubbles have formed and are enclosed by ice.

Mean net annual surface mass balance: Summary of terms contributing to the solid, liquid, and gaseous transfer of water across the surface of the ice sheet; commonly normalized to kg m^{-2} a^{-1} but often given in millimeters water equivalent.

Radiochronology: Determination of age from the natural decay of radioactive species.

Snow pit: Trench excavated in the snow, often of rectangular cross section, with a vertical wall on one side to investigate the stratigraphy and to take samples.

Stake: Pole put into the snow (often bamboo, sometimes aluminium or similar). The height above snow or ice surface is measured at intervals to determine mass balance.

Stake farm: Combination of stakes in a two-dimensional setup, often as a rectangular grid.

Stake line: Combination of stakes along a one-dimensional line, often hundreds of kilometers long.

Surface mass balance: Short for mean net annual surface mass balance.

Time marker: Unambiguously identifiable feature of known age in time series records.

Ultrasonic sounder: Device to measure the distance to the surface. Operates with sound wave at ultrasonic frequencies.

Volcanic horizon: Deposits from volcanic eruptions (acids, ash) identifiable in layers, which were deposited at the ice sheet surface, buried, and submerged over time.

[129] **ACKNOWLEDGMENTS.** Special thanks to Tas van Ommen for his encouragement and contributions to the initial kick-off of the paper and to Martin Sharp and Ian Goodwin for their reviews. Data contributed by Robert Arthern for Figure 2 are greatly acknowledged. The background of this work is based on decades of field measurements and generations of scientists, made possible by the different national polar research institutions. We acknowledge their long-term support for designing and organizing ground-based measurements of Antarctic surface mass balance and the efforts by logistics to making them real. This work, moreover, greatly profited from discussions with numerous colleagues at the different institutions, too many to list them all here. This research was partly funded by the Italian National Antarctic Research Program (PNRA) and the Deutsche Forschungsgemeinschaft through an "Emmy Noether" scholarship, grant EI 672/1, to O.E. The Editor responsible for this paper was Ian Fairchild. He thanks Ian Goodwin as the technical reviewer and Martin Sharp as the cross-disciplinary reviewer.

REFERENCES

Alley, R. B., et al. (1997), Visual-stratigraphic dating of the GISP2 ice core: Basis, reproducibility, and application, *J. Geophys. Res.*, *102*(C12), 26,367–26,381.

Andreas, E. L. (2002), Parameterizing scalar transfer over snow and ice: A review, *J. Hydrometeorol.*, *3*, 417–432.

Annan, A. P., and J. L. Davis (1976), Impulse radar sounding in permafrost, *Radio Sci.*, *11*(4), 383–394.

Anschütz, H., O. Eisen, W. Rack, and M. Scheinert (2006), Periodic surface features in coastal East Antarctica, *Geophys. Res. Lett.*, *33*, L22501, doi:10.1029/2006GL027871.

Anschütz, H., O. Eisen, H. Oerter, D. Steinhage, and M. Scheinert (2007), Investigating small-scale variations of the recent accumulation rate in Central Dronning Maud Land, East Antarctica, *Ann. Glaciol.*, *46*, 14–21.

Anschütz, H., D. Steinhage, O. Eisen, H. Oerter, M. Horwath, and U. Ruth (2008), Small-scale spatio-temporal characteristics of accumulation rates in western Dronning Maud Land, Antarctica, *J. Glaciol.*, in press.

Arcone, S. A., V. B. Spikes, and G. S. Hamilton (2005a), Phase structure of radar stratigraphic horizons within Antarctic firn, *Ann. Glaciol.*, *41*, 10–16.

Arcone, S. A., V. B. Spikes, and G. S. Hamilton (2005b), Stratigraphic variation within polar firn caused by differential accumulation and ice flow: Interpretation of a 400 MHz short-pulse radar profile from West Antarctica, *J. Glaciol.*, *51*(174), 407–422.

Arthern, R. J., D. P. Winebrenner, and D. G. Vaughan (2006), Antarctic snow accumulation mapped using polarization of 4.3-cm wavelength microwave emission, *J. Geophys. Res.*, *111*, D06107, doi:10.1029/2004JD005667.

Barkov, N. I., and V. Y. Lipenkov (1978), Nakoplenie snega v rayone stantsii Vostok v 1970–1973 (Snow accumulation in the area of Vostok Station in 1970–1973), *Inf. Bull. Sov. Antarct. Exped.*, *98*, 63–68.

Barkov, N. I., and V. Y. Lipenkov (1996), Nakoplenie snega v rayone stantsii Vostok, Antarktida, v 1970–1992 (Snow accumulation in the area of Vostok Station, Antarctica, in 1970–1992), *Mater. Glyatsiol. Issled.*, *80*, 87–88.

Barnes, P. R. F., E. W. Wolff, R. Mulvaney, R. Udisti, E. Castellano, R. Röthlisberger, and J.-P. Steffensen (2002), Effect of density on electrical conductivity of chemically laden polar ice, *J. Geophys. Res.*, *107*(B2), 2029, doi:10.1029/2000JB000080.

Bindschadler, R., H. Choi, C. Shuman, and T. Markus (2005), Detecting and measuring new snow accumulation on ice sheets by satellite remote sensing, *Remote Sens. Environ.*, *98*(4), 388–402.

Bintanja, R. (1999), On the glaciological, meteorological, and climatological significance of Antarctic blue ice areas, *Rev. Geophys.*, *37*, 337–359.

Bintanja, R. (2003), The mass balance of a dry snow surface during a snowstorm, *Ann. Glaciol.*, *38*, 79–83.

Black, H. P., and W. Budd (1964), Accumulation in the region of Wilkes, Wilkes Land, Antarctica, *J. Glaciol.*, *5*(37), 3–15.

Blindow, N. (1994), The central part of the Filchner-Ronne Ice Shelf, Antarctica: Internal structures revealed by 40 MHz monopulse RES, *Ann. Glaciol.*, *20*, 365–371.

Bogorodsky, V. V., C. R. Bentley, and P. E. Gudmandsen (1985), *Radioglaciology*, D. Reidel, Dordrecht, Netherlands.

Braaten, D. A. (1994), Instrumentation to quantify snow accumulation and transport dynamics at two locations on the Ross Ice Shelf, *Antarct. J. U.S.*, *29*(5), 86–87.

Bromwich, D. H., A. J. Monaghan, J. G. Powers, J. J. Cassano, H. L. Wei, Y. H. Kuo, and A. Pellegrini (2003), Antarctic mesoscale prediction system (AMPS): A case study from the 2000–01 field season, *Mon. Weather Rev.*, *131*, 412–434.

Budd, W. F., and I. N. Smith (1982), Large-scale numerical modelling of the Antarctic ice sheet, *Ann. Glaciol.*, *3*, 42–49.

Bull, C. (1971), Snow accumulation in Antarctica, in *Research in the Antarctic*, edited by L. Quam, pp. 367–421, Am. Assoc. for the Adv. of Sci., Washington, D. C.

Carter, M. W., and A. A. Moghissi (1977), Three decades of nuclear testing, *Health Phys.*, *33*, 55–71.

Chen, J. L., C. R. Wilson, D. D. Blankenship, and B. D. Tapley (2006), Antarctic mass rates from GRACE, *Geophys. Res. Lett.*, *33*, L11502, doi:10.1029/2006GL026369.

Clarke, T. S., and C. R. Bentley (1994), High-resolution radar on Ice Stream B2, Antarctica: Measurements of electromagnetic wave speed in firn and strain history from buried crevasses, *Ann. Glaciol.*, *20*, 153–159.

Clough, J. W. (1977), Radio echo sounding: Reflections from internal layers in ice sheets, *J. Glaciol.*, *18*(78), 3–14.

Clough, J. W., and C. R. Bentley (1970), Measurements of electromagnetic wave velocity in the East Antartic ice sheet, in *International Symposium on Antarctic Glaciological Exploration (ISAGE), Proceedings SCAR/IASH Symposium*, edited by A. J. Gow et al., *IAHS Publ.*, *86*, 115–128.

Clow, G. D., C. P. McKay, G. M. Simmons Jr., and R. A. Wharton Jr. (1988), Climatological observations and predicted sublimation rates at Lake Hoare, Antarctica, *J. Clim.*, *1*, 715–728.

Coffey, M. T. (1996), Observations of the impact of volcanic activity on stratospheric chemistry, *J. Geophys. Res.*, *101*(D3), 6767–6780.

Cole-Dai, J., and E. Mosley-Thompson (1999), The Pinatubo eruption in South Pole snow and its potential value to ice-core paleovolcanic records, *Ann. Glaciol.*, *29*, 99–105.

Cole-Dai, J., E. Mosley-Thompson, and L. G. Thompson (1997), Annually resolved Southern Hemisphere volcanic history from two Antarctic ice cores, *J. Geophys. Res.*, *102*(D14), 16,761–16,771.

Cole-Dai, J. H., E. Mosley-Thompson, S. P. Wight, and L. G. Thompson (2000), A 4100-year record of explosive volcanism from an East Antarctica ice core, *J. Geophys. Res.*, *105*(D19), 24,431–24,441.

Corr, H. F. J., A. Jenkins, K. W. Nicholls, and C. S. M. Doake (2002), Precise measurement of changes in ice-shelf thickness by phase-sensitive radar to determine basal melt rates, *Geophys. Res. Lett.*, *29*(8), 1232, doi:10.1029/2001GL014618.

Craven, M., and I. Allison (1998), Firnification and the effects of wind-packing on Antarctic snow, *Ann. Glaciol.*, *27*, 239–245.

Crozaz, G., and C. C. Langway Jr. (1966), Dating Greenland firn-ice cores with ^{210}Pb, *Earth Planet. Sci. Lett.*, *1*(4), 194–196.

Crozaz, G., E. Picciotto, and W. D. Breuck (1964), Antarctic snow chronology with ^{210}Pb, *J. Geophys. Res.*, *69*(12), 2597–2604.

Curran, M. A. J., G. B. Jones, and H. Burton (1998), Spatial distribution of dimethylsulfide and dimethylsulfoniopropionate in the Australasian sector of the Southern Ocean, *J. Geophys. Res.*, *103*(D13), 16,677–16,689.

Dansgaard, W. (1964), Stable isotopes in precipitation, *Tellus*, *16*, 436–468.

Dansgaard, W., S. J. Johnsen, H. B. Clausen, and N. Gundestrup (1973), Stable isotope glaciology, *Medd. Groenl.*, *197*(2), 53.

Dansgaard, W., et al. (1993), Evidence for general instability of past climate from a 250-kyr ice-core record, *Nature*, *364*, 218–220, doi:10.1038/364218a0.

Davis, C. H., Y. Li, J. R. McConnell, M. M. Frey, and E. Hanna (2005), Snowfall-driven growth in East Antarctic ice sheet mitigates recent sea-level rise, *Science*, *308*(5730), 1898–1901.

Delmas, R., and M. Pourchet (1977), Utilisation de filtres échangeurs d'ions pour l'étude de l'activité Béta globale d'un carottage glaciologique, *IAHS Publ.*, *118*, 159–163.

Delmas, R. J., S. Kirchner, J. M. Palais, and J. R. Petit (1992), 1000 years of explosive volcanism recorded at the South Pole, *Tellus, Ser. B*, *44*, 335–350.

Dibb, J. E., and M. Fahnestock (2004), Snow accumulation, surface height change, and firn densification at Summit, Greenland: Insights from 2 years of in situ observation, *J. Geophys. Res.*, *109*, D24113, doi:10.1029/2003JD004300.

Dibb, J. E., P. A. Mayewski, C. S. Buck, and S. M. Drummey (1990), Scientific correspondence: Beta radiation from snow, *Nature*, *345*, 25.

Dixon, D., P. A. Mayewski, S. Kaspari, S. Sneed, and M. Handley (2004), A 200-year sub-annual record of the primary sources of sulfate in West Antarctica, *Ann. Glaciol.*, *39*, 545–556.

Doran, P. T., C. P. McKay, G. D. Clow, G. L. Dana, A. G. Fountain, T. Nylen, and W. B. Lyons (2002), Valley floor climate observations from the McMurdo dry valleys, Antarctica, 1986–2000, *J. Geophys. Res.*, *107*(D24), 4772, doi:10.1029/2001JD002045.

Eisen, O., U. Nixdorf, F. Wilhelms, and H. Miller (2002), Electromagnetic wave speed in polar ice: Validation of the CMP technique with high resolution DEP and γ-density measurements, *Ann. Glaciol.*, *34*, 150–156.

Eisen, O., F. Wilhelms, U. Nixdorf, and H. Miller (2003a), Identifying isochrones in GPR profiles from DEP-based forward modelling, *Ann. Glaciol.*, *37*, 344–350.

Eisen, O., F. Wilhelms, U. Nixdorf, and H. Miller (2003b), Revealing the nature of radar reflections in ice: DEP-based FDTD forward modeling, *Geophys. Res. Lett.*, *30*(5), 1218, doi:10.1029/2002GL016403.

Eisen, O., U. Nixdorf, F. Wilhelms, and H. Miller (2004), Age estimates of isochronous reflection horizons by combining ice core, survey, and synthetic radar data, *J. Geophys. Res.*, *109*, B04106, doi:10.1029/2003JB002858.

Eisen, O., W. Rack, U. Nixdorf, and F. Wilhelms (2005), Characteristics of accumulation rate in the vicinity of the EPICA deep-drilling site in Dronning Maud Land, Antarctica, *Ann. Glaciol.*, *41*, 41–46.

Eisen, O., I. Hamann, S. Kipfstuhl, D. Steinhage, and F. Wilhelms (2007), Direct evidence for radar reflector originating from changes in crystal-orientation fabric, *Cryosphere Discuss.*, *1*(1), 1–16.

Ekaykin, A. A. (2003), Meteorological regime of central Antarctica and its role in the formation of isotope composition of snow thickness, Ph.D. thesis, Univ. Joseph Fourier, Grenoble, France.

Ekaykin, A. A., V. Y. Lipenkov, N. I. Barkov, J. R. Petit, and V. Masson-Delmotte (2002), Spatial and temporal variability in isotope composition of recent snow in the vicinity of Vostok Station: Implications for ice-core interpretation, *Ann. Glaciol.*, *35*, 181–186.

Ekaykin, A. A., V. Y. Lipenkov, I. N. Kuzmina, J. R. Petit, V. Masson-Delmotte, and S. J. Johnsen (2004), The changes in isotope composition and accumulation of snow at Vostok Station over the past 200 years, *Ann. Glaciol.*, *39*, 569–575.

Endo, Y., and K. Fujiwara (1973), Characteristics of the snow cover in East Antarctica along the route of the JARE South Pole Traverse and factors controlling such characteristics, *JARE Sci. Rep., Ser. C*, *Earth Sci.*, *7*, 38 pp.

Fahnestock, M. A., T. A. Scambos, C. A. Shuman, R. J. Arthern, D. P. Winebrenner, and R. Kwok (2000), Snow megadune fields on the East Antarctic Plateau: Extreme atmosphere-ice interaction, *Geophys. Res. Lett.*, *27*(22), 3719–3722.

Feely, H. W., H. Seitz, R. J. Lagomarsino, and P. E. Biscaye (1966), Transport and fallout of stratospheric radioactive debris, *Tellus*, *18*, 316–328.

Fischer, H., D. Wagenbach, and J. Kipfstuhl (1998), Sulfate and nitrate firn concentrations on the Greenland ice sheet: 2. Temporal anthropogenic deposition changes, *J. Geophys. Res.*, *103*(D17), 21,935–21,942.

Fisher, D. A., N. Reeh, and H. B. Clausen (1985), Stratigraphic noise in time series derived from ice cores, *Ann. Glaciol.*, *7*, 76–83.

Folco, L., A. Capra, M. Chiappini, M. Frezzotti, M. Mellini, and I. E. Tabacco (2002), The Frontier Mountain meteorite trap (Antarctica), *Meteorit. Planet. Sci.*, *37*, 209–228.

Fortuin, J. P. F., and J. Oerlemans (1990), The parameterization of the annual surface temperature and mass balance of Antarctica, *Ann. Glaciol.*, *14*, 78–84.

Freitag, J., F. Wilhelms, and S. Kipfstuhl (2004), Microstructure dependent densification of polar firn derived from X-ray microtomography, *J. Glaciol.*, *50*(169), 243–250.

Frezzotti, M., and O. Flora (2002), Ice dynamic features and climatic surface parameters in East Antarctica from Terra Nova Bay to Talos Dome and Dome C: ITASE Italian Traverse, *Terra Antarct.*, *9*(1), 47–54.

Frezzotti, M., S. Gandolfi, F. L. Marca, and S. Urbini (2002a), Snow dunes and glazed surfaces in Antarctica: New field and remote-sensing data, *Ann. Glaciol.*, *34*, 81–88.

Frezzotti, M., S. Gandolfi, and S. Urbini (2002b), Snow megadunes in Antarctica: Sedimentary structure and genesis, *J. Geophys. Res.*, *107*(D18), 4344, doi:10.1029/2001JD000673.

Frezzotti, M., et al. (2004), New estimations of precipitation and surface sublimation in East Antarctica from snow accumulation measurements, *Clim. Dyn.*, *23*(7–8), 803–813, doi:10.1007/s00382-004-0462-5.

Frezzotti, M., et al. (2005), Spatial and temporal variability of snow accumulation in East Antarctica from traverse data, *J. Glaciol.*, *51*(172), 113–124.

Frezzotti, M., S. Urbini, M. Proposito, C. Scarchilli, and S. Gandolfi (2007), Spatial and temporal variability of surface mass balance near Talos Dome, East Antarctica, *J. Geophys. Res.*, *112*, F02032, doi:10.1029/2006JF000638.

Fuhrer, K., A. Neftel, M. Anklin, and W. Maggi (1993), Continuous measurements of hydrogen peroxide, formaldehyde, calcium and ammonium concentrations along the new GRIP ice core from Summit, central Greenland, *Atmos. Environ., Part A*, *27*(12), 1873–1880.

Fuhrer, K., A. Neftel, M. Anklin, M. Staffelbach, and T. Legrand (1996), High-resolution ammonium ice core record covering a complete glacial-interglacial cycle, *J. Geophys. Res.*, *101*(D2), 4147–4164.

Fujii, Y. (1981), Formation of surface snow layer at Mizuho Station, Antarctica, *Mem. Nat. Inst. Polar Res. Spec. Issue*, *19*, 280–296.

Fujii, Y., and K. Kusunoki (1982), The Role of sublimation and condensation in the formation of ice sheet surface at Mizuho Station, Antarctica, *J. Geophys. Res.*, *87*(C6), 4293–4300.

Fujita, S., H. Maeno, S. Uratsuka, T. Furukawa, S. Mae, Y. Fujii, and O. Watanabe (1999), Nature of radio echo layering in the Antarctic ice sheet detected by a two-frequency experiment, *J. Geophys. Res.*, *104*(B6), 13,013–13,024.

Fujiwara, K., and Y. Endoh (1971), Preliminary report of glaciological studies, *Jpn. Antarct. Res. Exped. Sci. Rep., Special Issue*, *2*, 68–109.

Gallée, H., G. Guyomarch, and E. Brun (2001), Impact of snow drift on the Antarctic ice sheet surface mass balance: Possible sensitivity to snow surface properties, *Boundary Layer Meteorol.*, *99*, 1–19.

Gallée, H., V. Peyaud, and I. Goodwin (2005), Simulation of the net snow accumulation along the Wilkes Land transect, Antarctica, with a regional climate model, *Ann. Glaciol.*, *41*, 17–22.

Genthon, C. (2004), Space-time Antarctic surface mass balance variability from climate models, *Ann. Glaciol.*, *39*, 271–275.

Genthon, C., and G. Krinner (2001), Antarctic surface mass balance and systematic biases in general circulation models, *J. Geophys. Res.*, *106*(D18), 20,653–20,664.

Genthon, C., S. Kaspari, and P. A. Mayewski (2005), Interannual variability of the surface mass balance of West Antarctica from ITASE cores and ERA40 reanalyses, *Clim. Dyn.*, *24*, 759–770, doi:0.1007/s00382-005-0019-2.

Gerland, S., H. Oerter, J. Kipfstuhl, F. Wilhelms, H. Miller, and W. Miners (1999), Density log of a 181 m long ice core from Berkner Island, Antarctica, *Ann. Glaciol.*, *29*, 215–219.

Giovinetto, M. B., N. M. Waters, and C. R. Bentley (1990), Dependence of Antarctic surface mass balance on temperature, elevation, and distance to open ocean, *J. Geophys. Res.*, *95*(D4), 3517–3531.

Goldberg, E. D. (1963), Geochronology with lead-210, in *Radioactive Dating*, pp. 121–131, Int. At. Energy Agency, Vienna.

Goodwin, I. D. (1990), Snow accumulation and surface topography in the katabatic zone of eastern Wilkes Land, Antarctica, *Antarct. Sci.*, *2*(3), 232–235.

Goodwin, I. D. (1991), Snow-accumulation variability from seasonal surface observations and firn-core stratigraphy, eastern Wilkes Land, Antarctica, *J. Glaciol.*, *37*(127), 383–387.

Goodwin, I. D., M. Higham, I. Allison, and R. Jaiwen (1994), Accumulation variation in eastern Kemp Land, Antarctica, *Ann. Glaciol.*, *20*, 202–206.

Goodwin, I., M. de Angelis, M. Pook, and N. W. Young (2003), Snow accumulation variability in Wilkes Land, East Antarctica, and the relationship to atmospheric ridging in the 130°–170°E region since 1930, *J. Geophys. Res.*, *108*(D21), 4673, doi:10.1029/2002JD002995.

Gow, A. J. (1965), On the accumulation and seasonal stratification of snow at the South Pole, *J. Glaciol.*, *5*(40), 467–477.

Gow, A. J., and R. Rowland (1965), On the relationship of snow accumulation to surface topography at ''Byrd Station'', Antarctica, *J. Glaciol.*, *5*(42), 843–847.

Gudmandsen, P. (1975), Layer echoes in polar ice sheets, *J. Glaciol.*, *15*(73), 95–101.

Hamilton, G. (2004), Topographic control of regional accumulation rate variability at South Pole and implications for ice core interpretation, *Ann. Glaciol.*, *39*, 214–218.

Hammer, C. (1980), Acidity of polar ice cores in relation to absolute dating, past volcanism, and radio-echoes, *J. Glaciol.*, *25*(93), 359–372.

Hammer, C. U., H. B. Clausen, and C. C. Langway Jr. (1994), Electrical conductivity method (ECM) stratigraphic dating of the Byrd Station ice core, Antarctica, *Ann. Glaciol.*, *20*, 115–120.

Harrison, C. H. (1973), Radio echo sounding of horizontal layers in ice, *J. Glaciol.*, *12*(66), 383–397.

Hawley, R. L., E. M. Morris, R. Cullen, U. Nixdorf, A. P. Shepherd, and D. J. Wingham (2006), ASIRAS airborne radar resolves internal annual layers in the dry-snow zone of Greenland, *Geophys. Res. Lett.*, *33*, L04502, doi:10.1029/2005GL025147.

Helm, V., W. Rack, R. Cullen, P. Nienow, D. Mair, V. Parry, and D. J. Wingham (2007), Winter accumulation in the percolation zone of Greenland measured by airborne radar altimeter, *Geophys. Res. Lett.*, *34*, L06501, doi:10.1029/2006GL029185.

Helsen, M. M., R. S. W. van de Wal, M. R. van den Broeke, E. R. T. Kerstel, V. Masson-Delmotte, H. A. J. Meijer, C. H. Reijmer, and M. P. Scheele (2004), Modelling the isotopic composition of snow using backward trajectories: A particular precipitation event in Dronning Maud Land, Antarctica, *Ann. Glaciol.*, *39*, 293–299.

Helsen, M. M., R. S. W. van de Wal, M. R. van den Broeke, D. van As, H. A. J. Meijer, and C. H. Reijmer (2005), Oxygen isotope variability in snow from western Dronning Maud Land, Antarctica and its relation to temperature, *Tellus, Ser. B*, *57*, 423–435.

Hempel, L., F. Thyssen, N. Gundestrup, H. B. Clausen, and H. Miller (2000), A comparison of radio-echo sounding data and electrical conductivity of the GRIP ice core, *J. Glaciol.*, *46*(154), 369–374.

Hofstede, C. M., et al. (2004), Firn accumulation records for the past 1000 years on the basis of dielectric profiling of six cores from Dronning Maud Land, Antarctica, *J. Glaciol.*, *50*(169), 279–291.

Holmlund, P., et al. (2000), Spatial gradients in snow layering and ten metre temperatures at potential EPICA-DML drill sites, *Ann. Glaciol.*, *30*, 13–19.

Holtslag, A. A. M., and E. I. F. D. Bruijn (1988), Applied modelling of the nighttime surface energy balance over land, *J. Appl. Meteorol.*, *27*, 689–704.

Hori, A., et al. (1999), A detailed density profile of the Dome Fuji (Antarctica) shallow ice core by X-ray transmission method, *Ann. Glaciol.*, *29*, 211–214.

Isaksson, E., and W. Karlén (1994), Spatial and temporal patterns in snow accumulation, western Dronning Maud Land, Antarctica, *J. Glaciol.*, *40*(135), 399–409.

Isaksson, E., W. Karlén, N. Gundestrup, P. Mayewski, S. Whitlow, and M. Twickler (1996), A century of accumulation and temperature changes in Dronning Maud Land, Antarctica, *J. Geophys. Res.*, *101*(D3), 7085–7094.

Isaksson, E., M. R. van den Broeke, J.-G. Winther, L. Karlöf, J.-F. Pinglot, and N. Gundestrup (1999), Accumulation and proxy-temperature variability in Dronning Maud Land, Antarctica, determined from shallow firn cores, *Ann. Glaciol.*, *29*, 17–22.

Jacobel, R. W., and S. M. Hodge (1995), Radar internal layers from the Greenland summit, *Geophys. Res. Lett.*, *22*(5), 587–590.

Jacobel, R. W., B. C. Welch, E. J. Steig, and D. P. Schneider (2005), Glaciological and climatic significance of Hercules Dome, Antarctica: An optimal site for deep ice core drilling, *J. Geophys. Res.*, *110*, F01015, doi:10.1029/2004JF000188.

Jezek, K. C., and E. A. Roeloffs (1983), Measurements of radar wave speeds in polar glaciers using a down-hole radar target technique, *Cold Reg. Sci. Technol.*, *8*, 199–208.

Johnsen, S. J. (1977), Stable isotope homogenization of polar firn and ice, *IAHS Publ.*, *118*, 388–392.

Joughin, I., et al. (2005), Continued deceleration of Whillans Ice Stream, West Antarctica, *Geophys. Res. Lett.*, *32*, L22501, doi:10.1029/2005GL024319.

Jourdain, B., and M. Legrand (2001), Seasonal variations of atmospheric dimethylsulfide, dimethylsulfoxide, sulphur dioxide, methanesulfonate, and non-sea-salt sulphate aerosols at Dumont d'Urville (coastal Antarctica) (December 1998 to July 1999), *J. Geophys. Res.*, *106*(D13), 14,391–14,408.

Jouzel, J., L. Merlivat, M. Pourchet, and C. Lorius (1979), A continuous record of artificial tritium fallout at the South Pole (1954–1978), *Earth Planet. Sci. Lett.*, *45*(1), 188–200.

Jouzel, J., et al. (2007), Orbital and millennial Antarctic climate variability over the past 800,000 years, *Science*, *317*(5839), 793–796, doi:10.1126/science.1141038.

Kaczmarska, M., et al. (2004), Accumulation variability derived from an ice core from coastal Dronning Maud Land, Antarctica, *Ann. Glaciol.*, *39*, 339–345.

Kameda, T., H. Shoji, K. Kawada, O. Watanabe, and H. B. Clausen (1994), An empirical relation between overburden pressure and firn density, *Ann. Glaciol.*, *20*, 87–94.

Kameda, T., N. Azuma, T. Furukawa, Y. Ageta, and S. Takahashi (1997), Surface mass balance, sublimation and snow temperatures at Dome Fuji Station, Antarctica, in 1995, *Proc. NIPR Symp. Pol. Meteorol. Glaciol.*, *11*, 24–34.

Kameda, T., K. Fujita, O. Sugita, and G. Hashida (2007), Glaciological data collected by the 44th Japanese Antarctic Research Expedition during 2003–2004, *JARE Data Rep. Glaciol.*, *32*, 92 pp.

Kameda, T., H. Motoyama, S. Fujita, and S. Takahashi (2008), Temporal and spatial variability of surface mass balance at Dome Fuji, East Antarctica, by the stake method from 1995 to 2006, *J. Glaciol.*, *54*(84), 107–116.

Kamiyama, K., Y. Ageta, and Y. Fujii (1989), Atmospheric and depositional environments traced from unique chemical compositions of the snow over an inland high plateau, Antarctica, *J. Geophys. Res.*, *94*(D15), 18,515–18,519.

Kanagaratnam, P., S. P. Gogineni, N. Gundstrup, and L. Larsen (2001), High-resolution radar mapping of internal layers at the North Greenland Ice Core Project, *J. Geophys. Res.*, *106*(D24), 33,799–33,812.

Karlöf, L. (2004), Temporal and spatial variability of snow accumulation and redistribution, and its impact on the interpretation of ice cores, Ph.D. thesis, Fac. of Math. and Nat. Sci., Univ. of Oslo, Oslo.

Karlöf, L., et al. (2000), A 1500 years record of accumulation at Amundsenisen western Dronning Maud Land, Antarctica, derived from electrical and radioactive measurements on a 120 m ice core, *J. Geophys. Res.*, *105*(D10), 12,471–12,483.

Karlöf, L., T. A. Oigard, F. Godtliebsen, M. Kaczmarska, and H. Fischer (2005a), Statistical techniques to select detection thresholds for peak signals in ice-core data, *J. Glaciol.*, *51*(175), 655–662.

Karlöf, L., et al. (2005b), Accumulation variability over a small area in east Dronning Maud Land, Antarctica, as determined from shallow firn cores and snow pits: Some implications for ice-core records, *J. Glaciol.*, *51*(174), 343–352.

Karlöf, L., D. P. Winebrenner, and D. B. Percival (2006), How representative is a time series derived from a firn core? A study at a low-accumulation site on the Antarctic plateau, *J. Geophys. Res.*, *111*, F04001, doi:10.1029/2006JF000552.

Kaser, G. (1982), Measurement of evaporation from snow, *Meteorol. Atmos. Phys.*, *30*, 333–340.

Kaspari, S., P. A. Mayewski, D. A. Dixon, V. B. Spikes, S. B. Sneed, M. J. Handley, and G. S. Hamilton (2005), Climate variability in West Antarctica derived from annual accumulation rate records from ITASE firn/ice cores, *Ann. Glaciol.*, *39*, 585–594.

King, J. C., P. S. Anderson, M. C. Smith, and S. D. Mobbs (1996), The surface energy and mass balance at Halley, Antarctica, during winter, *J. Geophys. Res.*, *101*(D14), 19,119–19,128.

King, J. C., P. S. Anderson, and G. W. Mann (2001), The seasonal cycle of sublimation at Halley, Antarctica, *J. Glaciol.*, *47*(156), 1–8.

King, J. C., P. S. Anderson, D. G. Vaughan, G. W. Mann, S. D. Mobbs, and S. B. Vosper (2004), Wind-borne redistribution of snow across an Antarctic ice rise, *J. Geophys. Res.*, *109*, D11104, doi:10.1029/2003JD004361.

Klok, E. J., M. Noland, and M. R. van den Broeke (2005), Analysis of meteorological data and the surface energy balance of McCall Glacier, Alaska, USA, *J. Glaciol.*, *51*(174), 451–461.

Knüsel, S., D. E. Piguet, M. Schwikowski, and H. W. Gäggeler (2003), First results of trace element analysis in ice cores using Continuous Ice Melting (CIM) Inductively Coupled Plasma Sector Field Mass Spectrometry (ICP-SFMS), *J. Phys. IV Fr.*, *107*, doi:10.1051/jp4:20030399.

Kohler, J., J. C. Moore, and E. Isaksson (2003), Comparison of modelled and observed responses of a glacier snowpack to ground-penetrating radar, *Ann. Glaciol.*, *37*, 293–297.

Korth, W., and R. Dietrich (1996), *Ergebnisse geodätischer Arbeiten im Gebiet der Schirmacheroase/Antarctica 1988–1993*, *Publ. Ser. B Angew. Geod.*, vol. 301, Dtsch. Geod. Komm., Bayer. Akad. der Wiss., Munich, Germany.

Kovacs, A., A. J. Gow, and R. M. Morey (1995), The in-situ dielectric constant of polar firn revisited, *Cold Reg. Sci. Technol.*, *23*, 245–256.

Krinner, G., O. Magand, I. Simmonds, C. Genthon, and J.-L. Dufresne (2007), Simulated Antarctic precipitation and surface mass balance at the end of the 20th and 21st centuries, *Clim. Dyn.*, *28*, 215–230, doi:10.1007/s00382-006-0177-x.

Lambert, G., B. Ardouin, J. Sanak, C. Lorius, and M. Pourchet (1977), Accumulation of snow and radioactive debris in Antarctica: A possible refined radiochronology beyond reference levels, in *Symposium Isotopes et Impuretés dans les neiges et glaces, Colloque de Grenoble*, *IAHS Publ.*, *118*, 146–158.

Legrand, M., and R. J. Delmas (1984), The ionic balance of Antarctic snow: A 10-year detailed record, *Atmos. Environ.*, *18*, 1867–1874.

Legrand, M., and P. A. Mayewski (1997), Glaciochemistry of polar ice cores: A review, *Rev. Geophys.*, *35*, 219–243.

Li, J., and H. J. Zwally (2002), Modeled seasonal variations of firn density induced by steady-state surface air-temperature cycle, *Ann. Glaciol.*, *34*, 299–302.

Li, J., and H. J. Zwally (2004), Modeling the density variation in the shallow firn layer, *Ann. Glaciol.*, *38*, 309–313.

Li, L., and J. W. Pomeroy (1997), Estimates of threshold wind speeds for snow transport using meteorological data, *J. Appl. Meteorol.*, *36*, 205–213.

Lipenkov, V. Y., A. A. Ekaykin, N. I. Barkov, and M. Pourchet (1998), O svyazi plotnosti poverhnostnogo sloya snega v Antarktide so skorost'yu vetra (On the relationship of surface snow density in Antarctica and wind speed), *Mater. Glyatsiol. Issled.*, *85*, 148–158.

Looyenga, H. (1965), Dielectric constant of heterogeneous mixtures, *Physica*, *31*(3), 401–406.

Magand, O., M. Frezzotti, M. Pourchet, B. Stenni, L. Genoni, and M. Fily (2004), Climate variability along latitudinal and longitudinal transects in East Antarctica, *Ann. Glaciol.*, *39*, 351–358.

Magand, O., C. Genthon, M. Fily, G. Krinner, G. Picard, M. Frezzotti, and A. A. Ekaykin (2007), An up-to-date quality-controlled surface mass balance data set for the 90°–180°E Antarctica sector and 1950–2005 period, *J. Geophys. Res.*, *112*, D12106, doi:10.1029/2006JD007691.

Mann, G. W., P. S. Anderson, and S. D. Mobbs (2000), Profile measurements of blowing snow at Halley, Antarctica, *J. Geophys. Res.*, *105*(D19), 24,491–24,508.

Masson-Delmotte, V., et al. (2008), A review of Antarctic surface snow isotopic composition: Observations, atmospheric circulation and isotopic modelling, *J. Clim.*, in press.

Matsuoka, K., T. Furukawa, S. Fujita, H. Maeno, S. Uratsuka, R. Naruse, and O. Watanabe (2003), Crystal orientation fabrics within the Antarctic ice sheet revealed by a multipolarization plane and dual-frequency radar survey, *J. Geophys. Res.*, *108*(B10), 2499, doi:10.1029/2003JB002425.

Matsuoka, K., S. Uratsuka, S. Fujita, and F. Nishio (2004), Ice-flow induced scattering zone within the Antarctic ice sheet revealed by high-frequency airborne radar, *J. Glaciol.*, *50*(170), 382–388.

Mavrocordatos, C., E. Attema, M. Davidson, H. Lentz, and U. Nixdorf (2004), Development of ASIRAS (Airborne SAR/Interferometric Altimeter System), in *Geoscience and Remote Sensing Symposium IGARSS '04*, vol. 4, pp. 2465–2467, IEEE Int., New York, doi:10.1109/IGARSS.2004.1369792.

Mayewski, P. A., and I. D. Goodwin (1997), International Trans-Antarctic Scientific Expedition (ITASE), *PAGES Rep. 1997-1*, 48 pp., Past Global Changes Proj., Bern.

Mayewski, P. A., L. D. Meeker, S. Whitlow, M. S. Twickler, M. C. Morrison, R. B. Alley, P. Bloomfield, and K. Taylor (1993), The atmosphere during the Younger Dryas, *Science*, *261*(5118), 195–197, doi:10.1126/science.261.5118.195.

Mayewski, P. A., et al. (2005), The International Trans-Antarctic Scientific Expedition (ITASE): An overview, *Ann. Glaciol.*, *41*, 180–185.

McConnell, J. R., R. C. Bales, and D. R. Davis (1997), Recent intra-annual snow accumulation at South Pole: Implications for ice core interpretation, *J. Geophys. Res.*, *102*(D18), 21,947–21,954.

McMorrow, A. J., M. A. J. Curran, T. D. van Ommen, V. Morgan, I. Allison, and M. J. Pook (2001), Intercomparison of firn core and meteorological data, *Antarct. Sci.*, *13*(3), 329–337.

Meyerson, E. A., P. A. Mayewski, K. J. Kreutz, L. D. Meeker, S. I. Whitlow, and M. S. Twickler (2002), The polar expression of ENSO and sea-ice variability as recorded in a South Pole ice core, *Ann. Glaciol.*, *35*, 430–436.

Millar, D. H. H. (1981), Radio echo layering in polar ice sheets and past volcanic activity, *Nature*, *292*, 441–443.

Minikin, A., D. Wagenbach, W. Graf, and J. Kipfstuhl (1994), Spatial and seasonal variations of the snow chemistry at the central Filchner–Ronne Ice Shelf, Antarctica, *Ann. Glaciol.*, *20*, 283–290.

Monaghan, A. J., et al. (2006), Insignificant change in Antarctic snowfall since the International Geophysical Year, *Science*, *313*(5788), 827–831, doi:10.1126/science.1128243.

Moore, J. C. (1988), Dielectric variability of a 130 m Antarctic ice core: Implications for radar sounding, *Ann. Glaciol.*, *11*, 95–99.

Moore, J. C., and R. Mulvaney (1989), Dielectrical stratigraphy of ice: A new technique for determining total ionic concentrations in polar ice cores, *Geophys. Res. Lett.*, *16*(10), 1171–1179.

Moore, J. C., and J. G. Paren (1987), New technique for dielectric logging of Antarctic ice cores, *J. Physi. Colloq. C1)*, *48*(3), 155–160.

Moore, J. C., H. Narita, and N. Maeno (1991), A continuous 770-year record of volcanic activity from East Antarctica, *J. Geophys. Res.*, *96*(D9), 17,353–17,359.

Morey, R. M., and A. Kovacs (1985), Analysis of wide-angle reflection and refraction measurements, *CRREL Spec. Rep.*, *85-5*, 53–60.

Morgan, V. I., and T. H. Jacka (1981), Mass balance studies in East Antarctica, in *Sea Level, Ice, and Climatic Change*, edited by I. Allison, *IAHS Publ.*, *131*, 253–260.

Morgan, V. I., I. D. Goodwin, D. M. Etheridge, and C. W. Wookey (1991), Evidence from Antarctic ice cores for recent increases in snow accumulation, *Nature*, *354*, 58–60.

Morris, E. D., and J. D. Cooper (2003), Density measurements in ice boreholes using neutron scattering, *J. Glaciol.*, *49*(167), 599–604.

Mosley-Thompson, E., and L. G. Thompson (1982), Nine centuries of microparticle deposition at the South Pole, *Quat. Res.*, *17*, 1–13.

Mosley-Thompson, E., L. G. Thompson, J. F. Paskievitch, M. Pourchet, A. J. Gow, M. E. Davis, and J. Kleinman (1995), South Pole snow accumulation has increased in recent decades, *Ann. Glaciol.*, *21*, 131–138.

Mosley-Thompson, E., J. F. Paskievitch, A. J. Gow, and L. G. Thompson (1999), Late 20th century increase in South Pole snow accumulation, *J. Geophys. Res.*, *104*(D4), 3877–3886.

Mulvaney, R., H. Oerter, D. A. Peel, W. Graf, C. Arrowsmith, E. C. Pasteur, B. Knight, G. C. Littot, and W. D. Miners (2002), 1000 year ice-core records from Berkner Island, Antarctica, *Ann. Glaciol.*, *35*, 45–51.

Murray, T., G. W. Stuart, P. J. Miller, J. Woodward, A. M. Smith, P. R. Porter, and H. Jiskoot (2000), Glacier surge propagation by thermal evolution at the bed, *J. Geophys. Res.*, *105*(B6), 13,491–13,507.

Muszynski, I., and G. E. Birchfield (1985), The dependence of Antarctic accumulation rates on surface temperature and elevation, *Tellus, Ser. A*, *37*, 204–208.

Neftel, A. (1991), Use of snow and firn analysis to reconstruct past atmospheric composition, in *Seasonal Snowpacks*, *NATO ASI, Ser. G*, vol. 28, edited by T. D. Davies, M. Tranter, and H. Jones, pp. 385–415, Springer, Berlin.

Nemazi, M., G. Lambert, C. Lorius, and J. Labeyrie (1964), Mesure du taux d'accumulation de la neige au bord du continent Antarctique par la méthode du Plomb-210, *C. R. Hebd. Seances Acad. Sci.*, *259*(19), 3319–3322.

Nereson, N. A., C. F. Raymond, R. W. Jacobel, and E. D. Waddington (2000), The accumulation pattern across Siple Dome, West Antarctica, inferred from radar-detected internal layers, *J. Glaciol.*, *46*(156), 75–87.

Neumann, T. A., and E. D. Waddington (2004), Effects of firn ventilation on isotopic exchange, *J. Glaciol.*, *50*(169), 183–194.

Neumann, T. A., E. D. Waddington, E. J. Steig, and P. M. Grootes (2005), Non-climate influences on stable isotopes at Taylor Mouth, Antarctica, *J. Glaciol.*, *51*(173), 248–258.

Nishio, F., et al. (2002), Annual-layer determinations and 167 year records of past climate of H72 ice core in east Dronning Maud Land, Antarctica, *Ann. Glaciol.*, *35*, 471–479.

Noone, D., J. Turner, and R. Mulvaney (1999), Atmospheric signals and characteristics of accumulation in Dronning Maud Land, Antarctica, *J. Geophys. Res.*, *104*(D16), 19,191–19,211.

Oerlemans, J. (2003), Analysis of a 3 year meteorological record from the ablation zone of Morteratschgletscher, Switzerland: Energy and mass balance, *J. Glaciol.*, *46*(155), 571–579.

Oerter, H. (2005), Stable oxygen isotopes of snow pit DML25S02_03 (SS0203), *PANGAEA*, doi:10.1594/PANGAEA.264585.

Oerter, H., W. Graf, F. Wilhelms, A. Minikin, and H. Miller (1999), Accumulation studies on Amundsenisen, Dronning Maud Land, Antarctica, by means of Tritium, dielectric profiling and stable-isotope measurements: First results from the 1995–96 and 1996–97 field seasons, *Ann. Glaciol.*, *29*, 1–9.

Oerter, H., F. Wilhelms, F. Jung-Rothenhäusler, F. Göktas, H. Miller, W. Graf, and S. Sommer (2000), Accumulation rates in Dronning Maud Land as revealed by dielectrical-profiling measurements at shallow firn cores, *Ann. Glaciol.*, *30*, 27–34.

Oerter, H., W. Graf, H. Meyer, and F. Wilhelms (2004), The EPICA ice core Dronning Maud Land: First results from stable-isotope measurements, *Ann. Glaciol.*, *39*(39), 307–312.

Osterberg, E. C., M. J. Handley, S. B. Sneed, P. A. Mayewski, and K. J. Kreutz (2006), Continuous ice core melter system with discrete sampling for major ion, trace element and stable isotope analyses, *Environ. Sci. Technol.*, *40*, 3355–3361.

Palais, J. M., I. M. Whillans, and C. Bull (1982), Snow stratigraphic studies at Dome C, East Antarctica: An investigation of depositional and diagenetic processes, *Ann. Glaciol.*, *3*, 239–242.

Palais, J. M., M. S. Germani, and G. A. Zielinski (1992), Interhemispheric transport of volcanic ash from a 1259 A.D. volcanic eruption to the Greenland and Antarctic ice sheets, *Geophys. Res. Lett.*, *19*(8), 801–804.

Pälli, A., J. C. Kohler, E. Isaksson, J. C. Moore, J. F. Pinglot, V. A. Pohjola, and H. Samuelsson (2002), Spatial and temporal variability of snow accumulation using ground-penetrating radar and ice cores on a Svalbard glacier, *J. Glaciol.*, *48*(162), 417–424.

Palmer, A. S., T. D. van Ommen, M. A. J. Curran, V. Morgan, J. M. Souney, and P. A. Mayewski (2001), High-precision dating of volcanic events (A.D. 1301–1995) using ice cores from Law Dome, Antarctica, *J. Geophys. Res.*, *106*(D22), 28,089–28,095.

Parrenin, F., R. Hindmarsh, and F. Remy (2006), Analytical solutions for the effect of topography, accumulation rate and flow divergence on isochrone layer geometry, *J. Glaciol.*, *52*(177), 191–202.

Petit, J.-R., J. Jouzel, M. Pourchet, and L. Merlivat (1982), A detailed study of snow accumulation and stable isotope content in Dome C (Antarctica), *J. Geophys. Res.*, *87*(C6), 4301–4308.

Pettré, P., J. F. Pinglot, M. Pourchet, and L. Reynaud (1986), Accumulation in Terre Adélie, Antarctica: Effect of meteorological parameters, *J. Glaciol.*, *32*(112), 486–500.

Picciotto, E., and S. Wilgain (1963), Fission products in Antarctic snow, a reference level for measuring accumulation, *J. Geophys. Res.*, *68*(21), 5965–5972.

Picciotto, E., G. Crozaz, and W. D. Breuck (1964), Rate of accumulation of snow at South Pole as determined by radioactive measurements, *Nature*, *203*, 393–394.

Picciotto, E., G. Crozaz, and W. de Breuck (1971), Accumulation on the South Pole–Queen Maud Land Traverse, 1964–1968, in *Antarctic Snow and Ice Studies II*, *Antarct. Res. Ser.*, vol. 16, edited by A. Crary, pp. 257–315, AGU, Washington, D. C.

Pinglot, F., and M. Pourchet (1979), Low-level beta counting with an automatic sample changer, *Nucl. Instrum. Methods*, *166*(3), 483–490.

Pinglot, J. F., and M. Pourchet (1981), Gamma-ray bore-hole logging for determining radioactive fallout layers in snow, in *Methods of Low-Level Counting and Spectrometry*, pp. 161–172, Int. At. Energy Agency, Vienna.

Pinglot, J. F., and M. Pourchet (1994), Spectrométrie Gamma à trés bas niveau avec anti-compton NaI (T1) pour l'étude des glaciers et des sédiments, *J. Spectrom. Gamma X*, *93*, 291–296.

Pourchet, M., F. Pinglot, and C. Lorius (1983), Some meteorological applications of radioactive fallout measurements in Antarctic snows, *J. Geophys. Res.*, *88*(C10), 6013–6020.

Pourchet, M., et al. (1997), Distribution and fall-out of 137Cs and other radionuclides over Antarctica, *J. Glaciol.*, *43*(145), 435–445.

Pourchet, M., O. Magand, M. Frezzotti, A. A. Ekaykin, and J. G. Winter (2003), Radionuclides deposition over Antarctica, *J. Environ. Radioact.*, *68*, 137–158.

Qin, D. H., J. W. Ren, J. C. Kang, C. D. Xiao, Z. Q. Li, Y. S. Li, B. Sun, W. Z. Sun, and X. X. Wang (2000), Primary results of glaciological studies along an 1100 km transect from Zhongshan station to Dome A, East Antarctic ice sheet, *Ann. Glaciol.*, *31*, 198–204.

Ramillien, G., A. Lombard, A. Cazenave, E. R. Ivins, M. Llubes, F. Remy, and R. B. Ramilien (2006), Interannual variations of the mass balance of the Antarctica and Greenland ice sheets from GRACE, *Global Planet. Change*, *53*(3), 198–208, doi:10.1016/j.gloplacha.2006.06.003.

Rasmussen, S. O., K. K. Andersen, S. J. Johnsen, M. Bigler, and T. McCormack (2005), Deconvolution-based resolution enhancement of chemical ice core records obtained by continuous flow analysis, *J. Geophys. Res.*, *110*, D17304, doi:10.1029/2004JD005717.

Reijmer, C. H., and M. R. V. D. Broeke (2003), Temporal and spatial variability of the surface mass balance in Dronning Maud Land, Antarctica, as derived from automatic weather stations, *J. Glaciol.*, *49*(167), 512–520.

Reijmer, C. H., M. R. van den Broeke, and M. P. Scheele (2002), Air parcel trajectories to five deep drilling locations on Antarctica, based on the ERA-15 data set, *J. Clim.*, *15*, 1957–1968.

Reinhardt, H., M. Kriews, H. Miller, O. Schrems, C. Ludke, E. Hoffmann, and J. Skole (2001), Laser ablation inductively coupled plasma mass spectrometry: A new tool for trace element analysis in ice cores, *Fresenius J. Anal. Chem.*, *370*, 629–636.

Ren, J. W., Q. Dahe, and I. Allison (1999), Variations of snow accumulation and temperature over past decades in the Lambert Glacier basin, Antarctica, *Ann. Glaciol.*, *29*, 29–32.

Ren, J. W., I. Allison, C. D. Xiao, and D. H. Qin (2002), Mass balance of the Lambert Glacier basin, East Antarctica, *Sci. China Ser. D, Earth Sci.*, *45*(9), 842–850.

Richardson, C., and P. Holmlund (1999), Spatial variability at shallow snow-layer depths in central Dronning Maud Land, East Antarctica, *Ann. Glaciol.*, *29*, 10–16.

Richardson, C., E. Aarholt, S.-E. Hamram, P. Holmlund, and E. Isaksson (1997), Spatial distribution of snow in western Dronning Maud Land, East Antarctica, mapped by a ground-based snow radar, *J. Geophys. Res.*, *102*(B9), 20,343–20,353.

Richardson-Näslund, C. (2001), Spatial distribution of snow in Antarctica and other glacier studies using ground-penetrating radar, *Thesis Geogr. Emphasis Phys. Geogr.*, vol. 18, Dep. of Phys. Geogr. and Quat. Geol., Stockholm Univ., Stockholm.

Richardson-Näslund, C. (2004), Spatial characteristics of snow accumulation in Dronning Maud Land, Antarctica, *Global Planet. Change*, *42*, 31–43.

Robin, G. d. Q., S. Evans, and J. T. Bailey (1969), Interpretation of radio echo sounding in polar ice sheets, *Philos. Trans. R. Soc. London, Ser. A*, *146*, 437–505.

Röthlisberger, R., M. Bigler, M. Hutterli, S. Sommer, B. Stauffer, H. G. Junghans, and D. Wagenbach (2000), Technique for continuous high-resolution analysis of trace substances in firn and ice cores, *Environ. Sci. Technol.*, *34*, 338–342.

Rotschky, G., O. Eisen, F. Wilhelms, U. Nixdorf, and H. Oerter (2004), Spatial characteristics of accumulation patterns derived from combined data sets in Dronning Maud Land, Antarctica, *Ann. Glaciol.*, *39*, 265–270.

Rotschky, G., W. Rack, W. Dierking, and H. Oerter (2006), Retrieving snowpack properties and accumulation estimates from combination of SAR and scatterometer measurements, *IEEE Trans. Geos. Rem. Sens.*, *44*(4), 943–956, doi:10.1109/TGRS.2005.862524.

Rotschky, G., P. Holmlund, E. Isaksson, R. Mulvaney, H. Oerter, M. R. van den Broeke, and J.-G. Winther (2007), A new surface accumulation map for western Dronning Maud Land, Antarctica, from interpolation of point measurements, *J. Glaciol.*, *53*(182), 385–398, doi:10.3189/002214307783258459.

Saigne, C., and M. Legrand (1987), Measurements of methanesulphonic acid in Antarctic ice, *Nature*, *330*, 240–242, doi:10.1038/330240a0.

Satake, H., and K. Kawada (1997), The quantitative evaluation of sublimation and the estimation of original hydrogen and oxygen of a firn core at east Queen Maud Land, Antarctica, *Bull. Glacier Res.*, *15*, 93–97.

Schlosser, E., N. van Lipzig, and H. Oerter (2002), Temporal variability of accumulation at Neumayer station, Antarctica, from stake array measurements and a regional atmospheric model, *J. Glaciol.*, *48*(160), 87–94.

Schwander, J., A. Neftel, H. Oeschger, and B. Stauffer (1983), Measurement of direct current conductivity on ice samples for climatological applications, *J. Phys. Chem.*, *87*, 4157–4160.

Scott, J. B. T., D. Mair, P. Nienow, V. Parry, and E. Morris (2006), A ground-based radar backscatter investigation in the percolation zone of the Greenland ice sheet, *Remote Sens. Environ.*, *104*(4), 361–373.

Sigg, A., K. Fuhrer, M. Anklin, T. Staffelbach, and D. Zurmühle (1994), A continuous analysis technique for trace species in ice cores, *Environ. Sci. Technol.*, *28*(2), 204–209.

Sinisalo, A., A. Grinsted, J. C. Moore, E. Kärkäs, and R. Pettersson (2005), Snow-accumulation studies in Antarctica with ground-penetrating radar using 50, 100 and 800 MHz antenna frequencies, *Ann. Glaciol.*, *37*, 194–198.

Smeets, C. J. P. P., and M. R. van den Broeke (2008), Temporal and spatial variation of momentum roughness length in the ablation zone of the Greenland ice sheet, *Boundary Layer Meteorol.*, in press.

Smith, B. T., T. D. Van Ommen, and V. I. Morgan (2002), Distribution of oxygen isotope ratios and snow accumulation rates in Wilhelm II Land, East Antarctica, *Ann. Glaciol.*, *35*, 107–110.

Sommer, S., D. Wagenbach, R. Mulvaney, and H. Fischer (2000a), Glacio-chemical study spanning the past 2 kyr on three ice cores from Dronning Maud Land, Antarctica: 2. Seasonally resolved chemical records, *J. Geophys. Res.*, *105*(D24), 29,423–29,433.

Sommer, S., et al. (2000b), Glacio-chemical study covering the past 2 kyr on three ice cores from Dronning Maud Land, Antarctica: 1. Annually resolved accumulation rates, *J. Geophys. Res.*, *105*(D24), 29,411–29,421.

Spikes, V. B., G. S. Hamilton, S. A. Arcone, S. Kaspari, and P. A. Mayewski (2004), Variability in accumulation rates from GPR profiling on the West Antarctic plateau, *Ann. Glaciol.*, *39*, 238–244.

Stearns, C. R., and G. A. Weidner (1993), Sensible and latent heat flux estimates in Antarctica, in *Antarctic Meteorology and Climatology, Studies Based on Automatic Weather Stations*, *Antarct. Res. Ser.*, vol. 61, edited by D. H. Bromwich and C. R. Stearns, pp. 109–138, AGU, Washington, D. C.

Steffen, K., and J. Box (2001), Surface climatology of the Greenland ice sheet: Greenland Climate Network 1995–1999, *J. Geophys. Res.*, *106*(D24), 33,951–33,964.

Steig, E. J., et al. (2005), High-resolution ice cores from US ITASE (West Antarctica): Development and validation of chronologies and determination of precision and accuracy, *Ann. Glaciol.*, *41*, 77–84.

Stenberg, M., M. Hansson, P. Holmlund, and L. Karlöf (1999), Variability in snow layering and snow chemistry in the vicinity of two drill sites in western Dronning Maud Land, Antarctica, *Ann. Glaciol.*, *29*, 33–37.

Stenni, B., R. Caprioli, L. Cimino, C. Cremisini, O. Flora, R. Gragnani, A. Longinelli, V. Maggi, and S. Torcini (1999), 200 years of isotope and chemical records in a firn core from Hercules Néé, northern Victoria Land, Antarctica, *Ann. Glaciol.*, *29*, 106–112.

Stenni, B., F. Serra, M. Frezzotti, V. Maggi, R. Traversi, S. Becagli, and R. Udisti (2000), Snow accumulation rates in Northern Victoria Land (Antarctica) by firn core analysis, *J. Glaciol.*, *46*(155), 541–552.

Stenni, B., V. Masson-Delmotte, S. Johnsen, J. Jouzel, A. Longinelli, E. Monnin, R. Röthlisberger, and E. Selmo (2001), An oceanic cold reversal during the last deglaciation, *Science*, *293*(5537), 2074–2077, doi:10.1126/science.1059702.

Stenni, B., M. Proposito, R. Gragnani, O. Flora, J. Jouzel, S. Falourd, and M. Frezzotti (2002), Eight centuries of volcanic signal and climate change at Talos Dome (East Antarctica), *J. Geophys. Res.*, *107*(D9), 4076, doi:10.1029/2000JD000317.

Stenseng, L., R. Forsberg, K. Keller, S. M. Hvidegaard, and C. Leuschen (2005), Comparison of airborne laser scanning and D2P radar altimetry, *Geophys. Res. Abst.*, *7*, 06393.

Stroeven, A. P., and V. A. Pohjola (1991), Glaciological studies in Scharffenbergbotnen, in *The Expedition ANTARKTIS-VIII of RV "POLARSTERN" 1989/90*, *Report of Leg ANT-VIII/5, Ber. Polarforschung*, vol. 86, edited by H. Miller and H. Oerter, pp. 126–130, Alfred-Wegener-Inst. für Polar- und Meeresforsch., Bremerhaven, Germany.

Swedish Antarctic Research Programme (2003), Annual report, Stockholm.

Takahashi, S., and T. Kameda (2007), Snow density for measuring the surface mass balance using the stake method, *J. Glaciol.*, *53*(183), 677–680.

Takahashi, S., and O. Watanabe (1997), Snow accumulation in Antarctica: East Queen Maud Land, *Glaciol. Folio, sheet 3-1*, Natl. Inst. of Pol. Res., Tokyo.

Takahashi, S., Y. Ageta, Y. Fujii, and O. Watanabe (1994), Surface mass balance in east Dronning Maud Land, Antarctica, observed by Japanese Antarctic Research Expeditions, *Ann. Glaciol.*, *20*, 242–253.

Taylor, K. C., and R. B. Alley (2004), Two-dimensional electrical stratigraphy of the Siple Dome (Antarctica) ice core, *J. Glaciol.*, *50*(16), 231–235.

Taylor, K. C., et al. (2004), Dating the Siple Dome (Antarctica) ice core by manual and computer interpretation of annual layering, *J. Glaciol.*, *50*(170), 453–461.

Tiuri, M. T., A. H. Sihvola, E. G. Nyfors, and M. T. Hallikainen (1984), The complex dielectric constant of snow at microwave frequencies, *IEEE J. Oceanic Eng.*, *9*(5), 377–382.

Traufetter, F., H. Oerter, H. Fischer, R. Weller, and H. Miller (2004), Spatio-temporal variability in volcanic sulphate deposition over the past 2 kyr in snow pits and firn cores from Amundsenisen, Antarctica, *J. Glaciol.*, *50*(168), 137–146.

Traversi, R., S. Becagli, E. Castellano, A. Migliori, M. Severi, and R. Udisti (2002), High resolution fast ion chromatography (FIC) measurements of chloride, nitrate and sulphate along the EPICA Dome C ice core, *Ann. Glaciol.*, *35*, 291–298.

Udisti, R. (1996), Multiparametric approach for chemical dating of snow layers from Antarctica, *Int. J. Environ. Anal. Chem.*, *63*, 225–244.

Udisti, R., S. Becagli, E. Castellano, R. Mulvaney, J. Schwander, S. Torcini, and E. Wolff (2000), Holocene electrical and chemical measurements from the EPICA Dome C ice core, *Ann. Glaciol.*, *30*, 20–26.

Urbini, S., L. Vittuari, and S. Gandolfi (2001), GPR and GPS data integration: Examples of application in Antartica, *Ann. Geofis.*, *44*(4), 687–702.

Urbini, S., M. Frezzotti, S. Gandolfi, C. Vincent, C. Scarchilli, L. Vittuari, and M. Fily (2008), Historical behaviour of Dome C and Talos Dome (East Antarctica) as investigated by snow accumulation and ice velocity measurements, *Global Planet. Change*, *60*(3–4), 576–588, doi:10.1016/j.gloplacha.2007.08.002.

van de Berg, W. J., M. R. van den Broeke, C. H. Reijmer, and E. van Meijgaard (2006), Reassessment of the Antarctic surface mass balance using calibrated output of a regional atmospheric climate model, *J. Geophys. Res.*, *111*, D11104, doi:10.1029/2005JD006495.

van den Broeke, M. R., and N. P. M. van Lipzig (2003), Factors controlling the near-surface wind field in Antarctica, *Mon. Weather Rev.*, *131*, 733–743.

van den Broeke, M., C. Reijmer, and R. van de Wal (2004a), Surface radiation balance in Antarctica as measured with automatic weather stations, *J. Geophys. Res.*, *109*, D09103, doi:10.1029/2003JD004394.

van den Broeke, M. R., W. J. van de Berg, and E. van Meijgaard (2004b), A study of the surface mass balance in Dronning Maud Land, Antarctica, using automatic weather stations, *J. Glaciol.*, *50*(171), 565–582.

van den Broeke, M., W. J. van de Berg, and E. van Meijgaard (2006a), Snowfall in coastal West Antarctica much greater than previously assumed, *Geophys. Res. Lett.*, *33*, L02505, doi:10.1029/2005GL025239.

van den Broeke, M., W. J. van de Berg, E. van Meijgaard, and C. Reijmer (2006b), Identification of Antarctic ablation areas using a regional atmospheric climate model, *J. Geophys. Res.*, *111*, D18110, doi:10.1029/2006JD007127.

Van der Veen, C. J., and J. F. Bolzan (1999), Interannual variability in the net accumulation on the Greenland Ice Sheet: Observations and implications for the mass-balance measurements, *J. Glaciol.*, *34*(118), 355–357.

Van de Wal, R. S. W., W. Greuell, M. R. van den Broeke, C. Reijmer, and J. Oerlemans (2005), Mass balance observations and automatic weather station data along a transect near Kangerlussuaq, West Greenland, *Ann. Glaciol.*, *42*, 311–316.

van Lipzig, N. P. M., J. C. King, T. A. Lachlan-Cope, and M. R. van den Broeke (2004a), Precipitation, sublimation, and snow drift in the Antarctic Peninsula region from a regional atmospheric model, *J. Geophys. Res.*, *109*, D24106, doi:10.1029/2004JD004701.

van Lipzig, N. P. M., J. Turner, S. R. Colwell, and M. R. van den Broeke (2004b), The near-surface wind field over the Antarctic continent, *Int. J. Climatol.*, *24*(15), 1973–1982.

Vaughan, D. G. (2006), Recent trends in melting condition on the Antarctic Peninsula and their implications for ice-sheet mass balance and sea level, *Arctic Antarct. Alpine Res.*, *38*(1), 147–152.

Vaughan, D. G., J. L. Bamber, M. Giovinetto, and A. P. R. Cooper (1999a), Reassessment of net surface mass balance in Antarctica, *J. Clim.*, *12*, 933–946.

Vaughan, D. G., H. F. J. Corr, C. S. M. Doake, and E. D. Waddington (1999b), Distortion of isochronous layers in ice revealed by ground-penetrating radar, *Nature*, *398*, 323–326.

Vaughan, D. G., P. S. Anderson, J. C. King, G. W. Mann, S. D. Mobbs, and R. S. Ladkin (2004), Imaging of firn isochrones across an Antarctic ice rise and implications for patterns of snow accumulation rate, *J. Glaciol.*, *50*(170), 413–418.

Velicogna, I., and J. Wahr (2006), Measurements of time-variable gravity show mass loss in Antarctica, *Science*, *311*(5768), 1754, doi:10.1126/science.1120808.

Watanabe, O., et al. (1997), A preliminary study of ice core chronology at Dome Fuji Station, Antatactica, *Proc. NIPR Symp. Polar Meteorol. Glaciol.*, *11*, 9–13.

Weller, R., F. Traufetter, H. Fischer, H. Oerter, C. Piel, and H. Miller (2004), Postdepositional losses of methane sulfonate, nitrate, and chloride at the European Project for Ice Coring in Antarctica deep-drilling site in Dronning Maud Land, Antarctica, *J. Geophys. Res.*, *109*, D07301, doi:10.1029/2003JD004189.

Whillans, I. M., and J. F. Bolzan (1988), A method for computing shallow ice-core depths, *J. Glaciol.*, *34*(118), 355–357.

Whitlow, S., P. A. Mayewski, and J. E. Dibb (1992), A comparison of major chemical species input timing and accumulation at South Pole and Summit Greenland, *Atmos. Environ., Part A*, *26*(11), 2045–2054.

Wilgain, S., E. Picciotto, and W. D. Breuck (1965), Strontium 90 fallout in Antarctica, *J. Geophys. Res.*, *70*(24), 6023–6032.

Wilhelms, F. (1996), *Leitfähigkeits- und Dichtemessung an Eisbohrkernen* (Measuring the Conductivity and Density of Ice Cores), *Ber. Polarforsch.*, vol. 191, Alfred-Wegener-Inst. für Polar- und Meeresforsch., Bremerhaven, Germany.

Wilhelms, F. (2000), *Messung dielektrischer Eigenschaften polarer Eiskerne* (Measuring the Dielectric Properties of Polar Ice Cores), *Ber. Polarforsch.*, vol. 367, Alfred-Wegener-Inst. für Polar- und Meeresforsch., Bremerhaven, Germany.

Wilhelms, F. (2005), Explaining the dielectric properties of firn as a density-and-conductivity mixed permittivity (DECOMP), *Geophys. Res. Lett.*, *32*, L16501, doi:10.1029/2005GL022808.

Wilhelms, F., J. Kipfstuhl, H. Miller, K. Heinloth, and J. Firestone (1998), Precise dielectric profiling of ice cores: A new device with improved guarding and its theory, *J. Glaciol.*, *44*(146), 171–174.

Winebrenner, D. P., R. J. Arthern, and C. A. Shuman (2001), Mapping Greenland accumulation rates using observations of thermal emission at 4.5-cm wavelength, *J. Geophys. Res.*, *106*(D24), 33,919–33,934.

Wolff, E. B., J. C. Moore, H. B. Clausen, C. U. Hammer, J. Kipfstuhl, and K. Fuhrer (1995), Long-term changes in the acid and salt concentrations of the Greenland Ice Core Project ice core from electrical stratigraphy, *J. Geophys. Res.*, *100*(D8), 16,249–16,263.

Wolff, E. B., W. D. Miners, J. C. Moore, and J. G. Paren (1997), Factors controlling the electrical conductivity of ice from the polar reginos—A summary, *J. Phys. Chem. B*, *101*, 6090–6094.

Wolff, E. B., I. Basile, J.-R. Petit, and J. Schwander (1999), Comparison of Holocene electrical records from Dome C and Vostok, Antarctica, *Ann. Glaciol.*, *29*, 89–93.

Xiao, C. D., D. H. Qin, L. G. Bian, X. J. Zhou, I. Allison, and M. Yan (2005), A precise monitoring of snow surface height in the region of Lambert Glacier basin-Amery Ice Shelf, East Antarctica, *Sci. China, Ser. D, Earth Sci.*, *48*(1), 100–111.

Yilmaz, O. (1987), *Seismic Data Processing*, *Invest. Geophys.*, vol. 2, Soc. of Explor. Geophys., Tulsa, Okla.

Young, N. W., M. Pourchet, V. M. Kotlyakov, P. A. Korolev, and M. B. Dyugerov (1982), Accumulation distribution in the IAGP area, Antarctica: 90°E–150°E, *Ann. Glaciol.*, *3*, 333–338.

Zwally, H. J., and M. B. Giovinetto (1995), Accumulation in Antarctica and Greenland derived from passive-microwave data: A comparison with contoured compilations, *Ann. Glaciol.*, *21*, 123–130.

Zwally, H. J., M. B. Giovinetto, J. Li, H. G. Cornejo, M. A. Beckley, A. C. Brenner, J. L. Saba, and D. Yi (2005), Mass changes of the Greenland and Antarctic ice sheets and shelves and contributions to sea-level rise: 1992–2002, *J. Glaciol.*, *51*(175), 509–527, 19.

D. A. Dixon and S. Kaspari, Climate Change Institute, Department of Earth Sciences, University of Maine, 5790 Edward T. Bryand Global Sciences Center, Orono, ME 04469-5790, USA. (daniel_dixon@umit.maine.edu; susan.kaspari@maine.edu)

O. Eisen and H. Oerter, Stiftung Alfred-Wegener-Institut für Polar- und Meeresforschung, Postfach 120161, D-27515 Bremerhaven, Germany. (olaf.eisen@awi.de; hans.oerter@awi.de)

A. Ekaykin and V. Y. Lipenkov, Arctic and Antarctic Research Institute, 38 Bering Street, 199397 St. Petersburg, Russia. (ekaykin@aari.nw.ru; lipenkov@aari.nw.ru)

M. Frezzotti, ENEA Laboratory for climate observation, SP. Anguillarese, 301 I-00123 S.M. di Galeria (Roma), Roma, Italy. (frezzotti@casaccia.enea.it)

C. Genthon and O. Magand, LGGE, CNRS, Université Joseph-Fourier Grenoble, 54, Rue Molière, BP 96, Domaine Universitaire, F-38402 Saint-Martin d'H'eres, France. (genthon@lgge.obs.ujf-grenoble.fr; magand@lgge.obs.ujf-grenoble.fr)

P. Holmlund, Department of Physical Geography and Quaternary Geology, Stockholm University, SE-10691 Stockholm, Sweden. (per.holmlund@natgeo.su.se)

E. Isaksson, Norwegian Polar Institute, Polar Environmental Centre, N-9296 Tromsø, Norway. (elli@npolar.no)

T. Kameda and S. Takahashi, Snow and Ice Research Laboratory, Kitami Institute of Technology, 165 Koencho, Kitami, Hokkaido 090-8507, Japan. (kameda@mail.kitami-it.ac.jp; shuhei@mail.kitami-it.ac.jp)

L. Karlöf, Research and Development, SWIX SPORT AS, Servicebox, N-2626 Lillehammer, Norway. (l.karlof@swixsport.no)

M. R. van den Broeke, Institute for Marine and Atmospheric Research, Utrecht University, PO Box 80 005, NL-3508 TA Utrecht, Netherlands. (m.r.vandenbroeke@phys.uu.nl)

D. G. Vaughan, British Antarctic Survey, Natural Environment Research Council, High Cross, Madingley Road, Cambridge CB3 0ET, UK. (dgv@bas.ac.uk)

Small-scale spatio-temporal characteristics of accumulation rates in western Dronning Maud Land, Antarctica

Helgard ANSCHÜTZ,[1*] Daniel STEINHAGE,[1] Olaf EISEN,[1] Hans OERTER,[1] Martin HORWATH,[2] Urs RUTH[1]

[1] *Alfred-Wegener-Institut für Polar- und Meeresforschung, Postfach 120161, D-27515 Bremerhaven, Germany*
E-mail: helgard.anschuetz@npolar.no
[2] *Institut für Planetare Geodäsie, Technische Universität Dresden, D-01062 Dresden, Germany*

ABSTRACT. Spatio-temporal variations of the recently determined accumulation rate are investigated using ground-penetrating radar (GPR) measurements and firn-core studies. The study area is located on Ritscherflya in western Dronning Maud Land, Antarctica, at an elevation range 1400–1560 m. Accumulation rates are derived from internal reflection horizons (IRHs), tracked with GPR, which are connected to a dated firn core. GPR-derived internal layer depths show small relief along a 22 km profile on an ice flowline. Average accumulation rates are about 190 kg m^{-2} a^{-1} (1980–2005) with spatial variability (1σ) of 5% along the GPR profile. The interannual variability obtained from four dated firn cores is one order of magnitude higher, showing 1σ standard deviations around 30%. Mean temporal variations of GPR-derived accumulation rates are of the same magnitude or even higher than spatial variations. Temporal differences between 1980–90 and 1990–2005, obtained from two dated IRHs along the GPR profile, indicate temporally non-stationary processes, linked to spatial variations. Comparison with similarly obtained accumulation data from another coastal area in central Dronning Maud Land confirms this observation. Our results contribute to understanding spatio-temporal variations of the accumulation processes, necessary for the validation of satellite data (e.g. altimetry studies and gravity missions such as Gravity Recovery and Climate Experiment (GRACE)).

INTRODUCTION

Recent years have seen increasing discussions of observations of sea-level change (e.g. Van der Veen, 2002; Thomas and others, 2004; Alley and others, 2005; Church and White, 2006) and analysis of future sea-level rise (Gregory and Huybrechts, 2006). Uncertainties are still high, with the largest introduced by the contribution of the Antarctic ice sheet (e.g. Rignot and Thomas, 2002; Vaughan, 2005). New satellite missions such as the Gravity Recovery and Climate Experiment (GRACE; Tapley and others, 2004), the Ice, Cloud, and Land Elevation Satellite (ICESat; Zwally and others, 2002) and the forthcoming CryoSat-2 are expected to provide new insights into Antarctica's mass balance, especially in coastal and mountainous areas where European Remote-sensing Satellite (ERS) data could not determine surface elevation changes due to the steep slopes (Vaughan, 2005). Several recent studies report mass change rates for the West Antarctic and East Antarctic ice sheets (WAIS and EAIS) from GRACE. Although these studies generally agree that the WAIS is losing mass while the EAIS is gaining mass or is at least close to balance, their individual estimates yield different results (Table 1).

In the data presented by Velicogna and Wahr (2006), a significant ice-mass trend is only apparent after the removal of postglacial rebound from the GRACE solutions. Such corrections depend largely upon the models adopted for postglacial rebound, and thus form the main uncertainty in the ice-mass changes obtained from GRACE (Chen and others, 2006). The uncertainties and the differences highlight the necessity of obtaining ground-truth data for the estimates of ice-mass changes based on satellite gravity and altimetry data. Furthermore, ice-mass changes derived from GRACE are averaged over several hundred kilometres; small-scale effects are therefore not resolvable. Small-scale variations in parameters affecting the mass balance of the ice sheet are of major importance in validating satellite data. Together with the effects of ice dynamics, spatial and temporal variations of accumulation rates and density influence changes in ice-sheet elevation. It is therefore crucial to investigate these parameters and their spatio-temporal changes on small scales by ground-based observations.

Accumulation data have often been derived from point measurements such as firn cores, snow pits or stake readings (e.g. Isaksson and Karlén, 1994; Melvold and others, 1998; Oerter and others, 1999; Kreutz and others, 2000). However, these only yield accumulation data at the probing location, leaving open the question of spatial representation as discussed by Richardson and Holmlund (1999). They recommend ground-penetrating radar (GPR) studies in order to investigate the spatial variability of accumulation rates around a drilling site. GPR has been widely applied in such a way in recent years (e.g. Richardson and others, 1997; Sinisalo and others, 2003; Rotschky and others, 2004; Spikes and others, 2004; Eisen and others, 2005).

The observed internal reflection horizons (IRHs) are due to contrasting values of dielectric permittivity in the subsurface. Ice density has the most significant influence in the upper hundreds of metres of the firn/ice column, affecting the real part of the dielectric permittivity (e.g. Fujita and others, 1999). IRHs were demonstrated to be isochronous (Eisen and others, 2004; Vaughan and others, 2004). From their estimated age and a density–depth distribution, the mean

*Present address: Norwegian Polar Institute, Polar Environmental Center, NO-9005 Tromsø, Norway.

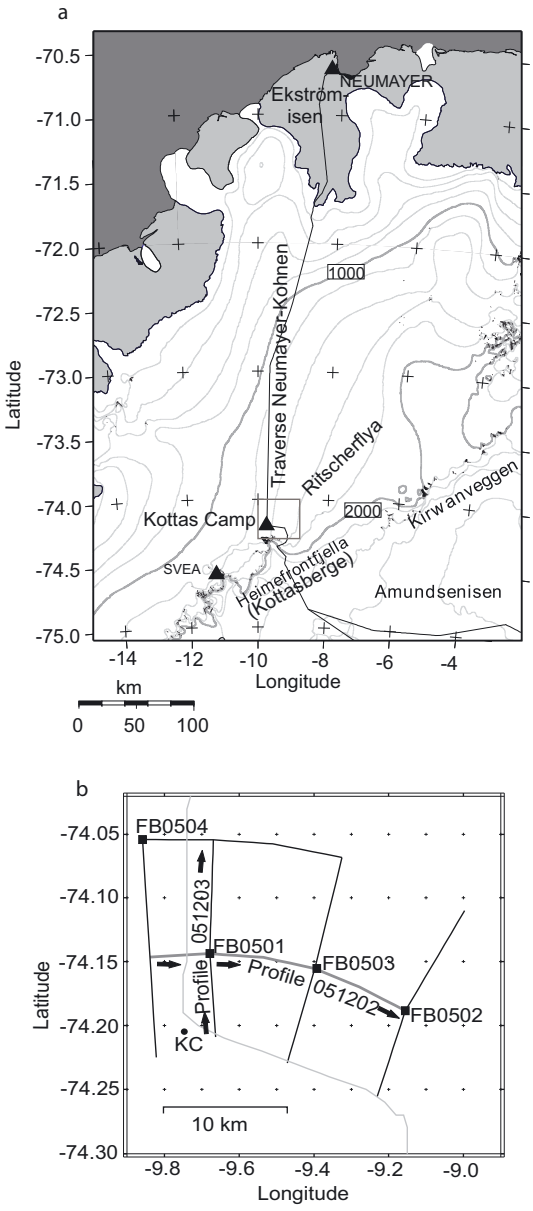

Fig. 1. (a) Thin grey curves: elevation contours at 200 m spacing; thick grey curves: 1000 m and 2000 m contours. The black curve indicates the traverse route from Neumayer station to Kohnen station (not shown). (Source: Antarctic Digital Database 4.0.) (b) GPR profiles and firn-core locations. Thick grey curve: profile on the ice flowline (measured against the flow direction); thin grey curve: stake line along traverse route Neumayer–Kottasberge. Arrows indicate direction of GPR profiles. Glacier flow is from right to left. KC: Kottas Camp and drilling location of FB9802.

accumulation rate for a particular period can therefore be calculated.

In this paper, we present ground-based data comprising GPR profiles and shallow firn cores from a small grid on Ritscherflya in western Dronning Maud Land (DML), Antarctica. Accumulation rates are obtained along tracked IRHs which are dated by firn-core parameters. We discuss the spatial variability of accumulation rates on the scale of a few kilometres and the temporal variability on decadal scales. Interannual variability of accumulation rates obtained from dated firn cores is also presented. We compare our results with other nearby studies from western DML as well as with similarly obtained data from a coastal site in central DML.

Table 1. Rates of volume change (in $km^3\ a^{-1}$) and uncertainties for WAIS and EAIS from GRACE

Study	WAIS	EAIS
Velicogna and Wahr (2006)	-148 ± 21	0 ± 56
Chen and others (2006)	-77 ± 14	$+80 \pm 16$
Ramillien and others (2006)	-107 ± 23	$+67 \pm 28$

STUDY AREA

The area of investigation is located near Kottas Camp in the grounded coastal part of DML, approximately 10 km north of Kottasberge, part of the Heimefrontfjella mountain range. Figure 1a depicts an overview of the area, where the dark grey rectangle corresponds to the area depicted in Figure 1b. This area is characterized by gentle surface undulations at 1400–1560 m a.s.l. and a glacier flow velocity of $50\ m\ a^{-1}$. The distance to the Weddell Sea coast is about 300 km. Ice thickness in the area of investigation reaches 2000 m with a smooth bedrock topography (Steinhage and others, 2001).

The Heimefrontfjella mountain range marks the boundary between the inland ice plateau (Amundsenisen) and Ritscherflya, with the mountains damming the ice flow from the plateau by channelling it through small outlets. The mountain chains are directed from the southwest to the northeast. Ice-sheet altitudes range from >2500 m on Amundsenisen to 1200–1500 m at the foot of the mountains.

DATA AND METHODS

GPR and GPS

In the Antarctic summer season 2004/05, GPR measurements were carried out along an ice flowline and on cross-profiles (Fig. 1b) using a bistatic shielded 500 MHz antenna (RAMAC, Malå Geoscience, Sweden) which was pulled by a snow vehicle at an average speed of $\sim 5\ km\ h^{-1}$. Traces were recorded every 0.5 m in a time window of 400 ns, triggered by an odometer. Simultaneously, kinematic GPS data were collected at a sampling interval of 1 s using a Trimble 4000SSi receiver and a choke-ring antenna. The roving station was mounted on the snow vehicle, and the reference station was located on Weigel Nunatak, 10 km south of Kottas Camp (Fig. 1).

Global positioning system (GPS) data provided information about the surface elevation and horizontal positions along the GPR profiles. The offset between the GPS and GPR antennae was taken into account for the positioning of the GPR traces. GPR data were filtered using a bandpass Butterworth filter with cut-off frequencies of 350 and 850 MHz, automatic gain control (AGC) and correction for the first arrival of the direct wave. From the processed GPR data, IRHs were tracked throughout the GPR profiles where possible. Conversion of travel time to depth is given below. However, the uppermost layers (up to 1.5–2 m depth) are not visible in the radargram since they are lost within the time window of the direct wave. We restrict ourselves to the upper 12 m since this is the maximum depth of isochronous layers which can be dated using the firn cores (see below). On the profile 051202, four IRHs are tracked within this depth range (Fig. 2) against the ice-flow direction on a flowline (Fig. 1b).

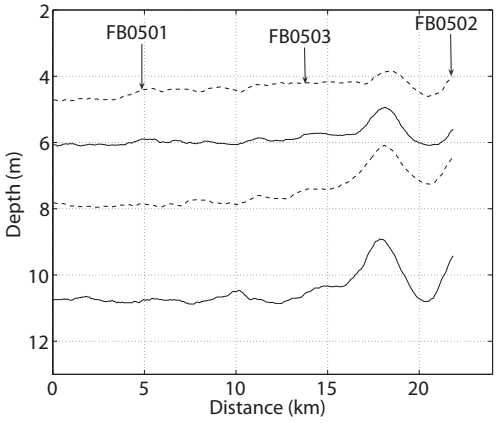

Fig. 2. Depth distribution of the tracked IRHs for profile 051202. The solid horizons are used to calculate accumulation rate.

Firn cores

At four selected points (Fig. 1b; Table 2) of the GPR profiles, shallow firn cores were drilled to depths of 12.0–12.7 m.

Firn-core analyses included density measurements using γ-attenuation profiling (GAP) over intervals of 2 mm and dielectric profiling (DEP) over 5 mm intervals (Wilhelms, 1996, 2005), yielding information about density, dielectric permittivity and the electrical conductivity of the firn. Chemical profiling was performed using a combination of continuous flow analyses (CFA) and ion chromatography (IC) (Ruth and others, 2004). Mass spectrometry was used to derive a $\delta^{18}O$ profile for each core with a sample size of 25–30 mm. Firn-core parameters from firn core FB0501 are exemplified in Figure 3.

Cumulative snow mass (i.e. the mass of overlying snow/firn up to a certain depth) was obtained by integrating GAP density profiles. Radar wave speed was calculated from the profiles of dielectric permittivity, to convert two-way travel time (TWTT) of tracked IRHs to depth and cumulative mass, following Eisen and others (2002) and Anschütz and others (2007), respectively. To establish models for TWTT–depth and cumulative mass–depth the mean profiles of density and dielectric permittivity for all four firn cores were used, since there is no further information about lateral variations of those variables between the drilling sites. However, profiles of density and dielectric permittivity show only small deviations between the four firn cores. In general, fluctuations within one specific core are higher than differences between the firn cores at the same depth (not shown).

Table 2. Locations of firn cores

Firn core	Longitude	Latitude	WGS84*
			m
FB0501	−9.6786	−74.1438	1447
FB0502	−9.1556	−74.1885	1569
FB0503	−9.3977	−74.1555	1488
FB0504	−9.8585	−74.0541	1420

World Geodetic System 1984 elevation.

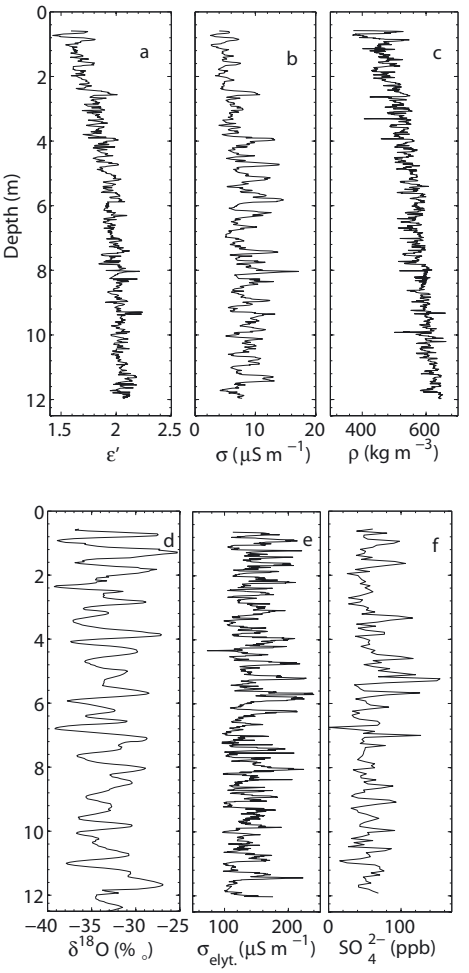

Fig. 3. Firn-core parameters from FB0501: (a) dielectric permittivity (from DEP); (b) electrical conductivity (from DEP); (c) density (from GAP); (d) $\delta^{18}O$ profile; (e) electrolytical conductivity (from CFA); and (f) sulphate (from IC).

Determination of accumulation rates

The $\delta^{18}O$ profile and the chemical profiles of FB0501 (Fig. 3d–f) have been used to establish a depth–age scale as a dating reference for the tracked IRHs on profiles 051202 and 051203 (cross-profile; see Fig. 1b). However, unambiguous dating was not possible by the chemical profiles alone. The chemical profiles were therefore used to support the dating based on the $\delta^{18}O$ profiles. Dating of the firn cores was carried out by annual-layer counting, with the $\delta^{18}O$ peaks indicating summer maxima. The density profiles of the firn cores were used to calculate annual accumulation rates from the snow mass of the annual layers. Note that the firn cores do not reach up to the year 2005 (the age of the surface at the time of data collection) due to poor core quality in the upper 1–2 m. A mean accumulation rate was therefore used to estimate the age of the first datable layer, obtained from two nearby snow pits. Strain rates for this particular area are unknown, so they are not taken into account in our calculation of accumulation rates. As we are focusing on shallow depths, layer thinning can be assumed to be negligible.

Using the depth–age scale obtained from the dated firn cores, the IRHs were dated by comparing their depth values at the coring location with the age given by the depth–age

Table 3. Accumulation values obtained from GPR (standard deviation at 1σ level given as per cent of the mean)

Profile	Time period	Accumulation			
		Mean	SD	Min.	Max.
		kg m^{-2} a^{-1}	%	kg m^{-2} a^{-1}	kg m^{-2} a^{-1}
051202	1980–90	209	7	171	226
051202	1990–2005	176	5	145	185
051202	1980–2005	191	5	159	199
051203	1980–90	192	11	135	232
051203	1990–2005	170	12	139	234
051203	1980–2005	170	9	149	220

scale. Accumulation rates along GPR profiles were calculated by dividing their cumulative mass difference by their age difference. Following the approach of earlier studies, the isochronous property of the IRHs on profile 051202 was tested by comparing the age of the two IRHs at the positions of FB0501, FB0502 and FB0503, yielding differences of up to ± 1 year which is within the range of the dating uncertainties. We thus regard the IRHs as isochrones.

In order to account for temporal differences td of accumulation rates of IRH intervals along the GPR profiles, we define

$$\mathrm{td} = \frac{a(t_1) - a(t_2)}{a(t_2)} \times 100\%, \qquad (1)$$

where a denotes accumulation along the profile and t_i the respective time period.

Calculation of errors in accumulation rates follows the discussion of Anschütz and others (2007). Deviation of the density profiles from the different firn cores is as large as 7%, including measurement errors from GAP (up to 10 kg m^{-3}; Wilhelms, 2005). This value represents the errors introduced by local density fluctuations with respect to the mean density profile used for the calculation of cumulative mass–depth. Errors from DEP measurements are 1% or less (Wilhelms, 1996), and conversion from TWTT to depth likewise yields errors of 1% (Eisen and others, 2002). Conversion of the tracked IRHs to cumulative mass results in errors of ~1% (Anschütz and others, 2007). The dating uncertainty for the IRHs used here is ± 1 year and the uncertainty in tracking the IRHs is up to ± 2 ns, equivalent to a depth uncertainty of about ± 0.2 m. The latter introduces an additional uncertainty of another ± 1 year with respect to the depth–age scale of FB0501. Using the values given above, measurement and model errors result in a mean error of 10–15% for the accumulation data presented here, similar to that reported by Anschütz and others (2007) for a different area.

Table 4. Accumulation values obtained from firn cores (standard deviation at 1σ level given as per cent of the mean)

Firn core	Time period	Accumulation			
		Mean	SD	Minimum	Maximum
		kg m^{-2} a^{-1}	%	kg m^{-2} a^{-1}	kg m^{-2} a^{-1}
FB0501	1976–2003	221	28	108	328
FB0502	1976–99	227	32	98	370
FB0503	1970–2002	199	28	96	359
FB0504	1984–99	195	33	112	305

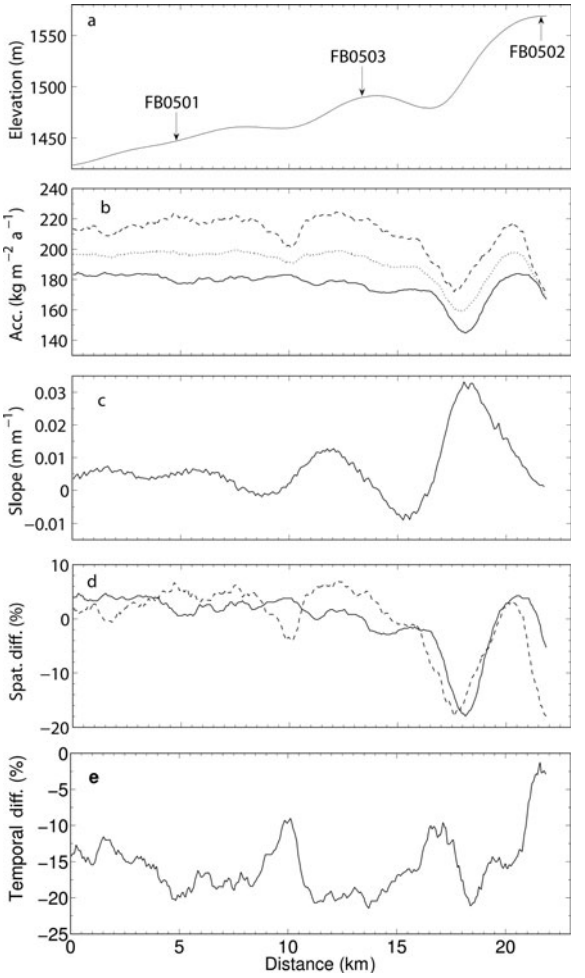

Fig. 4. (a) Surface elevation along profile 051202 near Kottas Camp, from west to east; (b) accumulation: 1980–90 (dashed curve), 1980–2005 (dotted curve) and 1990–2005 (solid curve); (c) surface slope; (d) spatial differences in per cent of the respective mean for the time periods 1990–2005 (solid curve) and 1980–90 (dashed curve); and (e) temporal differences between 1980–90 and 1990–2005, calculated from Equation (1). The locations of firn cores FB0501, FB0502 and FB0503 are given in (a). FB0501 marks the intersection with profile 051203 (Fig. 5).

RESULTS

We focus on the accumulation rates obtained from the firn cores and the two IRHs of profile 051202 (Fig. 2, solid curves). Due to ambiguities in tracing the IRHs throughout the GPR profiles and dating uncertainties, the two other IRHs are omitted. For comparison, we also present accumulation data from the cross-profile 051203 (see Fig. 1b). The two profiles intersect at the drilling location of FB0501. The estimated time of origin of the two IRHs represented by the solid curves in Figure 2 is 1980 ± 1 and 1990 ± 1 years, respectively. GPR-based accumulation rates are given in Table 3 for profiles 051202 and 051203. The accumulation rates presented here are horizontally averaged over 5 m.

The spatial variability of the accumulation values can be expressed by the standard deviation (1σ level), which amounts to 5–7% of the respective mean value for profile

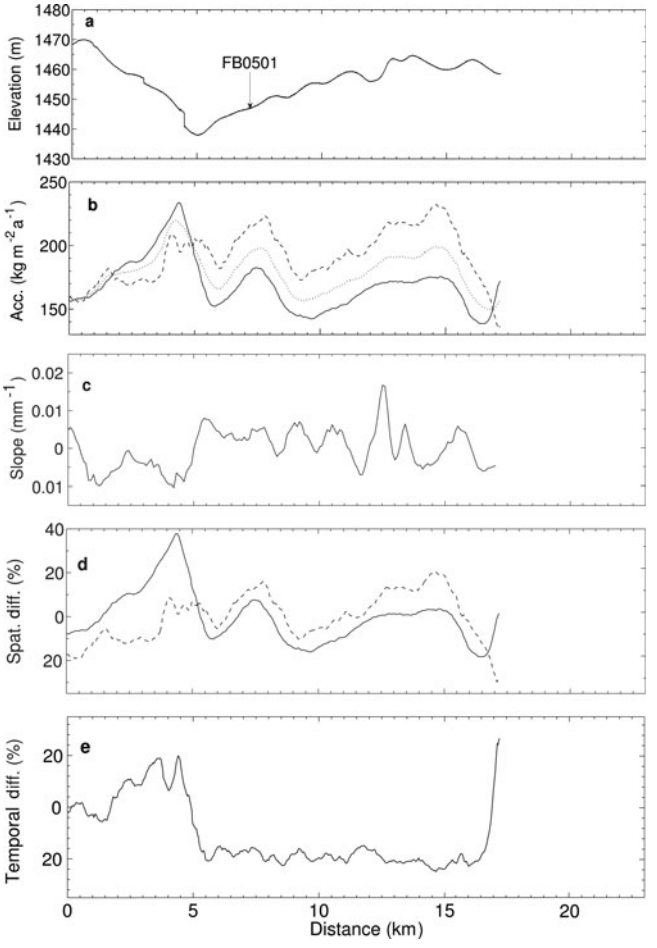

Fig. 5. (a) Surface elevation along profile 051203 near Kottas Camp, from south to north, and crossing profile 051202 perpendicularly at FB0501; (b) accumulation: 1980–90 (dashed curve), 1980–2005 (dotted curve) and 1990–2005 (solid curve); (c) surface slope; (d) spatial differences in per cent of the respective mean for the time periods 1990–2005 (solid curve) and 1980–90 (dashed curve); and (e) temporal differences between 1980–90 and 1990–2005, calculated from Equation (1). The location of firn core FB0501 is given in (a).

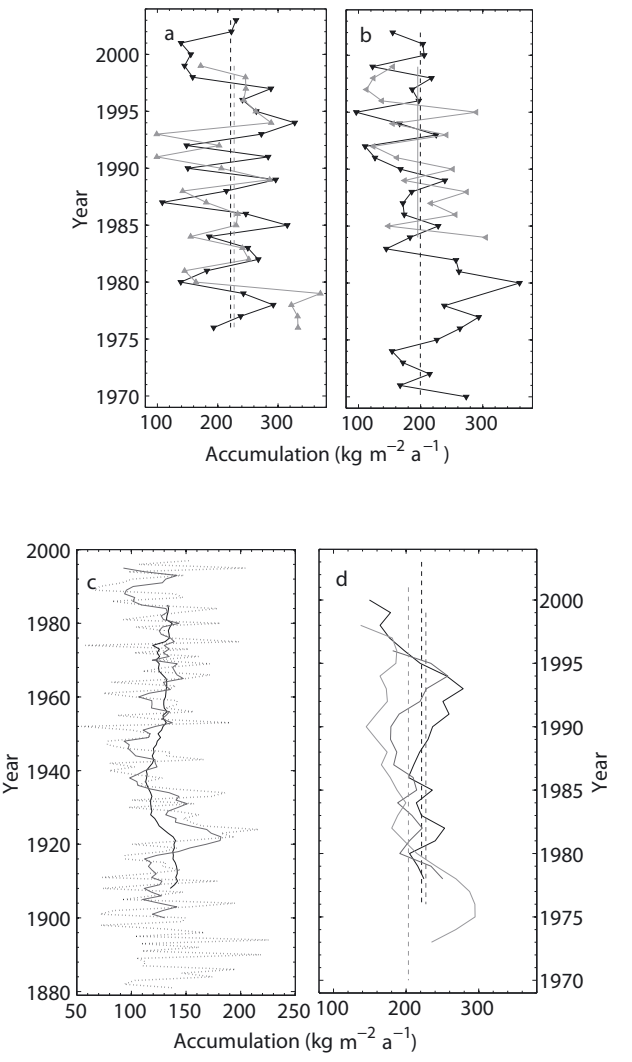

Fig. 6. (a) Year-to-year accumulation: FB0501 (solid black curve), FB0502 (solid grey curve), mean of FB0501 (dashed black curve), mean of FB0502 (dashed grey curve); (b) year-to-year accumulation: FB0503 (solid black curve), FB0504 (solid grey curve), mean of FB0503 (dashed black curve), mean of FB0504 (dashed grey curve); (c) FB9802: annual accumulation rates (dotted curve), 5 year running mean (dark grey curve), 25 year running mean (black curve) (Oerter and others, 1999); and (d) 5 year running mean of FB0501 (black solid curve), FB0502 (dark grey solid curve) and FB0503 (light grey solid curve). Mean values are shown as dashed curves with the respective shading.

051202 (Table 3). Along this profile, spatial differences of the mean value for time periods 1980–90 and 1990–2005 vary from −18% to +8% (Fig. 4d). The cross-profile 051203 reveals accumulation values that are in the same range compared to those on profile 051202, but with a slightly higher spatial variability, as expressed by a standard deviation of approximately 10% (Table 3). Here, the spatial differences for the time periods 1980–90 and 1990–2005 show values between −30% and +38% of the mean (Fig. 5d).

Mean accumulation values of the four firn cores as well as minima and maxima are given in Table 4. The interannual variability derived from the dated firn cores (Fig. 6a and b) is one order of magnitude higher than the spatial variability along the connecting GPR profile (Table 4), emphasizing that accumulation rates exhibit large fluctuations on annual scales. To gather information about temporal variations averaged over the projected mission duration of GRACE and ICESat, we apply a 5 year running mean to the accumulation series of FB0501, FB0502 and FB0503 (Fig. 6d). The standard deviations of the 5 year running means show values of 14% (FB0501), 12% (FB0502) and 17% (FB0503).

DISCUSSION

The accumulation pattern on the ice flowline near Kottas Camp is quite smooth (Fig. 4b), except for the local minimum between 17 and 22 km. This feature can be explained by the surface elevation profile (Fig. 4a; elevation above WGS84 ellipsoid) which shows a steeper increase along this section. Since the discussed IRHs are very shallow (Fig. 2) compared to the ice thickness (Steinhage and others, 2001), the ice thickness is only varying slowly. We therefore propose that the local variations in accumulation observed here arise mainly from the surface undulations and the interaction of surface topography and wind influence (e.g. King and others, 2004).

In general, the wind field and especially predominant wind direction significantly influence the accumulation pattern

(e.g. King and others, 2004). An accumulation profile along the main wind direction should therefore exhibit accumulation maxima at local surface elevation troughs and on the windward sides of surface undulations, whereas accumulation minima are to be expected on hills and on the leeward sides. Such patterns have been discussed in several studies throughout Antarctica (e.g. Black and Budd, 1964; Pettré and others, 1986; Eisen and others, 2005; Frezzotti and others, 2007).

Van den Broeke and Van Lipzig (2004) report predominantly easterly winds in this area of Antarctica, but the horizontal resolution of their model is about 55 km, which does not capture small-scale effects. Predominantly easterly winds agree only partly with the distribution of accumulation and surface features along profile 051202, from west to east (Fig. 4). Interestingly, accumulation pattern and surface topography show more coincidence along profile 051203, from south to north (Fig. 5). However, local wind field is unknown and the nearby Kottasberge are capable of modifying the regional wind direction. Assuming katabatic wind flow down from the nearby plateau region south of Kottasberge, the accumulation pattern of profile 051203 can be explained by wind influence. However, King and others (2004) show that correspondence between surface slope and accumulation is rather complex, especially if climatological wind direction and profile direction do not concur.

Another reason for the deviation from the general pattern on profile 051202 probably arises from consideration of glacier flow velocity. We used a mean surface flow speed of $50\,\mathrm{m\,a^{-1}}$ to correct our GPR layers and derive accumulation rates on profile 051202. This value is only determined by GPS observations of one reference point on the ice flowline during the expedition and might vary locally (personal communication from L. Eberlein, 2005). We therefore assume that interaction of local wind pattern and surface topography significantly influences the local accumulation pattern.

Comparison with nearby studies

Oerter and others (1999) report accumulation values at Kottas Camp of $129\,\mathrm{kg\,m^{-2}\,a^{-1}}$, with a standard deviation of 29%, obtained from a firn core (FB9802) drilled in December 1997 covering the time period 1881–1997. Similar to our firn cores, a 5 year running mean has also been applied to FB9802. To account for the timescales covered by our GPR data, we also apply a 25 year running mean to the accumulation series of FB9802 to enable a better comparison of temporal variations between GPR and firn-core data. The 5 year running mean and 25 year running mean of FB9802 show standard deviations of 14% and 6% of the core mean, respectively. Hence, firn core FB9802 reveals a rather smooth accumulation pattern on longer timescales and a high annual variability (Fig. 6c).

Together with our firn cores, this indicates that the temporal accumulation pattern on scales of 5–25 years is fairly stable, most probably because post-deposition noise and interannual fluctuations are averaged out. Using a mean standard deviation of 14%, as evident from the firn-core data, a surface density of $350\,\mathrm{kg\,m^{-3}}$ and a mean accumulation rate of $180\,\mathrm{kg\,m^{-2}\,a^{-1}}$ results in height fluctuations of $\sim 7\,\mathrm{cm\,a^{-1}}$ that can be explained by temporal accumulation variations. The response of ice flow to temporal variations in accumulation is much longer than the 5 years used for averaging accumulation series. This suggests that height changes of up to $\sim 7\,\mathrm{cm\,a^{-1}}$ may result from interannual variations of accumulation rates that are not instantaneously balanced by ice export. Accordingly, this result has implications for the correct interpretation of satellite-derived mass and elevation changes in this area.

Comparison of the standard deviation for the 25 year running mean of FB9802 with the spatial variability of our GPR-derived accumulation rates shows that temporal variability on the scale of decades and spatial variability on the scale of 20 km are very similar (6% and 5%, respectively). In contrast, studies from the polar plateau report that spatial variability on the kilometre scale is one order of magnitude higher than temporal variability on multi-decadal scales (Frezzotti and others, 2007). We suggest that these different characteristics are due to the different areas and timescales covered by our study, as the Heimefrontfjella forms a dominant topographic feature influencing wind regimes over a large area.

Considering the area-wide mean values (Table 3), our study reveals somewhat higher accumulation rates than those reported by Oerter and others (1999). The same holds for comparison of FB9802 with our firn-core data (Table 4). In order to take into account the different time periods covered by FB9802 and our firn cores, we calculate the mean accumulation of FB9802 over 1975–97 (i.e. the time period that overlaps with our firn cores) as $126\,\mathrm{kg\,m^{-2}\,a^{-1}}$. Hence, the time periods covered do not seem to be responsible for the different accumulation rates between FB9802 and our study. However, the spatial representativeness of firn cores is generally rather small (e.g. Richardson-Näslund, 2004; Rotschky and others, 2004; Spikes and others, 2004), and FB9802 is separated by 7–18 km from our firn-core locations and by about 3 km from the start of profile 051203. Comparing only accumulation rates from locations within our investigation that are nearest to FB9802, i.e. the start of profile 051203 (Fig. 1b), we derive annual accumulation rates of around $150\,\mathrm{kg\,m^{-2}\,a^{-1}}$ (Fig. 5b). These values are more in accordance with the value of $129\,\mathrm{kg\,m^{-2}\,a^{-1}}$ reported by Oerter and others (1999).

Rotschky and others (2006) present accumulation data obtained from stake readings along the transect from Neumayer station (70°39′ S, 08°15′ W) to Kottas Camp and farther on to the Kottasberge mountain range (Fig. 1a). Data obtained from stakes within 20–30 km of our GPR profiles range from 150 to $250\,\mathrm{kg\,m^{-2}\,a^{-1}}$ (Fig. 7a), with a high spatial variability. The transect up to Kottas Camp and the spatial variability of the accumulation data, complemented by GPR profiling, is further discussed by Richardson-Näslund (2004) with similar results. The stake-line data confirm the observation that in the immediate vicinity of Kottas Camp, accumulation values are slightly lower. Moreover, Rotschky and others (2007) obtained an accumulation map of western DML by interpolation of all available firn-core data, reporting values of about $180\,\mathrm{kg\,m^{-2}\,a^{-1}}$ for our investigation area. Our study therefore provides values within the range of current observations, but contributes a variability of accumulation rates on smaller spatial and temporal scales than has been previously published.

Temporal variation of spatial characteristics

We consider the temporal difference td, as defined by Equation (1), of GPR-based accumulation rates on profile 051202 between the time intervals $t_1 = 1990$–2005 and $t_2 = 1980$–90. The result is a mean value of −16%, i.e. accumulation rates in the time period t_1 are on average 16% lower than during t_2. This value is not constant along the profile 051202,

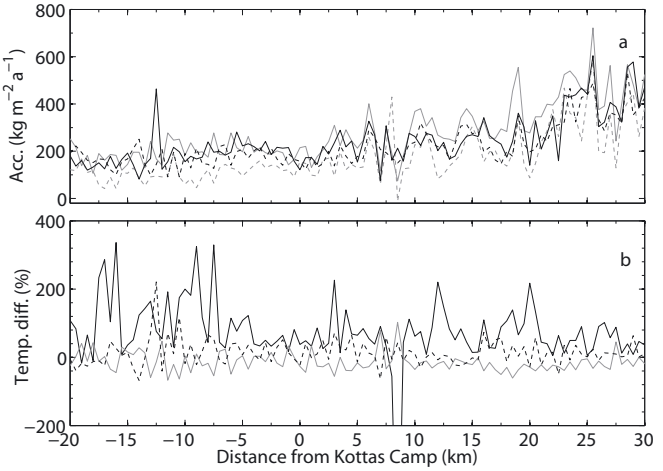

Fig. 7. (a) Accumulation values from stakeline readings in the vicinity of Kottas Camp: 1998 (black solid curve), 1999 (black dashed curve), 2000 (grey solid curve), 2001 (grey dashed curve). (b) Temporal differences calculated as in Equation (1): 1998–99 (black solid curve), 1999–2000 (grey solid curve), 2000–01 (black dashed curve). Negative values on the abscissa correspond to stakes located north of Kottas Camp; positive values are stakes to the south.

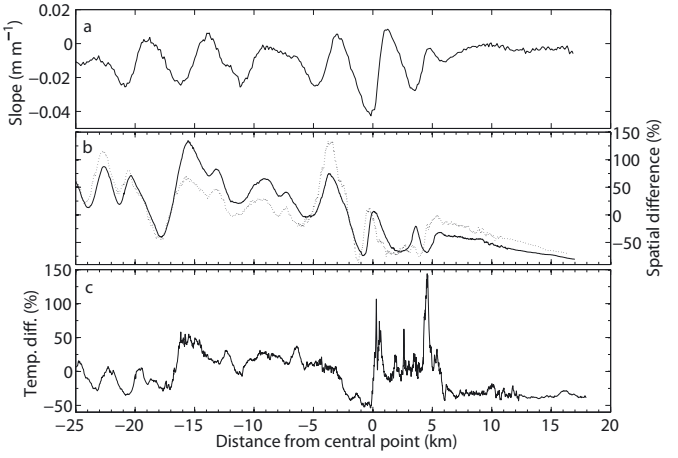

Fig. 8. (a) Main Potsdam Glacier flowline slope. (b) Potsdam Glacier accumulation spatial variation, expressed as differences from the mean, in per cent of the mean: 1980–2004 (solid curve) and 1970–80 (dashed curve). (c) Temporal variations between the time periods 1970–80 and 1980–2004 as calculated from Equation (1).

however. In fact, considering td pointwise along 051202 we see that temporal variations range from −1.3% to −23% (Fig. 4d). Comparing spatial and temporal differences along this profile, the variations seem to be linked, i.e. the largest temporal differences tend to occur at the places with largest relative spatial differences. Analysis of td on the cross-flow profile 051203 results in similar findings: the temporal differences likewise vary locally. Spatio-temporal characteristics of the stake-line data within 20–30 km around Kottas Camp (Fig. 7) confirm this observation, showing again a quite similar pattern of spatial and temporal accumulation, for instance between −15 and −10 km and ∼20 km.

Caution should be exercised with this comparison, however, as the stake-line data yield only annual variability whereas our GPR data consider decadal variability. In total, it seems that the spatial characteristics of accumulation are not constant in time in the considered region and timescales. Thus, it is important to derive the temporal differences pointwise along profiles and not only from the mean values. Small-scale features seem to affect both the temporal pattern and the spatial distribution.

Accumulation rates have been obtained likewise by combined analysis of GPR and firn-core studies on Potsdam Glacier, a near-coastal site in central Dronning Maud Land, in 2003/04. Similar to the area near Kottas Camp, the investigation area on Potsdam Glacier is characterized by the down-flow of ice from the polar plateau through mountain ranges. The spatial variability is discussed in detail by Anschütz and others (2007), reporting standard deviations of about 50% which is one order of magnitude higher than the standard deviations along the GPR profiles near Kottas Camp. On Potsdam Glacier, spatial differences from the respective mean value vary from −87 to +128% for the time period 1970–80 and from −79 to +130% for 1980–2004 (Fig. 8b). The temporal variation of accumulation rate of a few per cent as reported by Anschütz and others (2007) is obtained from the area-wide mean values of the time periods 1970–80 and 1980–2004, yet analysis of temporal variations along the profile on the main glacier flowline yields a varying pattern (Fig. 8c) as at Kottas Camp. The mean temporal difference of accumulation rates on Potsdam Glacier for the observed time periods t_1 and t_2 amounts to −3%, with values varying from −53% up to as much as +145%, as calculated from Equation (1) with t_1 = 1980–2004 and t_2 = 1970–80. Again, the largest temporal variations occur near maxima of spatial variability, indicating that temporal and spatial variations are not independent on these scales. The point-to-point variations of the temporal accumulation pattern near Kottas Camp (Figs 4e and 5e) exhibit less pronounced differences compared to those on Potsdam Glacier (Fig. 8c).

Anschütz and others (2006) discuss the influence of the surface topography on the spatial accumulation pattern on Potsdam Glacier and find dune-like features of relatively short distance between troughs, comparable to the megadunes observed on the polar plateau (Frezzotti and others, 2002). Upstream migration of these dunes at an average rate of 45 m a^{-1} (Anschütz and others, 2006) as well as locally varying glacier flow speed might also influence the variations in temporal accumulation observed on Potsdam Glacier.

Comparing the spatial and the temporal variations on Potsdam Glacier (Fig. 8b and c) and near Kottas Camp (Figs 4d and e and 5d and e) with the respective surface slopes (Figs 8a, 4c and 5c), we suggest that in areas of strong interaction between surface elevation, slope and accumulation, temporally varying mean accumulation rates lead to changing spatial accumulation patterns.

In order to analyze a possible correlation between spatial and temporal variations, we calculate the correlation coefficients R for spatial differences, in per cent, of the respective mean and temporal differences td along the GPR profiles near Kottas Camp and on Potsdam Glacier. We obtain values of 0.24 (t_1 = 1990–2005) and 0.69 (t_2 = 1980–90) for profile 051202 and correlation coefficients of 0.66 (t_1 = 1990–2005) and 0.55 (t_2 = 1980–90) for profile 051203 near Kottas Camp. The profile on the glacier flowline of Potsdam Glacier reveals R = 0.48 for t_1 = 1980–2004 and R = 0.28 for t_2 = 1970–1980.

This indicates that spatial and temporal variations are at least weakly correlated in our investigation areas. However,

inaccuracies of glacier flow velocity as well as dating uncertainties prevent a more detailed investigation. Influence of two-dimensional topography on accumulation rates might also be responsible for the observed spatio-temporal accumulation pattern. The topography in some of our investigation area can only be determined in high resolution along the GPR/GPS profiles, however. Due to the spacing between the profiles and the lack of a sufficient digital elevation model, we are unable to discuss possible small-scale topographical effects on our accumulation pattern.

Several other studies discussing temporal and spatial accumulation characteristics find different results. Vaughan and others (2004) reported accumulation data from Lyddan Ice Rise where spatial and temporal variability can be separated. They found that the regional mean accumulation is modified locally by persistent spatial variation and a non-persistent residual variability which is most likely due to minor changes in wind regime. As we do not have wind data for our investigation areas, we cannot determine whether our profiles are aligned with the main wind direction.

The results of Eisen and others (2005) on the East Antarctic plateau and Spikes and others (2004) in West Antarctica also indicate that spatial and temporal variability are separable. At this point we are unable to determine whether our findings are representative for larger areas of the grounded coastal parts of the Antarctic ice sheet. We therefore suggest that in our investigation areas the influence of surface topography, wind field and glacier flow are responsible for the relation between spatial and temporal accumulation pattern.

Near-surface winds tend to be complicated in nunatak-dominated areas (Jonsson, 1995), as would be seen on Potsdam Glacier. Since spatial variability is usually implicated when considering accumulation rates obtained from GPR (e.g. Richardson and others, 1997; Richardson-Näslund, 2004; Rotschky and others, 2004), further research is necessary to reveal possible correlations between spatial and temporal variability. As temporal variability obtained from ice-core records can be influenced by spatial variability of accumulation rates upstream of the drilling site and glacier flow (e.g. Spikes and others, 2004; Eisen and others, 2005; Frezzotti and others, 2007), detailed analysis of spatio-temporal characteristics is therefore important for the correct interpretation of climate signals obtained from ice cores.

Satellite observations such as those from GRACE allow the determination of ice-mass changes over several years with a spatial resolution of a few hundred kilometres. The spatial resolution of our ground-based observations on ice-mass changes is probably too low with too small a temporal overlap to validate the GRACE data. Our observations can contribute, however, to the assessment of statistical characteristics of the snow accumulation fluctuations which, in turn, is needed for the interpretation of satellite data. Ice-mass trends observed by satellite over a few years may be due either to interannual fluctuations in net ice surface mass balance or to long-term ice dynamics. In order to distinguish between these two effects, the temporal and spatial covariance of surface mass-balance fluctuation has to be known at least approximately.

Our GPR data analysis reveals the spatial behaviour of temporal changes in the investigation area. From Figures 4 and 5 it is evident that temporal variations can be spatially correlated over approximately 10 km. To determine the correlation length, and to draw conclusions about a comparison with GRACE data, it would be desirable to assess the correlation characteristics over larger distances. Clearly, for variations averaged over several hundred kilometres, the small-scale variations (deposition noise) are probably averaged out, therefore the standard deviation of temporal fluctuations will be smaller than the values of 28–33% obtained from the firn-core time series (Table 4). Such large fluctuations will therefore not be observed by GRACE.

Our observations and analyses help to qualify the spatio-temporal behaviour of the ice surface mass balance in larger areas and, together with studies from adjacent regions (e.g. Oerter and others, 1999; Richardson-Näslund, 2004; Rotschky and others, 2007), will support the interpretation of GRACE (and other satellite) observations.

CONCLUSIONS

Small-scale spatial variations of the recent accumulation rate as well as decadal and interannual temporal variations on Ritscherflya obtained from combined analysis of GPR and firn-core data have been discussed. Our GPR data indicate that spatial variability in this investigation area is rather low compared with other coastal sites, yet the year-to-year accumulation values obtained from firn cores reveal a large variability. Mean accumulation rates near Kottas Camp for the time period 1980–2005 amount to 190 kg m^{-2} a^{-1} on the flowline profile, with a standard deviation of 5–9%. The cross-profile yields a mean accumulation rate of 170 kg m^{-2} a^{-1} and a standard deviation of 9% for the same time period. Our results confirm the values from previous studies and provide additional detailed information about small-scale spatial and temporal variability.

We find that temporal fluctuations of accumulation coincide widely with spatial variations in our investigation area. Comparison with surface elevation and slope suggests that temporally varying accumulation rates lead to changes in the spatial pattern. It remains to be investigated how representative this result is for larger areas of Antarctica.

Furthermore, our results indicate that height changes of up to 7 cm a^{-1} may not be due to actual elevation changes but to accumulation variability in this area. This has implications for validation of satellite-based estimates of mass and elevation changes. Our study therefore provides valuable insight into local characteristics of temporal and spatial accumulation patterns, supporting the interpretation of satellite data and of ice-core records.

ACKNOWLEDGEMENTS

This work was supported by the Deutsche Forschungsgemeinschaft (DFG) through the VISA project, funded under grants Di 473/17 and Jo 191/8. O.E. was supported by the DFG 'Emmy Noether' programme. M. Scheinert (TU Dresden) provided the processed GPS data. B. Bayer is thanked for help with the figures. The support of the field team and in the ice laboratory is gratefully acknowledged. Comments from D. Vaughan and O. Brandt led to great improvements in the manuscript.

REFERENCES

Alley, R.B., P.U. Clark, P. Huybrechts and I. Joughin. 2005. Ice-sheet and sea-level changes. *Science*, **310**(5747), 456–460.

Anschütz, H., O. Eisen, W. Rack and M. Scheinert. 2006. Periodic surface features in coastal East Antarctica. *Geophys. Res. Lett.*, **33**(22), L22501. (10.1029/2006GL027871.)

Anschütz, H., O. Eisen, H. Oerter, D. Steinhage and M. Scheinert. 2007. Investigating small-scale variations of the recent accumulation rate in coastal Dronning Maud Land, East Antarctica. *Ann. Glaciol.*, **46**, 14–21.

Black, H.P. and W. Budd. 1964. Accumulation in the region of Wilkes, Wilkes Land, Antarctica. *J. Glaciol.*, **5**(37), 3–15.

Chen, J.L., C.R. Wilson, D.D. Blankenship and B.D. Tapley. 2006. Antarctic mass rates from GRACE. *Geophys. Res. Lett.*, **33**(11), L11502. (10.1029/2006GL026369.)

Church, J.A. and N.J. White. 2006. A 20th century acceleration in global sea-level rise. *Geophys. Res. Lett.*, **33**(1), L01602. (10.1029/2005GL024826.)

Eisen, O., U. Nixdorf, F. Wilhelms and H. Miller. 2002. Electromagnetic wave speed in polar ice: validation of the common-midpoint technique with high-resolution dielectric profiling and γ-density measurements. *Ann. Glaciol.*, **34**, 150–156.

Eisen, O., U. Nixdorf, F. Wilhelms and H. Miller. 2004. Age estimates of isochronous reflection horizons by combining ice core, survey, and synthetic radar data. *J. Geophys. Res.*, **109**(B4), B04106. (10.1029/2003JB002858.)

Eisen, O., W. Rack, U. Nixdorf and F. Wilhelms. 2005. Characteristics of accumulation rate around the EPICA deep-drilling site in Dronning Maud Land, Antarctica. *Ann. Glaciol.*, **41**, 41–56.

Frezzotti, M., S. Gandolfi and S. Urbini. 2002. Snow megadunes in Antarctica: sedimentary structure and genesis. *J. Geophys. Res.*, **107**(D18), 4344. (10.1029/2001JD000673.)

Frezzotti, M. *and 13 others*. 2007. Spatial and temporal variability of snow accumulation in East Antarctica from traverse data. *J. Glaciol.*, **51**(177), 113–124.

Fujita, S. *and 6 others*. 1999. Nature of radio-echo layering in the Antarctic ice sheet detected by a two-frequency experiment. *J. Geophys. Res.*, **104**(B6), 13,013–13,024.

Gregory, J. and P. Huybrechts. 2006. Ice-sheet contributions to future sea-level change. *Philos. Trans. R. Soc. London, Ser. A*, **364**(1844), 1709–1731.

Isaksson, E. and W. Karlén. 1994. Spatial and temporal patterns in snow accumulation, western Dronning Maud Land, Antarctica. *J. Glaciol.*, **40**(135), 399–409.

Jonsson, S. 1995. Synoptic forcing of wind and temperature in a large cirque 300 km from the coast of East Antarctica. *Antarct. Sci.*, **7**(4), 409–420.

King, J.C., P.S. Anderson, D.G. Vaughan, G.W. Mann, S.D. Mobbs and S.B. Vosper. 2004. Wind-borne redistribution of snow across an Antarctic ice rise. *J. Geophys. Res.*, **109**(D11), D11104. (10.1029/2003JD004361.)

Kreutz, K.J., P.A. Mayewski, L.D. Meeker, M.S. Twickler and S.I. Whitlow. 2000. The effect of spatial and temporal accumulation rate variability in West Antarctica on soluble ion deposition. *Geophys. Res. Lett.*, **27**(16), 2517–2520.

Melvold, K., J.O. Hagen, J.F. Pinglot and N. Gundestrup. 1998. Large spatial variation in accumulation rate in Jutulstraumen ice stream, Dronning Maud Land, Antarctica. *Ann. Glaciol.*, **27**, 231–238.

Oerter, H., W. Graf, F. Wilhelms, A. Minikin and H. Miller. 1999. Accumulation studies on Amundsenisen, Dronning Maud Land, by means of tritium, dielectric profiling and stable-isotope measurements: first results from the 1995–96 and 1996–97 field seasons. *Ann. Glaciol.*, **29**, 1–9.

Pettré, P., J.F. Pinglot, M. Pourchet and L. Reynaud. 1986. Accumulation in Terre Adélie, Antarctica: effect of meteorological parameters. *J. Glaciol.*, **32**(112), 486–500.

Ramillien, G. *and 6 others*. 2006. Interannual variations of the mass balance of the Antarctica and Greenland ice sheets from GRACE. *Global Planet. Change*, **53**(3), 198–208.

Richardson, C. and P. Holmlund. 1999. Spatial variability at shallow snow-layer depths in central Dronning Maud Land, East Antarctica. *Ann. Glaciol.*, **29**, 10–16.

Richardson, C., E. Aarholt, S.E. Hamran, P. Holmlund and E. Isaksson. 1997. Spatial distribution of snow in western Dronning Maud Land, East Antarctica, mapped by a ground-based snow radar. *J. Geophys. Res.*, **102**(B9), 20,343–20,353.

Richardson-Näslund, C. 2004. Spatial characteristics of snow accumulation in Dronning Maud Land, Antarctica. *Global Planet. Change*, **42**(1–4), 31–43.

Rignot, E. and R.H. Thomas. 2002. Mass balance of polar ice sheets. *Science*, **297**(5586), 1502–1506.

Rotschky, G., O. Eisen, F. Wilhelms, U. Nixdorf and H. Oerter. 2004. Spatial distribution of surface mass balance on Amundsenisen plateau, Antarctica, derived from ice-penetrating radar studies. *Ann. Glaciol.*, **39**, 265–270.

Rotschky, G., W. Rack, W. Dierking and H. Oerter. 2006. Retrieving snowpack properties and accumulation estimates from a combination of SAR and scatterometer measurements. *IEEE Trans. Geosci. Remote Sens.*, **44**(4), 943–956.

Rotschky, G. *and 6 others*. 2007. A new surface accumulation map for western Dronning Maud Land, Antarctica, from interpolation of point measurements. *J. Glaciol.*, **53**(182), 385–398.

Ruth, U. *and 6 others*. 2004. Comprehensive 1000 year climatic history from an intermediate-depth ice core from the south dome of Berkner Island, Antarctica: methods, dating and first results. *Ann. Glaciol.*, **39**, 146–154.

Sinisalo, A., A. Grinsted, J.C. Moore, E. Kärkäs and R. Pettersson. 2003. Snow-accumulation studies in Antarctica with ground-penetrating radar using 50, 100 and 800 MHz antenna frequencies. *Ann. Glaciol.*, **37**, 194–198.

Spikes, V.B., G.S. Hamilton, S.A. Arcone, S. Kaspari and P. Mayewski. 2004. Variability in accumulation rates from GPR profiling on the West Antarctic plateau. *Ann. Glaciol.*, **39**, 238–244.

Steinhage, D., U. Nixdorf, U. Meyer and H. Miller. 2001. Subglacial topography, internal structure of central, western Dronning Maud Land Land, Antarctica, determined from airborne radio echo sounding. *J. Appl. Geophys.*, **47**(3–4), 183–189.

Tapley, B.D., S. Bettardpur, M. Watkins and C. Reigber. 2004. The gravity recovery and climate experiment: mission overview and early results. *Geophys. Res. Lett.*, **31**(6), L09607. (10.1029/2004GL019920.)

Thomas, R. *and 17 others*. 2004. Accelerated sea level rise from West Antarctica. *Science*, **306**(5694), 255–258.

Van den Broeke, M.R. and N.P.M. van Lipzig. 2004. Changes in Antarctic temperature, wind and precipitation in response to the Antarctic Oscillation. *Ann. Glaciol.*, **39**, 119–126.

Van der Veen, C.J. 2002. Polar ice sheets and global sea level: how well can we predict the future? *Global Planet. Change*, **32**(2–3), 165–194.

Vaughan, D.G. 2005. How does the Antarctic ice sheet affect sea level rise? *Science*, **308**(5730), 1877–1878.

Vaughan, D.G., P.S. Anderson, J.C. King, G.W. Mann, S.D. Mobbs and R.S. Ladkin. 2004. Imaging of firn isochrones across an Antarctic ice rise and implications for patterns of snow accumulation rate. *J. Glaciol.*, **50**(170), 413–418.

Velicogna, I. and J. Wahr. 2006. Measurements of time-variable gravity show mass loss in Antarctica. *Science*, **311**(5768), 1754–1756.

Wilhelms, F. 1996. Leitfähigkeits- und Dichtemessung an Eisbohrkernen. *Ber. Polarforsch.* 191.

Wilhelms, F. 2005. Explaining the dielectric properties of firn as a density-and-conductivity mixed permittivity (DECOMP). *Geophys. Res. Lett.*, **32**(16), L16501. (10.1029/2005GL022808.)

Zwally, H.J. *and 15 others*. 2002. ICESat's laser measurements of polar ice, atmosphere, ocean and land. *J. Geodyn.*, **34**(3–4), 405–445.

MS received 14 December 2006 and accepted in revised form 5 September 2007

Characteristics and small-scale variability of GPR signals and their relation to snow accumulation in Greenland's percolation zone

Thorben DUNSE,[1,2] Olaf EISEN,[1,3] Veit HELM,[1] Wolfgang RACK,[1,4] Daniel STEINHAGE,[1] Victoria PARRY[5]

[1] *Alfred Wegener Institute for Polar and Marine Research, Am Allen Hafen 26, D-27568 Bremerhaven, Germany*
[2] *Department of Geosciences, University of Oslo, Box 1047, Blindern, NO-0316 Oslo, Norway*
E-mail: thorben.dunse@geo.uio.no
[3] *Versuchsanstalt für Wasserbau, Hydrologie und Glaziologie, ETH-Zürich, CH-8092 Zürich, Switzerland*
[4] *Gateway Antarctica, University of Canterbury, Private Bag 4800, Christchurch, New Zealand*
[5] *School of GeoSciences, University of Edinburgh, Drummond Street, Edinburgh EH8 9XP, UK*

ABSTRACT. We investigate snowpack properties at a site in west-central Greenland with ground-penetrating radar (GPR), supplemented by stratigraphic records from snow pits and shallow firn cores. GPR data were collected at a validation test site for CryoSat (T05 on the Expéditions Glaciologiques Internationales au Groenland (EGIG) line) over a 100 m × 100 m grid and along 1 km sections at frequencies of 500 and 800 MHz. Several internal reflection horizons (IRHs) down to a depth of 10 m were tracked. IRHs are usually related to ice-layer clusters in vertically bounded sequences that obtain their initial characteristics near the surface during the melt season. Warm conditions in the following melt season can change these characteristics by percolating meltwater. In cold conditions, smaller melt volumes at the surface can lead to faint IRHs. The absence of simple mechanisms for internal layer origin emphasizes the need for independent dating to reliably interpret remotely sensed radar data. Our GPR-derived depth of the 2003 summer surface of 1.48 m (measured in 2004) is confirmed by snow-pit observations. The distribution of IRH depths on a 1 km scale reveals a gradient of increasing accumulation to the northeast of about 5 cm w.e. km^{-1}. We find that point measurements of accumulation in this area are representative only over several hundred metres, with uncertainties of about 15% of the spatial mean.

1. INTRODUCTION

The Greenland ice sheet is rapidly responding to changing climatic conditions. Recent analyses indicate that the amount of surface melt has been increasing during the last decade (Fettweis and others, 2007). Its mass-balance characteristics are therefore the focus of investigations by various methods using satellite and airborne platforms (e.g. Shepherd and Wingham, 2007). One standard method to determine mass changes is provided by altimetry. Surface elevation measurements are acquired at several different times to yield ice volume changes, which are converted to mass changes (D.J. Wingham and others, http://esamultimedia.esa.int/docs/Cryosat/CVC_14Nov01.pdf). Using airborne laser altimetry acquired in 1994 and 1999, Krabill and others (2000) showed that the Greenland ice sheet is thinning at lower elevations and is generally in balance above an elevation of 2000 m. They found an overall mass loss for the last decade of the 20th century. In contrast, Zwally and others (2005) postulated a small overall mass gain for the period 1992–2002 derived from satellite radar altimetry. They observed ice-sheet growth in interior areas which compensates for the thinning at the margins.

Accumulation maps of Greenland inferred by snow-pit and shallow-firn-core analysis have reported uncertainties in accumulation rates as high as 24% (Bales and others, 2001). To overcome these problems and obtain reliable ground truth for interpretation of satellite data, several validation campaigns have been carried out on the Greenland ice sheet for the European Space Agency's upcoming CryoSat2 mission. Validation objectives focus on the relation of elevation changes to variations in accumulation and the densification process, major issues for conversion of observed volume changes to mass changes. Spatial extrapolation of point-based results can be evaluated and significantly improved by continuous profiles of snow and firn layering using ground-penetrating radar (GPR).

Within the CryoSat pre-validation study area using the Airborne SAR Interferometric Radar Altimeter System (ASIRAS; Helm and others, 2007), we made simultaneous GPR measurements in the percolation zone together with stratigraphic studies to investigate distribution of accumulation and physical properties of snow. The survey area (Fig. 1) was located at an altitude of 1940 m at point T05 (69.87° N, 47.33° W) on the Expéditions Glaciologiques Internationales au Groenland (EGIG) line, where geodetic and glaciological investigations have been repeatedly performed since 1956 (Hofmann, 1986).

The validation of CryoSat is of great importance because of the complex process of snow metamorphosis, particularly in the percolation zone. Pfeffer and Humphrey (1996, 1998) showed that the frequency of ice-layer occurrence in polar and subpolar firn is not only dependent on the amount of surface-generated meltwater during a particular summer season. They point out the importance of the initial snowpack conditions at the onset of melt, such as snow temperature or its 'cold content', as well as the presence of stratigraphic interfaces including buried wind or radiation crusts (Male, 1980). The cold content describes the energy which is needed to heat a unit volume of snow up to melting point.

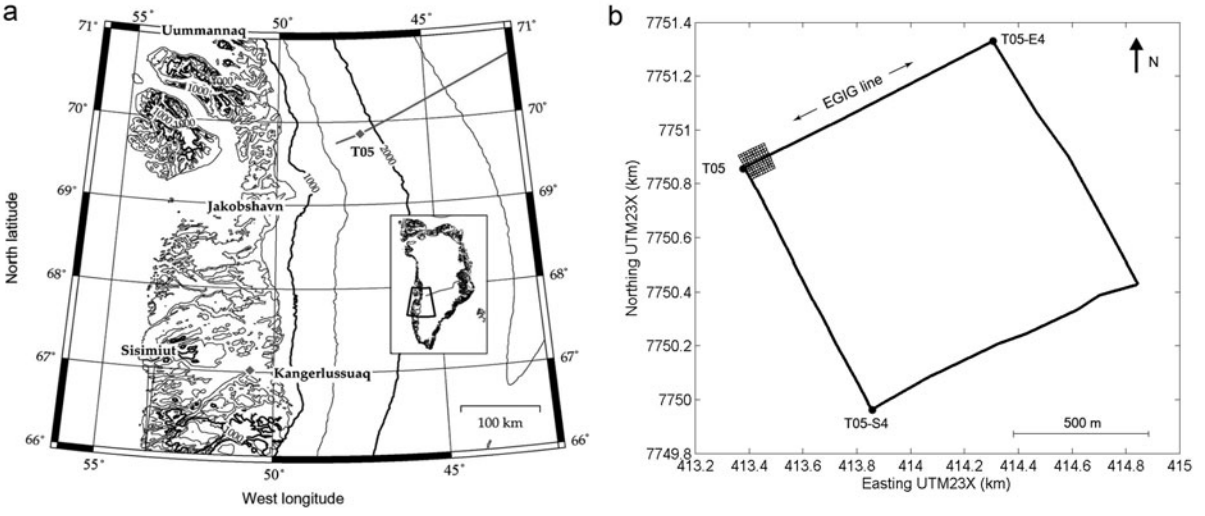

Fig. 1. (a) Map of the survey area around point T05 in the west-central region of the Greenland ice sheet. The line across the ice sheet indicates the position of the EGIG line. (b) Location of radar profiles near T05, forming a 100 m × 100 m grid with 10 m spacing and a 1 km × 1 km square.

If the initial snow temperature is low, and the snow density is moderate or high, the resulting high cold content limits the infiltration of meltwater, and typical ice layers may form and concentrate in a zone just below the summer surface. The larger, deeper fraction of the winter snowpack is left unaffected. In snowpack of low cold content, severe percolation will lead to extensive ice-layer formation and is likely to affect a greater fraction of the winter accumulation. In the case of high initial snow temperatures and warm summers, extensive breakthrough and limited ice-layer formation results in isolated ice lenses. The majority of refreezing meltwater is expected in the lowermost fraction of the winter accumulation, eventually accreted as thick ice on top of the previous summer surface (Pfeffer and Humphrey, 1996).

Summer surface melting and internal refreezing of percolating meltwater cause significant densification of the snowpack and large seasonal variability of radar backscatter properties at T05 (Parry and others, 2007). Solid ice structures in the snowpack from the previous winter, stemming from meltwater penetration, produce strong dielectric inhomogeneities which cause rapid signal attenuation with depth (Kanagaratnam and others, 2004). Earlier GPR studies, along with physical snow properties measurements, were undertaken in the vicinity of T05 at Crawford Point (Jezek and others, 1994) and near Dye-2 (Zabel and others, 1995) at centre frequencies in the C-band (5.3 GHz) and Ku-band (13.5 GHz) with bandwidths of 700 MHz and 2 GHz, respectively.

Intense radar reflections originated from a volume immediately below the previous summer surface. They were associated with solid ice structures in an upper fraction of the annual accumulation. While Zabel and others (1995) could track these features over long distances, more recent GPR measurements at T05 (Scott and others, 2006), applying the same frequency range, did not produce continuous internal reflection horizons (IRHs). Simultaneous observations of the snow and firn stratigraphy showed little evidence of lateral continuous ice layers, even at short length scales of 1 m. Prior to the onset of surface melt, ASIRAS proved capable of detecting a strong volume signal which could be traced continuously. The volume signal originated from solid ice structures below the undisturbed winter accumulation (Helm and others, 2007), enabling the mapping of winter accumulation along the flight-line.

In this study, we present GPR data collected at the same location, but at significantly lower frequencies in the P-band (500 and 800 MHz). We investigate the origin of continuous IRHs and interpret the formation process of related features in the snowpack. Further data, presented in section 2, comprise meteorological data from an automatic weather station (AWS) at Crawford Point (Steffen and others, 1996) and stratigraphic observations at the study site. The isochronous properties of the IRHs are finally used to interpret their distribution in terms of spatial variation of accumulation, and the relation to topography.

2. DATASETS AND METHODS

2.1. Climatological observations

Meteorological information is available through the Greenland Climate Network (Steffen and others, 1996) from an AWS at Crawford Point, in the vicinity of T05. The station has been in operation since April 1995, and the available record includes hourly mean values of surface air temperature, wind speed and direction as well as snow temperatures (Steffen and Box, 2001). We extract mean surface air temperatures for the three warmest months: June, July and August (JJA). In addition, we calculate a modified positive degree-day factor for each year. This factor is the sum of daily mean temperatures above 0°C during a particular period, typically a year (Braithwaite, 1995). Daily mean temperatures generally do not exceed the melting point at this location, as warm air masses are effectively cooled over the ice surface. The factor used here is based on positive hourly mean temperatures and referred to as the positive degree-hour (PDH) factor to distinguish it from the classical positive degree-day factor. In order to yield comparable dimensions, hourly mean values are weighted by a factor of 1/24. Artefacts caused by insufficient ventilation of the temperature sensor are avoided by taking wind speeds above 1 m s^{-1} as a constraint for the

inclusion of temperatures. The PDH factor is only minimally altered by this constraint.

To determine the onset of melt we use the day of year (DOY) at which two threshold values of PDH factors are reached: $DOY_{0.1}$ (PDH factor = 0.1) indicates the DOY when the first short events with above-zero temperatures occur; $DOY_{1.0}$ (PDH factor = 1.0) provides the DOY at which a stage of more persistent positive temperatures is present, likely causing some surface melt. For the time period between these days, the mean-snow temperature has been calculated using the record of a thermistor deployed at an initial depth of 1.1 m below the surface. This set of parameters describes the magnitude of meltwater generated at the surface as well as the cold content of the snow at the onset of melt. It gives a qualitative picture of the conditions to determine meltwater percolation and refreezing during a particular summer season. A detailed analysis of the AWS data is beyond the scope of the present study.

Data analysis indicates warm summers in 1995, 1999, 2002, 2003 and 2004 (Table 1). The years 1995, 1998, 2002 and 2003 were reported earlier as years of extreme melt throughout large parts of the Arctic, both in terms of the aerial extent and total amount of melt (ACIA, 2004; Steffen and others, 2004). Enhanced summer melting during these years covers the western slope of the Greenland ice sheet. The PDH factors from 1995 to 2004 range from 0.3 to 11.0. The highest values (>9.0) occurred in 1999, 2002, 2003 and 2004, a moderate value in 1995, and small values (<5.0) in the other years. The $DOY_{0.1}$ is in the range 142–188, and $DOY_{1.0}$ varies from 152 to 224. The time period between these two threshold values ranges from 2 to 44 days. In 1996, the year with the coldest summer and lowest PDH factor, the second threshold value was not reached at all. The period between the threshold values is generally longer for cold summers than for warm summers. Snowpack temperatures at the onset of melt range from –15.9 to –19.0°C, indicating a large cold content of the snow for all years in the record.

Table 1. Parameters characterizing onset and amount of meltwater generation at the surface as well as initial conditions affecting percolation into the snowpack, derived from AWS data from Crawford Point (Steffen and others, 1996)

Year	T_{air} (JJA)	PDH	$DOY_{0.1}$	$DOY_{1.0}$	T_{snow}	M_m	T_i
	°C	°C			°C		
2004	−4.7	9.7	171	173	−15.9	+	+
2003	−5.5	11.0	174	212	−17.3	+	o
2002	−5.9	10.5	161	163	−19.0	+	−
2001	−6.2	2.6	163	189	−18.0	−	o
2000	−6.6	4.4	188	191	−16.9	o	o
1999	−5.6	9.7	177	179	−16.1	+	+
1998	−5.2	2.9	142	152	−18.5	o	−
1997	−6.6	4.1	180	224	−19.0	o	−
1996	−8.6	0.3	171	−	−16.6	−	o
1995	−4.9	7.0	159	183	−16.5	+	o

Notes: T_{air}: air temperature for June, July and August (JJA); PDH: positive degree-hour factor; $DOY_{0.1,1.0}$: DOY when PDH reaches threshold value (0.1,1.0); T_{snow}: snow temperature; M_m: qualitative magnitude of melt; T_i: initial snow temperature at the onset of melt. M_m and T_i are divided into three qualitative classes: low (−), moderate/undecided (o) and high (+).

2.2. Snow-pit and firn-core data

During spring (19 April–13 May) and late summer 2004 (28 August–21 September), stratigraphic records were retrieved from the survey area from nine snow pits and shallow firn cores. The sites were located at point T05 and at distances of 1, 10, 100 and 1000 m east-northeast and south-southeast from T05, parallel and perpendicular to the EGIG line. These points are referred to as T05-E1 to E4, and T05-S1 to S4, respectively. Observations and measurements comprise visual snow stratigraphy, a qualitative description of layers and snow density. In spring, the last-summer melt surface (LSS) was reached in snow pits at a mean depth of 1.43 m. The LSS was characterized by a flat and hard ice layer beneath the late-summer depth hoar (Parry and others, 2007). The mean snowpack density ρ of all sites was 420 kg m^{-3}. Density variations in the winter layer were small. From the bottom of each pit, a shallow core with an approximate length of 2 m was drilled. The cores penetrated into a heterogeneous zone of metamorphosed snow, containing ice lenses and discontinuous ice layers below the LSS. At point T05-E3, 100 m east of T05, a longer core down to 18.9 m depth below the surface was additionally retrieved.

Repeated measurements in late summer reached the LSS at 1.51 m depth (5.3% increase compared to the spring depth) and a mean density of 530 kg m^{-3}(+26.2% compared to spring). Consequently, the water equivalent (w.e.) depth of the layer accumulated from the previous summer increased from 60.5 cm in spring to 79.6 cm in late summer, an increase of 31.6% (Parry and others, 2007). The density profiles showed more complex variations in late summer than in spring due to the presence of solid ice structures. Ice layers showed little spatial continuity, even at length scales as short as 1 m. An exception was a spatially continuous, 10–15 cm thick ice layer located at 3–3.5 m depth, potentially related to extreme summer melting in 2002 (Scott and others, 2006). Ice layers were present at all depths of the snow pits, more or less evenly distributed with no preferable depth of higher number density.

2.3. GPR data acquisition and processing

The GPR data were collected from 29 April to 11 May 2004 using a commercial radar system (RAMAC, Malå GeoScience) operating with shielded antennae at frequencies of 500 and 800 MHz. The GPR profiles form a grid of 100 m × 100 m with 10 m line spacing and were oriented parallel (west-southwest–east-northeast) and perpendicular (south-southeast–north-northwest) to the EGIG line. Additional GPR measurements were performed along 1 km sections forming a square (Fig. 1). A global positioning system (GPS) receiver was operated together with the GPR for simultaneous kinematic positioning. Static GPS measurements were additionally performed at the beginning and end of each profile. Gaps in the GPS data, resulting from the kinematic operation, were filled by linear interpolation between nearest kinematic or static points. A GPS reference station was operated at T05 and used for post-processing differential GPS data.

GPR shots were triggered every 0.1 m by means of an odometer attached to the sledge, which was pulled by hand. However, some slip caused the actual trace interval to vary between 0.10 and 0.12 m, reducing the number of traces along the profiles by up to 15%. To increase the signal-to-noise ratio during data acquisition, eight traces were recorded at each shot point location at a repetition rate of 200 kHz (quasi-instantaneously) and stacked. The receiving

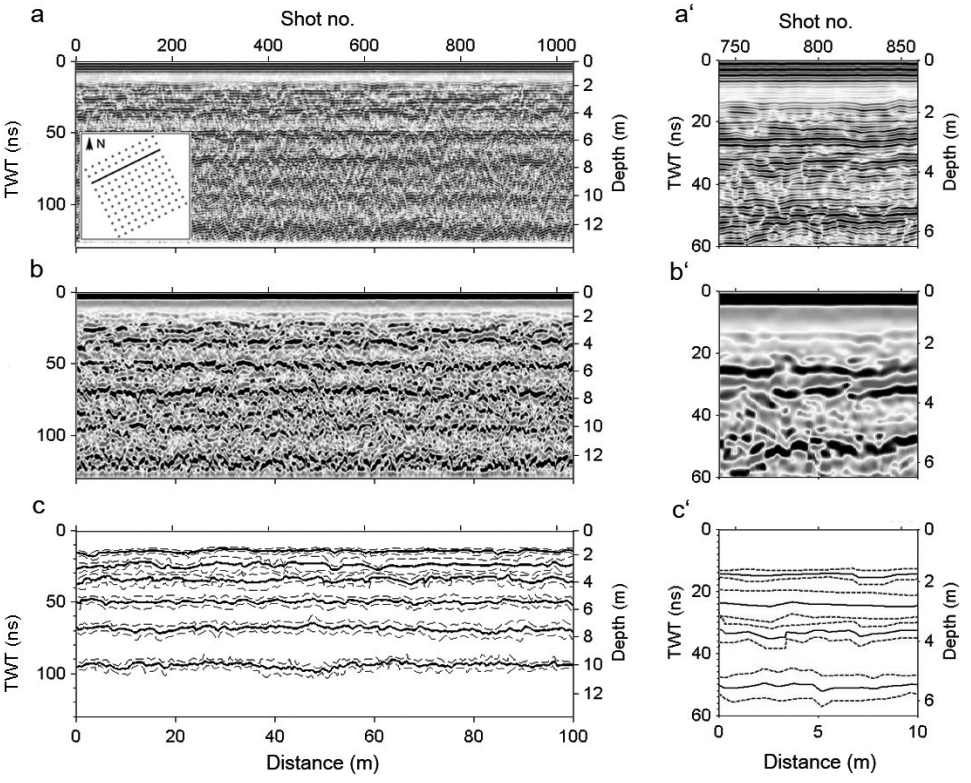

Fig. 2. Sample 500 MHz GPR profile, aligned approximately east–west as indicated in the inset in (a). Panels on the left (a, b, c) cover 100 m; panels on the right (a′, b′, c′) provide a 10 m wide close-up. (a, a′) Statically corrected, filtered and gain-corrected radargram, displaying signal amplitude; (b, b′) as (a), displaying signal envelope; (c, c′) tracked bands of high reflectivity of IRHs (upper and lower edge as dashed lines, computed centre line as solid line).

time window was 130 ns, corresponding to a depth range of about 13.5 m with 1024 samples and a sample interval of ∼0.13 ns. The wavelength λ in dry firn ($\rho = 500\,\mathrm{kg\,m^{-3}}$) is ∼0.42 m and ∼0.26 m for the 500 MHz and 800 MHz antennae, respectively. The GPR system is designed such that the centre frequency corresponds to the bandwidth. The theoretical resolution ($\lambda/4$) of the 500 MHz and 800 MHz antennae is therefore about 0.1 m and 0.06 m, respectively. This is limited by the length of the transmitted wavelets, however, comprising two to three cycles at 500 MHz and three to five cycles at 800 MHz, as interferences from partial reflections at inhomogeneities within the length of the wavelets occur.

Radar data were processed using the seismic software Focus/Disco (Paradigm Geophysical). Processing steps included static correction, bandpass filtering, complex trace analysis and gain adjustment (linear gain function and automatic gain control). For the static correction, individual traces were shifted such that the arrival times of the direct waves correspond to the theoretical arrival time in air, determined by the antennae spacing. Semi-automatic tracking routines in the Landmark software package SeisWorks2D (Halliburton) facilitated the tracking of continuous IRHs (Fig. 2a). To ensure that the same horizon was tracked throughout the record, intersections of previously tracked horizons were displayed as markers in the current profile. Cross-point errors in IRH depths from intersecting profiles are thus reduced.

Displaying the amplitude of the received signals, IRHs appear as bands of high reflectivity. Due to the above-mentioned length of the transmitter wavelet, the reflection horizons encompass multiple cycles of high amplitude (Fig. 2a). The uppermost 10–15 ns of the radargrams are masked by the arrival of the direct wave and cannot be used for analysis. Likewise, the lowermost 10 ns are blanked by the gain function.

The bands of high reflectivity become more clearly visible and focused when instead of the signal amplitude the signal envelope is displayed (Fig. 2b). The envelope display emphasizes zones of high reflectivity (strong instantaneous signal magnitude) vs zones of low reflectivity as it omits the zero-amplitude transitions. As the recorded radar data represent the real part of a complex signal, the imaginary part can be reconstructed by the Hilbert transform. Complex trace analysis yields the envelope, also termed the instantaneous magnitude of the complex signal, while the phase information is lost (Mari and others, 1999).

The upper and lower edges of each band were tracked by logging trace number and two-way travel time (TWT) of the sample exceeding a threshold magnitude. The mean TWT of both values determines the centre line of the IRH, which coincides approximately with the maximum signal magnitude (Fig. 2c). The difference in the TWT between the upper and lower edge is referred to as the IRH width.

For later analysis, we converted the recorded radar signals from the time domain to the depth domain. The wave speed v of the radar signal in snow is determined by the permittivity, $v = c/\sqrt{\varepsilon'_\mathrm{r}}$, where c is the speed of light in vacuum. We used the empirical relation of Kovacs and others (1995), $\varepsilon'_\mathrm{r} = (1 + 0.000845\rho)^2$, to link density and permittivity ε' where the snow density ρ is in $\mathrm{kg\,m^{-3}}$. Finally, the results for reflector depth are half the TWT multiplied by the average wave speed to that depth. A typically observed mean density of $500\,\mathrm{kg\,m^{-3}}$ corresponds to a wave speed

Table 2. Mean values of two-way travel time, depth and cumulative mass of IRHs and associated IRH width. Variation refers to one standard deviation of the spatial mean. Accumulation values apply to the layer above the IRH, bounded by the upper adjacent IRH

IRH	TWT	Depth	Cumulative mass	IRH width	Age	Possible origin	Accumulation
	ns	m	$kg\,m^{-2}$	m	years		$kg\,m^{-3}\,a^{-1}$
IRH-15	13.6 ± 0.9	1.48 ± 0.10	636 ± 43	0.49 ± 0.13	1.4 ± 0.5	LSS 2003	636 ± 43
IRH-25	21.3 ± 1.2	2.29 ± 0.17	1012 ± 82	0.73 ± 0.21	2.2 ± 0.8	LSS 2002*	376 ± 125
IRH-35	32.5 ± 1.9	3.45 ± 0.17	1604 ± 93	0.87 ± 0.25	3.5 ± 1.2	LSS 2001*	592 ± 175
IRH-50	49.9 ± 2.1	5.21 ± 0.21	2480 ± 99	0.80 ± 0.21	5.4 ± 1.8	LSS 1999	438 ± 96
IRH-70	67.9 ± 2.8	7.04 ± 0.19	3490 ± 87	0.83 ± 0.23	7.6 ± 2.4	LSS 1997	505 ± 93
IRH-95	94.7 ± 3.3	9.86 ± 0.17	4960 ± 99	0.76 ± 0.22	10.8 ± 3.4	LSS 1994*	490 ± 62

*Ice may have accreted on top of the LSS during the following summer, thereby altering the origin of the IRH.

of $2.1 \times 10^8\,m\,s^{-1}$. During data acquisition in spring, the snow was completely frozen (as evident from thermistor data at Crawford Point). Effects of liquid water on the propagation of the radar signal can therefore be safely neglected.

The error in the depth determination of a tracked reflection can be split into range-dependent and range-independent contributions. The former include inaccuracies in the correction of arrival times, assumed to be on average no larger than one sample (0.13 ns or ~1.5 cm), and inaccuracies in IRH tracking. Tracking IRHs is a partly subjective process; quantifying the related error is therefore difficult. We estimate the related error to be five samples (0.6 ns or ~6 cm).

Range-dependent errors are introduced in the conversion of TWT to depth, due to deviations from the snow density–depth model. Because of the depth-averaging of the velocity profile, the conversion from time to depth domain is less prone to errors from variations in density on short vertical length scales at a single location. Rather, it is a deviation of the mean or bulk density along the GPR profiles that introduces depth errors. We analyze density–depth profiles from seven snow pits and firn cores within 100 m of T05. The standard deviation of bulk densities from one pit to another rapidly decreases with depth and falls below 4% at 1 m depth. For simplicity, we assume a maximum error of 4% in the density–depth model, constant over the whole depth range of the GPR. The related maximum error in TWT–depth conversion increases from 0 cm at the surface to >15 cm at 10 m depth. The sum of the three error contributions adds up to a maximum error in IRH depth of ≤10 cm in the upper 2 m to almost 25 cm in 10 m depth.

3. ORIGIN AND INTERPRETATION OF INTERNAL REFLECTION HORIZONS

Exploiting the distribution of IRHs to derive information about spatio-temporal variations in accumulation requires that the IRHs are isochrones. This implies that an individual IRH obtains its physical properties at the same time and maintains this characteristic while being submerged to a larger depth. The origin of the IRHs is investigated in this section. We first compare GPR results obtained at the two different frequencies, and then interpret the IRHs by comparison with observed snow stratigraphy. Based on these results, an age–depth model is established by employing earlier accumulation estimates from ice-core analysis. We finally discuss reasons for the observation of continuous IRHs in comparison to other studies.

3.1. Comparison of IRHs observed at 500 and 800 MHz

Altogether, six IRHs down to about 10 m depth could be clearly identified and tracked at both frequencies, within the grid as well as along the 1 km sections. These are referred to as IRH-15 to IRH-95, with numbers indicating their approximate depth in nanoseconds of TWT near T05 (Table 2). To validate the measurements, 500 and 800 MHz results were first treated independently and later combined. The data at both frequencies reveal the same number of clearly identifiable IRHs, located at approximately the same depths with respect to the IRH centre line. IRHs obtained at 800 MHz appear on average 4.8% deeper than in the 500 MHz record. The differences in IRH depths increase with depth and range from 0.00 m for IRH-15 up to 0.52 m for IRH-95.

To investigate this further, we quantify the spatial variation in depth of each IRH in terms of its standard deviation (depth-SD). This property will serve as a first-order approximation of the small-scale spatial variability in snow accumulation. We consider it to be a measure of the representativeness of layer depths derived from individual point measurements within a certain area. Applying it to the comparison of 500 and 800 MHz data, it turns out that the depth-SD is on average 7.0% smaller for the 800 MHz than for the 500 MHz measurements for corresponding IRHs. No trend with respect to depth is present for the ratios of the depth-SD at both frequencies. Regarding differences in IRH widths, the 800 MHz survey yields slightly larger values: +6.0% on average. The observed differences in both IRH depths and widths can be considered small. They are most likely caused by variations in constructive and destructive interference from inhomogeneities because of the different frequencies and wavelets. The small differences indicate that IRHs obtained at 500 and 800 MHz likely arise from the same cluster of physical subsurface features.

Unless explicitly stated otherwise, we use mean values of both 500 and 800 MHz measurements for the discussion and interpretation in the rest of this paper. We will focus on the upper edges of IRHs, as they were the easiest to identify, usually occurring below a zone of low reflectivity and thus providing high tracking accuracy. The physical explanation for this observation is discussed in section 3.2.

3.2. Relation of GPR reflectivity to snow stratigraphy

Changes in density dominate the reflectivity of the firn pack, while changes in conductivity can be neglected. We now investigate which density features could cause the observed

IRHs. The upper edge of IRH-15 is located at 1.48 ± 0.10 m. It corresponds well with the depth of the LSS (end of 2003 summer surface) of 1.43 ± 0.04 m (Parry and others, 2007). We therefore consider it likely that IRH-15 arises from strong density contrast at the LSS formed during summer 2003. The IRH width and associated variability of IRH-15 is significantly smaller than for the deeper IRHs. We explain this with the time of data acquisition. As the data were acquired prior to melting conditions in summer, the overlying snowpack has not yet experienced metamorphosis through meltwater intrusion from above. The significantly larger reflector widths of deeper IRHs suggest that these may be influenced or even arise from ice-layer clusters formed during multiple summer seasons.

The depth range below IRH-15, down to approximately 4 m, is characterized by very complex and strong reflections. Two IRHs have been tracked in this depth range. The upper is IRH-25, at and below 2.29 m depth at T05. IRH-25 is laterally discontinuous and partly splits into two separate IRHs. IRH-35, at and below 3.45 m depth, is laterally well confined towards larger depths, where only weak signal returns are possible.

The AWS data at Crawford Point and the stratigraphic observations at TO5 in late summer 2004 provide an archetype for the development of the snowpack in warm summers, useful for interpreting deeper reflection patterns. The conditions during the melt period 2004 resemble those in the wet snow zone rather than the percolation zone. This is the year (2004) for which the AWS record yields the warmest summer months (June–August) with a mean temperature of -4.7°C, a high PDH factor and the highest initial snowpack temperature at the onset of melt (-15.9°C). Accordingly, after the melt season, discontinuous ice layers were found at all depths of the snow pits (Parry and others, 2007).

Similar conditions can also be expected for the years 2003 and 2002, for which the AWS data show clearly above-average summer temperatures. An example is the 0.10–0.15 m thick ice layer at 3–3.5 m depth (Scott and others, 2006; Parry and others, 2007), which is probably related to the extreme summer melt in 2002. Strong percolation of surface-generated meltwater in 2002 eventually accreted as ice on top of the underlying summer surface. We therefore suggest that IRH-35 partly arises from ice which probably formed during summer 2002 on top of LSS 2001. The complex appearance of IRH-25 above IRH-35 may be a consequence of extensive downward meltwater flow and soaking of the previous accumulation layer during summers 2003 and 2002. IRH-25 could therefore represent both the 2002 summer surface and lower clusters of solid ice structures as well as the ice accreted on top during the following summer.

The 4–5.5 m depth range shows weak signal returns in the GPR data compared to the depth range above. The AWS data for the years 2000 and 2001 show significantly colder summer temperatures expressed in low PDH values as well as colder initial snow temperatures. The winter accumulation during this time period is expected to be less affected by meltwater infiltration and refreezing. To date, an independent age–depth model is not available to confirm these interpretations. However, we can utilize earlier estimates of accumulation to determine a tentative age–depth model.

3.3. Continuous IRHs

The detection of continuous IRHs is encouraging for deriving accumulation characteristics. Interestingly, other studies did not observe continuous IRHs. Scott and others (2006) performed measurements at the same site in late summer 2004. Their data, collected along profiles of length 100 m, did not reveal continuous near-surface IRHs.

Three factors are likely to cause this discrepancy. First, they used a ground-based step-frequency radar with a centre frequency of ~13 GHz, one set-up with a bandwidth 1 GHz, and in a second operational mode with a bandwidth of 8 GHz. The higher resolution of their system, compared to that used in the present study, causes higher volume backscatter and a reduced penetration depth. Laterally coherent reflections from layers or similarly layered sequences are therefore less likely to be observed. Second, the trace interval of 0.5 m up to almost 1.5 m chosen by Scott and others (2006) is very large with respect to the high antennae resolution. It is therefore possible that despite a small antenna footprint, laterally consecutive first Fresnel zones did not overlap, therefore disabling laterally coherent reflections. In comparison, we used a trace interval of 0.1 m combined with a significantly lower resolution. Future experiments in comparable areas should take this into account. Finally, the complexity of the radar returns is further enhanced by the change in physical snow properties in the transition from pre- to late-summer conditions.

3.4. Age–depth model

Cumulative mass within a depth section divided by the corresponding time of accumulation yields the accumulation rate. We can therefore estimate the age of the IRHs by dividing the ice-core-derived cumulative mass above a particular horizon, obtained by integrating the density down to this horizon, by an independently determined mean accumulation rate at the site (available from earlier studies). We focus on the upper edges of IRHs, interpreted to represent LSSs for which the overlying winter layer is relatively undisturbed by ice accreted on top of the LSS.

Fischer and others (1995) derived accumulation rates along the EGIG line based on isotopic and chemical analysis of shallow firn cores, drilled in 1992. They found the annual mean snow accumulation over an 8 year period at T05 to be 46.0 ± 10.2 cm w.e. We attribute the variation of 22% to interannual variability of accumulation. Guided by the hypothetical time-span of accumulation, we appoint age estimates to the upper edges of IRHs (Table 2). This yields mean accumulation rates of 37.6–63.6 cm w.e. for periods enclosed by adjacent horizons. The mean accumulation rate over the period 1994–2004 is found to be 49.6 cm w.e. We estimate a temporal variability of 9.6 cm w.e. by the standard deviation of the six values, corresponding to the six IRHs. This value has to be considered as a lower limit for the interannual variability, as three of the periods average over 2 and 3 years, respectively. The relative uncertainty in the time since accumulation, and consequently the age estimate, amounts to roughly 30%. The absolute uncertainties therefore increase significantly with depth.

3.5. Scenarios for IRH formation

The stratigraphy in the percolation zone is very complex and its interpretation is based more on similar layered sequences than on the identification of specific layers (Benson, 1962). The initial processes for formation of a lateral continuous IRH occur at the snow surface mainly during the summer season. For the subsurface processes, which finally lead to amplification of the initial characteristics to produce

strong IRHs in the upper ~10 m, we propose the following scenarios.

In general, the IRHs are based on the integral effect of solid ice clusters on GPR signals at 500 and 800 MHz, as individual lateral continuous ice layers may be absent. Occasional melt–refreeze cycles during summers with little to moderate surface melt form an ice crust at the surface. Some meltwater infiltrates the snowpack and refreezes in the upper fraction of the layer of the previous winter's accumulation, immediately below the summer surface. Once this layer is submerged and overlain by new accumulation, these features probably appear in the GPR record as a continuous IRH with a defined upper boundary and a rather diffuse lower boundary consisting of isolated signals of high reflectivity. Extensive breakthrough of percolating meltwater during warm summers with severe surface melt produces isolated ice lenses throughout the snowpack, but percolating meltwater may accrete as thick ice on top of the LSS.

This was the case in late summer 2004 where accretion of ice was observed at the bottom of a snow pit at T04 on the EGIG line, at an elevation of 1860 m, just 80 m lower than T05 (Scott and others, 2006). Because of the strong density contrast between the porous snow matrix and the solid ice layer, this constitutes an inhomogeneity of high reflectivity in the GPR record. However, due to its proximity to the underlying LSS, this feature is barely separable from the LSS below. In case of persistent warm temperatures, extreme surface melt and subsequent meltwater percolation could cause a wetting front to propagate from the surface downwards. This may lead temporarily to snowpack conditions similar to those in the wet-snow zone at lower elevations. It can then form a unit of uniform wetting in an upper fraction of the snowpack, containing a complex mixture of small but numerous ice structures surrounded by coarse-grained snow crystals. As the complete layer thickness down to the underlying LSS is affected, this unit likely appears in the GPR record as a band of high backscatter with no defined lower boundary. Therefore, the continuous reflection from the LSS may be lost as a result of high clutter.

If no melting takes place during the summer, the conditions in the uppermost snow layer resemble those of the dry snow zone. The density, and thus the dielectric contrast, of layers originating from different accumulation events is small compared to normal percolation conditions. Only the formation of distinct layers of hoar or wind crust could provide a large enough density contrast to produce continuous IRHs. However, if this is not the case, then no continuous IRH might be observed with GPR, making it difficult to separate accumulation from subsequent years.

3.6. Spatio-temporal variation of accumulation

Here we discuss the spatial distribution of IRHs and the underlying accumulation pattern on different spatial scales. The results are first discussed independently of an age–depth scale in terms of depth and cumulative mass. We then apply the age–depth model established above to discuss the variation of accumulation in the larger regional context.

Over the area of the 100 m × 100 m grid, IRHs appear as interfaces aligned parallel to the reference surface (Fig. 2). The depth distribution of each IRH is basically of Gaussian shape. The depth-SD of the IRHs varies from 0.10 to 0.21 m, with a mean of 0.17 m, with the smallest value for the uppermost IRH-15, but shows no further systematic trend with depth (Table 2). As all depth-SD values are of the same

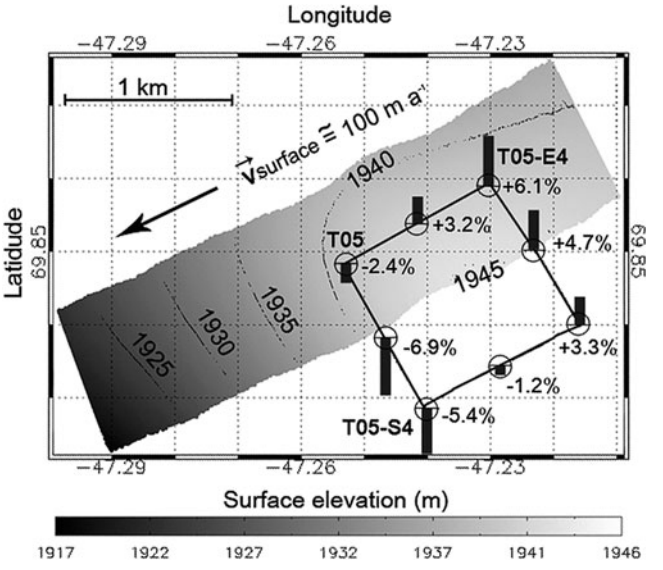

Fig. 3. Digital elevation model with 5 m contour lines, based on laser scanning during the ASIRAS campaign (Helm and others, 2007). Also shown is the location of the 1 km × 1 km square and the variation of cumulative mass above IRH-50 along its profiles. Bars visualize percentage deviations of inverse-distance weighted cumulative mass within a search radius of 100 m with respect to overall mean.

order of magnitude for all horizons, we assume that a consistent spatial gradient in snow accumulation cannot be detected at scales of 100 m at this location. For this length scale we can therefore estimate the accumulation variation to be 8.5 cm w.e., derived by multiplying the mean depth-SD with a typical density of 500 kg m^{-3}.

To identify a possible spatial gradient in snow accumulation over the area enclosed by the 1 km × 1 km square, we investigate the distribution of IRH-50. This IRH produces strong and relatively undisturbed return signals, providing reliable results. We compute inverse-distance weighted mean values of cumulative mass for measurements within a search radius of 100 m from mid- and end-points of the 1 km sections. Deviations are expressed as percentages of the average mass along all 1 km sections, indicated as bars in Figure 3. The analysis reveals increasing accumulation towards the northeast, a trend not recognized over the area of the 100 m × 100 m grid. Values range from –6.9% at the mid-point of the line connecting point T05 and point T05-S4 in the southwest to +6.1% at point T05-E4 in the northeast. IRHs along the 1 km sections show an increasing depth-SD with depth, varying between 0.11 m for IRH-15 and 0.34 m for IRH-95, with an overall mean of 0.22 m.

Spatial gradients in accumulation of such magnitude have been observed in many areas on ice sheets. They usually represent local effects caused by topographic undulations on small scales (few kilometres) that affect wind-driven redistribution of snow (King and others, 2004). To investigate if this process is also of relevance here, we use the new digital elevation model of the survey area, acquired during the ASIRAS campaign in spring 2004 by laser scanning (Helm and others, 2007).

The topography data indicate that our survey area lies on a plateau, with a nearby slope break to the southwest (Fig. 3). ASIRAS detected a slope-dependent, bimodal distribution of the uppermost-layer snow thickness along a 2.7 km crossover flight of T05 (Helm and others, 2007). A layer thickness of

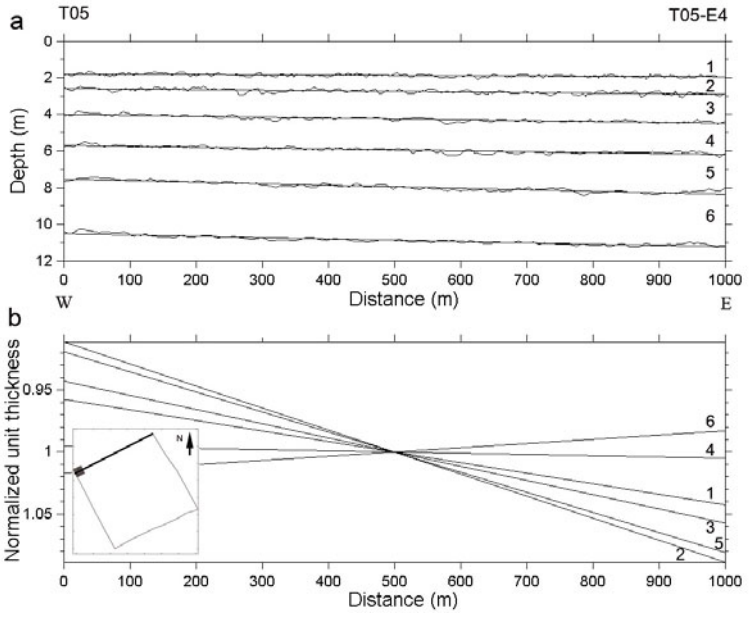

Fig. 4. (a) IRHs along the 1 km profile east of T05 (see inset in (b)). The positions of IRH centre lines and corresponding linear regression lines are plotted. (b) Normalized thickness for layers enclosed by adjacent horizons, with profile centres crossing the mean (normalized unit thickness ≡1).

1.30 ± 0.05 m was found on the slope (eastwards-rising elevation of 1920–1940 m), and 1.50 ± 0.13 m on the plateau (elevations of 1940–1945 m). Our 1 km GPR profiles are situated on the plateau, close to the edge of the area covered by ASIRAS, and obviously fall in a transition zone between the two accumulation modes. The ASIRAS-based layer thickness for the plateau corresponds very well with the depth of IRH-15 and the depth of the LSS from snow-pit analysis. While the strong response of the LSS causes complete power loss of the ASIRAS signal for the depth range below, we showed above that the GPR system is capable of detecting continuous IRHs down to 10 m depth. This enables us to investigate the spatial variability for earlier time periods.

To this end we use selected 800 MHz sections oriented parallel and perpendicular to the EGIG line. IRHs appear to be parallel to the surface along the section perpendicular to the EGIG line. The section following the EGIG line from T05 in a direction east-northeast reveals that IRHs are clearly dipping in that direction (Fig. 4a). To analyze the temporal variability of the spatial gradient in snow accumulation, we determine the thicknesses of units enclosed by adjacent horizons (see unit numbering in Fig. 4). The units were normalized by their corresponding mean thickness. We then performed a linear regression for all units. The fitted lines pass through the centroid (x mean, y mean; Fig. 4b). It is evident that the trends along this GPR profile are well represented by linear ap-proximations, indicating that the underlying gradient in snow accumulation is also linear. In general, the gradient appears less strong for deeper and older units than for younger units. The positive gradient in accumulation towards the east-northeast persists for most of the accumulation periods covered by our data.

Layer thicknesses increase by about 10% from southwest to northeast for units 1, 2, 3 and 5. The trend is reversed for the deepest unit 6, for which normalized thickness is about 3% greater at the northeast than at the southwest end. The thickness of unit 4 is almost constant. The observed weakening of the gradient with depth could be explained by the fact that we neglect ice advection. The surface velocity of the ice flow at the survey site is about 100 m a^{-1}. Ten-year-old firn originates about 1 km upstream from the present location, further up on the plateau, where ASIRAS detected little variability in snow accumulation (Helm and others, 2007).

The age estimate of the six IRHs enables us to convert the observed IRH depths and cumulative mass discussed above to accumulation values. The previous year's accumulation (summer 2003–spring 2004) yields 63.6 ± 4.3 cm w.e. This value is about 40% larger than previously derived accumulation rates (Fischer and others, 1995), but is in agreement with the snow-pit derived accumulation of 60.5 ± 3.4 cm w.e. (Parry and others, 2007). It should be noted that this is a preliminary lower-limit result, since the mass-balance year was not fully completed by the time of data acquisition. The observed northeast gradient in snow accumulation is of the order 5.0 cm w.e. km^{-1}, roughly 10% of the mean per km. This value is one order of magnitude larger than the regional trend on a 100 km scale on existing maps of accumulation rates over Greenland (Bales and others, 2001). We explain this discrepancy as the result of the difference between local and regional elevation trends influencing the katabatic wind speed and thus post-depositional redistribution of snow. Whereas the regional slope inland of the study site is of the order $1–5 \times 10^{-3}$ (i.e. 100–500 m over 100 km; Fig. 1), local slopes in the plateau-like area of the 1 km square amount to $\sim 10^{-2}$ (Fig. 3). The ASIRAS observation of further decreasing accumulation on the larger slope in the west confirms this relation.

The redistribution of mass by percolation in years of strong melt could cause a higher uncertainty for the estimated accumulation values. Percolating meltwater during summer 2003 could have caused ice accretion on top of the LSS of 2002 (IRH-25). This mass would therefore contribute to the value computed for the previous period 2001/02, but would be lacking in the period 2002/03. Thus, the minimum accumulation rate of 37.6 ± 12.5 cm w.e. for the period 2002/03 (Table 2) is likely an underestimate of the full balance year.

Mass loss by percolation may also apply for the the period 2001/02. If the amount of loss by percolation and gain by internal accumulation were comparable in both periods, the downward loss of mass and the gain from above would be compensated.

4. CONCLUSIONS

We analyzed GPR measurements at one particular location in the percolation zone of Greenland using frequencies of 500 and 800 MHz on scales of up to 1 km. The characteristics of the GPR record in the upper 5–6 m depth were related to meteorological conditions during previous melt seasons. The GPR-derived depth of the LSS (2003) around 1.4–1.5 m is in very good agreement with the depth as observed both in snow pits and by ASIRAS. The very complex radar response at 1.5–4.0 m depth is probably related to severe percolation and subsequent refreezing of large amounts of surface-generated meltwater during the extreme summers of 2003 and 2002. Reflections in the depth range 4.0–5.5 m are of significantly lower energy and less complex. They likely coincide with cold to moderate summer conditions in 2000 and 2001.

Relating the GPR record to snow stratigraphy, we conclude that the continuous IRHs are basically isochrones in the sense that each was generated during one melting season. Not only can they arise from specific ice layers, but also from clusters of solid ice structures in vertically bounded sequences. The structure of the IRH seems to depend upon initial snowpack conditions at the onset of melt and summer temperatures in the melt season that generated the IRH. Features leading to coherent and laterally continuous horizons can encompass isolated typical ice layers in the upper part of the snowpack, small but numerous ice clusters in a layer that was previously wetted considerably and accretion of ice or highly compacted firn at the bottom of an annual accumulation layer.

In the case of extreme melting, the characteristics of deeper IRHs may be altered by strong meltwater percolation. As a consequence, IRHs may not be clearly identifiable every year. The choice of wavelengths of the order several decimetres and high spatial sampling are a prerequisite for detecting continuous IRHs. At higher frequencies in the Ku-band, stronger volume backscatter, less distinct integral effects of ice-layer clusters on the radar return, and significantly lower signal penetration, may inhibit detection of laterally continuous sequences.

The distribution of the IRHs over the area of investigation is related to accumulation. For an area of approximately 100 m × 100 m around T05, accumulation values derived from individual snow pits or firn cores have uncertainties of about 8.5 cm w.e. or 15% of the mean accumulation, as determined through depth-SD analysis of the GPR survey. Over a distance of 1 km, an additional local trend in accumulation of 5.0 cm w.e. km^{-1} is present parallel to the EGIG line. This trend is about 10 times larger than the regional gradient. The variation in accumulation is likely related to topographic undulations, which affect wind-driven redistribution of snow. An observed weakening of the gradient for accumulation derived from deeper IRHs may be due to the fact that deeper units originate further upstream where surface slopes are comparably small, and accumulation is thus more uniform.

Compared with currently applicable airborne radar altimeters such as ASIRAS, or upcoming satellite sensors such as CryoSat's Synthetic Aperture Radar Interferometric Radar Altimeter (SIRAL), GPR systems naturally achieve a much lower spatial coverage. However, especially in the percolation zone, GPR has the advantage that deeper, older IRHs can be detected, allowing investigations not only of spatial but also temporal variability of accumulation. As full utilization of either dataset requires independent age–depth models, regular snow-pit and firn-core studies will remain necessary in operational stages of remote-sensing missions.

ACKNOWLEDGEMENTS

CryoVEx 2004 was funded by the European Space Agency (C18677/04/NL/GS) and supported by the German Aerospace Research Center (DLR) (50EE0505). O. Eisen was supported through an 'Emmy Noether' scholarship EI 672/1 of the Deutsche Forschungsgemeinschaft. We gratefully acknowledge the Greenland Climate Network for providing the AWS record from Crawford Point. Thanks to P. Nienow and D. Mair for collection of the snow stratigraphy records in the field and to T. V. Schuler for inspiring discussions of the AWS record. We also thank T. Scambos and two anonymous reviewers for critical remarks on the manuscript.

REFERENCES

Arctic Climate Impact Assessment (ACIA). 2004. *Impacts of a warming Arctic: Arctic Climate Impact Assessment*. Cambridge, etc., Cambridge University Press.

Bales, R.C., J.R. McConnell, E. Mosley-Thompson and G.W. Lamorey. 2001. Accumulation map for the Greenland ice sheet: 1971–1990. *Geophys. Res. Lett.*, **28**(15), 2967–2970.

Benson, C.S. 1962. Stratigraphic studies in the snow and firn of the Greenland ice sheet. *SIPRE Res. Rep.* 70.

Braithwaite, R.J. 1995. Positive degree-day factors for ablation on the Greenland ice sheet studied by energy-balance modelling. *J. Glaciol.*, **41**(137), 153–160.

Fettweis, X., J.P. van Ypersele, H. Gallée, F. Lefebre and W. Lefebvre. 2007. The 1979–2005 Greenland ice sheet melt extent from passive microwave data using an improved version of the melt retrieval XPGR algorithm. *Geophys. Res. Lett.*, **34**(5), L05502. (10.1029/2006GL028787.)

Fischer, H., D. Wagenbach, M. Laternser and W. Haeberli. 1995. Glacio-meteorological and isotopic studies along the EGIG line, central Greenland. *J. Glaciol.*, **41**(139), 515–527.

Helm, V. *and 6 others*. 2007. Winter accumulation in the percolation zone of Greenland measured by airborne radar altimeter. *Geophys. Res. Lett.*, **34**(6), L06501. (10.1029/2006GL029185.)

Hofmann, W. 1986. Bewegung des Inlandeises im West-Ost-Profil von 1959 bis 1967. *In Die deutschen geodätischen Arbeiten in Rahmen der Internationalen glaziologischen Grönland Expedition (EGIG) 1959–1974*. München, Bayerische Akademie der Wissenschaften. Deutsche Geodätische Kommission, 43–61.

Jezek, K.C., P. Gogineni and M. Shanableh. 1994. Radar measurements of melt zones on the Greenland ice sheet. *Geophys. Res. Lett.*, **21**(1), 33–36.

Kanagaratnam, P., S.P. Gogineni, V. Ramasami and D. Braaten. 2007. A wideband radar for high-resolution mapping of near-surface internal layers in glacial ice. *IEEE Trans. Geosci. Remote Sens.*, **42**(3), 483–490.

King, J.C., P.S. Anderson, D.G. Vaughan, G.W. Mann, S.D. Mobbs and S.B. Vosper. 2004. Wind-borne redistribution of snow across an Antarctic ice rise. *J. Geophys. Res.*, **109**(D11), D11104. (10.1029/2003JD004361.)

Kovacs, A., A.J. Gow and R.M. Morey. 1995. The in-situ dielectric constant of polar firn revisited. *Cold Reg. Sci. Technol.*, **23**(3), 245–256.

Krabill, W. *and 9 others*. 2000. Greenland Ice Sheet: high-elevation balance and peripheral thinning. *Science*, **289**(5478), 428–430.

Male, D.H. 1980. The seasonal snowcover. *In* Colbeck, S.C., *ed. Dynamics of snow and ice masses*. New York, Academic Press, 305–395.

Mari, J.L., F. Glangeaud and F. Coppens. 1999. *Signal processing for geologists and geophysicists*. Paris, Éditions Technip.

Parry, V. *and 6 others*. 2007. Investigations of meltwater refreezing and density variations in the snowpack and firn within the percolation zone of the Greenland Ice Sheet. *Ann. Glaciol.*, **46**, 61–68.

Pfeffer, W.T. and N.F. Humphrey. 1996. Determination of timing and location of water movement and ice-layer formation by temperature measurements in sub-freezing snow. *J. Glaciol.*, **42**(141), 292–304.

Pfeffer, W.T. and N.F. Humphrey. 1998. Formation of ice layers by infiltration and refreezing of meltwater. *Ann. Glaciol.*, **26**, 83–91.

Scott, J., D. Mair, P. Nienow, V. Parry and E. Morris. 2006. A ground-based radar backscatter investigation in the percolation zone of the Greenland Ice Sheet. *Remote Sens. Environ.*, **104**(4), 361–373.

Shepherd, A. and D. Wingham. 2007. Recent sea-level contributions of the Antarctic and Greenland ice sheets. *Science*, **315**(5818), 1529–1532.

Steffen, K. and J. Box. 2001. Surface climatology of the Greenland ice sheet: Greenland Climate Network 1995–1999. *J. Geophys. Res.*, **106**(D24), 33,951–33,964.

Steffen, K., J. Box and W. Abdalati. 1996. Greenland climate network: GC-Net. *CRREL Spec. Rep.* 96-27, 98–103.

Steffen, K., S. Nghiem, R. Huff and G. Neumann. 2004. The melt anomaly of 2002 on the Greenland Ice Sheet from active and passive microwave satellite observations. *Geophys. Res. Lett.*, **31**(20), L20402. (10.1029/2004GL020444.)

Zabel, I.H.H., K.C. Jezek, P.A. Baggeroer and S.P. Gogineni. 1995. Ground-based radar observations of snow stratigraphy and melt processes in the percolation facies of the Greenland ice sheet. *Ann. Glaciol.*, **21**, 40–44.

Zwally, H.J. *and 7 others*. 2005. Mass changes of the Greenland and Antarctic ice sheets and shelves and contributions to sea-level rise: 1992–2002. *J. Glaciol.*, **51**(175), 509–527.

MS received 9 October 2006 and accepted in revised form 13 November 2007

Investigating small-scale variations of the recent accumulation rate in coastal Dronning Maud Land, East Antarctica

Helgard ANSCHÜTZ,[1] Olaf EISEN,[1,2] Hans OERTER,[1] Daniel STEINHAGE,[1] Mirko SCHEINERT[3]

[1]*Alfred-Wegener-Institut für Polar- und Meeresforschung, Postfach 120161, D-27515 Bremerhaven, Germany*
E-mail: hanschuetz@awi-bremerhaven.de
[2]*Versuchsanstalt für Wasserbau, Hydrologie und Glaziologie (VAW), Eidgenössische Technische Hochschule, ETH-Zentrum, CH-8092 Zürich, Switzerland*
[3]*Institut für Planetare Geodäsie, Technische Universität Dresden, D-01062 Dresden, Germany*

ABSTRACT. The accumulation rate on Potsdam Glacier, East Antarctica, and its spatial and temporal variations are examined using ground-penetrating radar, snow samples and firn-core studies. Physical properties in snow samples and along firn cores provide distributions of density with depth, showing only small spatial variation. Counting of peaks in $\delta^{18}O$ along the firn cores yields an age–depth distribution that is transferred to the stratigraphy of isochronal internal layers observed with radar. From two radar horizons we determine the spatial accumulation pattern, averaged over the periods 1970–80 and 1980–2004. The shape of internal layers indicates an ablation area at the eastern margin of the investigation area. Accumulation rates show a very high spatial variability, with a mean value of 141 kg m^{-2} a^{-1} for the period 1970–2004 and a standard deviation of almost 50%. Mean temporal variation of only a few per cent throughout the investigated area for the observed time interval is much less than the spatial variations. The mean accumulation values are somewhat less than values reported before from this region. Accumulation pattern and surface topography are linked in a way indicating that wind-borne redistribution of snow significantly contributes to the observed spatial variations of accumulation rates. The accumulation data and their variability complement and validate present and future satellite studies of Antarctica's mass balance.

1. INTRODUCTION

Surface mass-balance studies of the Antarctic ice sheet are of vital importance for an enhanced understanding of the Earth's climate and its changes (Rignot and Thomas, 2002; Van der Veen, 2002), as the polar regions are able to contribute significantly to global sea-level change (Wingham and others, 1998). It is therefore crucial to determine the mass fluxes of the Antarctic ice sheet, for example by using remote-sensing techniques and satellite-based methods. Variations of accumulation and density on temporal and spatial scales also influence the relation between elevation changes and changes in gravity and mass. Knowledge of spatial and temporal patterns of ice-mass changes provides key information especially for validation of the time-varying gravity field as sensed by the Gravity Recovery and Climate Experiment (GRACE). (For a general overview of the GRACE mission see Tapley and others, 2004.) For this reason, small-scale variations of the accumulation rate play a significant role and need to be investigated closely by ground-borne operations.

Accumulation data are usually derived from firn cores, snow pits or stake readings (Isaksson and Karlén, 1994; Melvold and others, 1998; Kreutz and others, 2000; Oerter and others, 2000), but they yield only information about the local accumulation rate at the probing location. In recent years, ground-penetrating radar (GPR) measurements have proved a useful tool to map relative variations in surface mass balance over larger areas and connect snow pits and firn-core drilling sites (e.g. Richardson and others, 1997; Pinglot and others, 2001; Sinisalo and others, 2003; Rotschky and others, 2004; Spikes and others, 2004). Internal reflection horizons (IRHs) detected by GPR can be used to match signals found in different firn cores along the GPR profiles and assist proper correlations between the firn cores. The observed IRHs arise from contrasts of dielectric permittivity in the subsurface. In the upper hundreds of metres, density has the most significant influence, affecting the real part of the dielectric permittivity (Fujita and others, 1999). IRHs are shown to be of isochronal origin (Eisen and others, 2004; Vaughan and others, 2004), and from their estimated age and a density–depth distribution the mean accumulation rate for a certain period can be calculated.

In this study, we present GPR and firn-core data from a relatively small area in East Antarctica where no reliable accumulation data of high resolution have been available so far. High-frequency GPR measurements were carried out on Potsdam Glacier in Neuschwabenland, the coastal part of Dronning Maud Land (DML), during the Antarctic summer season 2003/04. Shallow firn cores were drilled at selected locations along the radar profiles. Two IRHs are traced throughout several GPR profiles and dated by a reference firn core. The firn-core analyses give travel-time–depth and density–depth relations that can be used to derive the regional accumulation pattern from these tracked IRHs.

2. STUDY AREA

The study area is located south of the Schirmacheroase and north of Wohlthat Massif (Fig. 1a). Most parts of Potsdam Glacier are above 1000 m a.s.l. and have a mean annual air temperature below –20°C (Bormann and Fritzsche, 1995). The average ice thickness is >1200 m, and subglacial

topography is characterized by deep valleys with some subglacial highs (Damm and Eisenburger, 2005; Meyer and others, 2005). The surface elevation declines from almost 1350 m a.s.l. in the southwestern part of the study area to about 850 m a.s.l. in the northeastern part. Accumulation dominates in this region, with the exception of small ablation areas around several nunataks. In the most northeasterly part of this glacier, near and east of the Schirmacheroase, a large ablation area is found that reaches up to the eastern Wohlthat Massif (Bormann and Fritzsche, 1995). Analysis of a firn core drilled at 70°58′ S, 11°22′ E, about 15 km away from our radar profiles, showed snow and firn with some ice layers down to 27 m depth. From 27 to 51 m, stratified ice layers were found, and below 50 m unstratified ice with small bubbles occurred (Bormann and Fritzsche, 1995 and references therein).

Ice-flow studies in this region have been undertaken, among others, by Korth and Dietrich (1996). They carried out differential global positioning system (GPS) measurements and stake readings along the GPS signals on traverse lines going from Novolazarevskaya station to Humboldtfjella and Gruberfjella, respectively (Fig. 1a). The flow pattern of Potsdam Glacier has also been deduced by interferometric synthetic aperture radar (SAR) analysis (Dietrich and others, 1999), as well as the line of highest flow velocity, hereinafter referred to as the main flowline. The velocities in the direction of glacier flow in the study area increase from about 20–30 m a^{-1} in the higher-elevation parts to 70–80 m a^{-1} in the lower region. The vertical velocity is unknown. Glacier flow is mainly divergent in the higher-elevation parts of the glacier, whereas in the lower-elevation parts laterally convergent flow is observed (M. Bäßler and others, unpublished information).

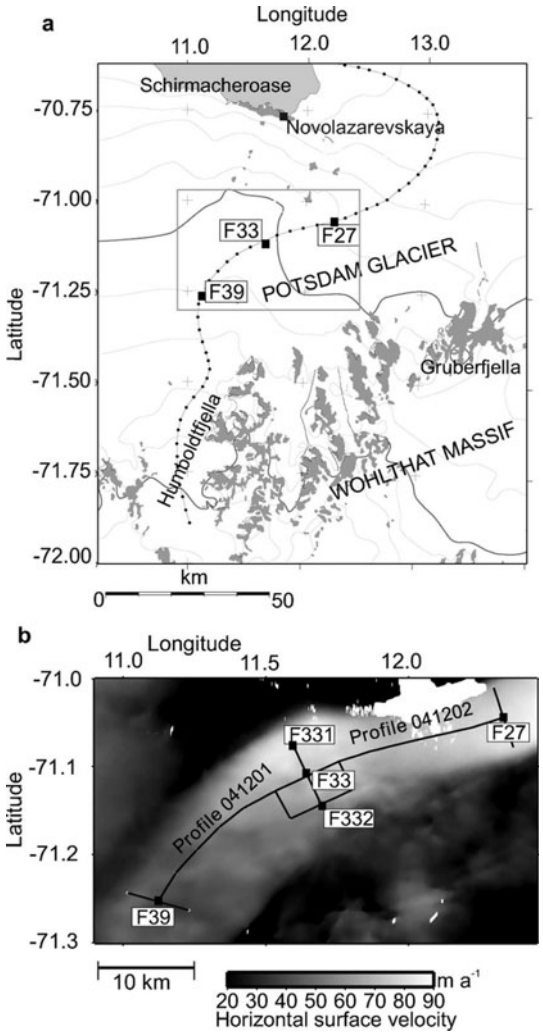

Fig. 1. (a) Overview of the study area. Black line: main flowline of Potsdam Glacier (Bäßler and others, 2003); black squares: start/end points of GPR profiles along the flowline. (Map source: Antarctic Digital Database 4.0.) Grey lines: contour lines of elevation at 200 m intervals; thick grey line: 1000 m contour line; large grey rectangle: area depicted in (b). (b) Sketch of GPR profiles (black lines) and firn-core locations (black squares) with point names (Fxxx). Profiles 041201/041202 correspond to the main flowline; glacier flow is from left to right. Distances F39–F33 and F33–F27 amount to 25 km each. Greyscale indicates magnitude of glacier flow velocity.

3. METHODS

3.1. GPR and GPS data

During the 2003/04 expedition, a 50 km long radar survey line was collected along the main flowline of Potsdam Glacier. Three cross-profiles were surveyed, each one being 8 km long (Fig. 1b). We used a commercial RAMAC radar system (Malå Geoscience, Sweden) with a bistatic shielded 500 MHz antenna that was connected to the central unit via fibre optic cables. Data were stored on a Husky Px5 computer. The GPR antenna was mounted behind a Nansen sledge pulled by a snowmobile at an average speed of ~5 km h^{-1}. Traces were recorded every 0.5 m, triggered by a distance wheel. Each trace consisted of 2048 samples in a 400 ns time window, thus mapping the upper ~35–38 m of the snowpack. Differential GPS data were collected simultaneously with GPR data. The roving station was mounted on the snowmobile, and two reference stations were situated at the field camp, i.e. about 1 km south of point F33 (see Fig. 1), and at the Schirmacheroase, respectively. The GPS data were collected every 1 s using a Trimble 4000SSi receiver and a choke-ring antenna. Processing of GPS data yields positions for the GPR profiles as well as surface elevation. The relative accuracy between the differential GPS points is generally in the range of several millimetres to a few centimetres for longitude and latitude, and of some centimetres to about one decimetre for the elevation. However, due to the movement of the roving station over severe sastrugi fields, we assume that actual accuracy declines to some centimetres for longitude and latitude and reaches a few decimetres for the elevation. The radar data were processed using Paradigm Geophysical FOCUS version 5.0 software by applying gain control, filtering using a bandpass Butterworth filter with cut-off frequencies of 350 and 850 MHz, and correction for the first arrival of the direct wave. From the processed radargrams, IRHs were tracked semi-automatically using Landmark OpenWorks release 2003.0 software. Within the depth section covered by the firn cores (given below), two internal horizons could be tracked throughout more than one GPR profile.

3.2. Firn cores and snow samples

At five locations (Fig. 1b; Table 1) along the radar profiles, shallow, 12.5–13.5 m deep, firn cores were drilled. At the same sites 2 m deep snow pits were dug which were probed in intervals of 5 cm, giving 40 samples per pit. The density of the snow samples was determined in situ from the weight and the known volume of the probing cylinder.

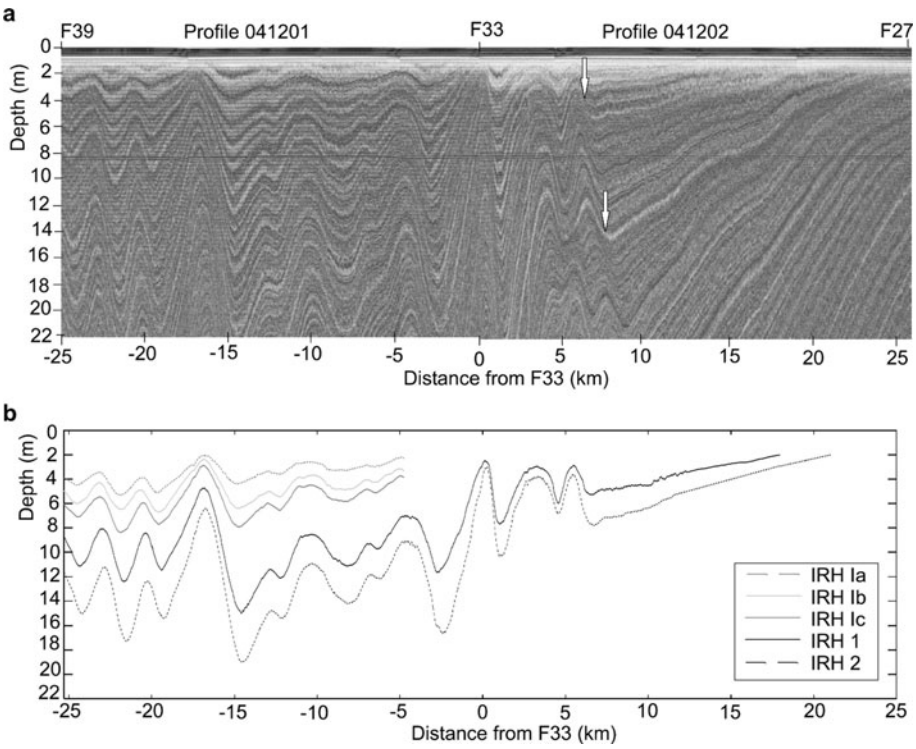

Fig. 2. (a) Processed radargrams from profiles 041201 and 041202. The white arrows mark the IRHs chosen to determine the approximate beginning of the transition zone from accumulation to ablation. (b) Depth distribution of tracked and dated IRHs. Black solid line: IRH 1 (1980); black dashed line: IRH 2 (1970); grey dashed line: IRH Ia (1995); light grey line: IRH Ib (1992); dark grey line: IRH IC (1989).

The firn cores and snow samples were transported to Germany and analyzed in the cold laboratory at the Alfred Wegener Institute, Bremerhaven, for physical and chemical properties. Snow-sample data were used to link firn-core data to the surface due to poor core quality in the upper 1–2 m of drilling. The $\delta^{18}O$ ratio was determined by mass spectrometry for both the firn cores as well as the snow samples. Firn-core analysis covered measurements of density using gamma-attenuation profiling (GAP) as well as dielectric profiling (DEP) that yield density, dielectric permittivity and electrical conductivity of the firn (Wilhelms, 1996, 2005).

3.3. Determination of accumulation rates

We derive distributions of electromagnetic wave speed and cumulative mass with depth from the firn-core data. The mean values of density, dielectric permittivity and conductivity of all five firn cores are used, since no further information about the lateral variations of those parameters between the firn-core drilling sites is available. Cumulative snow mass is obtained by integration of the mean density profile derived from the GAP measurements. Calculation of electromagnetic wave speed from DEP-derived parameters follows the procedure described by Eisen and others (2002). Error estimates are given below. Since the firn cores reach only a depth of about 12 m below the surface, the data of the two-way-travel-time (TWT)–depth and cumulative-mass–depth models were extrapolated down to 25 m depth. Extrapolation was done using the MATLAB™ polyfit routine by fitting a third-order polynomial (Richardson and others, 1997; Frezzotti and others, 2005) yielding a correlation coefficient of $R = 0.90$. Age–depth profiles are determined by counting the $\delta^{18}O$ peaks which indicate summer maxima (McMorrow and others, 2004 and references therein).

Consistent dating of the different firn cores proved difficult due to local variations in the $\delta^{18}O$ profiles which did not allow clear identification of maxima and minima for every firn core. However, firn core F39 shows a $\delta^{18}O$ profile with pronounced maxima and minima (Fig. 3d), so it was used as a reference core for interpreting the radar data. F332 could likewise be dated sufficiently by its $\delta^{18}O$ profile. However, since the tracked IRHs do not reach up to this core, F332 could not be used for dating the GPR layers. The two tracked horizons (IRH 1 and IRH 2; see Fig. 2b) are dated against F39 by comparing the depth of the respective IRH at the coring location with the depth–age scale of the firn core. The depth values for the IRHs at the drilling location are 8.65 m (IRH 1) and 11.55 m (IRH 2), and their estimated time of origin is 1970 and 1980, respectively, ±2 years for each dating. Three more IRHs (IRH Ia, Ib and Ic; see Fig. 2b) that could only be tracked throughout the uppermost ~20 km along the main flowline are also dated by the depth–age scale of F39: their estimated times of origin are 1995, 1992 and 1989 (±1 year for each dating).

The accumulation rate along the GPR profiles can be calculated by dividing the cumulative mass difference of two selected IRHs by their respective age difference.

3.4. Estimation of errors

Errors in our density–depth distribution are assumed to be up to 14% at 12 m depth, determined from the difference between the mean values (i.e. the model used) and F39 and F27, respectively (Fig. 4c). This includes errors from the density measurements using GAP which are up to 10 kg m^{-3} (Wilhelms, 2005). Accuracy of DEP-derived parameters is within 1% (Wilhelms, 1996). Errors in TWT–depth conversion using DEP data are up to 1% as shown by Eisen and others (2002). Errors in calculations of the cumulative mass

Table 1. Location of firn cores

Firn core	Point name*	Latitude °S	Longitude °E	Elevation m
FB0401	F33	71.110709	11.646268	1013
FB0402	F332	71.143130	11.693510	1076
FB0403	F39	71.253401	11.122667	1315
FB0404	F331	71.078270	11.599180	1008
FB0405	F27	71.044023	12.332327	848

*As in Figure 1b.

from the density profiles are likewise up to 1% due to error propagation. The dating uncertainty of the two IRHs used for determination of area-wide accumulation rates is ±2 years. Errors in tracking of IRHs are up to ±2 ns, which yields depth variations of up to ±0.2 m. However, for the two dated IRHs (IRH 1 and 2) this latter uncertainty does not affect the estimated age since 8.65 ± 0.2 m and 11.55 ± 0.2 m still correspond to the years 1980 and 1970, respectively (Fig. 4d). From analytic error propagation, the overall root-mean-square error in accumulation rates becomes 11.5% for profile 041201. The largest error was found to be 20%. We therefore assume that the accumulation values presented in this paper are accurate within about 12% on average. Errors from ray-path geometry due to the separation of transmitting and receiving antenna are neglected, since transmitter and receiver are separated by only 0.18 m. For the same reason, refraction within the snowpack can be neglected (Sinisalo and others, 2003).

4. RESULTS

4.1. GPR profiles

In the processed radargrams the undulations of internal layers can clearly be seen (Fig. 2a). Internal layers show large slopes along profile 041201. At some locations the vertical distance between separate layers is very small (e.g. at –16 to –17 km), whereas a few kilometres away the same layers are spaced more widely (e.g. from about –10 to –15 km). Comparable undulating patterns have been reported before in DML, for example by Richardson-Näslund (2001). Closely spaced layers indicate areas with less accumulation, whereas more widely spaced layers are associated with regions of higher accumulation. Along profile 041202 (Fig. 2a), layers ascend in the direction of glacier flow (with the exception of the local undulations in the first 6–7 km). Such patterns are characteristic for ablation areas and the transition from an accumulation area to an ablation area, where internal horizons come to the surface due to surface erosion. However, it is not possible to resolve actual ablation from very low accumulation by GPR internal layering. A layer outcropping at the surface at a certain location along the GPR profile would only yield zero values for accumulation or ablation for this point. Besides, the isochronal layers cannot be traced up to the surface since they are lost within the time window of the direct wave (here the upper ~20 ns, equivalent to ~2 m; Fig. 2a). Assuming zero advection, ascending layers with angles <90° relative to the surface would still provide accumulation, albeit low values (Fig. 2a, near $x = 25$ km). Without advection, therefore, only layers emerging perpendicularly at 90° indicate

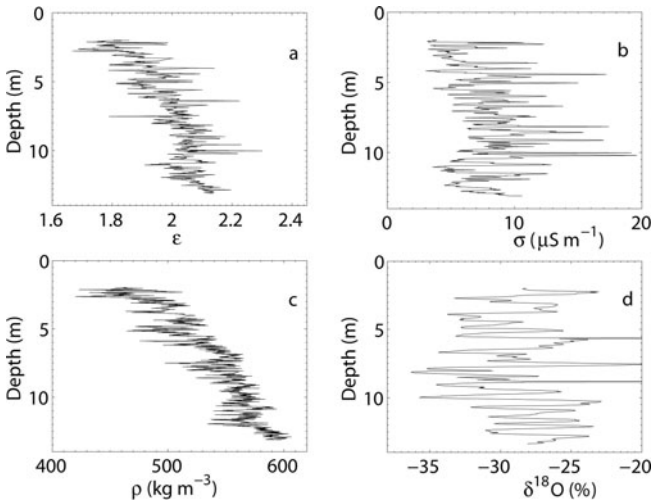

Fig. 3. Data from firn core F39: (a) dielectric permittivity; (b) electrical conductivity; (c) density (from GAP); and (d) $\delta^{18}O$.

ablation. Yet in our case we can conclude from the ascending IRHs that the transition zone from accumulation to ablation is present and visible in the radargram. Since we do have advection effects here, we cannot clearly define the beginning of the ablation area. Thus, we do not address the actual ablation area, but rather the transition zone where very low accumulation and also local ablation might occur. We define the beginning of this zone by the point where the first IRH would reach the surface. Using two different IRHs marked by the white arrows in Figure 2a, and extrapolating from their respective slopes the points where they would reach the surface, results in $x = 21.35$ km and $x = 23.84$ km, respectively. Since these IRHs could not be dated, we are unable to apply a sufficient correction for glacier flow velocity. By choosing one very shallow and one rather deep IRH we can at least conclude that the transition zone from very low accumulation to ablation starts at this part of Potsdam Glacier between about 21 and 24 km downstream of F33. Thus, the actual ablation area is to be expected slightly farther down-glacier, which is in accordance with the description of Bormann and Fritzsche (1995) and Horwath and others (2006).

4.2. Firn-core data and density distribution

The parameters derived from the firn-core analysis are depicted in Figure 3 for firn core F39. Dielectric permittivity as well as density increase with depth (Fig. 3a and c), but the parameters do not reach values of solid ice ($\rho = 917\,\mathrm{kg\,m^{-3}}$) within the depth section covered by the firn cores. Some of the peaks of the density coincide with observed ice lenses in the firn core.

Figure 3 shows the models for TWT–depth (Fig. 3b) and cumulative mass–depth (Fig. 3c) as derived from the mean values and from the 'extreme' cores, i.e. the core with the lowest mean density (F39) and the core with the highest mean density (F27). Down to about 5–6 m depth, the density values of the different firn cores are very similar (Fig. 4a). Below this depth they start to differ slightly, up to ~100–150 kg m^{-3} at about 12 m depth. In the upper 6–7 m, density variations within one specific firn core are usually larger than the variations between the different cores at the same depth. Generally, F27 shows the largest density values. This core

Table 2. Accumulation values in the study area, given in kg m^{-2} a^{-1}. Note that the top three rows (GPR-based accumulation rates) represent spatial means from the study area, whereas the bottom two rows (firn-core derived accumulation series) represent temporal accumulation means for the time period covered by the firn cores at the respective coring locations

Method	Period	Mean acc.	Std*	Min.	Max.
GPR–IRHs	1970–80	142	51	18	335
GPR–IRHs	1980–2004	140	48	27	318
GPR–IRHs	1970–2004	141	47	31	290
Firn core F332	1966–2003	161	39	60	327
Firn core F39	1968–2003	176	30	96	289

*One-fold standard deviation in % of the mean.

was drilled on the lower-elevation part of the glacier where the radar data indicate an ablation area nearby. Farther east a blue-ice area is found (Bormann and Fritzsche, 1995; Korth and Dietrich, 1996; Horwath and others, 2006) where the surface density should be higher than in the firn areas. Thus it can be assumed that density in the study area will increase in the direction of glacier flow, which is in accordance with our findings. However, density values of F27 are still in the range of firn density and do not reach the density of solid ice. Therefore we conclude that this part of the glacier is dominated by firn, at least in the uppermost 12 m.

4.3. Accumulation rates

The mean accumulation rate in the study area is derived for the periods 1970–80, 1970–2004 and 1980–2004, with 2004 corresponding to the surface at the time of data collection (Table 2). The depth distribution of the dated IRHs is depicted in Figure 2b. Taking into account a mean glacier flow velocity of 45 m a^{-1} results in the accumulation distribution along the main flowline (Fig. 5c). Furthermore, annual accumulation rates are obtained from the two dated firn cores (Table 2; Fig. 5a).

5. DISCUSSION OF ACCUMULATION FEATURES

5.1. Temporal characteristics

Comparing the mean values of the GPR-derived accumulation rates from Table 2, we conclude that the spatial variability exceeds the mean temporal variability for the periods considered. This has been reported before at other places in East Antarctica, for example by Frezzotti and others (2005). The temporal variations in accumulation rates derived from GPR measurements for the periods 1970–80 and 1980–2004 are about 1.5%, calculated from the mean values of the respective periods. However, interannual variability obtained from the two dated firn cores (Fig. 5a) is high, showing one-fold standard deviations of 30% and 39%, respectively (Table 2). Differences in per cent of the firn-core mean values range from –63% to +103% for F332 and from –46% to +65% for F39 (Fig. 5c). A mean over 10 years of the accumulation series obtained from the firn cores indicates a slight decrease at F332 and an even smaller increase at F39 for the period 1984–93 (Fig. 5b). Although the timescales are rather short, this suggests that the accumulation pattern comprising the last 30 years is quite stable on decadal scales in relation to the annual variability.

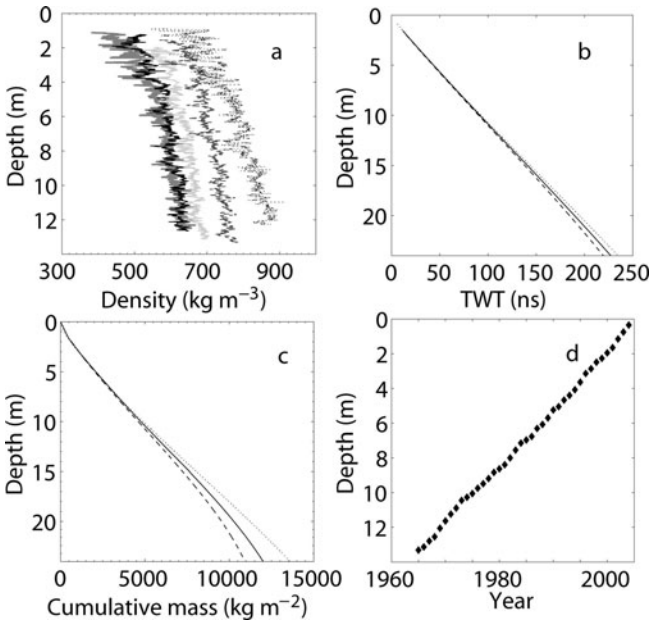

Fig. 4. (a) Density distribution of all firn cores. Thick grey line: F33; solid black line: F332; light grey line: F39; dark grey line: F331; black dotted line: F27. The density plots are offset by intervals of 50 kg m^{-3} in order to distinguish the individual cores. (b, c) Model for TWT–depth (b) and cumulative mass–depth (c). In each plot the solid line corresponds to the model derived from the mean values, the dashed line to the model derived from F39, and the dotted line to the model derived from F27. (d) Depth–age scale as derived from the dating of F39.

5.2. Spatial characteristics

Generally, our mean core-derived accumulation rates are about 12–23% higher than the average GPR-based accumulation rates in the investigation area. We therefore conclude that the spatial representativity of the firn cores is limited, as has been discussed before for West Antarctica (Spikes and others, 2004) and the western part of DML (Richardson-Näslund, 2001). The spatial variability of GPR-derived accumulation rates along the main flowline is very high (Fig. 6c). Differences in per cent of the mean range from –81% to +125% for the period 1980–2004, showing an undulating pattern. Accumulation rates show strong spatial gradients of up to 105 kg m^{-2} a^{-1} km^{-1}, with pronounced changes from increasing to decreasing accumulation in the direction of glacier flow, sometimes even within <1 km. For example, going 1 km upstream from near F33 yields a 10-fold increase in accumulation (from about 30 to 330 kg m^{-2} a^{-1}) for the interval 1970–80. Average accumulation gradients are on the order of 23 kg m^{-2} a^{-1} km^{-1}. Generally, a decrease in accumulation in the direction of glacier flow is visible. The linear trend along profiles 041201/041202 amounts to –4.9 kg m^{-2} a^{-1} km^{-1}. This is in accordance with the observation that IRHs tend to come to the surface at lower elevations on the main flowline (Fig. 2a).

Surface slope and slope of accumulation (Fig. 6d) show regular undulations similar to those in surface elevation (Fig. 6a and b) and in accumulation (Fig. 6c). Anschütz and others (2006) show that these undulations are likely caused by a feedback system between atmosphere and cryosphere similar to the features ruling the genesis of megadunes on the polar plateau (Frezzotti and others, 2002). Comparable association between surface slope and accumulation has

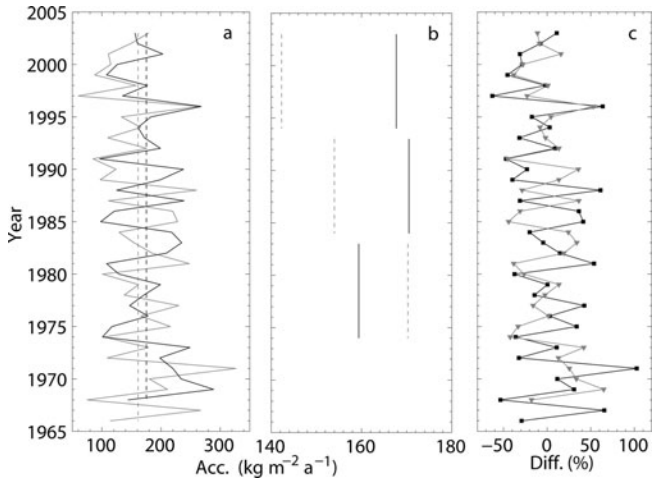

Fig. 5. (a) Year-to-year accumulation values obtained from firn cores F39 (black solid line) and F332 (grey solid line); the respective core means are depicted by the black dashed line (F39) and the grey dashed line (F332). (b) Accumulation rates for a 10 year mean for F332 (grey dashed line) and F39 (black solid line). (c) Variability expressed as per cent difference of the respective core mean. Grey line/grey triangles: F332; black line/black squares: F39.

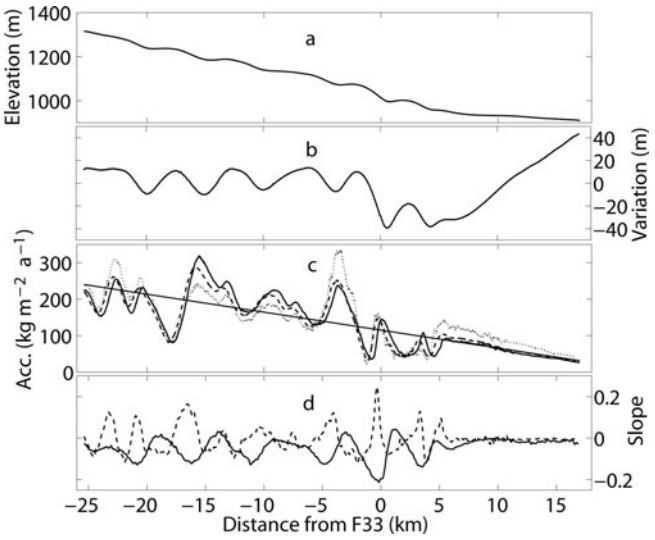

Fig. 6. (a) Surface elevation; (b) linearly detrended surface elevation; (c) accumulation pattern; and (d) gradient of accumulation and surface slope on the main flowline. The solid curve in (c) corresponds to the period 1980–2004, the dashed curve to 1970–2004 and the dotted curve to 1970–80. The solid line shows the linear trend fitted to the accumulation pattern. The solid line in (d) corresponds to the slope of surface elevation (vertically exaggerated by a factor of 5) in m m^{-1}, and the dashed line represents the slope of accumulation (1980–2004) in kg m^{-2} a^{-1} m^{-1}.

been reported before in Antarctica (e.g. Black and Budd, 1964; Pettré and others, 1986; Goodwin, 1990; Vaughan and others, 2004; Eisen and others, 2005) and is attributed to wind influence (King and others, 2004) where accumulation maxima are located within surface elevation troughs and on the windward slopes. Local deviations from this general pattern in our data are possibly due to different local-scale near-surface winds. Another reason probably arises from the correction for glacier flow where we used a measured mean flow speed of 45 m a^{-1} to correct the GPR layer depths and thus the accumulation pattern. Flow speed is not constant along the main flowline but increases with decreasing elevation. Measurements of spatial variations of ice flow are too inaccurate to allow a more detailed correction of the isochronal layers. Thus, accumulation maxima can be slightly misplaced due to locally incorrect consideration of glacier flow speed. However, the spatial variability of the accumulation rate is not affected by these errors.

5.3. Comparison with other studies

Other ground-borne data in this region are sparse, but there are a few accumulation values available from pit studies and stake readings.

Bormann and Fritzsche (1995) report a mean accumulation value derived from pit studies in the vicinity of a drillhole at 70°58′ S, 11°22′ E, about 15 km north of our radar profiles 041201/041202, that is about 130 kg m^{-2} a^{-1} (1950–84) which is in accordance with our mean values.

The mean annual accumulation from the stake readings presented by Korth and Dietrich (1996) on the Insel traverse route (going from Novolazarevskaya station to Humboldtfjella; see Fig. 1a) is 131 kg m^{-2} a^{-1}, with a standard deviation of 140% because some of the stakes are located in an ablation area. This comparison should be viewed with caution since the stake readings cover the period 1988–93, so the time interval of the different accumulation values is not the same. Furthermore, Korth and Dietrich (1996) do not state actual values for the densities used to calculate the accumulation. However, their mean value is in the range of our mean values, indicating that the overall distribution of accumulation is quite stable for the different time periods, although there are obvious small-scale differences. Their values obtained at stakes in the vicinity of our profiles, about 1 km away from the main flowline, are ~250 kg m^{-2} a^{-1} which is much larger than our nearby values of ~50 kg m^{-2} a^{-1}. Yet accumulation rates for the intervals 1980–89, 1980–92 and 1980–95 along profile 041201 (calculated from IRH Ia, Ib and Ic; see Fig. 2b) are 18–35% higher than the other values in our study. Taking into account the report from Korth and Dietrich (1996), this might indicate a higher accumulation at this part of the glacier during the 1980s and early 1990s of about 25% compared with the previous period (1970–80). Due to the dating uncertainty of F39, caution has to be used with these findings. However, dating uncertainty does not affect the accumulation pattern itself or the spatial variability which is clearly demonstrated by our study.

The accumulation values in the study area presented here are less than those reported by Giovinetto and Zwally (2000) who derive values of ~200–250 kg m^{-2} a^{-1} for this region of Antarctica. Vaughan and others (1999) report the same as Giovinetto and Zwally (2000). Both studies are concerned with larger areas and neglect small-scale features. Our mean value of 141 kg m^{-2} a^{-1} (1970–2004) is less than these findings because there is an ablation area in the vicinity of our study area, which influences our results. Van de Berg and others (2006) derive specific surface mass balance (SSMB) from a regional atmospheric climate model, estimating precipitation, sublimation and melt. Snowdrift processes are not considered. The horizontal resolution is about 55 km. They derive values of ~200 kg m^{-2} a^{-1} for the vicinity of our study area, which is likewise larger than our mean accumulation values. Our study reveals a significant influence of blowing snow on the accumulation values in the area of investigation, so neglecting this process likely

results in an overestimated SSMB for this area as given by Van de Berg and others (2006). Large-scale compilations like those cited above are usually based on a limited number of scattered observations. They do not take into account the spatial representativity of the respective point measurements which may be obscured by local-scale variability. Our study demonstrates a very high spatial variability in this area of coastal DML and indicates a limited representativity of firn-core derived accumulation data which are on average higher than the GPR-derived accumulation values. This might explain the higher accumulation rates in large-scale compilations of this area.

5.4. Implications for satellite-data interpretation

Satellite observations of surface elevation, for instance by European Remote-sensing Satellites-1 and -2 (ERS-1/-2) and the Ice, Cloud and land Elevation Satellite (ICESat), and gravity from the GRACE mission (Tapley and others, 2004) can provide mass-distribution changes according to the mission-specific spatial and temporal resolutions. Combining GRACE data and altimetry data helps to discriminate ice-mass changes (Zwally and others, 2005) from height changes induced by glacial isostatic adjustment or by changes in snow and firn density (Wahr and others, 2000). However, the effective spatial resolution of GRACE monthly solutions is only several hundred kilometres. To account for the GRACE error behavior and to separate mass signals from different geographic origins, adapted filter techniques have to be utilized (Swenson and Wahr, 2002; Horwath and Dietrich, 2006b). Hence, GRACE provides only integrated mass-balance estimates over large areas.

Trends in ice-mass changes over a few years derived from satellite observations may be either due to interannual fluctuations in net ice surface mass balance or due to long-term ice dynamics. To distinguish between the two effects, information on the temporal and spatial covariance of the interannual surface mass-balance fluctuation is needed.

With regard to spatial covariance, Anschütz and others (2006) report spatial autocorrelation lengths of only about 1 km for surface mass-balance fluctuations. For values averaged over ~100 km the small-scale variations (deposition noise) are averaged out, so the standard deviation of temporal fluctuations will be smaller than the values of 30–39% obtained from the firn-core time series (Table 2). Therefore, such small-scale fluctuations will not be resolved by GRACE. Concerning temporal covariance, there is, again, a large portion of small-scale deposition noise in the firn-core data: the autocorrelation length of the firn-core time series is only 0.6 years (Fig. 5a). However, the accumulation pattern seems fairly stable on decadal scales (Fig. 5b).

The GRACE mission, launched in 2002, is planned to cover 8 years in total. Considering the discussion above, long-term surface mass-balance changes showing a considerably large spatial pattern would be sensed by GRACE. Hence, regional studies of mass fluctuations are very important to qualify the spatio-temporal behaviour of the ice surface mass balance in larger areas and to discriminate surface mass-balance fluctuations from long-term ice dynamics. In this context, the results presented by this study, combined with further estimates yielded by other authors for adjacent regions (e.g. Richardson-Näslund, 2001; Rotschky and others, 2004; Frezzotti and others, 2005), provide valuable ground-based information to validate and interpret GRACE observations.

6. CONCLUSIONS

We have combined GPR data and firn-core data to investigate the accumulation pattern on Potsdam Glacier. Accumulation rates show a very high spatial variability in the study area, with a standard deviation of almost 50%. The generally decreasing trend of accumulation in the direction of glacier flow is overlain by local features. In accordance with other authors (Richardson-Näslund, 2001; Rotschky and others, 2004; Spikes and others, 2004; Arcone and others, 2005; Frezzotti and others, 2005), we conclude that it is important to take into account the spatial representativity of point measurements such as firn cores, snow pits or stake readings when examining accumulation rates.

Comparing the results from our study with previous work based on stake readings nearby, we found locally lower accumulation values; however, the previous study comprises a shorter time period. We found indications that accumulation during the late 1980s and early 1990s was slightly higher (about 25% higher than in the period 1970–80). Large-scale studies of Antarctic accumulation show values of 200–250 kg m^{-2} a^{-1} for our investigation area. The lower values found in our study are presumably owed to an ablation area that influences our results and has not been accounted for in the large-scale compilations, as well as significant influence of blowing snow on the local accumulation rates.

Our results provide useful insight into small-scale features affecting the accumulation in this area and can be helpful in further studies, especially for validating satellite-based mass-balance estimates. Monitoring of local-scale accumulation changes in coastal areas provides valuable information to increase our knowledge of ice-mass fluxes from ice streams and outlet glaciers like Potsdam Glacier (Hamilton and others, 2005).

This study also complements published datasets and enhances the evaluation and interpretation of ice-mass changes in this area of East Antarctica.

ACKNOWLEDGEMENTS

This work was supported by the Deutsche Forschungsgemeinschaft (DFG) through the VISA project, funded under grants Di 473/17 and Jo 191/8. O.E. was supported by the DFG 'Emmy Noether' scholarship EI 672/1. Comments from G. Hamilton, R. Pettersson and an anonymous reviewer greatly improved the manuscript. The contribution of the field team and help in the laboratory is gratefully acknowledged.

REFERENCES

Anschütz, H., O. Eisen, W. Rack and M. Scheinert. 2006. Periodic surface features in coastal East Antarctica. *Geophys. Res. Lett.,* **33**(22), L22501. (10.1029/2006GL027871.)

Arcone, S.A., V.B. Spikes and G.S. Hamilton. 2005. Stratigraphic variation in polar firn caused by differential accumulation and ice flow: interpretation of a 400 MHz short-pulse radar profile from West Antarctica. *J. Glaciol.,* **51**(174), 407–422.

Bäßler, M., R. Dietrich and C.K. Shum. 2003. Investigations of ice dynamics at the grounding zone of an Antarctic ice shelf utilizing SAR-interferometry. *In* Jekeli, C., *ed. Proceedings of the Weikko A. Heiskanen Symposium in Geodesy, 1–4 October 2002, Columbus, Ohio, USA.* Columbus, OH, Ohio State University. Laboratory for Space Geodesy and Remote Sensing.

Black, H.P. and W. Budd. 1964. Accumulation in the region of Wilkes, Wilkes Land, Antarctica. *J. Glaciol.,* **5**(37), 3–15.

Bormann, P. and D. Fritzsche, *eds*. 1995. *The Schirmacher Oasis, Queen Maud Land, East Antarctica, and its surroundings*. Gotha, Justus Perthes Verlag.

Damm, V. and D. Eisenburger. 2005. Ice thickness and sub-ice morphology in central Dronning Maud Land deduced by radio echo sounding. *Geol. Jahrb.,* **B97**, 109–127.

Dietrich, R., R. Metzig, W. Korth and J. Perlt. 1999. Combined use of field observations and SAR interferometry to study ice dynamics and mass balance in Dronning Maud Land, Antarctica. *Polar Res.,* **18**(2), 291–298.

Eisen, O., U. Nixdorf, F. Wilhelms and H. Miller. 2002. Electromagnetic wave speed in polar ice: validation of the common-midpoint technique with high-resolution dielectric-profiling and γ-density measurements. *Ann. Glaciol.,* **34**, 150–156.

Eisen, O., U. Nixdorf, F. Wilhelms and H. Miller. 2004. Age estimates of isochronous reflection horizons by combining ice core, survey, and synthetic radar data. *J. Geophys. Res.,* **109**(B1), B01406. (10.1029/2003JB002858.)

Eisen, O., W. Rack, U. Nixdorf and F. Wilhelms. 2005. Characteristics of accumulation around the EPICA deep-drilling site in Dronning Maud Land, Antarctica. *Ann. Glaciol.,* **41**, 41–56.

Frezzotti, M., S. Gandolfi and S. Urbini. 2002. Snow megadunes in Antarctica: sedimentary structure and genesis. *J. Geophys. Res.,* **107**(D18), 4344. (10.1029/2001JD000673.)

Frezzotti, M. *and 13 others*. 2005. Spatial and temporal variability of snow accumulation in East Antarctica from traverse data. *J. Glaciol.,* **51**(172), 113–124.

Fujita, S. *and 6 others*. 1999. Nature of radio-echo layering in the Antarctic ice sheet detected by a two-frequency experiment. *J. Geophys. Res.,* **104**(B6), 13,013–13,024.

Giovinetto, M.B. and H.J. Zwally. 2000. Spatial distribution of net surface accumulation on the Antarctic ice sheet. *Ann. Glaciol.,* **31**, 171–178.

Goodwin, I.D. 1990. Snow accumulation and surface topography in the katabatic zone of eastern Wilkes Land, Antarctica. *Antarct. Sci.,* **2**(3), 235–242.

Hamilton, G.S., V.B. Spikes and L.A. Stearns. 2005. Spatial patterns in mass balance of the Siple Coast and Amundsen Sea sectors, West Antarctica. *Ann. Glaciol.,* **41**, 105–110.

Horwath, M. and R. Dietrich. 2006. Errors of regional mass variations inferred from GRACE monthly solutions. *Geophys. Res. Lett.,* **33**(7), L07502. (10.1029/2005GL025550.)

Horwath, M. *and 7 others*. 2006. Nivlisen, an Antarctic ice shelf in Dronning Maud Land: geodetic–glaciological results from a combined analysis of ice thickness, ice surface height and ice-flow observations. *J. Glaciol.,* **52**(176), 17–30.

Isaksson, E. and W. Karlén. 1994. Spatial and temporal patterns in snow accumulation, western Dronning Maud Land, Antarctica. *J. Glaciol.,* **40**(135), 399–409.

King, J.C., P.S. Anderson, D.G. Vaughan, G.W. Mann, S.D. Mobbs and S.B. Vosper. 2004. Wind-borne redistribution of snow across an Antarctic ice rise. *J. Geophys. Res.,* **109**(D11), D11104. (10.1029/2003JD004361.)

Korth, W. and R. Dietrich. 1996. Ergebnisse geodätischer Arbeiten im Gebiet der Schirmacheroase/Antarktika 1988–1993. *Bayer Akad. Wiss., Deut. Geod. Komm.* B301.

Kreutz, K.J., P.A. Mayewski, L.D. Meeker, M.S. Twickler and S.I. Whitlow. 2000. The effect of spatial and temporal accumulation rate variability in West Antarctica on soluble ion deposition. *Geophys. Res. Lett.,* **27**(16), 2517–2520.

McMorrow, A.J., T.D. van Ommen, V. Morgan and M.A.J. Curran. 2004. Ultra-high-resolution seasonality of trace-ion species and oxygen isotope ratios in Antarctic firn over four annual cycles. *Ann. Glaciol.,* **39**, 34–40.

Melvold, K., J.O. Hagen, J.F. Pinglot and N. Gundestrup. 1998. Large spatial variation in accumulation rate in Jutulstraumen ice stream, Dronning Maud Land, Antarctica. *Ann. Glaciol.,* **27**, 231–238.

Meyer, U., D. Steinhage, U. Nixdorf and H. Miller. 2005. Airborne radio echo sounding survey in Central Dronning Maud Land, East Antarctica. *Geol. Jahrb.,* **B97**, 129–140.

Oerter, H. *and 6 others*. 2000. Accumulation rates in Dronning Maud Land, Antarctica, as revealed by dielectric-profiling measurements of shallow firn cores. *Ann. Glaciol.,* **30**, 27–34.

Pettré, P., J.F. Pinglot, M. Pourchet and L. Reynaud. 1986. Accumulation distribution in Terre Adélie, Antarctica: effect of meteorological parameters. *J. Glaciol.,* **32**(112), 486–500.

Pinglot, J.F., J.O. Hagen, K. Melvold, T. Eiken and C. Vincent. 2001. A mean net accumulation pattern derived from radioactive layers and radar soundings on Austfonna, Nordaustlandet, Svalbard. *J. Glaciol.,* **47**(159), 555–566.

Richardson, C., E. Aarholt, S.E. Hamran, P. Holmlund and E. Isaksson. 1997. Spatial distribution of snow in western Dronning Maud Land, East Antarctica, mapped by a ground-based snow radar. *J. Geophys. Res.,* **102**(B9), 20,343–20,353.

Richardson-Näslund, C. 2001. Spatial distribution of snow in Antarctica and other glacier studies using ground-penetrating radar. (PhD thesis, Stockholm University.)

Rignot, E. and R.H. Thomas. 2002. Mass balance of polar ice sheets. *Science,* **297**(5586), 1502–1506.

Rotschky, G., O. Eisen, F. Wilhelms, U. Nixdorf and H. Oerter. 2004. Spatial distribution of surface mass balance on Amundsenisen plateau, Antarctica, derived from ice-penetrating radar studies. *Ann. Glaciol.,* **39**, 265–270.

Sinisalo, A., A. Grinsted, J.C. Moore, E. Kärkäs and R. Pettersson. 2003. Snow-accumulation studies in Antarctica with ground-penetrating radar using 50, 100 and 800 MHz antenna frequencies. *Ann. Glaciol.,* **37**, 194–198.

Spikes, V.B., G.S. Hamilton, S.A. Arcone, S. Kaspari and P. Mayewski. 2004. Variability in accumulation rates from GPR profiling on the West Antarctic plateau. *Ann. Glaciol.,* **39**, 238–244.

Swenson, S. and J. Wahr. 2002. Methods for inferring regional surface-mass anomalies from Gravity Recovery and Climate Experiment (GRACE) measurements of time-variable gravity. *J. Geophys. Res.,* **107**(B9), 2193. (10.1029/2001JB000576.)

Tapley, B.D., S. Bettardpur, M. Watkins and C. Reigber. 2004. The gravity recovery and climate experiment: mission overview and early results. *Geophys. Res. Lett.,* **31**(9), L09607. (10.1029/2004GL019920.)

Van de Berg, W.J., M.R. van den Broeke, C.H. Reijmer and E. van Meijgaard. 2006. Reassessment of the Antarctic surface mass balance using calibrated output of a regional atmospheric climate model. *J. Geophys. Res.,* **111**(D11), D11104. (10.1029/2005JD006495.)

Van der Veen, C.J. 2002. Polar ice sheets and global sea level: how well can we predict the future? *Global Planet. Change,* **32**(2–3), 165–194.

Vaughan, D.G., J.L. Bamber, M.B. Giovinetto, J. Russell and A.P.R. Cooper. 1999. Reassessment of net surface mass balance in Antarctica. *J. Climate,* **12**(4), 933–946.

Vaughan, D.G., P.S. Anderson, J.C. King, G.W. Mann, S.D. Mobbs and R.S. Ladkin. 2004. Imaging of firn isochrones across an Antarctic ice rise and implications for patterns of snow accumulation rate. *J. Glaciol.,* **50**(170), 413–418.

Wahr, J., D. Wingham and C. Bentley. 2000. A method of combining ICESat and GRACE satellite data to constrain Antarctic mass balance. *J. Geophys. Res.,* **105**(B7), 16,279–16,294.

Wilhelms, F. 1996. Leitfähigkeits- und Dichtemessung an Eisbohrkernen. *Ber. Polarforsch.* 191.

Wilhelms, F. 2005. Explaining the dielectric properties of firn as a density-and-conductivity mixed permittivity (DECOMP). *Geophys. Res. Lett.,* **32**(16), L16501. (10.1029/2005GL022808.)

Wingham, D.J., A.J. Ridout, R. Scharroo, R.J. Arthern and C.K. Shum. 1998. Antarctic elevation change from 1992 to 1996. *Science,* **282**(5388), 456–458.

Zwally, H.J. *and 7 others*. 2005. Mass changes of the Greenland and Antarctic ice sheets and shelves and contributions to sea-level rise: 1992–2002. *J. Glaciol.,* **51**(175), 509–527.

Strong spatial variability of snow accumulation observed with helicopter-borne GPR on two adjacent Alpine glaciers

H. Machguth,[1] O. Eisen,[2,3] F. Paul,[1] and M. Hoelzle[1]

Received 12 April 2006; revised 23 May 2006; accepted 7 June 2006; published 13 July 2006.

[1] This study compares high-resolution helicopter-borne radar measurements to extensive ground-based profiling of the snow cover on Findel- and Adler Glacier, Switzerland. The results demonstrate that derived accumulation values of either method are well in accordance. The spatial distribution of radar based snow depth allows a clear distinction of three zones of different accumulation characteristics: (1) The lower part of Findel Glacier shows a clear altitudinal trend while (2) the upper part has no trend in altitude but high spatial fluctuations in snow depth. (3) Adler Glacier's accumulation characteristics are similar to zone (2). However, despite their close vicinity, accumulation on (3) is reduced by 40% compared to (2). The observed strong spatial variability emphasises the need for spatially continuous measurements for studies involving accumulation on glaciers. Finally, reasons for observed variations (e.g., preferential snow deposition and snow redistribution) are discussed.
Citation: Machguth, H., O. Eisen, F. Paul, and M. Hoelzle (2006), Strong spatial variability of snow accumulation observed with helicopter-borne GPR on two adjacent Alpine glaciers, *Geophys. Res. Lett.*, *33*, L13503, doi:10.1029/2006GL026576.

1. Introduction

[2] Utilisation of radio-echo sounding techniques to determine past and present accumulation rates has become a standard method, especially in polar glaciology. On polar ice sheets and polythermal glaciers this method is rewarding because of the low absorption of electromagnetic energy in cold firn. On temperated glaciers, application is usually restricted to sounding of ice thicknesses with low frequencies (<100 MHz). High-resolution measurements are mostly performed with so-called ground-penetrating radar systems (GPR) [e.g., *Richardson et al.*, 1997; *Kohler et al.*, 1997], operating directly from the surface. They are thus relatively time consuming and the spatial coverage is limited to accessible areas. Application of high-resolution airborne radar, capable of mapping annual accumulation, is still rare and mostly limited to fixed-wing aircraft [e.g., *Kanagaratnam et al.*, 2004]. To cope with the difficulties imposed by measurements in mountainous terrain and valley glaciers, airborne radar is most suitable. Apart from quasi-airborne measurements from an aerial tramway [*Yankielun et al.*, 2004], helicopter-borne radar provides the most reasonable platform and has been applied for studies of sea and river ice [*Wadhams et al.*, 1987; *Arcone and Delaney*, 1987; *Melcher et al.*, 2002], snow on ground [*Marchand et al.*, 2003] or glacier thickness measurements [*Thorning and Hansen*, 1987; *Damm*, 2004]. However, on mountain glaciers only few studies use helicopter-borne radar to investigate the properties of the snow cover and none was so far dedicated to the spatial accumulation distribution. For instance, *Arcone and Yankielun* [2000] focus on intraglacial features in the ablation zone of a glacier, whereas *Arcone* [2002] investigates processing techniques and autonomously derives physical properties of temperate firn.

[3] Today's glacier mass-balance models are based on sophisticated formulations of the energy fluxes while accumulation processes are treated in a very simple way: precipitation varies only with altitude and any processes of snow redistribution are neglected [*Hock*, 2005]. Using a similar model (described by *Machguth et al.* [2006]) we have calculated the mass balance distribution for a glacierized catchment in southwestern Switzerland, including Findel Glacier (length 7.2 km, area 15.3 km^2) and its neighbour Adler Glacier (3.1 km, 2.0 km^2) (Figure 1). (In this paper we refer to ''Findel Glacier''. According to the maps of the Swiss Federal Office for Topography (swisstopo) this is the official name of the glacier. However, in most glacier inventories the glacier is called Findelen Glacier.) The modelling for the 1971–1990 time period resulted in a very positive mass balance for Adler Glacier of 0.7 m water equivalent (m we) while its larger neighbour's mass balance was negative (−0.25 m we). In fact, the shrinkage of both glaciers indicates that a very positive mass balance is unrealistic. We assume that, in reality, accumulation on Adler- and Findel Glacier differs strongly. The model's failure is most probably caused by treating precipitation as a function of altitude alone and by ignoring snow redistribution.

[4] In this study we combine high-resolution helicopter-borne GPR measurements and extensive ground-based profiling of the snow cover to determine the spatial distribution of accumulation and to validate our assumption of a strong local variability in accumulation. In contrast to methods that require measurements at two points in time (e.g., mapping of elevation changes with laser altimetry, accumulation stakes without snowpits), GPR has the strong advantage that changes over time in surface elevation (e.g., melt, settlement of the underlying snow cover and glacier movement after the first measurement) do not affect the accuracy of the measurements. Furthermore, measuring only once requires less logistical efforts.

2. Methods

2.1. Radar System and Data Acquisition

[5] A commercial Noggin Plus 500 radar (Sensors & Software Inc., Canada,) was operated with a shielded

[1]Geographisches Institut, Universität Zürich, Zurich, Switzerland.
[2]Versuchsanstalt für Wasserbau, Hydrologie und Glaziologie, ETH Zürich, Zurich, Switzerland.
[3]Alfred-Wegener-Institut für Polar- und Meeresforschung, Bremerhaven, Germany.

0094-8276/06/2006GL026576$05.00

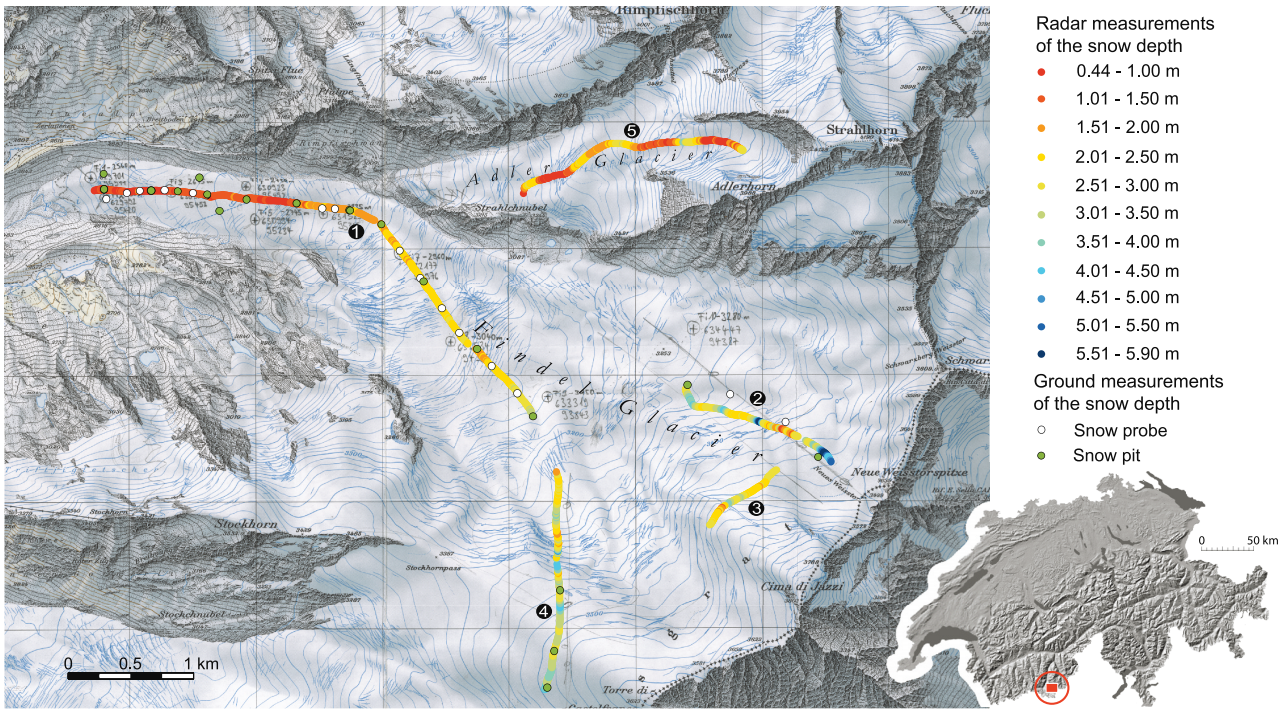

Figure 1. Map of Findel and Adler Glacier (red square in inset on Swiss map) with radar profiles (black numbered circles) and ground measurements. Color indicates radar-based snow depth. Reproduction of the background map with permission from swisstopo (BA067878).

antenna (15 cm transmitter-receiver separation) at a centre frequency of 500 MHz and 400 MHz bandwidth. The helicopter–radar combination was developed by Airborne Scan, Visp, Switzerland. The antenna was mounted to the helicopter runner. Data acquisition was performed in a constant-time triggering mode, with a time increment of 0.1 s between traces. Helicopter speed was about 6 m/s on average, resulting in a mean trace increment of 0.6 m. Helicopter altitude above ground was between 2.5 and 30 m, being 11 m on average, resulting in a footprint size in the order of a few tens of m^2. 1876 samples were recorded per trace with a 0.2 ns sampling interval, resulting in a 375 ns time window. Four-fold pre-storage stacking of traces at a pulse repetition frequency of 25 kHz was applied. A GPS antenna was mounted at the nose of the helicopter. For each recorded trace the GPS-position was simultaneously stored. Real-time GPS results in a position accuracy of <10 m.

[6] The radar flight was accomplished on 9 May 2005, ground measurements for validation were conducted on 6 and 7 May 2005. During all four days air temperature at the glacier terminus was slightly below the freezing point. Below 2700 m a.s.l. the snow was wet and some water drained off at the snow-ice interface. Above 3200 m the entire snow pack was dry. In approximately 25 minutes of flight 10.0 km of radar profiles were collected, thereof 1.9 km on Adler Glacier (Figure 1). On Findel Glacier radar profiles reach from 2570 to 3560 m a.s.l., on Adler Glacier they reach from 3240 to 3690 m a.s.l. Under the favourable weather conditions the sites of snow pits and -probes were visible from the helicopter allowing a consecutive visual determination of the flight direction. According to GPS data, the helicopter passed 26 snow pits and probes at a distance of <5 m, four at 5–15 m and two at 15–30 m. Two snow probes and one snow pit were missed by 60–130 m because they could not be found again.

2.2. Radar Data Processing

[7] Post-recording processing and radar-data analyses were carried out with ReflexWin (Sandmeier Scientific Software, Germany). Processing steps include dewowing (high-pass filter), background removal, application of a gain function to mainly compensate for spherical spreading, and additional filtering. The varying helicopter altitude above ground required a static correction of each trace to the first break of the surface reflection (time-zero correction). Due to the relatively smooth surface topography and small layer thickness compared to the helicopter altitude no migration was necessary. Along most profiles one or more distinct reflections of different magnitude are visible (see sample radar profile (Figure 2 or Figure S1 in auxiliary material[1]). Tracking of the uppermost strong continuous reflection horizon resulted in continuous profiles of last winters snow layer thickness (Figure 1). No interpretation was performed where no distinct reflection horizon was visible. Density measurements in the snow pits (see below) yielded a mean density of 400 kg m^{-3}. Based on the linear and quadratic conversion formulas of *Tiuri et al.* [1984] and *Kovacs et al.* [1995], respectively, conversion of the radar data from time to depth domain is carried out with a mean wave speed in snow of 2.2 10^8 ms^{-1}. Using the same mean density of 400 kg m^{-3} the layer thickness is converted to water equivalent.

[1] Auxiliary material is available in the HTML.

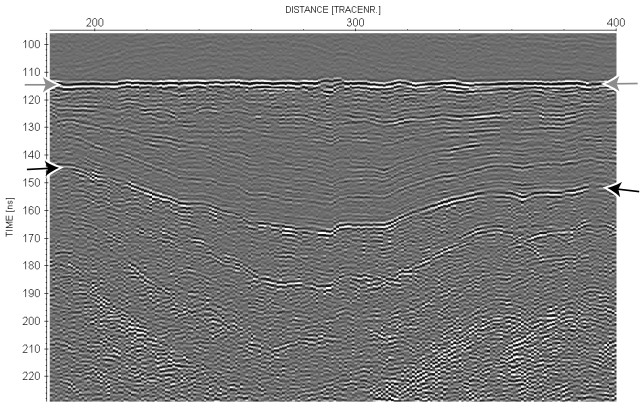

Figure 2. A section of the radar profile 2 at 3460 m a.s.l. The horizontal axis corresponds to approximately 130 m. The varying snow depth, the internal layering of the snow pack as well as previous years' firn layers with some internal structures are clearly recognizable. Grey arrows indicate the air-snow interface and black arrows indicate the snow-firn interface.

2.3. Snow Pits and Snow Probes

[8] Snow pits and snow probes were used to measure snow depth and density from the actual snow surface down to the ice surface. Where the snow cover outlasted the previous melting season (the remaining accumulation zone of 2004 is located above 3300 m a.s.l. on Findel Glacier, for Adler Glacier no data is available), snow pits were dug down to the horizon of the previous autumn's snow surface. According to data from the meteo station Gornergrat (located 5 km west of Findel Glacier at 3100 m a.s.l.), the long melt season of 2004 ended with heavy snow falls on 10 October. Consequently, the snow depth measured with radar, snow pits and -probes was accumulated within the time span of about 10 October 2004 to 7 May 2005. Coordinates of snow pits and -probes were captured with a hand-held GPS (position accuracy of 5–15 m). Within an altitudinal range from 2590 to 3510 m a.s.l. 20 snow pits have been sampled and snow depth and density as well as the internal layering of the snow pack was determined in all of them. This sample size was enhanced by 19 measurements of snow depth with snow probes. However, defining previous autumn's snow surface using snow probes is sometimes difficult (e.g., misinterpretations due to ice layers within the winter snow pack). Consequently, snow probes were restricted to the ablation area and for every test site the mean value of nine snow probes, sampled within a radius of 7 m, was calculated.

2.4. Data Merging

[9] Field measurements were only used to validate the interpretation of the radar profiles, analyses were conducted separately. Neither GPS data nor a map were used for the interpretation of the radar profiles, thus the interpreter's knowledge about the field measurements could not influence his interpretation of the profiles. The data sets were joined within a GIS software (ArcGIS 9.1). The twenty closest radar traces to every ground measurement were selected and their mean value is used below for comparison with the corresponding ground measurement.

3. Results

[10] The transition between winter snow and ice or winter snow and snow having outlasted the previous summer is in general clearly recognizable in the radar profiles. A total of 0.6 km radar profiles (6% of the total length) did not allow any tracking due to lacking or disturbed layering. Most of these zones are located within crevassed areas. Further analysis of the data is based on almost 15000 radar traces, representing the remaining 9.4 km of radar profiles. The thickness of the winter's snow layer varied in the ground measurements (radar measurements) from 0.32 (0.44) to 4.4 (5.9) m. The specific density measured in the snow pits is not correlated with altitude and varies from 360 to 470 kg m^{-3}. The mean density is 400 kg m^{-3} with a standard deviation of 30 kg m^{-3}. Figure 3 shows the agreement between radar profiles and all snow pits and -probes where the horizontal distance to the radar track is less than 30 m. The linear regression yields a correlation coefficient of $R^2 = 0.84$. Three data points must be considered outliers, as discussed below. Excluding these data points yields $R^2 = 0.96$.

[11] According to the radar profiles three zones of different accumulation characteristics can be distinguished: the lower part (profile 1) and the upper part of Findel glacier (profiles 2, 3 and 4), as well as Adler Glacier (profile 5). The lower part of Findel Glacier shows a clear correlation between altitude and snow cover thickness ($R^2 = 0.81$) and the fluctuations in snow depth are small (Figure 4). On Adler Glacier and the upper part of Findel Glacier accumulation has no altitudinal trend ($R^2 \leq 0.01$). Fluctuations in snow depth are very large. The correlation coefficient

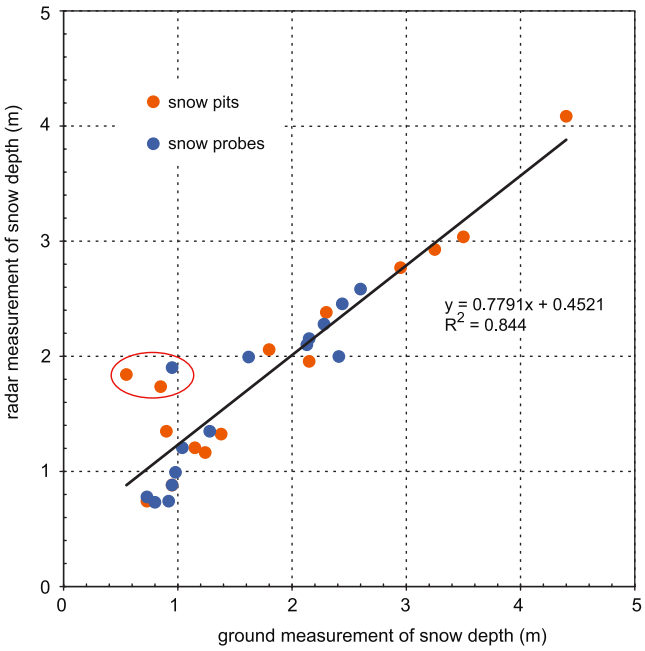

Figure 3. Comparison of radar- and ground-based measurements of snow depth. The three outliers are marked with a red circle.

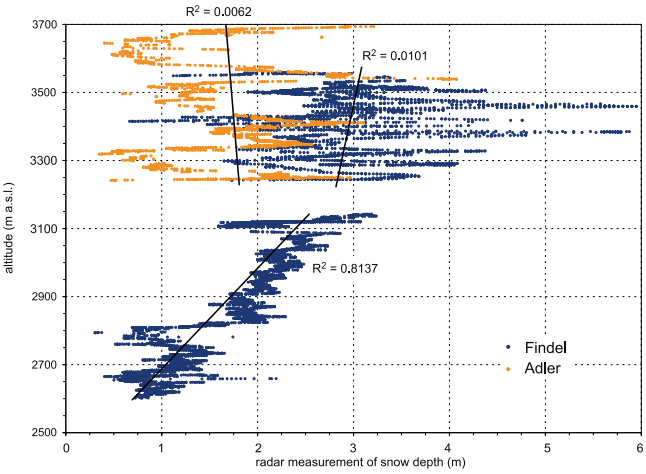

Figure 4. Snow depth versus altitude for all profiles on Findel and Adler Glacier.

calculated for the upper part of Findel Glacier is based on all traces of the profiles 2, 3 and 4 but also represents well the characteristics of every individual profile: none shows any significant trend with altitude; and all show large fluctuations of snow depth. At altitudes where radar profiles exist on both glaciers (3240 to 3560 m a.s.l.) the average accumulation is 2.98 m snow (5704 traces) on Findel and 1.80 m snow (2164 traces) on Adler Glacier. The accumulation on Adler Glacier is 0.5 m we or 40% lower than on Findel Glacier.

4. Discussion

[12] Our correlation between ground and radar measurements confirms the results of earlier studies with helicopter-borne radar in non glacierized landscapes, having achieved correlation coefficients of 0.82–0.97 [e.g., *Marchand et al.*, 2003]. The three outliers mentioned above are presumably caused by misinterpretations in the field. Snow-probe measurements at those three sites (see Figure S2 in auxiliary material), located within a diameter of 100 m at 2850 m a.s.l. are contradictory (0.5–1.7 m snow). A massive ice layer at 0.5 m depth was recorded in the snow profile closest to them. We assume that this layer was interpreted as the ice surface. The layer is visible in the radar profile as a long, massive and smooth reflection horizon at a depth of 0.5 to 1 m. Normally, the snow-ice interface appears more uneven because of previous surface melt and is similar to the second, less distinct reflection horizon at about 1.8 m in that profile. The example shows that in situ measurements might present only partial truth. A correct interpretation of the internal layering of the snow pack is essential for both methods. Consequently, mutual comparison is important to combine their strengths. In the ablation area snow pits allow precise point measurements while the large footprint of helicopter-borne GPR has the advantage of averaging out the bumpiness of the ice surface. In the accumulation area, both methods have to deal with the difficulty to correctly identify last autumn's snow horizon.

[13] The overall pattern of accumulation distribution on Findel Glacier corresponds well to the observations based on snow probes on other alpine glaciers (e.g., Vernagtferner in Austria, *Plattner et al.* [2006]). On the lower part of Findel Glacier the correlation between altitude and snow depth can partly be explained by melt during long warm weather periods in March and April 2005. The large deviations in accumulation between Findel and Adler Glacier are very unlikely to be caused by enhanced melt in March and April due to differing surface exposition: assuming that the entire difference in global radiation due to exposition (20 W m^{-2}) is available for melt and considering the high snow albedo of approximately 0.8 for this period, melt on Adler Glacier is estimated to be 0.05 m we higher than on Findel. We therefore assume that the large deviations in accumulation are primarily due to spatial variability of precipitation and redistribution of snow by wind. The area of investigation receives high amounts of precipitation under southerly wind directions. Reduced wind speed leeward from ridges results in enhanced precipitation and additional snow deposition from wind transport [e.g., *Föhn and Meister*, 1983; *Gauer*, 2001]. Findel glacier is located directly leeward of the main ridge and profits from this effect, whereas Adler Glacier is farther away. In addition, strongly reduced accumulation is also observed in crevassed zones, probably caused by topography and microscale turbulences. Within this study we have only assessed the spatial and not the temporal variability of accumulation. However, taking into account the concurrent shrinkage of both glaciers, we assume that the observed deviations in accumulation of both glaciers for the winter 2004/05 are not exceptional.

5. Conclusions and Outlook

[14] The data of both methods used in this study are in very good agreement. The observed distribution of the snow cover confirms our assumption of strongly reduced accumulation on Adler Glacier. Our results emphasize that the distribution of accumulation is not simply a function of altitude, confirming other studies [e.g., *Winstral et al.*, 2002]. We suppose that the spatial variability of precipitation as well as the redistribution of snow are mainly governing the accumulation distribution. The observed variability of the mass balance for the accumulation period (0.5 m we) is one order of magnitude higher than the error of melt calculations for the entire ablation period with energy balance models [compare *Arnold et al.*, 1996; *Obleitner and Lehning*, 2004]. The results underline that major improvements in glacier mass balance modelling can be achieved by focusing on the accumulation processes. Helicopter-borne GPR is recommended as a reliable tool for time-saving and accurate mapping of the snow cover. The method allows to enhance the sparse database on accumulation distribution toward both spatial and temporal variability, providing a sound data basis for glacier monitoring (e.g., yearly repeated measurement of winter balance), for statistical analyses (e.g., digital elevation model attributes) or for validation and calibration of physical modelling. Field measurements remain essential for mutual validation and to determine snow density.

[15] **Acknowledgments.** Simon Allen, Sabine Baumann, Xavier Bodin, Esther Hegglin, Christian Huggel, Jeannette Nötzli, Theresa Tribaldos, Michi Zemp and Michael Ziefle have helped us on field work. Their large effort made this study possible and is gratefully acknowledged. We very much appreciate the cooperation with Hubert Andereggen, Airborne Scan and Air

Zermatt. We would like to thank Michael Lehning and an anonymous reviewer for their valuable comments. H.M. was funded by the grant 21-105214/1 of the Schweizer Nationalfonds, O.E. was supported through an "Emmy Noether"-scholarship EI 672/1 of the Deutsche Forschungsgemeinschaft.

References

Arcone, S. (2002), Airborne-radar stratigraphy and electrical structure of temperate firn: Bagley Ice Field, Alaska, U.S.A., *J. Glaciol.*, *48*, 317–334.

Arcone, S., and A. Delaney (1987), Airborne river-ice thickness profiling with helicopter-borne UHF short-pulse radar, *J. Glaciol.*, *33*, 330–340.

Arcone, S. A., and N. E. Yankielun (2000), 1.4 GHz radar penetration and evidence of drainage structures in temperate ice: Black Rapids Glacier, Alaska, U.S.A., *J. Glaciol.*, *46*, 477–490.

Arnold, N., I. Willis, M. Sharp, K. Richards, and W. Lawson (1996), A distributed surface energy balance model for a small valley glacier: I. Development and testing for Haut Glacier d'Arolla, Valais, Switzerland, *J. Glaciol.*, *42*, 77–89.

Damm, V. (2004), Ice thickness and bedrock map of Matusevich Glacier drainage basin (Oates Coast), *Terra Antarct.*, *11*, 85–90.

Föhn, P. M. B., and R. Meister (1983), Distribution of snow drifts on ridge slopes: Measurements and theoretical approximations, *Ann. Glaciol.*, *4*, 52–57.

Gauer, P. (2001), Numerical modelling of blowing and drifting snow in Alpine terrain, *J. Glaciol.*, *47*, 97–110.

Hock, R. (2005), Glacier melt: A review of processes and their modelling, *Prog. Phys. Geogr.*, *29*, 362–391.

Kanagaratnam, P., S. Gogineni, V. Ramasami, and D. Braaten (2004), A wideband radar for high-resolution mapping of near-surface internal layers in glacial ice, *IEEE Trans. Geosci. Remote Sens.*, *42*, 483–490.

Kohler, J., J. Moore, M. Kennett, R. Engeset, and H. Elvehøy (1997), Using ground-penetrating radar to image previous years' summer surfaces for mass-balance measurements, *Ann. Glaciol.*, *24*, 355–360.

Kovacs, A., A. Gow, and R. Morey (1995), The in-situ dielectric constant of polar firn revisited, *Cold Reg. Sci. Technol.*, *23*, 245–256.

Machguth, H., F. Paul, M. Hoelzle, and W. Haeberli (2006), Distributed glacier mass-balance modelling as an important component of modern multi-level glacier monitoring, *Ann. Glaciol.*, in press.

Marchand, W. D., A. Killingtveit, P. Wilen, and P. Wikstrom (2003), Comparison of ground-based and airborne snow depth measurements with georadar systems, case study, *Nord. Hydrol.*, *34*, 427–448.

Melcher, N. B., et al. (2002), River discharge measurements by using helicopter-mounted radar, *Geophys. Res. Lett.*, *29*(22), 2084, doi:10.1029/2002GL015525.

Obleitner, F., and M. Lehning (2004), Measurement and simulation of snow and superimposed ice at the Kongsvegen glacier, Svalbard (Spitzbergen), *J. Geophys. Res.*, *109*, D04106, doi:10.1029/2003JD003945.

Plattner, C., L. N. Braun, and A. Brenning (2006), Spatial variability of snow accumulation on Vernagtferner, Austrian Alps, in winter 2003/2004, *Z. Gletscherkd. Glazialgeol.*, in press.

Richardson, C., E. Aarholt, S.-E. Hamram, P. Holmlund, and E. Isaksson (1997), Spatial distribution of snow in western Dronning Maud Land, East Antarctica, mapped by a ground-based snow radar, *J. Geophys. Res.*, *102*, 20,343–20,353.

Thorning, L., and E. Hansen (1987), Electromagnetic reflection survey 1986 at the Inland Ice margin of Pakitsoq basin, central Greenland, *Rapp. Groenl. Geol. Unders.*, *135*, 87–95.

Tiuri, M., A. Sihvola, E. Nyfors, and M. Hallikainen (1984), The complex dielectric constant of snow at microwave frequencies, *IEEE J. Oceanic Eng.*, *9*, 377–382.

Wadhams, P., M. A. Lange, and S. F. Ackley (1987), The ice thickness distribution across the Atlantic sector of the Antarctic Ocean in midwinter, *J. Geophys. Res.*, *92*, 14,535–14,552.

Winstral, A., K. Elder, and R. Davis (2002), Spatial snow modeling of wind-redistributed snow using terrain-based parameters, *J. Hydrometeorol.*, *3*, 524–538.

Yankielun, N., W. Rosenthal, and R. E. Davis (2004), Alpine snow depth measurements from aerial FMCW radar, *Cold Reg. Sci. Technol.*, *40*, 123–134.

O. Eisen, Laboratory of Hydraulics, Hydrology, and Glaciology, ETH Zürich, CH-8092 Zurich, Switzerland.

M. Hoelzle, H. Machguth, and F. Paul, Physical Geography Division, Department of Geography, University of Zurich, Winterthurerstr. 190, CH-8057 Zurich, Switzerland. (hoelzle@geo.unizh.ch; machguth@geo.unizh.ch)

GEOPHYSICAL RESEARCH LETTERS, VOL. 33, L22501, doi:10.1029/2006GL027871, 2006

Periodic surface features in coastal East Antarctica

Helgard Anschütz,[1] Olaf Eisen,[1,2] Wolfgang Rack,[1] and Mirko Scheinert[3]

Received 21 August 2006; revised 25 September 2006; accepted 3 October 2006; published 25 November 2006.

[1] We found evidence for highly periodic dunes in a near-coastal area of Dronning Maud Land, East Antarctica. Analysis of accumulation patterns, derived from ground-penetrating radar (GPR) internal layering, and GPS-based characteristics of surface topography, by means of auto- and cross-covariance, indicate quasi-harmonic oscillations of surface undulations, surface slope, and accumulation. The dunes occur at an elevation range of 1000–1350 m with the dominant wavelength of 5 km and undulations of ~10 m. Accumulation and slope are anticorrelated at zero lag, with a mean annual accumulation of some 140 kg m^{-2} yr^{-1} and variations on the order of ±100 kg m^{-2} yr^{-1}. Our findings have implications for studies aiming at the mass balance of coastal areas in Antarctica. **Citation:** Anschütz, H., O. Eisen, W. Rack, and M. Scheinert (2006), Periodic surface features in coastal East Antarctica, *Geophys. Res. Lett.*, *33*, L22501, doi:10.1029/2006GL027871.

1. Introduction

[2] Undulating features of surface topography and snow accumulation are a well-known phenomenon throughout Antarctica. Covarying undulations in topography, surface slope, and accumulation pattern have been reported since the earlier days of Antarctic research. *Black and Budd* [1964] report oscillations in the accumulation pattern derived from stake readings in Wilkes Land. Their profiles range from 180–380 km inland at an elevation range of 1000 to 3000 m. Surface slope along their stake line also shows oscillations, related to those in accumulation. *Pettré et al.* [1986] observed undulating patterns in accumulation in Tèrre Adélie, with a wavelength of 40 km. In order to explain those features they suggested a gravity-inertia wave at the break of slope. However, their stakes are spaced at intervals of 10 km so they are not able to derive any small-scale variations on the order of only a few kilometers. *Goodwin* [1990] discusses the influence of katabatic winds and the dependence of accumulation rates on surface aspect. He associates locally higher accumulation rates with the occurrence of longitudinal dunes, with lateral dimensions of 10–100 m, at elevations between 1870–2230 m. Referring to *Black and Budd* [1964], he furthermore explains that circulations forced by meso-scale topography modify wind flow induced by broad-scale orography, offsetting the accumulation minima to the West with respect to the elevation maxima. Although these earlier observations indicate dune-like patterns in more coastal areas, one has to be aware that they are based on stake readings with stake spacing of some 100 m or even more, thus lacking small-scale continuity as well as high-precision elevation data due to the lack of GPS equipment. All these observations are expressions of the generally accepted process that blowing snow tends to accumulate in local depressions, whereas local rises experience less accumulation or even ablation (see *King et al.* [2004] for a recent summary). Surface slope in the prevailing wind direction is a key parameter in the description of this process [*Frezzotti et al.*, 2002a].

[3] The probably most stunning phenomenon of interaction between accumulation distribution and surface topography are the megadune fields on the East Antarctic plateau, covering areas of roughly 500 000 km^2. Detailed descriptions were derived from satellite imagery showing the ripple-like patterns extending over hundreds of kilometers [*Fahnestock et al.*, 2000]. Megadunes are characterized as gentle but highly regular undulations on the surface, whose genesis is ruled by an unusual feedback mechanism between cryosphere and atmosphere [*Frezzotti et al.*, 2002a]. Wavelengths are on the order of a few kilometers and amplitudes of a few meters, their subparallel crests extending over several hundred kilometers. Increased accumulation occurs on the windward side and less accumulation on the leeward side, thus producing a dune-like nearly-periodic accumulation pattern related to the surface topography [*Frezzotti et al.*, 2002a]. Windward slopes are often covered with severe sastrugi, whereas on the leeward faces and in the interdune troughs glazed surfaces dominate surface characteristics in snow-megadune areas [*Frezzotti et al.*, 2002b]. A recent map of megadune distribution, based on ICESat's GLAS altimetry data, locates megadune fields only in the interior of the East Antarctic ice sheet, several hundreds of kilometers away from the coast [*Shuman et al.*, 2006]. Moreover, *Scambos and Bauer* [2006] observed that megadunes occur in areas of moderate regional slope and low accumulation on the flanks of the ice sheet at an elevation range between 2500–3800 m.

[4] Here, we provide evidence that highly periodic surface undulations are also present near coastal sites. We present ground-based data from Potsdam Glacier in Neuschwabenland, the coastal area of Dronning Maud Land, East Antarctica. Ground-penetrating radar (GPR) data complemented by firn-core studies indicate a strongly oscillating accumulation distribution that varies with surface slope. Statistical analysis by means of auto- and cross-covariance functions of accumulation series as well as of surface slope emphasizes the periodicity. In order to avoid confusion we will address these features as periodic dunes, especially since they lack the lateral extent and extreme morphology of the megadunes. As explained above, the latter experience extremely low accumulation on the leeward sides, where

[1] Alfred-Wegener-Institut für Polar- und Meeresforschung, Bremerhaven, Germany.
[2] Also at Versuchsanstalt für Wasserbau, Hydrologie und Glaziologie, ETH Zürich, Switzerland.
[3] Institut für Planetare Geodäsie, Technischen Universitt Dresden, Dresden, Germany.

0094-8276/06/2006GL027871$05.00

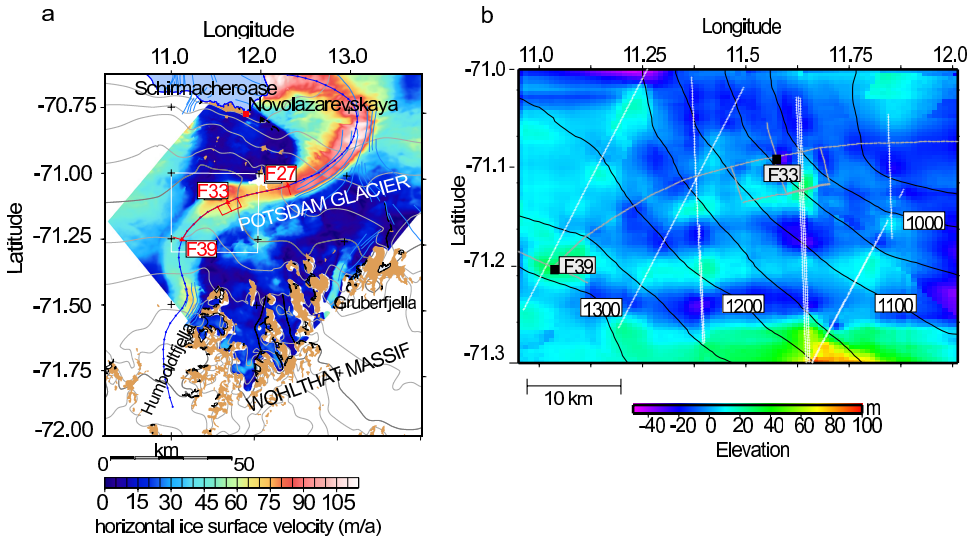

Figure 1. (a) Overview of the area of investigation. Dark line with dots: main glacier flow line; points marked Fxx: start/end points of the radar profiles along the main flow line; light (red) lines: additional GPR profiles. Distances from F39 to F33 and from F33 to F27 amount to 25 km each. Color scale indicates glacier-flow velocity [*Bäßler et al.*, 2002]. Flow direction is from F39 to F27. Light grey lines: elevation contour lines at 200 m spacing; dark grey line: 1000 m elevation contour line. The white rectangle corresponds to the area depicted in (b). (b) Undulations of elevation; color scale refers to differences between original and smoothed DEM. The DEM has been obtained from GPS (grey lines) and ICESat (white lines) data. Black lines indicate elevation contour lines at 50 m spacing (obtained from the smoothed DEM).

snow sampling reveals large grains and extensive depth hoar [*Albert et al.*, 2004; *Frezzotti et al.*, 2002b]. Comparable observations are not as pronounced or even missing in our study area near the Antarctic coast.

2. Area of Investigation and Data Set

[5] The study area is situated on Potsdam Glacier south of the Schirmacheroase and north of Wohlthat Massif (Figure 1a), about 120 km away from the ice-shelf edge. Wide areas of Potsdam Glacier are above 1000 m a.s.l. and have a mean annual temperature below −20°C. Ice thickness >1200 m in most parts of the glacier. Bedrock topography is generally smooth with some subglacial peaks [*Damm and Eisenburger*, 2005]. Generally the higher-elevation parts experience accumulation with the exception of small ablation areas around several nunataks. However, in the northeastern part of this glacier, near and east of the Schirmacheroase, a large ablation area is found [*Bormann and Fritzsche*, 1995, and references therein] that reaches up to the eastern Wohlthat Massif. Previous work in this area [e.g., *Korth and Dietrich*, 1996] consisted of geodetic-glaciological traverses to Humboldtfjella and Gruberfjella (Figure 1a). From the InSAR analysis of ERS-1/2 satellite data, *Dietrich et al.* [1999] established a horizontal velocity vector field. In the area of investigation glacier flow is about 20–30 m yr^{-1} at higher elevations and up to 70–80 m yr^{-1} in the lower parts. Laterally convergent flow occurs at the lower elevations, whereas at the higher parts lateral divergence is observed [*Bäßler et al.*, 2002; *Bäßler et al.*, 2003].

[6] During the Antarctic summer season 2003/2004 radar surveys at a frequency of 500 MHz were carried out along a profile of 50 km length on the main glacier-flow line (Figure 1). Traces were recorded every 0.5 m. Simultaneously, kinematic GPS data were collected at 1 s intervals, with the GPS equipment mounted to a snow mobile. An airborne radio-echo sounding survey near the main flow line was carried out as well. Snow pits and firn cores (12 m deep) complemented the field data, aiming for the determination of the recent accumulation rate. Along the firn cores measurements of density and dielectric profiling (DEP [*Wilhelms*, 2005]) were carried out in intervals of 5 mm as well as determination of $\delta^{18}O$ in 3 cm intervals, which was used for dating. (A detailed description of data acquisition and processing is given by H. Anschütz et al. (Investigating small-scale variations of the recent accumulation rate in coastal Dronning Maud Land, East Antarctica, submitted to *Annals of Glaciology*, 2006, hereinafter referred to as Anschütz et al., submitted manuscript, 2006).) From the processed GPR data two internal reflection horizons (IRHs) are tracked throughout the GPR profiles and dated by the $\delta^{18}O$ profile of one reference firn core. The respective dating uncertainty of each IRH amounts to ±2 a. Combining the age and the respective cumulative mass of the IRHs yields accumulation rates. Surface topography is derived from the processed GPS data.

3. Accumulation Characteristics and Surface Features

[7] The time-integrated effect of ice flow interacting with a variable accumulation pattern is memorized in the internal-layer architecture [e.g., *Arcone et al.*, 2005]. Our processed radargrams clearly show undulations of several meters over few kilometers of the internal layer depths, larger than expected for this area (Figure 2). Firn-core data (Anschütz et al., submitted manuscript, 2006) were input to convert GPR data from two-way traveltime (TWT) to depth [*Eisen et al.*, 2002]. Linking two continuous layers to the reference firn core provides estimates of along-profile

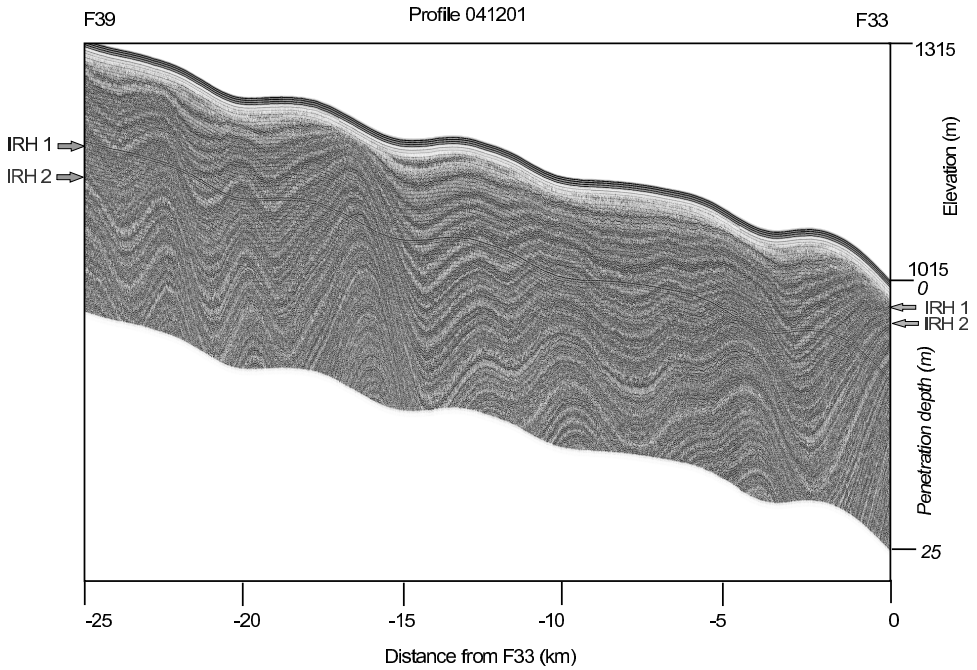

Figure 2. Processed radargram of profile 041201, going from F39 to F33 along the main flow line (see Figure 1). Arrows indicate the two tracked and dated IRHs. Note the vertically enlarged scale of the radar section in relation to the elevation scale.

accumulation (Anschütz et al., submitted manuscript, 2006) for the periods 1970–1980, 1970–2004, and 1980–2004, with a mean accumulation error of 12% (Figure 3c). Errors are mainly introduced by the dating uncertainty. However, this spatially systematic uncertainty only affects the temporal variability and the absolute accumulation values but not the spatial variability nor the undulations of the accumulation pattern and conclusions drawn in this study.

[8] The surface elevation declines from almost 1350 m a.s.l. in South-West to about 850 m a.s.l. in the North-East. On this decreasing trend a regularly undulating pattern is overlain, clearly visible in the linearly detrended surface elevation (Figure 3a) and in surface slope (Figure 3b). Topography undulations are around 10 m, and elevation maxima occur almost equidistantly at a 5 km interval. Beyond 7 km downstream of the central firn core (at F33, see Figure 1), towards a known blue-ice area, the undulations cease and surface slope is nearly constant.

[9] Undulations in GPR-layer depth coincide with the undulations in surface topography, but their peaks are displaced further downstream with increasing depth in relation to the local maxima in surface elevation. The accumulation pattern derived from the two dated IRHs (Figure 3c) shows a high spatial variability overlain on a generally decreasing trend in the direction of glacier flow down to 7 km beyond the central firn-core location. Although the accumulation oscillates less periodically than slope or surface elevation, it still seems regular.

4. Highly Periodic Dunes

[10] Other studies already reported anticorrelation of surface slope and accumulation [e.g., *Black and Budd*, 1964; *Frezzotti et al.*, 2005]. In order to further examine the periodicity described above, we calculated the autocovariance (ACV) functions of the accumulation and the surface slope as well as the cross-covariance (CCV) between those variables (Figure 4). The pronounced regular side maxima in the ACV functions emphasize the presence of oscillations. The largest magnitude of the CCV function of slope and accumulation occurs at zero lag with a value of −0.62, emphasizing that slope and accumulation are anticorrelated. Power spectral analyses of the accumulation and slope series reveal the wavelength of the features. The respective CCV function indicate a dominant wavelength at around 5.05 km. In all three spectra (auxiliary material) other wavelengths have much lower powers, and the respective main peaks are significant at the 99.7%-confidence level.[1] We therefore conclude that the observed surface undulations and accumulation variations are quasi harmonic and strongly linked to each other. These characteristics, being more detailed than reported in former analyses, remind of megadunes [*Frezzotti et al.*, 2002a], although they lack the spatial extension of the megadune fields. Moreover, observation of surface structure and its variability is basically in accordance with the description of *Frezzotti et al.* [2002a], who report large longitudinal sastrugi on the uphill sides of the megadunes and glazed surfaces on downhill sides. Generally, the mean accumulation in this coastal area is higher than on the polar plateau and the differences between the leeward and windward surface features are not as pronounced as in the megadune areas. We likewise observed large sastrugi fields, associated with locally increasing surface elevation, whereas smoother surfaces tended to be located in troughs.

[1] Auxiliary materials are available in the HTML. doi:10.1029/2006GL027871.

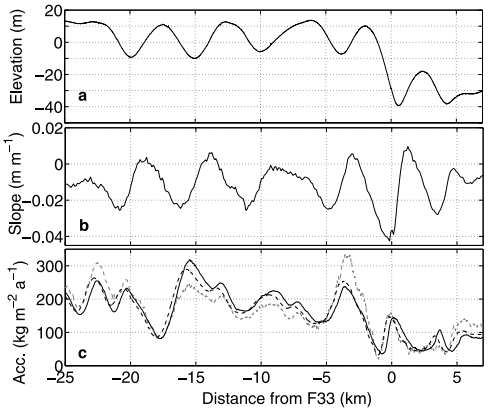

Figure 3. (a) Linearly detrended surface elevation, (b) surface slope, and (c) GPR-based accumulation pattern on the main flow line. The solid line in Figure 3c corresponds to the time period 1980–2004, the dashed to 1970–2004, and the dashed grey line to 1970–1980. Glacier flow is from left to right. Note that only features within the first 7 km downstream of the central firn core are shown.

[11] From the radargram along the uppermost 25 km of the main flow line (Figure 2) it is obvious that relative motion between the accumulation pattern and firn column takes place, as observed on the polar plateau [*Frezzotti et al.*, 2002a]. Buried crests of former dunes are slightly displaced to the crests of current surface dunes.

[12] By comparing the maxima in depth of the deepest continuous IRH (1970 ± 2 years) with those from the shallower continuous IRH (1980 ± 2 years) we can determine the relative migration velocities. From those phase lags between maxima in layer depth only half the velocity is derived due to interferences as demonstrated by *Arcone et al.* [2005] using trigonometric argumentation. Taking this into account, we calculated migration velocities which are basically in the range of glacier-flow velocities. However, uncertainties of this estimation, introduced by the horizontal placement of the troughs in depth distribution and especially by the dating uncertainty of the IRHs, prevent a clear prediction about possible dune migration from groundborne data. Analysis of SAR data from ERS-1/2 (April 1996) allows us to derive detrended elevation values along the main flow line which can be compared with the detrended surface elevation from the GPS data recorded during the expedition in January 2004 (Figure 3a). The detrended surface-elevation curve from the GPS data is displaced upstream in relation to the one derived from the SAR data (auxiliary material). From the displacements (peak-to-peak and trough-to-trough, respectively) we obtain mean migration velocities for the time period of 8 years (1996–2004). The mean relative migration velocity of the surface undulations results as 60 m yr^{-1} with a 1σ standard deviation of 20% in opposite direction to the glacier flow. The uncertainty of this estimation is about 8%. From Figure 1b it is obvious that the dunes are oriented mainly in East-West direction, thus introducing an angle of 25–45 degree between their orientation and the direction of the GPR profiles. Taking this into account, the obtained migration velocities reduce to values ranging from about 35–58 m yr^{-1} with an average velocity of 45 m yr^{-1} and a standard deviation of 22%. However, the DEM indicating the orientation of the dunes (discussed below) should be considered with caution because of the sparse data base.

5. Dune Extension and Genesis

[13] Unlike the megadune fields, our dune-like patterns are not clearly visible in satellite imagery, e.g. MODIS. This can be explained by the generally higher accumulation, about one order of magnitude higher compared to the polar plateau, and the less pronounced differences in reflection characteristics in our case. Analysis of ICESat altimetry data (Release-12, -24, and -26, http://nsidc.org/data/icesat) combined with groundborne GPS data allows us to derive a preliminary digital elevation model (DEM) of the investigation area. After smoothing this DEM using a median filter and calculating the differences between the original and the smoothed DEM we conclude that the periodic dune patterns laterally extend several tens of kilometers parallel to the mean surface slope (Figure 1b). Between about 11.2 E and 12.0 E they are almost parallel to the mountain range of the Wohlthat Massif, but further west they bend towards the North/North-East. Assuming katabatic winds from the mountains of Wohlthat Massif, the dunes would be transverse to the main wind direction. Beyond the western edge of Wohlthat Massif the wind pattern follows the main surface slope and changes direction, resulting in a bent dune orientation. No meteorological data are available so far to prove these assumptions. Up to now there are no AWS installed nearby and model data from atmospheric models are not able to resolve small-scale near-surface wind patterns in this orographically complicated region (M. v. d. Broeke, personal communication, 2006). The analysis of wind pattern in this area in future field campaigns would be helpful to further explain the existence of the dunes.

[14] In principle, bedrock topography could also cause an undulating surface, which then changes the accumulation pattern. Yet bedrock topography from a nearby airborne radio-echo sounding does not indicate any regular features that could be responsible for the observed small-scale surface undulations [*Damm and Eisenburger*, 2005; D. Steinhage, personal communication, 2006]. We thus suggest that the periodic dunes are generated by a feedback system between

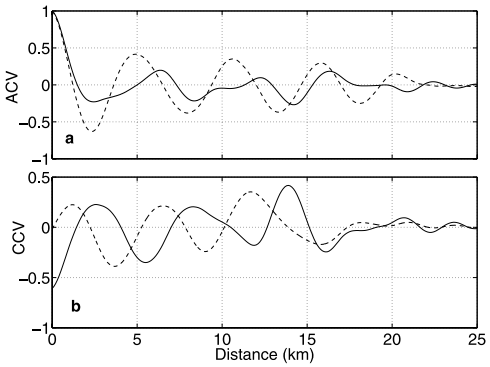

Figure 4. Auto-covariance functions (a) for surface slope (dashed line) and accumulation (solid line) and cross-covariance (b) between accumulation–slope (solid) and accumulation–detrended surface elevation (dashed).

atmosphere and cryosphere similar to the description by *Frezzotti et al.* [2002a] and *Pettré et al.* [1986], and not by dynamic influence of the bedrock topography on the surface.

[15] In summary, we conclude that undulations of surface slope interact with the wind pattern to generate highly regular dunes in this near-coastal area. This finding has implications for other coastal areas where similar periodic dunes exist. The regional representativity of firn-core interpretations in those areas is likely very limited, since orographic variations on the order of a few meters per kilometers significantly influence snow accumulation. Moreover, change detection for coastal areas is the focus of several remote sensing missions, like ICESat, GRACE, or Cryosat-2, aiming at Antarctica's continental mass balance. Although coastal accumulation patterns were expected to be complex due to wind action, as evident from blue ice areas, the occurrence of highly periodic dunes on small spatial scales further complicates the picture. Future studies in coastal areas should keep an eye on surface features and closely examine snow structure and surface topography in order to assess the distribution and magnitude of other dune patterns at coastal sites.

[16] **Acknowledgments.** Preparation of this work was supported by the Deutsche Forschungsgemeinschaft (DFG) through the VISA project, funded under grants Di 473/17 and Jo 191/8. O.E. was supported by the DFG "Emmy Noether"-scholarship EI 672/1. Comments from M. Frezzotti, T. Scambos, and C. Shuman significantly improved the manuscript.

References

Albert, M., C. Shuman, Z. Courville, R. Bauer, M. Fahnestock, and T. Scambos (2004), Extreme firn metamorphism: Impact of decades of vapor transport on near-surface firn at a low-accumulation glazed site on the East Antarctic plateau, *Ann. Glaciol.*, *39*, 73–78.

Arcone, S. A., V. B. Spikes, and G. S. Hamilton (2005), Stratigraphic variation within polar firn caused by differential accumulation and ice flow: Interpretation of a 400 MHz short-pulse radar profile from West Antarctica, *J. Glaciol.*, *51*(174), 407–422.

Bäßler, M., R. Dietrich, and C. Shum (2002), Investigation of ice dynamics at the grounding zone of an Antarctic ice shelf utilizing SAR interferometry, in *Proceedings of the Weikko A. Heiskanen Symposium in Geodesy 1–4 Oct 2002, Columbus, Ohio, USA*, edited by C. Jekeli and C. K. Shum, Ohio State Univ., Columbus.

Bäßler, M., R. Dietrich, and C. Shum (2003), Horizontal velocity field, strain analysis and grounding zone location for the area of Nivlisen ice shelf, Dronning Maud Land, poster presentation at FRINGE Workshop, Eur. Space Agency, Frascati, Italy, 1–5 Dec.

Black, H., and W. Budd (1964), Accumulation in the region of Wilkes, Wilkes Land, Antarctica, *J. Glaciol.*, *5*, 3–15.

Bormann, P., and D. Fritzsche (Eds.) (1995), *The Schirmacher Oasis, Queen Maud Land, East Antarctica, and Its Surroundings*, Justus Perthes, Gotha, Germany.

Damm, V., and D. Eisenburger (2005), Ice thickness and sub-ice topography in Central Dronning Maud Land deduced by radio echo sounding, *Geol. Jahrb., Reihe B*, *97*, 109–127.

Dietrich, R., R. Metzig, W. Korth, J. Polzin, and M. Scheinert (1999), Combined use of field observations and SAR interferometry to study ice dynamics and mass balance in Dronning Maud Land, Antarctica, *Polar Res.*, *18*, 291–298.

Eisen, O., U. Nixdorf, F. Wilhelms, and H. Miller (2002), Electromagnetic wave speed in polar ice: Validation of the CMP technique with high-resolution dielectric profiling and gamma-density measurements, *Ann. Glaciol.*, *34*, 150–156.

Fahnestock, M. A., T. A. Scambos, C. A. Shuman, R. J. Arthern, D. P. Winebrenner, and R. Kwok (2000), Snow megadune fields on the East Antarctic Plateau: Extreme atmosphere-ice interaction, *Geophys. Res. Lett.*, *27*(22), 3719–3722.

Frezzotti, M., S. Gandolfi, and S. Urbini (2002a), Snow megadunes in Antarctica: Sedimentary structure and genesis, *J. Geophys. Res.*, *107*(D18), 4344, doi:10.1029/2001JD000673.

Frezzotti, M., S. Gandolfi, F. L. Marca, and S. Urbini (2002b), Snow dunes and glazed surfaces in Antarctica: New field and remote-sensing data, *Ann. Glaciol.*, *34*, 81–88.

Frezzotti, M., et al. (2005), Spatial and temporal variability of snow accumulation in East Antarctica from traverse data, *J. Glaciol.*, *51*(172), 113–124.

Goodwin, I. (1990), Snow accumulation and surface topography in the katabatic zone of Eastern Wilkes Land, Antarctica, *Antarct. Sci.*, *2*, 235–242.

King, J. C., P. S. Anderson, D. G. Vaughan, G. W. Mann, S. D. Mobbs, and S. B. Vosper (2004), Wind-borne redistribution of snow across an Antarctic ice rise, *J. Geophys. Res.*, *109*, D11104, doi:10.1029/2003JD004361.

Korth, W., and R. Dietrich (1996), *Ergebnisse geodätischer Arbeiten im Gebiet der Schirmacheroase/Antarctica 1988–1993*, *Dtsch. Geod. Komm., Reihe B*, vol. 301, Bayer. Akad. der Wiss., Munich, Germany.

Pettré, P., J. Pinglot, M. Pourchet, and L. Reynaud (1986), Accumulation in Terre Adelié, Antarctica: Effect of meteorological parameters, *J. Glaciol.*, *32*, 486–500.

Scambos, T., and R. Bauer (2006), GPR and GPS data: Characteristics of snow megadunes and their potential effect on ice core interpretation, digital media, Natl. Snow and Ice Data Center, Boulder, Colo.

Shuman, C., M. Fahnestock, T. Scambos, M. Albert, R. Bauer, and V. Suchdeo (2006), Antarctic megadunes characteristics from ICESat elevation data, *Geophys. Res. Abstr.*, *8*, 08686.

Wilhelms, F. (2005), Explaining the dielectric properties of firn as a density-and-conductivity mixed permittivity (DECOMP), *Geophys. Res. Lett.*, *32*, L16501, doi:10.1029/2005GL022808.

H. Anschütz, O. Eisen, and W. Rack, Alfred-Wegener-Institut für Polar- und Meeresforschung, Am alten Hafen 26, D-27568 Bremerhaven, Germany. (hanschuetz@awi-bremerhaven.de; oeisen@awi-bremerhaven.de; wrack@awi-bremerhaven.de)

M. Scheinert, Institut für Planetare Geodäsie, Technischen Universität Dresden, D-01062 Dresden, Germany. (mikro@ipg.geo.tu-dresden.de)

Characteristics of accumulation around the EPICA deep-drilling site in Dronning Maud Land, Antarctica

Olaf EISEN,* Wolfgang RACK, Uwe NIXDORF, Frank WILHELMS

Alfred-Wegener-Institut für Polar- und Meeresforschung, Postfach 120161, D-27515 Bremerhaven, Germany
E-mail: oeisen@awi-bremerhaven.de

ABSTRACT. Based on ground-penetrating radar profiles, we analyze area-wide spatial and temporal characteristics of accumulation rate in the vicinity of the EPICA (European Project for Ice Coring in Antarctica) deep-drilling site in Dronning Maud Land, Antarctica (EDML). An area of 1600 km^2 is covered by 500 km of radar profiles, organized in a star-like pattern with eight 20–25 km legs and a 10 km grid with 1–3 km spacing, each pattern being centred on the EDML drilling location. Distributions of density, cumulative mass, age and the electromagnetic wave speed with depth are available from physical ice-core records. Nine internal reflection horizons are continuously tracked within the upper 110 m of ice over the whole area, yielding a spatial picture of accumulation rate history over >1000 years. The mean accumulation rate over the last 153 years varies between 50 and 75 kg m^{-2} a^{-1} over 50 km perpendicular to the ice divide; the spatial average is ~61 kg m^{-2} a^{-1}. This general pattern is overlain by small-scale variations of accumulation rate on the order of 10% of the mean. Maximum local gradients in accumulation rate are ~2–3 kg m^{-2} a^{-1} km^{-1}, about five times the regional accumulation rate gradient. Comparison of topography and accumulation rate along a 20 km profile in the direction of the mean winds indicates that variations in accumulation rate over short distances are linked to surface undulations. Our results show that advected spatial variations of accumulation rate are on the same order and even exceed temporal changes over the investigated periods. Ice flow and upstream effects therefore might influence accumulation rates reconstructed from the EDML ice core.

INTRODUCTION

Surface mass balance is a key parameter for estimating the contribution of the Antarctic ice sheet to global sea-level changes and deriving palaeoclimatic conditions from ice cores (Giovinetto and Zwally, 2000). A major problem for determining the net surface mass balance, hereafter referred to as accumulation rate, on continental scales is its irregular spatial characteristics. Regionally homogeneous precipitation is disturbed in the atmospheric boundary layer by small-scale variations in wind speed, leading to varying patterns of the surface mass balance on all scales.

Local changes in accumulation rate over time can be accurately reconstructed from ice cores retrieved at specific locations such as ice domes, provided their position was stationary over time. At other drilling locations, the surrounding setting of bedrock topography, ice thickness and surface slope determines whether observed local changes in annual layer thickness contain upstream effects (Hamilton, 2004), ice dynamics (Vaughan and others, 1999) or correspond to real temporal changes in the past (Spikes and others, 2004; Steinhage and others, in press).

In order to estimate the spatial representativity of deep ice-core measurements, drilling activities are usually accompanied by repeated readings of surface stakes, snow-pit sampling and deployment of shallow firn cores. Although ice-dynamic numerical modelling improves the separation of small-scale temporal and spatial effects, the limited spatial resolution of input datasets as well as models makes reliable interpretation of results difficult (Karlöf, 2004).

Especially over the last decade, several methodological studies on the application of high-resolution ground-penetrating radar (GPR) have been carried out to improve the spatial resolution of accumulation maps (Richardson-Näslund and others, 1997; Nereson and others, 2000; Richardson-Näslund, 2001; Frezzotti and others 2002; Pälli and others, 2002; Karlöf, 2004; Rotschky and others, 2004). In most cases, internal horizons imaged with GPR represent surfaces of isochronal deposition (Gudmandsen, 1975; Jacobel and Hodge, 1995). With its ability to penetrate the upper hundreds of metres of the ice column, equivalent to a deposition history of several hundreds to thousands of years on the Antarctic inland plateau, GPR provides a means to accurately map accumulation rates and their spatial variations along continuous profiles.

In this study, we present the spatial and temporal variation of the accumulation rate in the vicinity of the EPICA (European Project for Ice Coring in Antarctica) deep-drilling site in Dronning Maud Land, Antarctica, (EDML) based on extensive GPR measurements (Fig. 1). The EDML drill site near Kohnen station (75.00° S, 0.07° E; 2893 m a.s.l.) is located close to a topographic ice divide running approximately east-southeast–west-northwest. Repeated global positioning system (GPS) geodetic measurements during the period 2001–04 showed that surface velocities are ~0.7 m a^{-1}, with the main flow roughly parallel to the divide (personal communication from D. Schulte, 2004). The combination of continuous internal layers up to 110 m depth, obtained during several EPICA pre-site surveys, with physical properties from the EDML ice core allowed us to calculate the spatial distribution of the accumulation rate for eight time intervals during the last 1000 years.

Our results show that the spatial variations in accumulation rate, related to undulations in surface topography, and

*Present address: Versuchsanstalt für Wasserbau, Hydrologie und Glaziologie, Eidgenössische Technische Hochschule, ETH-Zentrum, CH-8092 Zürich, Switzerland.

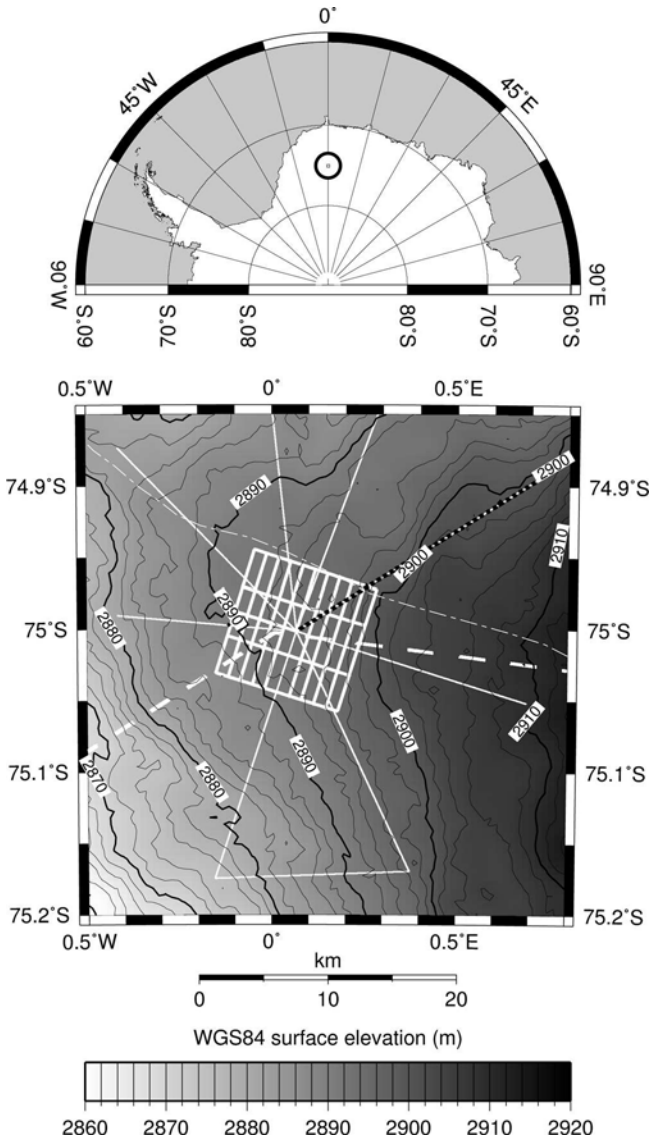

Fig. 1. Location of study area in Dronning Maud Land (top), and radar profiles surrounding the EPICA drill site (bottom). Contours (black) and greyscale refer to surface topography as derived from European Remote-sensing Satellite interferometry (see text for details). Superimposed as white lines are the 2000/01 grid- (thick) and star-like patterns (thin), with the 1998/99 traverse profiles as thick dashed white lines. The EDML drill site is in the centre of the star- and grid-profile patterns. Mean ice flow is from east-southeast to west-northwest at about 0.7 m a^{-1} near the drill site; mean wind direction is from ~60° true north (Reijmer, 2001). The black-and-white dashed line indicates the upwind profile 011203 discussed in the text and shown as a cross-section in Figure 4. The approximate position of the major topographic ice divide is shown as dotted-dashed line.

temporal variations seen in the ice core over the period considered are similar in magnitude. Interpretation of the EDML ice core therefore requires an understanding of how the spatial and temporal variations interact to form the record preserved in the core.

DATA AND METHODS

Ground-penetrating radar

We used a commercial RAMAC radar set (Malå Geosciences), operating with shielded 250 MHz antennae, and simultaneous positioning measurements with a Trimble GPS receiver, to map the internal structure of the upper 120 m of the ice sheet in 1 m increments. The radar profiles recorded in 2000/01 formed two patterns: the first was a 10×10 km^2 grid with 2 and 3 km spacing roughly parallel to the ice divide and 1 km spacing across. A second, star-like pattern consisted of eight legs up to 25 km long. Both patterns were centred on the EDML drilling location (Fig. 1). In addition, profiles recorded during the 1998/99 field season with the same system but unshielded 200 MHz antennae were also used for our analysis.

A series of nine continuous internal reflection horizons (IRHs), which are isochrones (Eisen and others, 2004), were tracked in all the profiles throughout the region of interest. Details of data processing, the tracking procedure and examples of the data quality are available in Eisen and others (2004). After tracking, all reflectors were available in the two-way travel-time domain.

Ice-core properties

Dielectric profiling (DEP) along the EDML core formed the basis for converting the structure of the IRHs to accumulation rates. The upper 13 m of the EDML core were missing because of the technical set-up of the deep drilling. They were replaced by DEP data from the nearby 150 m ice core B32, located 1.5 km to the west. The B32 and EDML records were matched by identifying unique volcanic peaks visible in both DEP conductivity records (personal communication from A. Lambrecht, 2003). This enabled us to transfer the age–depth profile from B32 to EDML, where the independent counting of annual layers is still underway. Dating uncertainty is ~5 years (Traufetter and others, 2004). Based on the age–depth model and density measurements along the EDML ice core, we determined the accumulation rates at the EDML drilling location used below.

Depth distribution of the electromagnetic wave speed and density was calculated from the DEP permittivity, allowing conversion of travel time to depth along the profiles. The integration of density yielded cumulative mass as a function of depth, thereby smoothing out small-scale variations in density. As we did not find significant spatial deviations of the mass–depth distribution from an analysis of eight ice and firn cores over >320 km (Rotschky and others, 2004), we assumed that it was constant throughout the region. The age of each reflector was determined by merging reflector depth and the age–depth distribution at EDML (for details of the IRH dating procedure see Eisen and others, 2004).

Synthesizing accumulation rates

The above datasets provided cumulative mass and age for each point along each IRH. The accumulation rate along the profiles was derived from adjacent pairs of IRHs for different time intervals by calculating the ratio of difference in cumulative mass and difference in age. The age difference of neighbouring IRHs ranges from <100 to 200 years. Hence, the calculated accumulation rates represent a low-pass filtered mean of the annual accumulation rate. The cumulative effect of strain thinning is comparably small in the upper part of the ice column. Vertical strain rates were on the order of 1–5 $\times 10^{-5}$ a^{-1} (personal communication from H. Oerter and O. Rybak, 2004), two orders of magnitude smaller than the value found to be significant for internal deformation of an ice cap by Vaughan and others (1999).

The spatial distribution of accumulation rate was obtained by gridding the dataset with a spatial increment of 0.5 km (Fig. 2). Prior to gridding with a tensioned minimum curvature technique, the data were spatially averaged within each gridcell to avoid aliasing of small wavelengths (Smith and Wessel, 1990). Within the 10 km grid, this resulted in one interpolated data point between adjacent radar profiles. However, in the outermost parts of the star-like pattern, adjacent radar profiles were up to 20 km apart. The maximum distance of interpolated points to the nearest profile was therefore on the order of the typical correlation lengths of accumulation rates, which were ~10 km in this area (Rotschky and others, 2004). Careful consideration of these values is therefore required.

The error in accumulation rates depends on the dating of the IRHs, conversion from travel time to depth, and integration of mass. From crossover point analyses within the grid we found a typical uncertainty of 5 ns in travel time, or 0.5 m in depth. This equals a statistical error of ~1.5 kg m^{-2} a^{-1} for accumulation rates close to the radar profiles. Dating uncertainty results in a systematic error in accumulation rates, ~1 kg m^{-2} a^{-1}. For discussion of the present accumulation rate pattern below, we use the accumulation rates derived from the depth of the uppermost continuous horizon, dated to AD 1848. The resulting pattern of accumulation rates (Fig. 2) therefore presents the mean over the period AD 1848–2001.

Surface topography

Surface topography was available from kinematic GPS measurements accompanying each GPR profile. The static GPS base station at Kohnen, tied into the global GPS network, was used as reference for the GPS rover with a time interval of 1 s. The kinematic GPS data result in a relative accuracy of surface elevations of 0.1 m. Unfortunately, only within the 10 km grid surrounding EDML were the GPS data spatially dense enough to interpolate a reasonably accurate surface topography. We therefore used satellite remote-sensing data to construct a digital elevation model (DEM) of the whole region, which provides an accurate datum for each gridpoint.

The topography was derived by European Remote-sensing Satellite (ERS-1 and -2) synthetic aperture radar (SAR) interferometry using two pairs of satellite data acquired in 1996 (Fig. 1). The ice motion and temporal changes in the investigation area were neglected. Precise orbits were refined using the GPS-based topography along our GPR profiles and ICESat's Geoscience Laser Altimetry System (GLAS) data (http://nsidc.org/data/icesat/). A coherence adaptive filter was applied to reduce the noise of the interferogram. Noise in the DEM was further reduced by averaging the original 25 m pixel spacing of the geocoded product with an estimated locational accuracy of 100 m onto the same grid used for gridding of the GPR data with 0.5 × 0.5 km^2 resolution (Fig. 1). The rms difference of the DEM in respect to the reference topographies is 0.9 m.

REGIONAL DISTRIBUTION OF ACCUMULATION RATE

Point sampling of accumulation rates by means of stake measurements, snow pits and ice cores during several field seasons in the 1990s yielded a generally decreasing trend of accumulation rate in DML away from the coast (Isaksson and others, 1996; Oerter and others, 2000). The data synthesis of our ice-core and regional radar measurements confirms this trend, but with a much enhanced spatial resolution (Fig. 2).

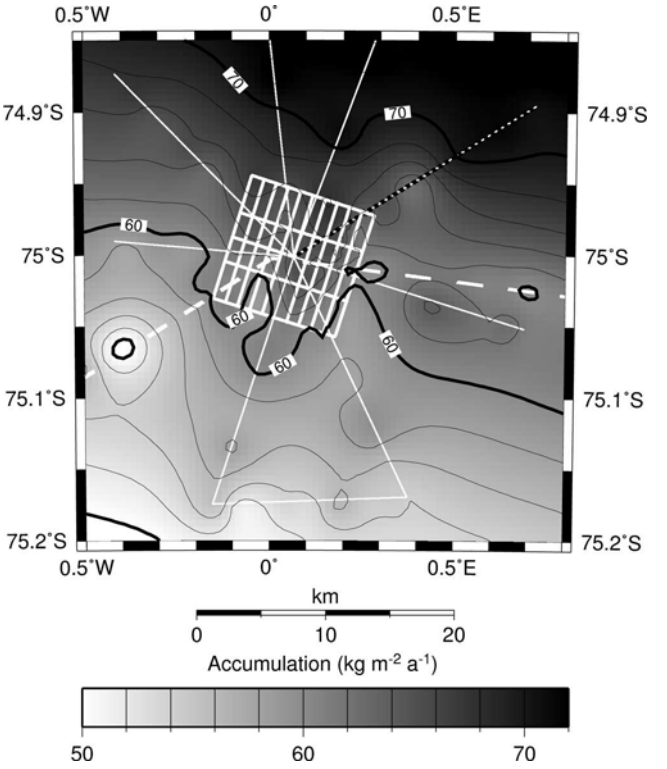

Fig. 2. Regional distribution of accumulation rate (grey values and contours) averaged over the period AD 1848–2001, derived from the uppermost isochronous IRH along the radar profiles. Line types as in Figure 1.

General characteristics

The mean accumulation rate at EDML from AD 1848 to 2001 is ~64 kg m^{-2} a^{-1}. The regional accumulation rate gradient is roughly perpendicular to the ice divide (Fig. 2). Based on the 153 year average, the accumulation rate decreases over a distance of 40 km in the north-northeast–south-southwest direction from ~72 kg m^{-2} a^{-1} to 54 kg m^{-2} a^{-1}, almost 30% of the accumulation rate at EDML. The average decreasing gradient perpendicular to the ice divide is ~0.5 kg m^{-2} a^{-1} km^{-1}, whereas the mean spatial trend in accumulation rate is close to zero parallel to the ice divide.

The general pattern is overlain by small-scale variations in accumulation rate, on the order of 5–15% of the accumulation rate at EDML over a few kilometres, the origin of which is discussed further below. Within the 10 km grid, where values reliably quantify the variations, maximum local accumulation rate gradients are up to 2.5 kg m^{-2} a^{-1} km^{-1}, about five times the regional gradient (Fig. 3). Even higher gradients occur on longer profiles outside the grid. The drill site is located on the eastern side of a southward-stretching tongue of higher accumulation rate, about 4 km wide (Fig. 3). Further upstream towards the east, accumulation rates decrease to <60 kg m^{-2} a^{-1} about 6 km away, before increasing again to 65 kg m^{-2} a^{-1} (Fig. 3).

Relation to surface topography

Snow accumulation rate in this region is mainly determined by precipitation, wind erosion and deposition (Van den

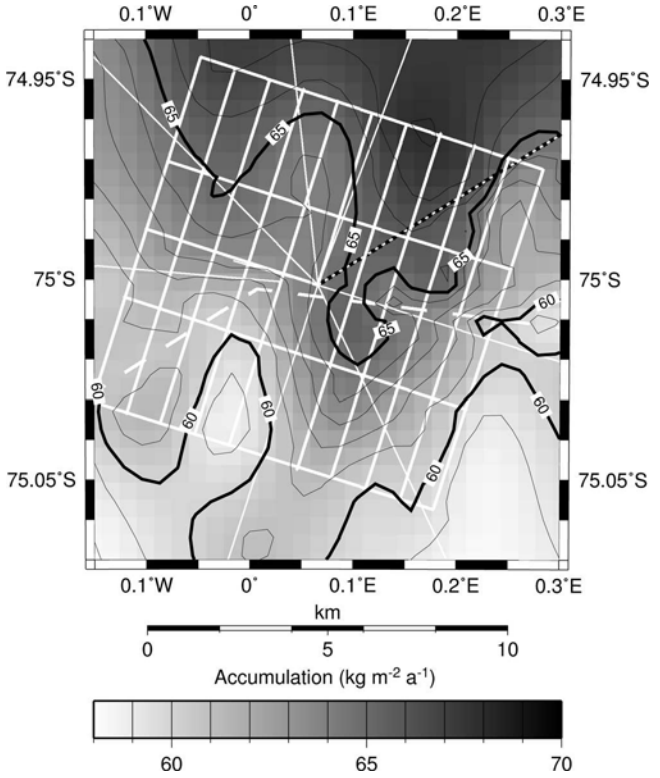

Fig. 3. Close-up of Figure 2, focusing on the 10 km grid, with radar profiles as shown above. Note that the range of grey values has changed.

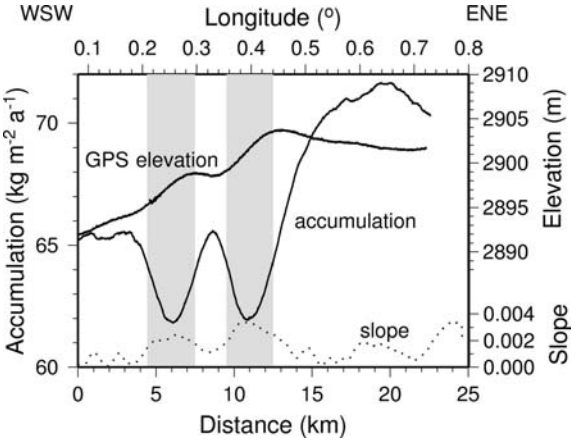

Fig. 4. Accumulation rate for the time interval AD 1848–2001, World Geodetic System 1984 (WGS84) surface elevation, and slope (dotted line) along upwind profile 011203 (Figs 1 and 2). Elevation is from kinematic GPS measurements; the magnitude of slope is derived from the DEM (Fig. 1) over segments of 1 km. Shaded areas mark the region of lower accumulation rates, as discussed in the text. The main wind direction is parallel to the profile from east-northeast to west-southwest (right to left).

Broeke and others, 1999). Varying wind speeds and turbulences in the boundary layer lead to disturbances in the regionally homogeneous precipitation pattern, finally resulting in inhomogeneous spatial accumulation rate (King and others, 2004). To qualitatively identify the relation of surface topography and the observed accumulation rate pattern, we compare both values along profile 011203 (Fig. 4), running in the upwind direction of EDML, which is from ~60° true north (Reijmer, 2001). The elevation along the profile rises gently east-northeastwards by an average of 10 m over a distance of 15 km. The general increase is interrupted by two local elevation maxima at distances of 7.5 and 13.5 km, separated by a local minimum around 8.5 km. The first convex rise is 2 km wide and about 0.5 m above the surrounding surface. The second rise is 4 km wide with a height of 2 m (Fig. 4).

The accumulation rate along this profile shows two pronounced minima along the same line (Fig. 4). For the first 3 km from EDML it is almost steady, then it drops by 3 kg m^{-2} a^{-1} over 2 km and increases again to the same level as at EDML at 8.5 km. The second minimum has slightly different characteristics than the first one. From its lowest value at ~11 km from EDML, the accumulation rate increases strongly over 5 km with a gradient of up to 2.5 kg m^{-2} a^{-1} km^{-1} and starts to level out around 16 km (Fig. 4). A small local maximum occurs about 19 km from EDML.

Comparison of the elevation and accumulation rates along this profile reveals two striking features: first, the local accumulation rate maximum at 8.5 km coincides with the local elevation minimum; second, both accumulation rate minima are on the leeward side of two elevation maxima and occur at locations where the local slope has a maximum. Moreover, the drop in accumulation rate downwind along the profile at 11 km is more than twice as deep (10 kg m^{-2} a^{-1}) as the accumulation rate minimum at 6 km. The larger drop seems to be related to the height of the upwind surface undulation and local slope.

Similar relations between surface undulations and accumulation rate patterns have been observed in other parts of Antarctica (e.g. the East Antarctic megadune fields (Frezzotti and others, 2002) and Lyddan Ice Rise (King and others, 2004)). Our interpretation of the observed features is in line with current understanding of the interaction of surface topography, wind field and accumulation rate. Undulations in the surface topography lead to variations in wind speed and turbulences, in turn resulting in varying depositional and erosional processes, as recently modelled by King and others (2004). Accumulation rate is lowest where wind speeds are likely to be higher than in the surrounding area, i.e. where surface gradients are larger. This leads to the 'in-phase' relation of local slope maxima and minima of accumulation rate (Fig. 4). Concave depressions, on the other hand, are likely places of lower wind speeds or even turbulences, resulting in higher accumulation rate. This is the case at the accumulation rate maximum at 8.5 km. Likewise, the small maximum around 20 km is also located in a small surface depression, which extends to about 23 km from EDML, downwind of a slope with higher gradients.

The observed accumulation rate anomalies, unlike those of East Antarctic megadunes, seem to be stationary (Fig. 5). The internal structure is advected with the mean ice flow of <1 m a^{-1}. It does not provide a consistent picture of surface features moving in the main wind direction, such as the displacement of the apexes of internal layers over time found by Frezzotti and others (2002).

TEMPORAL VARIATIONS

Patterns of accumulation rate derived for other time intervals over the >1000 year period show qualitatively the same distribution as that discussed above for the most recent time interval (Fig. 2). We show an example of this for the upwind

profile in Figure 5. Within each time interval, the position and value of spatial deviations from the mean accumulation rate are fairly constant. This means that the actual values of a distribution vary with the mean accumulation rate of the respective time interval. An exception is the region 19–22 km from EDML, where the four intervals before AD 1400 show lower accumulation.

The mean accumulation rate at EDML throughout the period amounts to 63 kg m^{-2} a^{-1}, as calculated from matching with the age–depth model of ice core B32 described above. To compare the spatial variations derived from the radar data with the temporal variations of the ice core, both records need to be based on comparable timescales. We therefore filtered the ice-core time series of accumulation rate with a 100 year running mean. This equals the order of magnitude of the time difference of adjacent IRHs. The corresponding standard deviation that resulted was 2.1 kg m^{-2} a^{-1}. As seen in Figure 5, the average accumulation rate within each time interval varies from the mean of the whole period by approximately the same amount. In contrast, the spatial standard deviation of accumulation rate for a single time interval along this profile is ~3.5 kg m^{-2} a^{-1}, almost twice as large.

As the EDML ice core is not located at an ice dome, its signal is formed along the upstream particle trajectories. From comparison of the temporal changes in accumulation rate observed in the ice core and the regional variations indirectly derived from radar surveys, it is evident that temporal and spatial changes are of the same order of magnitude. If the accumulation rate pattern varies along these trajectories, the ice-core signal also contains a spatial component stemming from advection. This may be part of the reason for the slightly lower accumulation between 19 and 22 km prior to AD 1400. An accurate interpretation of the ice-core record requires separation of temporal and spatial changes along the particle paths.

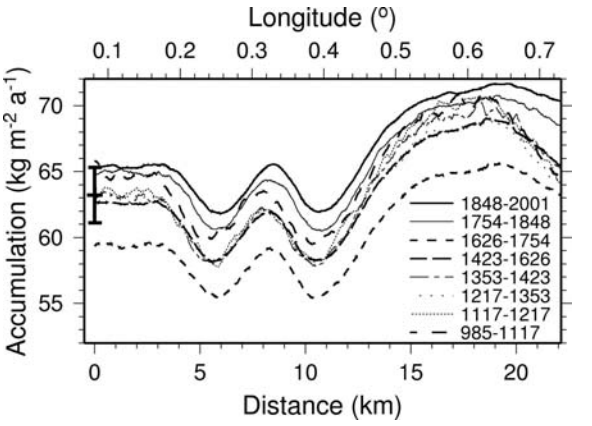

Fig. 5. Accumulation rates along the upwind profile 011203 (Fig. 2) for several time intervals (years AD). Based on the age–depth profile transferred from B32 to EDML and the density measurements at EDML, we calculated a time series of accumulation rate at EDML from AD 985 to 2001 (see text). The mean of accumulation rate over the complete period at EDML and the standard deviation of the 100 year filtered time series are indicated in error-bar type (grey) on the left.

IMPLICATIONS AND CONCLUSIONS

The accumulation rate pattern derived from joint GPR and ice-core data presented in this study reveals local variations in accumulation rate which have not previously been measured in a comparable spatial two-dimensional resolution in the vicinity of the EPICA deep-drilling site. Despite the low gradients in surface topography, tiny undulations alter accumulation rates by >10% over only a few kilometres.

Regarding climatic interpretations of ice-core records in terms of accumulation rates, these small-scale variations could lead to misinterpretations because of advection of the ice-core location through areas of different accumulation rates. Deconvolution of the ice-core record with respect to the spatial accumulation signal is therefore mandatory, and requires detailed knowledge of the upstream accumulation and velocity characteristics. Full understanding of the ice-dynamic mechanisms involved is also important when records from depth ranges subject to strain thinning are interpreted.

State-of-the-art satellite remote-sensing methods, such as passive microwave radiometers (Winebrenner and others, 2001), cannot yet map the accumulation rate to the degree of resolution and accuracy that is possible with ground-based measurements, but progress is expected during the next few years, with more accumulation datasets for ground-truthing becoming available from the satellite-borne active radar sensor (Drinkwater and others, 2001). The data presented here and in comparable studies (e.g. in this volume) will moreover make a valuable contribution to calibrating and validating satellite measurements, on board ICESat and CryoSat, aimed at determining the mass balance of the Antarctic continent. Once highly accurate topographies from those missions are available, their combination with numerical boundary-layer models and meteorological data will provide estimates of accumulation rates even in those areas of Antarctica where direct measurements are unavailable.

ACKNOWLEDGEMENTS

We acknowledge the contribution of the field parties during data acquisition, and especially G. Stoof for maintaining the system. Altimetry data were provided by the US National Snow and Ice Data Center, Boulder, CO (http://nsidc.org/data/icesat/). The ERS data were made available by the European Space Agency through the VECTRA project. Comments from C. Richardson-Näslund, D.G. Vaughan and an anonymous reviewer improved the manuscript. Preparation of this work was supported by the Deutsche Forschungsgemeinschaft grant Ni493/1 and two scholarships of the Studienstiftung des Deutschen Volkes. This work is a contribution to the 'European Project for Ice Coring in Antarctica' (EPICA), a joint European Science Foundation (ESF)/European Commission (EC) scientific programme, funded by the European Commission and by national contributions from Belgium, Denmark, France, Germany, Italy, the Netherlands, Norway, Sweden, Switzerland and the United Kingdom. This is EPICA publication No. 148.

REFERENCES

Drinkwater, M.R., D.G. Long and A.W. Bingham. 2001. Greenland snow accumulation estimates from satellite radar scatterometer data. *J. Geophys. Res.,* **106**(D24), 33,935–33,950.

Eisen, O., U. Nixdorf, F. Wilhelms and H. Miller. 2004. Age estimates of isochronous reflection horizons by combining ice core, survey, and synthetic radar data. *J. Geophys. Res.,* **109**(B4), B04106. (10.1029/2003JB002858.)

Frezzotti, M., S. Gandolfi and S. Urbini. 2002. Snow megadunes in Antarctica: sedimentary structure and genesis. *J. Geophys. Res.,* **107**(D18), 4344. (10.1029/2001JD000673.)

Giovinetto, M.B. and H.J. Zwally. 2000. Spatial distribution of net surface accumulation on the Antarctic ice sheet. *Ann. Glaciol.,* **31**, 171–178.

Gudmandsen, P. 1975. Layer echoes in polar ice sheets. *J. Glaciol.,* **15**(73), 95–101.

Hamilton, G.S. 2004. Topographic control of regional accumulation rate variability at South Pole and implications for ice core interpretation. *Ann. Glaciol.,* **39**, 214–218.

Isaksson, E., W. Karlén, N. Gundestrup, P. Mayewski, S. Whitlow and M. Twickler. 1996. A century of accumulation and temperature changes in Dronning Maud Land, Antarctica. *J. Geophys. Res.,* **101**(D3), 7085–7094.

Jacobel, R.W. and S.M. Hodge. 1995. Radar internal layers from the Greenland summit. *Geophys. Res. Lett.,* **22**(5), 587–590.

Karlöf, L. 2004. Temporal and spatial variability of snow accumulation and redistribution, and its impact on the interpretation of ice cores. (PhD thesis, University of Oslo.)

King, J.C., P.S. Anderson, D.G. Vaughan, G.W. Mann, S.D. Mobbs and S.B. Vosper. 2004. Wind-borne redistribution of snow across an Antarctic ice rise. *J. Geophys. Res.,* **109**(D1), D11104. (10.1029/2003JD004361.)

Nereson, N.A., C.F. Raymond, R.W. Jacobel and E.D. Waddington. 2000. The accumulation pattern across Siple Dome, West Antarctica, inferred from radar-detected internal layers. *J. Glaciol.,* **46**(152), 75–87.

Oerter, H. *and 6 others*. 2000. Accumulation rates in Dronning Maud Land, Antarctica, as revealed by dielectric-profiling measurements of shallow firn cores. *Ann. Glaciol.,* **30**, 27–34.

Pälli, A. *and 6 others*. 2002. Spatial and temporal variability of snow accumulation using ground-penetrating radar and ice cores on a Svalbard glacier. *J. Glaciol.,* **48**(162), 417–424.

Reijmer, C.H. 2001. Antarctic meteorology: a study with automatic weather stations. (PhD thesis, University of Utrecht.)

Richardson-Näslund, C. 2001. Spatial distribution of snow in Antarctica and other glacier studies using ground-penetrating radar. (PhD thesis, Stockholm University.)

Richardson-Näslund, C., E. Aarholt, S.E. Hamran, P. Holmlund and E. Isaksson. 1997. Spatial distribution of snow in western Dronning Maud Land, East Antarctica, mapped by a ground-based snow radar. *J. Geophys. Res.,* **102**(B9), 20,343–20,353.

Rotschky, G., O. Eisen, F. Wilhelms, U. Nixdorf and H. Oerter. 2004. Spatial distribution of surface mass balance on Amundsenisen plateau, Antarctica, derived from ice-penetrating radar studies. *Ann. Glaciol.,* **39**, 265–270.

Smith, W.H.F. and P. Wessel. 1990. Gridding with continuous curvature splines in tension. *Geophysics,* **55**, 293–305.

Spikes, V.B., G.S. Hamilton, S.A. Arcone, S. Kaspari and P. Mayewski. 2004. Variability in accumulation rates from GPR profiling on the West Antarctic plateau. *Ann. Glaciol.,* **39**, 238–244.

Steinhage, D., O. Eisen and B.H. Clausen. In press. Regional and temporal variation of accumulation around NorthGRIP derived from ground-based ice-penetrating radar. *Ann. Glaciol.,* **42**.

Traufetter, F., H. Oerter, H. Fischer, R. Weller and H. Miller. Spatio-temporal variability in volcanic sulphate deposition over the past 2 kyr in snow pits and firn ores from Amundsenisen, Antarctica. *J. Glaciol.,* **50**(168), 137–146.

Van den Broeke, M.R. *and 6 others*. 1999. Climate variables along a traverse line in Dronning Maud Land, East Antarctica. *J. Glaciol.,* **45**(150), 295–302.

Vaughan, D.G., H.F.J. Corr, C.S.M. Doake and E.D. Waddington. 1999. Distortion of isochronous layers in ice revealed by ground-penetrating radar. *Nature,* **398**(6725), 323–326.

Winebrenner, D.P., R.J. Arthern and C.A. Shuman. 2001. Mapping Greenland accumulation rates using observations of thermal emission at 4.5-cm wavelength. *J. Geophys. Res.,* **106**(D24), 33,919–33,934.

Regional and temporal variation of accumulation around NorthGRIP derived from ground-penetrating radar

Daniel STEINHAGE,[1] Olaf EISEN,[1] Henrik Brink CLAUSEN[2]

[1]*Alfred-Wegener-Institut für Polar- und Meeresforschung, Columbusstrasse, D-27568 Bremerhaven, Germany*
[2]*Niels Bohr Institutet for Astronomi, Fysik og Geofysik, Københavns Universitet, Juliane Maries Vej 30, DK-2100 Copenhagen, Denmark*

ABSTRACT. During the summer of 2003, a ground-penetrating radar survey around the North Greenland Icecore Project (NorthGRIP) deep ice-core drilling site (75°06′ N, 42°20′ W; 2957 m a.s.l.) was carried out using a shielded 250 MHz radar system. The drill site is located on an ice divide, roughly 300 km north-northwest of the summit of the Greenland ice sheet. More than 430 km of profiles were measured, covering a 10 km by 10 km area, with a grid centered on the drilling location, and eight profiles extending beyond this grid. Seven internal horizons within the upper 120 m of the ice sheet were continuously tracked, containing the last 400 years of accumulation history. Based on the age–depth and density–depth distribution of the deep core, the internal layers have been dated and the regional and temporal distribution of accumulation rate in the vicinity of NorthGRIP has been derived. The distribution of accumulation shows a relatively smoothly increasing trend from east to west from 145 kg m^{-2} a^{-1} to 200 kg m^{-2} a^{-1} over a distance of 50 km across the ice divide. The general trend is overlain by small-scale variations on the order of 2.5 kg m^{-2} a^{-1} km^{-1}, i.e. around 1.5% of the accumulation mean. The temporal variations of the seven periods defined by the seven tracked isochrones are on the order of ±4% of the mean of the last 400 years, i.e. at NorthGRIP ±7 kg m^{-2} a^{-1}. If the regional accumulation pattern has been stable for the last several thousand years during the Holocene, and ice flow has been comparable to today, advective effects along the particle trajectory upstream of NorthGRIP do not have a significant effect on the interpretation of climatically induced changes in accumulation rates derived from the deep ice core over the last 10 kyr.

INTRODUCTION

The mass balance of an ice sheet is determined by net precipitation and loss of mass by outflow and melting (Paterson, 1994). While ice thickness and surface velocities can be evaluated by means of remote sensing (e.g. ground-based and airborne ice-penetrating radar (GPR) and satellite interferometry) the accumulation rate has to be measured by using samples taken from the ice sheet with snow pits, firn and ice cores. Therefore the accumulation measurements are less frequent than ice-thickness or surface velocity data (Giovinetto and others, 1990). For Greenland, for instance, only approximately 360 estimates of accumulation rate were available by 2001 (Bales and others, 2001). GPR has become a common tool for determining the structure of ice sheets and glaciers (e.g. Nereson and others, 2000; Richardson-Näslund, 2001; Frezzotti and others, 2002; Pälli and others, 2002). While low-frequency GPR is used to determine ice thickness and subglacial bed elevation, high-frequency GPR is used to reveal internal structure and layering of the upper part of ice sheets and glaciers. The velocity of the electromagnetic waves in ice can be determined by so-called common-midpoint measurements or by measuring the dielectrical properties of an ice core. By applying the velocity–depth function on the measured travel times, the depths of detected internal horizons can be tied to firn and ice cores (Hempel and others, 2000). As buried erosional surfaces due to absence of surface melting and wind erosion can be excluded in the investigated area around the North Greenland Icecore Project (NorthGRIP) site, the internal horizons are isochrones (Gudmandsen, 1975; Jacobel and Hodge, 1995; Eisen and others, 2004); this allows determination of the accumulation rates along GPR profiles. Mapping internal horizons allows a vast increase in accumulation rate data and makes it possible to assess the representativeness of the data obtained from snow pits and ice-core drill sites and to reveal regional variations. In order to study the local accumulation pattern around the NorthGRIP deep ice-core drill site in north-central Greenland (Fig. 1), a ground-based GPR survey was carried out in 2003 by the Alfred-Wegener-Institut (AWI). By tracking seven internal reflection horizons (IRHs) along all profiles, the temporal variations for seven periods were mapped over the investigated area.

FIELD MEASUREMENTS

The aim of the survey was to map the internal structure of the upper 100 m of ice sheet within a 10 km by 10 km rectangle around NorthGRIP. The area covered was extended by a set of GPR profiles extending 5 km further along, and 20 km further perpendicular to, the ice divide. The resulting 'butterfly'-shaped survey pattern is shown as white lines in Figure 2. The line spacing of the grid is 1 km, with the 4 km line parallel to the ridge left out on both sides (Fig. 2). The surveyed area has been completed by a profile to NGT45, the end point of the AWI North Greenland traverse (Shuman and others, 2001). All measurements were carried out using a snowmobile equipped with global positioning system (GPS) for navigational purposes and geodetic measurements, towing a sledge with the operator, the GPR equipment and antennae. The total length of all profiles with GPS and GPR measurements is 430 km.

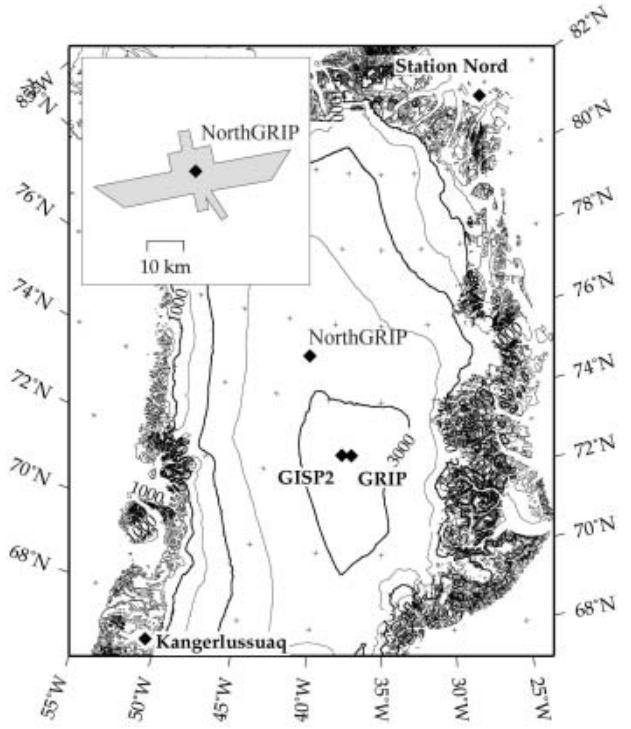

Fig. 1. Location map of NorthGRIP deep ice-core drill site and the survey area around NorthGRIP. The inset shows the investigated area around NorthGRIP.

Kinematic GPS

A Trimble 4000 SSI GPS receiver was operated at a sampling rate of 1 Hz for navigation as well as for determining surface topography along all GPR profiles with the antenna mounted on the towing snowmobile. For differential post-processing of the kinematic GPS data, a GPS reference station was established on the reference GPS point of the NorthGRIP camp site. The calculated surface heights were tied to this reference. The resulting surface topography based on all GPS observations interpolated onto a 1′ by 0.25′ (approximately 460 m by 460 m) grid is shown in Figure 2. Within the 450 km^2 area covered by the investigations, no height variation above 20 m was found. Along the ice divide running north-northwest the surface slope is 0.8‰, and perpendicular to the ridge 0.5‰.

Table 1. TWTs and depths of picked IRHs at NorthGRIP

IRH No.	TWT	Depth	Date	Interval
	ns	m	AD	years
1	155	16.5	1957	46
2	280	29.0	1914	43
3	410	42.0	1865	49
4	545	55.0	1811	44
5	680	66.5	1758	53
6	905	86.5	1662	96
7	1055	99.5	1597	65

Ground-penetrating radar

The GPR survey was performed with a commercial RAMAC radar set (Malå Geoscience, Sweden) with shielded antennae operating at a center frequency of 250 MHz. The traces were recorded in a 1500 ns time window with 1024 samples and eight-fold horizontal stacking at 1 m intervals using an odometer. The recorded two-way travel times (TWTs) have been converted to depths based on the density–depth information obtained from a shallow ice core drilled in the immediate vicinity of the NorthGRIP drill site. First analysis of the internal structure included mapping of seven continuous IRHs, the deepest of which is located at a TWT of 1055 ns near NorthGRIP (Fig. 3). TWTs and depths of all seven picked IRHs at NorthGRIP are summarized in Table 1.

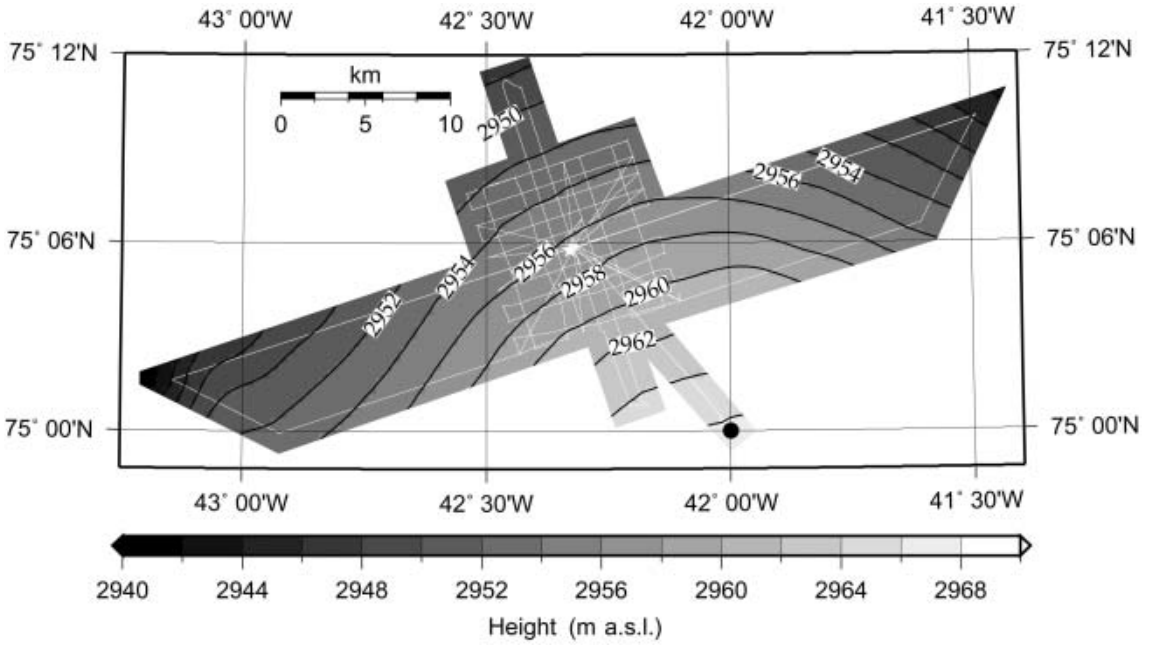

Fig. 2. Survey layout (white lines) and surface topography from kinematic post-differential GPS around NorthGRIP (white star). The black dot marks the drill site NGT 45. The contour line spacing is 2 m.

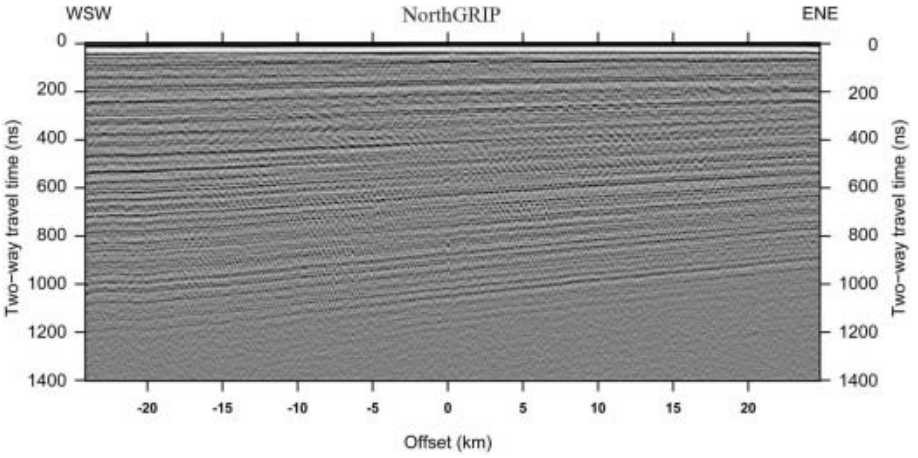

Fig. 3. GPR profile obtained with 250 MHz shielded antennae perpendicular to the ice divide across NorthGRIP. The profile runs from west-southwest to east-northeast over a distance of 50 km. NorthGRIP is located in the center; the offset is calculated relative to the drill site. The grayscale indicates strength of the signal envelope.

Reflector travel times increase steadily from east-northeast to west-southwest, perpendicular to the ice divide, by 40% over a distance of 50 km. Parallel to the ice flow the reflector travel times are nearly constant. The internal structure shows hardly any undulations, not surprisingly as the basal topography is known to be very flat (Göktaş, 1999; Nixdorf and Göktaş, 2001). The observed pattern is therefore most likely caused by a known variation of the accumulation rate across the ice divide, rather than by significant changes of the wave-speed–depth profiles or other dynamical effects. The GPR dataset is therefore used to derive the small-scale spatial variation of accumulation over the past 400 years.

ACCUMULATION RATE

The distribution of accumulation requires the dating of each IRH and calculation of cumulative mass. From dating of volcanic peaks in the electrical conductivity record along the shallow ice core, an age–depth function is available. At the drill site, each reflector is attributed an age from the shallow core. Integration of density yields the cumulative mass. As the horizontal distribution of density with depth is fairly constant across the region of interest, we assume that the cumulative mass–depth distribution is uniform along all GPR profiles, too. The accumulation rate along the profiles for different time intervals is derived from adjacent pairs of IRHs by calculating the ratio of their difference in cumulative mass and difference in age. The resulting time intervals vary between 43 and 96 years. Note that although the resulting accumulation rate is expressed in units of mass per unit area and year, the values represent a low-pass filtered average. The uncertainty of accumulation rate depends on the dating of the IRHs, conversion from travel time to depth, and calculation of cumulative mass. From crossover point analyses within the grid, we found that a typical uncertainty of 5 ns in travel time, corresponding to roughly 0.5 m in depth, results in a relative accumulation rate uncertainty of 6 kg m^{-2} a^{-1} on average. Including dating uncertainty, the estimated total uncertainty in accumulation is around ±8–9 kg m^{-2} a^{-1} for values close to the GPR profiles. This corresponds to some 5% of the mean accumulation rate at NorthGRIP of 171 kg m^{-2} a^{-1} for the complete period under consideration, AD 1597–2003.

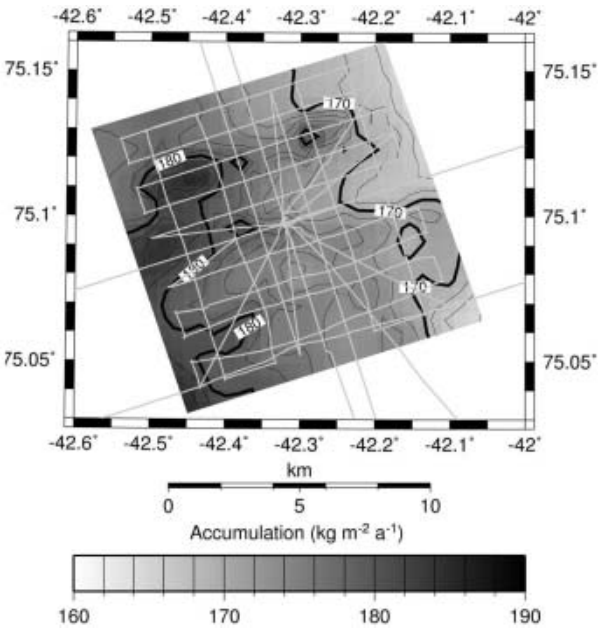

Fig. 4. Regional accumulation pattern around NorthGRIP derived from IRH-1, the shallowest tracked IRH, for the period 1953–2003. Contour line spacing is 2 kg m^{-2} a^{-1}.

Spatial distribution

Gridding of accumulation values along the profiles results in a distribution of accumulation around NorthGRIP. As an example, the areal variation of the accumulation rate for the most recent period, 1957–2003, is shown in Figure 4. Within the grid, accumulation rate decreases perpendicular to the ice divide in the west-southwest to east-northeast direction from 180 kg m^{-2} a^{-1} to 170 kg m^{-2} a^{-1} over 10 km. As would be expected from the distribution of IRH travel times, the accumulation parallel to the topographic divide is almost constant. Small-scale variations in accumulation are in general in the order of 2–3 kg m^{-2} a^{-1} km^{-1}. Larger gradients of up to 8 kg m^{-2} a^{-1} km^{-1} are observed over a distance of 1 km about 4 km directly north and east of the drill site. As these small-scale variations are around 5% of the mean accumulation at NorthGRIP, they are in the same order of

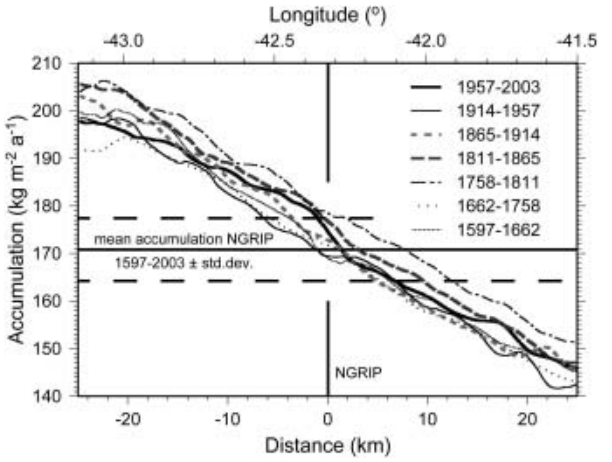

Fig. 5. Accumulation distribution for seven periods (see legend) perpendicular to the ice divide along GPR profile shown in Figure 3. The bar in the center marks the position of NorthGRIP and shows this variation as well as the temporal average.

magnitude as the uncertainty, and have to be considered with care. Accumulation maps for the other time interval show the same characteristics, with slightly different absolute values, but the same gradients, implying that the accumulation pattern has been constant for the last 400 years.

Comparison of temporal and spatial changes

We analyze the variations of accumulation along the 50 km long central profile perpendicular to the ice divide to investigate the temporal character of spatial changes in accumulation. For all seven time intervals, the accumulation decreases at 1.1 kg m^{-2} a^{-1} km^{-1} on average over the whole profile (Fig. 5). However, the mean accumulation at NorthGRIP for each period varies between 168 and 179 kg m^{-2} a^{-1}. The temporal variation of accumulation can be directly calculated from the original ice-core record over the last 400 years. Applying a 25 year running mean filter to reduce noise, the resulting 1σ level of standard deviation is 6.5 kg m^{-2} a^{-1} for the period 1597–2003.

DISCUSSION AND CONCLUSIONS

Based on a GPR survey, the structure of the upper 120 m of the ice sheet in the vicinity of the NorthGRIP deep ice-core drill site has been mapped. Dating of seven continuous IRHs in conjunction with data from a shallow core allowed us to evaluate the small-scale variations of the accumulation rate around the drill site. As the surface velocity at NorthGRIP is low (~1 m a^{-1} in the direction of the ice divide, north-northwest (Hvidberg and others, 2002)) and the strain rates are small ($\varepsilon_1 = -0.4 \times 10^{-5}$ a^{-1}, $\varepsilon_2 = 7.1 \times 10^{-5}$ a^{-1}, and $\varepsilon_z = 7.36 \times 10^{-5}$ a^{-1} (Hvidberg and others, 2002)), advection of ice parcels through stationary small-scale spatial variations in accumulation has a very small effect on values derived from ice cores compared to temporal changes. For instance, whereas the typical temporal changes over 25 years amount to almost 4% of the accumulation mean, transition of a particle trajectory through the largest accumulation anomaly observed in our data (4 km north of NorthGRIP, about 1 km wide) will last around 1000 years and result in an apparent decrease in accumulation of <2‰ over the same period. This is an advantage of the NorthGRIP drill site, in contrast to other drilling locations (e.g. South Pole (Hamilton, 2004) or Dronning Maud Land, Antarctica (Eisen and others, 2005)). The GPR survey also reveals that the accumulation rate of 171 kg m^{-2} a^{-1} for NorthGRIP is a representative value along the ice divide for the mapped area. Together with the clear west-to-east decrease in accumulation, our results are in agreement with the general trend in accumulation distribution as shown in the accumulation map of Bales and others (2001). Furthermore we conclude that the accumulation pattern did not change over the considered time period of 400 years, i.e. the spatial trend has been stable and the mean accumulation merely varied over time. If this has been the case for the last several thousand years during the Holocene and ice flow has been comparable to today, advective effects along the particle trajectory upstream of NorthGRIP do not have a significant effect on the interpretation of climatically induced changes in accumulation rates derived from the deep ice core over the last 10 kyr.

To investigate the influence of local variations in accumulation during the last ice age, accumulation should be analyzed from high-resolution GPR profiles along the upstream particle trajectories.

ACKNOWLEDGEMENTS

We thank the NorthGRIP team for their hospitality and support in the field. Thanks are also due to C. Wesche and S. Schober for data handling.

REFERENCES

Bales, R.C., J.R. McConnell, E. Mosley-Thompson and B. Csatho. 2001. Accumulation over the Greenland ice sheet from historical and recent records. *J. Geophys. Res.*, **106**(D24), 33,813–33,825.

Eisen, O., U. Nixdorf, F. Wilhelms and H. Miller. 2004. Age estimates of isochronous reflection horizons by combining ice core, survey, and synthetic radar data. *J. Geophys. Res.*, **109**(B4), B04106. (10.1029/2003JB002858.)

Eisen, O., W. Rack, U. Nixdorf and F. Wilhelms. 2005. Characteristics of accumulation around the EPICA deep-drilling site in Dronning Maud Land, Antarctica. *Ann. Glaciol.*, **41**, 41–46.

Frezzotti, M., S. Gandolfi, F. La Marca and S. Urbini. 2002. Snow dunes and glazed surfaces in Antarctica: new field and remote-sensing data. *Ann. Glaciol.*, **34**, 81–88.

Giovinetto, M.B., N.M. Waters and C.R. Bentley. 1990. Dependence of Antarctic surface mass balance on temperature, elevation, and distance to open ocean. *J. Geophys. Res.*, **95**(D4), 3517–3531.

Göktaş, F. 1999. Ergebnisse der Untersuchung des grönländischen Inlandeises mit dem elektromagnetischen Reflexionsverfahren in der Umgebung von NGRIP. *Ber. Polarforsch. Rep./Pol. Res.* 336.

Gudmandsen, P. 1975. Layer echoes in polar ice sheets. *J. Glaciol.*, **15**(73), 95–101.

Hamilton, G.S. 2004. Topographic control of regional accumulation rate variability at South Pole and implications for ice-core interpretation. *Ann. Glaciol.*, **39**, 214–218.

Hempel, L., F. Thyssen, N. Gundestrup, H.B. Clausen and H. Miller. 2000. A comparison of radio-echo sounding data and electrical conductivity of the GRIP ice core. *J. Glaciol.*, **46**(154), 369–374.

Hvidberg, C.S., K. Keller and N.S. Gundestrup. 2002. Mass balance and ice flow along the north-northwest ridge of the Greenland ice sheet at NorthGRIP. *Ann. Glaciol.*, **35**, 521–526.

Jacobel, R.W. and S.M. Hodge. 1995. Radar internal layers from the Greenland summit. *Geophys. Res. Lett.*, **22**(5), 587–590.

Nereson, N.A., C.F. Raymond, R.W. Jacobel and E.D. Waddington. 2000. The accumulation pattern across Siple Dome, West

Antarctica, inferred from radar-detected internal layers. *J. Glaciol.,* **46**(152), 75–87.

Nixdorf, U. and F. Göktaş. 2001. Spatial depth distribution of the subglacial bed and internal layers in the ice around NGRIP, Greenland, derived with airborne RES. *J. Appl. Geophys.,* **47**(3–4), 175–182.

Pälli, A. *and 6 others*. 2002. Spatial and temporal variability of snow accumulation using ground-penetrating radar and ice cores on a Svalbard glacier. *J. Glaciol.,* **48**(162), 417–424.

Paterson, W.S.B. 1994. *The physics of glaciers. Third edition.* Oxford, etc., Elsevier.

Richardson-Näslund, C. 2001. Spatial distribution of snow in Antarctica and other glacier studies using ground-penetrating radar. (PhD thesis, Stockholm University.)

Shuman, C.A., D.H. Bromwich, J. Kipfstuhl and M. Schwager. 2001. Multiyear accumulation and temperature history near the North Greenland Ice Core Project site, north central Greenland. *J. Geophys. Res.,* **106**(D24), 33,853–33,866.

Spatial distribution of surface mass balance on Amundsenisen plateau, Antarctica, derived from ice-penetrating radar studies

Gerit ROTSCHKY, Olaf EISEN, Frank WILHELMS, Uwe NIXDORF, Hans OERTER

Alfred-Wegener-Institut für Polar- und Meeresforschung, Postfach 120161, 27515 Bremerhaven, Germany
E-mail: grotschky@awi-bremerhaven.de

ABSTRACT. The distribution of surface mass balance on Amundsenisen, Dronning Maud Land, Antarctica, is investigated along a continous profile line. Ice-penetrating radar is used to map variations in ice-layer thickness within the upper 100 m of the ice sheet. The route passes several firn- and ice-core drilling sites over a distance of 320 km. Dielectric-profiling data of ice cores are used to calculate the depths of selected reflection horizons and the cumulative mass of the ice column. The local surface mass balance is determined as a temporal average, covering a time-span of almost two centuries. The findings indicate a complex accumulation pattern superimposed on a generally low surface mass balance, which is related to small-scale surface undulations. The results of the radar soundings are in general in good agreement with surface mass-balance data derived from firn-core studies. Discrepancies between these two datasets can be explained by spatial mismatch or by minor quality of either ice-core profiles or radar data. For regional comparison of radar-based accumulation data we use an accumulation distribution interpolated from point measurements. The surface mass balance varies up to 50% over short distances, with correlation lengths of <10 km. We conclude that the current utilization schemes of point sampling are only capable of reproducing local values and regional trends but provide no information on the small-scale variability of surface mass balance.

1. INTRODUCTION

The accumulation rate and its spatial pattern across Antarctica are the main influences determining the growth and movement of the ice sheet. The accumulation distribution is needed as a fundamental input factor in glacier mass-balance studies, necessary to, for instance, estimate current sea-level changes. The interpretation of physical and chemical properties measured along ice cores, used for paleoclimatic reconstruction, also relies on an exact knowledge about present and past surface mass-balance distribution across the Antarctic continent.

Surface mass-balance calculations are usually based on stake readings, snow-pit samples and shallow firn cores. These measurements yield parameters to estimate the spatial variability of the Antarctic surface mass balance, as well as its variation over the last few decades. Use of this information has the disadvantage that it is uncertain how these irregularly and sparsely collected datasets are able to represent general climatic trends of precipitation and wind-drift patterns for larger areas.

Over recent years, the traditional methods have been supplemented by methodological ice-penetrating radar (IPR) studies to improve the understanding of spatial accumulation patterns (e.g. Richardson and others, 1997; Nereson and others, 2000; Richardson-Näslund, 2001; Frezzotti and Flora, 2002; Pälli and others, 2002). High-frequency IPR is capable of imaging the physical structure of the upper hundreds of metres of the ice column. On the Antarctic inland plateau, this provides a means to derive information about the local surface mass balance over the last 100–1000 years. It has thus become possible to map accumulation rates and their spatial variations along continuous profiles within the upper parts of the snowpack.

The studies underlying this paper were carried out within the European Project for Ice Coring in Antarctica (EPICA), but are likewise a contribution to the International Trans-Antarctic Scientific Expedition (ITASE) programme. The latter was established in order to improve the collection and understanding of environmental parameters, representing the spatial variability of the Antarctic climate within the last 200 years. IPR data collected on Amundsenisen, Dronning Maud Land (DML), the Atlantic sector of Antarctica, allow us to derive spatial characteristics of the distribution of accumulation. Moreover, we estimate the spatial representativity of accumulation rates derived from point measurements, like firn and ice-core studies located on or near the profile line, by comparison with the IPR-based results. This enables us to judge the suitability of regional surface mass-balance estimation for Amundsenisen.

2. ORIGIN OF DATA

2.1. Deriving accumulation rates from IPR surveys

Coherent internal radar reflection horizons (IRHs) detected with IPR systems on ice sheets are generally considered to be features of equal age, often referred to as isochrones. The processes forming electromagnetic reflectors take place at or near the glacier surface at approximately the same time, with the submergence rate of the isochronic surface being determined by interaction of the flow field and surface accumulation rate (Robin and others, 1969; Gudmandsen, 1975; Millar, 1981). Knowledge of the depth of an IRH in respect to the surface, its age and the density–depth profile of the firn enables us to calculate the mass accumulated after formation of the IRH, and thus the average surface mass balance.

IPR data analyzed here result from common-offset measurements between various borehole locations and

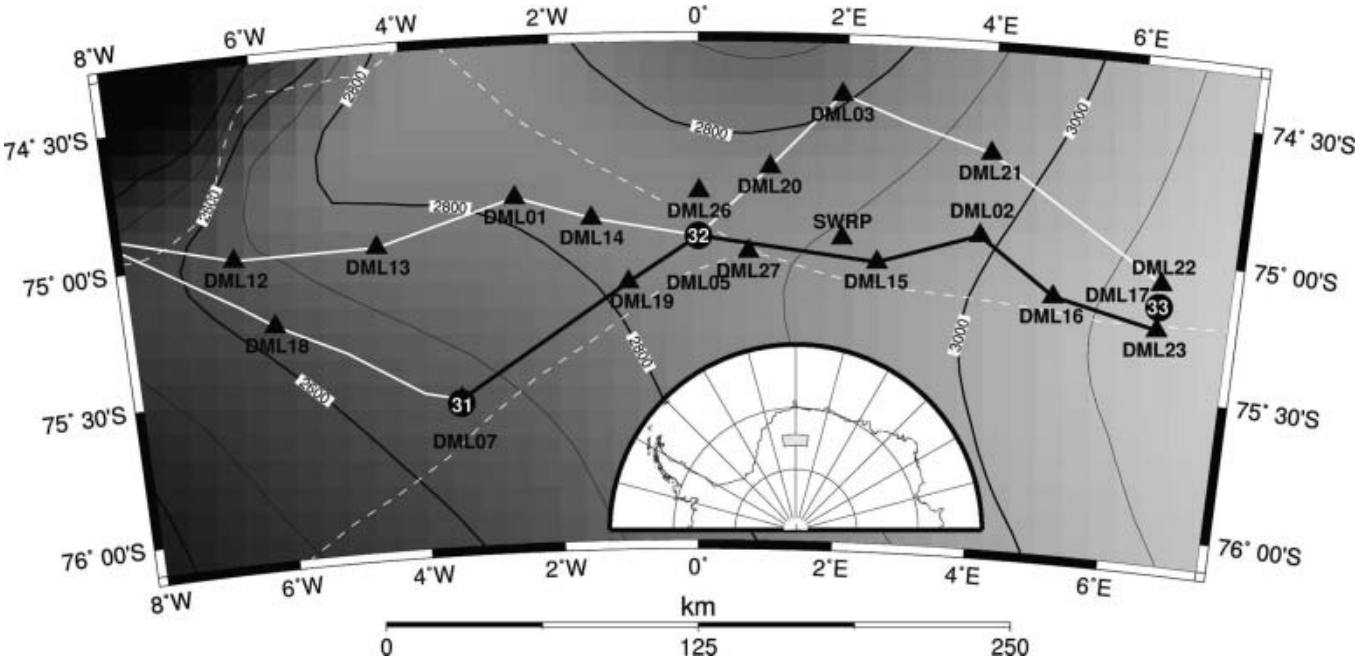

Fig. 1. Radar profiles and surface topography (Liu and others, 2001) in the region of interest on Amundsenisen plateau. Elevation contours (100 m interval and grey code) are given as thin solid black lines; the position of ice divides is indicated by the dashed white lines. The route of the radar survey (1999 and 2001) is shown as solid straight lines. The section of the radar profile analyzed here is shown as thick solid black line, extending from the ice-core drilling sites (circles) DML07 (B31) to DML17 (B33), passing DML05 (B32), near the EPICA deep-drilling camp Kohnen. Other firn-core sites in the vicinity of radar profiles within the study area are shown as triangles including site labels: DML: Alfred-Wegener-Institut pre-site surveys (Oerter and others, 2000); SWRP: Swedish Antarctic Research Programme (Isaksson and others, 1996). The location of the study area on the Antarctic continent is indicated as the shaded region in the inset.

were performed with a commercial RAMAC radar set (Malå Geoscience, Sweden). The monopulse bistatic radar system was operated with antennae at 200 and 250 MHz: unshielded dipoles at a fixed distance of 60 cm in the former, and shielded antennae at a distance of 36 cm in the latter case. Both set-ups are permanently mounted in skid-boxes and connected with the central processing unit via light-conducting cables, thus avoiding noise from ohmic conductors. The processing unit was operated by a Husky FC PX5 personal computer, using the radar system software. The 200 MHz survey was carried out in 1999 between ice cores B32 and B33, using a snow tractor for pulling at an average speed of 8 km h^{-1} (Fig. 1). Traces were recorded every 1.5 m, triggered by a distance wheel, in a 1500 ns time window consisting of 2400 samples. The 250 MHz data were recorded in 2001 between B32 and B31, pulling the device with a snowmachine at 12 km h^{-1} with traces recorded every metre in a 1570 ns time window with 2048 samples. For either measurement set-up, the stored traces consist of eight vertically stacked pulse recordings. Continuous geographical positioning of the GPR profiles was obtained from kinematic global positioning system (GPS) measurements.

Post-recording processing was performed using Paradigm Geophysical FOCUS version 4.2 software and includes five-fold horizontal stacking, bandpass filtering and automatic gain control. IRHs were semi-automatically tracked in the processed data with the Landmark OpenWorks release 2003.0 software, exploiting the coherency of signal features. IRHs were observed at numerous travel times and tracked continuously between the boreholes.

Dielectric profiling of the firn and ice cores at 5 mm intervals provides profiles of the wave speed–depth and the density–depth distribution (Wilhelms, 2000; Eisen and others, 2002). Wave speeds are used to convert radar data from travel time to depth, and integration of density profiles yields the distribution of cumulative mass with depth. The travel-time and cumulative mass profiles of all three ice cores are quasi-identical (Fig. 2) and show differences only on a high-resolution depth scale. It is therefore justified to assume a homogeneous density–depth distribution within the area of interest and thus using the data from B32, located between B31 and B33, for the whole radar profile.

Datings of IRHs are obtained by transferring the ice-core ages to the respective depth of the IRH at each drilling location. The ice cores are dated by annual-layer counting of multi-parameter chemical records combined with identification of volcanic horizons (Sommer and others, 2000). For further analysis in this study, we use the uppermost strong IRH that is continuously trackable along the whole profile. Near B32 it is located at around 25 m depth. Dating estimates of this IRH are AD 1815 at B31, AD 1822 at B32, and AD 1813 at B33, indicating that the IRH is likely related to the Tambora (Indonesia) volcanic eruption in AD 1815. The mean of all three datings, AD 1817, is used as the time of origin of this IRH, with an uncertainty of ± 5 years. This error accounts for uncertainties in the travel-time depth conversion, ice-core dating, and age transfer from ice-core depth to IRH depth (Eisen and others, 2004), as well as the 1–2 year delay of aerosol deposition related to the volcanic eruption (Traufetter and others, 2004). The total error of the IRH age and depth is thus a combination of different uncertainties, resulting from the resolution of the radar system (0.8 m), the error related to tracking of IRH (about 1 m), and dating accuracy, as described above.

Finally, we transfer the cumulative mass corresponding to the depth of the IRH along the profile. The average surface

mass balance then results from dividing the cumulative mass by the respective age of the reflector, i.e. 184 years for section B31–B32 (survey 2001) and 182 years for section B32–B33 (survey 1999).

2.2. Accumulation data based on point sampling

A compilation of accumulation data, consisting of 121 data points, is available for the DML region (Ühlein, 1999) and roughly comprises 10^6 km^2. It is based on snow-pit studies and firn-core data taken from the literature. The distribution of accumulation in the region of interest is presented and discussed by Oerter and others (2000). The averaging period of the different data points varies between 5 years for snow pits and up to 200 years for ice cores.

3. RESULTS

For comparison purposes, we focus on the accumulation measurements adjacent to the IPR route near the ice divide (Fig. 1). Profiles of surface topography, accumulation, internal structure and bedrock topography along the route are shown in Figure 3a–d. Before comparing and discussing the results of the two different methods in respect to accumulation rates, we briefly describe typical characteristics of each dataset separately.

3.1. IPR-based surface mass-balance profiles

In total, five strong IRHs are continuously tracked from B31 to B33. The variation of travel times around the mean increases from ~100 ns for the uppermost reflector to ~500 ns for the deepest (Fig. 3c). This amounts to changes in the horizons' depths between about 10 and 50 m, respectively, over short distances along the surveyed profiles. The annual surface mass-balance rate calculated from the AD 1817 horizon at around 20 m depth is shown in Figure 3b, together with accumulation rate estimates of firn and ice cores along the same profile line. The accumulation derived from the radar data varies between 32.6 and 74.3 kg m^{-2} a^{-1}. The resulting mean accumulation is 53.8 kg m^{-2} a^{-1}, with a standard deviation of 7.7 kg m^{-2} a^{-1} for an average sampling rate of 1.3 m. The autocorrelation function calculated from the IPR-based accumulation rate along the whole profile shows a strong decrease to 0.65 over the first 3 km separation (Fig. 4). The decrease continues less steep to around 10 km, to level out at a value of about 0.4.

The mass-balance information is complemented by surface and bedrock topography given along the IPR route (Fig. 3a and d). Bedrock heights are taken from Steinhage and others (1999), and surface altitude data from RADARSAT Antarctic Mapping Project (RAMP) digital elevation model version 2.0 (Liu and others, 2001). The elevation along our route gently rises from about 2650 to 3150 m a.s.l. over a distance of 320 km from DML07 to DML17. To emphasize small-scale surface variations of just a few metres over 10 km within the smooth surface topography, the difference of local surface elevation from a 50 km running mean is also calculated. They can be linked to undulations in the bedrock relief, a well-known phenomenon (Robinson, 1966; Budd and Carter, 1971; Robin and Millar, 1982), being on the order of hundreds of metres over the same distance. As most sections of our survey profiles are not parallel to the mean flow directions, the bedrock and surface undulations are slightly shifted.

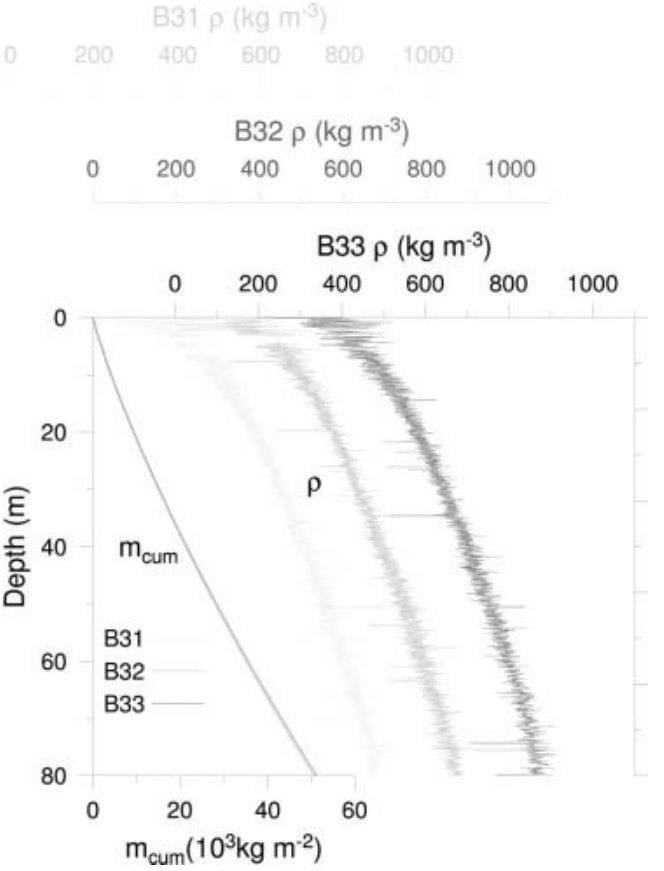

Fig. 2. Depth profiles of density ρ derived from dielectric profiling (x axes at top of graph) of ice cores B31 (light grey), B32 (dark grey) and B33 (black). Note the different x-axis offset for each density profile. The cumulative mass profiles (m_{cum}, bottom axis) result from integration of the density profiles. They are virtually indistiguishable, as small differences in density are smoothed out by integration. As the cumulative mass profiles are plotted without offset, only the black profile on top of the other two is visible.

3.2. Regional distribution of accumulation rates from point sampling

The accumulation distribution for the Amundsenisen plateau as derived from point measurements covers a 150 km wide stripe along both sides of latitude 75° S, between 5° W and 5° E. As described by Oerter and others (2000), the distribution shows a continuing general trend of decreasing accumulation rates from the coastal area towards the interior of the ice sheet. Along the whole profile, the mean surface balance between B31 and B33 is 56 kg m^{-2} a^{-1}, with a standard deviation of 9 kg m^{-2} a^{-1}. In the east as well as in the west of the studied area, spots with accumulation rates of <45 kg m^{-2} a^{-1} are found. In the centre, mainly eastwards of point DML05 along the ice divide, the accumulation rates vary between 45 and 65 kg m^{-2} a^{-1}. Towards the north, the accumulation rates increase to values around 90 kg m^{-2} a^{-1}, as determined at point DML03. The value of 77 kg m^{-2} a^{-1} reported by Isaksson and others (1996) at site SWRP in Figure 1 is exceptional compared to surrounding values of 65 kg m^{-2} a^{-1}.

4. DISCUSSION

The mass balances obtained from IPR data agree well with values gathered from several firn and three shallow ice

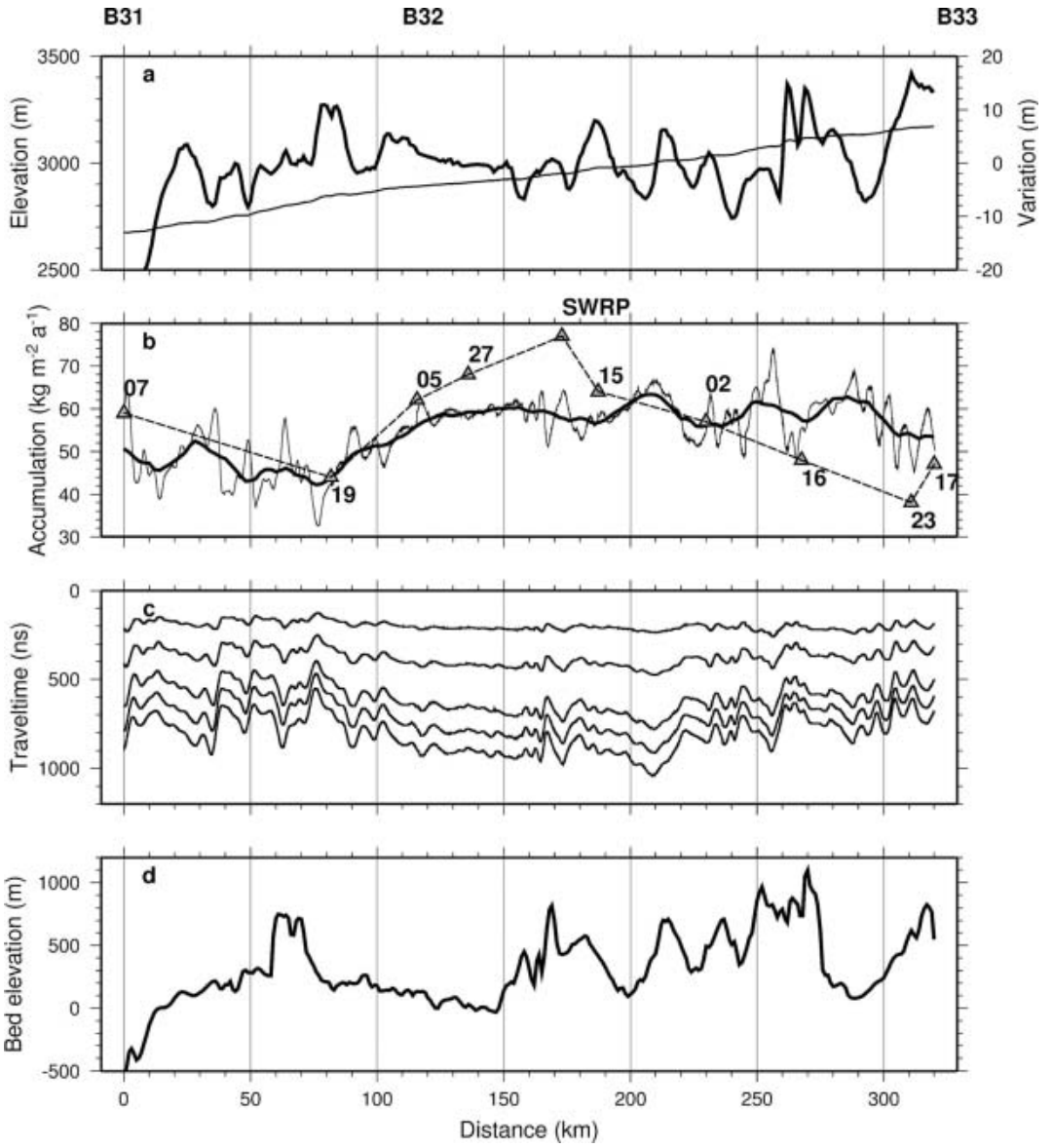

Fig. 3. (a) Surface topography (Liu and others, 2001) given as World Geodetic System 1984 ellipsoid (WGS84) elevation (thin line, left axis), and its variation as difference of local height from the 50 km running mean of the surface elevation (thick line, right axis). (b) Surface mass-balance profiles based on radar (thin line), its 50 km running mean (thick line) and linearly interpolated point samples (dashed line). Location and values of firn and ice cores are shown as triangles, with their site labels next to them (numbers: DML sites; see Fig. 1). (c) Depth distribution of selected internal horizons as a function of two-way travel time. The uppermost horizon, dated to AD 1817, is used to derive the surface mass balance shown in (b). (d) Bedrock topography (Steinhage and others, 1999). The location of the three ice cores B31–33 is shown on top of the graph.

cores which are located along the IPR travel route (Fig. 3). The values are nearly identical to most of the point samples. Exceptions are the locations DML15, DML23, DML27 and SWRP, where larger discrepancies of up to 13 kg m^{-2} a^{-1} are observed. The reasons for this will be discussed later.

Between the single core locations, the IPR results show large variations in layer thickness and thus local surface mass-balance rates, revealing a rather complex accumulation pattern for our study area. The standard deviation of 14% compares well with observations by Richardson-Näslund (2001), who quantified the spatial variability of the net snow accumulation to around 10% for undisturbed plateau areas of DML.

As the observed changes in accumulation are irregular in character beyond a separation of 10 km (Fig. 4), they cannot be systemized in terms of wavelength, unlike other features (e.g. snow megadunes: Frezzotti and others, 2002). Nevertheless, it seems likely that the surface mass-balance variations are related to small-scale undulations of the surface topography. In some parts of the survey profile (e.g. between DML07 and DML19), an increase in mass balance occurs at apparent surface depressions, while a lower accumulation rate can be observed where the elevation is higher then the average. In other parts, accumulation maxima occur rather in phase with surface heights. Care needs to be taken with these observations, however. An accurate relation between surface topography and accumulation rates requires a two-dimensional map of elevations in high resolution, as the topography along track is not necessarily the same in other directions.

Linear interpolation of the point data along the IPR profile line shows an alternating over- and underestimation of accumulation rates compared to the IPR-derived mass-

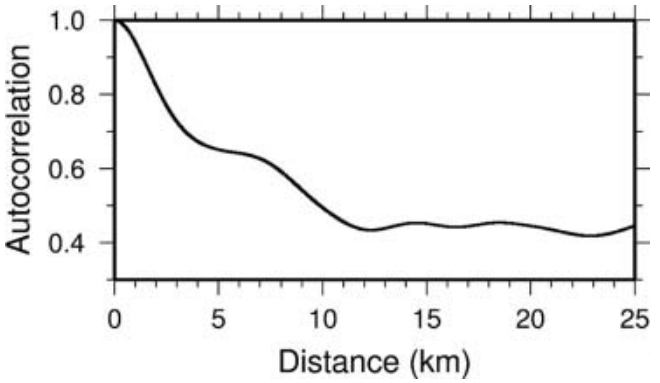

Fig. 4. Autocorrelation function of the unfiltered accumulation rates derived from tracking of the AD 1817 IRH.

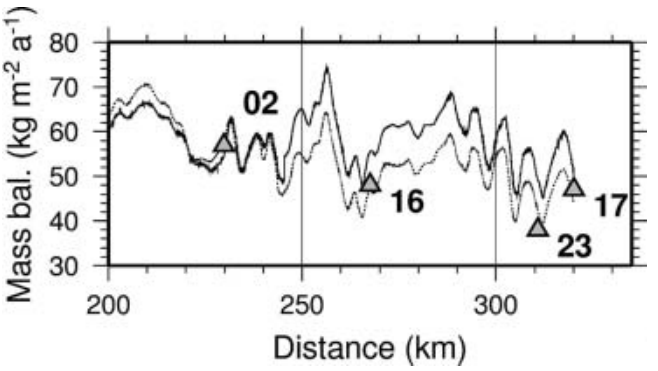

Fig. 5. Surface mass-balance profiles obtained from two IRHs of different age, dated to AD 1817 (upper solid line) and AD 1619 (lower dashed line). The deeper buried reflection horizon (dashed line) better reproduces mass-balance values obtained from core analysis (triangles) at locations DML16, DML23 and DML17 (indicated next to the symbols).

balance data. Applying a 50 km running mean to the IPR surface mass balance results in a distribution that is approximately in phase with the interpolated point samples (Fig. 3b). Starting in the west, a gradual decrease in accumulation is followed after a minimum near km 80 (DML19) by a strong increase up to km 170 in both profiles. However, whereas the smoothed IPR-based accumulation remains level with slight variations, the interpolated point samples continually decrease from km 175 (SWRP) to km 310 (DML23). One reason for the differences in the eastern half of the profiles is the strong influence of individual sample points representing local extremes. For example, the interpolated maximum at km 170 is a consequence of the relatively high accumulation rate of 77 kg m^{-2} a^{-1} mentioned above, and the strong minimum at km 310 results from the low value of 38 kg m^{-2} a^{-1}. Near these sites, the IPR-based accumulation rate shows strong variations, but still very different values than the interpolated ones.

In two cases, the point samples are not directly located on the radar route. DML27 is about 5 km to the south, and on the other side of the ice divide the SWRP site is about 8 km north of the IPR route. Given the strong decorrelation of the surface mass balance over the first 3 km (Fig. 4), the differences to the radar-based mass balance are not surprising.

The disagreement between radar- and core-based mass-balance values at DML15 and DML23 originates from two different kinds of miscalculation. Examination of the firn-core profile retrieved at DML15 reveals that bad core quality lead to gaps within the upper part of the density–depth profile, which were closed by linear interpolation. Thus, the increase of density with depth is too strong, which in turn leads to an overestimation of the cumulative mass.

In contrast, at DML23, increased antenna ringing causes a noisy radargram in the upper 20 m (~200 ns) of the ice column. Hence, our reference IRH has likely been incorrectly tracked, leading to an underestimation of the calculated accumulation rate. Noise caused by antenna ringing decreases with increasing travel time. Repeating the whole calculation process for a deeper reflection horizon, linked to the year AD 1619, produces an accumulation rate that again matches with the core data (Fig. 5), confirming that the AD 1817 IRH includes a larger error between DML16 and DML17.

5. CONCLUSIONS

We successfully used IPR to map the accumulation variation on the Amundsenisen plateau, increasing the spatial resolution of previous accumulation studies. Our results confirm findings of earlier studies that IPR surveys are capable of providing detailed information on surface mass-balance rates along continuous linear profiles, which cannot be provided by point sampling. Calculation of surface mass balance, however, still depends on an exact knowledge of the density–depth distribution along the survey route and dating of observed internal layers, which must be supplied by ice-core data. As radar surveys and point sampling of firn and ice cores along the route complement each other, the two methods should always be combined to ensure cross-check measurements.

Naturally, small-scale variations cannot be resolved by wide-spaced sampling locations. In general, however, point measurements are capable of determining regional trends, associated with meteorological conditions rather than flow features. Interpolations may thus yield an overview of the general distribution of accumulation for wider areas. However, being susceptible to over- and underestimations due to outliers, these have to be taken with care. Future studies should be optimized by a well-balanced aerial sampling scheme, sufficient for applying more sophisticated interpolation algorithms based on geostatistical correlation analyses.

Small surface undulations caused by bedrock topography are likely responsible for variations of the accumulation pattern on the generally smooth high-altitude plateau of DML. Deriving the temporal variation of accumulation rates from either ice-core profiles or IRHs at different depths of the ice column therefore requires a detailed understanding of the interaction between bedrock relief and ice flow, resulting in surface undulations and thus disturbances in a homogeneous precipitation pattern. To overcome two-dimensional limitations of IPR surveys, either an aerial IPR survey set-up or satellite remote sensing should be applied to obtain a three-dimensional picture of the internal structure, and thus accumulation. This will require the interpretation of backscattering signatures of other radar sensors in connection with known accumulation patterns.

ACKNOWLEDGEMENTS

Preparation of the manuscript profited greatly from discussions with W. Rack and D. Steinhage. The important contribution of the field parties during data acquisition is gratefully acknowledged. Preparation of this work was supported by Deutsche Forschungsgemeinschaft grant Ni493/1 and two scholarships of the Studienstiftung des Deutschen Volkes. This work is a contribution to the 'European Project for Ice Coring in Antarctica' (EPICA), a joint European Science Foundation (ESF))/European Commission (EC) scientific programme, funded by the EC and by national contributions from Belgium, Denmark, France, Germany, Italy, the Netherlands, Norway, Sweden, Switzerland and the United Kingdom. This is EPICA publication No. 116.

REFERENCES

Budd, W. F. and D. B. Carter. 1971. An analysis of the relation between the surface and bedrock profiles of ice caps. *J. Glaciol.,* **10**(59), 197–209.

Eisen, O., U. Nixdorf, F. Wilhelms and H. Miller. 2002. Electromagnetic wave speed in polar ice: validation of the common-midpoint technique with high-resolution dielectric-profiling and γ-density measurements. *Ann. Glaciol.,* **34**, 150–156.

Eisen O., U. Nixdorf, F. Wilhelms and H. Miller. 2004. Age estimates of isochronous reflection horizons by combining ice core, survey and synthetic radar data. *J. Geophys. Res.* **109**(B4). (10.1029/2003JB002858.)

Frezzotti, M. and O. Flora. 2002. Ice dynamic features and climatic surface parameters in East Antarctica from Terra Nova Bay to Talos Dome and Dome C: ITASE Italian traverses. *Terra Antartica,* **9**(1), 47–54.

Frezzotti, M., S. Gandolfi and S. Urbini. 2002. Snow megadunes in Antarctica: sedimentary structure and genesis. *J. Geophys. Res.,* **107**(D18). (10.1029/2001JD000673.)

Gudmandsen, P. 1975. Layer echoes in polar ice sheets. *J. Glaciol.,* **15**(73), 95–101.

Isaksson, E., W. Karlén, N. Gundestrup, P. Mayewski, S. Whitlow and M. Twickler. 1996. A century of accumulation and temperature changes in Dronning Maud Land, Antarctica. *J. Geophys. Res.,* **101**(D3), 7085–7094.

Liu, H., K. C. Jezek, B. Li and Z. Zhao. 2001. *RADARSAT Antarctic Mapping Project digital elevation model. Version 2*. Boulder, CO, National Snow and Ice Data Center.

Millar, D. H. M. 1981. Radio-echo layering in polar ice sheets and past volcanic activity. *Nature,* **292**(5822), 441–443.

Nereson, N. A., C. F. Raymond, R. W. Jacobel and E. D. Waddington. 2000. The accumulation pattern across Siple Dome, West Antarctica, inferred from radar-detected internal layers. *J. Glaciol.,* **46**(152), 75–87.

Oerter, H. *and 6 others*. 2000. Accumulation rates in Dronning Maud Land, Antarctica, as revealed by dielectric-profiling measurements of shallow firn cores. *Ann. Glaciol.,* **30**, 27–34.

Pälli, A. *and 6 others*. 2002. Spatial and temporal variability of snow accumulation using ground-penetrating radar and ice cores on a Svalbard glacier. *J. Glaciol.,* **48**(162), 417–424.

Richardson, C. 2001. Spatial distribution of snow in Antarctica and other glacier studies using ground-penetrating radar. (PhD thesis, Stockholm University.)

Richardson-Näslund, C., E. Aarholt, S.-E. Hamran, P. Holmlund and E. Isaksson. 1997. Spatial distribution of snow in western Dronning Maud Land, East Antarctica, mapped by a ground-based snow radar. *J. Geophys. Res.,* **102**(B9), 20,343–20,353.

Robin, G. de Q. and D. H. M. Millar. 1982. Flow of ice sheets in the vicinity of subglacial peaks. *Ann. Glaciol.,* **3**, 290–294.

Robin, G. de Q., S. Evans and J. T. Bailey. 1969. Interpretation of radio echo sounding in polar ice sheets. *Philos. Trans. R. Soc. London, Ser. A,* **265**(1166), 437–505.

Robinson, E. S. 1966. On the relationship of ice-surface topography to bed topography on the South Polar plateau. *J. Glaciol.,* **6**(43), 43–54.

Sommer, S. *and 9 others*. 2000. Glacio-chemical study spanning the past 2 kyr on three ice cores from Dronning Maud Land, Antarctica. 1. Annually resolved accumulation rates. *J. Geophys. Res.,* **105**(D24), 29,411–29,421.

Steinhage, D., U. Nixdorf, U. Meyer and H. Miller. 1999. New maps of the ice thickness and subglacial topography in Dronning Maud Land, Antarctica, determined by means of airborne radio-echo sounding. *Ann. Glaciol.,* **29**, 267–272.

Traufetter, F., H. Oerter, H. Fischer, R. Weller and H. Miller. 2004. Spatio-temporal variability in volcanic sulphate deposition over the past 2 kyr in snow pits and firn cores from Amundsenisen, Antarctica. *J. Glaciol.*, **50**(168), 137–146.

Ühlein, S. 1999. Anwendung verschiedener Interpolationsverfahren im Geografischen Informationssystem (GIS) auf Akkumulationsdaten in Dronning Maud Land (Antarktis). (Diploma thesis, Bayerische Julius-Maximilians-Universität, Würzburg.)

Wilhelms, F. 2000. Messung dielektrischer Eigenschaften polarer Eiskerne *Ber. Polarforsch./Rep. Pol. Res.* 367, 1–171.

Die "Berichte zur Polar- und Meeresforschung" (ISSN 1866-3192) werden beginnend mit dem Heft Nr. 569 (2008) ausschließlich elektronisch als Open-Access-Publikation herausgegeben. Ein Verzeichnis aller Hefte einschließlich der Druckausgaben (Heft 377-568) sowie der früheren **"Berichte zur Polarforschung** (Heft 1-376, von 1982 bis 2000) befindet sich im Internet in der Ablage des electronic Information Center des AWI (**ePIC**) unter der URL http://epic.awi.de. Durch Auswahl "Reports on Polar- and Marine Research" auf der rechten Seite des Fensters wird eine Liste der Publikationen in alphabetischer Reihenfolge (nach Autoren) innerhalb der absteigenden chronologischen Reihenfolge der Jahrgänge erzeugt.

To generate a list of all Reports past issues, use the following URL: http://epic.awi.de and select the right frame to browse "Reports on Polar and Marine Research". A chronological list in declining order, author names alphabetical, will be produced, and pdf-icons shown for open access download.

Verzeichnis der zuletzt erschienenen Hefte:

Heft-Nr. 614/2010 — "The Expedition of the Research Vessel 'Polarstern' to the Antarctic in 2009 (ANT-XXVI/1)", edited by Saad el Naggar and Andreas Macke

Heft-Nr. 615/2010 — "The Expedition of the Research Vessel 'Polarstern' to the Arctic in 2009 (ARK-XXIV/3)", edited by Wilfried Jokat

Heft-Nr. 616/2010 — "The Expedition of the Research Vessel 'Polarstern' to the Antarctic in 2009 (ANT-XXV/4)", edited by Christine Provost

Heft-Nr. 617/2010 — "The Expedition of the Research Vessel 'Polarstern' to the Amundsen Sea, Antarctica, in 2010 (ANT-XXVI/3)", edited by Karsten Gohl

Heft-Nr. 618/2010 — "Sozialhistorische Studie zur Polarforschung anhand von deutschen und österreich-ungarischen Polarexpeditionen zwischen 1868-1939", by Ursula Rack

Heft-Nr. 619/2010 — "Acoustic ecology of marine mammals in polar oceans", by Ilse Van Opzeeland

Heft-Nr. 620/2010 — "Cool Libraries in a Melting World - Proceedings of the 23rd Polar Libraries Colloquy 2010, June 13-18, 2010, Bremerhaven, Germany", edited by Marcel Brannemann and Daria O. Carle

Heft-Nr. 621/2010 — "The Expedition of the Research Vessel 'Polarstern' to the Arctic in 2010 (ARK-XXV/3)", edited by Volkmar Damm

Heft-Nr. 622/2010 — "Environmentally induced responses of *Donax obesulus* and *Mesodesma donacium* (Bivalvia) inhabiting the Humboldt Current System", by Daniel Carstensen

Heft-Nr. 623/2010 — "Research in the Laptev Sea region - Proceedings of the joint Russian-German workshop, November 8-11, 2010, St. Petersburg, Russia", edited by Sebastian Wetterich, Paul Pier Overduin and Irina Fedorova

Heft-Nr. 624/2010 — "The Expedition of the Research Vessel 'Polarstern' to the Arctic in 2010 (ARK-XXV/2)", edited by Thomas Soltwedel

Heft-Nr. 625/2011 — "The Expedition of the Research Vessel 'Polarstern' to the Arctic in 2010 (ARK-XXV/1)", edited by Gereon Budéus

Heft-Nr. 626/2011 — "Towards data assimilation in ice-dynamic models: the (geo)physical basis", by Olaf Eisen